



Research Article

ISSN : 0975-7384
CODEN(USA) : JCPRC5

Sequence analysis, Homology Modeling, Docking and Pharmacophore Studies of Phosphocholine Cytidylyltransferase in *Plasmodium Falciparum*

Pavanchand Akkiraju¹, V. Vijaya Lakshmi², P. Praveen Reddy³, Shailima R. D. Vardhini⁴, Syed Mohamed Abubacker⁵ and Sreenivas Enaganti^{4*}

¹Head & Assistant Professor, Department of Biotechnology, PVP College of Arts, Science & Commerce, Pravaranagar, Maharashtra, India

²Associate Professor, Department of Chemistry, Government Degree College for Women, Begumpet, Hyderabad, India

³Research Scholar, Department of Microbiology, Acharya Nagarjuna University, Guntur, India

⁵Dept.of Chemistry, Sadakathullah Appa College, Rahmath Nagar, Tirunelveli, India

⁴Averin Biotech Pvt.Ltd, 208, 2ndfloor, Windsor Plaza, Nallakunta, Hyderabad, India

ABSTRACT

By virtue of the most fatal pandemic disease, Malaria, about a million individuals reach lethality globally every year and with ever consummating drug-resistant malarial parasite species, there occurred a coercive demand for the identification of incipient drug targets. Here we have evaluated a new drug target in phospholipid metabolic pathway such as Phosphocholine cytidylyltransferase (PfCCT) which is involved in the synthesis of Phosphatidylcholine, a class of phospholipids that significantly sways the developmental aspects of malarial parasite along with its replication and longevity within human red blood cells. The Objective of Present study is to identify potential lead molecule against PfCCT through docking with homology model of our target protein and common pharmacophore approach of our target inhibitor molecules. In this study, we computationally modeled the structure of PfCCT using Molsoft and validated by PROCHECK, ProSA and RMSD. With the finally refined target structure we performed docking using GOLD 3.1 and pharmacophore studies using Discovery Studio with 12 natural compounds. The predicted homology model of PfCCT is reliable. On the basis of the docking scores and pharmacophoric features, we have identified the compounds Amodiaquine and Quinidine showing better binding affinity towards PfCCT respectively with good fit values. In conclusion, the two compounds Amodiaquine and Quinidine shows potential inhibition against PfCCT respectively as targeted for malaria and also having better pharmacophoric features that could aid in the design of new lead molecules.

Keywords: Docking, Malaria, pharmacophore, Phosphatidylcholine, Phosphocholine cytidylyltransferase, Phospholipids.

INTRODUCTION

An inductive agent of the world's uttermost significant parasitic malady, Malaria, is an intraerythrocytic protozoan parasite belonging to the genus *Plasmodium* among which *Plasmodium falciparum* is found felonious for severe human malarial cases with death rates beyond 1 million every year [1,2]. Advancements in strategies to encounter this disease has been made obligatory, in view of predicaments in the treatment and prophylaxis of malaria with an ever emerging drug resistant strains of *P. falciparum*, which paved the path for an incipient approach that suggests to target critical metabolic pathways known to be regulated parasite infection and transmission. Excellent targets have been provided by the recent studies on *P. falciparum* for lipid-based antimalarial therapy development involving the metabolic pathways which lead to the major *P. falciparum* phospholipids synthesis that requires enzymes, which are afflictive for a Brisky parasitic multiplication within human erythrocytes [3,4,5]. During the

course of intraerythrocytic longevity of the parasite, the *P. falciparum* takes up either of the two pathways for the production of phosphatidylcholine viz., The serine-decarboxylase phosphoethanolamine methyltransferase (SDPM) pathway and the CDP-choline pathway [4]. The SDPM pathway avails serine as a starting precursor either from human serum or from host hemoglobin degradation wherein, by the action of the parasite this serine gets decarboxylated with the aid of serine decarboxylase to form ethanolamine which is later phosphorylated by an ethanolamine kinase to form phosphoethanolamine (P-EA). This P-EA undergoes a three-step methylation to form phosphocholine [5,6,7] catalyzed by a parasite Sadenosylmethionine (SAM) -dependent methyltransferase, PfPMT, followed by its conversion into phosphatidylcholine (PtdCho) by the action of two parasite enzymes PfCCT and PfCEPT. As an alternative approach, CDP choline pathway might be employed for Phosphatidyl choline synthesis, which involves phosphorylation of choline to phosphocholine by a parasite-specific choline kinase (PfCK), that consequentially gets coupled to CTP to generate CDP-Cho by a CDP-choline cytidylyltransferase (PfCCT).

On the general grounds that the three-dimensional (3D) structure of proteins determines its function, a manoeuvre has been attempted in the present study to generate three-dimensional (3D) structure of PfCCT from *Plasmodium falciparum* based on the available template (3HL4) structural homologue from Protein Data Bank with the aid of homology modelling, a predominantly esteemed technique which work towards foreboding the 3D structure of bio molecules, as the three-dimensional structures of PfCCT (Q9BMP5) from *Plasmodium falciparum* still remain uncharted and the model has been validated by PROCHECK & ProSA. In Further studies. The developed structures were subjected to docking studies with selected ligands to validate the efficiency against PfCCT.

EXPERIMENTAL SECTION

Primary and secondary structure analysis of PfCCT

Physicochemical characterization, theoretical isoelectric point (pi), the total number of positive and negative residues, extinction coefficient [8], instability index [9], half life time, aliphatic index [10] and grand average hydropathy (GRAVY) [11] were computed using Expasy's Prot-Param server [12]. Secondary structure analysis was performed with the aid of PSI-PRED server.

Sequence Alignment of PfCCT

The FASTA sequence of PfCCT from *Plasmodium falciparum* was fetched from the Swiss-prot database which has a length of 370 amino acids (Accession No: Q9BMP5 Protein name: Phosphocholine cytidylyltransferase (PfCCT)). Customarily, Comparative modelling starts with the search for known protein structures in the PDB taking the target sequence for query [13] which is attained by comparing the target sequence with the sequences of the structures already present in the database using the Basic Local Alignment Search Tool (BLAST) [14] against PDB. The BLAST results thus obtained yielded X-ray structure of 3HL 4 of *Mammalian* ctp: Phosphocholine cytidylyltransferase that showed 47% identity to PfCCT from *Plasmodium falciparum*.

Homology Modelling of PfCCT

The theoretical structure of PfCCT from *Plasmodium falciparum* is generated using Molsoft ICM v3. 5 software by comparative modeling of protein structure prediction. In ICM-Homology modeling algorithm after the initial placement of the aligned polypeptide chain onto the template structure, the side-chain torsion angles are predicted by simultaneous global optimization of the energy for all non-identical residues.

Methodology for conformational modeling of protein side chains and loops, implemented in ICM, relies on the internal coordinate definition of the molecular object combined with computationally efficient ICM Biased Probability Monte Carlo (BPMC) optimization [15] An extended force field includes surface terms, electrostatics with the boundary element solution of the Poisson equation [16], side chain entropy terms, and a fast algorithm for calculating molecular surfaces.

Validation of of PfCCT Model

The developed model is further evaluated by Procheck, ProSA and RMSD. The validation of protein structure model is carried out by means of the Procheck [17] which was employed in verifying the Ramachandran plot quality and the Protein Structure Analysis program (ProSA) which was used for comparing the Z-scores of the target and the template structures wherein the Z-scores of a model is the measure of compatibility between its sequence and structure [18]. Root Mean Squared Deviation (RMSD) which was calculated by SPDBV is customarily exercised to ascertain the distance between two objects.

Active site Identification

As the final model is obtained, the probable binding sites of PfCCT is positioned pertaining to the structural comparison of the template and the model built with the aid of CASTP server [19].

Ligand preparation and Optimization

By the agency of ACD/ ChemSketch (12.0), 12 natural compounds were drawn and saved [20,21] which later were imported into the Argus Lab and were minimized after adding hydrogen bonds. The 3D structures of the compounds are shown in Figure 1.

Docking studies

All the possible conformations of the drug binding to the protein were generated by means of the Genetic algorithm GOLD v 3.0.1 [22] wherein the population size-100, the number of islands-5, the niche size-2, the selection pressure-1.1, the migrate-2, the number of operators-100,000, the mutate-95, and the cross over-95 were employed as the working parameters for the docking process [23], considering a maximum of 10 different conformations for the drug. The conformer that yielded the highest binding score was used for further analysis [24]. The possible active site co-ordinates for PfcCT is identified using Discovery Studio [25]. It is found that the active site pocket one has X= -7.707200, Y=44.167400, Z=3.714400 coordinate values for PfcCT.

Generation of pharmacophore models: common feature based approach

Common feature based pharmacophore modeling is performed with a set of highly active inhibitors of our target protein PfcCT which utilizes the common chemical features present in the most active compounds for the generation of pharmacophore. Common feature hypotheses are generated by the HipHop algorithm of catalyst program in Accelrys Discovery Studio. To derive the best featured model, conformers for each compound are generated within DS Diverse Conformation Generation protocol using the Best Conformation Method with a value of 255 as the maximum number of conformers for each compound and an energy threshold of 20 kcal/mol. All the possible pharmacophore feature mappings with desired chemical groups were identified for the generated conformers of all the compounds with Feature Mapping module. Based on the feature mapping results, using the "common feature pharmacophore generation" protocol, a pharmacophore query is created with chemical features like hydrogen bond donor (HBD), hydrogen bond acceptor (HBA), hydrophobic (HY), ring aromatic (RA) and positive ionizable with a minimum of 0 to a maximum of 5 features to include in the generated pharmacophore. Multiple common-feature pharmacophore generation runs were carried out with a principal value of '2', maximum omit the feature value of '0' and minimum inter feature distances of '2.97 Å' that ensures that all the chemical features in the molecules were considered to build the pharmacophore space and must map to the compounds. Also the parameters such as maximum pharmacophores as 10, Number of Leads That May Miss and Feature Misses, were used as a value of '1' to allow that one of the compounds may not contain all the features when building hypothesis space. The Complete Misses option is set to '0', which is used for specifying the number of compounds that do not have to map to any features in the hypothesis. With the result of common feature pharmacophore model generation, 10 possible pharmacophore hypotheses having a different arrangement of constituent features are generated and the best one is selected based on the ranking score of the hypothesis. To the best featured hypothesis, compounds were screened for mapping on to the pharmacophore model and analysed the best mapped compound is selected based on the fitvalues and aligned pharmacophoric features.

RESULTS AND DISCUSSION

Primary and secondary structure analysis

The predicted physicochemical characteristics showed that the molecular formula of PfcCT is C1866H2926N506O622S8. The amino acid composition of PfcCT has 71 (Asp+Glu) and 53(Arg+Lys). The computed pI values of Modeled PfcCT is less than 7 (pI<7) indicating that target protein is considered as acidic. The computed GRAVY of PfcCT is -0.990, which implied that the solubility of protein is supported by their hydrophilic nature. This has the potentiality to solve the major issue with the isolation of soluble protein by acquiring high-concentrations of soluble proteins which still remains an intensive experimental challenge [26].

Homology modelling of pfcct

Homology modelling used to predict the 3D structure of PfcCT, (target) based on its alignment with the identified templates. The PfcCT sequence is having 47% amino acid sequence identity with the crystal structure of 3HL4 (Mammalian ctp: phosphocholine cytidyltransferase). Based on the crystal structures of the template, the 3D structures of PfcCT is modelled using Molsoft ICM and visualized in Rasmol as shown in Figure 2.

Validation of modeled protein structures

The Ramachandran plot analysis was carried out for evaluating the stereo chemical quality and accuracy of the predicted model of PfcCT after the refinement process by means of the PROCHECK program which revealed the contribution of the phi and psi angles in conformation of amino acids excluding glycine and proline with the results displaying 94.5% residues in the core region, 4.0% in the allowed region, 1.5% in the generous region. The Ramachandran's map for PfcCT model and statistics is represented in Figure 3 and Table 1.

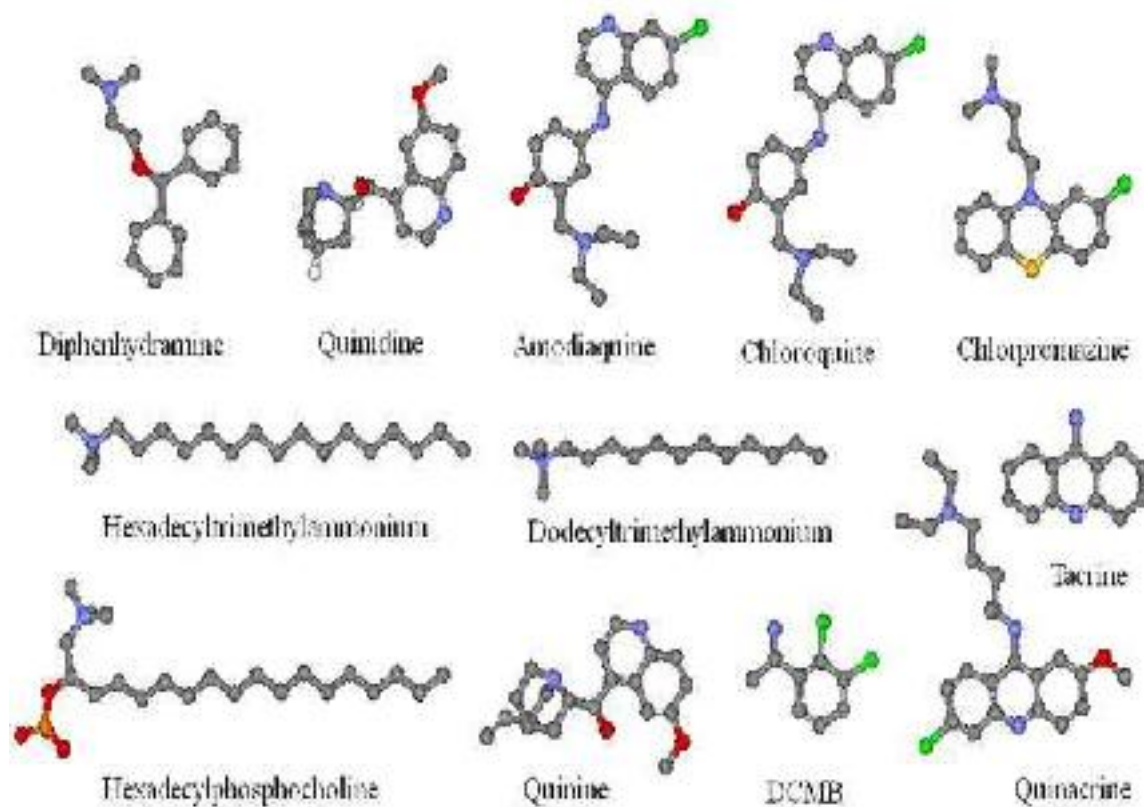


Figure 1: The three dimensional structures of selected ligand molecules represented in ball-stick

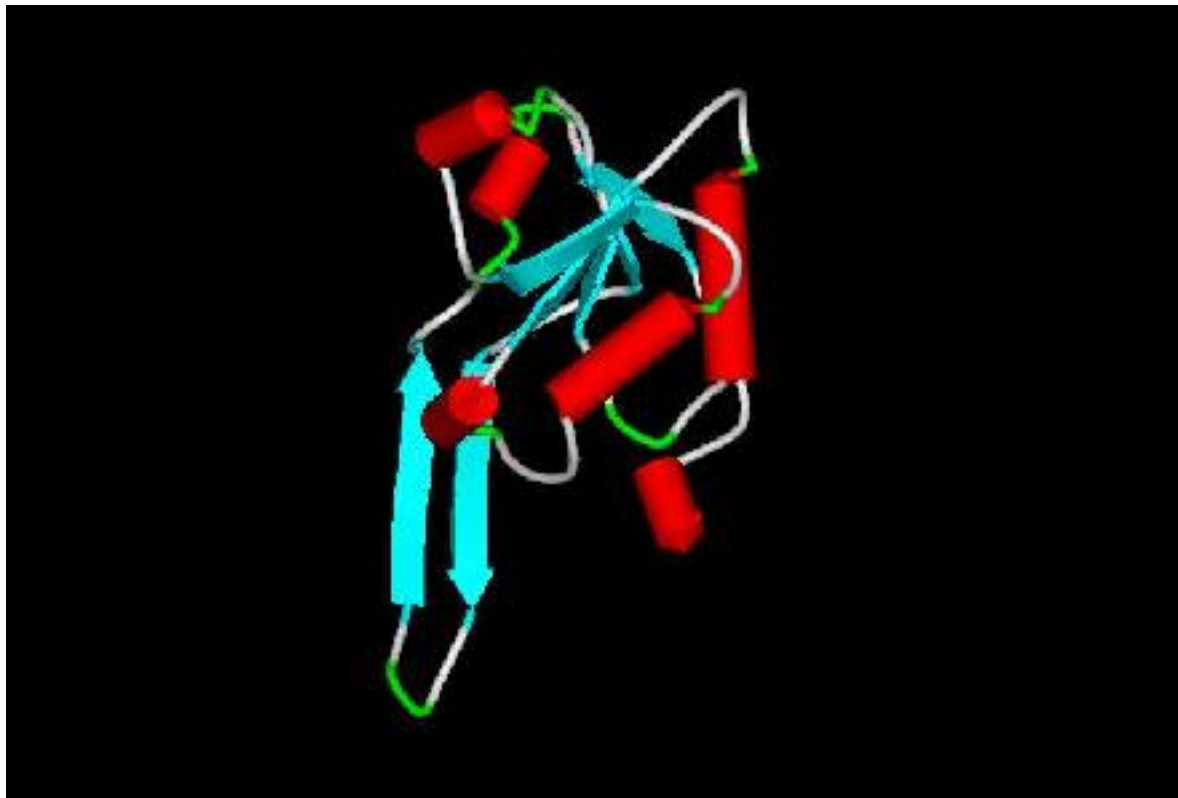


Figure 2. Modeled structure of PfCCT from *Plasmodium falciparum* as visualized in Rasmol

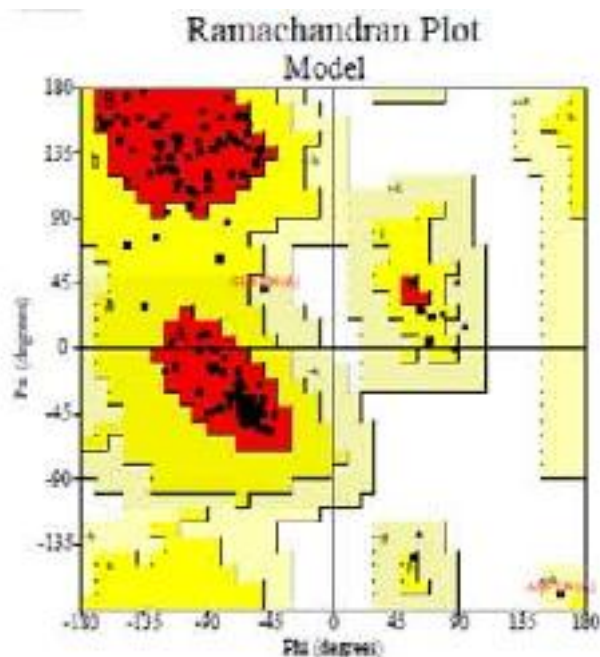


Figure 3: Ramachandran's Plot of PfcCT Model

Z-Score: -5.21

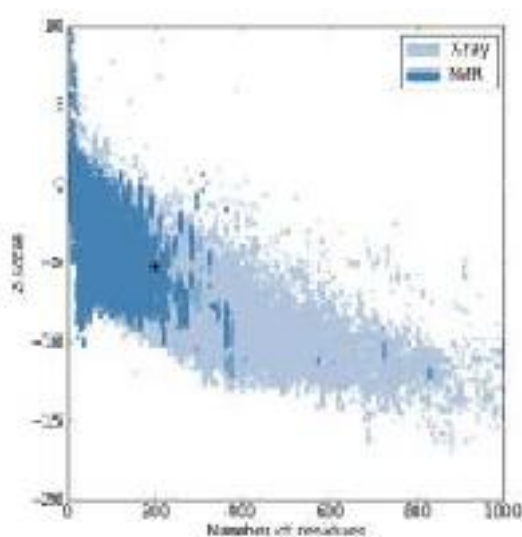


Figure 4: The plot of the Z-Score shows spot for Z score value of protein that is determined by NMR (represented in dark blue colour) and x ray (represented in light blue colour) with the aid of ProSA program. The black dot encircled by orange circles represent Z-Scores of our model PfcCT (-5.21) which indicates the overall quality of the modeled 3D structures of PfcCT

ProSA was employed to analyse energy criteria comparing with Z scores between the modeled protein and 3D template structure. The Z-scores of the obtained modeled Structure of PfcCT is -5.21 (shown in Figure 4) located within the space of proteins determined by X ray crystallography derived structures. The RMSD value calculated based on Alpha carbon atoms by superimposing template and modeled structure is calculated to be 1.12 Å for PfcCT using SPDBV.

Docking Studies

Docking of 12 drawn ligands is studied against Modeled PfcCT using GOLD. The best docking solutions were analysed with the assistance of GOLD scores generated for all the 12 compounds. Comparison of Gold scores of 12 compounds with PfcCT is shown in Figure 5. Among all the docked complexes of PfcCT with the 12 ligands, Quinidine shows highest binding affinity towards PfcCT with a Gold score of 36.61 forming interactions with the amino acids Asp 41, Lys137, Val 45, and Val42 respectively. Diphenhydramine is shown the next highest docking score with PfcCT having a fitness score of 36.38 respectively. The interaction patterns of Quinidine and

Diphenhydramine with PfCCT is shown in (Figure 5). The docking results of all the 12 compounds with PfCCT along with their Fitness scores are shown in Table 2.

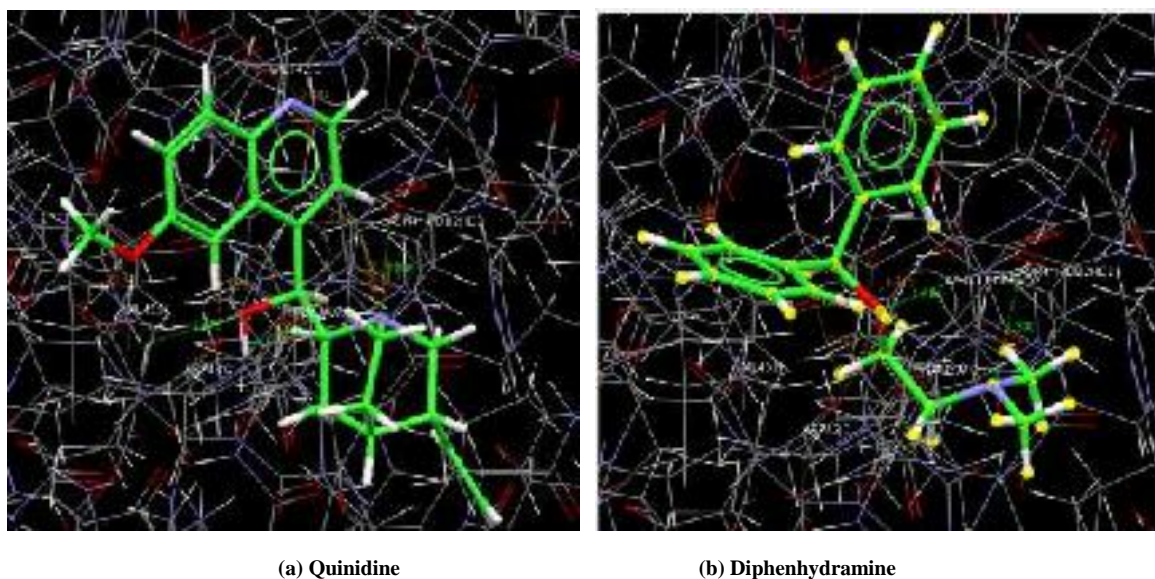


Figure 5: Shows H-Bond interactions of (a) Quinidine and (b) Diphenhydramine with PfCCT

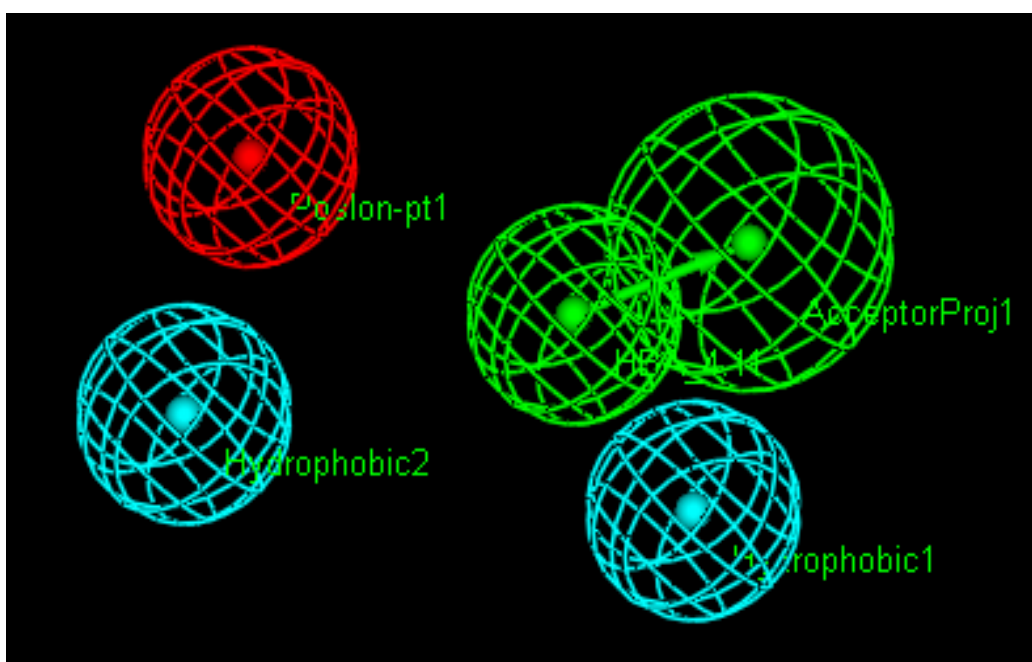


Figure 6: Best DS catalyst pharmacophore model (Hypo 1) illustrating the hydrophobic regions (light blue), the hydrogen bond acceptor (green) and the positive ionizable region (red)

Pharmacophore model generation and validation

Important common pharmacophore hypotheses are computed by HipHop algorithm for the selected inhibitors of pfpmt and pfcct, in order to find the chemical features shared by them and also for assuming the relative alignment of the compounds with the best derived common feature pharmacophore model. By selecting the features obtained through the results of Feature Mapping protocol, the pharmacophore generation run was performed along with 902 diverse conformers of all the active inhibitor molecules. The common pharmacophoric features are obtained as top 10 hypotheses with their ranking scores ranging from 65.093 to 57.783 (Table 3). Table 3 reports the top 10 pharmacophore models along with the displayed features and maxFit values. Among the generated hypotheses, Hypo1 to 8 consisting of four features, one positive ionizable, one hydrogen bond acceptor and two hydrophobic features while the Hypo9 and 10 containing three features, one ring aromatic one positive ionizable and one hydrophobic features. The pharmacophore which scored the highest ranking score is chosen as the most accurate pharmacophore hypothesis (Hypo 1) (Figure 6). The top ranking pharmacophore model Hypo 1 was used to

determine the mapping of the most active compounds and estimate the fit values for each compound. The predicted fit values of the active compounds from the most accurate hypothesis Hypo 1 is given in Table 4. The fit values of all the compounds molecules were ranging from 3.99 to 0.674 of highly mapped molecule to molecule showing low mapping. Remarkably, the highest active compounds Quinidine mapped well on all the chemical features of the Hypo1 model with good fitting scores of 3.786 indicating that the Hypo1 model provides reasonable pharmacophoric characteristics of PfCCT inhibitors for components of their activities. The features mapping of high active molecule Quinidine on the generated best pharmacophore Hypo 1 is shown in Figures 8.

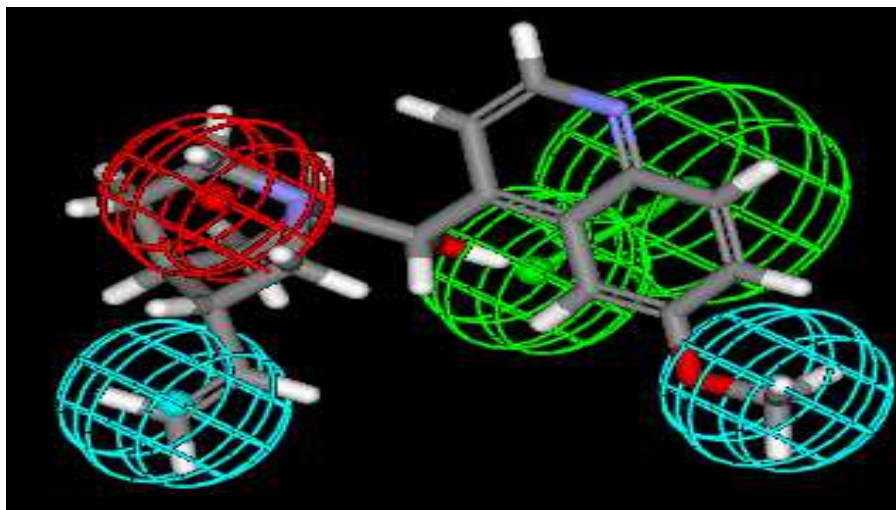


Figure 7: The most active compound Quinidine mapping the common feature pharmacophore Hypo 1

Table 1: Percentage of the residues in the core region of the Ramachandran Plot

Structure	Modeled <i>PfCCT</i>
Core	94.5
Allowed	4.0
Generous	1.5
Disallowed	0.0

Table2: Gold Scores and interaction of 12 ligands with PfCCT

Compound	Fitness score	S(hb_ext)	S(Vdw_ext)	S(hb_int)	S(int)	Interacting atoms	H-Bond Distance
Diphenhydramine	36.38	0.0	37.60	0.0	-91.67	Asn41:ND2...N10(L)	1.875
Quinidine	36.61	0.0	32.19	0.0	-7.66	Asp41 :ND2...N3(L) Asp41 :ND2...C14(L) Lys137:OH...O1H(L) Val 45: NH...O1H(L) Val142:OH...C20(L)	2.085 2.631 2.448 2.475 2.484
Amodiaquine	29.70	0.28	37.60			Val 45: NH...O1H(L) Asp41 :ND2...N3(L)	2.475 2.085
Chloroquine	23.77	0.0	29.87	0.0	-19.52	Arg140:HA...C3(L) Pro46:HD1...H35(L)	1.875 1.307
Chlorpromazine	34.17	2.80	31.16	0.0	-9.54	Asp41:ND2...N10(L)	2.397
DCMB	31.36	0.0	29.98	0.0	-4.84	Asp41 :ND2...N3(L) Lys137:OH...O1H(L)	1.821 1.479
Dodecyltrimethyl Ammonium	31.98	0.0	29.63	0.0	-16.68	Lys137:OH...O1H(L) Val 45: NH...O1H(L)	2.448 2.475
Hexadecylphosphocholine	26.43	0.0	46.81	0.0	-33.34	-	
Hexadecyltrimethylammonium	23.43	0.0	31.11	0.0	-17.21	-	
Quinacrine	26.72	0.0	36.78	0.0	-27.58	Arg140: HA...C3(L)	1.875
Quinine	34.73	0.0	29.90	0.0	-7.37	Val142:O...N15(L) Lys187:O...C5(L)	1.977 2.376
Tacrine	32.90	5.78	19.73	0.0	0.0	Asp43:O...N10(L) Asn41:ND2...N10(L) Arg140:HA...C3(L) Val142:O...N15(L)	2.288 2.397 1.875 1.977

Table 3: Features shared by top 10 hypotheses in common feature pharmacophore generation

Hypo	Features	Rank	Direct Hit	Partial Hit	Max Fit
01	PHHA	65.093	1111111	0000000	4
02	PHHA	64.240	1111111	0000000	4
03	PHHA	62.002	1111111	0000000	4
04	PHHA	60.719	1111111	0000000	4
05	PHHA	60.156	1111111	0000000	4
06	PHHA	59.228	1111111	0000000	4
07	PHHA	58.553	1111111	0000000	4
08	PHHA	58.403	1111111	0000000	4
09	RPH	57.834	1111111	0000000	3
10	RPH	57.783	1111111	0000000	3

Table 4: Predicted fit values of the active compounds from the hypothesis Hypo 1

Compound name	Fit value	Pharmprint
Amodiaquine	3.999	'1111'
Quinidine	3.786	'1111'
Chloroquine	3.703	'1111'
Quinacrine	2.443	'1111'
Quinine	1.907	'1111'
Chloropromazine	0.793	'1111'
Diphenhydramine	0.674	'1111'

CONCLUSION

In the present study, based on the selected template 3HL4, the 3D structural model for PfCCT is predicted and validated. Further molecular docking of 12 natural compounds with our modeled target structure reveals that the binding affinity of compound Quinidine with PfCCT is high showing significant interactions suggesting their inhibitory activity. The pharmacophore results also indicate that the compound Quinidine is well matched with the obtained pharmacophore model features with good fitvalues. This study reveals that Quinidine is a potential inhibitors of PfCCT respectively as targeted for malaria, to act as a drug candidate. Yet pharmacological study will confirm it to be promising in future.

REFERENCES

- [1]. World Health Organization, *WHO Tech. Rep. Ser.* **2000**:892, 1–74.
- [2]. WHO: World Malaria Report 2008. Geneva: World Health Organisation **2008**.
- [3]. Pessi, G., and Ben Mamoun, C. *Future Lipidology* **2006**: 1(2):173-180.
- [4]. Pessi, G., Kociubinski, G., and Mamoun, C. B.. *Proc Natl Acad Sci USA* **2004**: 101:6206-6211.
- [5]. Vial HJ, Ben Mamoun C. Plasmodium lipids: metabolism and Function. Molecular approaches to malaria. Washington, DC: ASM Press; **2005**. pp. 327–352.
- [6]. Pessi G, Choi JY, Reynolds JM, Voelker DR, Mamoun CB. *J Biol Chem* **2005**: 280(13):12461-12466.
- [7]. Reynolds JM, Takebe S, Choi JY, El Bissati K, Witola WH, Bobenchik AM et al. *J Biol Chem* **2008**:283(12):7894-7900.
- [8]. Gill S.C. *et al.*, (1998). *Annual Biochem.* 182: 319-328.
- [9]. Guruprasad K, Reddy BVP, Pandit MW. *Prot. Eng.* **1990**:4: 155-164.
- [10]. Ikai A. J. *J Biochem.* **1980**:88: 1895-1898
- [11]. Kyte J, and Doolittle R. F.. *J Mol. Biol.* **1982**: 157: 105- 132.
- [12]. Gasteiger E, Hoogland C, Gattiker A, Duvaud S, Wilkins MR, Appel RD, et al, Protein Identification and Analysis Tools on the ExPASy Server, (In) John M. Walker (ed): The Proteomics Protocols Handbook, Humana Press **2005**. 571-607.
- [13]. Westbrook J, Feng Z, Jain S, Bhat TN, Thanki N, Ravichandran V, Gilliland GL, Bluhm W, et al. *Nucleic Acids Res* **2002**:30:245–248.
- [14]. Altschul SF, Gish W, Miller W, Myers EW, Lipman DJ. *et al. Nucleic Acids Res.* **1997**:25: 3389 [PMID: 9254694].
- [15]. Abagyan, R.A., M.M. Totrov. *Abstr. Pap. Am. Chem. Soc.* **1996**: 211:35-COMP.
- [16]. Totrov. M. and Abagyan. R. *Biopolymers.* **2001**:60(2):124-133.
- [17]. Laskowski R A, Rullmann J A C, MacArthur M W, Kaptein R, Thornton J M. *J Biomol NMR.* **1996**: 8:477–486.
- [18]. Sippl, M.J. *Curr. Opin. Struct. Biol.* **1995**: 5 (2): 229–235.
- [19]. Alex Mathew J, Nixon Raj N Docking Studies on Anticancer Drugs for Breast Cancer Using Hex Proceedings of the International Multi Conference of Engineers and Computer Scientists Vol. I IMECS **2009**, March 18 - 20, 2009, Hong Kong.

-
- [20]. J. C. Cole, J. W. M. Nissink, R. Taylor. Protein-Ligand Docking and Virtual Screening with GOLD. Virtual Screening in Drug Discovery (Eds. B. Shoichet, J. Alvarez), Taylor & Francis CRC Press, Boca Raton, Florida, USA ,**2005**.
- [21]. Joe Dundas, Zheng Ouyang, Jeffery Tseng, Andrew Binkowski, Yaron Turpaz, and Jie Liang. *Nucleic Acid Research*. **2006**; 34:W116-W118.
- [22]. Jones G, Willett P, Glen RC. *J Mol Biol*. **1995**;245:43–53.
- [23]. Nissink JW, Murray C, Hartshorn M, Verdonk ML, Cole JC, Taylor R. *Proteins*. **2002**;49:457–471.
- [24]. Gregory L. Warren, C. Webster Andrews, Anna-Maria Capelli, Brian Clarke, Judith LaLonde, Millard H. Lambert, *et al*. *J Med Chem*. **2006**; 49(20): 5912–5931.
- [25]. Pawel Smialowski, Antonio J. Martin-Galiano, Aleksandra Mikolajka, Tobias Girschick, Tad A. Holak, Dmitrij Frishman. *Bioinformatics* **2007**; 23 (19): 2536-2542.

2D- and 3D-QSAR Study of Acyl Homoserine Lactone Derivatives as Potent Inhibitors of Quorum Sensor, SdiA in *Salmonella typhimurium*

Gnanendra Shanmugam^{1,3}, Syed Mohamed², Jeyakumar Natarajan^{3*}

¹Bioinformatics Division, Center for Research and Development
Mahendra Educational Institutions, Mallasamudram
Tiruchengode, Tamil Nadu, India
E-mail: gnani_science@gmail.com

²Department of Molecular Modeling
Sadakathullah Appa College
Tirunelveli, Tamil Nadu, India
E-mail: asm2032@gmail.com

³Department of Bioinformatics
Bharathiar University
Coimbatore, Tamil Nadu, India.
E-mail: n.jeyakumar@yahoo.co.in

*Corresponding author

Received: February 12, 2016

Accepted: November 10, 2016

Published: December 31, 2016

Abstract: A series of Acyl homoserine lactone derivatives against quorum sensing (QS) enhanced transcriptional regulator SdiA of *S. typhimurium* were used to establish the physicochemical and structural requirements for the inhibition of QS using 2D- and 3D-QSAR methods. The QSAR model was developed by employing 35 compounds as a training set and the predictive ability was assessed by a test set of 12 compounds. The best 2D-QSAR model for the prediction of SdiA, quorum sensor inhibitory activity has been developed using Multiple Linear Regression (MLR) method (giving $r^2 = 0.8012$ and $q^2 = 0.657$), Principal Component Regression (PCR) method (giving $r^2 = 0.8104$ and $q^2 = 0.625$), and Partial Least Squares Regression (PLS) method (giving $r^2 = 0.8023$ and $q^2 = 0.648$). The best model for 3D-QSAR has been obtained using Comparative Molecular Field Analysis (CoMFA) method, giving $r^2 = 0.896$ and $q^2 = 0.772$. The 2D-QSAR results revealed that the most important descriptors for predicting the anti-quorum sensing activity were alignment-independent descriptors and the topology index descriptors. The 3D-QSAR results of CoMFA contour maps impart some important structural features-like electronegative substituent (Br, Cl, F) on lactone ring favors the strong inhibitory activity. These results will be further useful for development of new quorum sensing inhibitors with structural diversity.

Keywords: *Salmonella typhimurium*, 2D-QSAR, 3D-QSAR, CoMFA, QS inhibitors.

Introduction

Salmonella typhimurium is an enteric bacterium causing gastroenteritis, a life threatening disease in human beings. In recent years problems related to *Salmonella* have increased both in terms of prevalence and severe cases of human salmonellosis and millions of human cases are reported worldwide every year resulting in thousands of mortality [26]. Worldwide, nearly 21.6 million cases of typhoid fever resulting in 200,000 deaths are estimated every year [3]. In Asia, the rate of incidence of typhoid fever is estimated to be 900 per 100,000 people per annum [17]. In contrast, human gastroenteritis is increasing because of food contamination.

The Ernest surveillance program reported *S. typhimurium* on gastrointestinal disorders characterized by high morbidity but low mortality [27]. Globally, the incidence of gastroenteritis is estimated at 1.7 billion cases per year resulting about 3 million deaths. In United States, there are an estimated 1.5 million new cases of non-typhoidal *Salmonella* infections every year [24]. Computational techniques are commonly applied for structure determination and functional elucidation of specific proteins of *S. typhimurium* [20, 31].

In general, gram-negative bacteria including *S. typhimurium* communicate with each other by producing chemical signal molecules that are released into the surrounding environment. These signal molecules upon reaching the quorum, activate certain target genes to respond to the population density which is termed as quorum sensing (QS) [9, 33]. Most of the gram-negative bacteria encodes LuxR/LuxI QS system of *Vibrio fischeri*, where the N-(3-oxo) homoserine lactone (AHLs) are produced by signal synthase, LuxI and reaches LuxR, a signal receptor to modulate the gene expression of various genes and virulence factors [8, 22]. The species of our interest *S. typhimurium* encodes only LuxR homologue, termed as SdiA (Suppressor of cell division inhibition A). Due to the absence of LuxI homologs [25], *S. typhimurium* sense the AHLs produced by *Yersinia enterocolitica* [12] which activates two *Salmonella*-specific loci, *srgE* (SdiA regulated gene E) and the *rck* (resistance to complement killing) operon and also the *Salmonella*'s colonization in the intestine [28].

In gram-negative bacteria including *S. typhimurium*, brominated furanones were reported to have inhibitory activity against SdiA, the LuxR homologue [4, 29]. Gnanendra et al. [12] earlier studied and reported the binding interactions of SdiA and the four AHLs of *Y. enterocolitica*. Their studies revealed that the lactone ring and alkyl chains of AHL molecules are crucial in forming the interactions with in the active site of SdiA. The importance of crucial active site residues favoring the interaction with ligands suggested that the compounds substituted with suitable groups on the lactone ring and alkyl chain might be the best inhibitors of *Salmonella* SdiA [23].

Since there were only a few reports concerning the activity of halogenated furanones on *Salmonella* [15], here we present our quantitative structure-activity relationship (QSAR) analysis of the series of brominated furanones and N-Acyl homoserine lactone derivatives by 2D- and 3D-QSAR models, which may guide rational synthesis of potent novel compounds.

The 2D-QSAR model was derived from various regression methods such as Multiple Linear Regression (MLR), Principle Component Regression (PCR), Partial Least Squares (PLS) and the development of 3D-QSAR models was derived from the most widely used computational 3D-CoMFA method [1]. The study was performed by using structurally diverse sets of N-Acyl homoserine lactone QS inhibitors from the literature with reported IC₅₀ values. In total 47 compounds were used for the study and the 2D- and 3D-QSAR models were developed using a training set of 35 compounds, and the predictive ability of the QSAR models was assessed by using a test set of 12 compounds.

Materials and methods

Biological activities and dataset for 2D-QSAR

Reported quorum sensing inhibitors ex-vivo dataset of 47 brominated furanones and N-Aryl homoserine lactone derivatives with the experimental biological activities, in the form of IC₅₀ (μ M) values (Fig. 1) were selected from the literature [11, 19, 30]. The IC values spanning a range of 0.21 μ M to 1000 μ M provide a broad spectrum data set for 2D-QSAR study. The biological activities were converted into pIC₅₀ to correlate the linear data to the free energy

change and to use as a dependant variable for the development of a valid 2D- and 3D-QSAR models. For all these compounds 2D structures were sketched using ACD-chemsketch and converted to 3D structures using their SMILES notation at “Online SMILES convertor and Structure file generator” [16]. Merck molecular force field and charge were used for Energy minimization and geometry optimization running at maximum number of 1000 cycles and RMS gradient at 0.01 using “small molecule” module at Discovery Studio [6].

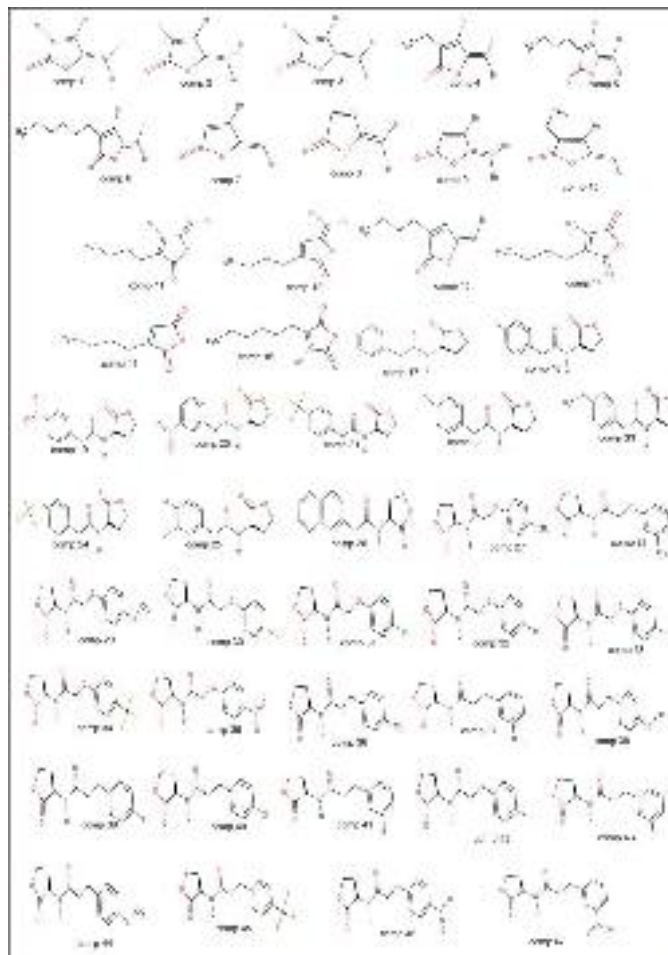


Fig. 1 Dataset of 47 brominated furanones and N-Aryl homoserine lactone derivatives

Molecular descriptors

As the 2D-QSAR studies require the molecular descriptors, the optimized geometries of the molecules were used to calculate the 4 different types of descriptors namely *topological*, *electronic*, *geometrical* and *constitutional descriptors*. These descriptors encode different aspects of molecular structure and consist of electronic, element counts, molecular weight, molecular refractivity, logP and topological descriptors (Table 1). The invariable (constant) columns of independent variables (i.e., descriptors) were removed and later used for QSAR analysis. The 2D-QSAR and molecular descriptors calculations were done using “*QSAR module*” at Discovery Studio [6] and Molecular descriptor calculation server [14].

Selection of training and test set

The dataset of 47 molecules was divided into training set (35 compounds, Table 2) and test set (12 compounds, Table 3) by Sphere Exclusion (SE) method [16]. The unicolon statistics

(Table 4) reveals the perfect selection test and training sets. A total of 178 descriptors were calculated using Molecular descriptor calculation server [14]. The calculated molecular descriptors with same value and highly correlating with other descriptors were excluded. The remaining 9 significant descriptors were calculated for all the 47 molecules. The top five significant descriptors were considered for generating the 2D-QSAR using regression analysis.

Table 1. Types of descriptors used in the study

Sl. No.	Type of descriptor	Descriptor used	Symbol	Description
1.	Topological	Eccentric connectivity index	ECCEN	A descriptor combining distance and adjacency information.
2.	Topological	Zagreb index	Zagreb	The sum of the squared atom degrees of all heavy atoms
3.	Topological	WHIM	Weta3.unity	Holistic descriptors described by Todeschini et al.
4.	Topological	Autocorrelation charge	ATSc1	The Moreau-Broto autocorrelation descriptors using partial charges.
5.	Topological	Wiener numbers	WPOL	Calculates Wiener path number and Wiener polarity number.
6.	Electronic	Charged partial surface area	RNCS	Descriptors combining surface area and partial charge information.
7.	Constitutional	HBond donor count	nHBon	Calculates the number of hydrogen bond donors.
8.	Geometrical	Gravitational index	GRAV-1	Descriptor characterizing the mass distribution of the molecule.
9.	Geometrical	Moment of inertia	MOMI-R	Calculates the principal moments of inertia and ratios of the principal moments. Also calculates the radius of gyration.

Regression analysis

The regression analysis of dataset comprising of 35 training set molecules was carried out by MLR, PCR, and PLS as model building methods. The pIC₅₀ values of the 35 molecules were used as dependent variable and various descriptors as independent variables to generate the QSAR models with the parameters of cross-correlation limit of 0.5 [32]. The models were evaluated by means of statistical measures such as number of data points n , multiple correlation co-efficient r , standard error of estimate s , Fisher ratio between the variances of observed and predicted activities F , cross-validated r^2 obtained by the Leave-One-Out (LOO) method q^2 .

Multiple linear regression (MLR) analysis

The linear relationship between a dependent variable Y (pIC₅₀) and independent variable X (2D descriptors) is established by Multiple Linear regression. The method least square curve fitting is used in MLR to estimate the regression coefficients (r^2) values as the MLR is based on least squares. A relationship in the form of linear straight line that estimates all the individual data points is created by the model.

Table 2. Training set molecules with IC50 and pIC50 values

Sl. No.	Compound number	IC50 value	pIC50 value
1.	Comp 1	17	4.76
2.	Comp 3	11	4.95
3.	Comp 4	45	4.34
4.	Comp 6	50	4.3
5.	Comp 7	17.9	4.74
6.	Comp 8	199.9	3.699
7.	Comp 10	23.12	4.63
8.	Comp 11	10.74	4.96
9.	Comp 13	1000	3
10.	Comp 14	19.42	4.71
11.	Comp 16	65.89	4.18
12.	Comp 17	1.25	5.9
13.	Comp 18	4.63	5.33
14.	Comp 20	0.61	6.21
15.	Comp 21	0.81	6.09
16.	Comp 22	0.92	6.036
17.	Comp 24	4.7	5.32
18.	Comp 25	2.4	5.61
19.	Comp 27	1.8	5.74
20.	Comp 28	1.1	5.98
21.	Comp 29	4.3	5.36
22.	Comp 30	2.7	5.56
23.	Comp 31	0.62	6.2
24.	Comp 33	0.44	6.35
25.	Comp 34	1.6	5.79
26.	Comp 35	0.29	6.53
27.	Comp 36	4.3	5.36
28.	Comp 38	6.8	5.16
29.	Comp 39	12	4.92
30.	Comp 40	3.3	5.48
31.	Comp 42	2.1	5.67
32.	Comp 43	1.8	5.74
33.	Comp 44	1.1	5.95
34.	Comp 46	1.6	5.79
35.	Comp 47	3.4	5.46

Table 3. Test set molecules with IC50 and pIC50 values

Sl. No.	Compound number	IC50 value	pIC50 value
1.	Comp 2	13	4.88
2.	Comp 5	90	4.04
3.	Comp 9	57.46	4.24
4.	Comp 12	160.1	3.79
5.	Comp 15	1000	3
6.	Comp 19	2.25	5.64
7.	Comp 23	8.4	5.07
8.	Comp 26	4.2	5.37
9.	Comp 32	0.51	6.29
10.	Comp 37	8.9	5.05
11.	Comp 41	3.3	5.48
12.	Comp 45	0.21	6.67

Table 4. Uni-column statistics of the training and test sets for QSAR models

Data set	Column name	Average	Max	Min	SD	Sum
2D-QSAR						
Training set	pIC50	5.30	6.53	3.00	0.7808	185.80
Test set	pIC50	4.96	6.67	4.88	1.0529	59.52
3D-QSAR						
Training set	pIC50	5.30	6.53	3.00	0.7808	185.80
Test set	pIC50	4.96	6.67	4.88	1.0529	59.52

MLR analysis includes more than one independent variable based on the regression analysis where the conditional mean of dependant variable (pIC50) Y depends on independent variable (descriptors) X . Regression equation has the form

$$Y = b_1x_1 + b_2x_2 + b_3x_3 + c,$$

where Y is dependent variable; b_i are regression coefficients; x_i are independent variables and; c is regression constant [2, 5].

Principal component regression (PCR) method

Principal component regression is a data compression method for finding the structures in datasets and aims to group correlated variables and replace the original descriptors by new set termed as principal components (PCs). The PC value at each point is obtained by rotating the data into a new set of axes such that most of the variations within the data reflect the first few axes. The data in the decreasing order of variance is selected by PCA as a new set of axes to estimate the dependent variable value based on the selected Principle Components of independent variables [7].

Partial least squares regression (PLSR) method

The relationship of one or more dependent variable (Y) with several independent (X) variables can be established by PLS. This popular regression method is used when the number of independent variables exceeds the number of observations. PLSR aims to describe the common structure by predicting the activity (Y) from X [15].

Validation of QSAR model

The generated models were evaluated by using following statistical measures: correlation coefficient r , which accounts for variance in activity. The internal consistency of equation predictive powers is cross-validated by LOO method expressed as the cross-validated squared correlation coefficient (q^2). The q^2 is defined as

$$q^2 = 1 - \sum (Y_{\text{pred}} - Y_{\text{act}})^2 / (Y_{\text{act}} - Y_{\text{mean}})^2,$$

where Y_{pred} , Y_{act} , Y_{mean} are predicted, actual and mean values of the target property (pIC50) respectively; $\sum (Y_{\text{pred}} - Y_{\text{act}})^2$ is the predictive residual error sum of squares (PRESS), an important cross-validation parameter as is a good approximation of the real predictive error of the model [21].

3D-QSAR studies and dataset

The same dataset of 47 molecules used in 2D-QSAR studies were again used for 3D-QSAR analysis. For the 3D-QSAR analysis we used CoMFA model [1]. This method enables to predict biological activity of specific molecules by deriving a relationship between electrostatic/steric properties and biochemical activities, which can be plotted on contour maps. Comparative molecular field analysis calculates steric fields using Lennard-Jones potential and electrostatic fields using a Coulombic potential. For this CoMFA model, the IC₅₀ values were converted to the corresponding logPIC₅₀ and used as dependent variables. The 3D-QSAR analyses were carried out using “3D-QSAR module” of Discovery Studio [6].

Alignment procedure

Molecular alignment is an important method in 3D-QSAR, related to the conformational flexibility of molecules. Using Systemic conformational search method (grid search) all possible conformations were generated with varying torsion angles and the lowest energy conformers were selected. The template-based alignment method was used to align all the 35 compounds by defining template structure as a basis [18] in the create QSAR option from small molecule module of Discovery studio [6]. To generate the predictive QSAR model, the most active compound's lactone ring was used a template to align all the compounds.

Descriptors calculation

The Tripos force field and Gasteiger and Marsili charge types are used to calculate the electrostatic, steric and hydrophobic field descriptors [10]. The distance-dependent dielectric function probe as carbon atom with charge 1.0 and dielectric constant of 1.0 are considered to calculate the field descriptors (electrostatic and steric).

Comparative molecular field analysis (CoMFA)

The regular space grid of 2.0 Å in all the three dimensions is used to calculate the CoMFA steric and electrostatic potential fields at each lattice intersection within the defined region [1]. The sp³ carbon atom with a radius of 1.52 Å and +1.0 charge was used to calculate the steric and electrostatic fields representing the van der Waals potential (Lennard-Jones 6-12) and columbic terms. The contributions of steric and electrostatic interactions are terminated at ±30 kcal/mol and the electrostatic contributions are ignored with the maximum steric interactions of lattice intersections.

Partial least squares (PLS) analysis

The CoMFA interaction energies pertaining to structural parameters and biological activities relationship is quantified by PLS analysis. The PLS regression takes advantages of greater number of descriptors (independent variables) comparable to number of compounds (data points) [13]. LOO method is used for cross-validation analysis in which the activity is predicted by leaving one compound from the dataset. The optimum number of components and the cross-validated q^2 value were obtained by using a minimum column filtering value (σ) of 2.00 kcal/mol to speed up the analysis with reduced noise [34]. The non-cross-validated r^2 value was obtained by employing the optimum number of previously identified components used to analyse the CoMFA result.

Results and discussion

Generation of 2D-QSAR models

The detailed description of the descriptors used to generate the 2D-QSAR models were given in Table 1. Several QSAR models were derived for the 2D-QSAR studies on a series of

Brominated Furanones and N-Aryl homoserine lactone and the statistically significant QSAR models is discussed.

Multiple linear regression analysis

$$\begin{aligned} \text{pIC50} = & + 0.0025 (\pm 0.0094) \text{ECCEN} - 0.0180 (\pm 0.0436) \text{Zagreb} + 4.9151 (\pm 9.8709) \\ & \text{weta3.unity} - 0.0610 (\pm 0.0772) \text{RNCS} + 0.5308 (\pm 1.5955) \text{nHBDon} + 3.5910 (\pm 5.5780) \\ & (n = 35; r = 0.937; r^2 = 0.8012; s = 0.462; F = 21.611; p < 0.0001; q^2 = 0.657; \\ & S_{\text{Press}} = 0.563; \text{SDEP} = 0.520) \end{aligned}$$

Principle component regression method

$$\begin{aligned} \text{pIC50} = & + 0.2863 (\pm 0.0758) \text{MOMI} + 0.3045 (\pm 0.2636) \text{ECCEN} - 0.2580 (\pm 0.5120) \text{Zagreb} \\ & + 0.5124 (\pm 0.6640) \text{GRAV-1} - 0.5533 (\pm 0.7446) \text{Wpol} + 5.3087 (\pm 0.1573) \\ & (n = 35; r = 0.943; r^2 = 0.8104; s = 0.455; F = 21.226; p < 0.0001; q^2 = 0.625; \\ & S_{\text{Press}} = 0.582; \text{SDEP} = 0.538) \end{aligned}$$

Partial least square method

$$\begin{aligned} \text{pIC50} = & + 0.2965 (\pm 0.0776) \text{weta3.unity} + 0.2869 (\pm 0.2959) \text{ECCEN} - 0.0367 (\pm 0.3149) \\ & \text{ATSc-1} + 0.4306 (\pm 0.5850) \text{GARV-1} - 0.6770 (\pm 1.3104) \text{Zagreb} + 5.3087 (\pm 0.1595) \\ & (n = 35; r = 0.938; r^2 = 0.8023; s = 0.461; F = 20.683; p < 0.0001; q^2 = 0.648; \\ & S_{\text{Press}} = 0.568; \text{SDEP} = 0.525) \end{aligned}$$

The above QSAR equations explain the variance in biological activity by a correlation coefficient r^2 and the models predictability is evaluated by q^2 using LOO method. In the model, ratio of variance due to error in regression is reflected by high F value indicating statistically significant.

Interpretation of 2D-QSAR models

Generated equations of MLR, PCR and PLS indicate the negative contribution of topological descriptor – Zagreb. The electronic descriptor, Charged Partial surface Area denoted by RNCS indicates negative contribution in MLR. In PCR, The topological descriptor, Weiner polarity number denoted by Wpol is showing negative contribution. The topological descriptor auto correlation charge denoted by ATSc-1 indicates the negative contribution in PLS. Topological descriptors, Eccentric Connectivity Index denoted by ECCEN used for combining distance and adjacency information and weta3.unity (holistic descriptor) WHIM and Constitutional Descriptor, nHDon are indicating the positive contribution in MLR equation.

In PCR equation, topological descriptors, ECCEN and the geometrical descriptors GRAV-1 used for mass distribution of the molecule and MOMI (Moment of inertia) explaining the radius of gyration indicate the positive contribution. In case of PLS equation, the topological descriptors, ECCEN and weta3.unity and geometrical descriptor, GRAV-1 indicate positive contribution. The descriptors contribution is shown in Fig. 2. The regression analysis equation is statistically significant with better correlation coefficient (r) which accounts for more than 90% of variance in activity. The LOO cross-validation method, PRESS, cross-validated q^2 and standard deviation were considered for the validation of the predictive powers of the equations for the models. The statistically significant parameter values of MLR, PCR and PLS are summarized in Table 5. The actual and predicted values of the best models of MLR, PCR and PLS of the training set are given in Table 6 with the residual values and their respective plots in Fig. 3.

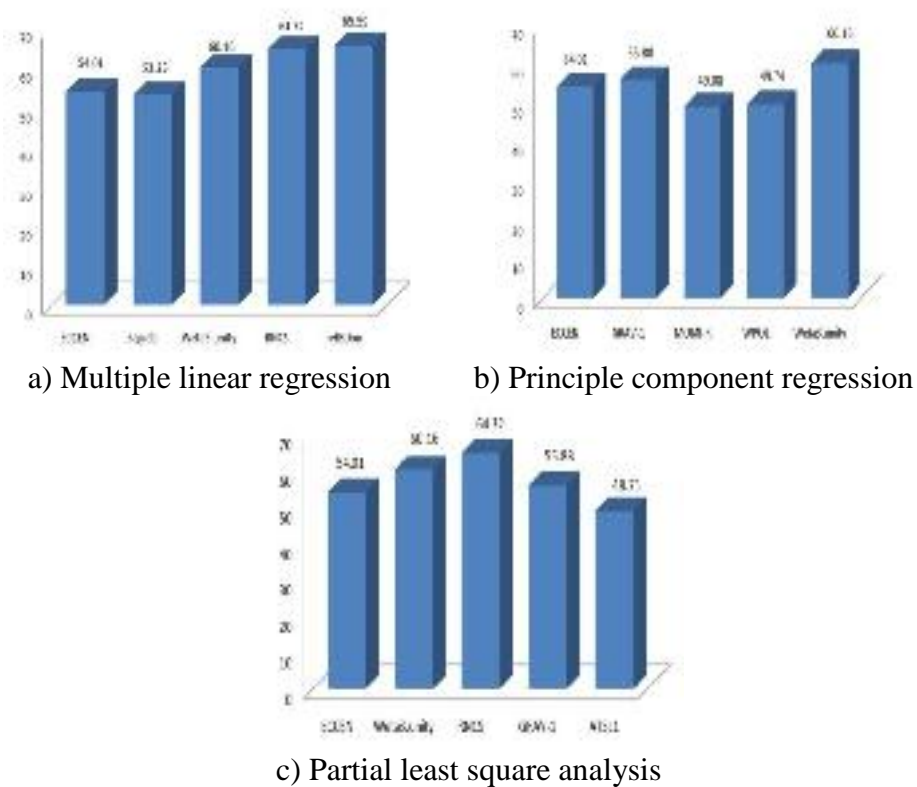


Fig. 2 Descriptors contribution chart for 2D-QSAR

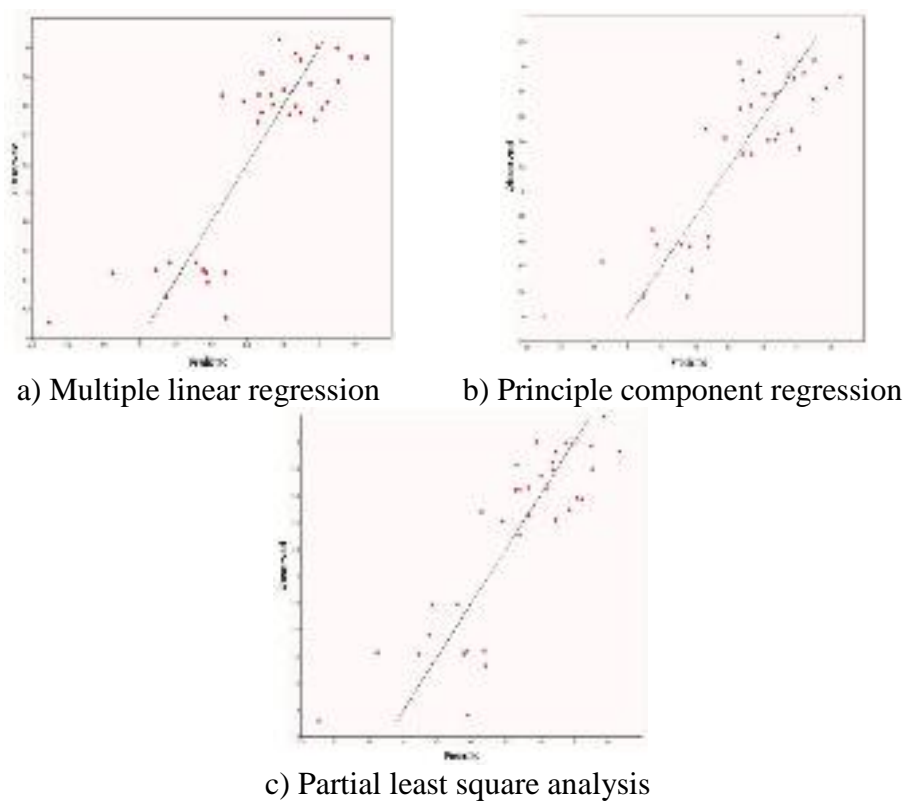


Fig. 3 Observed vs predicted activities plot of best models of training set

Table 5. Statistical results of 2D-QSAR equation generated by MLR, PCR and PLS methods

Sl. No.	Statistical parameters	Results		
		MLR	PCR	PLS
1.	n	35	35	35
2.	r	0.937	0.943	0.938
3.	r^2	0.8012	0.8104	0.8023
4.	s	0.462	0.455	0.461
5.	F	21.611	21.226	20.683
6.	p	< 0.0001	< 0.0001	< 0.0001
7.	q^2	0.657	0.625	0.648
8.	S_{press}	0.563	0.582	0.568
9.	SDEP	0.520	0.538	0.525

The MLR, PCR and PLS models were validated by the test (12 compounds) that are excluded from the training set during the model development. Their residual values were given in Table 7 and respective plots in Fig. 4. The plots of observed versus predicted activity of MLR, PCR and PLS training set reveals the model accuracy with training set and the plots of test set show the activity prediction of the external test set. The result from cross-validated analysis was expressed in the terms of cross-validated squared correlation coefficient (q^2). The approximation of real predictive error of the model is given in the terms of PRESS, an important cross-validation parameter. In general the coefficient of determination r^2 (> 0.7); cross-validated r^2 , q^2 (> 0.5) F -test (higher is better) represents the models as a statistically significant. The generated MLR, PCR and PLS equations shows the r^2 of 0.8012, 0.8104 and 0.8023 respectively. The cross-validated squared coefficient q^2 of 0.657 (MLR), 0.625 (PCR) and 0.648 (PLS) suggests good correlation between the topological, constitutional and geometrical descriptors and inhibitory activity.

3D-QSAR model generation and interpretation

CoMFA method is used for 3D QSAR modelling to generate relationships between molecular fields and inhibitory activity of AHL analogs. In general, despite of drug-receptor interactions, the CoMFA analysis can give a statistically significant model. The training set comprising of 35 compounds was used to generate the CoMFA model and validated by using test set comprised of 12 compounds. The increase or decrease in the activities based on the variation in the structural features of the different compounds were specified by the steric (S) and electrostatic (E) descriptors accompanied by its number indicating its position in 3D MFA grid. The criteria for the model selection are based on the q^2 values and its internal predictive ability. In CoMFA QSAR models, distorted grid spacing is observed as a change in the q^2 values.

The model with the grid spacing of 2.0 Å was selected as the best model by cross-validating value (q^2) after LOO cross-validation. The statistical parameters of CoMFA analysis is compiled in Table 8. A cross-validated value (q^2) of 0.772 of the best model was obtained through LOO analysis, which suggests that the model is a helpful tool for predicting inhibitory activity of Salmonella SdiA binding inhibitors.

The 0.834 relative contributions of steric and 0.612 of electrostatic fields indicates that steric field is more predominant. Further, the new q^2 and r^2 values of 0.772 and 0.869 respectively was studied in a condition without electrostatic field. Basically the electrostatic contribution was taken to be negligible. The contour plot generated as scalar products of coefficients and standard deviation associated with each CoMFA column are shown in Fig. 5.

Table 6. Observed, predicted activities, and residual values of statistically significant models obtained by MLR, PCR and PLS (2D-QSAR) of training set compounds

Sl. No.	Compound	Observed pIC50	Predicted		Predicted		Predicted	
			pIC50 by MLR	Residual	pIC50 by PCR	Residual	pIC50 by PLS	Residual
1.	Comp 1	4.76	4.39	0.37	4.37	0.39	3.96	0.8
2.	Comp 3	4.95	4.45	0.5	4.56	0.39	4.44	0.51
3.	Comp 4	4.34	4.52	-0.18	4.58	-0.24	4.79	-0.45
4.	Comp 6	4.3	4.29	0.01	4.70	-0.4	4.56	-0.26
5.	Comp 7	4.74	4.45	0.29	4.56	0.18	4.44	0.3
6.	Comp 8	3.699	4.45	-0.751	4.44	-0.741	4.43	-0.731
7.	Comp 10	4.63	4.52	0.11	4.58	0.05	4.79	-0.16
8.	Comp 11	4.96	4.14	0.82	4.64	0.32	4.33	0.63
9.	Comp 13	3	4.11	-1.11	4.00	-1	3.92	-0.92
10.	Comp 14	4.71	4.47	0.24	4.16	0.55	4.42	0.29
11.	Comp 16	4.18	4.47	-0.29	4.16	0.02	4.42	-0.24
12.	Comp 17	5.9	5.75	0.15	5.95	-0.05	5.99	-0.09
13.	Comp 18	5.33	5.67	-0.34	5.67	-0.34	5.83	-0.5
14.	Comp 20	6.21	5.77	0.44	6.05	0.16	5.80	0.41
15.	Comp 21	6.09	5.62	0.47	5.95	0.14	5.57	0.52
16.	Comp 22	6.036	5.58	0.456	5.34	0.696	5.58	0.456
17.	Comp 24	5.32	5.49	-0.17	6.03	-0.71	5.64	-0.32
18.	Comp 25	5.61	5.71	-0.1	5.78	-0.17	5.75	-0.14
19.	Comp 27	5.74	5.96	-0.22	5.77	-0.03	5.85	-0.11
20.	Comp 28	5.98	6.01	-0.03	5.91	0.07	5.98	0
21.	Comp 29	5.36	5.82	-0.46	5.89	-0.53	5.64	-0.28
22.	Comp 30	5.56	6.06	-0.5	5.96	-0.4	6.00	-0.44
23.	Comp 31	6.2	6.00	0.2	5.74	0.46	5.97	0.23
24.	Comp 33	6.35	5.93	0.42	5.83	0.52	6.19	0.16
25.	Comp 34	5.79	5.91	-0.12	6.24	-0.45	5.93	-0.14
26.	Comp 35	6.53	5.93	0.6	5.92	0.61	5.93	0.6
27.	Comp 36	5.36	5.55	-0.19	5.30	0.06	5.31	0.05
28.	Comp 38	5.16	5.63	-0.47	5.43	-0.27	5.41	-0.25
29.	Comp 39	4.92	5.67	-0.75	5.51	-0.59	5.48	-0.56
30.	Comp 40	5.48	5.61	-0.13	5.30	0.18	5.44	0.04
31.	Comp 42	5.67	5.54	0.13	5.41	0.26	5.65	0.02
32.	Comp 43	5.74	5.60	0.14	5.42	0.32	5.79	-0.05
33.	Comp 44	5.95	5.50	0.45	5.50	0.45	5.50	0.45
34.	Comp 46	5.79	5.55	0.24	5.47	0.32	5.42	0.37
35.	Comp 47	5.46	5.67	-0.21	5.69	-0.23	5.66	-0.2

In Fig. 5a green contours indicate steric bulk groups needed to increase activity, while yellow contours are unfavourable regions that can decrease the activity. In Fig. 5c blue contours indicate electro positive charges correlating with activity and the H-bond donor regions and the red contour indicates the relationship between negative charge and activity and also the H-bond acceptor regions. The green and yellow colored contours represent steric interactions whereas red and blue colored contours represent electrostatic interactions. The green colour indicates the favourable region for bulky substituents and yellow showing unfavourable regions.

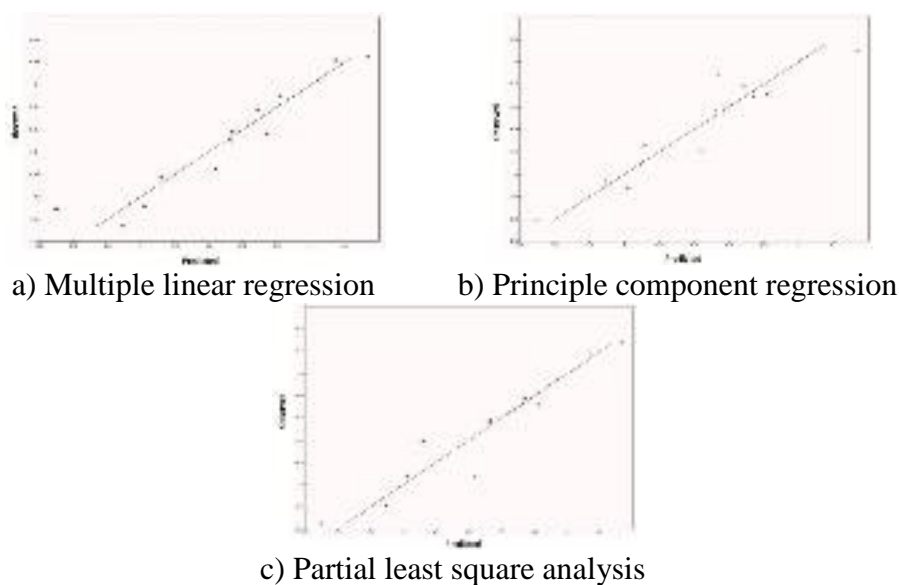


Fig. 4 Observed vs predicted activities plot of best models of test set

Table 7. Observed, predicted activities, and residual values of statistically significant models obtained by MLR, PCR and PLS (2D-QSAR) of training set compounds

Sl. No.	Compound	Observed pIC50	Predicted pIC50 by		Predicted pIC50 by		Predicted pIC50 by	
			MLR	Residual	PCR	Residual	PLS	Residual
1.	Comp 2	4.88	4.50	0.38	4.44	0.44	4.14	0.74
2.	Comp 5	4.04	3.84	0.20	3.75	0.29	4.15	-0.11
3.	Comp 9	4.24	4.34	-0.10	4.52	-0.28	4.78	-0.54
4.	Comp 12	3.79	3.48	0.31	3.87	-0.08	3.63	0.16
5.	Comp 15	3.00	3.79	-0.79	3.19	-0.19	3.30	-0.30
6.	Comp 19	5.64	5.80	-0.16	5.43	0.21	5.44	0.20
7.	Comp 23	5.07	5.16	-0.09	5.78	-0.71	5.15	-0.08
8.	Comp 26	5.37	5.56	-0.19	5.57	-0.2	5.33	0.04
9.	Comp 32	6.29	6.43	-0.14	6.29	0	6.35	-0.06
10.	Comp 37	5.05	5.01	0.04	5.13	-0.08	5.13	-0.08
11.	Comp 41	5.48	5.13	0.35	5.37	0.11	5.57	-0.09
12.	Comp 45	6.67	6.49	0.18	6.18	0.49	6.55	0.12

Table 8. PLS statistics of CoMFA 3D-QSAR

Sl. No.	PLS statistics	CoMFA values
1.	q^2 (LOO cross-validated predicted power of model)	0.772
2.	r^2 (correlation coefficient squared of PLS analysis)	0.896
3.	N (optimum number of components obtained from cross-validated PLS analysis)	3
4.	Standard error of estimate (SEE)	0.036
5.	F -test value	1598.65
6.	R^2 prediction	0.368
7.	Steric field contribution from CoMFA	0.834
8.	Electrostatic field contribution from CoMFA	0.612

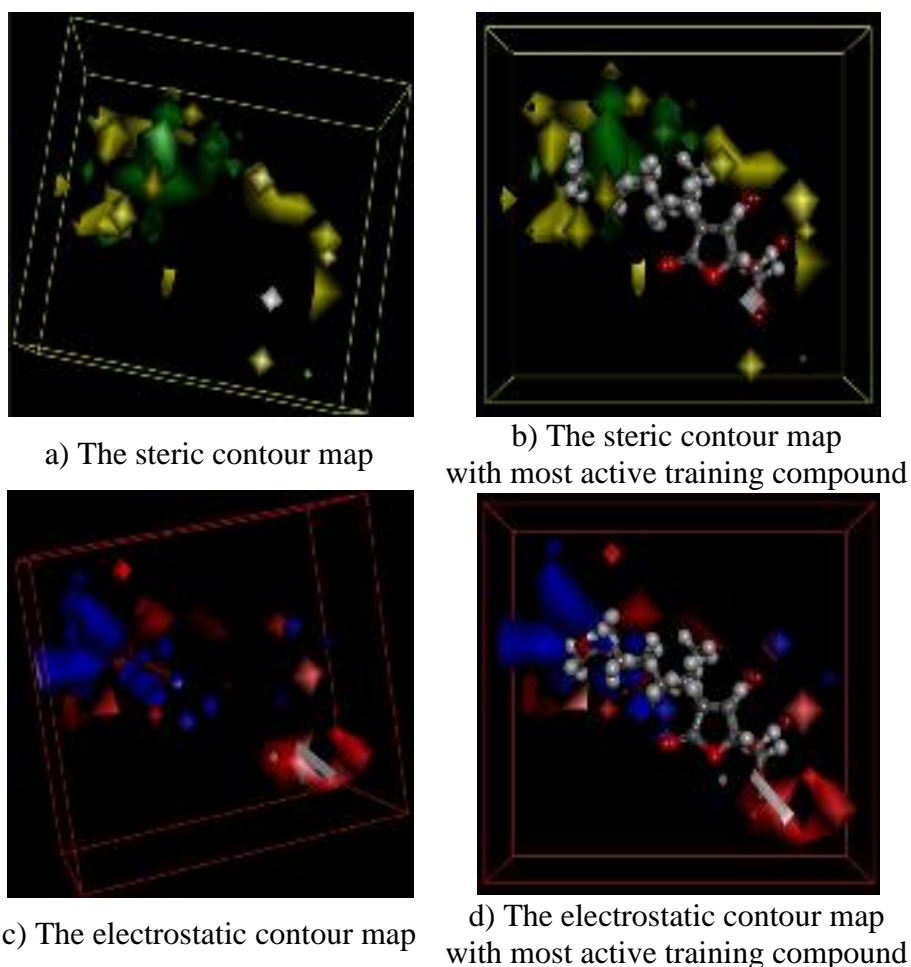


Fig. 5 CoMFA contour maps

The increase in positive charge and H-bond donor regions are favored in blue region while increase in negative charge and H-bond acceptor regions are favored in red region. The steric bulk substituents at green color regions are required to increase the inhibitory activity, while the substitution of steric bulk substituents at yellow color regions are unfavourable for the inhibitory activity. The electropositive charged groups enhancing inhibitory activity are shown in blue colored regions, whereas the electronegative charged groups to improve the activity with the presence of H-bond acceptors are shown in red regions. Therefore, electron withdrawing groups like Br, Cl and F substitutions on lactone ring may significantly increase the inhibition activity of halogen substituted AHLs against SdiA, a potent quorum sensor responsible for *Salmonella typhimurium* pathogenicity.

Conclusion

The 2D-QSAR results revealed that the most important descriptors for predicting the anti-quorum sensing activity were the topological and geometrical descriptors. Further, this QSAR study provides a significant approach to understand the structural and electrostatic requirements of the ligand and its derivative for efficient binding within the SdiA receptor. The 3D-QSAR studies revealed that the steric bulk groups present on the preferred location of analogs plays a crucial role to improve the activity and also the possible role of vander waals and electrostatic interactions. The CoMFA contour maps impart some important structural features-like electronegative substituent (Br and Cl) on lactone ring favors the strong inhibitory activity. These results are helpful to design more potent and selective SdiA, quorum sensor inhibitors and also provide hints for the design of new quorum sensing inhibitors with structural diversity.

Acknowledgements

The authors wish to thank S. Anusuya at Data Mining and Text Mining Research Group, Department of Bioinformatics, Bharathiar University, Coimbatore, India for this invaluable help and support.

References

1. Cramer R. D. III, D. E. Patterson, J. D. Bunce (2008). Comparative Molecular Field Analysis (CoMFA): Effect of Shape on Binding Steroids to Carrier Proteins, *J Am Chem Soc*, 110, 5959-5967.
2. Croux C., K. Joossens (2005). Influence of Observations on the Misclassification Probability in Quadratic Discriminant Analysis, *J Multivar Anal*, 96, 348-403.
3. Curtis T., D. J. Wheeler (2006). Typhoid Fever, *Emedicine Ophthalmology*, <http://emedicine.medscape.com/article/1204093-overview>.
4. Defoirdt T., C. M. Miyamoto, T. K. Wood, E. A. Meighen, P. Sorgeloos, W. Verstraete, P. Bossier (2007). The Natural Furanone (5Z)-4-bromo-5-(bromomethylene)-3-butyl-2(5H)-furanone Disrupts Quorum Sensing-regulated Gene Expression in *vibrio* *Harveyi* by Decreasing the DNA-binding Activity of the Transcriptional Regulator Protein luxR, *Environmental Microbiology*, 9, 2486-2495.
5. Devillers J. (1996). *Neuronal Network in QSAR and Drug Design*, Academic Press, London.
6. *Discovery Studio Modeling Environment*, Release 2.5 (2011). Accelrys Software Inc., San Diego.
7. Doucet J. P., F. Barbault, H. Xia, A. Panaye, B. Fan (2007). Nonlinear SVM Approaches to QSPR/QSAR Studies and Drug Design, *Currently Computationally Aided Drug Designing* 3, 263-289.
8. Eberhard A., A. L. Burlingame, C. Eberhard, G. L. Kenyon, H. K. Nealson, N. J. Oppenheimer (1981). Structural Identification of Autoinducer of *Photobacterium fischeri* Luciferase, *Biochemistry*, 20, 2444-2449.
9. Fuqua C., M. R. Parsek, E. P. Greenberg (2001). Regulation of Gene Expression by Cell-to-cell Communication: Acyl-homoserine Lactone Quorum Sensing, *Annual Review Genetics*, 5, 439-468.
10. Gasteiger J., M. Marsili (1980). Iterative Partial Equalization of Orbital Electronegativity – A Rapid Access to Atomic Charges, *Tetrahedron*, 36, 3219-3228.
11. Geske G. D., M. E. Mattmann, H. E. Blackwell (2008). Evaluation of a Focused Library of N-Aryl L-homoserine Lactones Reveals a New Set of Potent Quorum Sensing Modulators, *Bioorganic & Medicinal Chemistry Letters*, 18, 5978-5981.
12. Gnanendra S., S. Anusuya, J. Natarajan (2012). Molecular Modeling and Active Site Analysis of SdiA Homolog, a Putative Quorum Sensor for *Salmonella typhimurium* Pathogenicity Reveals Specific Binding Patterns of AHL Transcriptional Regulators, *J Mol Model*, 18, 4709-4719.
13. Høskuldsson A. (1988). PLS Regression Methods, *J Chemometrics*, 2, 211-228.
14. <http://crdd.osdd.net/descriptors.php> (Web server for Molecular Descriptor Calculator, Access date 01 December 2016).
15. Huberty C. J. (1994). *Applied Discriminant Analysis*, Wiley, New York.
16. Hudson B. D., R. M. Hyde, E Rahr, J. Wood (1996). Parameter Based Methods for Compounds Selection from Chemical Databases, *Quant Struct Act Relat*, 15, 285-289.
17. Ivanoff B. (1994). Typhoid Fever: Global Situation and WHO Recommendations, *Proceedings of the 2nd Asia Pacific Symposium on Typhoid Fever and other Salmonellosis*, Bangkok: Infectious Disease Association of Thailand, 39.

18. Jain S. V., M. Ghate, K. S. Bhadoriya, S. B. Bari, A. Chaudhari, J. S. Borse (2012). 2D, 3D-QSAR and Docking Studies of 1,2,3-thiadiazole Thioacetanilides Analogues as Potent HIV-1 Non-nucleoside Reverse Transcriptase Inhibitors, *Organic and Medicinal Chemistry Letters*, 2:22, doi: 10.1186/2191-2858-2-22.
19. Janssens J. C. A., H. Steenackers, S. Robijns, E. Gellens, J. Levin, H. Zhao, K. Hermans, D. De Coster, T. L. Verhoeven, K. Marchal, J. Vanderleyden, D. E. De Vos, S. C. J. De Keersmaecker (2008). Brominated Furanones Inhibit Biofilm Formation by *Salmonella enterica* Serovar Typhimurium, *Applied and Environmental Microbiology*, 74, 6639-6648.
20. Khan A., H. Ahmed, N. Jahan, S. R. Ali, A. Amin, M. N. Morshed (2016). An *in silico* Approach for Structural and Functional Annotation of *Salmonella enterica* Serovar Typhimurium Hypothetical Protein R_27, *Int J Bioautomation*, 20(1), 5-18.
21. Kubyani H. (1994). Variable Selection in QSAR Studies: An Evolutionary Algorithm, *Quant Struct Act Relat*, 13, 285-294.
22. Marketon M. M., M. R. Gronquist, A. Eberhard, J. E. Gonzalez (2002). Characterization of the *Sinorhizobium meliloti* sinR/sinI Locus and the Production of Novel N-Acyl Homoserine Lactones, *J Bacteriol*, 184, 5686-5695.
23. Michael B., J. N. Smith, S. Swift, F. Heffron, B. M. Ahmer (2001). SdiA of *Salmonella enterica* is a LuxR Homolog that Detects Mixed Microbial Communities, *J Bacteriol*, 183, 5733-5742.
24. Pang T. Z., A. Bhutta, B. B. Finlay, M. Altwegg (1995). Typhoid Fever and Other Salmonellosis: A Continuing Challenge, *Trends Microbiol*, 3, 253-255.
25. Parsek M. R., E. P. Greenberg (2005). Sociomicrobiology, the Connections between Quorum Sensing and Biofilms, *Trends Microbiol*, 13, 27-33.
26. Scherer C. A., S. I. Miller (2001). Molecular Pathogenesis of Salmonellae, In: Groisman E. A. (Ed.), *Principles of Bacterial Pathogenesis*, Academic Publishers, New York, 266-333.
27. Singh S., R. K. Agarwal, C. S. Tiwari, H. Singh (2011). Antibiotic Resistance Pattern among the Salmonella Isolated from Human, Animal and Meat in India, *Tropical Animal Health and Production*, 44, 665-674.
28. Smith D., J. H. Wang, J. E. Swatton, P. Davenport, B. Price, H. Mikkelsen, H. Stickland, K. Nishikawa, N. Gardio, D. R. Spring, M. Welch (2006). Variations on a Theme: Diverse N-Acyl Homoserine Lactone-mediated Quorum Sensing Mechanisms in Gram-negative Bacteria, *Sci Prog*, 89, 167-211.
29. Smith J. N., B. M. Ahmer (2003). Detection of Other Microbial Species by Salmonella: Expression of the SdiA Regulon, *J Bacteriol*, 185, 1357-1366.
30. Steenackers H. P., J. Levin, J. C. Janssens, A. De Weerd, J. Balzarini, J. Vanderleyden, D. E. De Vos, C. S. De Keersmaecker (2010). Structure-activity Relationship of Brominated 3-alkyl-5-methylene-2(5H)-furanones and Alkylmaleic Anhydrides as Inhibitors of Salmonella Biofilm Formation and Quorum Sensing Regulated Bioluminescence in *Vibrio Harveyi*, *Bioorganic & Medicinal Chemistry*, 18, 5224-5233.
31. Tabassum R., M. Haseeb, S. Fazal (2016). Structure Prediction of Outer Membrane Protease Protein of *Salmonella typhimurium* Using Computational Techniques, *Int J Bioautomation*, 20(1), 31-42.
32. Vyas V. K., M. Ghate, H. Katariya (2011). 2D and 3D-QSAR Study on 4-anilinoquinazoline Derivatives as Potent Apoptosis Inducer and Efficacious Anticancer Agent, *Organic and Medicinal Chemistry Letters*, 1-13.
33. Waters C. M., B. L. Bassler (2005). Quorum Sensing Cell-to-cell Communication in Bacteria, *Annual Review of Cell Developmental Biology*, 21, 319-346.
34. Zhaoqi Y., S. Pinghua (2007). 3D-QSAR Study of Potent Inhibitors of Phosphodiesterase-4 Using a CoMFA Approach, *Int J Mol Sci*, 8, 714-722.

Assist. Prof. Gnanendra Shumugam, Ph.D.E-mail: gnani_science@gmail.com

Dr. G. Shanmugam was the Ph.D. research scholar in Department of Bioinformatics, Bharathiar University, Coimbatore, India. He is recently awarded with Ph.D. degree in Bioinformatics from the same institute. He is currently working as an Assistant Professor at Bioinformatics Division, Center for Research and Development, Mahendra Educational Institutions, Tiruchengode, India. His research interest includes structural bioinformatics and high throughput bioinformatics data analysis.

Assist. Prof. Syed Mohamed, Ph.D.E-mail: asm2032@gmail.com

Dr. A. Syed Mohamed is an Assistant Professor in the Department of Chemistry in Sadakathullah Appa College, Tirunelveli, India since 2001. He completed two post graduate degrees, M.Sc. Chemistry and M.Sc. Environmental Science. He also qualified in CSIR-NET & GATE examination. He completed Ph.D. in the field of theoretical & computational chemistry from University of Madras. He has 15 years of teaching experience and 8 years research experience. His research interest includes computational chemistry, molecular modeling & drug design. At present is serving as Head, Department of Molecular Modeling & Drug Design. He is also serving as Coordinator of Career Oriented Program (COP) in water and soil analysis.

Prof. Jeyakumar Natarajan, Ph.D.E-mail: n.jeyakumar@yahoo.co.in

Dr. J. Natarajan is a Professor in Department of Bioinformatics, Bharathiar University, Coimbatore, India. He obtained his Ph.D. from University of Ulster, UK and post-doctorial training from Northwestern Medical School, Northwestern University, Chicago, USA. He holds research experience from reputed research institutes like Jawaharlal Nehru University, New Delhi, and Madurai Kamaraj University, Madurai. His area of research interest includes data mining and text mining of biomedical data. He is currently working on various research problems in this domain.

Molecular Insights of Hyaluronic Acid as Potential Source of Polymer-Drug Conjugate in the Target-Mediated Treatment of Cancer

Gnanendra Shanmugam^a, Rajesh Salem Varadharajan^b, Desika Prabakar^c, Syed Mohammed^d, Sathiyapriya Renganathan^e, Murano Erminio^{f,g} and Vincent Aroulmoji^{e*}

^aDepartment of Biotechnology, Yeungnam University, Gyeongsan, South Korea

^bDepartment of Botany, Vivekanandha College of Arts and Science, Tiruchengode, Tamilnadu, India

^cBioinformatics Division, Origene Biosolutions, Salem, Tamilnadu, India

^dDepartment of Chemistry, Sadakathullah Appa College, Tirunelveli, Tamilnadu, India

^eCenter for Research & Development, Mahendra Educational Institutions, Namakkal, Tamilnadu, India

^fProtos Research Institute, Via Flavia 23/1, 34148, Trieste, Italy

^gNealys srl, Via Flavia 23/1, 34148, Trieste, Italy

aroulmoji@gmail.com

Received: June 24th, 2016; Accepted: December 28th, 2016

The naturally occurring polysaccharide hyaluronic acid (HA) is a major component of the extracellular matrix and is found over expressed in many cancer cells. Hyaluronic acid is reported to be a potential carrier for drug delivery with the dual advantage of accumulation at the tumor site and receptor-mediated uptake. The use of drugs conjugated with macromolecules was shown to improve the drug pharmacokinetic profile. The various biological potentials such as biodegradability, biocompatibility, non-toxicity, hydrophilicity and non-immunogenicity, together with the availability of various chemical groups that allow the conjugation of drugs, put forward HA as a potential choice for the development of drug conjugates. In this context, the present study is focused to provide, through docking studies, insights on the activity of cancer drugs such as methotrexate, 3',5'-dichloromethotrexate and ornithine-methotrexate and their activity against the receptor caspase-1, which is a well-established drug target in the treatment of cancer. The docking study envisages that the usage of methotrexate properly conjugated to the natural polysaccharide HA might serve as a potential drug to effectively treat some cancer diseases.

Keywords: Hyaluronic acid, Methotrexate, Cancer, Docking studies, Drug-conjugate.

INTRODUCTION

The naturally occurring polysaccharide hyaluronic acid (HA) is a major component of the extracellular matrix and, additionally, it is found in the synovial fluid of joints and scaffolding that comprises cartilages. Peculiarly, one of its cellular receptors (CD44) it is found over expressed in many cancer cells [1,2]. Structurally, HA consists of β -(1 \rightarrow 4)-linked D-glucopyranuronic acid and β -(1 \rightarrow 3)-linked 2-acetamido-2-deoxy-D-glucopyranose. Its basic disaccharide repeating unit presents a carboxyl group at C-5' and two free hydroxyl groups at the C-2' and C-3' positions in the β -D-GlcpA and two hydroxyl groups at C-4 and C-6 position in the β -D-GlcpNAc moiety; chemical and enzyme-catalyzed reactions at some of these positions have led to a wide range of derivatives [3-5].

The well documented physico-chemical and biochemical characteristics such as network-forming and viscoelastic and polyelectrolytic behaviour of HA signifies its importance in contributing the biochemical properties of living tissues and also put forward this polymer as a potential nano carriers for the development of new anticancer drug-conjugates [6]. HA appears to be important in cell-cell interactions and takes part in regulating cell behavior during various morphogenic processes in the body [7]. The role of this natural polysaccharides in diseases such as various forms of cancers, arthritis and osteoporosis has led to the development of both biomaterials for surgical implants and drug conjugates for targeted delivery [8-10]. The use of drugs conjugated with macromolecules improves their pharmacokinetic

profile. The various biological potentials such as biodegradability, biocompatibility, non-toxicity, hydrophilicity and non-immunogenicity together with the presence of chemical groups favoring the conjugations with drugs put forward HA as a potential choice for carrier macromolecules to be employed for the development of drug conjugates.

In cancer disease, some cells display uncontrolled growth, invasion and sometimes metastasis. These malignant properties differentiate cancer from benign tumors, which are self-limited, do not invade or metastasize [11]. The development of cancer is generally considered a multistep process driven by carcinogen-induced genetic and epigenetic damage in susceptible cells, which as a result, gain selective growth damage. Subsequently, cells may undergo clonal expansion as the result of activation of proto-oncogenes and/or inactivation of tumor suppressor genes [12].

Nowadays, various types of cancers are reported spreading according to various mechanisms. The most frequently diagnosed cancers are bone, brain, breast, colon and skin cancers. There are many known causes of cancer like exposure to chemicals, drinking excess alcohol, excessive exposure to sunlight, and genetic differences, to name a few [13]. The caspase are a family of cysteine proteases that are one of the main executors of the apoptotic process and exist within the cell as inactive pro-forms or zymogens. These zymogens can be cleaved to form active enzymes following the induction of apoptosis [14]. The origin of cancer involves deregulated cellular proliferation and the suppression of

apoptotic processes, ultimately leading to tumor establishment and growth. Several lines of evidence point toward the family of proteins playing a role in oncogenesis, via their effective suppression of apoptosis. The central mechanisms of apoptotic suppression appear to be through direct caspase and pro-caspase inhibition.

Thus, the present study is focused to provide insights, through docking studies, on the activity of cancer drugs such as methotrexate, 3',5'-dichloromethotrexate and ornithine-methotrexate and their activity against the receptor of caspase-1, a well established drug target in the treatment of cancer.

RESULT AND DISCUSSION

Globally, it is estimated that deaths from cancer will raise to 13.1 million in 2030 [15,16] with lung, stomach, liver, colon and breast cancers being the most prominent causes for cancer deaths each year. Even though a number of advancing techniques have been put forward in delineating the molecular and cellular biology of cancer cell, the urgency in the treatment of metastatic diseases remains challenging. Due to certain limitation such as low specificity and efficacy, and high toxicity of anticancer drugs, great effort is devoted to the research of improved therapeutics based on molecular targeted approaches as alternatives to treat malignant tumor cells.

In most of the target-based therapeutics, the drugs are made to differentiate the malignant and healthy tissues on the basis of their physiological and biochemical differences. Most prominently, the poor intra-tumor lymphatic drainage and the vascular leakage are exploited by employing passive drug delivery systems that allow large molecules, such as polymeric conjugates [17], liposomes [18], micro-particles, and nanoparticles [19], to accumulate at the tumor site. In addition to this, due to the biochemical differences of cancerous and normal tissues, the usage of conjugated drugs may be proposed to selectively target over-expressed tumor specific receptors. Interestingly, evidence was provided that the conjugation of drugs with macromolecules enhances the pharmacokinetic profiles of the drugs themselves [20]. Furthermore, the sustained high intra-tumor drug levels and its lower plasma concentrations are driven by the slow release of the drug from the macromolecular carrier. This process can be effectively achieved by employing specific macromolecules with biodegradable linkage and suitable spacer, which can hold a potent anticancer agent that can preferentially be released within the tumor tissue [21]. The natural polysaccharide hyaluronic acid (HA) has the dual advantage of a potential accumulation at the tumor site and of a receptor-mediated uptake. Thus the anticancer activity of methotrexate, 3',5'-dichloromethotrexate, ornithine-methotrexate and its HA-drug conjugates HA-methotrexate, HA-3',5'-dichloromethotrexate and HA-ornithine-methotrexate against caspase-1, a well-established drug target in the treatment of cancer, was explored through docking studies.

The origin of cancer involves the deregulation of the cellular proliferation and the suppression of apoptotic processes that ultimately leads to the establishment of tumors and cell growth; caspase-1, as the main executor of the apoptotic process, exists within the cell as inactive pro-form or zymogen [22]. Since the central mechanisms of apoptotic suppression appear to involve direct caspase and pro-caspase inhibition, the choice of caspase-1 as potential cancer target is significantly worthy to be explored as alternative therapeutic choice of drugs that can exhibit their efficacy through the delivery by a polymer-drug conjugate. The crystal structure of the human caspase-1 [23] in complex with malonate,

determined by X-ray crystallography resolved at 1.80^Å with PDB ID: 1SC3, is shown in Figure 1. The drug target interactions between methotrexate, 3',5'-dichloromethotrexate, ornithine-methotrexate and HA-drug conjugates such as HA-methotrexate, HA-3',5'-dichloromethotrexate and HA-ornithine-methotrexate were explored through docking studies.

Ligands: The 2D structures of potential anticancer drugs such as methotrexate, 3',5'-Dichloromethotrexate and Ornithine-methotrexate and the HA-drug conjugates HA-methotrexate, HA-3',5'-dichloromethotrexate and HA-ornithine-methotrexate sketched in ACD ChemsSketch along with the HA dimer and HA-peptide linker (Phe-Phe used in HA-drug conjugates) are shown in Figure 2.

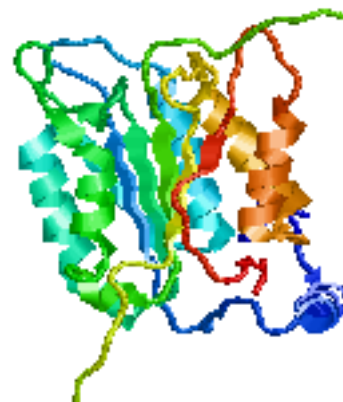


Figure 1: Crystal structure of the human caspase-1 (PDB ID: 1SC3).

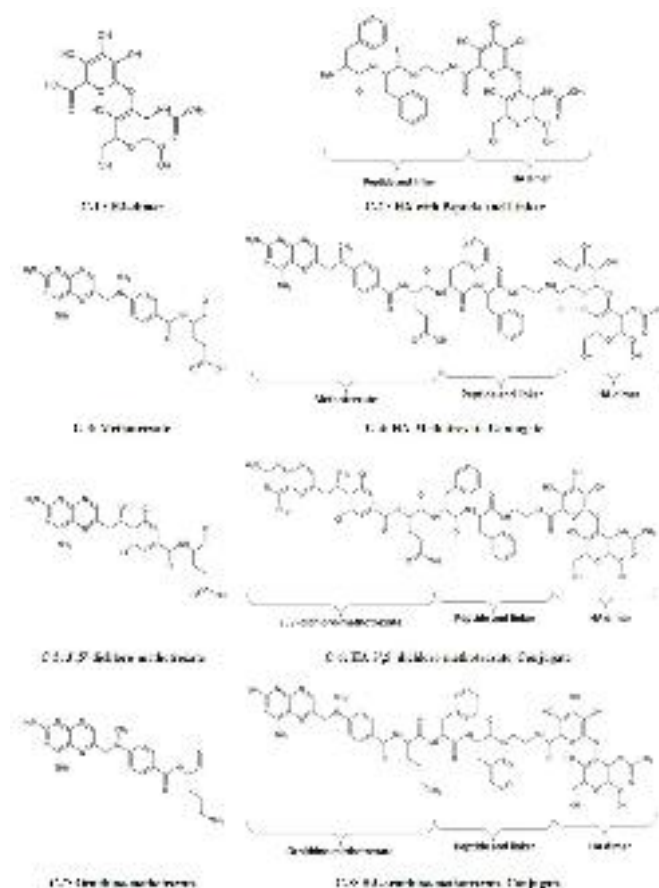


Figure 2: 2D structures of HA-dimer, HA-peptide linker, anti-cancer drugs and HA-drug conjugates used in docking studies.

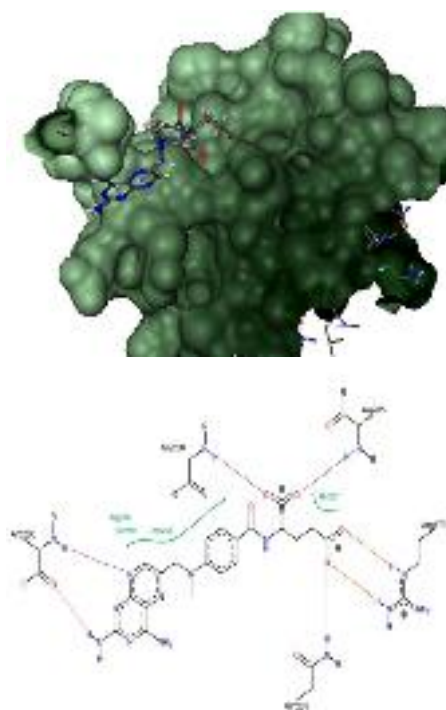


Figure 3: Docking complex and interactions of methotrexate within the active site of human caspase-1 (Dock score: -26.9011 kJ/mol).

Docking interactions of methotrexate: The compound methotrexate docked within the active site of human caspase-1 exhibited the dock score of -26.9011 kJ/mol. It was observed that the compound occupied the ligand binding site of malonate as in the crystal structure of human caspase-1 by favoring the H-bond interactions and non-bonded interactions. The amino acids Arg179, Gly238, Gln283, Ala285 and Arg286 favored the H-bond interactions and the non-bonded interactions are supported by His237, Ala285, Arg286 and Ser289. The docking complex and docking interactions of methotrexate within the active site of human caspase-1 is shown in Figure 3.

Docking interactions of 3',5'-dichloromethotrexate: The compound 3',5'-dichloromethotrexate docked within the active site of human caspase-1 exhibited the dock score of -21.6994 kJ/mol. It was observed that the compound occupied the ligand binding site of human caspase-1 by favoring the H-bond interactions with amino acids such as Arg179, Gly238, Gln283 and Ala285 while non-bonded interactions were exhibited by His237, Ala285, Arg286 and Ser289. The docking complex and docking interactions of 3',5'-dichloromethotrexate within the active site of human caspase-1 is shown in Figure 4.

Docking interactions of ornithine-methotrexate: The compound ornithine-methotrexate docked within the active site of human caspase-1 exhibited the dock score of -17.5100 kJ/mol. It was observed that the compound occupied the ligand binding site of malonate as in the crystal structure of human caspase-1 by favoring the H-bond interactions and non-bonded interactions. The amino acids Arg179, Gly238, Gln283, Arg286 and Ser289 favored the H-bond interactions and the non-bonded interactions are supported by His237, Gln283, Ala284, Ala285 and Arg286. The docking complex and docking interactions of ornithine - methotrexate within the active site of human caspase-1 is shown in Figure 5.

Docking interactions of HA: The compound HA docked within the active site of human caspase-1 exhibited the dock score of

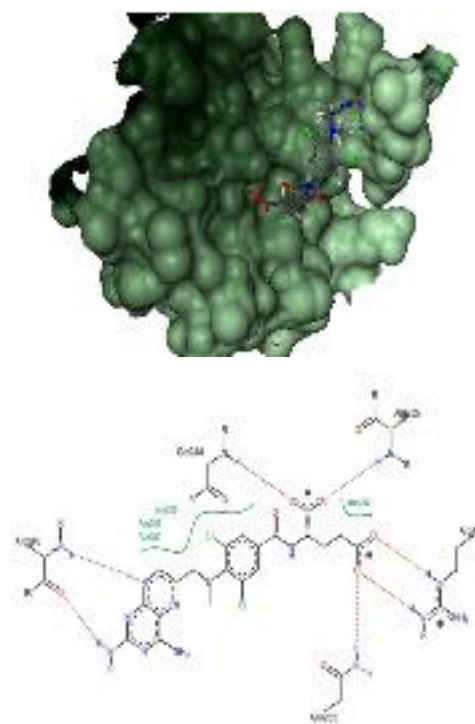


Figure 4: Docking complex and interactions of 3',5'-dichloromethotrexate within the active site of human caspase-1 (Dock score: -21.6994 kJ/mol).

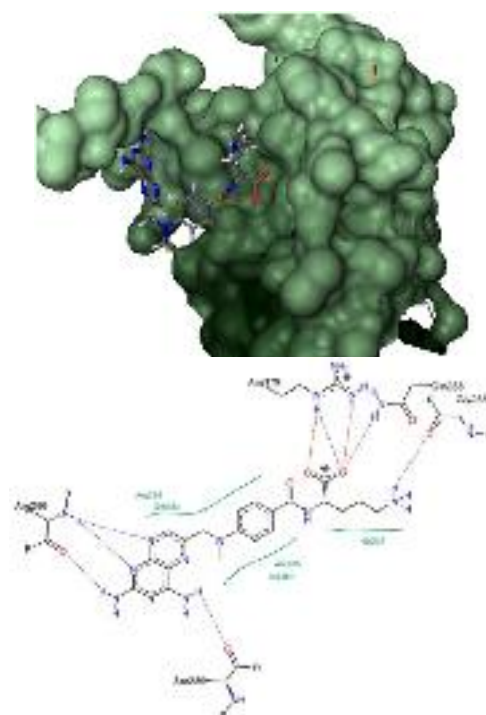


Figure 5: Docking complex and interactions of ornithine-methotrexate within the active site of human caspase-1 (Dock score: -17.5100 kJ/mol).

-24.4711 kJ/mol. It was observed that the compound partially occupied the ligand binding site of malonate as in the crystal structure of human caspase-1 by favoring the H-bond interactions and non-bonded interactions. The amino acids Arg179, Gly238, Gln283, Ala285 and Gly287 favored the H-bond interactions while non-bonded interactions are supported by His237, Gly238, Ala284 and Ala285. The docking complex and docking interactions of HA within the active site of human caspase-1 are shown in Figure 6.

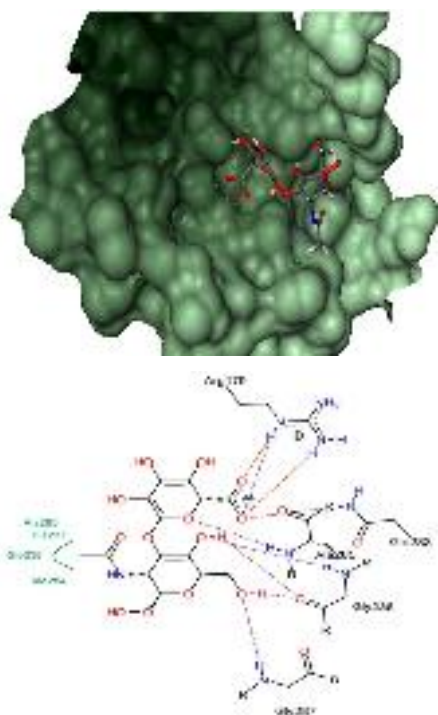


Figure 6: Docking complex and interactions of HA dimer within the active site of human caspase-1 (Dock score: -24.4711 kJ/mol).

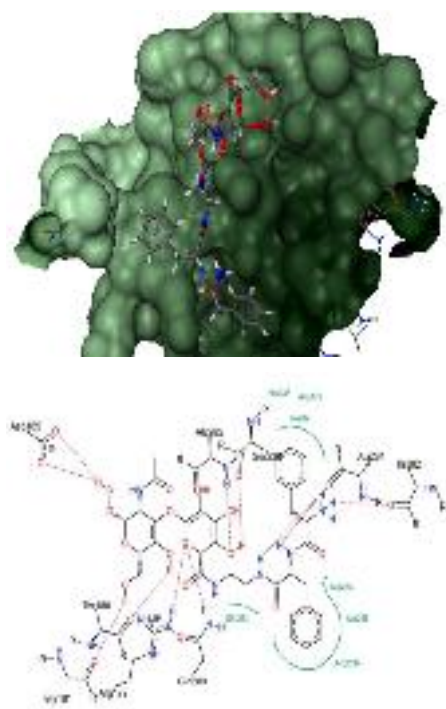


Figure 7: Docking complex and interactions of HA with Phe-Phe peptide linker within the active site of human caspase-1 (Dock score: -26.2475 kJ/mol).

Docking interactions of HA-peptide (Phe-Phe) linker: The compound HA-Phe-Phe peptide docked within the active site of human caspase-1 exhibited the dock score of -26.2475 kJ/mol. It was observed that the compound occupied the ligand binding site of malonate as in the crystal structure of human caspase-1 by favoring the H-bond interactions and non-bonded interactions. The amino acids Arg179, Thr180, Gly181, Asp185, Ser236, Ile282, Gln283, Ala284 and Ala285 favored the H-bond interactions while non-bonded interactions are favored by Arg179, His237, Ile282, Gln283,

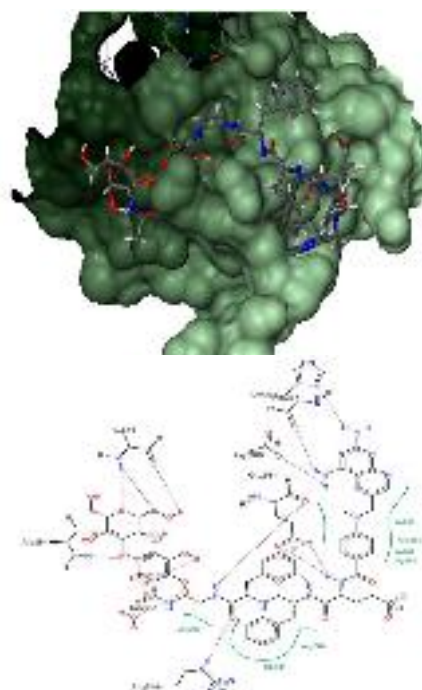


Figure 8: Docking complex and interactions of HA-methotrexate conjugate within the active site of human caspase-1 (Dock score: -34.3024kJ/mol).

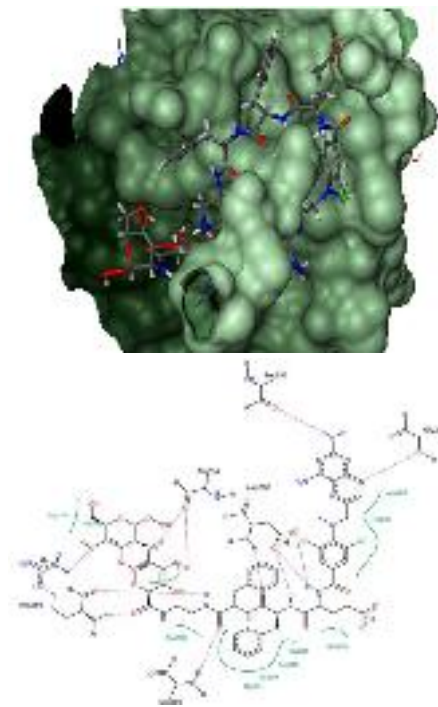


Figure 9: Docking complex and interactions of HA-3',5'-dichloromethotrexate conjugate within the active site of human caspase-1 (Dock score: -31.5882kJ/mol).

Ala284, Ala285 and Ala286. The docking complex and docking interactions of HA-peptide linker within the active site of human caspase-1 is shown in Figure 7.

Docking interactions of HA-methotrexate conjugate: The compound HA-methotrexate conjugate docked within the active site of human caspase-1 exhibited the dock score of -34.3024kJ/mol. It was observed that the compound occupied the ligand binding site of malonate as in the crystal structure of human caspase-1 by favoring the H-bond interactions and non-bonded interactions. The amino acids Arg179, Gly238, Gln283, Ala285 and Arg286 favored the

Table 1: Docking interactions (H-bond & non-bonded) and respective dock scores of the compounds within the predicted binding pocket of caspase-1 (*H-bond interactions).

C-1	C-2	C-3	C-4	C-5	C-6	C-7	C-8
-	-	-	-	-	-	-	*Glu171
-	-	-	-	-	-	-	Glu171
-	-	-	-	-	-	-	*Glu172
-	-	-	-	-	-	-	Arg178
*Arg179	*Arg179	*Arg179	-	*Arg179	-	*Arg179	*Arg179
-	Arg179	-	-	-	-	-	Arg179
-	*Thr180	-	-	-	-	-	-
-	*Gly181	-	-	-	-	-	*Gly181
-	-	-	-	-	-	-	*Ala182
-	-	-	-	-	-	-	Ala182
-	-	-	-	-	-	-	Glu183
-	-	-	-	-	-	-	*Glu183
-	-	-	-	*Arg286	-	-	*Val184
-	-	-	-	-	-	-	Val184
-	*Asp185	-	-	-	-	-	*Asp185
-	-	-	-	-	-	-	Asp185
-	*Ser236	-	-	-	*Ser236	-	-
-	-	-	*His237	-	-	-	-
His237	His237	His237	-	His237	His237	His237	His237
*Gly238	-	*Gly238	-	*Gly238	*Gly238	*Gly238	-
Gly238	-	-	-	-	-	-	-
-	-	-	Ile239	-	Ile239	-	-
-	-	-	*Arg240	-	-	-	-
-	-	-	Arg240	-	Arg240	-	-
-	-	-	*Glu241	-	-	-	-
-	-	-	Glu241	-	Glu241	-	-
-	-	-	Glu250	-	Glu250	-	-
-	-	-	Leu258	-	-	-	-
-	*Ile282	-	*Ile282	-	-	-	-
-	Ile282	-	Ile282	-	-	-	-
*Gln283	*Gln283	*Gln283	-	*Gln283	-	*Gln283	*Gln283
-	Gln283	-	-	-	-	Gln283	Gln283
-	*Ala284	-	*Ala284	-	*Ala284	-	-
Ala284	Ala284	-	-	-	Ala284	Ala284	-
*Ala285	*Ala285	*Ala285	-	*Ala285	-	-	-
Ala285	Ala285	Ala285	-	Ala285	Ala285	Ala285	Ala285
-	-	*Arg286	-	-	*Arg286	*Arg286	-
-	Arg286	Arg286	Arg286	Arg286	Arg286	Arg286	-
*Gly287	-	-	*Gly287	-	-	-	-
-	-	-	-	-	Gly287	-	-
-	-	-	*Asp288	-	*Asp288	-	*Asp288
-	-	-	-	-	Asp288	-	-
-	-	-	-	-	*Ser289	*Ser289	-
-	-	Ser289	-	Ser289	-	-	-
-24.4711	-26.2475	-26.9011	-34.3024	-21.6994	-31.5882	-17.5100	-28.7427

C-1: HA dimer; C-2: HA-peptide linker; C-3: methotrexate; C-4: HA-methotrexate conjugate; C-5: 3',5'-dichloro-methotrexate;
C-6: HA-3',5'-dichloro-methotrexate conjugate; C-7: ornithine-methotrexate; C-8: HA-ornithine-methotrexate conjugate.

H-bond interactions and the non-bonded interactions are supported by His237, Ala285, Arg286 and Ser289. The docking complex and docking interactions of HA-methotrexate conjugate within the active site of human caspase-1 are shown in Figure 8.

Docking interactions of HA-3',5'-dichloromethotrexate conjugate: The compound HA-3',5'-dichloromethotrexate conjugate docked within the active site of human caspase-1 exhibited the dock score ligand binding site of human caspase-1 by favoring the H-bond interactions with amino acids such as Arg179, Gly238, Gln283 and Ala285 while non-bonded interactions were exhibited by His237, Ala285, Arg286 and Ser289. The docking complex and docking interactions of HA-3',5'-dichloromethotrexate conjugate within the active site of human caspase-1 is shown in Figure 9.

Docking interactions of HA-ornithine-methotrexate conjugate: The compound HA-ornithine-methotrexate conjugate docked within

the active site of human caspase-1 exhibited the dock score of -28.7427 kJ/mol. It was observed that the compound occupied the ligand binding site of malonate as in the crystal structure of human caspase-1 by favoring the H-bond interactions and non-bonded interactions. The amino acids Arg179, Gly238, Gln283, Arg286 and Ser289 favored the H-bond interactions and the non-bonded interactions are supported by His237, Gln283, Ala284, Ala285 and Arg286. The docking complex and docking interactions of HA-ornithine-methotrexate conjugate within the active site of human caspase-1 is shown in Figure 10.

The docking interactions of HA dimer, HA-peptide (Phe-Phe) linker, methotrexate, 3',5'-dichloromethotrexate, ornithine-methotrexate, HA-methotrexate conjugate, HA-3',5'-dichloromethotrexate conjugate and HA-ornithine-methotrexate conjugate with their docking scores were given in Table 1.

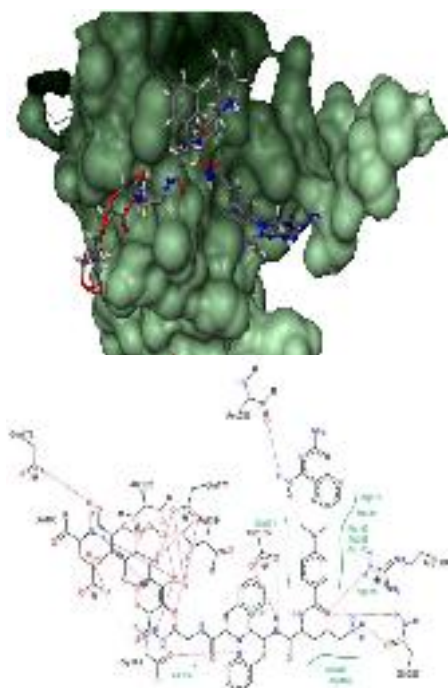


Figure 10: Docking complex and interactions of HA-ornithine-methotrexate conjugate within the active site of human caspase-1 (Dock score: -28.7427kJ/mol).

Theoretically, it was observed that all the compounds exhibited better binding efficacy in terms of highest dock score, which significantly reveals the lowest binding energy of stable confirmation. The best dock score of -34.3024 kJ/mol was exhibited by HA-methotrexate conjugate, while the poor dock score of -17.5100 kJ/mol was obtained for ornithine-methotrexate interactions with caspase-1. It is note-worthy to mention that the dock score of anti-cancer drugs methotrexate, 3',5'-dichloromethotrexate and ornithine-methotrexate is poor when compared to the dockscore of the corresponding HA-drug conjugates HA-methotrexate, HA-3',5'-dichloromethotrexate and HA-ornithine-methotrexate, thus indicating that these compounds would certainly possess a better activity when employed as HA-drug conjugate. It is also worth to mention that the dock score of -24.4711 kJ/mol and -26.2475 kJ/mol, exhibited by HA dimer and HA-peptide linker molecules, are almost the same as the dock score of -26.7427 exhibited by methotrexate within the binding pocket of human caspase-1. This finding suggests that the HA-dimer and the use of a peptide linker for the design of HA-drug conjugate would also plays a major role in drug interactions.

The HA-drug conjugates designed to specifically target overexpressed CD44 in lung carcinoma cells as reported by Akima *et al.*, [24] reveals the uptake of a fluorescent HA conjugate, of HA-conjugated mitomycin C (MMC), and of epirubicin.

Similarly, HA-butyrate and HA-paclitaxel conjugates showed increased apoptosis activity [25, 26] and inhibited cell growth in vitro, with significant decrease in tumor burden in vivo [27]. However, only few studies on HA-drug conjugation were reported to be promising. In this regards, the docking study reported here indicates that H-bond interactions favored by Arginine (Arg179 and 286), Glycine (Gly238) and Glutamine (Gln283) plays a crucial role in binding the methotrexate, 3',5'-dichloromethotrexate, ornithine-methotrexate compounds with human caspase-1. While the amino acids Aspartic acid (Asp288) plays a crucial role in binding the HA-methotrexate, HA-3',5'-dichloromethotrexate and HA-ornithine-methotrexate compounds, the amino acid Arginine (Arg286) is

found to be crucial in favoring the non-bonded interactions with all the compounds.

These docking interactions imply that the keto group (C=O) of the compounds and the amino group (NH) on the amino acids of caspase-1 molecule favor the H-bond interactions. In line with this, the efficacy of the conjugation of methotrexate, 3',5'-dichloromethotrexate and ornithine-methotrexate with HA macromolecules would certainly envisages that, as anti-cancer agent, HA-methotrexate is a better choice and might be employed in the treatment of various cancers and also provides a suggestion for the selection of novel HA-based anti-cancer agents with more target specificity.

CONCLUSIONS: As the estimated deaths from cancer continues to raise to 13.1 million in 2030 with lung, stomach, liver, colon and breast cancers being the most prominent causes for cancer deaths each year, the identification of potential drug conjugate with dual advantages of accumulation at the tumor site and receptor-mediated uptake would serve as a potential alternative to effectively treat cancer. In this scenario, the naturally-occurring polysaccharide hyaluronic acid (HA), a major component of the extracellular matrix whose cellular receptor CD44 is over expressed in many cancer cells, was selected as a potential carrier of anticancer drugs to synthesize new selective, potent drug-conjugates. Thanks to its biological potentials such as biodegradability, biocompatibility, non-toxicity, hydrophilicity and non-immunogenicity, and the presence, in the macromolecular backbone, of chemical groups that may favor drug conjugations make HA a potential choice for the development of anticancer drug conjugates. Thus, in the present study the binding efficacy of the selected cancer drugs such as methotrexate, 3',5'-dichloromethotrexate and ornithine-methotrexate and their activity against the receptor caspase-I, were explored through docking studies. The docking study envisages that the Aspartic acid (Asp288) and Arginine (Arg286) plays a crucial role in favoring H-bond and non-bonded interactions with all the compounds. The binding efficacy of the methotrexate, 3',5'-dichloromethotrexate and ornithine-methotrexate and the HA conjugate of these drugs has revealed that the usage of methotrexate as HA-methotrexate conjugate might represent a potential alternative to effectively treat cancer through the caspase-1 pathway.

Methodology

Potential drug Target: The 3D structure of caspase-1, that plays a central role as an executor of the apoptotic process, is retrieved from PDB [28]. The crystal structure of the human caspase-1 in complex with malonate, determined by X-ray crystallography resolved at 1.80Å⁰ with PDB ID: 1SC3 was selected as a potential drug target.

Binding Site determination: To determine the interactions of methotrexate, 3',5'-dichloromethotrexate, ornithine-methotrexate and HA-drug conjugates such as HA-methotrexate, HA-3',5'-dichloromethotrexate and HA-ornithine-methotrexate with crystal structure of the human caspase-1, the potential binding pockets were predicted by submitting the co-ordinate file to DoGsite scorer [29]. The potential binding sites with predicted high drug score value was considered as potential binding site for further docking studies.

Drugs and HA-drug conjugates: The 3D structures of specified cancer drugs such as Methotrexate, 3',5'-Dichloromethotrexate and Ornithine-methotrexate were retrieved in SDF format from Pubchem database [30]. Further, the 2D structures of HA-drug

conjugates such as HA-Methotrexate, HA-3',5'-Dichloromethotrexate and HA-Ornithine-methotrexate were sketched by using ACD ChemsSketch and their respective 3D structures were converted into SDF by using 'Online Smiles translator'.

Molecular Docking: All the compounds in SDF file format were docked with the amino acids in the predicted binding pocket of human caspase-1 by using the following parameters [31]: (i) default docking information's; (ii) base placement using triangle matching; (iii) scoring of full score contribution and threshold of 0,30 and No score contribution and threshold of 0,70;(iv) chemical parameters of clash handling values for protein ligand clashes with

maximum allowed overlap volume of 2.9 Å³ and intralegend clashes with clash factor of 0.6 and considering the hydrogen in internal clash tests; and (v) default docking details values of 200 for both the maximum number of solutions per iteration and maximum number of solutions per fragmentation.

Ligand- Receptor Interactions: The interactions of the compounds Methotrexate, 3',5'-Dichloromethotrexate, Ornithine-methotrexate and HA-drug conjugates such as HA-Methotrexate, HA-3',5'-Dichloromethotrexate and HA-Ornithine-methotrexate with human caspase-1 in the docked complex were analyzed by the pose-view of LeadIT [32].

References

- [1] Murano E, Perin D, Khan R, Bergamin M. (2011) Hyaluronan: from biomimetic to industrial business strategy. *Natural Product Communications*, **6**, 555-572.
- [2] Khan R, Mahendhiran B, Aroulmoji V. (2013) Chemistry of hyaluronic acid and its significance in drug delivery strategies: A review. *International Journal of Pharmaceutical Sciences and Research*, **4**, 3699-3710.
- [3] Lapčík Jr L, Lapčík L, De Smedt S, Demeester J, Chabreck P (1998) Hyaluronan: preparation, structure, properties and applications. *Chemical Reviews*, **98**, 2663-2684.
- [4] Khan R, Bella J, Konowicz PA, Paoletti S, Vesnaver R, Linda P (1998) Selective acetylation reactions of hyaluronic acid. *Carbohydrate Research*, **306**, 137-146.
- [5] Khan R, Vesnaver R (1991) New derivatives of hyaluronic acid: Synthesis and characterization. *Ph.D Thesis*, University of Trieste, Italy.
- [6] Schanté CE, Zuber G, Herlin C, Vandamme TF (2011) Chemical modifications of hyaluronic acid for the synthesis of derivatives for a broad range of biomedical applications. *Carbohydrate Polymers*, **85**, 469-489.
- [7] Goodarzi N, Varshochian R, Kamalinia G, Atyabi F, Dinarvand R. (2013) A review of polysaccharide cytotoxic drug conjugates for cancer therapy. *Carbohydrate Polymers*, **92**, 1280-1293.
- [8] Laurent TC (1998) *The Chemistry, Biology and Medical Applications of Hyaluronan and its derivatives*. Cambridge University Press, Cambridge, UK
- [9] Davidson JM, Nanney LB, Broadley KN, Whitsett JS, Aquino AM, Beccaro M, Rastrelli A (1991) Hyaluronate derivatives and their application to wound healing: Preliminary observations. *Clinical Materials*, **8**, 171-177.
- [10] Lipponen P, Aaltoma S, Kosma V, Ala-Opas M, Eskelinen M (1998) Expression of CD44 standard and variant-v6 proteins in transitional cell bladder tumours and their relation to prognosis during a long term follow up. *Journal of Pathology*, **186**, 157-164.
- [11] Siegel R, Desantis C, Virgo K, Stein K, Mariotto A, Smith T, Cooper D, Gansler T, Lerro C, Fedewa S (2012) Cancer treatment and survivorship statistics. *CA: A Cancer Journal for Clinicians*, **62**, 220-241.
- [12] Tsurumi T, Fujita M, Kudoh A (2005) Latent and lytic Epstein-Barr virus replication strategies. *Reviews in Medical Virology*, **15**, 3-15.
- [13] Anand P, Kunnumakkara AB, Kunnumakara AB, Sundaram C, Harikumar KB, Tharakan ST, Lai OS, Sung B, Aggarwal BB. (2008) Cancer is a preventable disease that requires major lifestyle changes. *Pharmacological Research*, **25**, 2097-2116.
- [14] Kerr JF, Wyllie AH, Currie AR (1972) Apoptosis: a basic biological phenomenon with wide-ranging implications in tissue kinetics. *British Journal of Cancer*, **26**, 239-257.
- [15] Ferlay J, Shin HR, Bray F, Forman D, Mathers C, Parkin DM. (2010) Estimates of worldwide burden of cancer in 2008. *International Journal of Cancer*, **127**, 2893-2917.
- [16] Jemal A, Bray F, Center MM, Ferlay J, Ward E, Forman D. (2011) Global cancer statistics CA: *A Cancer Journal for Clinicians*, **61**, 69-90.
- [17] Torchilin V (2011) Tumor delivery of macromolecular drugs based on the EPR effect. *Advanced Drug Delivery Reviews*, **63**, 131-135.
- [18] Stapleton S, Allen C, Pintilie M, Jaffray DA. (2013) Tumor perfusion imaging predicts the intra-tumoral accumulation of liposomes. *Journal of Controlled Release*, **172**, 351-357.
- [19] Brigger I, Dubernet C, Couvreur P (2012) Nanoparticles in cancer therapy and diagnosis. *Advanced Drug Delivery Reviews*, **64**, 24-36.
- [20] Arpicco S, Milla P, Stella B, Dosio F. (2014) Hyaluronic acid conjugates as vectors for the active targeting of drugs, genes and nanocomposites cancer treatment. *Molecules*, **19**, 3193-3230.
- [21] Arpicco S, De Rosa G, Fattal E (2013) Lipid-based nano vectors for targeting of CD44-overexpressing tumor cells. *Journal of Drug Delivery* **860780**, 78-86.
- [22] Shi Y. (2004) Caspase activation. *Cell*, **117**, 855-858.
- [23] Romanowski MJ, Scheer JM, O'Brien T, McDowell RS. (2004) Crystal structures of a ligand-free and malonate-bound human caspase-1: implications for the mechanism of substrate binding. *Structure*, **12**, 1361-1371.
- [24] Akima K, Ito H, Iwata Y, Matsuo K, Watari N, Yanagi M, Hagi H, Oshima K, Yagita A, Atomi Y (1996) Evaluation of antitumor activities of hyaluronate binding antitumor drugs: Synthesis, characterization and antitumor activity. *Journal of Drug Targeting*, **4**, 1-8.
- [25] Benitez A, Yates TJ, Lopez LE, Cerwinka WH, Bakkar A, Lokeshwar VB. (2011) Targeting hyaluronidase for cancer therapy: Antitumor activity of sulfated hyaluronic acid in prostate cancer cells. *Cancer Research*, **71**, 4085-4095.
- [26] Mero A, Campisi M. (2014) Hyaluronic acid bioconjugates for the delivery of bioactive molecules. *Polymers*, **6**, 346-369.
- [27] Coradini D, Pellizzaro C, Miglierini G, Daidone MG, Perbellini A. (1999) Hyaluronic acid as drug delivery for sodium butyrate: Improvement of the anti-proliferative activity on a breast-cancer cell line. *International Journal of Cancer*, **81**, 411-416.
- [28] Berman HM, Westbrook J, Feng Z, Gilliland G, Bhat TN, Weissig H, Shindyalov IN, Bourne PE. (2000). The Protein Data Bank. *Nucleic Acids Research*, **28**, 235- 242.
- [29] Volkamer A, Kuhn D, Rippmann F, Rarey M. (2012) DoGSiteScorer: a web server for automatic binding site prediction, analysis and druggability assessment. *Bioinformatics*, **28**, 2074-2075.
- [30] Kim S, Thiessen PA, Bolton EE, Chen J, Fu G, Gindulyte A, Han L, He J, He S, Shoemaker BA, Wang J, Yu B, Zhang J, Bryant SH (2015) PubChem Substance and Compound databases. *Nucleic Acids Research*, **44**, D1202-13.
- [31] GnanendraShanmugam, Syed Mohamed, Jeyakumar Natarajan (2013) Identification of potent inhibitors for *Salmonella typhimurium* quorum sensing via virtual screening and pharmacophore modeling. *Combinatorial Chemistry & High Throughput Screening*, **16**, 826-839.
- [32] Rarey M, Kramer B, Lengauer T, Klebe G (1996) A fast flexible docking method using an incremental construction algorithm. *Journal of Molecular Biology*, **261**, 470-489.

See discussions, stats, and author profiles for this publication at: <https://www.researchgate.net/publication/319004696>

Identification of Potent Angiotensin Converting Enzyme 2 Inhibitors through Virtual Screening and Structure-Based Pharmacophore Design

Article in *International Journal of Advanced Science and Engineering* · January 2017

CITATION

1

READS

464

9 authors, including:



Zozimus Divya Lobo C

St.Mary's College , Thoothukudi, India

6 PUBLICATIONS 1 CITATION

[SEE PROFILE](#)



Syed Mohamed

Sadakathullah Appa College

29 PUBLICATIONS 34 CITATIONS

[SEE PROFILE](#)



Chinnapiyan Vedhi

V. O. Chidambaram College

114 PUBLICATIONS 1,297 CITATIONS

[SEE PROFILE](#)



S. V. Rajesh

Ramakrishna Mission Vivekananda College, Mylapore, Chennai

16 PUBLICATIONS 54 CITATIONS

[SEE PROFILE](#)

Some of the authors of this publication are also working on these related projects:



M.Sc Project [View project](#)



Synthesis, characterization and applications of metal oxide nanoparticles [View project](#)

Identification of Potent Angiotensin Converting Enzyme 2 Inhibitors through Virtual Screening and Structure-Based Pharmacophore Design

C. Zozimus Divya Lobo¹, A. Syed Mohamed^{1*}, C.Vedhi², S.V. Rajesh³, V. Aroulmoji⁴ and Gnanendra Shanmugam^{5*}

¹Department of Chemistry, Sadakathullah Appa College (Autonomous), Tirunelveli, Tamilnadu, India.

²Department of Chemistry, VOC College, Tuticorin, Tamilnadu, India

³Department of Botany, Vivekanandha college of Arts and Sciences (Autonomous), Tiruchengode, Namakkal, Tamilnadu.

⁴Center for Research & Development, Mahendra Educational Institutions, Namakkal-637503, Tamilnadu, India

⁵Department of Biotechnology, College of Life and Applied Sciences, Yeungnam University, Gyeongsan, South Korea.

ABSTRACT: Angiotensin Converting Enzyme (ACE), a metallo-peptidase is the best known important drug target in the treatment of hypertension and responds to broad range ACE inhibitors such as Captopril. Whilst, many phytochemical compounds including alkaloids and flavonoids were also reported with anti-hypertensive activity. On the other hand, ACE2 is considered as an interesting new cardio-renal disease target as it is close and unique ACE homologue. In this scenario, the anti-hypertensive activities of 17 phytochemical compounds were analyzed through docking studies with ACE2. Also, the other ACE inhibitors with reported IC₅₀ values were considered for docking interactions and used as training set. Further, the best docked phytochemical compound Rosemarinic acid and the training set compounds with ACE inhibitor activity were used to design the pharmacophore and validated. The generated 3D pharmacophore is subjected to screen the compounds with the significant chemical features against May bridged database consisting of more than one lakh compounds and subsequently, the hit compounds were screened using various filters such as estimated activity, Lipinski's rule of five, and ADMET properties and resulted Eight compounds. The anti-hypertensive activities of these 5 compounds with good fit values were selected for further docking studies with ACE2. The five compounds PD 00533, CD 01374, CD 04888, CD 01278 and BTB 04932 exhibited the best docking scores and also favors the necessary hydrogen bond interactions with in the activity site of ACE and thus identified as novel leads with anti-hypertensive activity.

KEYWORDS: Pharmacophore, Angiotensin Converting Enzyme, ACE inhibitors, ADMET, docking studies.

© 2015 mahendrapublications.com, All rights reserved

1. INTRODUCTION

Hypertension and congestive heart failures are becoming epidemic throughout the world [1]. In recent years, the drastic increase in the number in the adult population of the world with hypertension was recorded and more than 20 million people were affected with heart failure. Angiotensin-converting enzyme 2 (ACE2) is a newly discovered membrane-bound aminopeptidase [2]. This enzyme has been proven to be critical in impacting cardiovascular and immune systems by 2 distinct physiologically important mechanisms. ACE2 catalyzes the production of vasodilatory peptides, including angiotensin 1 to 7 and thus is responsible in counterbalancing the potent vasoconstrictor effects of angiotensin II. This counterbalancing property of ACE2 is proposed to be important for the development of novel pharmacotherapy against hypertension and related cardiovascular diseases [3-4]. In the process of hypertension, ACE plays an important role in regulating blood pressure, and ACE inhibitors are considered to be one of the therapeutic methods for treating anti-hypertension. Angiotensin-converting enzyme is secreted in the lungs and kidneys by cells in the endothelium of blood vessels, and it is the part of the renin-angiotensin system (RAS). It indirectly increases

blood pressure by causing blood vessels to constrict by converting angiotensin-I to angiotensin-II [5-6]. Thus, the ACE considered as an ideal target for controlling blood pressures and heart failures and synthetic compounds are being used as ACE inhibitors to treat heart problems. These inhibitors inhibit the conversion (angiotensin-I to angiotensin-II), dilate the blood vessels and control the blood pressures. Several ACE inhibitors, including captopril, lisinopril, fosinopril and enalapril, are synthetic molecules which are clinically used as anti-hypertension agents [7].

In 1990 Paul Ehrlich [8] introduced pharmacophore as 'a molecular framework that carries (phoros) the essential features responsible for a drug's (pharmacon) biological activity'. The design of pharmacophore are necessary to reveal specific functional group that are optimal for the interactions which can trigger the potential targets either by inhibiting or enhancing the biological function of those receptors [9]. The generation of pharmacophore plays a crucial role in the drug discovery pipeline in term of time and cost. The crucial step in the design of pharmacophore involves the alignment of multiple ligands (training set) which can determine the essential chemical features that are essential for their bioactivity. The alignment of these multiple ligand can be achieved by superposing a set of active molecules [10]. In general, the pharmacophore

*Corresponding Author: science@gmail.com & asm2032@gmail.com

Received: 12.05.2017

Accepted: 10.06.2017

Published on: 27.07.2017

Zozimus Divya Lobo et al.,

modelling involves the knowledge of two or more known active compounds. In this method, the known compounds (training set) are aligned and the commonly shared chemical entities are established common pharmacophore features [11]. These shared features of the training set compound are considered as the essential chemical entities. More commonly, the pharmacophore models are generated with the combination of known active and inactive compounds and been used to validate the models. Utmost care is taken while choosing the known active and inactive compounds for the training set, as they significantly influence the quality of the model [12]. Most preferably, the selection of inactive compounds in the training set is based on the activity low binding affinities and high IC₅₀ values to avoid the generation of inappropriate pharmacophore model. Ultimately, to achieve the good pharmacophore models, the training set should contain the structurally diverse set of compounds. Thus the present study is designed to explore the chemical features that ascertain the ACE inhibitors activity was put-forth through pharmacophore designing.

2. METHODOLOGY

Virtual Screening of AHL Analogue Library

The target ACE2 and selected ACE inhibitors were converted in to PDBQT files by using the PyRx software [13] for virtual screening studies. For docking purpose the grid was set to the predicted binding pocket of ACE2 as that inhibitors would have flexibility in binding. The ACE inhibitors were docked with ACE2 using AutoDock Vina option of PyRx. The docking was carried out using Lamarckian Genetic Algorithm and with parameters as follows: 10 docking trials, population size of 150, maximum number of energy evaluation ranges of 250000, maximum number of generations of 27,000, mutation rate of 0.02, cross-over rate of 0.8 and an elitism value of 1 [14]. The ACE inhibitors with the best docking score (binding energy) were used for the Pharmacophore modelling.

Pharmacophore modeling and 3D database Screening

The pharmacophore model was generated by using the Pharmacophore option of discovery studio software [15]. The best docked ACE inhibitor was used as training compound for the generation of a Pharmacophore by using option Auto Pharmacophore Generation which considers the Hydrogen bond acceptor (HB_ACCEPTOR), Hydrogen bond donor (HB_DONOR), Hydrophobic feature (HYDROPHOBIC), Negative ionizable feature (NEG_IONIZABLE), Positive ionizable feature (POS_IONIZABLE) and Aromatic ring (RING_AROMATIC) feature types to generate a selective pharmacophore model from a single ligand. The Principal value of 2 and the Maxis set to the Training ligand which ensures that all of the chemical features in the compound should be considered in building the pharmacophore space. The Auto Pharmacophore Generation option enumerates a set of candidate pharmacophore models from the features and chooses the pharmacophore with the highest selectivity as predicted by a Genetic Function Approximation (GFA) model. Using this generated pharmacophore hypothesis,

compound screening was performed against, Maybridge database [16] consisting of one lakh compounds and assessed the compounds matching the pharmacophore by considering the Fit Values.

Molecular Docking

The Top 5 obtained hits from Maybridge database with the highest Fit Value were docked with in the active site of ACE2 by using FlexX [17] with following parameters i) default general docking informations, ii) base placement using triangle matching, iii) scoring of full score contribution and threshold of 0,30 and No score contribution and threshold of 0,70. iv) chemical parameters of clash handling values for protein ligand clashes with maximum allowed overlap volume of 2.9 A³ and intra-ligand clashes with clash factor of 0.6 and considering the hydrogen in internal clash tests. v) default docking details values of 200 for both the maximum number of solutions per iteration and maximum number of solutions per fragmentation. Further, the interactions of database molecules with SdiA in the docked complex were analyzed by the pose-view of LeadIT.

3. RESULT AND DISCUSSION

Virtual Screening

The 3D structures of 24 ACE inhibitors as ligand compounds in SDF (structure data file) format are virtually screened to reveal their binding efficiencies through docking in the binding pockets of ACE2 receptor using FlexX module of LeadIT suite. Among these 24 compounds, 17 compounds (Figure.1) were the phytochemical with anti-hypertensive activities and 7 were the compounds with IC₅₀ values. The docking parameters such as triangle matching base placements, zero full score and No score contributions and threshold for full score and no score contributions of 30 and 70, respectively, Clash handling values of 2.9 A³ and 0.6 for protein ligand clashes with maximum allowed overlap volume and intra-ligand clash factors while considering the hydrogen in internal clash tests and 200 as the default docking values for maximum number of solutions per iteration and also per fragmentation [18].

Docking Interactions

The docking interactions that envisage the binding affinities of the lead compounds with the binding pockets amino acids in the modelled structures are analyzed by using pose-view module of LeadIT suite [19] which clearly picturizes the Hbond and non-bond interactions. Among these compounds the best docked phytochemical compound Rosemarinic acid (Figure.2) was selected for the further pharmacophore modelling studies.

Pharmacophore Modelling and Validation

The pharmacophore model is generated by using the pharmacophore module of Discovery Studio. The Pharmacophore hypothesis generation is achieved by using auto pharmacophore generation option in Discovery Studio which considers the chemical feature types such as the hydrogen bond acceptor (HB_ACCEPTOR), hydrogen bond donor (HB_DONOR),

Zozimus Divya Lobo et al.,

hydrophobic feature (HYDROPHOBIC), negative ionizable feature (NEG_IONIZABLE), positive ionizable feature (POS_IONIZABLE) and aromatic ring (RING_AROMATIC) for the selected ligand. The ten pharmacophore models are generated by using Common Feature pharmacophore Model Generation protocol in Discovery studio. For a statistically

significant pharmacophore model, correlation coefficient and root mean square deviation (RMSD) are calculated [20]. The best pharmacophore model was selected based on the high correlation coefficient and lower RMSD. The generated pharmacophoric features based on the Rosemarinic acid is shown in figure.3.

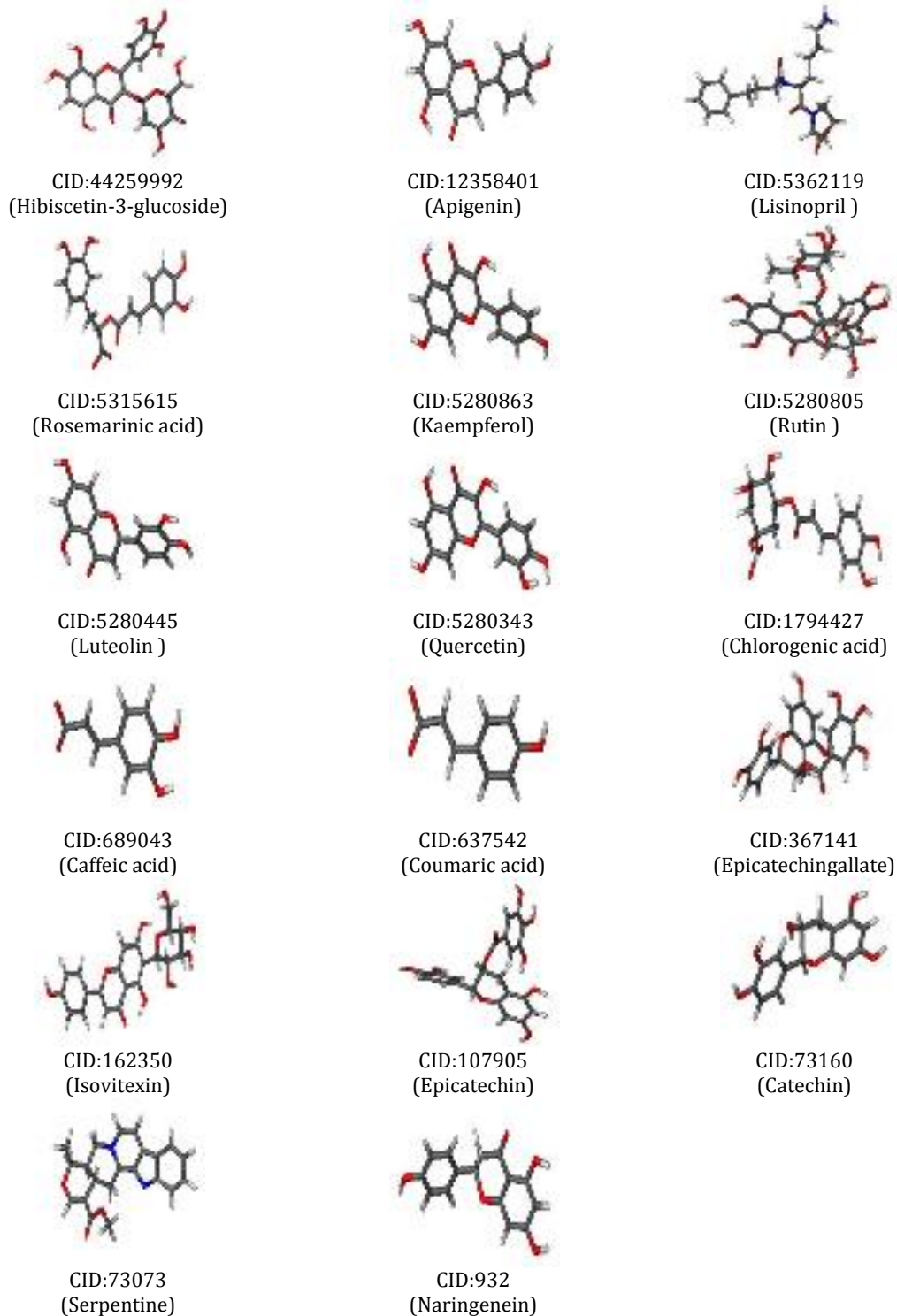


Figure.1: The 17 phytochemical compounds used in the study for the pharmacophore generation

Zozimus Divya Lobo et al.,

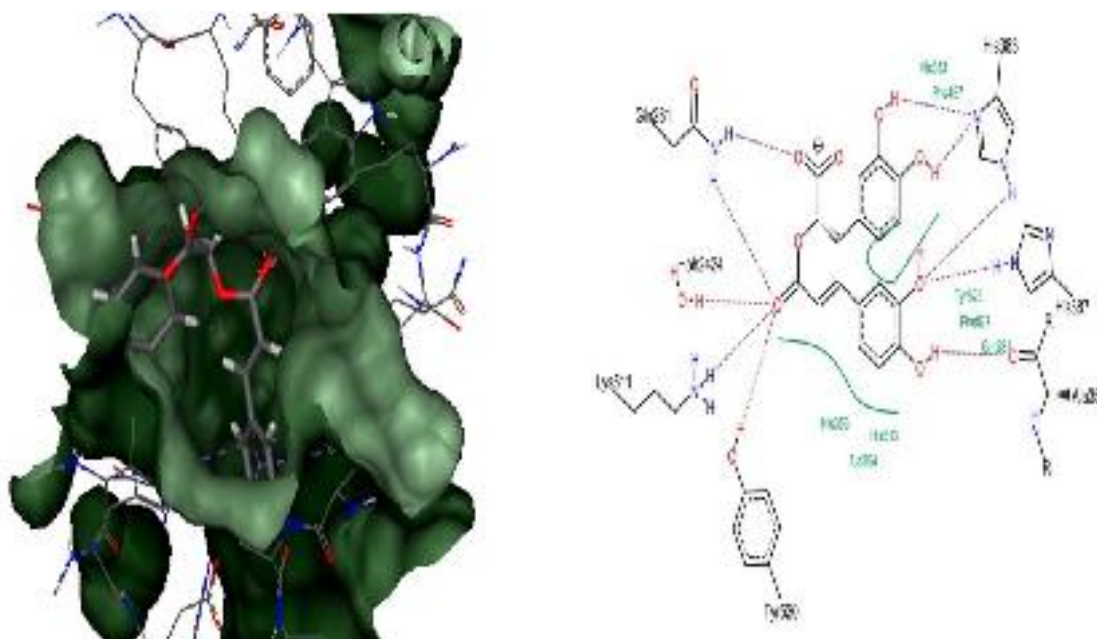


Figure.2 Docking complex and interactions of Rosemarinic acid (CID: 5315615) (-34.6473 kJ/mol)

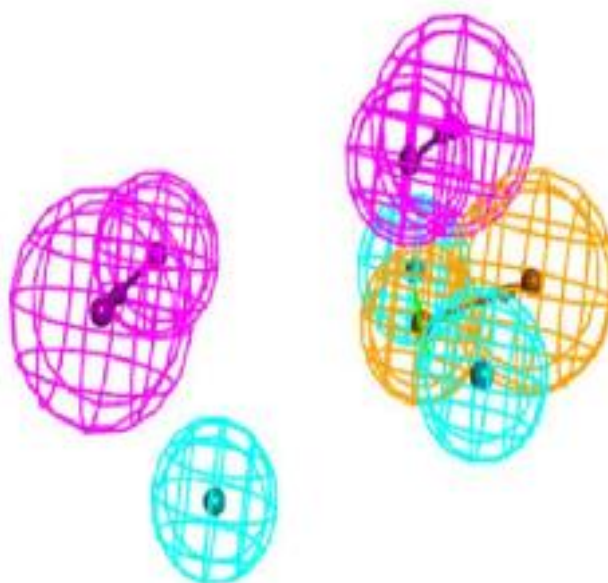


Figure.3: Generated Pharmacophore based on the Rosemarinic acid Hydrogen bond acceptor (green); Hydrogen bond donor (magenta) Hydrophobic (cyan) ; Ring aromatic (orange)






Compound	Mapped Pharmacophore	Fit value
PD 00533		4.66957
CD 01374		3.86604
CD 04888		2.56234
CD 01278		2.54782
BTB 04932		1.89542

Figure.4: Maybridge compounds mapped against the generated pharmacophore and their fit values

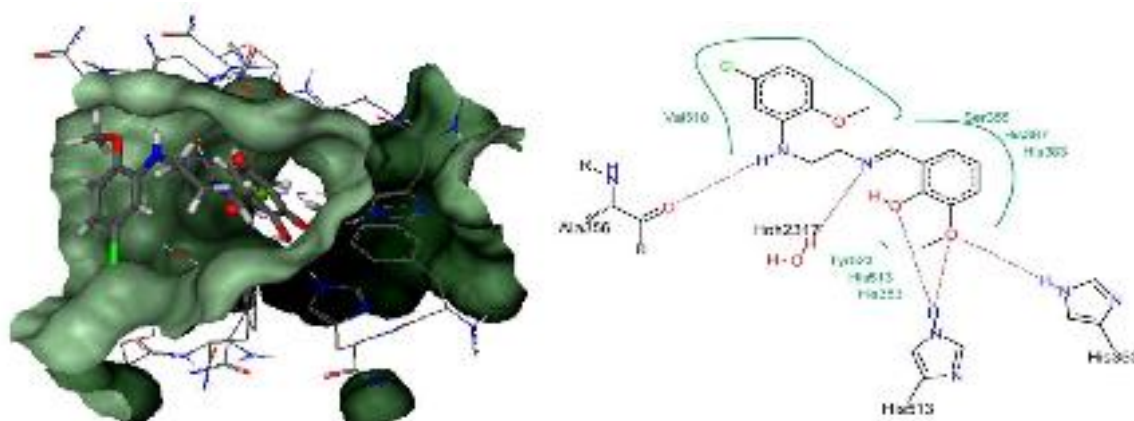


Figure.5: Docking complex and interactions of PD 00533 (-38.4372 kJ/mol)

Zozimus Divya Lobo et al.,

Table.1: Maybridge compounds with the fit values and docking scores

Compound	Fit value	Docking score
PD 00533	4.66957	-38.4372
CD 01374	3.86604	-34.5687
CD 04888	2.56234	-32.5624
CD 01278	2.54782	-30.4587
BTB 04932	1.89542	-28.25687

3D Database Screening

Search 3D Database screening protocol with best search option implemented in DS is used for database screening against Maybridge database consisting of more than one lakh compounds. The obtained database hits is screened using various filters such as estimated activity, Lipinski's rule of five [21], and ADMET properties [22]. The final hit compounds after filtering are known as hit list and ranked according to the fit value, which is the degree of consistency with the pharmacophore model. To decrease the number of hits, a minimum fit value of >3, which is the lowest limit to qualify as a hit compound, is applied. This lower limit of fit value is chosen according to the fit value obtained from the active molecule. The molecules with good fit scores are selected for further docking studies. The generated 3D pharmacophore is subjected to screen the compounds with the significant chemical features against May bridged database, exhibited 5 potential compounds that matches the generated pharmacophore. The five MayBridge Database compound, PD 00533, CD 01374, CD 04888, CD 01278 and BTB 04932 exhibited the best docking scores and also favors the necessary hydrogen bond interactions with in the activity site of ACE and thus identified as novel leads with anti-hypertensive activity. These Hits are defined as those compounds that possess chemical functionalities that spatially overlap with corresponding features within the pharmacophoric model. The hits were subsequently fitted against the pharmacophore and assessed by Fit Value (Figure.4).

Molecular Docking

The Top 5 obtained compounds PD 00533, CD 01374, CD 04888, CD 01278 and BTB 04932 were docked with in the active site of ACE2, and their docking interactions with their binding energies along with their pharmacophoric fit values were tabulated (Table.1). Among the obtained 5 hits from maybridge database, the compound PD 00533 exhibited the highest docking score of -38.4372 kJ/mol (Figure.5). The docking studies implies that the amino acids Alanine (Ala356), Histidine (His 513 and 353) and Water molecule (Hoh 2317) in the binding pockets of ACE are vital in posing the better binding interaction with the maybridge screened compound (PD 00533). While the non bonded interactions are favoured by Valine (Val518), Serine (Ser355), Histidine (His 353,387,383 and 513). These docking interactions also envisages that the =O (keto group) present in the compounds and NH (amino group)

on the amino acids favors the Hbond interactions. Thus the pharmacophoric design and 3D database search along with the docking studies revealed that the May Bridge compound PD00533 having the better binding energy of -38.4372 kJ/mol might have a better inhibition activity against the ACE2 receptor.

4. CONCLUSION

The ACE2, a metallo-peptidase is considered as a interesting cardio-renal disease target and is the best known important drug target in the treatment of hypertension that responds to Captopril. Alternatively many phytochemical compounds with their anti-hypertensive activities were also reported. In this study, the 17 phytochemical compounds and 7 other ACE inhibitors with reported IC₅₀ values were considered for docking interactions and used as training set to design the pharmacophore and validated. The best docked phytochemical compound Rosemarinic acid has resulted in the generation of 3D pharmacophore is used to screen against May bridged database. The hit compounds were screened using various filters such as estimated activity, Lipinski's rule of five, and ADMET properties and resulted five compounds PD 00533, CD 01374, CD 04888, CD 01278 and BTB 04932 with best fit values and also the best docking scores. This compound also favors the necessary hydrogen bond interactions with in the activity site of ACE and thus identified as novel leads with anti-hypertensive activity.

REFERENCES

- [1]. McMurray JJ, Petrie MC, Murdoch DR, Davie AP 1998. Clinical epidemiology of heart failure: public and private health burden. *Eur Heart J*. 19 (Suppl P):P9-P16.
- [2]. Turner AJ, Hooper NM 2002. The angiotensin-converting enzyme gene family: genomics and pharmacology. *Trends Pharmacol Sci*. 23:177-183.
- [3]. Ishiyama Y, Gallagher PE, Averill DB, Tallant EA, Brosnihan KB, Ferrario CM 2004. Upregulation of angiotensin-converting enzyme 2 after myocardial infarction by blockade of angiotensin II receptors. *Hypertension*. 43:970-976.
- [4]. Donoghue M, Wakimoto H, Maguire CT, Acton S, Hales P, Stagliano N, Fairchild-Huntress V, Xu J, Lorenz JN, Kadambi V, Berul CI, Breitbart RE 2003. Heart block, ventricular tachycardia, and sudden death in ACE2 transgenic mice with down-

- regulated connexins. *J Mol Cell Cardiol.* 35:1043-1053.
- [5]. Skeggs LT, Jr, Kahn JR, Lentz K, Shumway NP 1957. The existence of two forms of hypertensin. *J Exp Med.* 99: 275-282.
- [6]. Skeggs LT, Dorer FE, Kahn JR, Lentz KE, Levine M 1976. The biochemistry of the renin-angiotensin system and its role in hypertension. *Am J Med.* 60: 737-748
- [7]. Vázquez-Valadez VH, Abrego VH, Martínez PA, Torres G, Zúñiga O, Escutia D, Vilchis R, Velazquez AM, Martinez L, Ruiz M, Camacho B, Lopez-Castanares R, Angeles E 2013. Docking Studies of Methylthiomorpholin Phenols (LQM300 Series) with Angiotensin-Converting Enzyme (ACE). *The Open Medicinal Chemistry Journal*, 7: 30-38.
- [8]. Ehrlich P 1909. Ueber den jetzigen Stand der Chemotherapie. *Ber. Dtsch. Chem. Ges.* 42, 17-47.
- [9]. Sheng-Yong Yang 2010 Pharmacophore modeling and applications in drug discovery : challenges and recent advances *Drug discovery Today*, 15:444-450.
- [10]. Van Drie JH 2004. Pharmacophore discovery: a critical review. In *Computational Medicinal Chemistry for Drug Discovery* (Bultinck, P., ed.), pp. 437-460, Marcel Dekker.
- [11]. Poptodorov K 2006. Pharmacophore model generation software tools. In *Pharmacophores and Pharmacophore Searches* (Langer, T. and Hoffmann, R.D., eds): 17-47, Wiley-VCH
- [12]. Mutasem O Taha, Amal G Al-Bakri and Waleed A Zalloum 2006. Discovery of potent inhibitors of pseudomonas quorum sensing via pharmacophore modeling and in silico screening, *Bioorganic & Medicinal Chemistry Letters*, 16 : 5902-5906.
- [13]. Wolf LK. Digital briefs: New software and websites for the chemical enterprise. *C&EN.* 2009;87:32
- [14]. Gnanendra Shanmugam, Syed Mohamed, Jeyakumar Natarajan 2013. Identification of potent inhibitors for Salmonella typhimurium quorum sensing via virtual screening and pharmacophore modeling, *Combinatorial Chemistry & High Throughput Screening*, 16 (10): 826 - 839.
- [15]. Accelrys Software Inc., 2011. *Discovery Studio Modeling Environment, Release 2.5*, San Diego: Accelrys Software Inc.,.
- [16]. Maybridge Database www.maybridge.com/
- [17]. Rarey M, Kramer B, Lengauer T, Klebe G 1996. A fast flexible docking method using an incremental construction algorithm. *J Mol Biol.* 261:470-89.
- [18]. Gnanendra Shanmugam, Anusuya Shanmugam, Natarajan Jeyakumar 2012. Molecular modeling and active site analysis of SdiA homolog, a putative quorum sensor for Salmonella typhimurium pathogenicity reveals specific binding patterns of AHL transcriptional regulators, *J Mol. Model.*, 18 (10): 4709 - 4719.
- [19]. Stierand K, Maab P, Rarey M 2006. Molecular Complexes at a Glance: Automated Generation of two-dimensional Complex Diagrams. *Bioinformatics.* 22: 1710-1716.
- [20]. Sanam R, Vadivelan S, Tajne S, Narasu L, Rambabu G, Jagarlapudi SA 2009. Discovery of potential ZAP-70 kinase inhibitors: Pharmacophore design, database screening and docking studies. *Eur. J. Med. Chem.*, 44, 4793-4800.
- [21]. Lipinski CA, Lombardo F, Dominy BW, Feeney PJ 2001. Experimental and computational approaches to estimate solubility and permeability in drug discovery and development settings. *Adv. Drug Del. Rev.*, 46, 3-26.
- [22]. Walters WP, Murcko MA 2002. Prediction of 'drug-likeness'. *Adv. Drug. Deliv. Rev.*, 54: 255-271.



Share Your Innovations through JACS Directory

Journal of Nanoscience and Technology

Visit Journal at <http://www.jacsdirectory.com/jnst>

ISSN: 2455-0191



Influence of pH and Temperature on The Structure and Size of Tin Oxide Nanoparticles

I. Merlin^{1,2}, C.Vedhi³, K. Muthu⁴, A. Syed Mohamed^{5,*}

¹Research Scholar (Reg No: 8162), Department of Chemistry, Sadakathullah Appa College, Affiliated to Manonmaniam Sundaranar University, Abisekapatti, Tirunelveli – 627 012, Tamilnadu, India.

²Department of Nanoscience, Sarah Tucker College, Tirunelveli – 627 007, Tamilnadu, India.

³Department of Chemistry, V.O. Chidambaram College, Thoothukudi – 628 008, Tamilnadu, India.

⁴Department of Chemistry, Manonmaniam Sundaranar University, Abisekapatti, Tirunelveli – 627 012, Tamilnadu, India.

⁵Research Dept. of Chemistry, Sadakathullah Appa College, Tirunelveli – 627 011, Tamilnadu, India.

ARTICLE DETAILS

Article history:

Received 3 November 2018

Accepted 29 November 2018

Available online 22 December 2018

Keywords:

Tin Oxide

Nanoparticles

Semiconductor

ABSTRACT

A systematic study on the preparation of tin oxide nanoparticles using the precipitation method has been conducted. The preparation of nanomaterials was by varying reaction parameters such as pH and temperature. The tin oxide nanoparticles were characterized by using AFM, SEM, XRD and UV-Vis. Particle size was obtained using XRD studies the value is 28.8 nm, 35.2 nm, 30.8 nm and 33.8 nm. It was found that the alteration of pH and temperature changes the particle size.

1. Introduction

Nanoparticles have attracted great interest due to their intriguing properties, which are different from those of their corresponding bulk state. Enormous efforts are being taken towards the development of nanometer sized materials in studies related to one hand to their fundamental mechanism such as the size effect and the quantum effect and on the other hand towards application of these materials. The morphology of obtained materials is highly dependent on the chosen method, enabling to obtain nanoparticles, nanowires, nanorods, and other morphologies [1]. Tin oxide (SnO₂) is an n-type semiconductor with excellent optical and electrical properties, partly due to its wide band gap (E_g = 3.6 eV). In sensor research, many semiconducting metal oxides are used of which tin oxide is the most widely studied and employed owing to its physicochemical properties [2].

Nano-sized tin oxide is regarded as a highly preferred multitasking metal oxide such as gas sensors and lithium rechargeable batteries. The transparent conducting oxide (TCOs) materials has been widely used for various optoelectronic devices, flat panel displays, liquid crystal displays, organic light emitting diodes, solar cells and etc. It has specific properties and advantages of high sensitivity, including conductivity, transparency in the visible region in addition to mechanical and chemical stabilities. However, thermal treatments lead to an increase of the average grain size, spreading of the grain size distribution, and changes in the phase composition with increasing annealing temperature [3]. Among various classes of Nanoparticles (Metals, Semiconductors and Insulators), semiconductor particles have attracted more interests because of their size-dependent optical & electrical properties [4]. This study attempts to provide some findings to this research area [5]. Chemical sensors have played very important roles in the detection of pollutant, toxic, and industrially important gas species such as NO_x, NH₃, CO_x, H₂ and ethanol. The study of dielectric properties and a.c. electrical conductivity throws light on the behaviour of charge carriers under an a.c. field, their mobility and the mechanism of conduction. Tin oxide nanoparticles are suitable for gas sensing applications due to high surface to volume ratio, compared to bulk tin oxide [6]. The associated challenge with chemical precipitation

methods is; when the product is calcined at high temperatures the crystallite size increases and the surface area decreases due to the particle growth [7]. Tin oxide has been used as solid state sensor mainly due to its sensitivity towards different gaseous species, photovoltaic energy conversion to make indium tin dioxide (ITO) transparent thin film coatings, etc., [8]. Tin oxide is an important oxide semiconducting material, which has been widely used in many applications such as catalysts agent, hazardous gas sensors, heat reflecting mirrors, varistors, transport conducting electrodes for solar cells and optoelectronic devices. Recent studies have shown that many fundamental physical or chemical properties of semiconductor materials strongly depend on the size and morphology of the materials [9]. Many processes have been developed to synthesis tin oxide nanostructures, e.g., spray pyrolysis, hydrothermal methods, chemical vapour deposition, thermal evaporation of oxide powders and sol-gel method. Annealing the SnO₂ nanoparticles prepared adding hydrochloric acid improved the crystallite size [10]. In the present work the fabrication and characterization of crystalline tin oxide nanoparticles powders by chemical precipitation method.

2. Experimental Methods

2.1 Chemical Precipitation Method

About 6 g (0.1 M) of stannous chloride dehydrate (SnCl₂·2H₂O) was dissolved in 300 mL of distilled water. After complete of dissolution, the ammonia solution was added to the above solution by drop wise under stirring. The pH is measured and it was adjusted to 11. The particles were then allowed to settle down at the bottom of the flask. The resulting gels were filtered and dried at 80 °C for 24 hours. The obtained product was heated to the temperature of 500 °C and 600 °C for 2 hours. The same procedure was repeated by changing the pH=9 also. The final obtained product was white tin oxide nano powder.

3. Results and Discussion

3.1 AFM Analysis

The atomic force microscope (AFM) was ideally suited for characterization of nanoparticles. It offers the capability of 3D visualization and both qualitative and quantitative information on many

*Corresponding Author: asm2032@gmail.com (A. Syed Mohamed)

physical properties including size, morphology, surface texture and roughness. A wide range of particle sizes can be characterized in the same scan, from 1 nanometer to 8 micrometers. In addition, the AFM can characterize nanoparticles in multiple media ambient air, controlled environments and even in liquid dispersions. Resolution of AFM for SnO₂ sample was 300x300 pixels. The sample was analyzed in non-contact mode with nominal diameter of tip 10 nm.

The height of the nanoparticles roughness can be measured by atomic force microscope. Figs. 1(a, b) show tin oxide nanoparticles of maximum height 40 nm prepared in pH=8.0 at 500 °C and 100 nm prepared at 600 °C. Figs. 1(c, d) present the prepared tin oxide nanoparticles of maximum height 50 nm and 200 nm in pH=10.0 at 500 °C and 600 °C respectively.

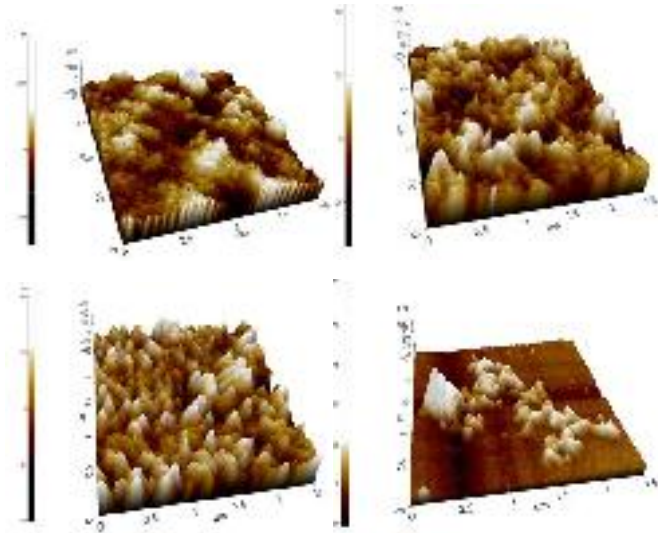


Fig. 1 AFM image of tin oxide nanoparticles prepared at pH=8 and pH=10 a) 500 °C, b) 600 °C and c) 500 °C d) 600 °C respectively

3.2 SEM Study

Scanning electron microscope (SEM) was used for the morphological study of tin oxide nanoparticles. Figs. 2(a-d) show SEM image of tin oxide nanoparticles. In Fig. 2a (pH=8, 500 °C) cauliflower like morphology structure can be seen. In Fig. 2b (pH=8, 600 °C) spherical like morphology structure was observed. In Fig. 2c (pH=10, 500 °C), highly porous foam like structure is observed and Fig. 2d (pH=10, 600 °C) few agglomeration has been observed. The particle sizes and the structures are varied due to the change in the reaction parameters such as pH and temperature.

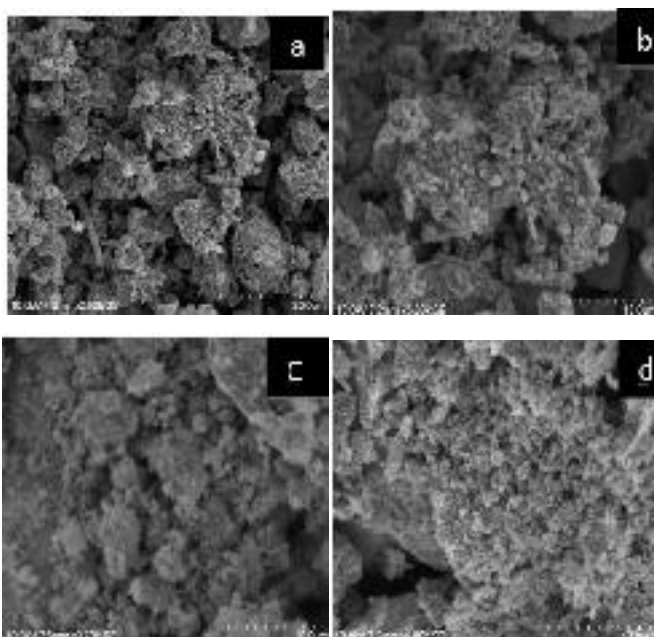


Fig. 2 SEM images of tin oxide nanoparticles prepared at pH=8 and pH=10 a) 500 °C, b) 600 °C and c) 500 °C d) 600 °C respectively

3.3 XRD Analysis

In order to determine the size and structural properties of the synthesized tin oxide nano particles, the powdered XRD analysis was performed. Structural identification of SnO₂ nanoparticles were carried out with X-ray diffraction in the range of angle 2θ between 10° to 80°. Moreover, a sharper and higher relative intensity peaks at higher reaction temperature was attributed to highly crystallinity of SnO₂ NSs as the degree of crystallinity increase with reaction temperature [11]. Figs. 3(a-d) show XRD patterns for tin oxide nanoparticles, which was crystalline in nature. The diffraction peaks are markedly broadened, which indicates the crystalline. XRD spectrum of tin oxide nanoparticles sizes of samples are very small. According to the Debye-Scherrer's equation [12], $D = 0.9\lambda / \beta \cos \theta$, where λ is the wavelength, β is the width of half maximum of the diffraction peak and θ is Bragg diffraction angle. Fig. 3 shows the average crystalline size calculated using Scherrer formula are 28.77 nm, 35.19 nm, 30.82 nm and 33.8 nm respectively.

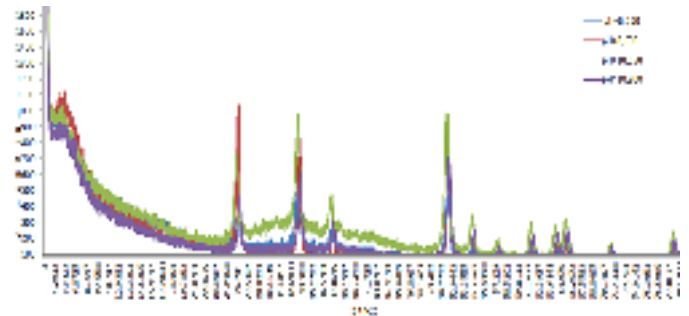


Fig. 3 XRD spectrum of tin oxide nanoparticles prepared at pH=8 & 10 at 500 °C, 600 °C respectively

3.4 UV Analysis

The size of the nanoparticles plays an important role in changing the entire properties of materials. Thus, size evolution of semiconducting nanoparticles becomes very essential to explore the properties of the materials. UV-visible absorption spectroscopy is widely being used technique to examine the optical properties of nanosized particles. Absorption bands confirm the formation of the tin oxide nanoparticles. Fig 4 shows that peaks were observed at 403 nm at 500 °C and 407 nm at 600 °C in pH=8.0, 410 nm for 500 °C and 413 nm for 600 °C in pH 10.0.

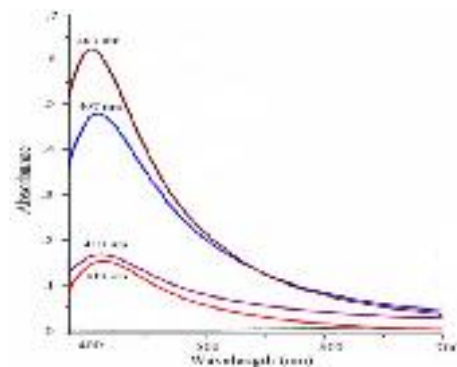


Fig. 4 UV spectrum of tin oxide nanoparticles prepared at pH=8 & 10 at 500 °C, 600 °C respectively

4. Conclusion

Tin oxide nanoparticles have been synthesized using chemical precipitation method. The resulting product was crystalline with agglomeration and hence more surface area. Surface morphology was studied using SEM and crystalline size calculated using XRD of tin oxide nanoparticles showed different structures and sizes due to variation in reaction parameters such as pH and temperature. The surface roughness of the tin oxide nanoparticles were also measured using AFM. The maximum absorbance were observed at 403 nm at 500 °C and 407 nm at 600 °C in pH=8.0, 410 nm for 500 °C and 413 nm for 600 °C in pH 10.0 by UV-vis absorption spectrum. Also, the process used the economically lower cost chemical, tin (II) chloride as the precursor. The present study provides inexpensive and easy method to improve the quality of tin oxide nanoparticles. Thus, this synthesis method is fast, simple, convenient and feasible on industrial scale to synthesize SnO₂ nanomaterial. The possible applications of SnO₂ nanoparticles are in gas sensor, solar cells, optoelectronic devices, paint industry, and surface coating industry.

References

- [1] F.M.B. Oliveira, J.A. Varela, M.O. Orlandi, Influence of pH in obtaining indium tin oxide nanoparticles by microwave assisted solvothermal method, *Mater. Res.* 21(2) (2018) 1516-1439.
- [2] Olga Rac, S.W. Patrycja, F. Marta, Influence of stabilising agents and pH on the size of SnO₂ nanoparticles, *Beilstein J. Nanotech.* 5 (2014) 2192–2201.
- [3] L. Jiang, G. Sun, Z. Zhou, S. Sun, et al., Size-controllable synthesis of monodispersed SnO₂ nanoparticles and application in electrocatalysts, *J. Phys. Chem. B* 109 (2005) 8774-8778.
- [4] R. Sudha Periathai, J. Pandiarajan, N. Jeyakumaran, N. Prithivikumaran, Role of temperature on the properties of SnO₂ nanoparticles synthesised by Sol-Gel Process, *Int. J. ChemTech Res.* 6 (2014) 2132-2134.
- [5] F. Boran, S. Çetinkaya, M. Şahin, Effect of surfactant types on the size of tin oxide nanoparticles, *Acta Phys. Polonica A* 132(3) (2017) 546-548.
- [6] S. Tazikeh, A. Akbari, A. Talebi, E. Talebi, Synthesis and characterization of tin oxide nanoparticles via the co-precipitation method, *Mater. Sci. Poland* 32(1) (2014) 98-101.
- [7] A. Gaber, M.A. Abdel-Rahim, A.Y. Abdel-Latif, M.N. Abdel-Salam, Influence of calcination temperature on the structure and porosity of nanocrystalline SnO₂ synthesized by a conventional precipitation method, *Int. J. Electrochem. Sci.* 9 (2014) 81-95
- [8] A.K. Singh, U.T. Nakate, Microwave synthesis, characterization and photocatalytic properties of SnO₂ nanoparticles, *Adv. Nanopart.* 3 (2012) 66-70.
- [9] R. Padmavathy, K.V. Rajendran, Influence of surfactants on the synthesis of SnO₂ nanoparticles and nanorods, *A Zojomo* 6 (2009) 1-6.
- [10] S. Mohana Priya, A. Geetha, K. Ramamur, Structural, morphological and optical properties of tin oxide nanoparticles synthesized by sol-gel method adding hydrochloric acid, *J. Sol-Gel Sci. Technol.* 78 (2016) 365-372.
- [11] M.A.M. Akhira, K. Mohameda, H.L. Lee, S.A. Rezanc, Synthesis of tin oxide nanostructures using hydrothermal method and optimization of its crystal size by using statistical design of experiment, *Proc. Chem.* 19 (2016) 993-998.
- [12] P. Manisankar, C. Vedhi, G. Selvanathan, Synthesis of nano size copolymer of 3,4-ethylenedioxythiophene with diclofenac and characterization, *J. Polym. Sci. A: Polym. Chem.* 45(13) (2007) 2787-2796.

See discussions, stats, and author profiles for this publication at: <https://www.researchgate.net/publication/325761645>

Structure-Based Pharmacophore Design and Natural Bond orbital analysis of Angiotensin Converting Enzyme inhibitors

Article in *International Journal of Current Research in Science Engineering & Technology* · April 2018

DOI: 10.30967/ijcrset.1.2.2018.10-21

CITATIONS

0

READS

89

3 authors:



Zozimus Divya Lobo C

St. Mary's College , Thoothukudi, India

6 PUBLICATIONS 1 CITATION

[SEE PROFILE](#)



Syed Mohamed

Sadakathullah Appa College

29 PUBLICATIONS 34 CITATIONS

[SEE PROFILE](#)



Chinnapiyan Vedhi

V. O. Chidambaram College

114 PUBLICATIONS 1,297 CITATIONS

[SEE PROFILE](#)

Some of the authors of this publication are also working on these related projects:



MEDICINAL CHEMISTRY [View project](#)



Nano-material synthesis [View project](#)

Structure-Based Pharmacophore Design and Natural Bond orbital analysis of Angiotensin Converting Enzyme inhibitors

Zozimus Divya Lobo C^a, Syed Mohamed A^{b*} and Vedhi C^c

^aDepartment of Chemistry, St.Mary's College (Autonomous), Thoothukudi, Tamilnadu, India.

^bDepartment of Chemistry, Sadakathullah Appa College (Autonomous), Tirunelveli, Tamilnadu, India.

^cDepartment of Chemistry, VOC College, Tuticorin, Tamilnadu, India.

Received: 02 March 2018; Revised: 29 March 2018; Accepted: 04 April 2018; Published online: 07 April 2018;

ABSTRACT: Hypertension and congestive heart failures are becoming epidemic throughout the world. Angiotensin Converting Enzyme (ACE), a metallo-peptidase is the best known important drug target in the treatment of hypertension and responds to broad range ACE inhibitors such as Captopril. Though there are many synthetic drugs that are being used as ACE inhibitors, the usage of natural compounds has its significance with less adverse effects. In this regard, many phytochemical compounds including alkaloids and flavonoids has been reported with anti-hypertensive activity. In this connections, the present study is focused on determining the anti-hypertensive actively of certain phytochemical compounds and synthetic drugs through docking studies and to explore their pharmacophoric features. The docking study implies that rosmarinic acid was relatively better that that of Standard drugs Lisinopril and Captopril. The pharmacophore modelling, validation and screening studies on rosmarinic acid along with Lisinopril and Captopril resulted in two compounds from Maybridge compound database (CD 01374 and CD 01278). Also the Density function theory (DFT) studies on these compounds explained the charge transfer (HOMO-LUMO energy gap of 2.90 eV) interactions that are taking place within the molecule through strong N-H...N and N-H...O hydrogen bonding is essential for the bioactivity of these compounds. Thus the finding of this study clearly emphasized that the rosmarinic acid could significantly possess better ACE inhibition activity and could be an alternative therapeutic agent to replace the drugs with severe side effects.

Keywords: Angiotensin Converting Enzyme; ACE inhibitors; Pharmacophore; Lisinopril; Captopril; rosmarinic acid;

1. INTRODUCTION

In recent years, cardiovascular diseases have become a serious problem worldwide. The World Health Organization has reported an increase in the number of patients suffering from this disease. Currently, existing treatments for high blood pressure are not very effective and are generally uncomfortable for patients. This relies in that the patient need to have a very strict control in the dosage and in the moment of the administration of the drug [1]. And also some patients have an unfavorable response after the administration, leading them to a fast blood

pressure reduce. One of the most widely used compounds for the treatment of hypertension is captopril. Like many others on the market, this drug was designed with computational tools. Over the last few decades, computational studies, together with rational drug design, have become a critical part in the development of new drugs. Currently, cardiovascular diseases are a serious health problem worldwide. One example of cardiovascular disease is arterial hypertension, which is defined as increased systolic pressure, diastolic pressure, or both [2].

Hypertension is a silent, asymptomatic disease, and as a result, not many people know that they suffer from it. Hypertension is an important risk factor, contributing to other cardiovascular diseases such as blood vessel disorders, coronary heart disease, aortic aneurysm, stroke, etc [3]. Cardiac arrhythmia is another cardiovascular problem. An arrhythmia is any disorder of the heart rate that may cause stroke. Heart rhythm disorders may be caused by genetic factors or occur when the heart muscle (myocardium) is damaged, sometimes by hypertension [4]. Raised blood pressure, especially systolic pressure (hypertension), confers a significant cardiovascular risk and

Correspondence

Sayed Mohamed A; asm2032@gmail.com

Competing interests

The authors have declared that no competing interests exist.

DOI: 10.30967/ijcset.1.2.2018.10-21

Cite this article

Zozimus Divya Lobo, C., Syed Mohamed, A., & Vedhi, C. (2018). Structure-Based Pharmacophore Design and Natural Bond orbital analysis of Angiotensin Converting Enzyme inhibitors. *Int J Cur Res Eng Sci Tech*, 1(2), 10-21.

Copyright

© 2018 Zozimus Divya Lobo et al. This is an open access article distributed under the terms of the Creative Commons Attribution License.

public health concern and should be actively treated.

One of the major systems involved in the elevation of the pressure is the renin-angiotensin system (RAS) and subsequently its inhibition will have beneficial effects to lower blood pressure and improve cardiovascular health [5]. The RAS is regulated by a series of highly specific enzymatic reactions. The first enzymatic reaction in the pathway starts with renal production of renin that cleaves angiotensinogen to generate angiotensin I. Angiotensin I is then cleaved by angiotensin-converting enzyme (ACE) to generate the active peptide vasoconstrictive hormone angiotensin II.

In the last three decades, several intensive efforts have been conducted into researching the antihypertensive therapeutic values of medicinal plants [6-8]. While compared to allopathic treatment, medicinal and bioactive plants have become a vital resource for the treatment of heart problems [9]. Nearly 80% of the global population including many developed and developing countries prefers to use natural medicines, due to their minimal side effects and better usage ability of humans [10]. In this scenario, the present study was emphasized to provide the insights of alkaloid from various medicinal plant source and to explore their binding mechanism within the active site of ACE, explore the chemical features that ascertain the ACE inhibitors activity through pharmacophore designing and to understand the chemical entities through DFT studies which might pave path to design of novel ACE inhibitors with potential inhibition activity.

2. METHODOLOGY

2.1 Target Selection

The X-ray Crystal Structure of Human Angiotensin Converting Enzyme complexed with Lisinopril (PDB ID: 1O86) [11] was retrieved from Protein Databank [12]. The protein energy was minimized through 20 steps of steepest descent and conjugate gradient by using GROMOS [13] of SwissPDBviewer and final energy minimized model used for further Docking studies.

2.2 Ligand selection

The SMILES notation of eighteen phytochemical compounds including alkaloids and flavonoids from various medicinal plants were obtained by drawing their 2D structures in ACD-Chemsketch (Version 12) (www.acdlabs.com). The 3D structures of these compounds were generated and converted into SDF format by using 'Online SMILES convertor and Structure file generator' server [14].

2.3 Binding site prediction

The amino acid residues in binding site of ACE protein are defined by using the reference Ligand of Angiotensin

Converting Enzyme complexed with Lisinopril [11]. The acid residues within 6 Å radius of reference Ligand was included in the predicted binding site by using LeadIT (Version 2.1.9) [15].

2.4 Virtual Screening

The 3D structures of all the selected eighteen phytochemical compounds and two ACE inhibitors were virtually screened to reveal their binding efficiencies through docking in the predicted binding site of ACE using FlexX [16] module of LeadIT. The docking was performed with the default parameters such as triangle matching base placements, zero full score and No score contributions and threshold for full score and no score contributions of 30 & 70 respectively, Clash handling values of 2.9 Å and 0.6 for protein ligand clashes with maximum allowed overlap volume and intra-ligand clash factors while considering the hydrogen in internal clash tests and 200 as the default docking values for maximum number of solutions per iteration and also per fragmentations [17].

2.5 Docking interactions

The docking interactions revealing H-bond and van-der Waal forces among the phytochemical compounds and the amino acid residues of ACE were analyzed by using pose-view module of LeadIT.

2.6 Pharmacophore modeling and 3D database Screening

The pharmacophore model was generated by using the Pharmacophore option of discovery studio software (Accelrys Software Inc.) The best docked ACE inhibitor was used as training compound for the generation of a Pharmacophore by using option Auto Pharmacophore Generation which considers the Hydrogen bond acceptor (HB_ACCEPTOR), Hydrogen bond donor (HB_DONOR), Hydrophobic feature (HYDROPHOBIC), Negative ionizable feature (NEG_IONIZABLE), Positive ionizable feature (POS_IONIZABLE) and Aromatic ring (RING_AROMATIC) feature types to generate a selective pharmacophore model from a single ligand. The Principal value of 2 and the Maxis set to the Training ligand which ensures that all of the chemical features in the compound should be will be considered in building the pharmacophore space. The Auto Pharmacophore Generation option enumerates a set of candidate pharmacophore models from the features and chooses the pharmacophore with the highest selectivity as predicted by a Genetic Function Approximation (GFA) model. Using this generated pharmacophore hypothesis, compound screening was performed against, Maybridge database (www.maybridge.com/) consisting of one lakh compounds and assessed the compounds matching the pharmacophore by considering the Fit Values.

2.7 DFT studies

The determination of the energy gap between HOMO (highest occupied molecular orbital) and LUMO (lowest unoccupied molecular orbitals) could provide the chemical reactivity and kinetic stability of molecules. The molecules were optimized and proposed for theoretical calculations (DFT studies) by using Gaussian software. The chemical hardness, that reveals the compounds stability and reactivity are expressed as: $\eta = (-EHOMO + ELUMO)/2$. While, the escaping tendency of electrons from an equilibrium system is defined through electronic chemical potential (μ) of the compound as $\mu = (EHOMO + ELUMO)/2$. In extension to this, the stabilization in compound energy acquired through an additional electronic charge from the environment is measured by arriving its global electrophilicity expressed as $\omega = \mu^2/2\eta$ that significantly expressed the power of a ligand molecule.

3. RESULT AND DISCUSSION

3.1 Target

Considering the role of ACE in controlling the blood pressure and in conversion of angiotensin I to angiotensin II, the protein structure of Human Angiotensin Converting Enzyme complexed with Lisinopril (PDB ID: 1086) (Figure.1) was retrieved from Protein Databank and used as receptor for further docking studies.

3.2 Ligands

The selected 16 Phytochemical compounds along with their Pubchem ID and their plant sources were given in Table 1. The two well known first class therapeutic drugs of ACE inhibitors such as Captopril and Lisinopril were considered as references for docking studies. The structures of these phytochemical compounds and standard drugs were shown in Figure.2.

Table 1. Selected phytochemical compounds and their plant sources

Pubchem ID	Compound	Plant Source
CID:44259992	Hibiscetin-3-glucoside	<i>Hibiscus sabdariffa</i> L.
CID: 12358401	Apigenin	<i>Allium sativum</i>
CID: 5315615	Rosemarinic acid	<i>Mentha spicata</i>
CID: 5280863	Kaempferol	<i>Allium sativum</i>
CID: 5280805	Rutin	<i>Sophora secundiflora</i>
CID: 5280445	Luteolin	<i>Allium sativum</i>
CID: 5280343	Quercetin	<i>Allium sativum</i>
CID: 1794427	Chlorogenic acid	<i>Calluna vulgaris</i>
CID: 689043	Caffeic acid	<i>Argania spinosa</i>
CID: 637542	Coumaric acid	<i>Solanum lycopersicum</i>
CID: 367141	Epicatechingallate	<i>Camellia sinensis</i>
CID: 162350	Isovitexin	<i>Camellia sinensis</i>
CID: 107905	Epicatechin	<i>Theobroma cacao</i>
CID: 73160	Catechin	<i>Theobroma cacao</i>
CID: 73073	Serpentine	<i>Rauwolfia serpentine</i>
CID: 932	Naringenein	<i>Solanum lycopersicum</i>

3.3 Virtual Screening

It is observed that all the compounds in the study exhibited theoretically encouraging docking scores. Among these selected 18 compounds, two compounds namely Rosemarinic acid and Caffeic acid showed relatively good binding affinity as compared to the standard ACE inhibitor Lisinopril, which exhibited the dock score of -33.8026 kJ/mol. While, other eight compounds exhibited higher binding affinity scores when compared to Captopril (-28.0001 kJ/mol). Whereas the other six compounds such as Kaempferol (-27.3849 kJ/mol), Apigenin (-27.2702 kJ/mol), Catechin (-26.7584 kJ/mol), Serpentine (-25.1353 kJ/mol), Hibiscetin-3-glucoside (-23.9487 kJ/mol) and Naringenein (-23.3107 kJ/mol) exhibited relatively poor dock score when compared to that of the standard drugs emphasized in this study.

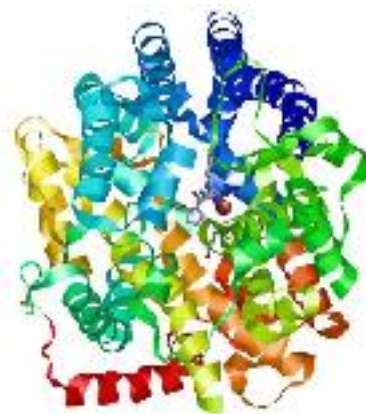


Figure 1. The protein structure of Human Angiotensin Converting Enzyme complexed with Lisinopril (PDB ID: 1086)

Table 2. Docking interactions of the phytochemical compounds with higher docking affinities in comparison with Captopril

COMPOUNDS PUBCHEM ID								
44093	637542	367141	162350	107905	5280805	5280445	5280343	1794427
Gln281*	Gln281*	Gln281*	-	Glu281*	-	Gln281#	Gln281*	Gln281#
His353\$	His353\$	His353*	His353#	His353#	His353\$	His353\$	His353#	His353\$
-	-	Ala354#	-	Ala354#	Ala354#	Ala354\$	Ala354*	-
-	-	-	-	-	Ser355\$	-	-	-
-	-	Val380\$	-	Val380\$	Val380\$	-	-	-
His383\$	His383\$	His383#	His383#	His383#	His383#	His383\$	His383#	His383*
-	-	-	Glu384*	-	Glu384*	Glu384*	-	Glu384*
-	His387*	-	His387*	-	-	His387*	His387*	His387*
Glu411*	-	-	Glu411*	-	-	Glu411*	-	-
-	-	-	Phe457\$	-	Phe457\$	Phe457\$	Phe457\$	-
Lys511*	Lys511*	-	-	-	Lys511*	Lys511*	Lys511*	Lys511*
His513#	His513\$	His513#	His513#	-	His513#	-	-	His513\$
Tyr520#	Tyr520*	-	-	-	Tyr520#	Tyr520*	Tyr520*	Tyr520*
Tyr523#	Tyr523\$	Tyr523\$	Tyr523\$	Tyr523\$	Tyr523\$	Tyr523\$	Tyr523\$	Tyr523\$
-	-	-	Phe527\$	-	Phe527\$	Phe527\$	Phe527\$	-
Docking Scores (kJ/mol)								
-28.0001	-28.0932	-28.3753	-30.0155	-28.2712	-29.4384	-30.8914	-33.0149	-28.6159

*Amino acid residues favouring H-bond interactions;

\$Amino acid residues favouring Non-bonded (Hydrophobic) interactions;

#Amino acid residues involved in both interactions.

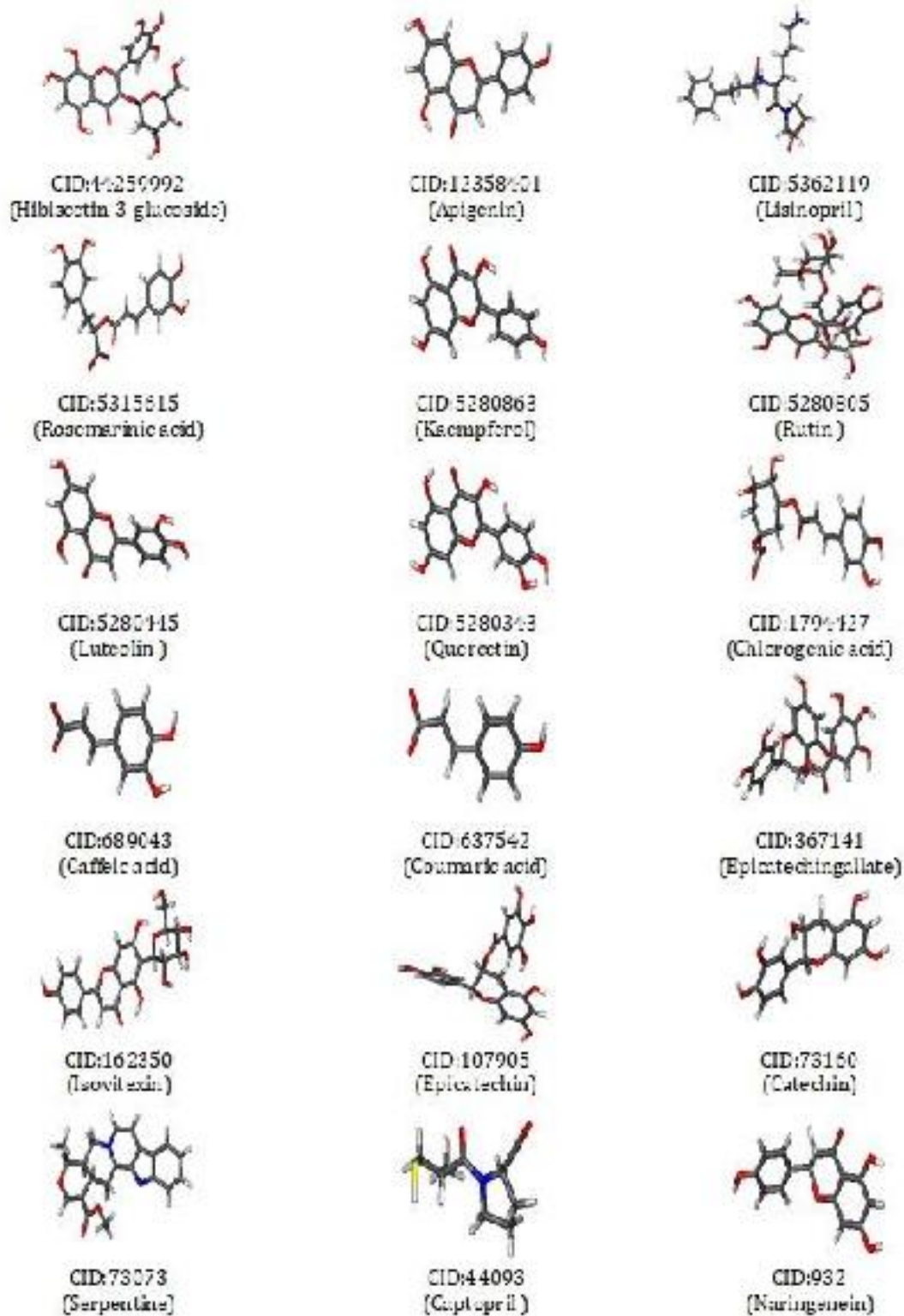


Figure 2. Structures of phytochemical compounds and standard drugs

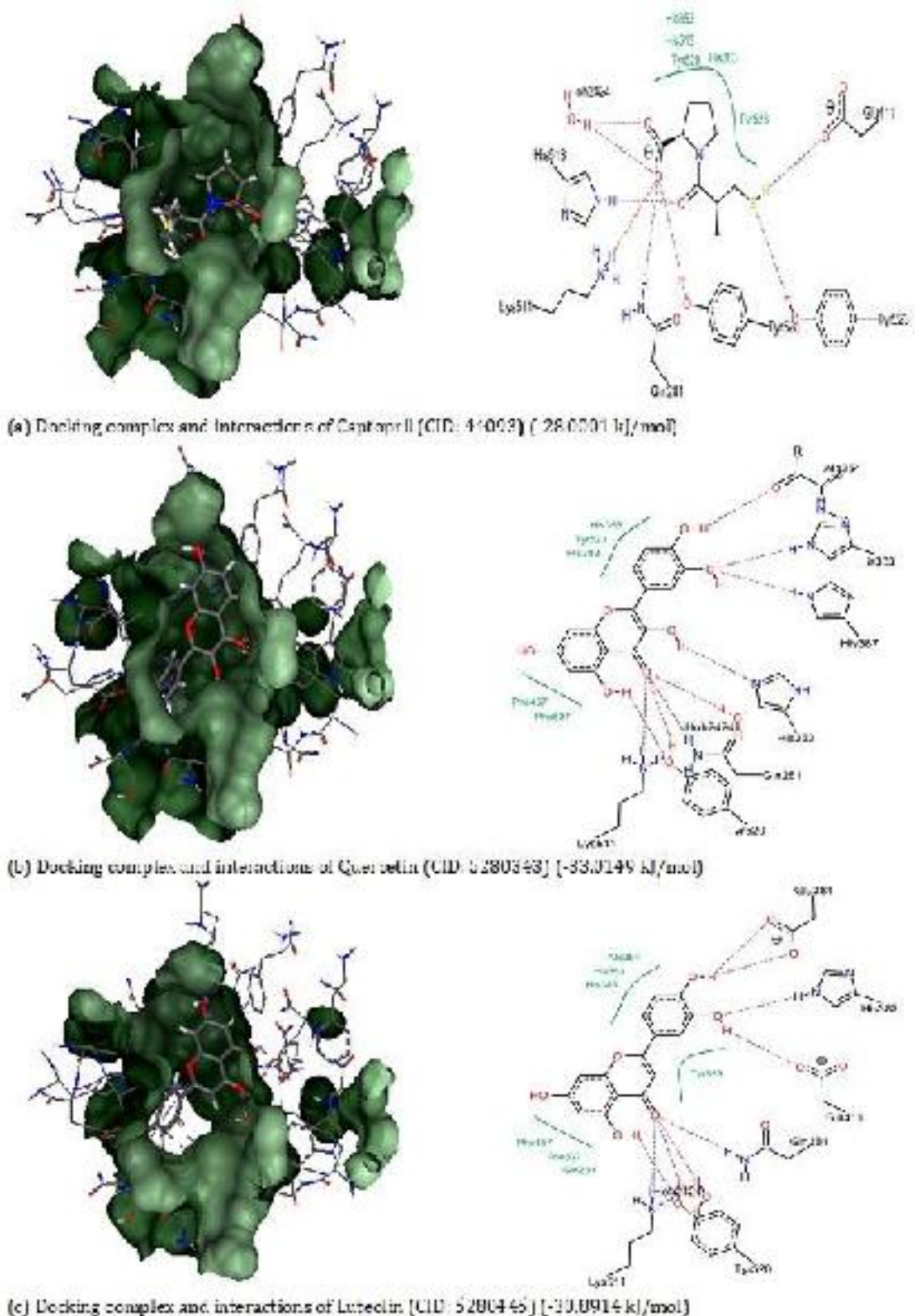


Figure 3. Docking interactions of the phytochemical compounds with higher docking affinities in comparison with Captopril

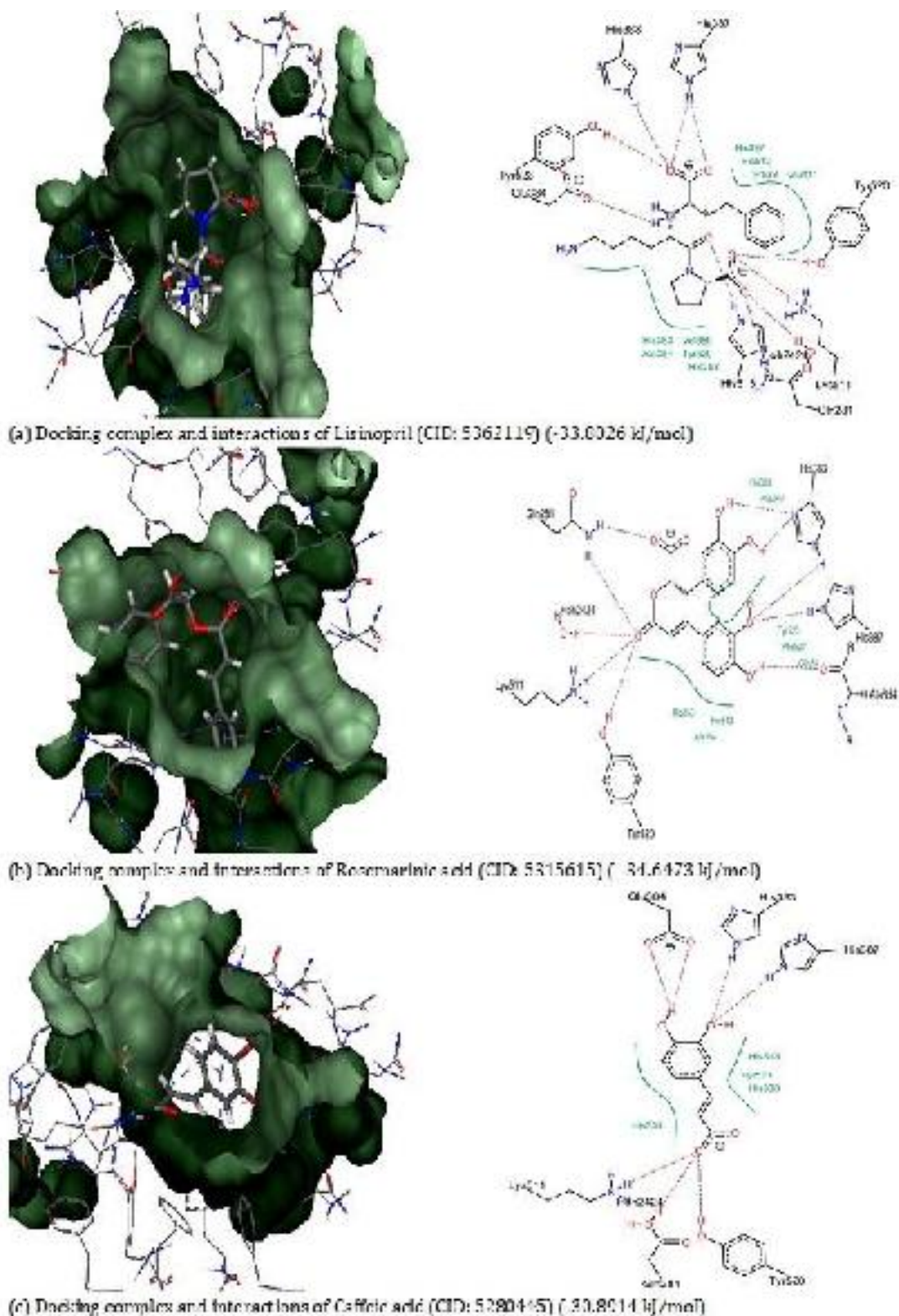


Figure 4. Docking interactions of the phytochemical compounds with higher docking affinities in comparison with Lisinopril

Table 3. Docking interactions of the phytochemical compounds with higher docking affinities in comparison with Lisinopril

COMPOUNDS PUBCHEM ID		
5362119	5315615	689043
Gln281*	Gln281#	Gln281*
His353#	His353\$	His353\$
Ala354*	Ala354#	-
Ser355\$	-	-
-	-	-
His383#	His383#	His383#
-	-	Glu384*
His387#	His387*	His387*
Glu411\$	-	-
Phe457\$	Phe457\$	-
Lys511*	Lys511*	Lys511*
His513\$	His513\$	His513\$
Tyr520#	Tyr520*	Tyr520*
Tyr523#	Tyr523\$	Tyr523\$
-	Phe527\$	-
Docking Scores (kJ/mol)		
-33.8026	-34.6473	-33.9872

*Amino acid residues favouring H-bond interactions;

\$Amino acid residues favouring Non-bonded (Hydrophobic) interactions;

#Amino acid residues involved in both interactions.

3.4 Docking interactions

The binding affinities among ACE and best two phytochemical compounds (Quercetin and Luteolin) that exhibited higher docking affinities in comparison with Captopril, a Sulfhydryl-containing agent were shown in Figure.3a-c. The docking interactions revealing the formation of H-bond interactions and Non-bonded (van-der Waal's) interactions between the nine phytochemical compounds and ACE binding site residues were explored in Table 2. It is observed that the interaction of standard drug Captopril is favoured by the formation of H-bonds with Gln281, Glu411, Lys511, His513, Tyr520 and Tyr523 while hydrophobic interactions with His353, His383, His513, Tyr520 and Tyr523. Interestingly, it is observed that the amino acids Histidine (His353, His383, and His513) and Tyrosine (Tyr523) in the binding site of ACE protein are crucial in favouring the interactions with all the nine compounds, which exhibited better dock score than that of captopril. It is noteworthy to mention that the compounds such as Quercetin (-33.0149 kJ/mol), Luteolin (-30.8914 kJ/mol), Isovitexin (-30.0155 kJ/mol) and Rutin (-29.4384 kJ/mol) exhibited significantly better binding affinities than

the standard drug captopril. Interestingly, the interaction of these four compounds suggests are favoured by formation of vander Waals interaction with Phenyl alanine (Phe 457 and 527), which possibly that the Phenyl alanine in the active site of ACE protein plays a crucial role for their better binding affinities.

The docking interactions along with their docking scores of three compounds that exhibited higher docking affinities in comparison with Lisinopril, a dicarboxylate-containing agent were shown in Figure.4a-c. The docking interactions revealing the formation of H-bond interactions and Non-bonded (van-der Waal's) interactions between these three phytochemical compounds along with standard drug Lisinopril and ACE binding site residues were explored in Table 3. It is observed that the interaction of standard drug Lisinopril is favoured by the formation of H-bonds with Gln281, His353, Ala354, His383, His387, Lys511, Tyr520 and Tyr523 and hydrophobic interactions with His353, Ser355, His383, His387, Glu411, Phe457, His513, Tyr520 and Tyr523. Similarly, it is observed that the amino acids Glutamine (Gln281), Histidine (His353), Lysine (Lys511) and Tyrosine (Tyr523) plays a crucial role in favouring the

interactions with all the three compounds including Lisinopril. Interestingly it is observed that the docking score of Rosemarinic acid (-34.6473 kJ/mol) is relatively better than that of Standard drug Lisinopril dock score (-33.8026 kJ/mol), While the dock score of Caffeic acid (-33.9872 kJ/mol) is also found to be slightly better than standard. It is observed the Rosemarinic acid interactions are supported by an additional amino acid Phenylalanine (Phe527) in the formation of nonbonded interactions while compared to other compound interactions. Thus it possibly suggests that the Pheny alanine in the active site of ACE protein plays a crucial role for its better binding affinities.

Thus the docking studies implies that the conserved amino acids such as Histidine (H) and Tyrosine (Y) in the binding pockets of ACE are vital in posing the better binding interaction with the phytocompounds than that of Sulfhydryl-containing ACE therapeutic, Captopril. Whereas the amino acids such as Glutamine (Q) and Valine (V) are significant in favouring the better interaction with phytocompounds than that Lisinopril, a dicarboxylate-containing agent. These docking interactions also envisages that the =O (keto group) present in the compounds and -NH (amino group) on the amino acids favors the H-bond interactions. Hence these findings clearly picturizes that the Rosemarinic acid could significantly possess better ACE inhibition activity and could be an alternative therapeutic agent to replace the drugs with severe side effects.

3.5 Pharmacophore Modeling and Validation

The pharmacophore model is generated by using the pharmacophore module of Discovery Studio. The Pharmacophore hypothesis generation is achieved by using auto pharmacophore generation option in Discovery Studio which considers the chemical feature types such as the hydrogen bond acceptor (HB_ACCEPTOR), hydrogen bond donor (HB_DONOR), hydrophobic feature (HYDROPHOBIC), negative ionizable feature (NEG_IONIZABLE), positive ionizable feature (POS_IONIZABLE) and aromatic ring (RING_AROMATIC) for the selected ligand.

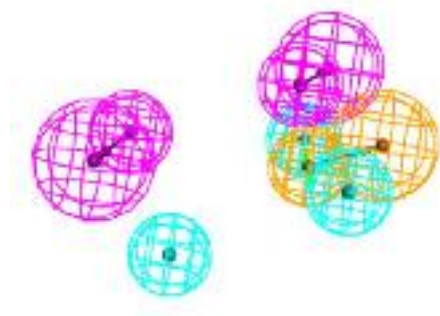


Figure.5: Generated Pharmacophore based on the Rosemarinic acid, Hydrogen bond donor (magenta) Hydrophobic (cyan) ; Ring aromatic (orange)

The ten pharmacophore models are generated by using Common Feature Pharmacophore Model Generation protocol in Discovery studio. For a statistically significant pharmacophore model, correlation coefficient and root mean square deviation (RMSD) are calculated. The best pharmacophore model was selected based on the high correlation coefficient and lower RMSD. The generated pharmacophoric features based on the Rosemarinic acid is shown in figure.5.

3.6 3D Database Screening

Search 3D Database protocol with best search option implemented in DS is used for database screening against Maybridge database consisting of more than one lakh compounds. The obtained database hits is screened using various filters such as estimated activity, Lipinski's rule of five, and ADMET properties. The final hit compounds after filtering are known as hit list and ranked according to the fit value, which is the degree of consistency with the pharmacophore model. To decrease the number of hits, a minimum fit value of >3, which is the lowest limit to qualify as a hit compound, is applied.

This lower limit of fit value is chosen according to the fit value obtained from the active molecule. The molecules with good fit scores are selected for further docking studies. The generated 3D pharmacophore of rosmeric acid is subjected to screen the compounds with the significant chemical features against May bridged database, exhibited 9 potential compounds that matches the generated pharmacophore (Table.4). These Hits are defined as those compounds that possess chemical functionalities that spatially overlap with corresponding features within the pharmacophoric model. The hits were subsequently fitted against the pharmacophore and assessed by Fit Value (Figure.6).

Table 4 The compounds matching pharmacophore and their fit values (Rosemeric acid)

S.No.	Maybridge compound	Fit Value
1.	PD 00533	2.66957
2.	CD 01374	1.86604
3.	CD 04888	1.74073
4.	CD 01278	1.17254
5.	BTB 04932	1.14923
6.	SPB 00952	0.866112
7.	RJC 03634	0.840245
8.	RJC 03429	0.36152
9.	RDR 01978	0.152094

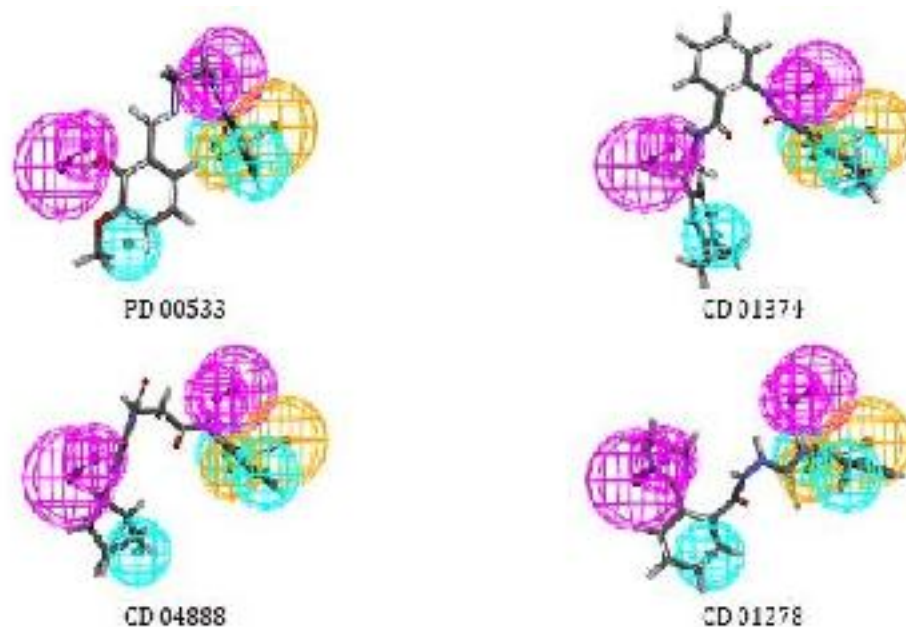


Figure.6 : The top four compounds matching the Pharmacophore

3.7 Molecular Docking

The Top 4 obtained compounds PD 00533, CD 01374, CD 04888 and CD 01278 were docked with in the active site of ACE2, and their docking interactions with their binding energies along with their pharmacophoric fit values were tabulated (Table.5). Among the obtained 4 hits from maybridge database, the compound PD 00533 exhibited the highest docking score of -38.4372 kJ/mol. The docking studies implies that the amino acids Alanine (Ala356), Histidine (His 513 and 353) and Water molecule (Hoh 2317) in the binding pockets of ACE are vital in posing the better binding interaction with the maybridge screened compound (PD 00533). While the non bonded interactions are favoured by Valine (Val518), Serine (Ser355), Histidine (His 353,387,383 and 513). These docking interactions also envisages that the =O (keto group) present in the compounds and NH (amino group) on the amino acids favors the Hbond interactions.

Table.5: Maybridge compounds with the fit values and docking scores

Compound	Fit value	Docking score
PD 00533	4.66957	-38.4372
CD 01374	3.86604	-34.5687
CD 04888	2.56234	-32.5624
CD 01278	2.54782	-30.4587
BTB 04932	1.89542	-28.25687

Thus the pharmacophoric design and 3D database search along with the docking studies revealed that the May Bridge compound PD00533 having the better binding energy of -38.4372 kJ/mol might have a better inhibition activity against the ACE2 receptor.

3.8 Natural bond Analysis (HOMO-LUMO)

The Eigen value of LUMO-HOMO energy gap reflects the chemical activity of the molecule. The HOMO-LUMO Plot of PD00533 is shown in figure.8.

The HOMO-LUMO energy gap for PD 00533calculated at DFT level:

$$\begin{aligned} \text{HOMO Energy} &= -6.8077 \text{ eV} \\ \text{LUMO Energy} &= -3.9086 \text{ eV} \\ \text{HOMO - LUMO energy gap} &= 2.90 \text{ eV} \end{aligned}$$

The Eigen value of LUMO-HOMO energy gap reflects the chemical activity of the molecule. The decrease in the HOMO and LUMO energy gap explains the eventual charge transfer interactions that are taking place within the molecule which might be due to the strong electron-accepting ability of the electron-acceptor groups. It is observed that the HOMOs have an overall π bonding character along with a considerable non-bonding character and LUMOs have an anti-bonding π^* character. The strong charge transfer interaction is responsible for the bioactivity of the molecule. Thus it is observed that two compounds namely Rosemarinic acid and Caffeic acid showed relatively good binding affinity that the standard ACE inhibitor Lisinopril. Lisinopril.

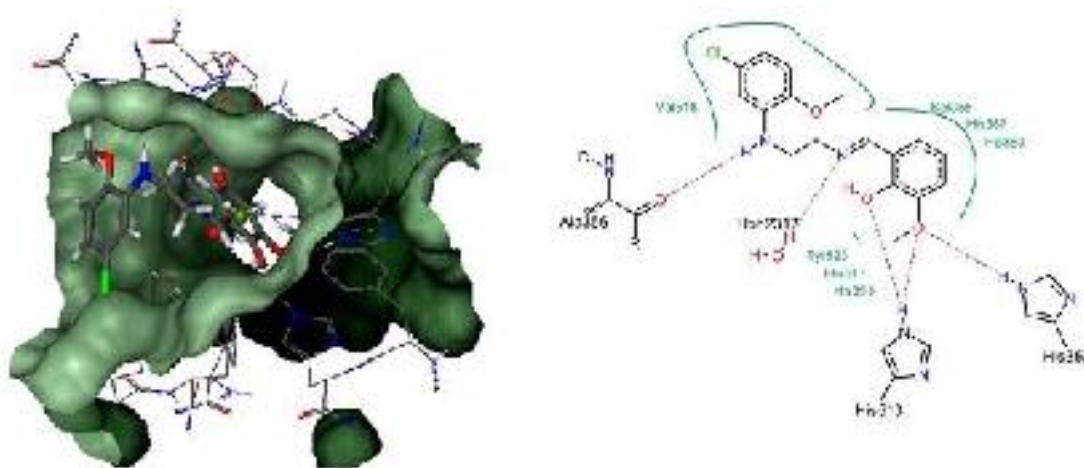


Figure.7: Docking complex and interactions of PD 00533 (-38.4372 kJ/mol)

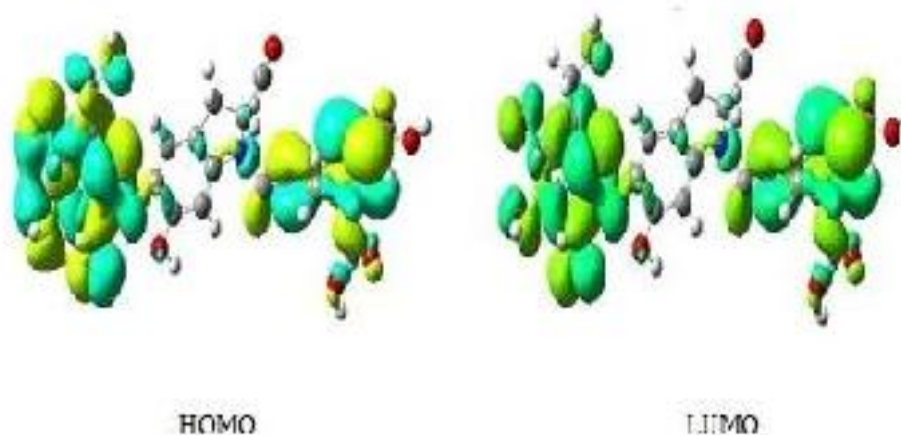


Figure 8 : The HOMO-LUMO plot for PD 00533 (compound obtained from Rosemmeric pharmacophore)

The compound PD 00533 also favors the necessary hydrogen bond interactions with in the activity site of ACE and thus identified as novel leads with anti-hypertensive activity. The HOMO–LUMO energy gap has a substantial influence on the calculated value that is found to be 2.90 eV. The lowering of HOMO–LUMO energy gap, a quantum-chemical descriptor, explains the charge transfer interactions taking place within the molecule through strong N–H···N and N–H···O hydrogen bonding which strengthens that compound PD00533 is bioactive and pharmaceutical in nature and thus suggested as novel leads with anti-hypertensive activity.

CONCLUSION:

Hypertension is a highly prevalent cardiovascular risk factor. Angiotensin Converting Enzyme (ACE), a metallo-peptidase is the best known important drug target in the treatment of hypertension and responds to broad range ACE inhibitors such as Captopril. In this study, 18 phytochemical compounds were screened for their anti-hypertensive activity against the x-ray crystal structure of human ACE in complex with lisinopril. It is observed that Rosemarinic acid showed relatively good binding affinity that the standard ACE inhibitor Lisinopril. Further, the 3D pharmacophore generated on Rosemarinic acid was screened against May bridged database and found that PD 00533 as novel leads with anti-hypertensive activity.

The hydrogen bonds network of PD 00533 has been thoroughly analyzed using NBO analysis and the molecular hydrogen bonding and charge transfer interaction present in the molecule emphasized the charge transfer interactions taking place within the molecule through strong N-H...N and N-H...O hydrogen bonding is crucial for its bioactivity. Further it implies that the NH group and =O present in the compounds favors the hbond interactions. The findings from these studies pave a path for the design of novel ACE inhibitors and also envisage that the amino acids Aspartic acid, Phenylalanine, Leucine and Glycine should be considered during its design for implying its action as a best ACE inhibitor compound against the potential target of angiotensin-converting enzyme.

REFERENCES

- [1] Charifson, P. S., Corkery, J. J., Murcko, M. A., & Walters, W. P. (1999). Consensus scoring: A method for obtaining improved hit rates from docking databases of three-dimensional structures into proteins. *Journal of medicinal chemistry*, 42(25), 5100-5109.
- [2] Chow, W. H., Gridley, G., Fraumeni Jr, J. F., & Järholm, B. (2000). Obesity, hypertension, and the risk of kidney cancer in men. *New England Journal of Medicine*, 343(18), 1305-1311.
- [3] Clark, R. D., Strizhev, A., Leonard, J. M., Blake, J. F., & Matthew, J. B. (2002). Consensus scoring for ligand/protein interactions. *Journal of Molecular Graphics and Modelling*, 20(4), 281-295.
- [4] Gehlhaar, D. K., Verkhivker, G., & FREER, S. (1995, April). DOCKING CONFORMATIONALLY FLEXIBLE SMALL MOLECULES INTO A PROTEIN-BINDING SITE THROUGH SIMULATED EVOLUTION. In *ABSTRACTS OF PAPERS OF THE AMERICAN CHEMICAL SOCIETY* (Vol. 209, pp. 146-COMP). PO BOX 57136, WASHINGTON, DC 20037-0136: AMER CHEMICAL SOC.
- [5] Izzo, J. L., Black, H. R., & Goodfriend, T. L. (2003). Hypertension primer: the essentials of high blood pressure. ed.
- [6] Yang, Y. C., Lu, F. H., Wu, J. S., Wu, C. H., & Chang, C. J. (2004). The protective effect of habitual tea consumption on hypertension. *Archives of internal medicine*, 164(14), 1534-1540.
- [7] Gilani, A. U. H., & Aftab, K. (1994). Hypotensive and spasmolytic activities of ethanolic extract of Capparis cartilaginea. *Phytotherapy Research*, 8(3), 145-148.
- [8] Gilani, A. H., Aftab, K., & Ahmed, W. (1991). Antihypertensive activity of methanolic extract of *Castanospermum australe* leave. *J. Anim. Plant Sci*, 1, 113-116.
- [9] Muhammad, S. A., & Fatima, N. (2015). In silico analysis and molecular docking studies of potential angiotensin-converting enzyme inhibitor using quercetin glycosides. *Pharmacognosy magazine*, 11(Suppl 1), S123.
- [10] Tabassum, N., & Ahmad, F. (2011). Role of natural herbs in the treatment of hypertension. *Pharmacognosy reviews*, 5(9), 30.
- [11] Natesh, R., Schwager, S. L., Sturrock, E. D., & Acharya, K. R. (2003). Crystal structure of the human angiotensin-converting enzyme-lisinopril complex. *Nature*, 421(6922), 551.
- [12] Thorn, K. S., & Bogan, A. A. (2001). ASEdb: a database of alanine mutations and their effects on the free energy of binding in protein interactions. *Bioinformatics*, 17(3), 284-285.
- [13] Scott, W. R., Hünenberger, P. H., Tironi, I. G., Mark, A. E., Billeter, S. R., Fennen, J., ... & van Gunsteren, W. F. (1999). The GROMOS biomolecular simulation program package. *The Journal of Physical Chemistry A*, 103(19), 3596-3607.
- [14] Weininger, D. (1988). SMILES, a chemical language and information system. 1. Introduction to methodology and encoding rules. *Journal of chemical information and computer sciences*, 28(1), 31-36.
- [15] Rarey, M., Kramer, B., Lengauer, T., & Klebe, G. (1996). A fast flexible docking method using an incremental construction algorithm. *Journal of molecular biology*, 261(3), 470-489.
- [16] Stierand, K., Maaß, P. C., & Rarey, M. (2006). Molecular complexes at a glance: automated generation of two-dimensional complex diagrams. *Bioinformatics*, 22(14), 1710-1716.
- [17] Gnanendra, S., Anusuya, S., & Natarajan, J. (2012). Molecular modeling and active site analysis of SdiA homolog, a putative quorum sensor for *Salmonella typhimurium* pathogenicity reveals specific binding patterns of AHL transcriptional regulators. *Journal of molecular modeling*, 18(10), 4709-4719.

Synthesis and characterization of L-Isoleucine Maleate and L-Isoleucine Oxalate crystals

A.Zeenath Bazeera^a, S.Selvaraj^b, A.Syed Mohamed^c

^aResearch Scholar, Reg.No.12100 Department of Physics, M.D.T.Hindu College, Tirunelveli.

^aDepartment of Physics, Sadakathullah Appa College, Tirunelveli, Tamilnadu, India.

^bDepartment of Physics, M.D.T.Hindu College, Tirunelveli, Tamilnadu, India.

^cDepartment of Chemistry, Sadakathullah Appa College, Tirunelveli, Tamilnadu, India.

Affiliated to Manonmaniam Sundaranar University, Tirunelveli, Tamilnadu, India.

Email id: meeran.jul1@gmail.com, phone no: 9486558176

Abstract: A novel organic single crystal of L-Isoleucine Maleate (LIM) and L-Isoleucine Oxalate (LIO) were grown by slow evaporation solution growth method using water as the solvent at room temperature. X-ray Powder diffraction studies have been carried out in order to calculate the lattice parameter values. The FT-IR spectrum of the materials were recorded on BRUKER IFS 66V FT-IR SPECTROMETER using KBr pellet technique. FT-IR studies revealed the functional groups present in the compounds.

Key words: L-Isoleucine Maleate (LIM), L-Isoleucine Oxalate (LIO), XRD, FT-IR

1.1 Introduction

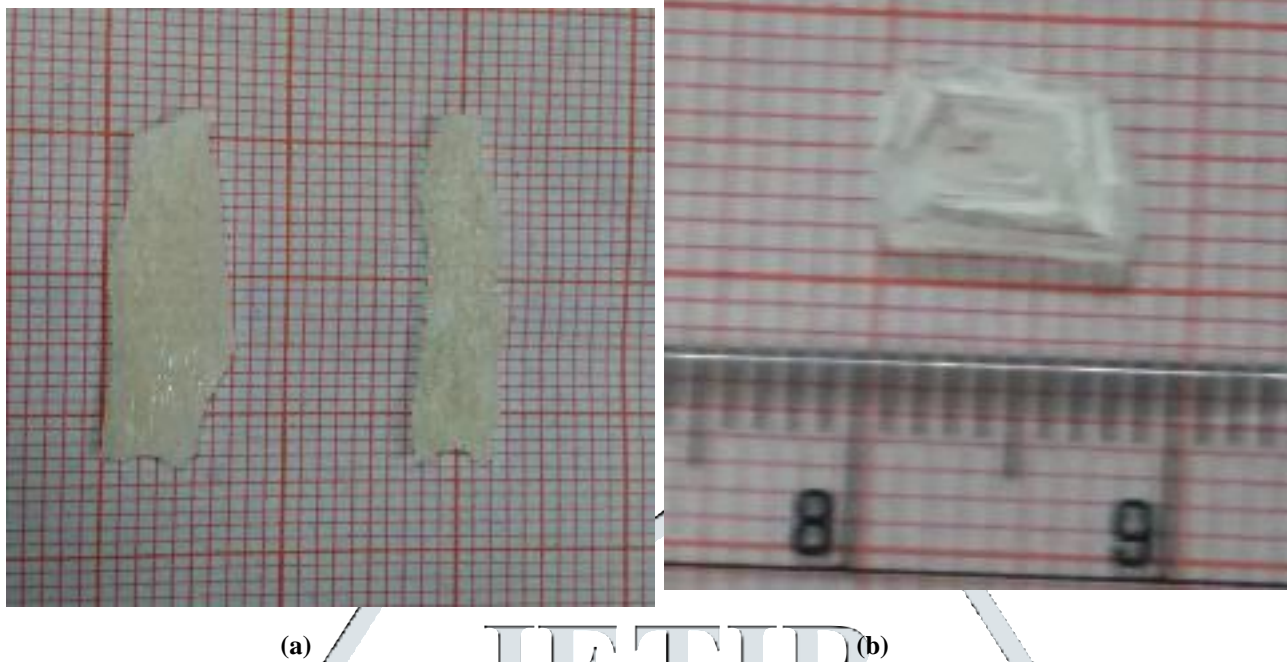
Crystal growth plays an important role in modern technology. A crystal is nothing but a solid in which the constituents atoms molecules or ions are packed in a regular ordered, repeating pattern extending in all three spatial dimensions in the present study. Amino acids are crystalline solids. They are generally soluble in water and insoluble in non-polar organic solvents. The predictable formation of networks or assemblies through intermolecular interactions such as hydrogen bonding or co-ordination bonds in the entire crystal lattice of crystalline materials having desired chemical and physical properties is the main objective of crystal engineering. It is a multi-disciplinary area and it has implications for materials chemistry, supramolecular chemistry, molecular recognition and biology [1-4]. Among the organic molecules, α -amino acids exhibit specific features of interest such as molecular chirality, absence of strongly conjugated π -bonds, wide transparency window in the entire UV, Visible and NIR regions of the electromagnetic spectrum and zwitter ionic nature as a consequence of internal acid-base reactions[5]. The α -amino acids are the building blocks of poly-peptides and proteins and are linked to one another by means of peptide bonds. L-Isoleucine is both glucogenic and ketogenic amino acid. This is one of the amino acids having branched hydro carbon side chains. It is non polar and aliphatic in nature. On the basis of infra red spectroscopic study, the crystal of L-Isoleucine was assumed to belong to a rather unusual type in which the molecules two type of conformation[6,7]. In the present paper, the synthesis and single crystal growth of L-Isoleucine organic acids followed by characterization by Powder X-ray diffraction (XRD) and FT-IR have been described.

1.2 Experimental Details

L-Isoleucine Maleate (LIM) was synthesized by the reaction between a weak organic maleic acid and the strongly basic amino acid L-Isoleucine (Hi-media) taken in equimolar proportions.

L-Isoleucine Oxalate (LIO) was synthesized by taking L-Isoleucine (Hi-media) and Oxalic acid in equimolar ratio.

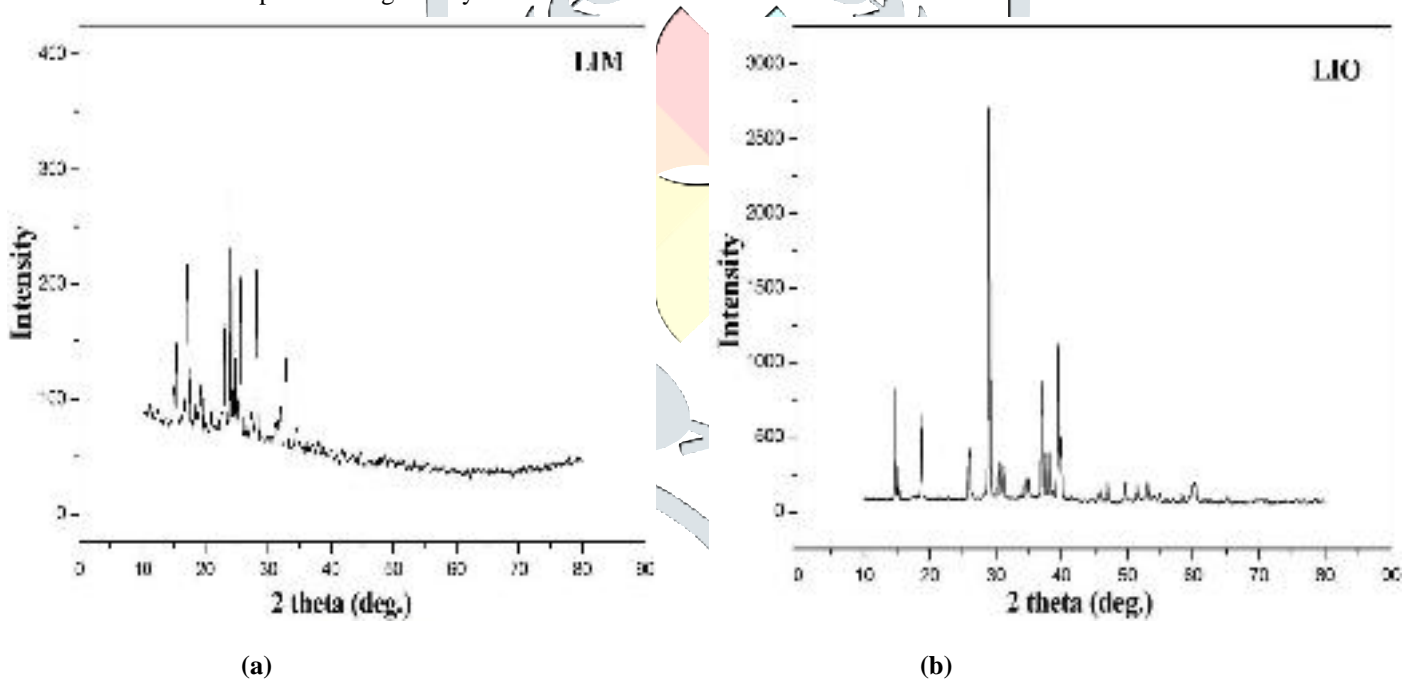
The calculated amounts of reactants in each of the reactions were thoroughly dissolved in double distilled water and stirred well for about 6h using a magnetic stirrer to ensure homogenous temperature and concentration over the entire volume of the solutions. The solution was filtered using a Whatmann filter paper of pore size eleven μ m, transformed to crystal growth vessels and crystallizations were allowed to take place by slow evaporation under room temperature. Transparent colorless LIM and LIO were harvested in a period of 45 days and 60 days, respectively by slow evaporation and are shown in Fig. 1(a and b).



(a) (b)
Fig. 1 (a & b) Photograph of LIM and LIO crystals

1.3 XRD Studies

Powder X-Ray diffraction studies of L-Isoleucine Maleate and L-Isoleucine Oxalate crystals are carried out. The samples were scanned for 2θ values from 10° to 80° at a rate of 2° per minute. The resulted powder XRD pattern is shown in Fig. 2 (a & b). The sample displays sharp and well resolved diffraction peaks with good crystalline nature.



(a) (b)
Fig. 2 (a & b) XRD pattern of LIM and LIO crystals

1.4 FT-IR Studies

The FT-IR spectrum of the candidate materials were recorded on BRUKER IFS 667 FT-IR SPETROMETER using KBr pellet technique. The FT-IR analysis of L-Isoleucine Maleate and L-Isoleucine Oxalate crystals have been carried out in the wave number range of 4000 to 450cm^{-1} are shown in fig.3(a and b). In LIM the higher energy region, peak at 2961cm^{-1} is assigned to C-H stretching vibration [8]. The C-O and C=O stretching modes produce peaks at 2878cm^{-1} and 1720cm^{-1} . Multiple fine structures at the lower energy mode of the envelope indicates the strong hydrogen bonding interaction of NH_3^+ group with strong absorptions of COO^- group at 1568cm^{-1} [9]. The C-O stretching mode is observed at 1307cm^{-1} . The CH_2 wagging and rocking modes produce peaks at 1240 and 866cm^{-1} , respectively. Further medium band observed at about 1069cm^{-1} is due to C-N stretching. The COO^- scissoring (694cm^{-1}) vibration is also observed[10].

Investigating the absorption bands of LIO below 1000cm^{-1} three characteristic bands were identified, one at 675cm^{-1} (COO^- in plane deformation), one at 580cm^{-1} (COO^- wagging mode) and the third one at 851cm^{-1} (C-C stretching). The band corresponding to NH_3^+ asymmetric deformation vibration occurs at 1683cm^{-1} , COO^- asymmetric stretching at 1512cm^{-1} . High wave number region (3377 - 2350cm^{-1}) contains NH and CH stretching vibration and combination of them. Band at 3377cm^{-1} is due to the presence of water molecules.

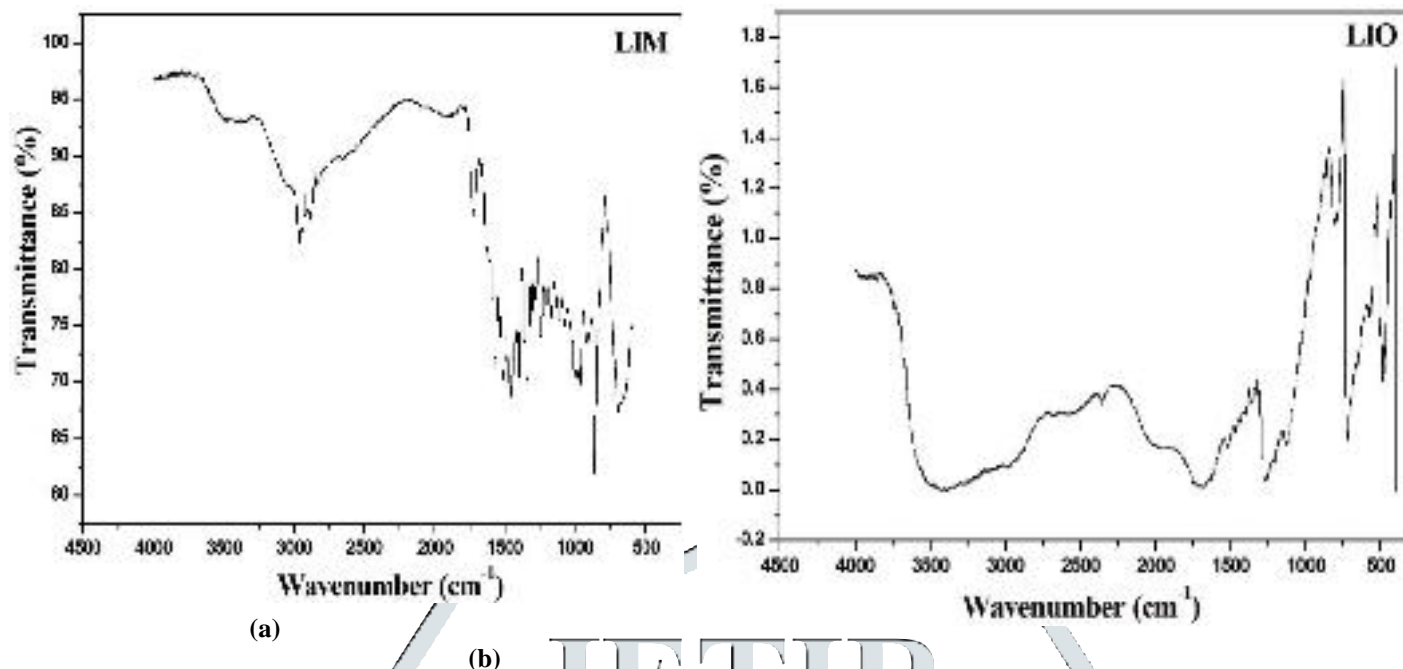


Fig. 3 (a & b) FTIR spectrum of LIM and LIO crystals

The observed vibrational frequencies and their tentative assignments of LIM and LIO are listed in Table 1 (a & b)

Table 1a. Band Assignments of LIM

Wave number cm^{-1}	Assignments
2961	C-H stretching
2878	C-O stretching
1720	C=O stretching
1568	COO ⁻ asymmetric stretching
1307	C-O stretching
1240	CH ₂ wagging
1069	C-N stretching
866	CH ₂ rocking
694	COO ⁻ scissoring

Table 1b. Band Assignments of LIO

Wave number cm^{-1}	Assignments
3377-2350	NH and C-H stretching vibration
1683	NH ₃ ⁺ asymmetric deformation
1512	COO ⁻ asymmetric stretching
1262	CH ₂ wagging
1080	C-N stretching
851	C-C stretching
675	COO ⁻ plane deformation
580	COO ⁻ wagging mode
478	N-H deformation

1.5 Conclusion

Transparent crystals of **L-Isoleucine Maleate** and **L-Isoleucine Oxalate** were grown by slow evaporation solution growth method. Grown crystals were characterized by X-ray diffraction. The modes of vibration of the molecules and the presence of functional groups were identified using FT-IR technique.

Acknowledgement

The authors thank the Manonmaniam Sundaranar University, Tirunelveli for providing the research support.

References

- [1] GM J Schmidt, Pure Appl. Chem. 27(1971) 647-678.
- [2] G R Desiraju, Angew. Chem. Int. Ed. 34 (1995) 2311-2327.
- [3] Michael j, Zaworotko, chem. Commun. (2001) 1-9.
- [4] G R Desiraju, Crystal Engineering, the Design of Organic Solids in Material Science Monographs, vol.54, Elsevier, Amsterdam, 1989.
- [5] Z H Sun, G H Zhang, X Q Wang, G Yu, L Y Zhu, H L Fan, D Xu, j. cryst. Growth 311 (2009) 3455-3460.

- [6] Tsuboi M, Takenishi T & Iitaka Y, (1959), Bull. Chem. Soc. Japan, 32, 305.
- [7] Kazuo Torji, Yoichi Iitaka, Acta Cryst. (1971). B27, 2237.
- [8] P Geetha, S Arulmozhi, J Madhavan and M Victor Antony Raj, International Journal of Chem Tech Research, Vol.6, No.3, pp 1647-1650, 2014.
- [9] M Dinesh Raja, S Arulmozhi, J Madhavan and S Senthil, International Journal of Chem Tech Research, Vol.6, No.1, pp 31-35, 2014.
- [10] U Karunanithi, S Arulmozhi, and J Madhavan, IOSR Journal of Applied Physics, Volume 1, (July-Aug. 2012), PP 14-18.



VIRTUAL SCREENING OF HETEROCYCLIC COMPOUNDS AGAINST ANGIOTENSIN-CONVERTING ENZYME FOR POTENTIAL ANTIHYPERTENSIVE INHIBITORSZOZIMUS DIVYA LOBO C¹, SYED MOHAMED A², GNANENDRA SHANMUGAM^{3*}

¹Department of Chemistry, St. Mary's College (Autonomous), Tuticorin, Tamil Nadu, India, Affiliated to Manonmanium Sundaranar University, Tirunelveli, Tamil Nadu, India. ²Department of Chemistry, Sadakathullah Appa College (Autonomous), Tirunelveli, Tamil Nadu, India. ³Department of Biotechnology, Mahendra Arts and Science College, Namakkal, Tamil Nadu, India. Email: gnani.science@gmail.com

Received: 30 August 2018, Revised and Accepted: 30 October 2018

ABSTRACT

Objective: The objective of this study was to investigate the antihypertensive activity of heterocyclic compounds against angiotensin-converting enzyme (ACE) through molecular docking studies.

Methods: The X-ray crystal three-dimensional (3D) structure of human ACE complexed with lisinopril (PDB ID: 1O86) was retrieved from protein databank. The two-dimensional structures of 10 selected heterocyclic compounds were drawn in ACD-Chemsketch and converted into 3D structures. The 3D structures of compounds were virtually screened in the binding pockets of ACE using FlexX docking program. Further, the chemical entities revealing the molecular electronic structures of the best docked compound (Compound-4) were explored through density functional theory studies.

Results: The Compound-4 showed the highest docking score of -26.6290 kJ/mol with ACE. The Hbond and non-bonded interactions are favored by phenylalanine, leucine, and arginine. The energy gap of 1.60 eV between highest occupied molecular orbital and lowest unoccupied molecular orbitals explained the presence of strong electron-acceptor group. Furthermore, the molecular electrostatic potential studies clearly envisaged the requirement of electropositive and electronegative groups are crucial for the ACE inhibitor activities.

Conclusion: The identification of good ACE inhibitors requires the understanding of the current ACE inhibitors. Thus, the docking interactions of Compound-4 and its molecular electronic structure significantly imply its potential as antihypertensive agent. However, further clinical studies are required to ascertain its potential toxic effects.

Keywords: Angiotensin-converting enzyme, Angiotensin-converting enzyme inhibitors, Docking, Density functional theory studies, Highest occupied molecular orbital, Lowest unoccupied molecular orbitals, Molecular electrostatic potentials.

© 2019 The Authors. Published by Innovare Academic Sciences Pvt Ltd. This is an open access article under the CC BY license (<http://creativecommons.org/licenses/by/4.0/>) DOI: <http://dx.doi.org/10.22159/ajpcr.2019.v12i2.29106>

INTRODUCTION

In recent years, cardiovascular diseases have become a serious problem worldwide. The World Health Organization has reported an increase in the number of patients suffering from this disease. Hypertension is an important risk factor, contributing to other cardiovascular diseases such as blood vessel disorders, coronary heart disease, aortic aneurysm, and stroke [1]. Cardiac arrhythmia is another cardiovascular problem. An arrhythmia is any disorder of the heart rate that may cause stroke. Heart rhythm's disorders may be caused by genetic factors or occur when the heart muscle (myocardium) is damaged, sometimes by hypertension [2].

At present, existing treatments for high blood pressure (BP) are not very effective and are generally uncomfortable for patients. This relies in that the patient needs to have a very strict control in the dosage and in the moment of the administration of the drug [3]. Moreover, also, some patients have an unfavorable response after the administration, leading them to a fast BP reduced. One of the most widely used compounds for the treatment of hypertension is Captopril. Like many others on the market, this drug was designed with computational tools. Over the past few decades, computational studies, together with rational drug design, have become a critical part in the development of new drugs.

Raised BP, especially systolic pressure (hypertension), confers a significant cardiovascular risk and public health concern and should be actively treated. One of the major systems involved in the elevation of the pressure is the renin-angiotensin system (RAS), and subsequently, its inhibition will have beneficial effects to lower BP and improve cardiovascular health [4]. The RAS is regulated by a series

of highly specific enzymatic reactions. The first enzymatic reaction in the pathway starts with renal production of renin that cleaves angiotensinogen to generate angiotensin I. Angiotensin I is then cleaved by angiotensin-converting enzyme (ACE) to generate the active peptide vasoconstrictive hormone angiotensin II.

Many ACE inhibitors are known to be useful in the treatment of hypertension. The search for ACE inhibitors that lacked the sulfhydryl group also leads to the investigation of phosphorus-containing compounds. The phosphinic acid is capable of binding to ACE in a manner similar to enalapril. The interaction of the zinc atom with the phosphinic acid is similar that is seen with sulfhydryl groups. The purpose of the study is to determine the ability of some derivatives as ACE inhibitors through docking studies and the derivative with the highest potency and understanding its chemical entities through density functional theory (DFT) studies might pave path to design of novel ACE inhibitors with potential inhibition activity.

METHODS**Ligand selection**

A total of 10 antihypertension inhibitor molecules reported in the studies of Yu *et al.*, 2015, were selected in this study to explore their chemical entities required for the ACE inhibitory activity. The two-dimensional (2D) structures of compounds drawn in ACD-Chemsketch (Version 12) [5] were obtained as simplified molecular-input line-entry system (SMILES). Further, the three-dimensional (3D) structures were generated and converted into standard delay file format at "online SMILES convertor and Structure file generator" server [6].

Target and binding site prediction

The X-ray crystal structure of human ACE complexed with lisinopril (PDB ID: 1086) [7] was retrieved from protein databank [8]. The amino acid residues within 6 Å radius of reference ligand lisinopril was considered as binding site using LeadIT (Version 2.1.9) [9].

Virtual screening

The 3D structures of all the 10 selected ACE inhibitors were virtually screened to reveal their binding efficiencies through docking in the predicted binding site of ACE using FlexX module of LeadIT. The docking was performed with the default parameters [10-12].

Docking interactions

The docking interactions revealing Hbond and Van der Waal forces among the selected ACE inhibitors and the amino acid residues of ACE were analyzed using pose-view [13] module of LeadIT.

DFT studies

The molecular structure of the best docked compound was computed using Gaussian software to retrieve the molecular geometric coordinates. Both DFT and time-dependent DFT calculations were performed using Gaussian 03W software. B3LYP hybrid functional 6-311G (d) basis set was used in the calculation methods. The models of the electron density of various energy levels of the compound were visualized using Gauss View 3.0 [14].

RESULTS AND DISCUSSION

Hypertension is a highly prevalent cardiovascular risk factor and an increase in BP increases the risk of developing heart disease, obesity, kidney disease, eye damage, and stroke. Excessive salt intake has been suspected as a cause of high prevalence of hypertension. A high dietary salt intake contributes to the risk of hypertension, which further antagonizes the BP-lowering effect of most antihypertensive drugs. It has been reported that a combination of diet rich in fruits, vegetables, and low-fat dairy products could substantially lower BP levels [15].

Vázquez-Valadez *et al.* [16] reported that main target in the treatment of hypertension is the ACE. This enzyme is responsible for producing angiotensin II, a potent vasoconstrictor. Therefore, one of the targets in the treatment of hypertension is to inhibit ACE activity. Hence, this study's aim is to use computational studies and to demonstrate that the heterocyclic compounds have a molecular affinity for ACE and are capable of inhibiting ACE activity, thus avoiding the production of the vasopressor angiotensin II. The 3D structure of ACE protein as target is shown in Fig. 1 and the 2D structures of 10 selected heterocyclic compounds considered in this study are shown in Fig. 2.



Fig. 1: The protein structure of human angiotensin-converting enzyme complexed with lisinopril (PDB ID: 1086)

Docking interactions

The docking interactions of all the selected compounds in the study exhibited theoretically encouraging docking scores. Among the selected compounds, Compound-4 has exhibited relatively good binding affinity as compared to the other ACE inhibitors considered in this study. The docking interactions of the each compound exploring the amino acids favoring Hbond interactions and non-bonded interactions and their docking scores are discussed.

Docking interactions of Compound-1

The Compound-1 showed the docking score of -11.3060 kJ/mol with the ACE. It is observed that the Compound-1 exhibited critical interactions with the catalytic amino acid residues present in the active site cavity of the ACE by favoring the Hbond interactions and non-bonded interactions. The amino acid Leu380, Phe381, and Arg110 favored the Hbond interactions and the non-bonded interactions are supported by Phe130, Phe487, Phe381, Leu382, Glu383, and Arg110. Thus, this compound can be considered as potential ACE inhibitor molecule. The docking complex and docking interactions of Compound-1 within the active site of ACE is shown in Fig. 3a.

Docking interactions of Compound-2

The Compound-2 showed the docking score of -17.9469 kJ/mol with the ACE. It is observed that the Compound-2 exhibited critical interactions with the catalytic amino acid residues present in the active site cavity of the ACE by favoring the Hbond interactions and non-bonded interactions. The amino acid Phe381, Arg110, and Leu380 favored the Hbond interactions and the non-bonded interactions are supported by Arg110, Glu383, Leu382, Phe130, Phe487, and Phe381. Thus, this compound can be considered as potential ACE inhibitor molecule. The docking complex and docking interactions of Compound-2 within the active site of ACE is shown in Fig. 3b.

Docking interactions of Compound-3

The Compound-3 showed the docking score of -18.9100 kJ/mol with the ACE. It is observed that the Compound-3 exhibited critical interactions with the catalytic amino acid residues present in the active site cavity of the ACE by favoring the Hbond interactions and non-bonded interactions. The amino acid Phe381, Leu380, and Arg110 favored the Hbond interactions and the non-bonded interactions are supported by Phe487, Arg110, Leu382, Phe381, Glu383, and Phe130. Thus, this compound can be considered as potential ACE inhibitor molecule. The docking complex and docking interactions of Compound-3 within the active site of ACE is shown in Fig. 3c.

Docking interactions of Compound-4

The Compound-4 showed the highest docking score of -26.6290 kJ/mol with the ACE. It is observed that the Compound-4 exhibited critical interactions with the catalytic amino acid residues present in the active site cavity of the ACE by favoring the Hbond interactions and non-bonded interactions. The amino acid Phe381, Leu380, and Arg110 favored the Hbond interactions and the non-bonded interactions are supported by Arg110, Glu383, Leu382, Phe130, Phe487, and Phe381. Thus, this compound can be considered as potential ACE inhibitor molecule. The docking complex and docking interactions of Compound-4 within the active site of ACE is shown in Fig. 3d.

Docking interactions of Compound-5

The Compound-5 showed the docking score of -14.2283 kJ/mol with the ACE. It is observed that the Compound-5 exhibited critical interactions with the catalytic amino acid residues present in the active site cavity of the ACE by favoring the Hbond interactions and non-bonded interactions. The amino acid Phe381, Leu380, and Arg110 favored the Hbond interactions and the non-bonded interactions are supported by Arg110, Glu383, Leu382, Phe130, Phe487, and Phe381. Thus, this compound can be considered as potential ACE inhibitor molecule. The docking complex and docking interactions of Compound-5 within the active site of ACE is shown in Fig. 3e.

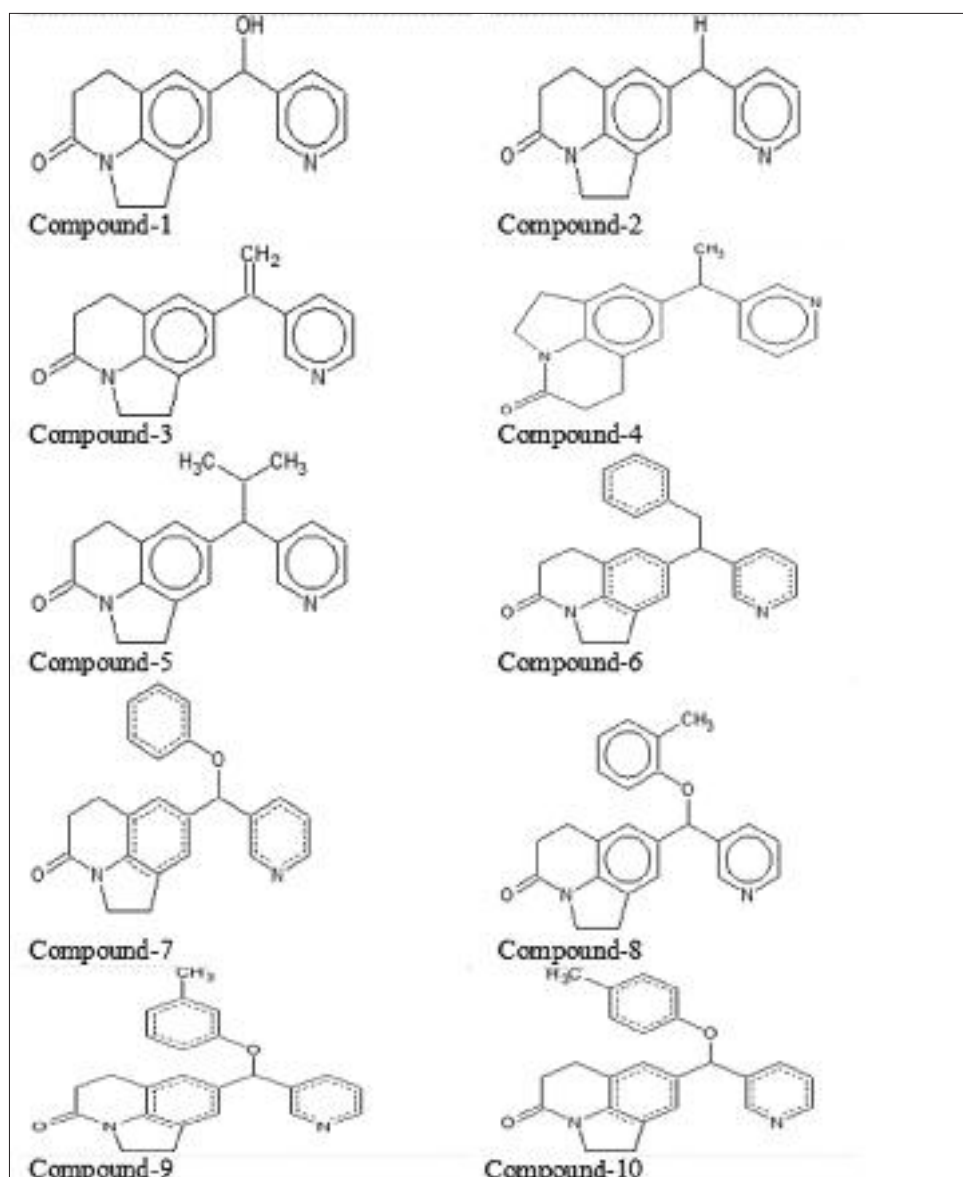


Fig. 2: The two-dimensional structure of 10 selected heterocyclic compounds

Docking interactions of Compound-6

The Compound-6 showed the docking score of -11.1612 kJ/mol with the ACE. It is observed that the Compound-6 exhibited critical interactions with the catalytic amino acid residues present in the active site cavity of the ACE by favoring the Hbond interactions and non-bonded interactions. The amino acid Phe381, Leu380, and Arg110 favored the Hbond interactions and the non-bonded interactions are supported by Arg110, Glu383, Leu382, Phe130, Phe487, and Phe381. Thus, this compound can be considered as potential ACE inhibitor molecule. The docking complex and docking interactions of Compound-6 within the active site of ACE is shown in Fig. 3f.

Docking interactions of Compound-7

The Compound-7 showed the docking score of -15.9906 kJ/mol with the ACE. It is observed that the Compound-7 exhibited critical interactions with the catalytic amino acid residues present in the active site cavity of the ACE by favoring the Hbond interactions and non-bonded interactions. The amino acid Phe381, Leu380, and Arg110 favored the Hbond interactions and the non-bonded interactions are supported by Arg110, Glu383, Leu382, Phe130, Phe487, and Phe381. Thus, this compound can be considered as potential ACE inhibitor molecule. The docking complex and docking

interactions of Compound-7 within the active site of ACE is shown in Fig. 3g.

Docking interactions of Compound-8

The Compound-8 showed the docking score of -17.1659 kJ/mol with the ACE. It is observed that the Compound-8 exhibited critical interactions with the catalytic amino acid residues present in the active site cavity of the ACE by favoring the Hbond interactions and non-bonded interactions. The amino acid Phe381, Leu380, and Arg110 favored the Hbond interactions and the non-bonded interactions are supported by Arg110, Glu383, Leu382, Phe130, Phe487, and Phe381. Thus, this compound can be considered as potential ACE inhibitor molecule. The docking complex and docking interactions of Compound-8 within the active site of ACE is shown in Fig. 3h.

Docking interactions of Compound-9

The Compound-9 showed the docking score of -15.7295 kJ/mol with the ACE. It is observed that the Compound-9 exhibited critical interactions with the catalytic amino acid residues present in the active site cavity of the ACE by favoring the Hbond interactions and non-bonded interactions. The amino acid Phe381, Leu380, and Arg110 favored the Hbond interactions and the non-bonded interactions are supported by

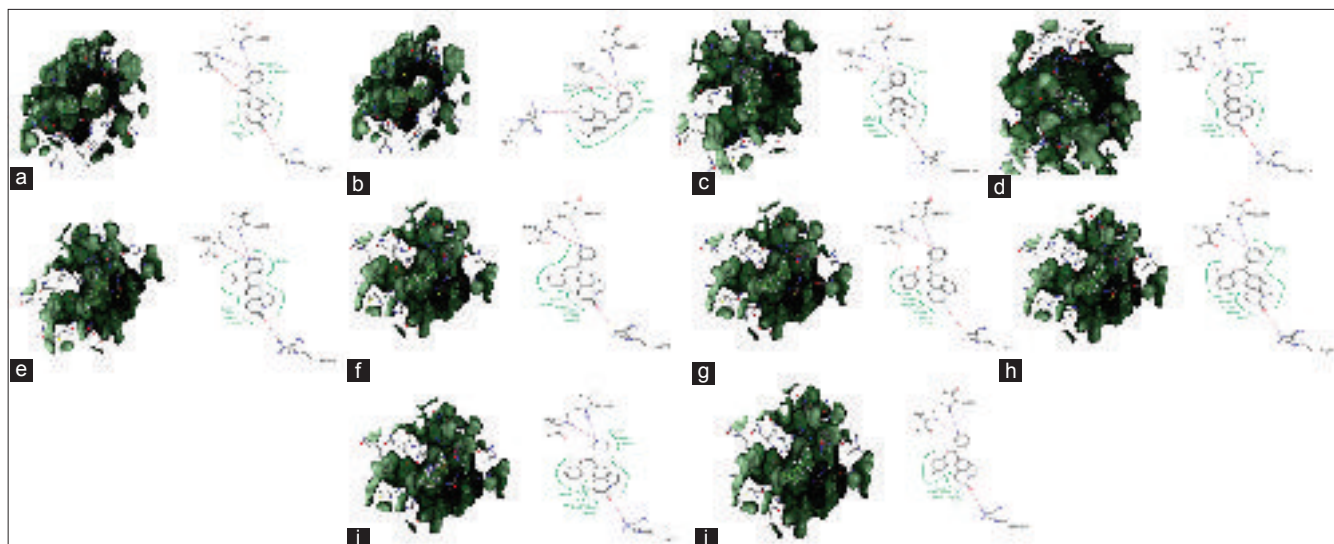


Fig. 3 (a) Docking complex and interactions of Compound-1 with angiotensin-converting enzyme (ACE) (Score: -11.3060 kJ/mol). (b) Docking complex and interactions of Compound-2 with ACE (Score: -17.9469 kJ/mol). (c) Docking complex and interactions of Compound-3 with ACE (Score: -18.9100 kJ/mol). (d) Docking complex and interactions of Compound-4 with ACE (Score: -26.6290 kJ/mol). (e) Docking complex and interactions of Compound-5 with ACE (Score: -14.2283 kJ/mol). (f) Docking complex and interactions of Compound-6 with ACE (Score: -11.1612 kJ/mol). (g) Docking complex and interactions of Compound-7 with ACE (Score: -15.9906 kJ/mol). (h) Docking complex and interactions of Compound-8 with ACE (Score: -17.1659 kJ/mol). (i) Docking complex and interactions of Compound-9 with ACE (Score: -15.7295 kJ/mol). (j) Docking complex and interactions of Compound-10 with ACE (Score: -14.7761 kJ/mol)

Phe487, Phe381, Gly379, Phe130, Trp116, Thr318, Phe231, Leu382, Ile488, and Arg110. Thus, this compound can be considered as potential ACE inhibitor molecule. The docking complex and docking interactions of Compound-9 within the active site of ACE is shown in Fig. 3i.

Docking interactions of Compound-10

The Compound-10 showed the docking score of -14.7761 kJ/mol with the ACE. It is observed that the Compound-10 exhibited critical interactions with the catalytic amino acid residues present in the active site cavity of the ACE by favoring the Hbond interactions and non-bonded interactions. The amino acid Phe381, Leu380, and Arg110 favored the Hbond interactions and the non-bonded interactions are supported by Arg110, Glu383, Leu382, Phe130, Phe487, and Phe381. Thus, this compound can be considered as potential ACE inhibitor molecule. The docking complex and docking interactions of Compound-10 within the active site of ACE is shown in Fig. 3j.

DFT studies

Among the selected 10 ACE inhibitors, the Compound-4 exhibited the highest docking score, and thus, the Compound-4 was considered to explore its structural features and also the chemical entities required for the activity of the compound. The compound geometry was analyzed through predicting Fourier transform infrared (FT-IR) and FT Raman spectra of the optimized Compound-4. Further, considering that the determination of the energy gap between highest occupied molecular orbital (HOMO) and lowest unoccupied molecular orbitals (LUMO) could provide the chemical reactivity and kinetic stability of molecules, the Compound 4 was optimized and proposed for theoretical calculations (DFT studies) using Gaussian software.

Vibrational analysis

The vibration spectral analysis is performed on the basis of the characteristic vibrations of the amino group, hydroxyl group, carbonyl group, and methyl group. The optimized 3D structure of Compound-4 is shown in Fig. 4.

The theoretically predicted FT-IR and FT Raman spectra using B3LYP/6-311 G (d,p) method and the observed experimental FT-IR and FT Raman spectra are shown in Figs. 5 and 6, respectively. The

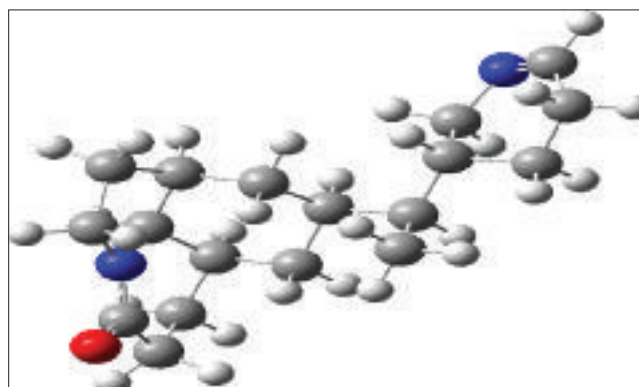


Fig. 4: The optimized geometry of the Compound-4

respective FT-IR spectra and FT Raman spectra were recorded in the range from 4000 to 400 cm^{-1} .

The Compound-4 exhibits a sharp peak at 2000 cm^{-1} associated with the -C-H- stretching vibrations of CH and CH_3 groups. The signal characteristic bands of C=O (carbonyl) stretching vibration at 1600 – 1750 cm^{-1} are due to the presence of some aromatic esters.

The compounds containing methyl groups and C-H groups are electron donating substituent in the aromatic ring system. Absorption arising from C-H stretching in the alkenes occurs in the region 3000 – 2840 cm^{-1} . The lowering of the wave numbers from the normal values is due to the intermolecular charge transfer from the dimethyl group to the hydroxyl group through π conjugation system.

The changes in intensity of the CH_3 stretching mode are also due to the influence of electronic effects resulting from hyperconjugation of methyl group with nitrogen atom and the aromatic ring system. Thus, the hyperconjugation of methyl group, causing changes in intensity in IR, clearly indicates that methyl hydrogen is directly involved in the donation of electronic charge. The asymmetric and symmetric bending

vibrations of methyl group normally appear around 1446 and 1375 cm^{-1} , respectively. The relatively large value of intensity in IR and Raman wave numbers of the rocking modes suggests the presence of hyperconjugation. The twisting and torsion vibrations are identified below 503 cm^{-1} , which are also supported by the computed wave numbers.

The fundamental modes involving the amino group are stretching and bending of NH bonds, torsion, and inversion. The Compound-4 under investigation possesses one NH₂ group, and hence, one expects one symmetric and one asymmetric N-H stretching vibrations. In all the primary aromatic amines, the N-H stretching frequency occurs in the region 3300–3500 cm^{-1} and. The antisymmetric stretching mode appears to be higher wave number than the symmetric. In Compound-4, the NH₂ asymmetric stretching vibration is observed in IR at 2500 as a medium band; the symmetric stretching vibration is observed in IR around 3520 cm^{-1} and in Raman around 3580 cm^{-1} . The frequency lowering present in the molecule is due to the intermolecular interaction.

The ring modes which are found to be active in both IR and Raman spectra enable the molecule to be an effective π conjugation system. Due to the existence of one directional charge transfer from the donor to the acceptor through the single-double bond conjugated path induces large variations of both the molecular dipole moment and the molecular polarizability during the same vibrations, thus gaining the activity of both IR and Raman at the same time. The simultaneous activation of IR and Raman ring modes also supports the charge transfer interaction between CH₃ and the aromatic ring which also plays an important role in the biological activity of the compound to establish as a pharmaceutical compound with inhibitory activities.

Natural bond analysis (HOMO-LUMO)

The Eigenvalue of LUMO-HOMO energy gap reflects the chemical activity of the molecule. The HOMO-LUMO plot of Compound-4 is

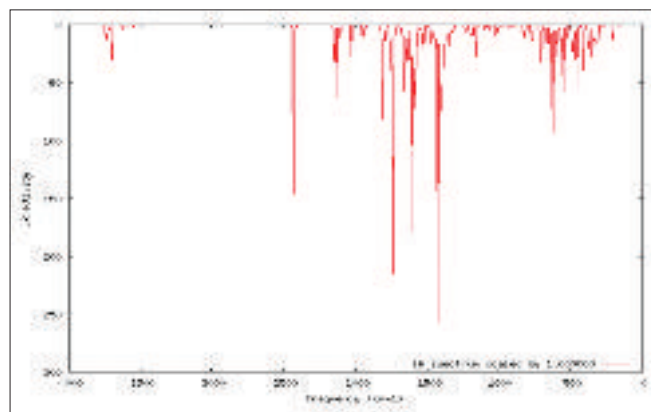


Fig. 5: Theoretical Fourier transform infrared of Compound-4

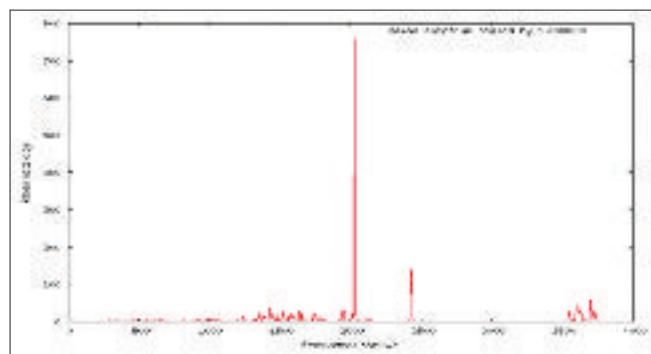


Fig. 6: Theoretical Fourier transform Raman spectra of Compound-4

shown in Fig. 7. The calculated HOMO of -4.46eV and LUMO of -2.86eV are observed.

The decrease in the HOMO and LUMO energy gap (1.60 eV) explains the eventual charge transfer interaction taking place within the molecule, due to the strong electron-accepting ability of the electron-acceptor group. It is worth noting that HOMOs have an overall π bonding character along with a considerable non-bonding character and LUMOs have an antibonding π^* character. The strong charge transfer interaction is responsible for the bioactivity of the molecule.

Molecular electrostatic potentials

The electrostatic contour map of the Compound-4 is shown in Fig. 8. The blue contours indicate electropositive charges correlating with activity and the Hbond donor regions, and the red contour indicates the relationship between negative charge and activity and also the Hbond acceptor regions.

The increase in positive charge and H-bond donor regions are favored in blue region while increase in negative charge and H-bond acceptor regions are favored in red region. Blue-colored regions show areas where electropositive charged groups enhance inhibitory activity by the presence of H-bond donors, while red regions represent where electronegative charged groups improve the activity with the presence of H-bond acceptors. The green colored contours indicates the steric bulk groups that are required to increase the activity while the yellow contours indicates the unfavorable steric bulk groups that can decrease the activity.

Thus, considering the docking interactions of Compound-4 with ACE protein and geometry, HOMO-LUMO energy gaps and electrostatic contour map of the Compound-4 clearly envisage that the presence of electropositive charged groups is very essential to enhance the inhibitory activity along with the H-bond donors, and the presence of electronegative charged groups can possibly improve the activity along the presence of H-bond acceptors.

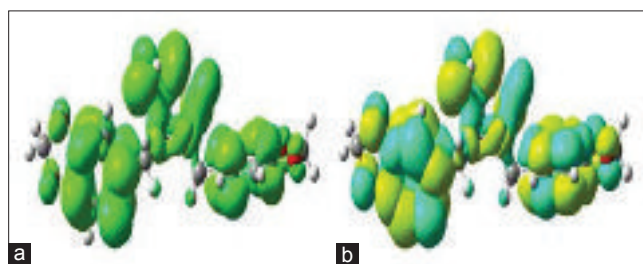


Fig. 7: The highest occupied molecular orbital-lowest unoccupied molecular orbitals plot of the Compound-4

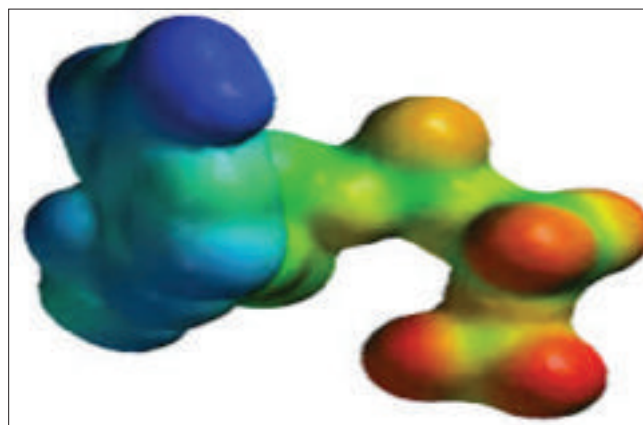


Fig. 8: Electrostatic contour map of the Compound-4

CONCLUSION

Hypertension is an important risk factor, contributing to other cardiovascular diseases such as blood vessel disorders, coronary heart disease, aortic aneurysm, and stroke. The search for many novel ACE inhibitors is in progress that can be effective in the treatment of hypertension. Hence, the clear understanding of the present ACE inhibitors might give envisage the required chemical entities for the better ACE inhibition activity. Thus, in this study, a set of ACE inhibitors is used to explore their binding mechanisms with ACE protein and the Compound-4 with the highest activity is considered for further DFT analysis. The DFT studies revealed the HOMO (-4.46eV) and LUMO (-2.86 eV) and the energy gap (1.60 eV). This NBO analysis explained the eventual charge transfer is due to the strong electron-accepting ability of the compound. Furthermore, the electrostatic contour map revealed that the presence of electropositive charged groups is very essential to enhance the inhibitory activity along with the H-bond donors, and the presence of electronegative charged groups can possibly improve the activity along the presence of H-bond acceptors.

AUTHORS' CONTRIBUTIONS

CZDL carried out of the experimental part of the work. The CV and ASM guided and monitored the experimental design; GS carried the data compilation and drafted the manuscript.

CONFLICTS OF INTEREST

The authors do not have any conflicts of interest to declare.

REFERENCES

- Clark RD, Strizhev A, Leonard JM, Blake JF, Matthew JB. Consensus scoring for ligand/protein interactions. *J Mol Graph Model* 2002;20:281-95.
- Gehlhaar DK, Verkhivker G, Rejto PA, Fogel DB, Fogel LJ. Docking Conformationally Flexible Small Molecules into a Protein Binding Site through Evolutionary Programming. *Proceedings of the Fourth International Conference on Evolutionary Programming*; 1995. p. 615-27.
- Charifson PS, Corkery JJ, Murcko MA, Walters WP. Consensus scoring: A method for obtaining improved hit rates from docking databases of three-dimensional structures into proteins. *J Med Chem* 1999;42:5100-9.
- Izzo JL, Black HR, Goodfriend TL. *Hypertension Primer: The Essentials of High Blood Pressure*. Philadelphia, PA: Lippincott Williams and Wilkins; 2003.
- Advanced Chemistry Development, Inc. ACD/Chem Sketch Freeware. Version 12. Toronto, ON, Canada: Advanced Chemistry Development, Inc. Available from: <http://www.acdlabs.com>.
- Weininger D. SMILES, a chemical language and information system. Introduction to methodology and encoding rules. *J Chem Inf Comput Sci* 1998;28:31-6.
- Natesh R, Schwager SL, Sturrock ED, Acharya KR. Crystal structure of the human angiotensin-converting enzyme-lisinopril complex. *Nature* 2003;421:551-4.
- Sussman JL, Lin D, Jiang J, Manning NO, Prilusky J, Ritter O, et al. Protein data bank (PDB): Database of three-dimensional structural information of biological macromolecules. *Acta Crystallogr D Biol Crystallogr* 1998;54:1078-84.
- Rarey M, Kramer B, Lengauer T, Klebe G. A fast flexible docking method using an incremental construction algorithm. *J Mol Biol* 1996;261:470-89.
- Gnanendra S, Anusuya S, Natarajan J. Molecular modeling and active site analysis of sdiA homolog, a putative quorum sensor for salmonella typhimurium pathogenicity reveals specific binding patterns of AHL transcriptional regulators. *J Mol Model* 2012;18:4709-19.
- Sari BL, Mun'im A, Yanuar A, Riadhi R. Screening of α -glucosidase inhibitors from *Terminalia catappa* L. fruits using molecular docking method and *in vitro* test. *Int J Pharm Pharm Sci* 2016;8:184-9.
- Anjugam C, Sridevi M, Gnanendra TS. Structure-based docking studies toward exploring the potential anticancer activity of morin against non-melanoma skin cancer therapeutic drug targets. *Asian J Pharm Clin Res* 2018;11:61-6.
- Stierand K, Maass PC, Rarey M. Molecular complexes at a glance: Automated generation of two-dimensional complex diagrams. *Bioinformatics* 2006;22:1710-6.
- Suresh DM, Amalanathan M, Sebastian S, Sajan D, Hubert Joe I, Bena Jothy V, et al. Vibrational spectral investigation and natural bond orbital analysis of pharmaceutical compound 7-amino-2,4-dimethylquinolinium formate-DFT approach. *Spectrochim Acta A Mol Biomol Spectrosc* 2013;115:595-602.
- White WB, Prisant LM, Wright JT Jr. Management of patients with hypertension and diabetes mellitus: Advances in the evidence for intensive treatment. *Am J Med* 2000;108:238-45.
- Vázquez-Valadez VH, Abrego VH, Martínez PA, Torres G, Zúñiga O, Escutia D, et al. Docking studies of methylthiomorpholin phenols (LQM300 series) with angiotensin-converting enzyme (ACE). *Open Med Chem J* 2013;7:30-8.

Identification Of Potential Drug Targets From Intrinsically Disordered Proteins (Idps)

MeeraBanu A, Shakina J, Syed Mohamed A, Bushra U S

Abstract: Intrinsically Disordered Proteins (IDPs) are lack in their stable tertiary and/or secondary structures under physiological conditions. IDPs can adopt a fixed three-dimensional structure after binding to other macromolecules. Parkinson's Disease (PD) is a degenerative, neurological disease that causes a person to lose control over some body functions. Symptoms start gradually with a barely noticeable tremor in just one hand. Tremors are common, but the disorder also commonly causes stiffness or slowing of movement. Many amino acids which are responsible for the disorderness they are aspartic acid, methionine, lysine, arginine, serine, glutamine, proline, glutamic acid. Withaniasomnifera (Ws) is an Indian Ayurvedic traditional medicinal herb root extract is rich in steroidal lactones including withanone, withaferin, withanolides, withasomidienone, and withanolide. These compounds have been reported to inhibit metastasis and quinonereductase activity and preferentially affect the cholinergic signal transduction cascade of the cortical and basal forebrain, and thus may be beneficial for the treatment of PD. The outcome of this research project can lead a reflective standard shift in the treatment of Parkinson's Disease (PD). The outcome of this project can also significantly support our understanding and analysis of biological networks of Human diseases.

Keywords: Intrinsically Disordered Proteins (IDPs) , signaling interactions, Parkinson's Disease(PD), Withaniasomnifera, quinonereductase, α - synuclein, 6FLT

1. INTRODUCTION

Intrinsically Disordered Proteins (IDPs) are lack in their stable tertiary and/or secondary structures under physiological conditions¹. IDP can adopt a fixed three-dimensional structure after binding to other macromolecules. They have important functions both in vitro and in vivo². They are highly abundant in nature and their functional range complements the signaling and control. Intrinsic disorder opens a unique binding capability when they are binding to the partners and to gain different bound structures. They can also form highly stable complexes in "signaling interactions". Aspartic acid, methionine, lysine, arginine, serine, glutamine, proline, glutamic acid are said to be the disorder promoting residues of the protein molecule³. According to the physico-chemical point of view, the majority of order-promoting residues are non-polar and commonly found within the hydrophobic cores of ordered proteins, whereas the majority of disorder-promoting residues are polar, often charged, and commonly found on the surfaces of ordered proteins⁴. Finally interesting interconnections among intrinsic disorder, cell signaling and many human diseases suggest that protein conformational diseases are not only formed by the protein mis-foldings but also from misidentification, missignaling and unnatural and nonnative folding of the protein. Thus, the project aims to investigate such proteins sequences from human proteome containing disordered regions, and implicated in diseases with a specific objective of classifying these disordered proteins as potential drug targets. Conventional tasks such as identification of active

sites and inventing new protocols for docking at the active site and estimating the accuracy of docking in such disordered regions.

IDPs AND PARKINSON'S DISEASE

Parkinson's Disease (PD) is a degenerative, neurological disease that causes a person to lose control over some body functions. Symptoms start gradually, with a barely noticeable tremor in just one hand. Tremors are common, but the disorder also commonly causes stiffness or slowing of movement. Withaniasomnifera (Ws) is an Indian Ayurvedic traditional medicinal herb grown in India, Africa, and the Mediterranean region. The root extract is rich in steroidal lactones including withanone, withaferin, withanolides, withasomidienone, and withanolide. The above compounds are skilled of inhibiting metastasis and quinonereductase activity and preferentially affect the cholinergic signal transduction cascade of the cortical and basal forebrain, and thus may be beneficial for the treatment of PD.



Fig:1. *Withaniasomnifera* (Ws)

MATERIALS AND METHODS

Protein Preparation:

The protein 6FLT was loaded from RCSB protein data bank (www.rcsb.org/pdb/) on the PyRx then the force field Uff and is applied to the structure then minimization was carried out the algorithms is Conjugate Gradient and Smart Minimizer along with the maximum steps were 200 to minimize the molecule to results satisfied.

Ligand Preparation

The ligands were sketched using ACD/ ChemSketch (12.0) software and saved in (.mol) file format. The saved ligand

- Research Scholar, PG and Research Dept. of Chemistry, Sarah Tucker College (Affiliated to Manonmaniam Sundaranar University), Tirunelveli, Tamil Nadu, India. meera3306@gmail.com
- **Asst. Professor, PG and Research Dept. of Chemistry, Sarah Tucker College (Affiliated to Manonmaniam Sundaranar University), Tirunelveli Tamil Nadu, India. shakinajudson@gmail.com
- \$Corresponding author, Research Head, Research Dept. of Chemistry, Sadakathullah Appa College, Tirunelveli, Tamilnadu, India. asm2032@gmail.com
- #Research Scholar, Research Dept. of Chemistry, Sadakathullah Appa College, Tirunelveli, Tamilnadu, India. s.bushra91@gmail.com

compounds were later imported in was loaded on the PyRx and minimised using Dreiding Minimizer.

Docking

The Protein and Ligands molecules are loaded on the then the forcefield and minimization were applied to that and docking studies are carried out Auto Dock docking method is used for this the high positive docking score were to be consider the H-bond interaction are shown below with the docked protein and ligands.

RESULT AND DISCUSSION

The target protein receptor possessed satisfactory geometric parameters and was therefore used in the investigation of the ligand-protein interaction. In the present Docking analysis, all three ligand compounds were docked in active site of Human alpha-synuclein (α -syn). Docking analysis reveal that most active compound withaferin interacted with receptor through H-bond interactions. On mapping of all the ligands against generated features, it is shown the best compound is withaferin based on Auto Dock binding affinity. The results and discussion are shown below. α -SYNUCLEIN (α -syn) Human alpha-synuclein (α -syn) is predominantly conversed in the brain, especially in the neocortex, hippocampus, substantianigra(SN),thalamus and cerebellum and is found in Lewy bodies (LBs). α -Syn is an acidic protein with three domains namely N-terminallipid-binding α -helix, amyloid-binding central domain (NAC),and C-terminal acidic tail. α -Syn can be present as an α -helix structure in association with phospholipids or an unfolded conformation in the cytosol, suggesting that it plays special roles in divergent cellular locations based on its dynamic structure.

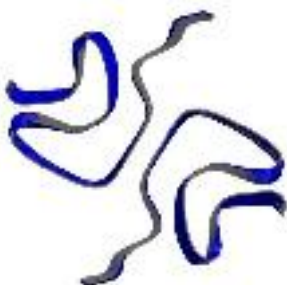


Fig. 2. SECONDARY STRUCTURE OF α -SYNUCLEIN

Primary Sequence of α -synuclein

```
>6FLT:A|PDBID|CHAIN|SEQUENCE
MDVFMKGLSKAKEGVVAAAEKTKQGVAAEAGKTEGVL
YVGSKTKEGVVHGVATVAEKTKEQVTNVGGAVVTGVT
VAQKTVEGAGSIAAATGFVKKDQLGKNEEGAPQEGILE
MPVDPDMDVFMKGLSKAKEGVVAAAEKTKQGVAAEAGK
TKEGVLYVGSKTKEGVVHGVATVAEKTKEQVTNVGGAVV
TGVTAVAQKTVEGAGSIAAATGFVKKDQLGKNEEGAPQE
GILEDMPVDPDMDVFMKGLSKAKEGVVAAAEKTKQGV
AAEAGKTEGVLVYVGSKTKEGVVHGVATVAEKTKEQVTN
GGAVVTGVTAVAQKTVEGAGSIAAATGFVKKDQLGKNEE
GAPQEGILEDMPVDPDMDVFMKGLSKAKEGVVAAAEK
TKQGVAAEAGKTEGVLVYVGSKTKEGVVHGVATVAEKT
KEQVTNVGGAVVTGVTAVAQKTVEGAGSIAAATGFVKKD
QLGKNEEGAPQEGILEDMPVDPDMDVFMKGLSKAKEGV
VAAAEKTKQGVAAEAGKTEGVLVYVGSKTKEGVVHGVAT
```

```
EKTKEQVTNVGGAVVTGVTAVAQKTVEGAGSIAAATGFV
KKDQLGKNEEGAPQEGILEDMPVDPDMDVFMKGLSKAK
EGVVAEAEKTKQGVAAEAGKTEGVLVYVGSKTKEGVVH
GVATVAEKTKEQVTNVGGAVVTGVTAVAQKTVEGAGSIA
AATGFVKKDQLGKNEEGAPQEGILEDMPVDPDMDVFMK
GLSKAKEGVVAAAEKTKQGVAAEAGKTEGVLVYVGSKT
KEGVVHGVATVAEKTKEQVTNVGGAVVTGVTAVAQKTVE
GAGSIAAATGFVKKDQLGKNEEGAPQEGILEDMPVDPD
MDVFMKGLSKAKEGVVAAAEKTKQGVAAEAGKTEGVLV
YVGSKTKEGVVHGVATVAEKTKEQVTNVGGAVVTGVT
VAQKTVEGAGSIAAATGFVKKDQLGKNEEGAPQEGILE
DMPVDPDMDVFMKGLSKAKEGVVAAAEKTKQGVAAEAG
KTKEGVLVYVGSKTKEGVVHGVATVAEKTKEQVTNV
GGAVVTGVTAVAQKTVEGAGSIAAATGFVKKDQLGKNEE
GAPQEGILEDMPVDPD
```

Selection of α -synuclein The protein data bank (PDB) is a collection of crystal structures for proteins with bound ligands and co-activators. Protein searched for the crystal structure of Human DNA α -synuclein has around many PDB structures. Among all of them, the best protein was selected as 6FLT based on the high resolution on X-Ray diffraction results and Ramachandran plot analysis. The Ramachandran plot of protein 6FLT is shown in Fig. 2. Number of residues in favoured region (~98.0% expected) : 480 (85.7%) Number of residues in allowed region (~2.0% expected) : 80 (14.3%) Number of residues in outlier region : 0 (0.0%)

Protein molecule in the PyRx:

The Protein 6FLT has loaded on the PyRx then the force field Uff and is applied to the structure then minimization was carried out the algorithms is conjugate gradient and smart minimizer along with the maximum steps were 200 to minimize the molecule to results satisfied.

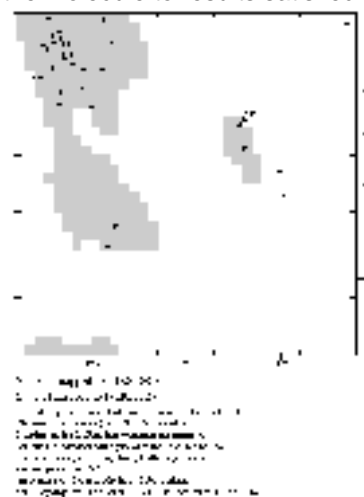


Fig. 3. Ramachandran plot analysis of 6FLT

(85.7% residues in most favored region and 0.0% residues in disallowed region)



Fig: 4. Protein Molecule in 3D -window

Docking Results:

The Protein and Ligands molecules are loaded on the PyRx then the forcefield and minimization were applied to that and docking studies are carried out Auto Dock docking method is used for this the high positive docking score were to be consider the H-bond interaction are shown in Table 1 with the docked protein and ligands.

CONCLUSION

The X-ray crystal structure of the human alpha-synuclein (α -syn) was retrieved from protein data bank and the Withaniasomnifera compounds were sketched using ACD/ChemSketch software. The target protein receptor possessed satisfactory geometric parameters and was therefore used in the investigation of the ligand-protein interaction. In the present Docking analysis, all three ligand compounds were docked in active site of Human alpha-synuclein (α -syn). Docking analysis reveal that most active compound withaferin interacted with receptor through H-bond interactions. On mapping of all the ligands against generated features, it is shown the best compound is withaferin based on Auto Dock binding affinity.

Ligand molecule in the PyRx :

The ligands were loaded on the PyRx and ligands are prepared by using the small molecules-general purpose-ligand preparation otherwise the dried minimizer were used to prepare the ligands all the ligands were load into the one 3D window.



Fig: 5. Ligand Molecules in 3D –window

Table 1: Binding Affinity for Selected Ligands

Ligand	Align (Total Score)	H-bond	Hydrophobic	Hydrophilic
Withaferin	1.2	1	1	1
Withanone	1.1	1	1	1
Withanone	1.0	1	1	1
Withanone	0.9	1	1	1
Withanone	0.8	1	1	1
Withanone	0.7	1	1	1
Withanone	0.6	1	1	1
Withanone	0.5	1	1	1
Withanone	0.4	1	1	1
Withanone	0.3	1	1	1
Withanone	0.2	1	1	1
Withanone	0.1	1	1	1
Withanone	0.0	1	1	1
Withanone	-0.1	1	1	1
Withanone	-0.2	1	1	1
Withanone	-0.3	1	1	1
Withanone	-0.4	1	1	1
Withanone	-0.5	1	1	1
Withanone	-0.6	1	1	1
Withanone	-0.7	1	1	1
Withanone	-0.8	1	1	1
Withanone	-0.9	1	1	1
Withanone	-1.0	1	1	1
Withanone	-1.1	1	1	1
Withanone	-1.2	1	1	1
Withanone	-1.3	1	1	1
Withanone	-1.4	1	1	1
Withanone	-1.5	1	1	1
Withanone	-1.6	1	1	1
Withanone	-1.7	1	1	1
Withanone	-1.8	1	1	1
Withanone	-1.9	1	1	1
Withanone	-2.0	1	1	1
Withanone	-2.1	1	1	1
Withanone	-2.2	1	1	1
Withanone	-2.3	1	1	1
Withanone	-2.4	1	1	1
Withanone	-2.5	1	1	1
Withanone	-2.6	1	1	1
Withanone	-2.7	1	1	1
Withanone	-2.8	1	1	1
Withanone	-2.9	1	1	1
Withanone	-3.0	1	1	1
Withanone	-3.1	1	1	1
Withanone	-3.2	1	1	1
Withanone	-3.3	1	1	1
Withanone	-3.4	1	1	1
Withanone	-3.5	1	1	1
Withanone	-3.6	1	1	1
Withanone	-3.7	1	1	1
Withanone	-3.8	1	1	1
Withanone	-3.9	1	1	1
Withanone	-4.0	1	1	1
Withanone	-4.1	1	1	1
Withanone	-4.2	1	1	1
Withanone	-4.3	1	1	1
Withanone	-4.4	1	1	1
Withanone	-4.5	1	1	1
Withanone	-4.6	1	1	1
Withanone	-4.7	1	1	1
Withanone	-4.8	1	1	1
Withanone	-4.9	1	1	1
Withanone	-5.0	1	1	1

Fig:6. Docking Results

REFERENCES

- [1] Intrinsically disordered proteins: regulation and disease; M adanBabu, Robinvander Lee, Natalia Sanchezde Groot and Jo"rgGspomer; ; Science Direct, Current Opinion in Structural Biology 2011, 21:1-9.
- [2] Targeting intrinsically disordered proteins in neurodegenerative and protein dysfunction diseases: another illustration of the D2 concept; Vladimir N Uversky; Expert Rev Proteomics. 2010 Aug; 7(4): 543–564.
- [3] The alphabet of intrinsic disorder II. Various roles of glutamic acid in ordered and intrinsically disordered proteins; Vladimir N Uversky. Intrinsicly Disord. Proteins. 2013.
- [4] The alphabet of intrinsic disorder I. Act like a Pro: On the abundance and roles of proline residues in intrinsically disordered proteins Francois-Xavier Theillet, Lajos Kalmar, Peter Tompa, Kyou-Hoon Han, Philipp Selenko,1 A. Keith Dunker, Gary W. Daughdrill, and Vladimir N Uversky. Intrinsicly Disord Proteins; January, 2013.
- [5] Protein Kinase C: An Attractive Target for Cancer Therapy; Barbara Marengo*, Chiara De Ciucis, Roberta Ricciarelli, Maria A. Pronzato, Umberto M. Marinari and CinziaDomenicotti. Cancers (Basel). 3(1): 531–567. 2011.
- [6] The alphabet of intrinsic disorder I. Act like a Pro: On the abundance and roles of proline residues in intrinsically disordered proteins Francois-Xavier Theillet, Lajos Kalmar, Peter Tompa, Kyou-Hoon Han, Philipp Selenko, A. Keith Dunker, Gary W. Daughdrill and Vladimir N. Uversky. Landes Bioscience, e24360-2 .volume1 ,issue 1.
- [7] Intrinsic disorder in Viral Proteins Genome-Linked: experimental and predictive analyses EugénieHébrard, YannickBessin, Thierry Michon, Sonia Longhi, Vladimir N Uversky5, François Delalande, Alain Van Dorsselaer, Pedro Romero, Jocelyne Walter, Nathalie Declerck and Denis Fargette. Virology Journal 2009, 6:23.
- [8] Unfoldomics of human diseases: linking protein intrinsic disorder with diseases Vladimir N Uversky, Christopher J Oldfield, UrosMidic, Hongbo Xie4, Bin Xue1, Slobodan Vucetic, Lilia M lakoucheva, ZoranObradovic and A Keith Dunker. BMC Genomics 2009, 10(Suppl-1):S7.
- [9] Intrinsic Disorder and Functional Proteomics PredragRadivojac,* Lilia M. lakoucheva, y Christopher J. Oldfield,* ZoranObradovic, z Vladimir N. Uversky, and A. Keith Dunker. Biophysical Journal Volume 92 March 2007 1439–1456.
- [10] Amino acid contribution to protein solubility: Asp, Glu, and Ser contribute more favorably than the other hydrophilic amino acids in RNaseSaSaul R. Trevino, Martin Scholtz, and C. Nick Pace; J Mol Biol. 2007 Feb 16; 366(2): 449–460., 2006.

Spectroscopic analysis (Raman, FT-IR, UV, NMR), HUMO, LUMO and first order hyper polarizability calculations of Nor Leucine Maleate (DLNM) using DFT methods

A.Zeenath Bazeera¹ Dr.S.Selvaraj² Dr.A.Syed Mohamed³

¹Part- time Ph.D Research Scholar, Reg. No. 12100, Department of physics, M.D.T.Hindu College, Tirunelveli, & Assistant professor, Department of Physics, Sadakathullah Appa College, Tirunelveli, Tamilnadu.

² Associate Professor, Department of Physics, M.D.T. Hindu College, Tirunelveli, Tamilnadu.

³ Assistant professor, Department of Chemistry, Sadakathullah Appa College, Tirunelveli, Tamilnadu.

Abstract

The investigations by various spectroscopic analysis for Nor Leucine Maleate were carried out in this study. The crystal characterizations were done using FT-IR ($4,000-400\text{cm}^{-1}$), FT-Raman ($3,500-500\text{cm}^{-1}$), UV-Vis (200-800nm) and NMR by SCF-GIAO method. HOMO-LUMO analysis for were done. The HUMO-LUMO energy gap of the Nor Leucine Maleate was calculated at B3LYP/6-31G (d, p) level, which aids in the revelation that the energy gap found in this analysis reflects the chemical activity of the molecule. The first order Hyper polarizability was also calculated. Finally, this study aids in the optimization of Non-Linear Optical property of Nor Leucine Maleate for various applications such as optoelectronic devices.

Key Words : Nor Leucine Maleate, First order hyper polarizability, HUMO-LUMO, FT-IR.

1. Introduction

The materials which possess optical non-linearity (NLO materials) are of great significance and are used in a number of optoelectronic and photonic devices. Materials which possess the property of optical linearity also has technological importance in areas such as optical communications, optical computing and data storage [1]. The semi-organic and organic materials are given more importance due to their high non-linearity, quick response and great diversities in opto-electric effect when compared to an inorganic NLO material. Organic crystals have a delocalized π -conjugated system [2, 3]. Conjugated donor-acceptor substituted organic materials are known to exhibit good NLO and electro-optical

effects. The optical-linearity can be intensified by adding a strong electron donating and also optimizing the donor-acceptor distance. The extensive choice of materials helped in improving high non-linearity, low transformation temperature, fast response and high transparency making these systems more demanding than any other systems. The interest in the optical non-linearity phenomena has increased after the advent of laser sources and they also play a very important role in the development of laser technology. DL-Norleucine is found to be both a glucogenic and a ketogenic amino acid. It is one among the three amino acids with a branched hydro carbon side chains. DL-Norleucine is hydrophobic, non polar and aliphatic in nature. DL-Norleucine has been used in various computational studies such as molecular dynamics simulations for elucidating the solid state transition mechanism in molecular crystals[4-7]. In the present study, we chose Norleucine maleate to enhance the property of optical non-linearity. DL-Norleucine and maleic acid are mixed to form DL-Norleucine maleate crystal. The structure of the crystal is studied. Several spectroscopic studies such as UV, FTIR, Raman, VCD, ECD were carried out. In addition HUMO LUMO analysis, hyperpolarizability were carried out. Moreover, theoretical calculations based on Density Functional Theory (DFT) were done for the investigation of NLO properties.

2. Experimental studies

Characterization of Nor Leucine Maleate

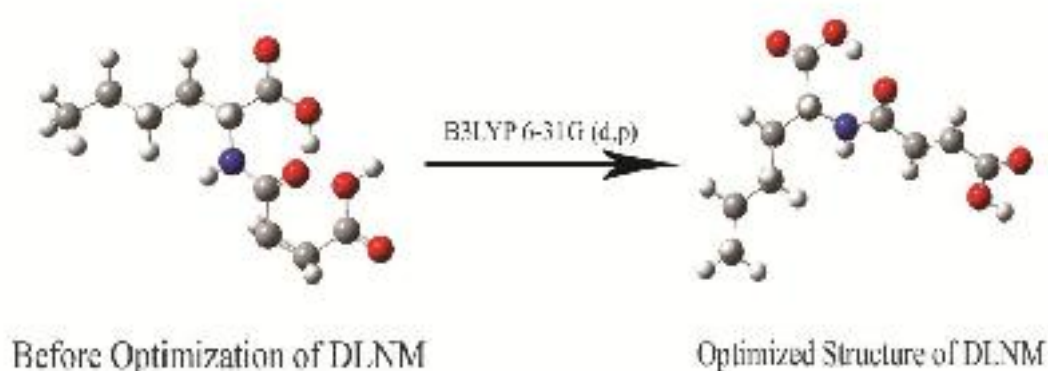
Several characterization studies of the crystal were undertaken to understand their structure. The FT-IR spectra were recorded in the range of $400\text{-}4000\text{cm}^{-1}$ with a resolution of $\pm 4\text{cm}^{-1}$ with an accuracy of $\pm 0.01\text{cm}^{-1}$ on a BRUKER IFS 667 FTIR. Other spectroscopic studies viz. UV-vis, Raman was done in the region $3,500\text{-}500\text{cm}^{-1}$ to ensure the crystal structure and the purity of the crystals. Various interpretations were done based on the spectrum obtained. Nuclear Magnetic Resonance is one of the most powerful tools for elucidating the structure of compounds making it an important method for the study of organic chemistry. The SCF-GIAO plot will show the assignments to each atom, the integration simulation and a reference curve if needed. When two atomic or molecular orbitals interact with each other it produces two new orbitals. Of the two orbitals one has higher energy (the anti-bonding orbitals) and another orbital with lower energy (the bonding orbitals). If one of the orbitals is filled with an electron pair (Lewis base) while the other is empty (a Lewis acid), we can place both the electron into lower energy of the two orbitals. Therefore the interaction between the “filled-energy” orbitals is stabilizing. If we deal with the interacting molecular orbitals, the two that interact are the highest energy occupied

molecular orbitals (HOMO) and lowest occupied molecular orbitals (LUMO) of the specific compound. These two orbitals are a pair of orbitals, allowing them to interact more strongly. As these orbitals lie at the outermost boundaries of the electron in the compound, they are known as the frontier orbitals. The intermolecular charge from the donor to the acceptor group through a single-bond conjugated path is able to induce a huge variation in the molecular dipole moment and also the molecular polarizability, making the activity of IR strong[8,9]. The HOMO-LUMO energy gap of the Nor Leucine Maleate was calculated at B3LYP/6-31G (d, p) level, which reveals that the energy gap found in this analysis reflects the chemical activity of the molecule of interest. Other than this, Hyper polarizability calculations were done for DLNT crystals by the DFT-B3LYP functional with the 6-31G (d, p) basis set. The output from GAUSSIAN 09 provides 10 components of the 3*3*3 matrix as β_{xxx} , β_{xxy} , β_{xyy} , β_{yyy} , β_{xxz} , β_{xyz} , β_{yyz} , β_{xzz} , β_{yzz} , β_{zzz} and also the total hyperpolarizability is also calculated.

3. Results and discussion

3.1 Optimized Molecular Geometry

The molecular geometry of DLNM was designed using Gaussian 09 and optimization was carried out with DFT-B3LYP functional with the 6-31G (d,p) basis set. Optimization corrects our molecular structure, the bond angle and bond length between the molecules. This optimized molecular structure is used for other characterizations.



3.2 FT-IR analysis

The FT-IR spectrum of DLNM is shown in figure 1:

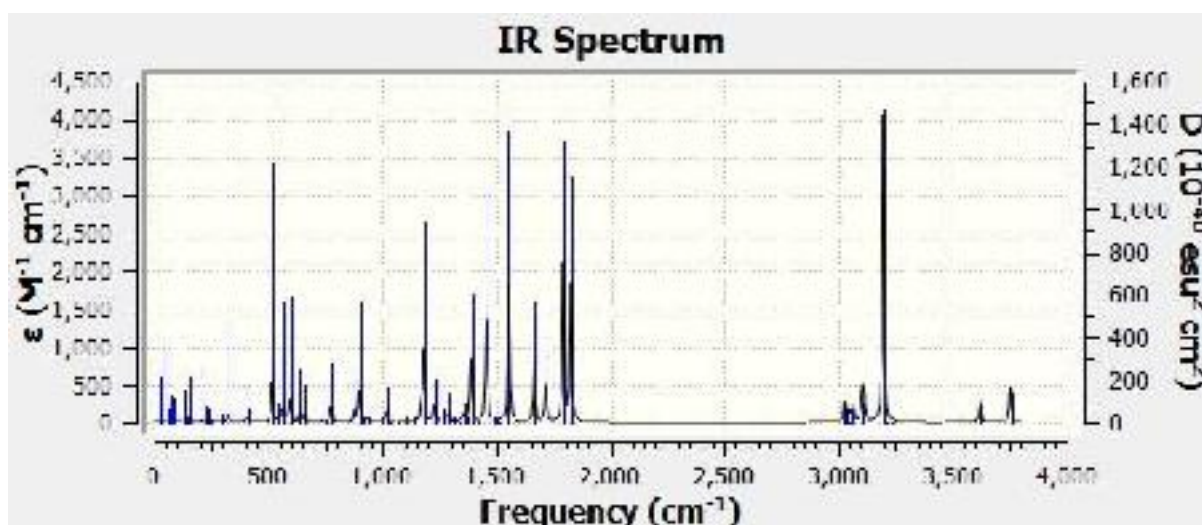


Fig.1: FT-IR of Nor Leucine Maleate

The B3LYP level at 6-31G (d,p) basis set and keyword freq=(raman) is used to calculate theoretical FT-IR and FT-Raman. The prominent peak at 3197cm^{-1} corresponds to C-H stretching. The C=O symmetric stretching is found at band 1795.45cm^{-1} . The C=C stretching and C-N stretching are found at bands 1555.21cm^{-1} , 1457.49cm^{-1} respectively. The tabulations are given below:

Table 1: Theoretical and experimental FT-IR spectrum of Nor Leucine Maleate

Wave number cm^{-1} (experimental)	Wave number cm^{-1} (computational)	Assignments
3197.43	3176	C-H stretching
1795.45	1705	C=O stretching
1555.21	1538	C=C stretching
1457.49	1495	C-N stretching

3.3 Raman activity spectra

The Raman activity spectrum observed for a particular frequency range is given in the figure 2:

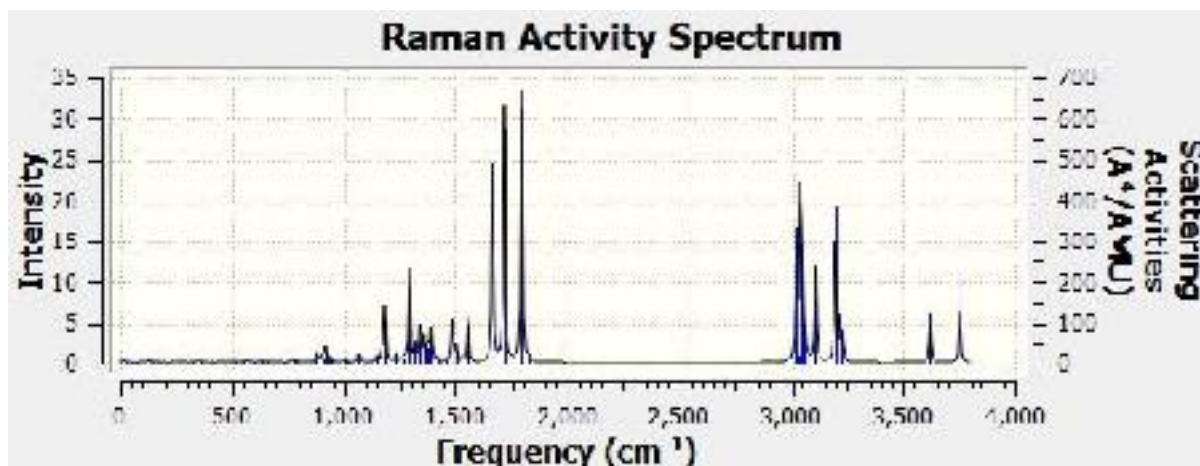


Fig. 2: Raman Activity spectrum of Nor Leucine Maleate

One of the prominent peaks near the region of 1666.60cm^{-1} corresponds to C=O stretch Alpha helix. Two more peaks at 3020cm^{-1} and 3197cm^{-1} ensures broadening and shifting by H-bonding.

3.4 UV-Vis spectral analysis

The UV-Vis Spectrum is obtained using TD-DFT calculation with solvent as water. The calculations results in values of excited state energy and oscillator strength in particular wavelengths. As we calculated the oscillator strength of the excited state in the wavelength 290 nm as 0.1414[10,11] By using oscillator strength, transition dipole moment can be calculated using the formula

$$\mu^2 = \frac{3e^2\hbar}{4\pi m_e v} \times f$$

Where, f is the oscillator strength As the result the transition dipole moment is **7.4011 debye**. Transition dipole moment is useful in designing non linear optical materials. This can be carried out for various solvents by which the first order hyperpolarizability varies. The observed UV-Vis spectrum is given in the figure 3:

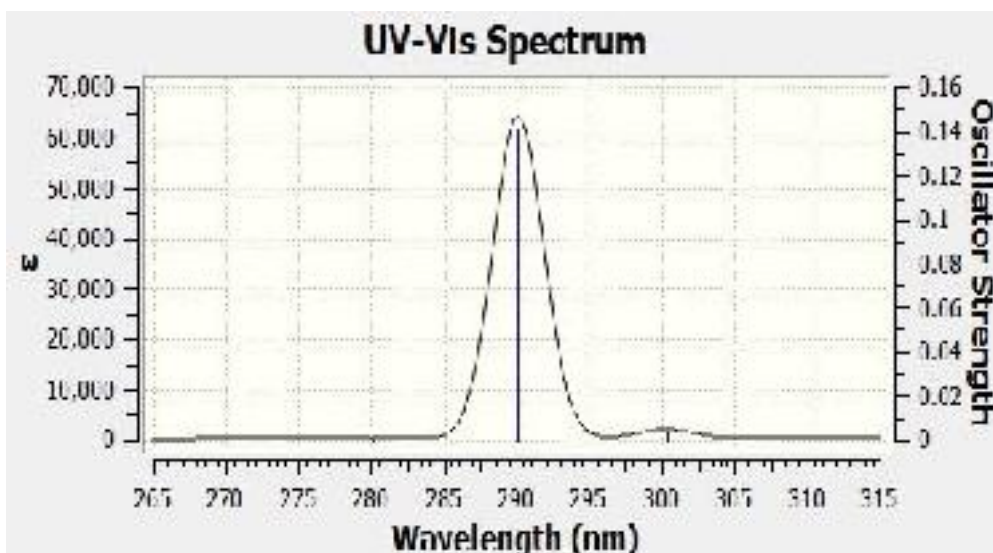


Fig.3: UV-Vis of Nor Leucine Maleate

Also various observations such as the excitation energy and the oscillator strengths are calculated the UV data and are the results are tabulated below:

Table 2: Calculated values of excitation energies and oscillator strength

Wavelength (nm)	Excitation energy (eV)	Oscillator strength
280.07	4.4270	0.0004
290.13	4.2734	0.1414
300.35	4.1280	0.0040

3.5 NMR analysis – SCF-GIAO method

The NMR spectrum for DLNM obtained using the SCF-GIAO method is given below in the figure 4:

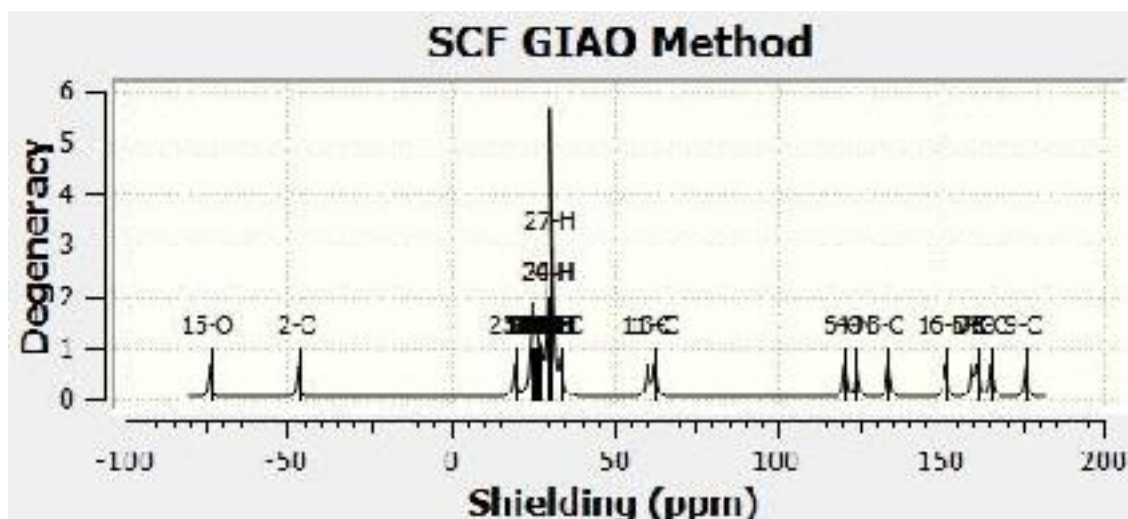


Fig.4: NMR study by SCF-GIAO method

3.6 HOMO-LUMO analysis

The energy gap value is a critical parameter in stability of the molecule. The calculated energy HOMO and LUMO are -0.26505 and -0.09008 respectively. The energy gap value is calculated as 0.17497 [12,13]. As we see smaller energy gap and high energy of HOMO indicates the larger value of microscopic first order hyperpolarizability.

The analyzed HOMO-LUMO energies are given below in the following figure 5.

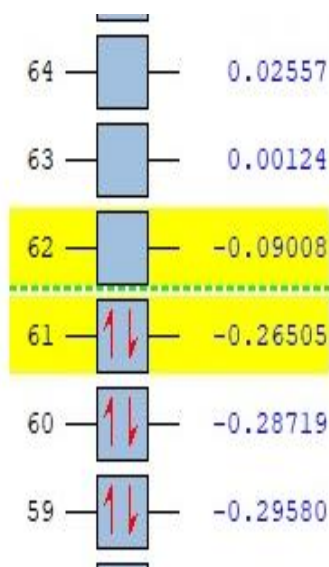
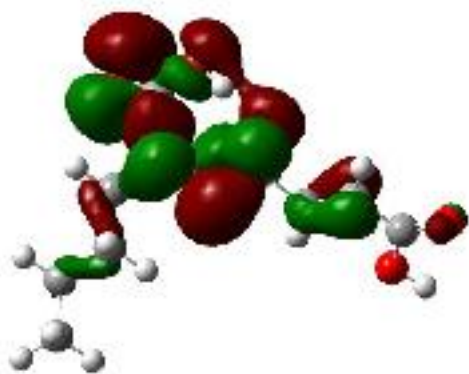
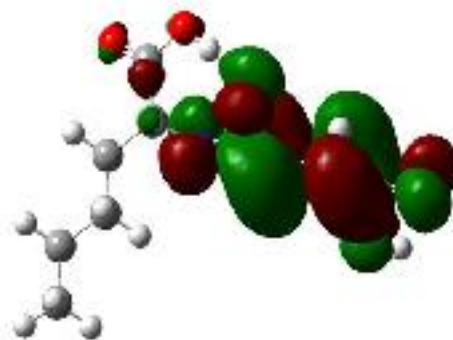


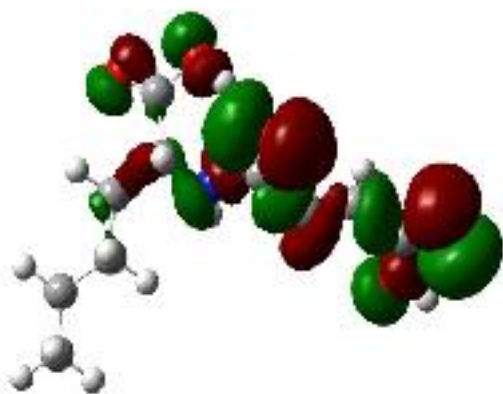
Fig.5: HUMO-LUMO energies of Nor Leucine Maleate



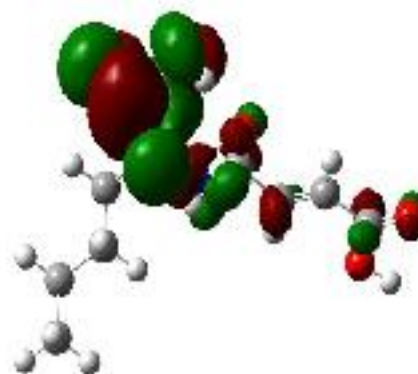
HOMO (61)



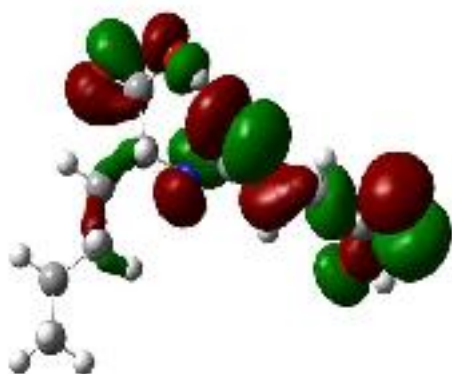
LUMO (62)



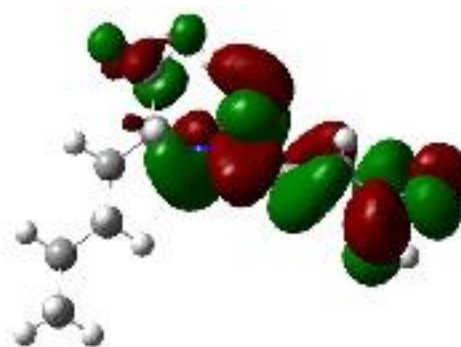
HOMO (60)



LUMO (63)



HOMO (59)



LUMO (64)

Table 3: HUMO-LUMO analysis and energy gap calculation

Parameter	Energy (eV) using B3LYP/6-31 G(d,p)
HOMO (61)	-0.26505
LUMO (62)	-0.09008
HOMO (61) – LUMO (62) Energy gap	-0.17497
HOMO -1 (60)	-0.28719
LUMO +1 (63)	0.00124
HOMO -1 (60) - LUMO +1 (63) Energy gap	-0.28843
HOMO -2 (59)	-0.29580
LUMO +2 (64)	0.02577
HOMO -2 (59) - LUMO +2 (64) Energy gap	-0.32157

3.7 Hyper polarizability

The hyperpolarizability is the second order electric susceptibility per unit volume. First order hyperpolarizability is a third rank tensor, which is described using 3*3*3 matrix. The 27 components of 3D matrix is reduced to 10 components using Kleinman symmetry.

The magnitude of hyperpolarizability value is calculated using the formula

$$\beta_{\text{tot}} = (\beta_x^2 + \beta_y^2 + \beta_z^2)^{1/2}$$

Where,

$$\beta_x^2 = (\beta_{xxx} + \beta_{xyy} + \beta_{xzz})^2$$

$$\beta_y^2 = (\beta_{yyy} + \beta_{yzz} + \beta_{yxx})^2$$

$$\beta_z^2 = (\beta_{zzz} + \beta_{zxx} + \beta_{zyy})^2$$

The calculation results obtained from Gaussian output file will be in atomic units (a.u) and it is converted into electrostatic units (e.s.u) where, 1 a.u = 8.6393×10^{-33} e.s.u. The hyperpolarizability value is found to be 9.6168×10^{-30} [14,15]. This first order hyperpolarizability shows the non linearity of DLNM molecule. Which results in Second Harmonic Generation (SHG). The first order hyper polarizability findings are listed below:

Table 4: The First order hyper polarizability calculations for Nor Leucine Maleate

$\beta_{xxx} = 114.54901$
$\beta_{xyy} = -289.18986$
$\beta_{xyy} = 468.96922$
$\beta_{xxz} = 2.08429$
$\beta_{xzz} = -44.74526$
$\beta_{yyy} = -957.0806$
$\beta_{yyz} = -25.49090$
$\beta_{yzz} = -50.32641$
$\beta_{zzz} = -35.17686$
$\beta_{total} = 9.6168 \times 10^{-30}$ e. s. u

4. Conclusion

In our work, we studied various structural properties of Nor Leucine Maleate crystals. The molecular structure is optimized using DFT method. FT-IR and FT-Raman spectrum shows the particular modes of stretching and bending of bonds. The HUMO-LUMO energy gap is found and the value of the energy gap can be used for the explanation of the eventual charge transfer interactions which takes place within the molecule. Moreover, the first order hyper polarizability of the Nor Leucine Maleate crystals ensures that the molecule of interest proves to be a fascinating object to study the NLO properties and hence can be used in a variety of applications.

5. References

1. Vijayalakshmi, S. Kalyanaraman, DFT and TD-DFT approach for the analysis of NLO and OLED applications of 9-anthraldehydeS, 2014, 2429-2432.
2. T. Pal, T. Kar, Mat. Chem. Phys 91, 2005, 343.
3. L. Jothi, K. Ramamurthi, Indian J. Sci. Technol. 4, 2011, 6.
4. S.A. Martin Britto Dhas, M. Suresh, G. Bhagavannarayana, S. Natarajan, Growth and characterization of L-Tartaric acid, an NLO material, Elsevier, 2007, 48-52.
5. N.Vijayan, G. Bhagavannarayana, R. Ramesh Kumar, R. Gopalakrishnan, K. K. Maurya, P. Ramasamy, Crystal Growth Des., 6 ,2006, 1452.
6. S. Natarajan, S. A. Martin Britto, E. Ramachandran, Cryst. Growth Des. 6 (2006) 137.
7. K. Sambathkumar, K. Settu, Elixir Vib. Spec. 91, 2016, 38087-38098.
8. Bhawani Datt Joshi, Rashmi Mishra, Poonam Tandon, Alcemirqa Conceicao Oliviera, Alejandro Pedro Ayala, J. Mol. Structure 1058 (2014) 31-40.
9. G. Ramesh, Jyothi Prashanth, J. Laxman Naik, Byru Venkatram Reddy, J. Mol. Structure, 59,5,1022-1031.
10. Krishna Chaitanya Gunturu, Anup Thomas, Sinu .C.R, Biju Francis, Indian J. of Chem Sec. 47a, 8, 1171-1180.
11. Kalpana Sharma, R. M. Melavanki, S. S. Patil, Raviraj, A Kusanur, J. Mol. Structure 1181, 2019, 474-487.
12. P. Devi, H. Parveen, S. Fatma, A. Bishnoi, Ind. J. of Pure and App. Phy. 56, 10, 814-829.
13. Asli Esme, Ind. J of Pure and App. Phy. 57:822-835.

14. Manivannan Arivazhagan, S. Prabhakaran, R. Gayathri, *Spectrochimica Acta Part A Molecular and Biomolecular Spec*, 82,1,332-9
15. Vadivelu Balachandran, K. Parimala, *J. Mol. Structure* 1007:136-145.

Green synthesis and characterization of reduced graphene oxide using polysaccharides extracted from *Solanum tuberosum* peels

Dr. M. A. Sabitha¹, Dr. A. Syed Mohamed²

¹Assistant Professor & PG Head, Department of Chemistry, Sadakathullah Appa College (Autonomous), Tirunelveli, Tamil Nadu, India, drsabithama@sadakath.ac.in

²Associate Professor & Research Head, Department of Chemistry, Sadakathullah Appa College (Autonomous), Tirunelveli, Tamil Nadu, India, asm2032@sadakath.ac.in

ABSTRACT

Green technique for the reduction of graphene oxide is utterly important on account of its industrial application. The available methods involve the use of hydrazine which is a very harmful chemical. Hence an eco-friendly method is to be suggested for producing reduced graphene oxide. The current study paves way for efficient, cost effective and greener synthesis of reduced graphene oxide using waste materials. The peels of *Solanum tuberosum* which is rich in polysaccharides are utilized for the reduction and stabilization of reduced graphene oxide. The extracted polysaccharides are tested and used for the reduction. The reduced graphene oxide is characterized using UV-Visible spectroscopy. The red shift of the spectrum to 274 nm and peak at 300 nm confirms the formation of reduced graphene oxide.

Key words: graphene oxide, polysaccharides, *Solanum tuberosum*, red shift, reduced graphene oxide.

I. INTRODUCTION

Graphene, graphene oxide and their derivatives is currently the subject of a great deal of research, both in terms of their fundamental physical, chemical, and materials science properties, as well as the exciting promise of their practical applications in diverse fields [1]. The tuning of defects in graphene based materials is of interest for application in several areas. The remarkable

potential of graphene-based technologies has prompted researchers to explore several areas of application centered on the controlled reduction of graphene oxide to varying degrees and consequently also a partial restoration of its network system [2].

Graphene has wide applications in the industries. It is very difficult to prepare graphene in pure form and in large quantity. The reduction of graphene oxide which is hydrophilic to reduced graphene oxide which is hydrophobic and similar in structure to graphene is easy [3]. Reduced graphene retains the hexagonal structure of graphene with sp^2 hybridized carbon-carbon bonds with all the functional groups removed.

Reduced graphene oxide with similar structure to graphene has wide range of applications. Reduced GO is preferable over graphene, because of the ease of production and low cost [4]. Bulk quantities can be produced at cheaper cost. The methods involved in the reduction of graphene oxide to reduced graphene are chemical reduction, thermal reduction, solvothermal, photolytic, hydrothermal and microwave irradiation. There are advantages and disadvantages involved in each process [5].

The sheets of graphene oxide sheets are insulating with sheet resistance (R_s) of $10^{12} \Omega/\text{sq}$. This is due to the presence of sp^3 hybridized carbon cluster and other defects. Reduction of graphene oxide can make it electrically conductive. Heat treatment of graphene oxide decomposes the oxygen functionalities and restores the sp^2 carbon clusters which lead to higher electrical conductivity [6].

Hence a greener, cost effective and easy method is to be designed for the bulk production of reduced graphene oxide. The present study involves an eco-friendly method utilizing the waste material for the production. Several nutritionally beneficial compounds were present in

Solanum tuberosum peels which can be utilized in many ways. The peel extract exhibits antioxidant property. Phenolic compounds are found predominantly (about 90%) in potato peels. Many researchers reported the presence of caffeic acid in *Solanum tuberosum* [7].

The peels also contain non-starch polysaccharides of about 30%. These polysaccharides show antioxidant properties. It exhibits radical scavenging activity and reducing capacity. Hence, it can be utilized in the reduction and stabilization of graphene oxide.

II. MATERIALS AND METHODS

Solanum tuberosum was obtained from a local market in Tirunelveli, Tamilnadu. The adhered surface dust particles on the peels were removed by washing in tap water and then in distilled water. After washing, the peels were removed. The peels were dried at 50°C in an oven for 48 h and ground in a mixer grinder (Moulinex). It was then stored at room temperature (25 ± 5°C) until use. The methodology for the extraction of polysaccharides was done as suggested by Ding *et al.*, (2012) with some modifications [8].

The peels (20 g) were mixed with 500 ml of distilled water in a 1 L flask, and boiled under reflux with a heating mantle. The solution was filtered and recovered after 4 hours. The extraction was repeated to ensure complete removal of polysaccharides. The filtrates obtained were combined and concentrated by means of a rotary evaporator maintained at 50°C under vacuum. Recovery of the polysaccharides was performed by ethanol precipitation for one night at -20°C, followed by centrifugation for 15 min at 5300xg. The polysaccharide was re-solubilized in distilled water. A dialysis step against double-distilled water was carried out for 3 days to remove inorganic salts, prior to freeze-drying for three days to obtain water-soluble polysaccharides [9, 10].

Test for polysaccharides

Iodine test

1 ml of a given sample is taken in a clean, dry test tube. Control of 1ml of distilled water is taken in another tube. About 2-3 drops of Lugol's solution is added to both the tubes and mixed in a vortex. The appearance of color in the test tube is observed. It is heated in the water bath until the color disappears. The test tubes are cooled. The appearance of color seen in the test tubes is noted. Appearance of blue black color indicates the presence of polysaccharides (starch) [11].

Reduction of graphene oxide

1 g of graphene oxide powder was mixed with 5 g of polysaccharides and dissolved in 250 ml water and stirred continuously for 72 hours. This process was done by using deionized water and centrifugation at 5000 rpm for 15 minutes. The step was repeated twice along with ultrasonification of 10 minutes before every centrifugation to disperse sample in deionized water. The product was dried in an oven at 80°C for 24 hours.

Characterization

The dried powder was characterized using UV-Visible spectrophotometer.

III. RESULTS AND DISCUSSION

A green method to reduce graphene oxide (RGO) was developed using polysaccharide obtained from *Solanum tuberosum* peels which acts as as both reducing agent and stabilizing agent. The reaction conditions are analyzed for optimum production of reduced graphene oxide and the product is characterized using UV-Visible spectrophotometer. Reduction of graphene oxide using polysaccharides obtained from waste proves to be an efficient and cost effective green methodology. The degree of reduction can be determined by λ_{\max} of UV–Visible spectrum. As conjugation increases, less energy is needed for π - π^* transitions and the λ_{\max} value increases [12].

The spectrum of graphene oxide has an absorption peak at 230 nm which is shifted to 274 nm in reduced graphene oxide. This is red shift due to electronic configuration in reduced graphene oxide. The absorption peak at 230 nm is attributed to π - π^* transition of aromatic C-C ring. The UV spectra of reduced graphene oxide on the other hand show the red shift at 274 nm. This absorption peak is due to n- π^* transition of C-O bonds. The UV spectrum for graphene oxide and reduced graphene oxide are given in the figures 5.1 and 5.2 respectively.

The optical absorption for graphene oxide appears at 230 nm corresponding to the π - π^* plasmon peak [13]. The nano meter scale sp^2 clusters and chromophore units such as C=C, C=O and C–O are responsible for π - π^* plasmon peak [11]. The conjugative effect of chromophore produces the π - π^* plasmon peak for graphene oxide. n- π^* transition of the carbonyl groups (C=O) appears as shoulder at 300 nm [14,15, 16].

The red shift to 274 nm suggests the presence of conjugation followed from graphene oxide after reduction. The peak at 300 nm in reduced graphene oxide results from the removal of oxygen. The change in color of the solution from brown to black also indicates the formation of reduced graphene oxide. Conventional methods involve the use of hydrazine which is very

harmful. This greener methodology provides cost effective route for the reduction of graphene oxide [17].

Although methodologies are available for reduction of graphene oxide using polysaccharides such as glucose, this method involves the use of polysaccharides extracted from waste peels. The incorporation of waste materials for the production of commercially important product paves way for cost effective, novel and eco-friendly process.

IV. CONCLUSION

The reduced graphene oxide has high commercial application. Hence an eco-friendly and cheap method to reduce graphene oxide will pave way for huge application in various fields. The present method involves the reduction of graphene oxide using easily available, cost effective and reuse of waste form vegetable (peels of *Solanum tuberosum*). The result indicated the formation of reduced graphene oxide which is characterized by UV-Visible spectrum with λ_{\max} at 230 and 274 nm for graphene oxide and reduced graphene oxide respectively. Further studies can be carried out to inspect the structural morphology and applications of reduced graphene oxide.

V. REFERENCES

1. B. L. Dasari, J. M. Nouri, D. Brabazon, and S. Naher, (2017). Graphene and derivatives – synthesis techniques, properties and their energy applications, *Energy*, vol. 140(1): 766–778.
2. B. C. Brodie, (1860). Researches on the atomic weight of graphite, *Quarterly Journal of the Chemical Society of London*, 12(1): 261–268.
3. O. Leenaerts, B. Partoens, and F. M. Peeters, (2009). Water on graphene: Hydrophobicity and dipole moment using density functional theory, *Phys. Rev. B*, 79(23): 235440-5.

4. D. A. Dikin, S. Stankovich, E. J. Zimney, R. D. Piner, G. H. B. Dommett, G. Evmenenko, S. T. Nguyen, and R. S. Ruoff, (2007). Preparation and characterization of graphene oxide paper, *Nature*, 448(7152): 457–460.
5. N. Syed, N. Sharma, and L. Kumar, (2017). Synthesis of graphene oxide (go) by modified hummers method and its thermal reduction to obtain reduced graphene oxide (rgo), *Graphene*, 6(1): 1-18.
6. S. Pei and H.-M. Cheng, (2012). The reduction of graphene oxide, *Carbon*, 50(9): 3210–3228.
7. Al-Weshahy A., Venket Rao A., (2009). Isolation and characterization of functional components from peel samples of six potatoes varieties growing in Ontario. *Food Res. Int.*, 42: 1062–1066.
8. Khawla Ben Jeddou, Fatma Chaari, SamehMaktouf, Oumèma Nouri-Ellouz, Claire Boisset Helbert and Raoudha Ellouz Ghorbel, (2016). Structural, functional, and antioxidant properties of water-soluble polysaccharides from potatoes peels, *Food Chemistry*, 205: 97-105.
9. Yi Ding, Huhu Cheng, Ce Zhou, Yueqiong Fan, Jia Zhu, Huibo Shao and Liangti Qu, (2012). Functional microspheres of graphene quantum dots, *Nanotechnology*, 23(25): 6494-6498.
10. Juan Yu, Hai-Yu Ji, Yu-Fang Wang and An-Jun Liu, (2018). Polysaccharides from Pomelo Peels: Extraction, Optimization and their Antioxidant Activity In Vitro, *Current Topics in Nutraceutical Research*, 17(1): 56-63.
11. Blance, D.E., GaillardNorman, S., Thompson Alfred J., Morak, (1969). The interaction of polysaccharides with iodine: Part I. Investigation of the general nature of the reaction, *Carbohydrate Research*, 11(4): 509-519.
12. D.C. Marcano, D.V. Kosynkin, J.M. Berlin, A. Sinitskii, Z. Sun, A. Slesarev, J.M. Tour, (2010). Improved synthesis of graphene oxide, *ACS Nano*, 4 (8): 4806-4814.

13. Goki Eda, Yun-Yue Lin, Cecilia Mattevi, Hisato Yamaguchi, Hsin-An Chen, I-Sheng Chen, Chun-Wei Chen, Manish Chhowalla, (2010). Blue Photoluminescence from Chemically Derived Graphene Oxide, *Advanced Materials*, 22(4): 505-509.
14. W. Cai, R.D. Piner, F.J. Stadermann, S. Park, M.A. Shaibat, Y. Ishii, R.S. Ruoff, (2008). Synthesis and solid-state NMR structural characterization of ^{13}C -labeled graphite oxide, *Science*, 321(5897): 1815-1817.
15. Lawrence Verbit, (1965). The Benzene Ring as an Optically Active Chromophore, *Journal of the American Chemical Society*, 87(7): 1617-1619.
16. Haruo Hosoya, Jiro Tanaka, and Saburo Nagakura, (1962). Ultraviolet absorption spectra of monomer and dimer of benzoic acid, *Journal of Molecular Spectroscopy*, 8(1-6): 257-275.
17. Adere Tarekegne Habte and Delele Worku Ayele, (2019). Synthesis and Characterization of Reduced Graphene Oxide (rGO) Started from Graphene Oxide (GO) Using the Tour Method with Different Parameters, *Advances in Materials Science and Engineering*, vol-2019, <https://doi.org/10.1155/2019/5058163>.

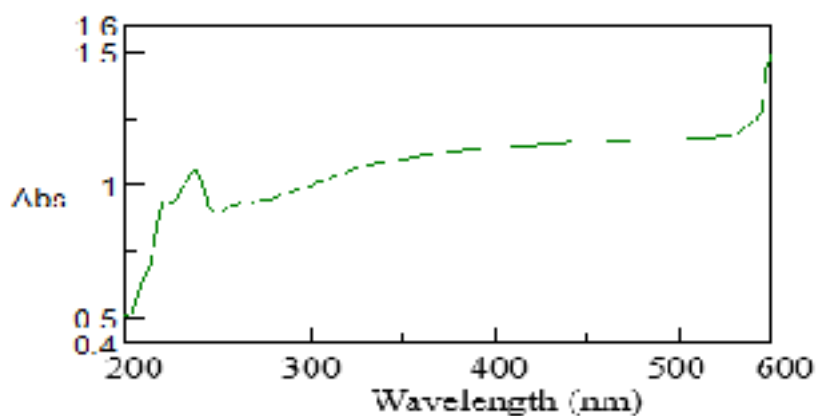


Figure 1 UV- Visible spectrum of Graphene oxide

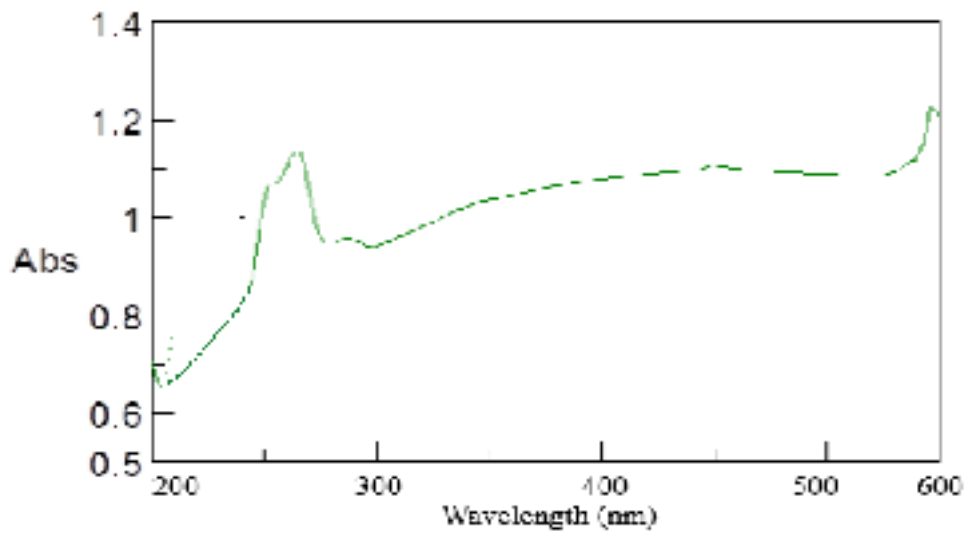
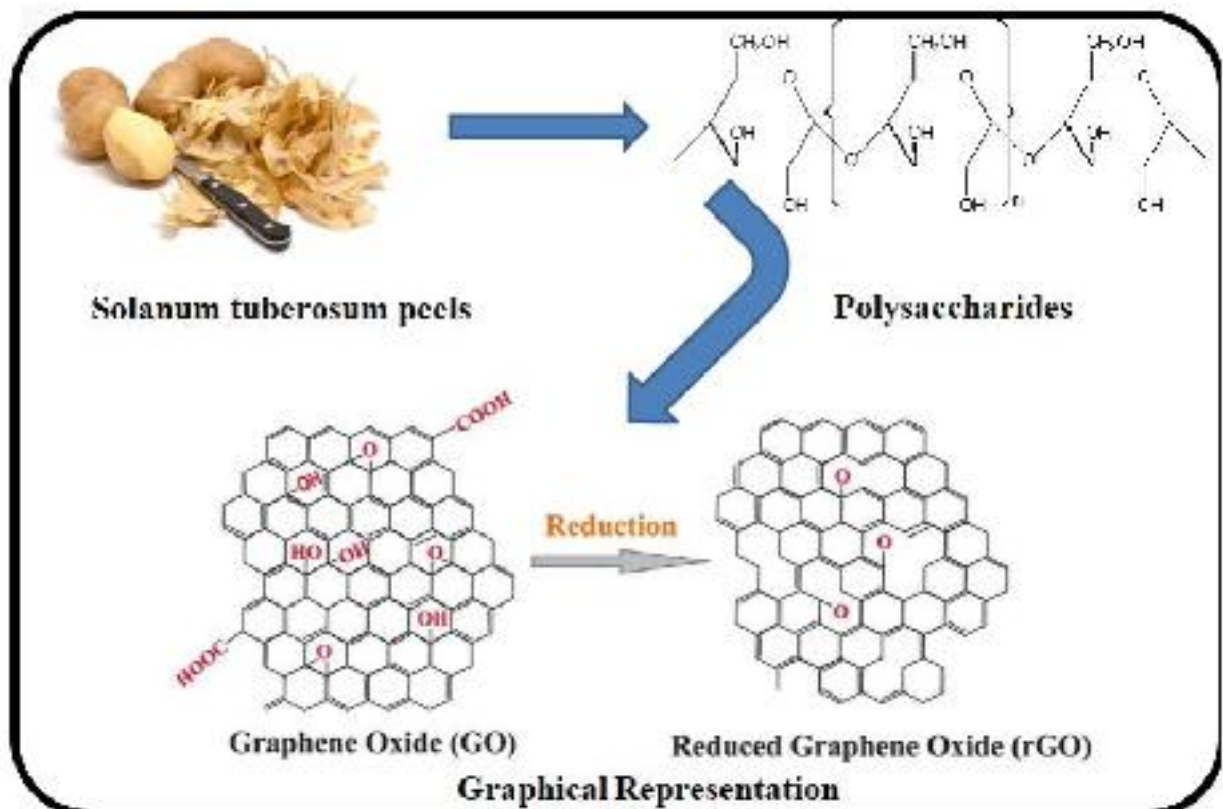


Figure 2 UV-Visible spectra of Reduced Graphene oxide



Antimicrobial activity of combined extracts of *Carica papaya* peels and *Glycyrrhiza glabra* roots

Dr. M. A. Sabitha^{1*}, Dr. A. Syed Mohamed²

¹Assistant Professor & PG Head, Department of Chemistry, Sadakathullah Appa College (Autonomous), Tirunelveli, Tamil Nadu, India.

²Associate Professor & Research Head, Department of Chemistry, Sadakathullah Appa College (Autonomous), Tirunelveli, Tamil Nadu, India.

Abstract: *The use of plants for medication in India is common among tribal and ethnic groups. The phytochemical constituents present in the plants ensure antibacterial, antifungal and anti-cancer properties. The present study is initiated to study the antimicrobial property of Carica papaya peels and Glycyrrhiza glabra roots. The extracts of these components are prepared in different ratios and analyzed for antimicrobial and phytochemical constituents. The results showed that the presence of phenol, saponins, flavonoids, steroids, terpenes and reducing sugar in the extract. The extract in the ratio of 2:1 exhibited effective antibacterial activity against Klebsiella pneumoniae whereas the ratio of 1:1 had effectiveness against Pseudomonas aeruginosa and Staphylococcus aureus. The antifungal studies provided the data that 1:1 extract is effective against Rhizopus microspores while 2:1 ratio proved to be effective against Aspergillus flavus and Candida albicans.*

Keywords: *Carica papaya, Glycyrrhiza glabra roots, phenol, Klebsiella pneumonia, Staphylococcus aureus, Rhizopus microspores.*

1. Introduction

Treatment with medicinal plants is the prime medication in many countries. Most of the world's population depends on crude plants for medicinal use. The tree barks, leaves, stem, flowers and roots are utilized for medication (Barrett and Kieffer 2001). The active phytochemical constituents are made use as starting materials for the preparation of drugs. The side effects produced in consuming the synthetic drugs provided importance to the ancient medicinal plant constituents. Numerous plants which are used in folk medication are approved as medicines by extracting the bioactive component of the mixture. An example is morphine extracted from opium.

Research on medicinal plants involves numerous fields of study and analysis. The different field of study involved is botanist to collect plants, ethnopharmacologist to diagnose the medicinal value, chemist to analyze the component responsible for therapeutic action and pharmacologist to isolate and make it suitable for medication (Baker et al., 1995). The phytochemical constituents are important source of new drugs and lead compounds (Newman et al., 2000; Newman et al., 2003).

India occupies an important place in the plant resources. About lakhs of traditional medicinal practitioners are available in India. Millions of people receive the welfare of Siddha, Unani and Ayurvedic medicine. Recent years the medical field is attracted much towards the use of plants. The reason lies in non-toxic and lack of side effects of using natural cure (Mukherjee 2001). The traditional medicine requires extensive research with technological advances and logical justifications to be utilized.

The use of plants as medicine has started from vedic period. Charak Samhita described about 341 medicinal plants in 1900 BC. Baghahtta of Sind, Madhab Nidana and Bhava Mishra wrote books on medicinal plants. About 1250 plants have been utilized in Ayurveda. Many Ayurvedic plants have now been used in preparing modern medicines. Nearly 70% of organic constituents in British Pharmacopoeia of 1932 are derived from plants. The lacking in the use of traditional medicine lies in the backlog of research in the plant derived products and scientific reasoning of the components (Miller and Gerean 1992).

Antibacterials derived from plants have served better than synthetic due to lesser side effects. The active components of plant origin are a best alternative to control pathogens (Kumaraswamy et al., 2008). The bioactive components are essential for the determination of therapeutic action and medicinal value of the plants. The chemical constituents mostly found in plants are flavonoids, alkaloids, phenolic compounds and tannins. Ethnopharmacological information in phytochemistry will pave way for discovery of new therapeutic agent with fewer side effects (Chhetri et al., 2008). The phenolic compounds and flavonoids present in plants have therapeutic values such as anti-inflammatory, analgesic, antimicrobial and antitumour properties (Wink, 1999). Flavonoids can also act as antioxidants (Gurib-Fakim, 2006).

Recent advancement in technology and isolation processes pave way for the extraction and purification of phytochemical constituents. Numerous plant species still remain unexplored. Some examples of plant components with high efficiency are mevastatin obtained from penicillin, quinine, rapamycin and etoposide (Kingston et al., 1992). According to the World Health Organization report, around 20, 000 medicinal plants are used worldwide as medicine.

The demand for herbal drugs is increasing day by day. The efficacy, lack of side effects and therapeutic long term action make these drugs essential for analysis of bioactive components. People rely on Ayurveda for medicinal purposes during ancient times and the period changed when their hope shifted to allopathic medicine. Now due to lack of long term therapeutic effects and safety, the attention is much diverted to herbal medicines. Hence it becomes important to analyze the bioactive ingredients of these plants for effective medicinal use.

International Pharmacopoeia has included several herbal drugs and traditional medicines. The guidelines and methodology must be regularized for the usage of these bioactive components. The plants must be chosen based on easy availability, phytochemical components and therapeutic value.

Glycyrrhiza glabra is one of the oldest traditional medicinal plants of India. The components of the plant are saponins, flavonoids, glycyrrhizin and in addition the root exhibits sugar and proteinous substances. Glycyrrhizin, a triterpenoid compound, represents the sweet taste of root. The yellow shade of *G. glabra* is due to the flavonoid substance such as liquiritin, isoliquiritin (a chalcone) and other compounds. The concentrates are frequently utilized as an enhancing agent in present day medication. The plant has been used as pigments, food additives, insecticides and in perfume industries. It has been used in folk medicine to reduce fever and curing tooth aches (Kumar and Dora, 2012). Alkaloids present in the roots are active constituent with therapeutic value.

Licorice hinders the growth and cytopathology of numerous random DNA and RNA viruses. Glycyrrhizic corrosive represses cyclooxygenase movement and prostaglandin development, as well as by implication restraining platelet aggregation (Acharya et al., 1993). Specifically, glycyrrhizin has antiviral action against and is prepared to do irreversibly inactivating the virus. Although it is an extensively studied plant, the effect of the root components against some particular bacteria and fungus remains unexplored (Ajagannavar et al., 2014).

Not only plant parts but also the wastes obtained from the fruits can also be used for medicine. One such plant is *Carica papaya* where the peels of fruits contain bioactive ingredients. The peels are rich in phenol, vitamin c, fibres, copper, sulphur, calcium, iron, magnesium and potassium. The presence of phenol provides antioxidant property. Also, vitamin c content helps to cure inflammation and can be utilized for antimicrobial activities (Didier et al., 2017).

The present study is carried out to analyze the combined effects of extracts of *Glycyrrhiza glabra* root and *Carica papaya* peels in different ratios against certain bacteria and fungi.

2. Materials and Methods

Carica papaya peels were cut in to small pieces and weighed. Samples were exposed to air dry for three days, lyophilized for 8 hours using a freeze dryer and exposed to temperatures of 50 °C and 80 °C using a laboratory oven for 3 hours. About 2 g of coarse powder was packed in Soxhlet apparatus using ethyl acetate, ethanol and hexane. The extract was collected and stored after evaporating the solvents. Fresh roots of *Glycyrrhiza glabra* Linn commonly known as athimathuram were collected. They were washed and shade dried for 5 to 6 days. The dried samples were finely ground into powder. The fine powdered roots of *Glycyrrhiza glabra* were weighed to determine the dry weight. The extraction was carried out using Soxhlet apparatus with chloroform as solvent. About 10g of dried *G. glabra* was dissolved in 100 ml of chloroform and stirred using stirrer. The sample and solvent was maintained at 1:10 ratio. After extraction, the contents were filtered using Whatmann filter paper No.1. The filtrate was kept on a hot water bath at 75 °C to concentrate the product by evaporating the residual solvents in the filtrate. The samples are mixed with one another in

two different ratios. Sample A and B. Sample A has the ratio of 1:1 (*Carica papaya* peel extract 1ml and extract of *Glycyrrhiza glabra* root 1ml) and sample B has the ratio of 2:1 (papaya peel extract 2ml and extract of *Glycyrrhiza glabra* 1ml), then the samples were analyzed for antimicrobial activity and phytochemical constituents. The presence of bioactive components such as phenols, saponins, flavonoids, steroids, terpenes and reducing sugars were tested. The samples were examined for antibacterial activity against *Klebsiella pneumoniae*, *Pseudomonas aeruginosa* and *Staphylococcus aureus*. Antifungal study was carried out against *Aspergillus flavus*, *Rhizopus microspores* and *Candida albicans* (Yogeshi et al., 2004; Perez et al., 1990).

3. Results and Discussion

Phytochemical analysis indicated the presence of phenol, saponins, flavonoids, steroids, terpenes and reducing sugar in the extract. The phytochemical constituents are tabulated in table 1

Table 1 Antibacterial activity of extracts of *Carica papaya* peels and roots of *Glycyrrhiza glabra*

Phytochemical test	Result
Phenol	+
Saponins	+
Flavonoids	+
Steroids	+
Terpenes	+
Reducing sugars	+

Antibacterial activity

In the present study the samples were subjected to evaluate its antimicrobial activity. Sample A represents *Carica papaya* peel extract of 1ml and *Glycyrrhiza glabra* extract of 1ml whereas Sample B represents the papaya peel extract of 2ml and *Glycyrrhiza glabra* of 1ml. Sample B was highly active against *Klebsiella pneumoniae* than Sample A. The zone of inhibition of sample A was 18 whereas sample B showed 16 against the bacteria *Pseudomonas aeruginosa*. The result for *Staphylococcus aureus* was similar to that of *Pseudomonas aeruginosa*, since sample A showed high zone of inhibition than sample B. Samples A and B displayed nearly equal activity against *Pseudomonas aeruginosa*. The antibacterial results are tabulated in table 2.

Table 2 Antibacterial activity of extracts of *Carica papaya* peels and roots of *Glycyrrhiza glabra*

Microorganisms	Zone of inhibition	
	A*	B*
<i>Klebsiella pneumoniae</i>	15	20
<i>Pseudomonas aeruginosa</i>	18	16
<i>Staphylococcus aureus</i>	20	14

*Sample A - *Carica papaya* peel extract 1ml and extract of *Glycyrrhiza glabra* 1ml

*Sample B- *Carica papaya* peel extract 2ml and extract of *Glycyrrhiza glabra* 1ml

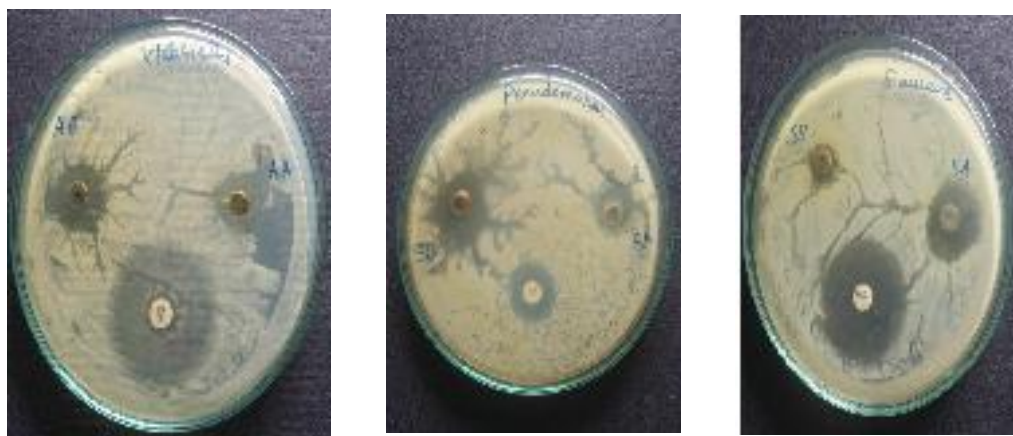


Figure 1 Antibacterial activity of Sample A and Sample B against *Klebsiella pneumoniae*, *Pseudomonas aeruginosa* and *Staphylococcus aureus*

Antifungal activity

Sample B was effective against *Aspergillus flavus* and *Candida albicans* than sample A. The zone of inhibition of sample B was 12 against *Aspergillus flavus*. Both samples A and B showed higher zone of inhibition for *Rhizopus microspores*. The antifungal activity was tabulated in table 3.

Fukai et al. (2002 a) reported certain flavonoids of licorice such as glabridin, glabrene, licochalcone A, licoisoflavone B which showed antibacterial activity against drug resistant *H. pylori*. Fukai et al. (2002 b) further reported antibacterial activity of flavonoid against methicillin resistant strain of *S. aureus*. The presence of these flavonoids resulted in the antibacterial activity of *Glycyrrhiza glabra*. The antimicrobial activity was reported due to the presence of glycyram and licuroside. Glabridin in *Glycyrrhiza glabra* was the main reason for antifungal activity (Fatima et al., 2009).

Table 3 Antifungal activity of extracts of *Carica papaya* peels and roots of *Glycyrrhiza glabra*

Microorganisms	Zone of inhibition	
	A*	B*
<i>Aspergillus flavus</i>	10	12
<i>Rhizopus microsporus</i>	18	16
<i>Candida albicans</i>	15	16

*Sample A - papaya peel extract 1ml and extract of *Glycyrrhiza glabra* 1ml, *Sample B- papaya peel extract 2ml and extract of *Glycyrrhiza glabra* 1ml



Figure 2 Antifungal activity of Sample A and Sample B against *Aspergillus flavus*, *Rhizopus microspores* and *Candida albicans*

The antibacterial activity of papaya peel was due to the presence of alkaloids and tannins (Khalili et al., 2012). The result was further supported by Maria et al., (2019). Their study showed that the presence of phytochemicals such as terpenes, alkaloids and saponins contents in peels of papaya which result in antimicrobial activity.

The mixture of extract was active against *Klebsiella pneumoniae* bacteria which cause severe infections in lungs, bladder, brain, liver, eyes, blood, and wounds. Also the extract was very much effective against *Rhizopus microspores* which can cause mucormycosis in immune-compromised humans.

4. Conclusion

The extracts of *Carica papaya* peels and roots of *Glycyrrhiza glabra* were effective against bacteria such as *Klebsiella pneumonia*, *Pseudomonas aeruginosa* and *Staphylococcus aureus*. The extract showed efficient antifungal activity against *Aspergillus flavus*, *Rhizopus microspores* and *Candida albicans*. The different ratio of mixtures depicted varying activity. The efficiency of the extract can be further increased by analyzing different ratio mixtures and separating the active components.

References

- Bruce Barrett and David Kieffer, Medicinal Plants, Science, and Health Care, *Journal of Herbs Spices & Medicinal Plants* 8(2-3), (2001), 1-36.
- Baker, J.T., Borris, R.P., Carté, B., Cordell, G.A., Soejarto, D.D., Cragg, G.M., Gupta, M.P., Iwu, M.M., Madulid, D.R. and Tyler, V.E. Natural products drug discovery and development: new perspective on international collaboration. *J. Nat. Prod.*, 1995, 58 (9), (1995, 1325-1357.
- Newman, D. J., Cragg, G.M. and Snader, K.M., The influence of natural products upon drug discovery, *Nat. Prod. Rep.* 17 (3), (2000), 215-234.
- Newman, D.J., Cragg, G.M. and Snader, K.M., Natural products as sources of new drugs over the period 1981-2002. *J. Nat. Prod.* 66 (7), (2003), 1022-1037.
- Mukherjee P.K., Quality control of Herbal Drugs, Business Horizons, Pharmaceutical Publisher, 1st ed, 1-29, (2001).

Miller J.S., Gerean R.E., Biologically Active natural products: Pharmaceuticals, ed. Cutler S.J., Cutler H.G., CRC Press, Boca Raton, Florida, 1st Ed. 25-38, (1992).

Kumaraswamy MV, Kavitha HU, Satish S. Antibacterial evaluation and phytochemical analysis of *Betula utilis*. *World Journal of Agricultural Sciences.*, (2008), 4: 661-4.

Himal Paudel Chhetri, Nisha Shrestha, Jyoti Sherchan Panna Thapa, Phytochemical and Antimicrobial Evaluations of some Medicinal Plants of Nepal, *Kathmandu University Journal of Science Engineering and Technology*, 1(5), (2008), 49-54.

Wink, M., Biochemistry of plant secondary metabolism. Annual plant reviews, volume 2. Ch. 1. p. 1-16. Sheffield Academic Press, (1999).

Gurib-Fakim, A., Medicinal plants: Tradition of yesterday and drugs of tomorrow. Review article. *Mol. Aspects Med.* 27 (1), (2006), 1-93.

Kingston D.G.I., Biologically active natural products Pharmaceuticals, ed Cutter S.J., Cutler H.G., CRC Press, Boca Raton, Florida 1st ed, 39-52, (1992).

Acharya SK, Dasarathy S, Tandon A, A preliminary open trial on interferon stimulator (SNMC) derived from *Glycyrrhiza glabra* in the treatment of subacute hepatic failure. *Indian J Med Res Sect A—Infect Dis.*;98, (1993), 69–74.

Ajagannavar SL, Battur H, Shamarao S, Effect of aqueous and alcoholic licorice (*Glycyrrhiza glabra*) root extract against *Streptococcus mutans* and *Lactobacillus acidophilus* in comparison to chlorhexidine: an in vitro study. *J Int Oral Health.*, 6, (2014), 29–34.

Adingra Kouassi Martial-Didier, Konan Kouassi Hubert, Kouadio Eugène Jean Parfait, Tano Kablan, Phytochemical Properties and Proximate Composition of Papaya (*Carica papaya* L. var solo 8) Peels, *Turkish Journal of Agriculture- Food Science and Technology*, 5(6), (2017), 676- 680.

Kumar A and Dora J, Review on *Glycyrrhiza glabra*: licorice. *Journal of Pharmaceutical & Scientific Innovations* 1, (2012), 1-4.

Yogeshi, K. V., Rathish, N., Mayur, S., Shipra, B., Sumitra, C., Synthesis, structural determination and antibacterial activity of compounds derived from vanillin and 4-aminoantipyrine. *J Serb Chem Soc.*, 69, (2004), 991-998.

Fukai T, Marumo A, Kaitou K, Anti-*Helicobacter pylori* flavonoids from licorice extract. *Life Sci.*, 7, (2002), 1449–1463.

Fatima, Z., Saleemi, M., Zia, M., Sultan, T., Aslam, M., Riaz-ur-Rehman, Chaudhary, M.F., Antifungal activity of plant growth-promoting rhizobacteria isolates against *Rhizoctonia solani* in wheat. *Afr. J. Biotechnol.* 8, (2009), 219-225.

Khalili JS, Hanson RW, Szallasi Z 2012. In silico prediction of tumor antigens derived from functional missense mutations of the cancer gene census. *OncolImmunology* 1, (2012), 1281–1289.

Ana Maria Zbancioc and Gabriela Tataringa, Coumarin derivatives with antimicrobial and antioxidant activities, *Intec Open Book Series*, (2019).



Density Functional Theory Investigation on the Mechanism of Chemiluminescent Decomposition in Adamantylideneadamantane-1,2-Dioxetane (BAAD) and Monoadamantylidene-1,2-Dioxetane (MAD)

Syed Mohamed A^{1*}, E. J. Padma Malar²

¹Research Department of Chemistry, Sadakathullah Appa College (Autonomous), Tirunelveli, Tamil Nadu

²Research Scientist-C, National Centre for Ultrafast Process, University of Madras, Chennai, Tamil Nadu

*Corresponding Author: Syed Mohamed A, Research Department of Chemistry, Sadakathullah Appa College (Autonomous), Tirunelveli, Tamil Nadu, 627 011, India. Tel: 9894388030; Email: asm2032@gmail.com

ABSTRACT

Chemiluminescence is the emission of light as a result of chemical reaction. The 4-membered dioxetane ring is also proposed as an intermediate in the chemiluminescent reactions. Bisadamantylidene Adamantane 1,2-Dioxetane (BAAD) have received special attention. The former is a very stable compound having half-life time of approximately 104 years at room temperature. The main aim of this study was to investigate the mechanism of chemiluminescent decomposition of dioxetane derivatives BAAD. The ground and the transition states in the closed shell singlet state were optimized by B3LYP/6-31G method.

Key words: Chemiluminescence, dioxetane, Bisadamantylidene adamantane 1,2-dioxetane, closed shell singlet state.

INTRODUCTION

Chemiluminescence is the emission of light as a result of chemical reaction [1]. There is no external light source used to initiate a chemiluminescence reaction. These reactions are generated by fundamental molecular transformations. In these reactions, “non-adiabatic surface jump” leads to the ground state reactant into excited state. Traditionally developed methods for atmospheric ozone and nitric oxide provide a good example of the advantage of CL reactions [2]. The 4-membered dioxetane ring is also proposed as an intermediate in the chemiluminescent reactions [3-10]. More results have been published on the experimental and theoretical studies of chemiluminescence of 1, 2-dioxetanes [11-15].

The first dioxetane namely 3, 3, 4-trimethyl 1,2-dioxetane by Kopecky and Mumford [16] in 1969, which decomposes rapidly at room temperature. In 1973, Turro and Lechtken [17-18] studied the decomposition and chemiluminescence of TMD was strongly solvent dependent, activation energy of TMD 25 kcal/mol has been measured and a reaction enthalpy of 60 kcal/mol was calculated [19]. In the case of simple dioxetanes chemiluminescence emission is from triplet state *via* biradical mechanism [20] Most studies showed that 3,3,4-trimethyl 1,2-dioxetane, TMD and simple dioxetane derivatives yield triplet products upon decomposition in solution [21-23]. More succeeding researches reveal that, thermal decomposition studies [24] on TMD using MCSCF method is used to study the mechanism of singlet state (S_1) formation.

According to the theoretical point of view 1,2-dioxetane (DO) and TMD are studied by using stepwise mechanism [24].

According to Tanaka and Tanaka [24] report, TMD is more stable than DO and the chemiluminescence yield is much higher when compared with DO. This report also proves that TMD follows biradical mechanism and it form the biradical was formed by the breaking of O-O bond in the rate determining step of the chemiluminescent reaction. TMD is more stable than parent system, because in contain more number of methyl substitution. More experimental results [25] are also reported on TMD that, the triplet yield for TMD is significantly higher than that for the parent system.

In the case of adamantyl substituted dioxetanes, such as spiro-adamantyl, spiro-acridyl and spiro-xanthyl are used as thermochemiluminescent immunoassays [26]. Bisadamantylidene Adamantane 1,2-Dioxetane (BAAD) was studied by Wynberg and coworkers [27-32] by using X-ray crystallography. In 1983, Adam [33] resolves the stability of BAAD. He proposed that, the biradical is formed after the breakage of O-O bond leads to fragmentation at transoid conformation rather cisoid conformation. The unusual thermal stability [32] of BAAD is due to the compression of bulky spiroadamantane units. X-ray structure [34] reveals that, BAAD is not planar and this compound also follows biradical mechanism, the initial O-O bond cleavage results a dioxygen biradical leads to energetically unfavorable compression they increase the activation energy. The length of O-O bond is 1.48 Å, average length of C-C bonds in the adamantyl group is 1.531 Å and the central C-C bond length is 1.549 Å. In BAAD [35], the ring opening mechanism invokes compression of the alkyl substituents in the initial step was the breaking of O-O bond either in concert with the spin flip (or) to form a singlet biradical. But the O-O and C-C bonds cleaves simultaneously it leads to steric compression. In 1982, Adam et al tried to synthesize the Monoadamantyl 1,2-Dioxetane (MAD) *via* Kopecky route still a failure process [36].

According to the theoretical point of view [24,37-43] and most previous studies showed that there are three mechanisms involved in the decomposition of 1,2-dioxetanes. In stepwise mechanism, according to White and Harding [44] and Richardson and O'Neal [20], cleavage of the weak O-O bond generates a short lived biradical intermediate which cleaves rapidly to carbonyl containing products. The initially formed singlet biradical is postulated to partition between singlet ground state and excited state carbonyl products. Singlet and triplet of the biradical should approach each other in energy with sufficient spatial separation of the oxygen atom. Hence, intersystem crossing to the triplet *via* spin-orbit coupling will be facilitated in the biradical. Cleavage of the triplet biradical should lead to the formation of a triplet excited state products. The asynchronous concerted mechanism was proposed by Adam [25]. It stated that, the first part of the chemiluminescent reaction should be concerted; the O-O bond will extend while the C-C bond undergoes some stretching. This is followed by a biradical phase (where the O-O bond is broken) prior to the decomposition (C-C bond breaking) into excited state products. The CIEEL mechanism, proposed by Schuster et al. , the sequence of reaction was initiated by one-electron transfer from a suitable donor molecule (activator ACT) to an organic molecule of high energy content. Subsequent rearrangement (or) loss of a neutral fragment transforms the reduced peroxide into a highly reducing species; in the form of a radical anion charge annihilation then generates an electronically excited state of ACT and the final step of the sequence is the emission from the ACT.

Among the derivatives, Bisadamantylidene Adamantane 1, 2-Dioxetane (BAAD) have received special attention. The former is a very stable compound having half-life time of approximately 10^4 years at room temperature. When it is heated to about 230°C, it decomposes rapidly and leads to the formation of excited state adamantanone which gives rise to chemiluminescence. The main aim of this study was to investigate the mechanism of chemiluminescent decomposition of dioxetane derivatives BAAD.

MATERIALS AND METHODS

All calculations were performed with the Gaussian 03 program [37] and Gaussian 09 program [38]. The main part of the calculations includes the geometry optimizations; vibrational frequencies and intrinsic reaction coordinate by stretching the C-C and O-O bond for the structures on the reaction path. The optimized geometries were characterized with the use of their vibrational frequencies. The ground and the transition states in the closed shell singlet state were optimized by B3LYP/6-31G* method. The open-shell systems, namely the biradical intermediate ^3BR , triplet transition state $^3\text{TS1}$ and singlet biradical transition state $^1\text{TS1}$ were optimized using UB3LYP/6-31G* calculations. The decomposition reaction of these simple dioxetanes was investigating the reaction paths by stretching the C-C and O-O bonds in the closed-shell singlet (S_0) and in the triplet (T_1) states. The ground state structures of BAAD were optimized by B3LYP/6-31+G* method.

RESULTS AND DISCUSSION

The optimized geometries of the ground state structure of BAAD are shown in Figure 1. The geometrical parameters of the dioxetane ring of these dioxetanes are listed in Table 1. The central C1-C2 bond in AAD has a length of 1.574 Å which is 0.025 Å greater than the X-ray structural data value of AAD (1.549 Å). Both the C1-O4 and C2-O3 lengths are having the same value of 1.472 Å. The length of the O3-O4 bond of AAD is 1.481 Å, which is 0.01 Å lesser than the reported X-ray value (1.491 Å), but is equal to that in H₂O₂. The calculations reveal that the dioxetane ring is not planar, but twisted out of plane by 20.5°. This deformation is due to the unfavorable non-bonded interaction of two pairs of equatorial hydrogen of the four methylene groups located under the dioxetane ring. Thus, the puckered peroxidic ring of AAD is correctly predicted by B3LYP/6-31G* method. Both the dioxetane ring angles C1-C2-O3 and C2-C1-O4 are 86.3° which is lesser than the ring angles of mono-substituted and tetra substituted dioxetanes (87.5°- 90.1°). In TMD, only four methyl groups are present. Due to two adamantyl groups, AAD becomes more strained. The ring angles are 1.2° lesser than the angles of TMD (87.5°). Hence the agreement between the calculated and the experimental values is satisfactory.

In MAD, the C1-C2 is 1.529 Å which is 0.02 Å lesser than X-ray structural data value of BAAD (1.549 Å). But it is very close to the theoretical value of MMD (1.524 Å). The C1-O4 bond length of MAD (1.473 Å) is same as the value observed in BAAD. The puckered nature is not observed in MAD and the ring is nearly planar (-0.34°). The dioxetane ring angles C1-C2-O3 and C2-C1-O4 are 90.17° and 88.23° respectively. The ground state structures of BAAD are optimized by B3LYP/6-31+G* method. The values are shown in Table 1. It reveals that the optimized geometrical parameters of BAAD is not much deviated from the results using 6-31G* basis set.

TRANSITION STATES AND INTERMEDIATE OF BAAD ALONG THE REACTION PATH

BAAD were investigated using B3LYP/6-31G* and UB3LYP/6-31G* methods. The transition states ¹TS1, ¹TS3 and ³TS1 and a triplet Biradical Intermediate (³BR) were characterized along the reaction path by structural optimization using UB3LYP/6-31G* method. The transition state ¹TS2 was characterized by structural optimization by B3LYP/6-31G*.

¹TS1 is formed from the ground state of the reactant by elongation of O-O bond. The C-C distance in ¹TS1 is 1.593 Å. Both the C-O lengths are having the same value (1.407 Å). The dioxetane ring angles, C1-C2-O3 and C2-C1-O4 are 97.2° and 97.1° respectively. The geometry of ¹TS1 is characterized by the dihedral angle O4-C1-C2-O3=41.6° and the O-O distance is 2.182 Å. The potential barrier for the formation of ¹TS1 is 28.2 kcal/mol. It is 5.8 kcal/mol lesser than the available experimental activation energy of BAAD (34 kcal/mol).

The Biradical Minimum (³BR) possesses a Relative Energy (RE) of 28.9 kcal/mol. The C1-C2, O3-O4, C1-O4 and C2-O3 lengths of ³BR are, respectively, 1.615 Å, 2.338 Å, 1.375 Å and 1.375 Å. The dioxetane ring angles, C1-C2-O3 and C2-C1-O4 of ³BR are increased from the value of 97.2° in ¹TS1 to 100.3°. From the ³BR, stretching of C-C length resulted in triplet Transition State (³TS1). The potential barrier for the formation of ³TS1 is 28.9 kcal/mol which is 0.9 kcal/mol higher than that of ¹TS1. The difference between the energies of ³TS1 state and ³BR intermediate is only 0.7 kcal/mol. The geometrical parameters of transition states of ¹TS2 and ¹TS3 are listed in Table 2 and also depicted in Figure 2.

The potential barrier of ¹TS2 is 50.0 kcal/mol. A transition state, ¹TS3 in the singlet excited state (S₁) is optimized using the time dependent (TD)-B3LYP calculations using 6-31G* basis set. The C1-C2, O3-O4, C1-O4 and C2-O3 lengths are 2.025 Å, 2.148 Å, 1.320 Å and 1.318 Å respectively. The dioxetane ring angles, C1-C2-O3 and C2-C1-O4 of BAAD are 86.2° and 86.1° respectively. The potential barrier for the formation of ¹TS3 from S₀ is 38.0 kcal/mol. when single point calculation done with UB3LYP/6-31G* method is also done at the TD-B3LYP/6-31G* the barrier is lowered to 24.8 kcal/mol.

The barrier for the formation of ¹TS3 (24.8 kcal/mol) is lower than the barriers of ¹TS1, ³TS1 and ¹TS2. The present study show that the feasibility of the chemifluorescent decomposition of AAD *via* the excited singlet transition state, ¹TS3. The present analysis reveals that the formation of chemifluorescence than chemiphosphorescence from BAAD has a lower activation barrier of 24.8 kcal/mol as compared to the latter having the barrier of 29.1 kcal/mol.

PRODUCTS FORMED FROM THE DECOMPOSITION OF BAAD

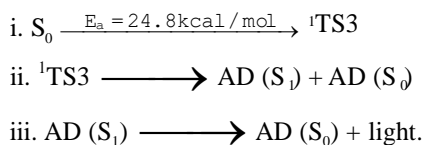
The total energies of the products formed from the chemiluminescence and thermal decomposition of dioxetanes,

BAAD is summarized in Table 4. The geometrical structures of the 2-Adamantanone (AD) is shown in Figure 3. In the S_0 state of 2-adamantanone, the C1-O4 length is 1.216 Å. The value is increased to 1.298 Å and 1.301 Å respectively for S_1 and T_1 states of 2-Adamantanone. The C atoms connected to C1 atoms are slightly increased to 1.546 Å and 1.562 Å respectively for S_1 and T_1 states of AD from 1.527 Å in S_0 of AD. The triplet excitation energy of 2-Adamantanone is 3.14 eV which is 0.16 eV which is 0.28 eV lesser than the experimental value (3.84 eV).

MECHANISTIC ASPECTS OF BAAD

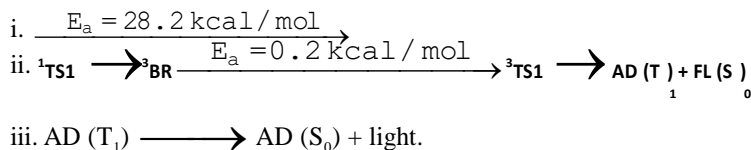
It is concluded that the chemifluorescence decomposition of BAAD follows a concerted mechanism proceeds via a singlet excited transition state 1TS3 leading to the formation of adamantanone in the singlet excited state.

In the first step, both the C-C and O-O bond lengths are stretching in a concerted manner leading to the transition state 1TS3 . This transition state leads to the products, one adamantanone in the singlet excited state (S_1) state and the other adamantanone in the ground (S_0) state. The mechanism for the chemifluorescent decomposition of BAAD is shown in Scheme 1. It is evident from the experimental results that the chemiluminescent decomposition of BAAD also yields adamantanone in the singlet excited state (S_1) along with the adamantanone in the triplet (T_1) state. Chemiphosphorescence in BAAD is explained by the step-wise mechanism. From the reactant BAAD the triplet biradical 3BR is formed via the transition state 3TS1 from 3BR leads to the products 3AD (T_1) and AD (S_0). The activation barrier for the above process is 29.1 kcal/mol which is higher than that for the formation of the products 1AD (S_1) and AD (S_0).



Scheme 1

The present study predicts the preference for the chemifluorescence process than the chemiphosphorescence process in AAD. The formation of 1TS1 from S_0 is the rate determining step. The activation barrier is 28.8 kcal/mol which is 5.8 kcal/mol lower than the experimental results (34 kcal/mol). The mechanism for the chemiphosphorescent decomposition of BAAD is shown in Scheme 2.



Scheme 2

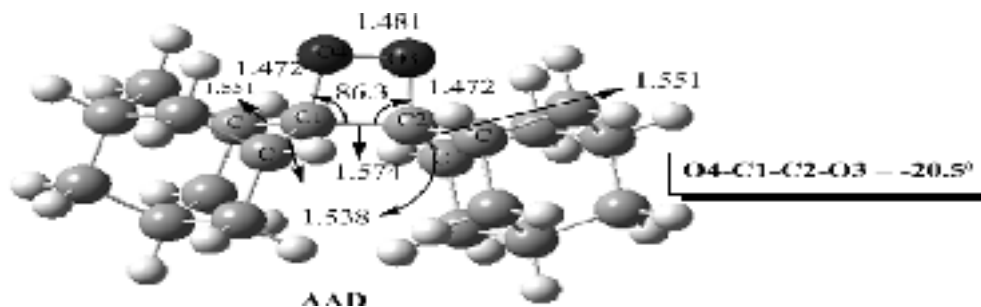


Figure 1. B3LYP/6-31G* optimized geometrical parameters of the BAAD. Bond length in Å, bond angle and dihedral angle in degrees.

Table 1 Selected bond lengths (Å) and angles (°) in the dioxetane BAAD

Parameters	B3LYP/ 6-31G* optimized Geometries		X-ray analysis	
	BAAD ^c		BAAD ^a	DMTOH ^b
C1-C2	1.574 (1.578)		1.549	1.584

C1-O4	1.472 (1.475)	1.476	1.485
C2-O3	1.472 (1.475)	1.474	1.459
O3-O4	1.481 (1.480)	1.491	1.497
C1-C2-O3°	86.3 (86.3)	--	--
C2-C1-O4°	86.3 (86.3)		
O3-O4/ C1-C2	0.941 (0.938)	0.963	0.945
O4-C1-C2-O3°	20.5 (20.3)	21.3	7.7
Energy (Hartree)	-929.3598661 (-929.3789027)		

a: X-ray crystal structure of BAAD – adamatylideneadamantane 1,2-dioxetane

b: X-ray crystal structure of DMTOH-1-aryl-5-(9-methylfluorene-9-yl)-4,4-dimethyl-2,6,7- trioxabicyclo [3,2,0] heptanes

c: Numbers in parenthesis indicate the values in B3LYP/6-31+G(d)

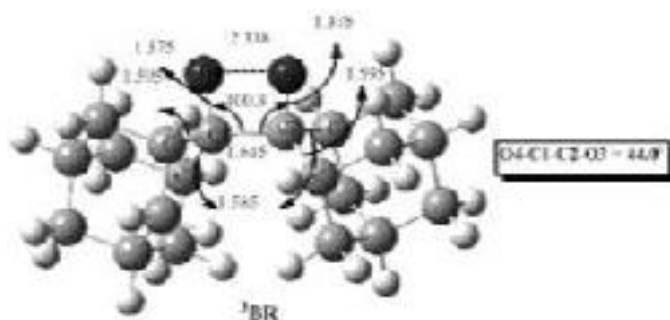
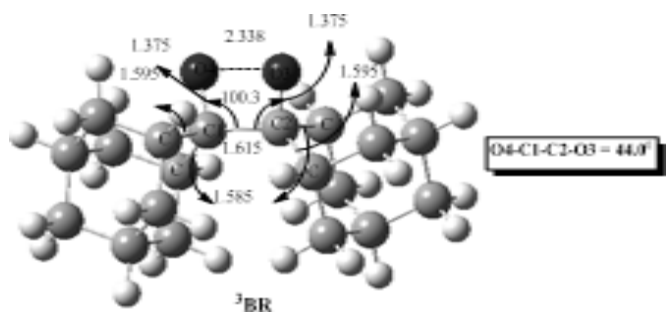
Table 2: Energies, selected bond lengths (Å) and angles (°) of different transition states and triplet biradical intermediate of BAAD using UB3LYP/ 6-31G(d)^a. Bond length in Å, bond angle and dihedral angle in degrees, total energy in Hartree, and relative energy, relative energy^b (RE) in kcal/moltr.

TS/BR	¹ TS1	¹ TS3	³ TS1	³ BR	¹ TS3	¹ TS2
C1-C2	1.593	1.751	1.979	1.615	2.025	1.840
C1-O4	1.407	1.347	1.337	1.375	1.320	1.345
C2-O3	1.407	1.347	1.285	1.375	1.318	1.344
O3-O4	2.182	2.115	2.148	2.338	2.148	2.011
C1-C2-O3°	97.2	92.9	88.7	100.3	86.2	86.7
C2-C1-O4°	97.1	92.9	89.4	100.3	86.1	90.8
O4-C1-C2-O3°	41.6	41.5	41.6	44.0	49.2	40.4
ZPE	0.450859	0.450865	0.451335	0.450920	0.449264	0.4482337
Frequency	401.9i	663.3i	115. 2i	67.1	919.6 i	1670.5 i
Spin densities on O ₃ ,O ₄	0.79, -0.79	0.11, -0.11	0.68, 0.72	0.85, 0.85	0.36, -0.36	--
RE (kcal/mol)	28.2	37.4	29.1	28.9	24.8 ^c	50.0

a: For closed-shell singlet transition state, ¹TS2, B3LYP/6-31G* method is used

b: Reference energy is -929.3598662 a.u. for S₀ ground state using B3LYP/6-31G* method

c: Relative energy is calculated using TD-B3LYP/6-31G*//UB3LYP/6-31G* method



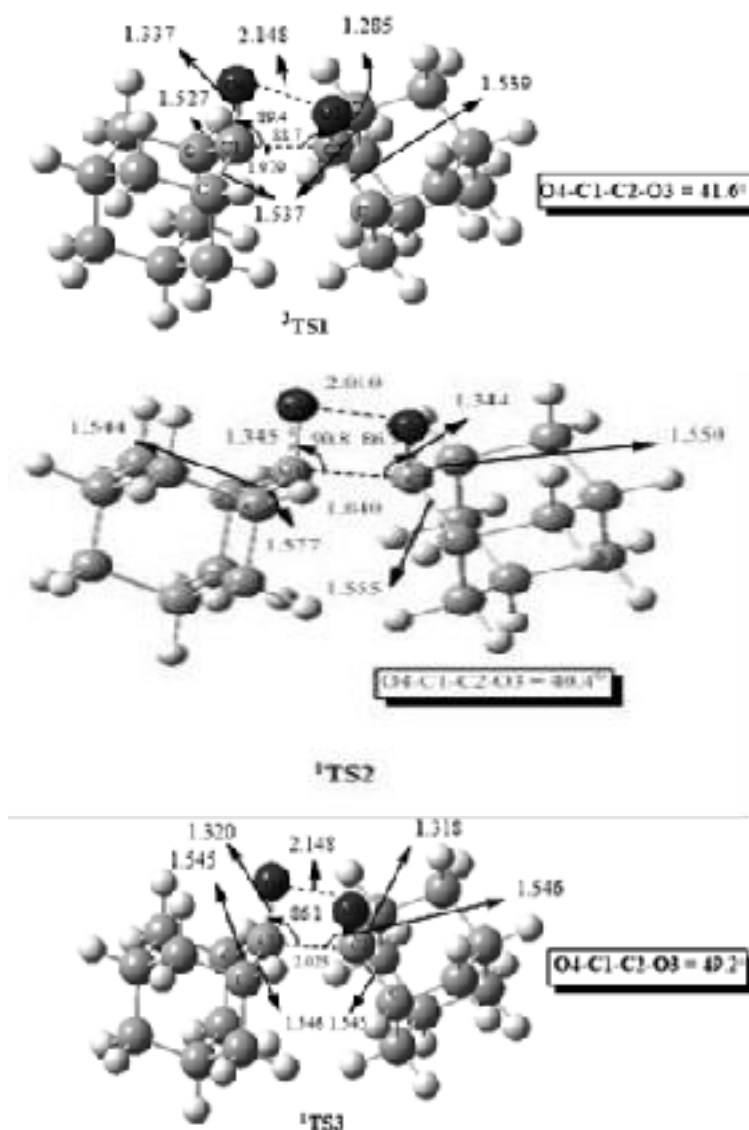


Figure 2. Optimized geometrical parameters of the dioxetane ring in the ¹TS1, ³BR, ¹TS2 and ³TS1 and ¹TS3 of BAAD. Bond length in Å, bond angle and dihedral angle in degrees.

Table 3: Total Energies of 2-Adamantanone (AD) and Formaldehyde (FL); B3LYP/6-31G* for S₀ and UB3LYP/6-31G* for T₁ states.

Products	Energy (Hartree)	Relative Energy (kcal/mol)
AD(S ₀) + AD(S ₀)	-929.4732772	-71.17
AD*(T ₁) + AD(S ₀)	-929.3580991	-1.17
AD(S ₀) + AD*(S ₁) ^a	-929.3321253	17.41
AD*(T ₁) + AD*(T ₁)	-929.242921	73.34
AD (S ₀) + FL (S ₀)	-579.2454792	-60.62
AD (S ₀) + FL*(T ₁)	-579.1375203	7.13
FL (S ₀) + AD*(T ₁)	-579.1303011	11.66
AD*(T ₁) + FL*(T ₁)	-579.0223422	79.4

a: TD-B3LYP/6-31G*
*: Excited state

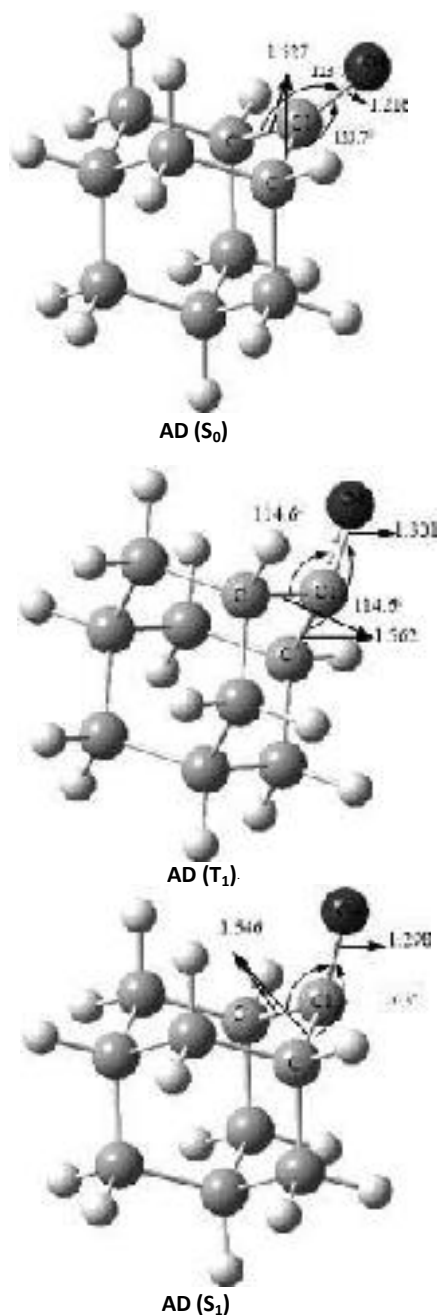


Figure 3. Geometrical structures of the adamantanone (AD) in S_0 , T_1 and S_1 states.

CONCLUSION

Unlike the other systems, it is observed that the mechanism of the chemiluminescent decomposition of AAD prefers a concerted pathway *via* the transition state 1TS3 in the singlet excited state with a lower activation barrier of 24.8 kcal/mol. The step-wise biradical pathway possesses a higher activation barrier of 29.1 kcal/mol. The analysis reveals different mechanisms for the chemifluorescent and chemiphosphorescent in AAD. The results are in agreement with the earlier experimental study.

REFERENCES

- [1] Turro, N., Modern Molecular Photochemistry. Benjamin/Cumming Publishing Co., Mento Park, CA. 1978.
- [2] Fontijn, A., Sadabell, J. and Ronolo, R.J., Chemiluminescence Techniques in Air Pollutant Monitoring. *Analytical Chemistry*,

1970. 42: p. 575.
- [3] Clogh, P.N. and Thrush, B.A., Mechanism of chemiluminescent reaction between nitric oxide and Ozone. *Transactions of the Faraday Society*, **1967**. 63: p. 915.
- [4] Fontijn, A., et al., Chemiluminescence and Bioluminescence, *Plenum Press*, New York, **1973**. p. 393-426
- [5] White, E.H. and Harding, M.J.C., The Chemiluminescence of Lophine and Its Derivatives. *Journal of American Chemistry Society*, **1984**. 86: p. 5686.
- [6] White, E.H. and Harding, M.J.C., Chemiluminescence of organic compounds. *Photochemistry and Photobiology*, **1965**. 4: p. 1129.
- [7] McCapra, F. and Chang, Y.C., Recent advances in research on the chemiluminescence of organic compounds. *Chemical Communications*, **1966**. p. 522.
- [8] McCapra, F., Richardson, D.G., and Chang, Y.C., Chemiluminescence Involving Peroxide Decompositions, *Photochemistry and Photobiology*, **1965**. 4: p. 111.
- [9] Rauhut, M.M., Chemiluminescence from concerted peroxide decomposition reactions, *Accounts of Chemical Research*, **1969**. 2: p. 80.
- [10] Urry, W.H. and Sheeto, J., The Autoxidation of Tetrakis-(Dimethylamino)-Ethylene. *Photochemistry and Photobiology*, **1965**. 4: p. 1067.
- [11] Carpenter, W., and Bens, E.M., The identification of some of the oxidation products of tetrakis (dimethylamino) ethylene. *Tetrahedron*, **1970**. 26: p. 59.
- [12] Wilson, T., Chemi- and bioluminescence of firefly luciferin. *Photochemistry and Photobiology*, **1995**. 62: p. 601.
- [13] Adam, W., and Cilento, G., Four-Membered Ring Peroxides as Excited State Equivalents. *Angewandte Chemie Int Ed. England*, **1983**. 22: p. 529.
- [14] Adam, W., et al., Epoxidation of vinylamides by dimethyldioxirane. In *Organic Peroxides*, John Wiley and Sons: Chichester, **1992**. p. 252.
- [15] Kopecky, K.R., and Mumford, Activation parameters for the decomposition of 3,3-dimethyl-1,2-dioxetane in 60% aqueous methanol. *Can Chemistry*, **1969**. 47: p. 709.
- [16] Turro, N.J. and Lechtken, P., Thermal and photochemical generation of electronically excited organic molecules. Tetramethyl-1,2-dioxetane and naphthalene. *Pure and Applied Chemistry*, **2009**. 33: p. 363.
- [17] Turro, N.J., and Lechtken, P., Thermal generation of organic molecules in electronically excited states. Evidence for a spin forbidden, diabatic pericyclic reaction. *Journal of American Chemistry Society*, **1973**. 95: p. 264.
- [18] Baumstark, A.L., and Rodriguez, A., CRC Handbook of Organic Photochemistry and Photobiology, *CRC press Inc.*, **1995**. p. 335.
- [19] Baader, W.J., Stevani, C.V., and Bastos, E.L., Chemiluminescence of Organic Peroxides. *Chemistry of Peroxides*, Wiley, Chichester, **2006**. 2(16): p. 1211.
- [20] Tanaka, C. and Tanaka, J., First-order transition in confined water between high-density liquid and low-density amorphous phases. *Journal of Physical Chemistry A*, **2000**. 104: p. 2078.
- [21] Adam, W., and Baader, W.J., Effects of Methylation on The Thermal Stability and Chemiluminescence Properties of 1,2-Dioxetanes. *Journal of American Chemistry Society*, **1985**. 107: p. 410-416.
- [22] Hummelen, J.C., Luider, T.M., and Wynberg, H., Xanthenylideneadamantane 1,2-dioxetane. preparation, properties and its potential use as an inherently thermochemiluminescent label. *Pure Applied Chemistry*, **1987**. 59: p. 639.
- [23] Hummelen, J.C., Luider, T.M., and Wynberg, H., Functionalized adamantylideneadamantane 1,2-dioxetanes: investigations on stable and inherently chemiluminescent compounds as a tool for clinical analysis. *Complimentary Immunoassays*, Wiley and Sons, New York, **1988**. p. 191
- [24] Hummelen, J.C., Luider, T.M., and Wynberg, H., Chemiluminescence: Properties of 1,2-Dioxetane Chemiluminescence. *Meth. Enzym*, **1986**. 133: p. 531.
- [25] Wynberg, H., Meijer, E.W., and Hummelen, J.C., Bioluminescence and Chemiluminescence. *Academic Press Inc.*, New York, **1981**. p. 687.
- [26] Hummelen, J.C., Inherently Chemiluminescent Compounds as New Labels in Clinical Analysis. *Thesis University of*

- Groningen, Groningen, **1985**. p. 229.
- [27] Luider, T.M., Thermochemiluminescence and its Application in Immunoassay. *Thesis, University of Groningen*, **1988**. p. 205.
- [28] Numan, H., et al., X-Ray structure of the 1,2-dioxetan dispiro (adamantane-2,3 [1,2] dioxetan-4,2-adamantane). *Journal of the Chemical Society, Chemical Communications*, **1977**. p. 591.
- [29] Schuster, G.B., et al., Adamantylideneadamantane-1,2-dioxetane. Chemiluminescence and decomposition kinetics of an unusually stable 1,2-dioxetane. *Journal of American Chemistry Society*, **1975**. 97: p. 7110.
- [30] Waldermar Adam, Thermal stability of spiro [adamantane [1,2] dioxetanes]. *Chemische Berichte.*, **1983**. 116: p. 839-846.
- [31] Schuster, G.B., et al., Empowering self-reporting polymer blends with orthogonal optical properties responsive in a broader force range. *Journal of American Chemistry Society*, **1975**. 97: p. 7110-7118.
- [32] Adam, W., and Encarnacion, L.A., Chemical and enzymatic triggering of 1,2-dioxetanes. 2: fluoride-induced chemiluminescence from tert-butyltrimethylsilyloxy-substituted dioxetanes. *Chemische Berichte.*, **1982**. 115: p. 2592
- [33] M. J. Frisch, et al., A potential energy profile of the catalytic cycle of pyruvate decarboxylase. *Pople Gaussian Inc.*, Wallingford CT, **2004**.
- [34] M. J. Frisch, et al., QSAR Studies of the Antifungal Activities of α -Diaminophosphonates Derived from Dapsone by DFT Method. *Gaussian, Inc.*, Wallingford CT, **2009**.
- [35] Lechtken, P., Thermal decomposition of tetramethyl-1,2-dioxetane. Selective and efficient chemoelectronic generation of triplet acetone. *Chemische Berichte.*, **1978**. 111: p. 1413-1419.
- [36] Yu, H., Chan, W. and Goddard, J.D., Ring-opening reactions of dioxetene, oxetene, dithiete, and thiete. *Journal of American Chemistry Society*, **1990**. 112: p. 7529-7537.
- [37] Wilsey, S., et al., The Thermal Decomposition of 1,2-Dioxetane Revisited. *Journal of Physical Chemistry*, **1999**. 103: p. 1669-1677.
- [38] White, E.H., and Harding, M., The Chemiluminescence of Lophine and Its Derivatives. *Journal of American Chemistry Society*, **1984**. 86: p. 5686.
- [39] Numan, H., et al., X-Ray structure of the 1,2-dioxetan dispiro(adamantane-2,3[1,2] dioxetan-4,2-adamantane). *Journal of Chemistry Society Comm.*, **1977**. p. 591.
- [40] Murov, S.L., et al. Hand-book of Photochemistry. 2nd Ed. *World Cat*, **1973**, New York.
- [41] Adam, W., Encarnacion, L.A.A. and Zinner, K., Thermal stability of spiro [adamantane [1,2] dioxetanes]. *Chemische Berichte*, **1982**. 116: p. 839.
- [42] Brouwer, A.C., et al., Xanthenylideneadamantane 12-dioxetane. preparation, properties and its potential use as an inherently thermochemiluminescent label. *Tetrahedron Letters*, **1988**. p. 3137.
- [43] Brouwer, A.C. et al., Xanthenylideneadamantane 12-dioxetane. preparation, properties and its potential use as an inherently thermochemiluminescent label. *Tetrahedron Letters*, **1988**. p. 3137
- [44] Matsumoto, M., et al. Synthesis of thermally stable 1,2-dioxetanes bearing a phenylethenyl or a phenylethynyl moiety and their base-induced decomposition. *Tetrahedron Letters*, **1997**. p. 2863.

**PHYTOREMEDIATION OF LABORATORY WASTE WATER USING
OCIMUM SANCTUM, *CYMBOPOGON CITRATUS*, *ALOE BARBADENSIS*
AND REUSING FOR DOMESTIC PURPOSES.**

Dr. M. A. Sabitha¹, Dr. A. Syed Mohamed²

¹Assistant Professor & PG Head, Department of Chemistry, Sadakathullah Appa College (Autonomous), Tirunelveli, Tamil Nadu, India, drsabithama@sadakath.ac.in

²Associate Professor & Research Head, Department of Chemistry, Sadakathullah Appa College (Autonomous), Tirunelveli, Tamil Nadu, India, asm2032@sadakath.ac.in

ABSTRACT

Water samples were collected from the chemistry laboratory. Daily lab discharge water was collected for one week. Water sample was treated by biosorption technique using *Ocimum sanctum*, *Cymbopogon citratus* (Lemon Grass) and *Aloe barbadensis miller*. The water analysis was carried out before and after treatment. 35 physico-chemical parameters were analyzed. pH, electrical conductivity, total dissolved solid and total hardness were reduced to permissible limits. Percentage of reduction was high in sodium, calcium, magnesium, bicarbonate and chloride. The decrease in carbonates, bicarbonates, nitrates, chloride, sulphate and phosphate were high. Even though the concentration of trace metals was low, the biosorption had reduced the concentration further. It was evident from this work that *Ocimum sanctum*, *Cymbopogon citratus* (Lemon Grass) and *Aloe barbadensis miller* could be efficiently used for treating laboratory waste water.

Keywords: *Aloe barbadensis miller*, biosorption, *Cymbopogon citrates*, *Ocimum sanctum*, total dissolved solid.

I. INTRODUCTION

Every natural response happen in water and it is the coordinated arrangement of organic metabolic responses in a fluid arrangement that is fundamental for the support of life. Human beings rely on water in one manner or other. It might be noticed that man's initial home and human advancement jumped up along the banks of waterways. In spite of the fact that the outside of our planet is about 71% water, just 3% of it is new. Of these 3% about 75% is tied up

in icy masses and polar ice sheets, 24% in groundwater and 1% is accessible as new water in streams, lakes and lakes appropriate for human utilization [1].

India faces a serious threat due to water pollution. Nearly 70% of surface water resources and groundwater reserves are contaminated by tones of various pollutants. These resources become unsafe for human consumption as well as for other activities. Because of the degradation of water quality, it will lead to water scarcity. In India, the Central Pollution Control Board (CPCB) in the year 1995 predicted that 18 major rivers are severely polluted. All these rivers run through urban area [2].

Wastes created in households, sewage, effluents from industries and agriculture run off pollutes the water resources. These wastes are loaded with chemicals and toxic substances which affect animals, plants and human beings. Solid wastes dumped in rivers and lakes affect the aquatic life. Due to the spilling of oil in sea pollutes the water becomes toxic for aquatic lives.

Iron coagulants are ferric sulphate ($\text{Fe}_2 (\text{SO}_4)_3$), ferrous sulphate (FeSO_4) and ferric chloride (FeCl_2). Iron compounds are generally cheaper, produce a heavier flocculent and perform over a wider pH range than aluminium coagulants. However, iron coagulants are not used as much as aluminium due to staining equipment, corrosiveness, and they require more alkalinity than alum.

Although water treatment chemicals are effective and used worldwide, scientific evidence shows that exposure to chemicals during coagulation with metal salts could be associated with adverse health effects [3]. Aluminium, which is the major component of aluminium sulphate (alum), polyaluminium chloride (PAC) and polyaluminium silica sulphate (PASS), could induce Alzheimer's disease and other similar related problems that are associated with residual aluminium in treated water [4].

It becomes important to pursue research for effective, more cheap and economic way of treating water using natural adsorbents. Hence the present work is carried out using *Ocimum sanctum*, *Cymbopogon citrates* and *Aloe barbadensis* to treat waste water from laboratory and paving way for reuse of lab water for domestic purposes.

II. MATERIALS AND METHODS

Water samples are collected from the Chemistry laboratory of Sadakathullah Appa College. Daily lab discharge water is collected for one week. Sample was preserved by addition of sulphuric acid to $\text{pH} < 2$ (USEPA 600/4-82/029) and stored in refrigerator. Water sample was treated by biosorption technique using *Ocimum sanctum*, *Cymbopogon citratus* (Lemon Grass) and *Aloe barbadensis miller*. The leaves of *Ocimum sanctum* and *Cymbopogon citratus* (Lemon Grass) were collected and dried along with the gel of *Aloe barbadensis miller*. Then dried content were powdered. The weighed 5g powder was kept in muslin cloth and packed. This packet was put in the one litre water sample and then tightly closed. This set up was kept undisturbed for one week. After one week this sample is filtered and again the physico-chemical parameters were analyzed.

The following physico-chemical parameters such as pH, electrical conductivity, total dissolved solids, salinity, total hardness, sodium, calcium, potassium, magnesium, bicarbonate, carbonate, chloride, sulphate, nitrate, phosphate and fluoride [5,6] were determined before and after treatment of water.

III. RESULTS AND DISCUSSION

The waste water collected from the laboratory was soaked with *Ocimum sanctum*, *Cymbopogon citratus* (Lemon Grass) and *Aloe barbadensis miller*. The water analysis was carried out before and after treatment and was tabulated in table 1 and represented in figure 1.

The waste water was also analyzed for trace metals such as lead, arsenic, beryllium, cadmium, vanadium, chromium, nickel, molybdenum, silver, strontium, barium, rubidium, copper, iron, zinc, manganese, aluminium, cobalt, selenium and antimony before and after treatment of water. The results were tabulated in table 2 and represented in figure 2.

pH level of laboratory water was above 8.5 which indicate that a high level of alkanity and minerals were present. High pH causes many problems such as

- ❖ Scale build up on fixtures and shower doors.
- ❖ Reduced water flow.
- ❖ Scale accumulation at the bottom of tank water heater.

❖ Bitter taste.

On treatment with *Ocimum sanctum*, *Cymbopogon citratus* (Lemon Grass) and *Aloe barbadensis miller* pH level was decreased and lies within the permissible level of 7.34 which is very much near to neutral pH. TDS permissible limit for domestic water was less than 300 mg/L. The laboratory water showed 20 times more than the allowed limit. The treatment made an effective purification of waste water and the TDS level fell to 50 mg/l. The value was reduced by 99% from the before treatment value. A high level of TDS creates health problems in human. The presence of potassium, sodium and chloride increase the TDS level in water.

The present study showed electrical conductivity of 11,280 and 74 $\mu\text{S}/\text{cm}$ for waste water and treated water respectively. The permissible limit for EC must be less than 400 $\mu\text{S}/\text{cm}$. The treated water indicated that the value was decreased by greater extent. High electrical conductivity was due to dissolved substances and the presence of heavy metals. These substances affect the aquatic life system when discharged untreated.

The total hardness of the waste water was found to be three times more than the prescribed limit of 0- 60 mg/l. The value was declined to 19 mg/l after treatment with bioadsorbent. The hardness was well below the limiting value. The classification of water based on hardness was given in the table 3.

Based on the classification, the untreated very hard water had been changed to soft water after treatment. Hard water can cause the following effects:

- ❖ Reduce the life of equipment,
- ❖ Raise the costs of heating the water,
- ❖ Lower the efficiency of electric water heaters, and clog pipes.

The permissible limit for sodium in domestic water was 30- 60 mg/l. The untreated water exhibited 652 mg/l and the treated water had 62 mg/l. Although the treated water exceeds the limit, there was 90% reduction in the value. The level of calcium was reduced to 23 mg/l when treated with bioadsorbents which was below the permissible limit of 40- 80 mg/l. The potassium and magnesium levels were highly reduced from 56 mg/l to 6 mg/l and 562 mg/l to 31 mg/l respectively. 94 % decline in magnesium values was observed. The classification of water based

on magnesium was tabulated in table S4. Based on magnesium level, the waste water was graded as very hard which had been modified to slightly hard.

The carbonate and bicarbonate levels reached 101 mg/l and 0 mg/ l from 3 mg/l and 333 mg/l respectively. The levels of carbonate and bicarbonate represent the alkalinity of the samples. When these salt increases, the usage of such water creates health issues.

Chloride and sulphate amounts were reduced by 77% and 85% respectively. The amount of nitrate, phosphate and fluoride also showed slight decrease. Phosphorus is an essential element for plant life, but when there is too much of it in water, it can speed up eutrophication (a reduction in dissolved oxygen in water bodies caused by an increase of mineral and organic nutrients) of rivers and lakes. This method using can be used to prevent those conditions.

Even though the concentrations of lead, arsenic, vanadium, nickel, strontium, barium, cobalt, selenium and antimony were very low, the bio-adsorbents were able to further reduce these amounts. Manganese, iron, copper, and zinc are essential micronutrients. When the concentrations of these elements increase, it creates serious threats to the environment. The bioadsorbents can effectively used to reduce the concentrations of micro nutrients and also trace elements. Concentration of beryllium and nickel were decreased to permissible limit. Similarly the concentrations of silver and molybdenum were declined below the limiting value of 0.2-0.3 μ g/l and < 10 μ g/l respectively. Also aluminium concentration was reduced from 0.23 mg/l to 0.15mg/l.

The flavinoids and tannins present in *Cymbopogon citratus* provide antibacterial effect against gram positive bacteria. Quercitin and tannic acid contained in *Cymbopogon citratus* has efficacious effect against *P. Aeruginosa* [7]. In addition to antibacterial activity, *Cymbopogon citratus* possess antiamoebic, antifilarial and antifungal properties [8]. Studies reveal that aromatic grasses such as lemon grass, vetiver and palmarosa are used for phytoremediation of heavy metal contaminated sites. Also, Ocimum, Metha and Lavender help to remove metals [9]. *Cymbopogon citratus* is used to reclaim the toxic copper tailings [10]. Lead can be conveniently removed from waste water using lemon grass [11].

The effective bioadsorbition capacity of lemon grass for metals such as lead, cadmium and zinc is proved by Hassan et al., [12]. *Cymbopogon citratus* is an efficient accumulator of

aluminium, zinc, cadmium, lead, chromium, arsenic and nickel [13,14]. The efficient biosorption of iron and lead using *Ocimum sanctum* is studied which revealed that alcohol, carboxylamino and sulphonic groups play significant role in biosorption [15]. The high phenolic contents in these medicinal plants pave way for removal of metals due to high metal chelation potential [16]. *Ocimum sanctum* is considered as queen of herbs as it shows antiviral, antioxidative and antimicrobial properties [17].

Aloe barbadensis miller is a hyper accumulator of chromium, copper, nickel, cadmium and lead [18]. Rai et al., [19] confirmed that aloe vera can be effectively used for the biosorption of potassium, sodium, calcium, magnesium, phosphorus, iron, copper, zinc, cadmium and lead. The surface studies of *Aloe barbadensis miller* is being carried out by Malik et al., in 2015 [20]. They showed that carboxyl group, hydroxyl group and carbonyl group are present on the surface. The mechanism for the removal of metals is that the electrostatic attraction between charged groups in cell wall and metals in the pH range of 1.0 to 4.0 [21]. At this pH range, ionic exchange will be the reason for the removal of metals and at high pH, the removal is possible by means of precipitation. High potential of antiviral, antibacterial and antifungal properties are shown by *Aloe barbadensis miller* [22,23].

The main reaction involved in metal removal in these plant leaves are chemical reaction between functional groups on the surface of adsorbent and metals which forms metal- organic complexes. When the pH varies, other possible mechanisms of diffusion, bulk transport in liquid phase and mass transport processes occur. The biosorption of *Cymbopogon citratus* for the metals are in the order Zn (II) > Cd (II) > Pb (II) [24]. The metal removal efficiency of *Ocimum sanctum* for iron is 73.62% and that of lead is 95.63%. When *Aloe barbadensis miller* along with coconut husk is used for metal removal, the efficiency is found to be 99.99% for lead, 86.41% for zinc, 91.97% for nickel and 93.21% for copper [25]. Different bioadsorbents show different removal efficiency for various metals. Hence the combination of these bioadsorbents will produce effective results. So, the three plant species are chosen to effect maximum removal of metals and to incorporate antimicrobial activities.

Conclusion

The increasing population and the demand for underground water have created awareness for rain water harvesting and search of new techniques to reuse waste water. This methodology of using *Ocimum sanctum*, *Cymbopogon citratus* (Lemon Grass) and *Aloe barbadensis miller* for purification of most polluted laboratory waste water was cost effective and efficient. It can be applied to purify any water and the water can be used for domestic purpose. The proposed work can be extended to large scale waste water purification by constructing water tank made with three layers of sand and pebbles, sand and ceramic membrane coated with *Ocimum sanctum*, *Cymbopogon citratus* (Lemon Grass) and *Aloe barbadensis miller* leaf powders.

Acknowledgments

The authors acknowledge the financial support received from Sadakathullah Appa College, Tirunelveli, for their support and encouragement in carrying out this work.

V. REFERENCES

1. Dugan, P.R. (1972). Bio Medical Ecology of Water Pollution. Plenum press London, 159.
2. Central Pollution Control Board (CPCB), (1995). Annual Report 1993/94, Central Pollution Control Board, Ministry of Environment & Forests, Government of India, New Delhi, 154 pp.
3. Hahn, H.H. and Kunte, R. (1990). Chemical Water and Wastewater Treatment. Proceedings of the 4th Gottenburg Symposium ed. Klute, R. Madrid, Spain. Oct.1990. pp 37-409.
4. American Water Works Association (AWWA), (1990). Water Quality and Treatment: A Hand book of Public Water Supplies, 4th edition, New York, McGraw Hill.
5. APHA (American Public Health Association), (2012). Standard Methods for the Examination of Water and Wastewater (22nd ed.), American Public Health Association, Washington, DC.
6. USEPA (1992). Guidelines for Exposure Assessment. EPA/600/Z-92/001. US Environmental Protection Agency, Risk Assessment Forum, Washington, DC.
7. Geetha Subramaniam, Xin YingYew and Lalita Ambigai Sivasamugham, (2020). Antibacterial activity of *Cymbopogon citratus* against clinically important bacteria, South African Journal of Chemical Engineering, 34: 26- 30.

8. Shah, A.P., Nongthomba, U., Kelly Tanaka, K.K., Denton, M.L., Meadows, S.M., Bancroft, N., Molina, M.R., Cripps, R.M. (2011). Cardiac remodeling in *Drosophila* arises from changes in actin gene expression and from a contribution of lymph gland-like cells to the heart musculature. *Mech. Dev.* 128(3-4): 222--233.
9. Janhvi Pandey, Rajesh Kumar Verma and Saudan Singh, (2019). Suitability of aromatic plants for phytoremediation of heavy metal contaminated areas: a review, *International Journal of Phytoremediation*, <https://doi.org/10.1080/15226514.2018.1540546>.
10. Das M, Maiti SK. 2009. Growth of *Cymbopogon citratus* and *Vetiveria zizanioides* on Cu mine tailings amended with chicken manure and manure-soil mixtures: a pot scale study. *Int J Phytoremediation*. 11(8):651–663.
11. Lal K, Yadav RK, Kaur R, Bundela DS, Khan MI, Chaudhary M, Meena RL, Dar SR, Singh G. 2013. Productivity, essential oil yield, and heavy metal accumulation in lemon grass (*Cymbopogon flexuosus*) under varied wastewater–groundwater irrigation regimes. *Ind Crops Prod.* 45:270–278.
12. Hassan E. 2016. Comparative study on the biosorption of Pb (II), Cd (II) and Zn (II) using Lemon grass (*Cymbopogon citratus*): kinetics, isotherms and thermodynamics. *Chem Int.* 2(2):89–102.
13. Gautam M, Pandey D, Agrawal M. 2017. Phytoremediation of metals using lemongrass (*Cymbopogon citratus* (DC) Stapf.) grown under different levels of red mud in soil amended with biowastes. *Int J Phytoremediation*. 19(6):555–562.
14. Lee LY, Lee XJ, Chia PC, Tan KW, Gan S. 2014. Utilisation of *Cymbopogon citratus* (lemon grass) as biosorbent for the sequestration of nickel ions from aqueous solution: equilibrium, kinetic, thermodynamics and mechanism studies. *J Taiwan Institut Chem Eng.* 45(4):1764–1772. doi:10.1016/j.jtice.2014.02.002.
15. Sreelakshmi C D, (2017). Heavy Metal Removal from Wastewater using *Ocimum Sanctum*, *International Journal of Latest Technology in Engineering, Management & Applied Science*, 6(4): 85- 90.
16. Rice-Evans CA, Miller NJ, Paganga G. Structure-antioxidant activity relationships of flavonoids and phenolic acids. *Free Radical Biol Med.* 1996;20:933–956. doi: 10.1016/0891-5849(95)02227-9.

17. Pramod K Raghav and Mitu Saini, (2018). Antimicrobial properties of Tulsi (*Ocimum sanctum*), *International Journal of Green and Herbal Chemistry*, 7(1): 20-32.
18. Fatemeh Shokri, Parisa Ziarati and Zahra Mousavi, (2016). Removal of Selected Heavy Metals from Pharmaceutical Effluent by Aloe Vera L., *Biomed Pharmacol. J.*, 9(2), <https://dx.doi.org/10.13005/bpj/993>
19. Rai TS, Puri A, McBryan T, Hoffman J, Tang Y, Pchelintsev NA, van Tuyn J, Marmorstein R, Schultz DC, Adams PD. 2011. Human CABIN1 is a functional member of the human HIRA/UBN1/ASF1a histone H3.3 chaperone complex. *Mol Cell Biol* 31: 4107–4118.
20. Malik, R. 1 Saini, N. 1 Ahlawat, S. 2 Singhal, S. 3 and Lata, S., (2019). Convenient and Efficient Elimination of Heavy Metals from Wastewater Using Smart Pouch with Biomaterial, *Pollution*, 5(1): 13- 31.
21. Sag Y, Ozer D and Kutsal T, (1995). A comparative study of the biosorption of lead (II) ions to *Z. ramigera* and *R. arrhizus*. *Process Biochemistry* 30 169–174.
22. Ramasubramanian TS, Sivakumar VT, Thirumalai AV., (2010). Antimicrobial activity of *Aloe vera* (L.) Burm. f. against pathogenic microorganisms. *J Bio Sci Res.*, 4:251–8.
23. Arunkumar S, Muthuselvam M., (2009). Analysis of phytochemical constituents and antimicrobial activities of *Aloe vera* L. against clinical pathogens. *World J Agric Sci.*, 5(5):572–6.
24. Babarinde A, Ogundipe K, Sangosanya KT, Akintola BD, Hassan AOE (2016) Comparative study on the biosorption of Pb(II), Cd(II) and Zn(II) using lemon grass (*Cymbopogon citratus*): kinetics, isotherms and thermodynamics. *Chem Int* 2:89–102.
25. Malik, R. 1 Saini, N. 1 Ahlawat, S. 2 Singhal, S. 3 and Lata, S., (2019). Convenient and Efficient Elimination of Heavy Metals from Wastewater Using Smart Pouch with Biomaterial, *Pollution*, 5(1): 13- 31.

TABLE 1: Physico-chemical parameters of waste water collected from laboratory before and after treatment

S. No.	Physico-chemical parameters	Value before treatment	Value after treatment	Standard value
1	pH	8.55	7.34	7.0-8.0
2	TDS mg/L	7400	50	Less than 300
3	EC μ S/cm	11280	74	< 400
4	Total hardness mg/L	270	19	0-60
5	Sodium mg/L	652	62	30-60
6	Calcium mg/L	159	23	40-80
7	Potassium mg/L	56	9	-
8	Magnesium mg/L	562	31	17.1-60
9	Bi carbonate mg/L	333	101	-
10	Carbonate mg/L	3	0	Below 60
11	Chloride	888	201	>250
12	Sulphate	651	89	1-770
13	Nitrate	10	7	10
14	Phosphate	6	2	0.5 -1.5
15	Fluoride	0.8	0.6	-

TABLE 2: Trace metals in waste water collected from laboratory before and after treatment.

S. No.	Trace metals	Values before treatment mg/L	Values after treatment mg/L	Standard value
1	Lead	0.006	0.001	400ppm
2	Arsenic	0.23	0.16	0.05mg/L
3	Beryllium	0.13	0.009	0.01µg/L
4	Cadmium	0.33	0.02	0.005mg/L
5	Vanadium	0.001	0	5.1µg/L
6	Chromium	0.42	0.12	0.1mg/L
7	Nickel	0.12	0.003	100-400µg/L
8	Molybdenum	0.002	0	<10µg/L
9	Silver	0.23	0.11	0.2-0.3µg/L
10	Strontium	0.0001	0.0001	7.0mg/L
11	Barium	0.001	0.001	2.0mg/L
12	Rubidium	0.002	0.002	-
13	Copper	0.13	0.05	<30mg/L
14	Iron	0.23	0.12	1-3mg/L
15	Zinc	0.45	0.14	0.01-0.05mg/L
16	Manganese	0.56	0.12	<300µg/L
17	Aluminum	0.23	0.15	-
18	Cobalt	0.002	0	0.02-53.2µg/L
19	Selenium	0.003	0.003	0.06µg/L
20	Antimony	0.002	0.001	0.1-0.2µg/L

TABLE 3: Classification of water based on hardness

S. No.	Classification	Hardness in mg-CaCO ₃ /L
1	Soft	0-60
2	Moderately hard	61-120
3	Hard	121-181
4	Very hard	≥ 181

TABLE 4: Classification of water based on magnesium level.

Classification	Magnesium level (mg/L)
Slightly hard	17.1-60
Moderately hard	60-120
Hard	120-180
Very hard	180 & over

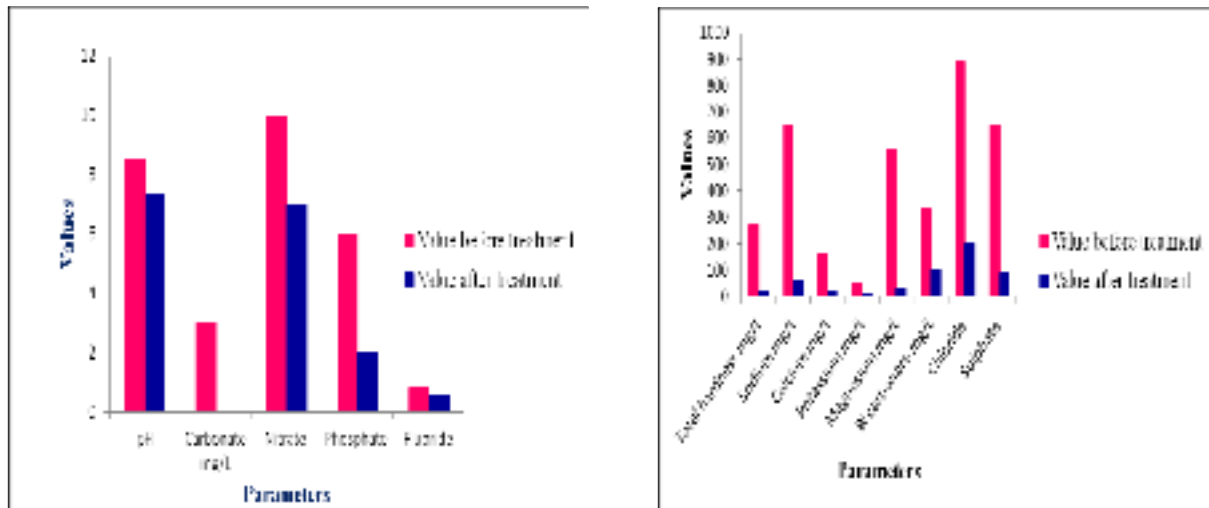


Fig. 1: Variation of physico-chemical parameters of laboratory waste water before and after treatment

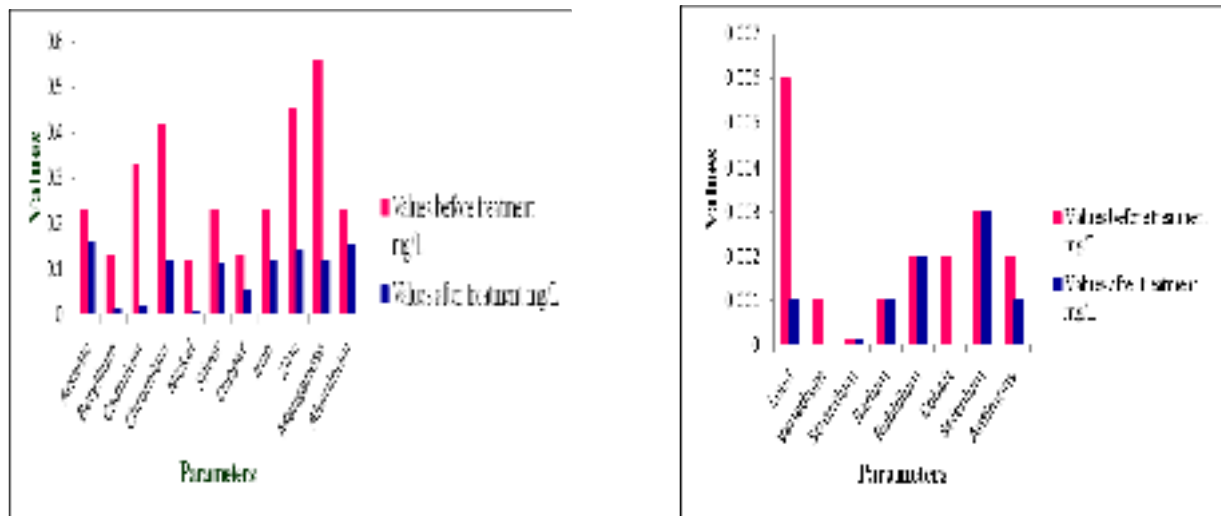


Fig. 2: Trace metals in waste water collected from laboratory before and after treatment.



Microwave assisted synthesis of ZnO and Co doped ZnO nanoparticles and their antibacterial activity

M. Sheik Muhideen Badhusha*

Department of Chemistry, SadakathullahAppa College, Tirunelveli, Tamilnadu, India

ABSTRACT

The aim of this study was to obtain and characterize ZnO and Co doped ZnO nanoparticles by Microwave assisted method. ZnO plays an important role in many semiconductors technological aspects. In this work, the Co doped ZnO nanoparticles prepared by varying the concentration of Co $(\text{CH}_3\text{COO})_2 \cdot 4\text{H}_2\text{O}$. The synthesized nanomaterials were characterized by XRD, FT-IR and SEM with EDX. The XRD patterns showed that ZnO nanoparticles have hexagonal wurtzite structure. The FT-IR study confirms the presence of functional group in ZnO. SEM photographs show that the synthesized pure ZnO and Co doped ZnO were in the shape of nanoneedles and nanospheres. The average size of nanoneedles and nano-spheres were found to be 25-35 nm and 20-30 nm.

Keywords: ZnO, Co-ZnO, Microwave, Antibacterial activity.

INTRODUCTION

Metallic oxide nanoparticles, specifically nano-scale ZnO, have gained considerable importance in recent years due to their wide range of applications in various fields of science notably biotechnology and pharmacology [1]. ZnO nanoparticles have been regarded as biocidal agents/disinfectants because of their safety, lower toxicity and biocompatibility towards humans [2].

Number of synthesis methods are available for the preparation of pure and doped ZnO nanomaterials, like hydrothermal, hydrolysis, sol-gel, vapor condensation, spray pyrolysis and organic precursor flame decomposition [3]. In conventional synthesis, energy is transferred to the material through convection, conduction and radiation, which results in temperature gradient between surface and bulk. The microwave heating causes the uniform distribution of temperature between the surface and the bulk material and thereby leading to the fast formation of nanoparticles. The microwave dielectric heating has resulted in acceleration of the chemical transformations in a microwave field, which cannot be achieved easily by the conventional method [4-5].

Due to the outbreak of the infectious diseases caused by different pathogenic bacteria, the scientists are searching for new antibacterial agents. In the present scenario, nanoscale materials have emerged up as novel antimicrobial agents owing to their high surface area to volume ratio and the unique chemical and physical properties [6]. Nowadays, ZnO is more focussed by researchers due to its stability and antibacterial activity during rough and tough processing and safe materials for human and ecosystem [7]. Antimicrobial activity of ZnO has enhanced due to the presence of water molecules on its surface, these aqueous suspensions of ZnO and water generate free radicals of hydroxyl and oxygen species which is responsible for remarkable oxidative stress in treated bacterial cells. Recently, many complexes and nanomaterials of Co(II) showing antimicrobial [8]. But, there are significant results over antibacterial

activity of cobalt doped ZnO while both zinc and cobalt are the essential elements of human and animal health in trace amounts. Earlier reports have been mainly focused on optical, electrical and magnetic properties of Co doped ZnO NPs [9], whereas very few attempts have been made to study the antibacterial properties of Co doped ZnO NPs. Hence, in the present study, Co doped ZnO nanostructured materials have been successfully synthesized by the microwave assisted method. Further, the influence of Co dopant concentration on the structural, optical, and antibacterial properties of ZnO NPs has been investigated.

MATERIALS AND METHODS

2.1. Chemicals

Zinc acetate dihydrate ($\text{Zn}(\text{CH}_3\text{COO})_2 \cdot 2\text{H}_2\text{O}$), cobalt acetate tetrahydrate ($\text{Co}(\text{CH}_3\text{COO})_2 \cdot 4\text{H}_2\text{O}$) and Sodium hydroxide (NaOH) were purchased from Merck Private Limited as Analytical grade chemicals.

2.2. Synthesis procedure

Pure and Co doped ZnO with compositional formula $\text{Zn}_{1-x}\text{Co}_x\text{O}$ ($x = 0.00, 0.01, 0.03$ and 0.05) were synthesized by Microwave assisted hydrothermal route. Appropriate amounts of zinc acetate and cobalt acetate were dissolved in water and stirred using magnetic stirrer for 10 min. 1M solution of NaOH was slowly added into above the mixture solution. Then PEG was added drop by drop into the above solution, which was stirred with a magnetic stirrer, until the pH reached 9.0 and the solution became green. The obtained solution was heated in a LG microwave oven at a power of 300W for 30 min. After microwave processing, the solution was cooled to room temperature. The resulted precipitate was separated by centrifugation, then washed with deionized water and ethanol for several times and finally the precipitate was dried in an oven at 60°C for 24 h and calcinated at 400°C for 1 h. ZnO nanoparticles were also prepared by the same procedure without the addition of cobalt acetate.

2.3. Characterization

Structural properties of the synthesized samples were characterized by powder x-ray diffraction (XRD) analysis (X'PERT-PRO diffractometer). Optical properties were analyzed with the help of UV-vis spectrometer (SHIMADZU-UV 1800 spectrometer). Functional group analysis of the synthesized samples was characterized using FT-IR (SHIMADZU- 8400) spectrometer. Morphological properties and composition of the samples were investigated using scanning electron microscopy (SEM, ZEISS Supra 40VP) with energy dispersive x-ray spectroscopy (EDX, Oxford).

2.4. Antibacterial assay

The antibacterial susceptibility test was performed by adopting the agar diffusion method [10]. Around 20 ml of Mueller-Hinton Agar was poured on to the petri plates and allowed to solidify in order to investigate susceptibility test against bacteria. Then 0.1 ml of standardized inoculums suspension was dispensed into the surface of the petri plates and allowed to dry for 5 min. The test solution was prepared with a known weight fraction in 0.01mg/mL of the samples were dissolved in 5% dimethyl sulphoxide (DMSO). Sterile discs (6mm) from Himedia Ltd, Mumbai, were impregnated with 20 μl of the prepared samples (corresponding to 0.05 and 0.1mg / ml) was allowed to dry at room temperature. After drying, the discs with respective samples were placed on the surface of the plate using sterile forceps and gently pressed to ensure contact with the agar surface. The petri dishes were subsequently incubated at 37°C for 24 hours. After incubation the growth inhibition rings were quantified by measuring the diameter of the zone of inhibition in mm using transparent ruler in millimeter (including the diameter of the disc) from the lower surface of the petri dishes and the control is consisted of paper disc soaked with appropriate solvent and evaporated to dryness.

RESULTS AND DISCUSSION

3.1 XRD Analysis

Fig. 1 shows the XRD pattern of pure and Co doped ZnO nanoparticles. The peaks that are observed at $2\theta = 31.70^\circ, 34.42^\circ, 36.19^\circ, 47.42^\circ, 56.50^\circ, 62.66^\circ$ and 67.74° represents the hexagonal wurtzite structure of ZnO with lattice parameters (1 0 0), (0 0 2), (1 0 1), (1 0 2), (1 1 0), (1 0 3) and (1 1 2) (JCPDS card no. 891397). Thus, X-Ray diffraction studies confirmed that the synthesized materials were ZnO and Co doped ZnO with hexagonal phase. Also, all the diffraction peaks agreed with the reported JCPDS data and no characteristic peaks were observed other than ZnO. The average crystallite size is estimated by measuring the change in full-width at the half-maximum of the diffraction peaks using scherrer's formula [11] $D = K\lambda/(\beta\cos\theta)$, where K is the scherrer constant, λ the X-ray

wavelength, β the peak width of half maximum, and θ is the Bragg diffraction angle. The average crystallite size is found to be ~ 45 , ~ 42 , ~ 21 , and ~ 10 nm correspond to Co concentration ($x = 0.00, 0.01, 0.03$ and 0.05), respectively. The results of the analysis indicate that the average crystallite size tends to decrease with increasing Co concentrations.

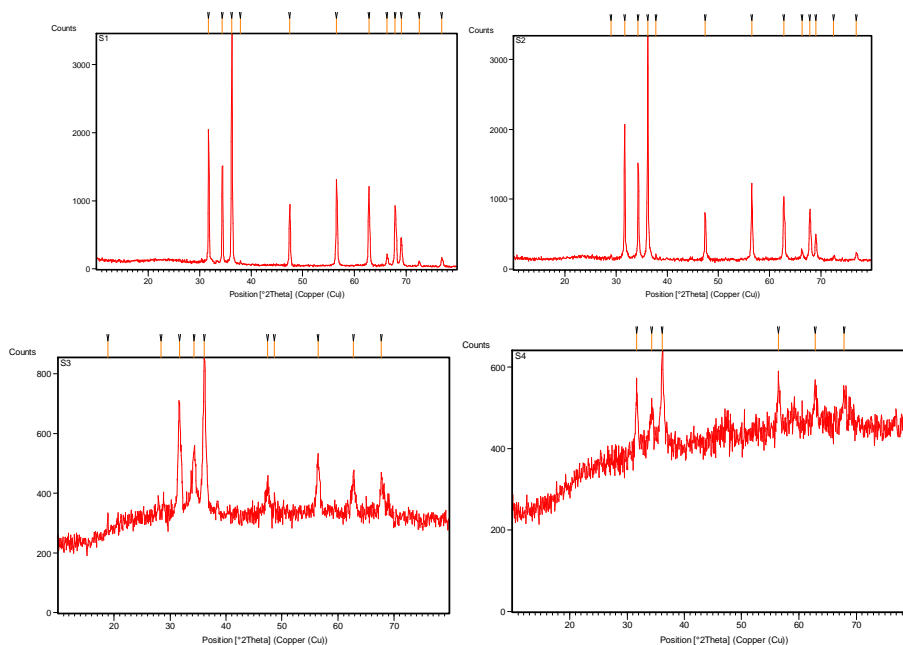


Fig. 1 XRD pattern of pure ZnO and Co doped ZnO NPs

3.2 UV- Vis Analysis

The UV-Vis spectrum of the ZnO and Co doped ZnO nanoparticles were observed by dispersing the powder in deionized water. Fig. 2(a), shows the UV-Vis spectrum of pure ZnO and Co doped ZnO nanoparticles. From the Co doped ZnO shows the higher optical absorption in the visible region than pure ZnO. The fundamental absorption which corresponds to electron excitation from the valence band to conduction band can be used to determine the value of the optical band gap. The value of the optical band gap is calculated by extrapolating the straight line position of $(\alpha h\nu)^2$ vs $h\nu$. It is obviously clear that doped ZnO NPs shows reduced the band gap energy than the pure ZnO (Fig. 2b) and it is better than the earlier report. The remarkable changes that, there is a decrease in the band gap for the Co doped ZnO which shows the clear red shift.

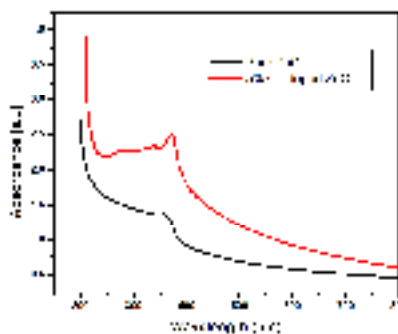


Fig 2 (a) UV-vis absorption spectra of ZnO and Co doped ZnO NPs

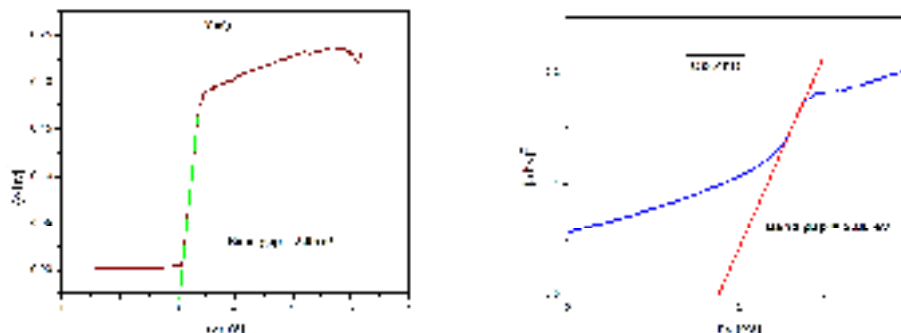


Fig. 2 (b) Tauc plot of $(\alpha h\nu)^2$ versus $(h\nu)$ of ZnO and Co doped ZnO NPs

3.3 FT-IR Analysis

The FT-IR spectra of ZnO and Co doped ZnO NPs recorded in the range $4000\text{--}400\text{ cm}^{-1}$ are shown in Fig. 3. The broad band located around 3450 cm^{-1} is due to O–H stretching vibration of adsorbed water molecules, while the band located about 1625 cm^{-1} is due to O–H bending vibration of the same atmospheric water [12]. The characteristic band at 2350 cm^{-1} is due to $\text{O}=\text{C}=\text{O}$ stretching vibrations of residual CO_2 that is adsorbed on particles surface. The strong absorption band at 444 cm^{-1} is due to Zn–O stretching mode of ZnO nanoparticles [13].

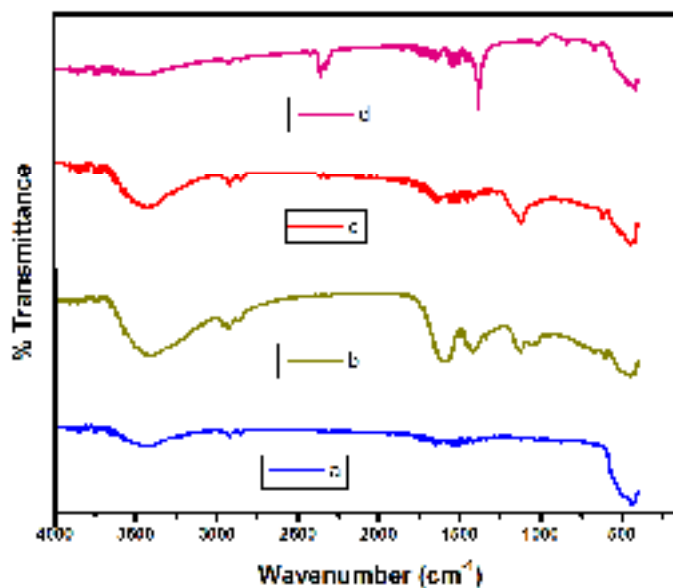


Fig. 3 FT-IR spectrum of ZnO and Co doped ZnO NPs

3.4 SEM Analysis

Surface morphological studies of undoped and Co doped ZnO NPs have been carried out using a scanning electron microscope. Fig. 4 shows representative SEM images for the $\text{Zn}_{1-x}\text{Co}_x\text{O}$ with $(x = 0.00, 0.01, 0.03 \text{ and } 0.05)$. These images show the presence of large aggregates of smaller individual nanoparticles of various sizes. Pure ZnO showed needle shaped microstructure, while the Co doped ZnO nanoparticles were obtained as nanospheres. For the pure ZnO, the average grain size was found to be around 25–35 nm. The average grain size slightly tends to decrease with increasing the Co doping. This tendency was also observed in the XRD measurements.

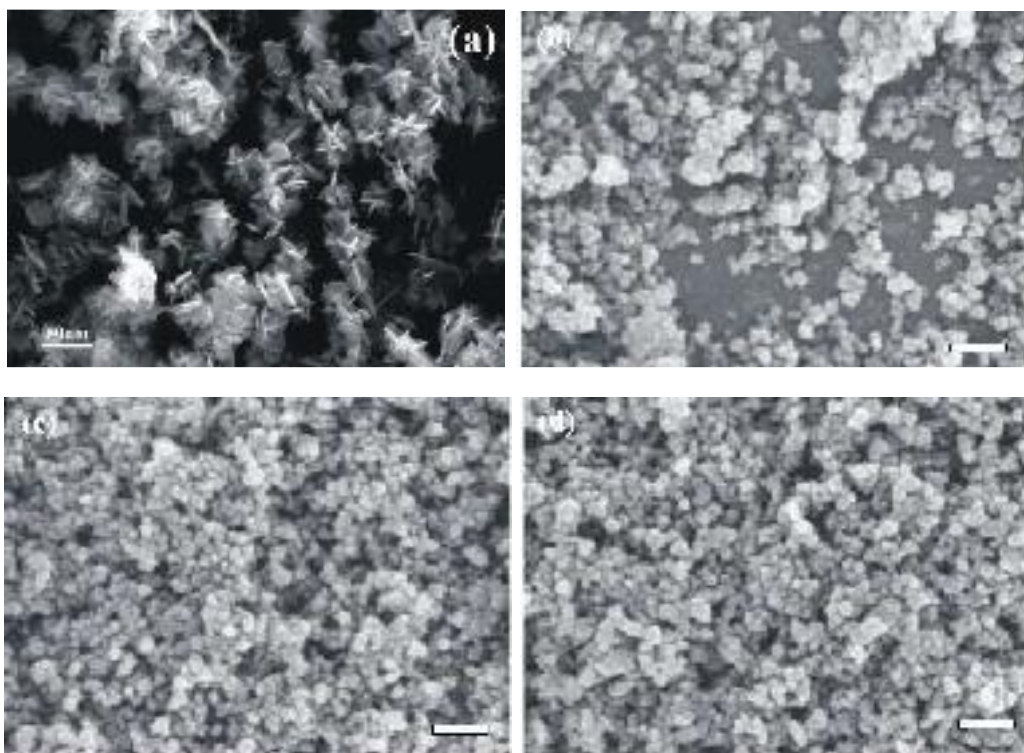


Fig. 4. SEM images for representative samples of $Zn_{1-x}Co_xO$ with (a) $x = 0.0$, (b) $x = 0.01$, (c) $x = 0.03$ and (d) $x = 0.05$

3.5 Elemental analysis (EDS)

The chemical compositions of synthesized Co doped ZnO NPs were measured by EDS spectra and shown in Fig. 5. The EDS spectrum showed signals of all the expected elements Zn, O and Co, which confirms the presence of Co^{2+} ions which are substituting the Zn^{2+} ions in the Zn matrix. Hence, these results conclude that Co ions have been doped into the ZnO lattice without any impurities.

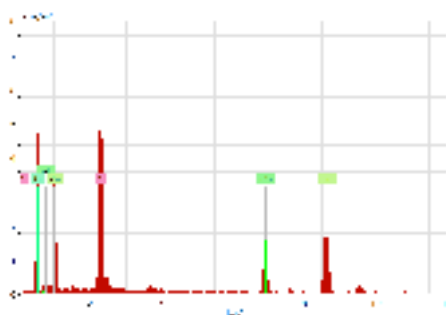


Fig. 5 EDS spectrum of Co doped ZnO NPs

3.6. Antibacterial activity

Antibacterial activity of the synthesized ZnO and Co doped ZnO NPs were evaluated using agar diffusion method. Figs. 6(a)–(f) shows the three different concentrations of bare ZnO and Co doped ZnO NPs suspensions tested against *Salmonella typhi* and *Klebsiella pneumonia*. This indicates the biocidal action of both the samples. For *Salmonella typhi*, bare ZnO NPs exhibited a maximum inhibition zone of 16 mm whereas Co-doped ZnO exhibited inhibition zone of 25 mm. In addition, against *Klebsiella pneumonia* with zone of inhibition of 18 mm is observed for Co-doped ZnO while 14 mm is measured for bare ZnO NPs. It is apparent that, as the concentration of nanoparticles increases the inhibition zone also gets increased. Also, Co-doped ZnO obtained better results in both the bacterial strains.

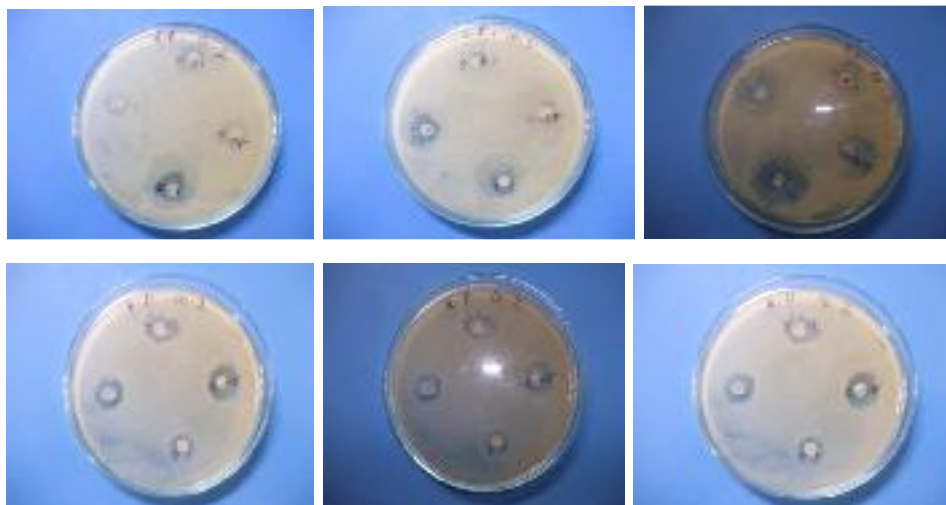


Fig. 6 Antibacterial-screening results against of *Salmonella typhi* and *Klebsiella pneumonia* with Pure ZnO and Co doped ZnO NPs

CONCLUSION

Nanostructured $Zn_{1-x}Co_xO$ ($x = 0.00$, $x = 0.01$, $x = 0.03$ and $x = 0.05$) nanopowders have been successfully fabricated by microwave-assisted method further analyzed through X-ray diffraction, UV-Visible spectrum, Scanning electron microscopy and Fourier transform infrared spectroscopy to analyzing the influence of Co doping on structural and optical properties of ZnO Nanoparticles. From XRD analysis it is witnessed that average crystalline size decreased with increase of dopant (Co) concentration. SEM images showed the formation of needle like ZnO nanoparticles and in the case of Co doped ZnO nanoparticles are almost spherical images due to the influence of Co doping. The vibration frequencies in the FT-IR spectra further confirm the formation of wurtzite structure. Further, focused on the applied part of synthesized cobalt doped ZnO nanoparticles as an effective and potent antibacterial agent against water borne bacteria. The future studies will probably witness important novel developments in applied nanoresearch regarding antimicrobial agent.

Acknowledgement

I am thankful to the University Grants Commission, Hyderabad, for the financial support provided to me for pursuing the Minor Research Project (Ref. No. F MRP-5363/14 (SERO/UGC)). Also, I express my sincere thanks to the Managing Committee and the Principle, Sadakathullah Appa College, Tirunelveli for having provided to me the necessary facilities to carry out the project successfully.

REFERENCES

- [1] R. Javed, M. Usman, S. Tabassum, M. Zia, *Applied Surface Science.*, **2016**, 386, 319–326
- [2] K.I. Bogutska, Y.P. Sklyarov, Y.I. Prylutsky, *Ukrainica Bioorganica Acta.*, **2013**, 1, 9-16.
- [3] I. Djerdj, J. Zvonko, A. Denis, N. Markus, *Nanoscale.*, **2010**, 2, 1096–1104.
- [4] C. Ragupathi, J. Judith Vijaya, L. John Kennedy, *Materials Science and Engineering B.*, **2014**, 184, 18–25.
- [5] Naghme Faal Hamedani, Ali Reza Mahjoub, Abbas Ali Khodadadi, Yadollah Mortazavi, *Sensors and Actuators B.*, **2011**, 156, 737–742.
- [6] Razieh Jalal, K. Elaheh, Goharshadia, Maryam Abareshi, Majid Moosavi, Abbas Yousefi, Paul Nancarrow, *Materials Chemistry and Physics.*, **2010**, 121, 198–201.
- [7] P.K. Stojimenov, R.L. Klinger, G.L. Marchin, K.J. Klabunde, *Langmuir.*, **2002**, 18, 679–6686.
- [8] Mohammad Oves, Mohd Arshad, Mohd S. Khan, Abraham S. Ahmed, Ameer Azam, Iqbal M.I. Ismail, *Journal of Saudi Chemical Society.*, **2015**, 19, 581–588.
- [9] H. S. Al-Salman and M. J. Abdullah., *Mater. Sci. Eng. B.*, **2013**, 178, 1048–56.
- [10] M. Sheik Muhideen Badhusha and C. Joel, *Der Pharmacia Lettre.*, **2016**, 8, (11) 218-223.
- [11] S. Som and S.K. Sharma, *J. Phys. D: Appl. Phys.*, **2012**, 45, 415102.

[12] A. Mesaros, D. Cristina, Ghitulica, M. Popa, R. Mereu, A. Popa, T. Petrisor, S. Vasile, *Ceramic International.*, **2014**, 40, 2835–2846.

[13] S. Fabbiyola, L. John Kennedy, Udaya Aruldoss, M. Bououdina, A.A. Dakhel, J. JudithVijaya, *Powder Technology.*, **2015**, 286, 757–765.



Scholars Research Library

Der Pharmacia Lettre, 2016, 8 (11):218-223
(<http://scholarsresearchlibrary.com/archive.html>)



Green synthesis of ZnO Nanoparticles using *Phyllanthus embilica* Stem extract and their Antibacterial activity

C. Joel¹ and M. Sheik Muhideen Badhusha^{2*}

¹P.G. Department of Chemistry, St. John's College, Tirunelveli-627002, Tamilnadu, India

²Department of Chemistry, Sadakathullah Appa College, Tirunelveli, Tamilnadu, India

ABSTRACT

In this paper, a green synthesis of ZnO nanoparticles using *Phyllanthus embilica* stem extract as a reducing/capping agent. The prepared ZnO nanoparticles were characterized using fourier transform infrared spectroscopy (FTIR), UV-visible diffuse reflectance spectroscopy (UV-vis-DRS), X-Ray diffraction (XRD) and Scanning Electron Microscopy (SEM). The synthesized ZnO nanoparticles are wurtzite hexagonal structure with an average average crystallite size of ZnO prepared using *Phyllanthus embilica* stem extract was smaller (25.96 nm) when compared to the same ZnO prepared using a chemical method (36.73 nm). FT-IR spectra revealed the functional groups and the presence of protein as the stabilizing agent for surrounding the ZnO nanoparticles. The antibacterial activity of the ZnO was tested against gram negative bacteria *Salmonella typhi* and *Klebsiella phnemonea* by disc diffusion method. ZnO nanoparticles were subjected to antimicrobial studies and significant results were obtained.

Keywords: Metal Oxide, Nanomaterial, XRD, Antibacterial activity

INTRODUCTION

ZnO is abundant in nature and environmentally friendly. These characteristics make this material attractive for many applications [1, 2]. The bacteriostatic and fungistatic behaviour of ZnO is well studied and utilized in personal care products. Zinc oxide is a material with many important and diverse applications. Approximately, 45% of the world year production of ZnO is used in the rubber industry to control the vulcanization process and as additive [3]. In the methanol synthetic process ZnO is part of the Cu, ZnO, Al₂O₃ catalyst [4]. In the pharmaceutical industry ZnO is applied in ointments because of its antiseptic properties [4]. The optical properties make ZnO also suitable for many applications, like as a pigment in paints, as a UV filter in products for sun protection and for the production of LEDs and TFTs [5]. In this wide range of applications ZnO is used often in the form of particles and the size of the particles plays an important role.

A number of synthetic routes have been employed to synthesize ZnO nanoparticles such as sol-gel processing, homogeneous precipitation [6], mechanical milling [7], organometallic synthesis [8], microwave method [9], spray pyrolysis [10], thermal evaporation [11] and mechano-chemical synthesis [12]. These methods used in organic solvents and toxic reducing agent majority of which are highly reactive and are unsafe to the environment, to avoid such implications and for sustainable synthesis of ZnO nanoparticles by biological approaches. Biosynthesis of nanoparticles is a bottom up approach where in the main reaction occurring is reduction/oxidation. Among the various biosynthetic approaches, the use of plant extracts has advantages such as easy availability, safe to metabolites. The plant extract has been used as a reducing and capping agent for the synthesis of nanoparticles which could be advantageous over chemical methods. Microbial contamination is a serious issue in healthcare. Hence, the developments of antimicrobial agents have attracted increasing attention in recent times [13]. The developments of nanoparticles with antimicrobial properties are of considerable interest now. ZnO is an antimicrobial agent and the particles are effective to inhibit both gram positive and gram negative bacteria [14, 15].

This study, therefore, is aimed to evaluate the toxicity of biological and chemically synthesized ZnO nanoparticles along with bulk formulations against plant and human pathogens under laboratory conditions.

MATERIALS AND METHODS

2.1 Preparation of aqueous *Phyllanthus embilica* stem extract:

The collected Fresh stem of *Phyllanthus embilica* was washed thrice with tap water and twice with distilled water to remove the adhering salts and other associated contaminants and they were cut into small pieces. 10 g of the stem was taken and boiled with 100 ml of double distilled water at 100 °C for half an hour. During the procedure of boiling, a light brown coloured solution was formed and which was cool at room temperature. After that, the boiled extract was filtered through Whatman No.1 and was stored in the refrigerator at 4 °C for further studies.

2.2 Synthesis of ZnO nanoparticles by chemical precipitation method:

ZnO nanoparticles were prepared by simple precipitation method. Zinc acetate used as the precipitator 0.1 M Zinc acetate and 0.52 M of potassium hydroxide were dissolved separately in 50 ml distilled water in two glass beakers with magnetic stirring, Potassium hydroxide was added to Zinc acetate solution dropwise with constant stirring which led to the rapid formation of white precipitation, it was stirred for 2 h to form a homogeneous precipitate. After filtering, the precipitate was washed with distilled water and dried at 80 °C for 5 h. The obtained nanoparticle was calcinated at 500 °C for 1 h.

1.3 Synthesis of ZnO nanoparticles by green method:

For the synthesis of ZnO nanoparticles, 50 mL of extract was taken and boiled at 60°C. Then, 5.5g of zinc acetate was added to the solution. This mixture was then boiled and stirred by using magnetic stirrer until it becomes brown coloured paste. Then it transferred to a ceramic crucible cup and calcinated at 500 °C for 3h. Finally, obtained brown coloured powder. The material was powdered using a mortar and pestle so, that got a fine powder.

2.4 Characterization of ZnO nanoparticles

The optical properties were investigated using a UV-Vis-DRS were recorded in air at room temperature in the wave length range of 200-800 nm using Shimadzu UV - 2450 spectrophotometer. Surface structure was characterized by a Fourier-transform infra red (FT-IR) spectrophotometer (JASCO FT-IR 460 plus). The crystalline structure of the nanoparticles was studied by an X-ray diffractometer (XRD; XPERT PRO X-RAY) with Cu K α radiation at 25 °C and the structural assignments were made with reference to the JCPDS powder diffraction files. The surface morphology was examined using scanning electron microscopy (SEM) (JSM 6701F - 6701) in both secondary and backscattered electron modes and the elemental analysis was also detected.

2.5 Measurement of antimicrobial activity

ZnO nanoparticles in sterilized distilled water were tested for their antimicrobial activity by the agar diffusion method. Two microbial strains, *Salomonella* and *Klebsiella* were used for this analysis. The samples ZnO(chemical) and ZnO(Green) are dissolved in dimethyl sulfoxide (DMSO) and their concentrations are fixed at 200 mg/mL (minimum inhibitory concentration) and Ketoconazole was used as a reference drug. A lawn of test organism was made on the agar plate using a sterile cotton swab and then the antimicrobial discs (Whatman No.1. filter disc with samples at 200 mg/mL) were placed on the agar plate. All the plates were incubated at 37 °C for 24 h. The zone of inhibition was measured and expressed as millimetre in diameter [16].

RESULTS AND DISCUSSION

3.1 UV –Visible spectroscopy

Optical properties of ZnO nanoparticle become important as the size of particle is reduced to nanoscale. Fig(1) shows the UV-visible absorption spectra of ZnO nanoparticle Synthesis by chemical method and green method. The absorption coefficient (α) where calculated an plotted for direct transition $(\alpha h\nu)^{1/2}$ Verses $h\nu$ of the sample the value of the band energy (E_g) of ZnO NPs synthesized by chemical method was an increase in band gap of ZnO NPs synthesized by green method. The band gap energy of samples is determined by the formula $\alpha h\nu = E_d(h\nu - E_g)^2$ where α is absorption coefficient, $h\nu$ is the energy of photon, E_g is the direct band gap and E_d is the constant. By plot of $(\alpha h\nu)^2$ vs $h\nu$ and extra plotting the linear region of the curve to absorption equal to zero as shown in the Fig(2a) and Fig(2b) gives the value of direct band gap (E_g). The unique exciton absorption and bang gap energy of ZnO (chemical) and green ZnO are shown in Table 1

Fig.1 UV-vis-DRS of ZnO (chemical) and ZnO (green)

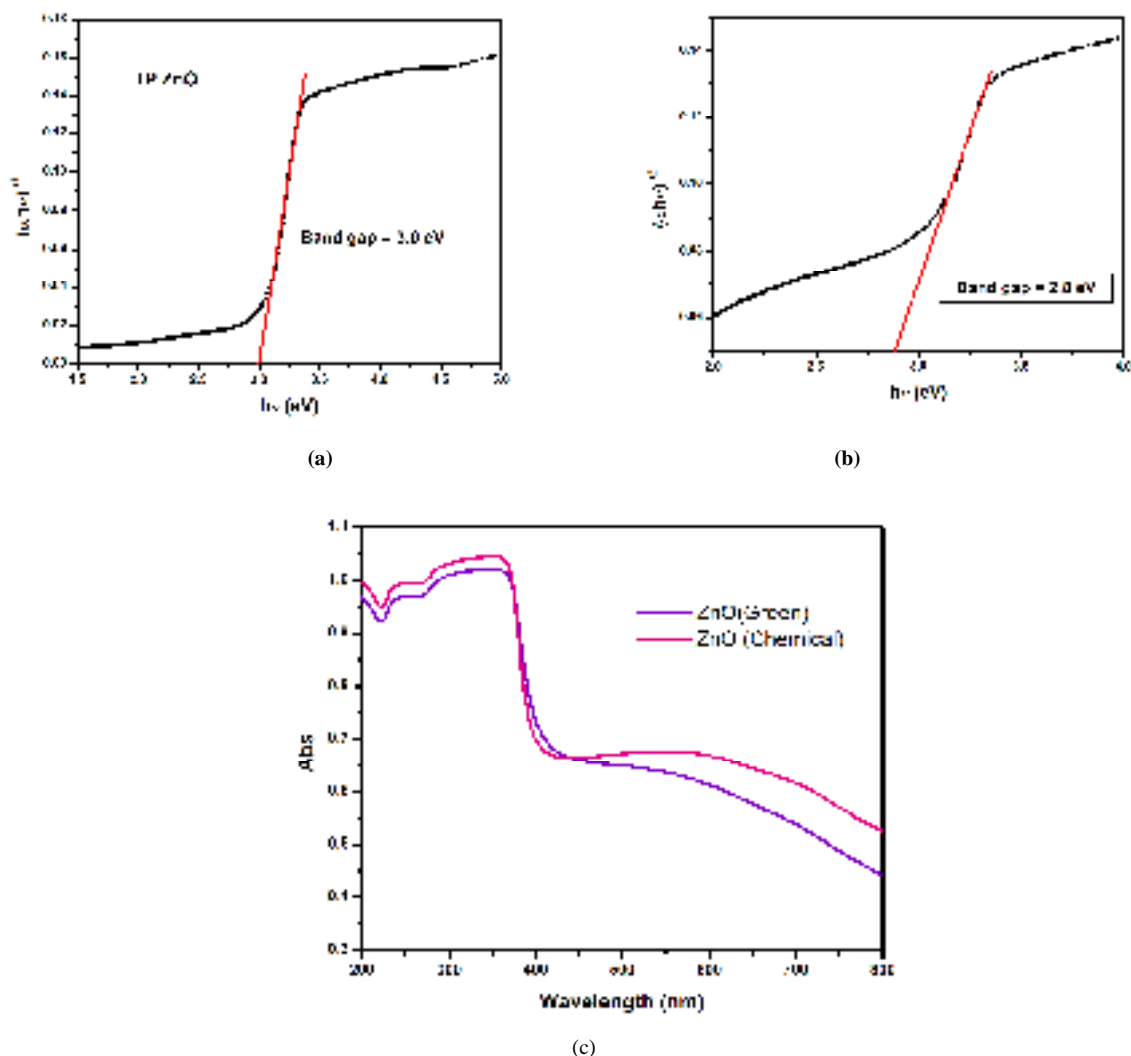


Fig.2 Tauc plots of (a) ZnO (chemical) (b) ZnO (green)

Table 1: UV –Visible absorption intensity and band gap energies ZnO nanoparticles synthesized by chemical and green method

SAMPLES	ABSORPTION INTENSITY (λ)	BAND GAP(eV)
ZnO (Chemical)	413nm	3.0 eV
ZnO (Green)	443nm	2.8 eV

3.2 Powder XRD studies

The end product in the chemical synthesized ZnO nanoparticles was pale white powder where in green synthesized ZnO is brown powder. XRD is used to investigate the changes of phase structure and crystallite size of the synthesized nanoparticles before and after addition of plant extract. Fig. 3 Shows the XRD pattern of chemical ZnO and green ZnO nanoparticles. From the diffractogram of XRD are very well matched with the hexagonal wurtzite structure by comparison with the data from JCPDS card No. 89-1397.

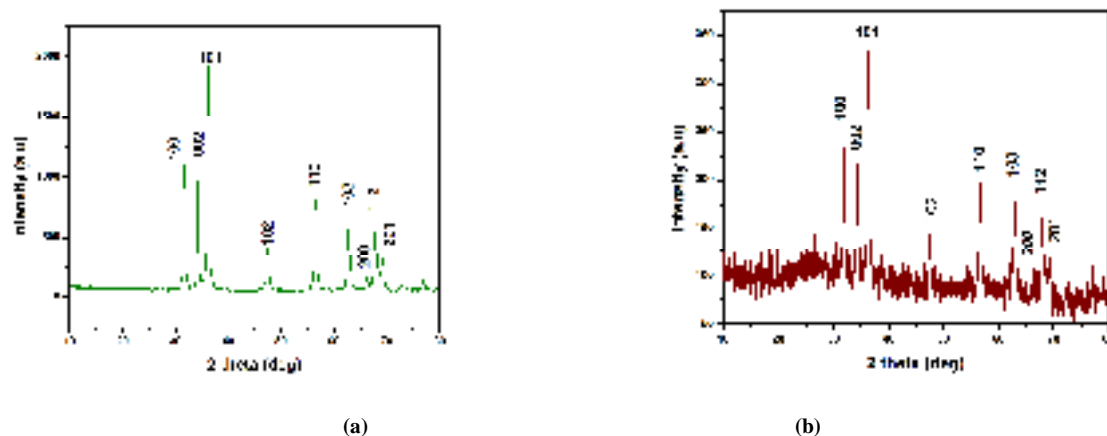


Fig.3 XRD patterns of a) ZnO (chemical) b) ZnO (green)

These peaks are broad, suggesting that the crystallites have sizes in the nanometer range and the diameter D was calculated using Debye-Scherrer formula [17] $D = K\lambda/(\beta\cos\theta)$, where K is the Scherrer constant, λ the X-ray wavelength, β the peak width of half maximum, and θ is the Bragg diffraction angle. The broad diffraction peaks of the sample after adding plant extract shown in Fig.3b confirmed that the crystal structure of ZnO nanoparticles was not altered during the plant extract. The XRD peaks give the diameter of about 25 nm for green synthesized ZnO and about 36 nm for chemical synthesized ZnO nanoparticles.

3.3 FT-IR spectral studies

The FT-IR spectra showed the presence of bonds due to O-H stretching around 3423 cm^{-1} . Peak at 1405 cm^{-1} may be assigned to symmetric stretching of the carbonyl side groups in the amino acid residues of the protein molecules [18]. The band at 1022 cm^{-1} corresponding to C-N stretching vibration of amine [19]. The peak at around 1340 cm^{-1} present in green ZnO signified amide III band of the random coil of protein [20].

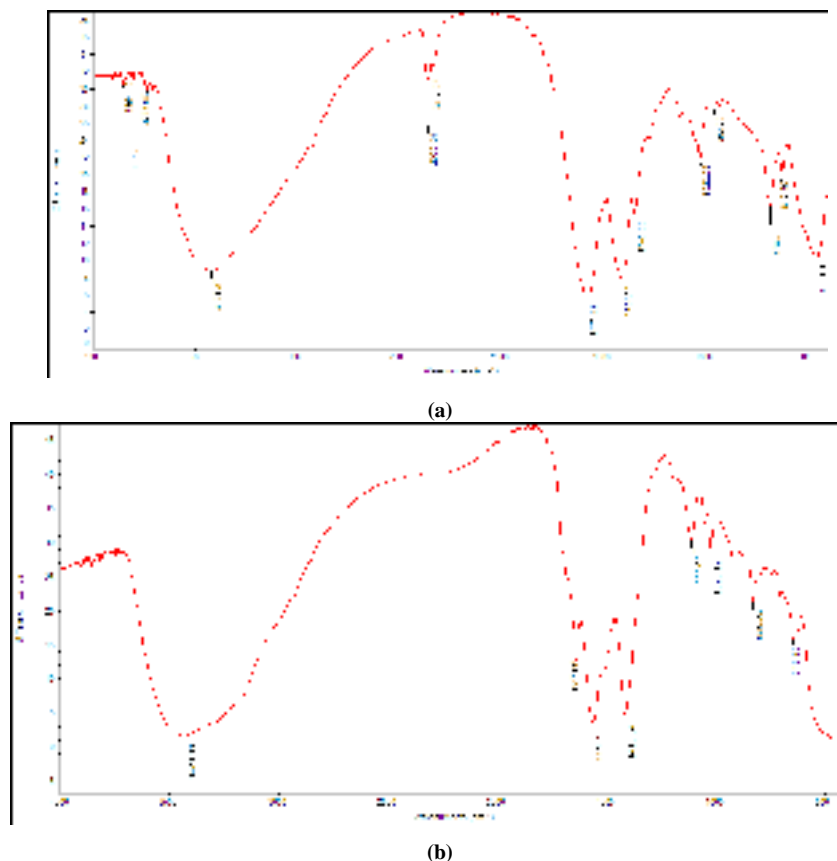


Fig.4 FT-IR spectrum of a) ZnO (chemical) b) ZnO (green)

3.4 Morphological studies:

The SEM images of ZnO (chemical) and ZnO (green) are shown in Fig. 5a and 5b which shows that the chemically synthesized ZnO nanoparticles are spherical shaped with particle size of 25 - 35 nm which is in line with the results from XRD while the Green synthesized ZnO nanoparticles were obtained as nanospheres with particle size of 15 -25 nm which proves the role of *Phyllanthus embilica* extract to change in the size and morphology of ZnO nanoparticles.

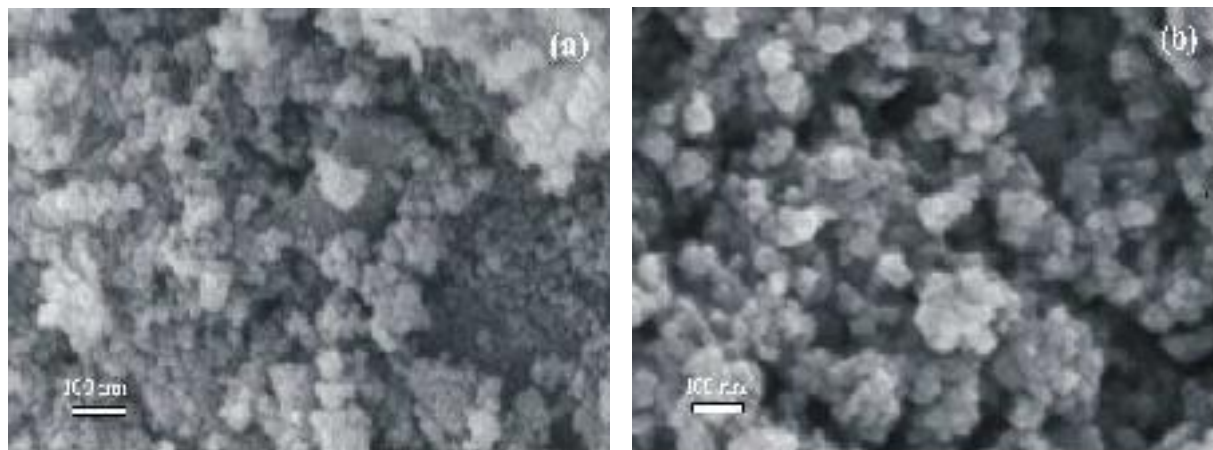


Fig. 5 SEM images of a) ZnO (chemical) b) ZnO (green)

3.5 Antibacterial activity

The antimicrobial activity of the ZnO nanoparticles was tested against gram negative bacteria *Salmonella typhi* and *Klebsiella phnemonea*. The results for the antimicrobial activity of ZnO (chemical) and green ZnO are shown in Table 2 and it is observed that green ZnO showed excellent anti-bacterial activity against *Salmonella typhi* and *Klebsiella phenomena*. The remarkable antimicrobial activities of green ZnO nanoparticles are due to the generation of surface oxygen species which leads to the killing of the pathogens [20].

Table 2: Antimicrobial activity of ZnO nanoparticles synthesized by chemical and green methods

Sample	<i>Salmonella typhi</i>	<i>Klebsiella phnemonea</i>
ZnO(Chemical)	10	11
ZnO(Green)	12	12
Control	R	R
Standard	06	R

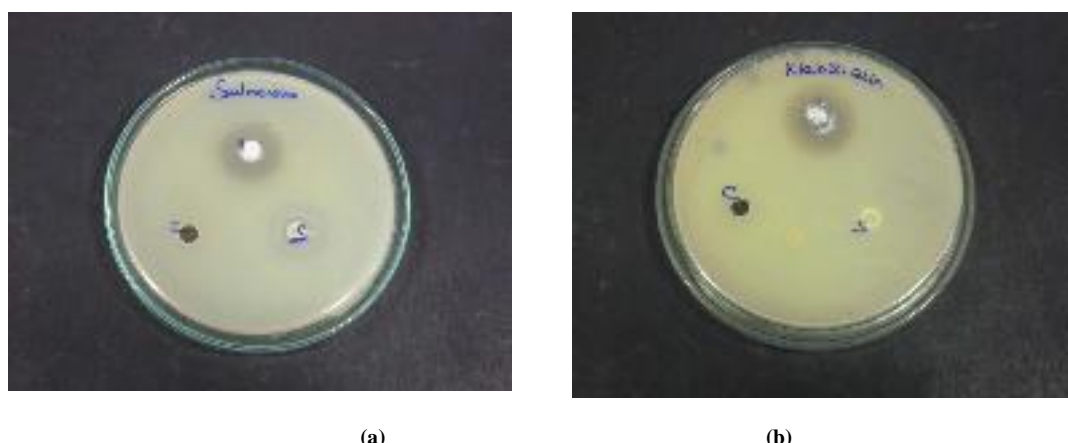


Fig. 6 The zone of inhibition of ZnO (chemical) against *Salmonella typhi* and *Klebsiella pneumonia*

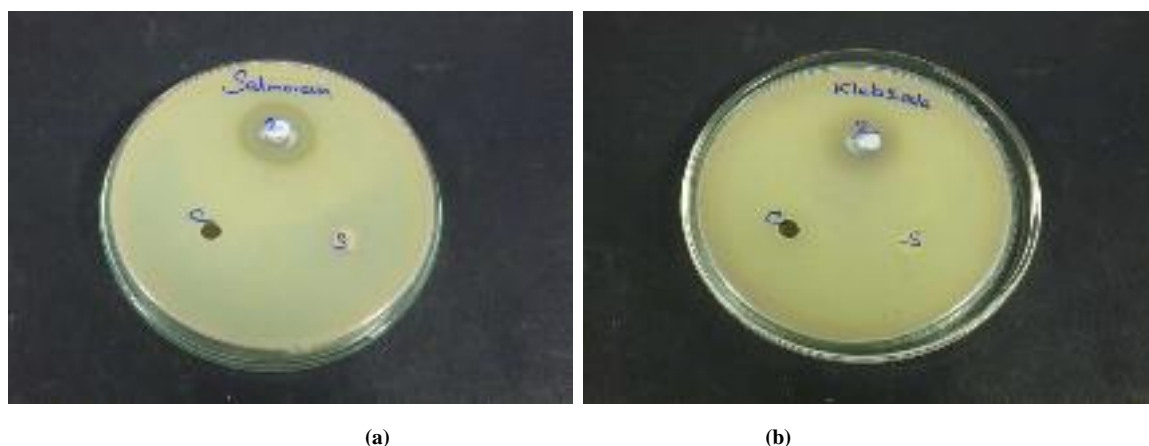


Fig. 7 The zone of inhibition of ZnO (green) against *Salmonella typhi* and *Klebsiella pneumonia*

CONCLUSION

ZnO nanoparticles are successfully synthesized via green method using *Phyllanthus embilica* plant extract. The structure, morphology and size of the prepared ZnO nanoparticles were characterized by XRD, FT-IR and SEM analysis. UV-vis DRS studies confirmed the indirect band gap 2.8 eV. The average grain size lies between 25 to 35nm were found from XRD. The FT-IR spectra revealed the functional groups of stretching bands for ZnO Nps were found around 800 – 400 cm^{-1} . The synthesized ZnO Nps was studied for antibacterial activities against diseases pathogenic bacteria like *Salmonella typhi* and *Klebsiella pneumonia*. Finally, the present study is so helpful and useful to the human and animals. In addition, the green synthesized ZnO Nps are inexpensive, stable and eco-friendly without side effect of human being.

Acknowledgement

The author (Dr. M. Sheik Muhideen Badhusha) gratefully acknowledges the financial support (MRP-5363/14(SERO/UGC)) from the University Grant Commission (UGC), Delhi, India.

REFERENCES

- [1] J.C. Pivin, G. Socol, I. Mihailescu, P. Berthet, F. Singh, M.K. Patel, *Thin Solid Films.*, **2008**, 517, 916.
- [2] K.Sato and H. Katayama-Yoshida, *Jpn. J. Appl. Phys.*, **2000**, 39, 555.
- [3] H.W. Engels, H.J. Weidenhaupt, M. Abele, M. Pieroth and W. Hofmann, in: *Ullmann's Encyclopedia of Industrial Chemistry*, sixth ed., **2001**.
- [4] H. Heine, H.G. Vo lz, J. Kischkewitz, P. Woditsch, A. Westhaus, W.D. Griebler, M. de Liederkerke, in: *Ullmann's Encyclopedia of Industrial Chemistry*, sixth ed., **2001**.
- [5] C.H. Yan, J. Zhang, L.D. Sun, in: H.S. Nalwa (Ed.), *Encyclopedia of Nanoscience and Nanotechnology*, **2004**, 10, 767.
- [6] J.H.Kim, W.C. Choi, H.Y. Kim, Y. Kang and Y.K. Park, *Powder Technol.*, **2005**, 153, 16
- [7] L.C. Damonte, L.A.Memdoza Zelis, B. Mari Soucase, M.A. Hernandez Fenollosa, *Powder Technol.*, **2004**, 148, 15.
- [8] M.L. Kahn and M. Monge, *Adv. Funct. Mater.*, **2005**, 3, 458.
- [9] S. Daniel Abraham, S. Theodore David, R. Biju Bennie, C. Joel, D. Sanjay Kumar, *J. Mol. Struct.*, **2016**, 1113, 174.
- [10] X.Y. Zhao, B.C. Zheng, C.Z. Li, H.C. Gu, *Powder Technol.*, **1998**, 100, 20.
- [11] T. Tani, L. Madler, S.E. Pratsinis, *J. Nanopart. Res.*, **2002**, 4, 337.
- [12] Z.R. Dai, Z.W. Pan, Z.L. Wang, *Adv. Funct. Mater.*, **2003**, 13, 9.
- [13] K.H. Tam, A.B. Djuricic, C.M.N. Chan, Y.Y. Xi, C.W. Tse, Y.H. Leung, W.K. Chan, F.C.C. Leung, D.W.T. Au, *Thin Solid Films*, **2008**, 516, 6167.
- [14] C. Karunakaran, P. Gomathisankar, G. Manikandan, *Material Chemistry and Physics*, **2010**, 123, 585.
- [15] Zarrindokht Emami-Karvani, Pegah Chehrazi, *African Journal of Microbiology Research*, **2011**, 5, 1368.
- [16] Venubabu Thati, Aashis.S.Roy, M.V.N.Ambika Prasad, C.T. Shivannavar, S.M.Gaddad., *J Biosci Tech*, **2010**, 1, 64.
- [17] B.D. Cullity, *Acta Crystallographica section A*, **1979**, 35, 255.
- [18] S. K Das, A. R. Das, A. K. Guha, *Langmuir*, **2009**, 25, 8192.
- [19] N. Islam Bhuiyan, J.Begum, M. Sultana, *J. Bangladesh. Pharmacol. Soc.*, **2009**, 4, 66.
- [20] S. Cai, B. R. Sing, *Biochemistry*, **2004**, 43, 2541.

See discussions, stats, and author profiles for this publication at: <https://www.researchgate.net/publication/316887286>

A study of physico-chemical analysis of ground water in and around SIPCOT, Tuticorin, Tamil Nadu, India

Article in *International Journal of Earth Sciences and Engineering* · January 2016

CITATION

1

READS

119

3 authors:



Thillai Arasu

Kalasalingam University

42 PUBLICATIONS 158 CITATIONS

SEE PROFILE



Arumugam Murugan

North Eastern Regional Institute of Science and Technology

6 PUBLICATIONS 19 CITATIONS

SEE PROFILE



Sheik Muhideen Badhusha

Sadakathullah Appa College

4 PUBLICATIONS 31 CITATIONS

SEE PROFILE

Some of the authors of this publication are also working on these related projects:



A pyrene based Schiff base probe for selective fluorescence turn-on detection of Hg²⁺ ions with live cell application [View project](#)



Green synthesis of metal oxide coreshell nanoparticles for biomedical applications [View project](#)



A Study of Physico-Chemical Analysis of Ground Water in and around SIPCOT, Tuticorin, Tamil Nadu, India

P THILLAI ARASU¹, A MURUGAN² AND M S M BADUSHA³

¹Department of Chemistry, Wollega University, Nekemte, ETHIOPIA

¹Department of Chemistry, North Eastern Regional Institute of Science and Technology, Nirjuli, Papum Pare (Dist.), Itanagar 791 109, Arunachal Pradesh, INDIA

³Department of Chemistry, Sadakathullah Appa college, Tirunelveli 627 011, Tamil Nadu, INDIA

Email: drpthillaiarasu@gmail.com, nspmurugan@gmail.com

Abstract: Physico-Chemical study was carried out in and around State Industries Promotion Corporation of Tamil Nadu Ltd (SIPCOT) area, Tuticorin, Tamilnadu, with an attempt to determine the characteristics of ground water status and public health in this region, which includes a network of some major industries. Twelve ground water sample were collected from different bore wells and open wells in the study area and were analyzed for pH, total dissolved solid (TDS), total hardness (TH), Nitrogen dioxide (NO₂), Sulphate (SO₄²⁻), Chloride (Cl⁻), Fluoride (F⁻), and Iron (Fe). The analysis show that all the twelve samples collected from the places located in and around the industrial belt of SIPCOT has been grossly polluted. The present study clearly highlight that the Physico-chemical parameters like pH, TDS, TH, NO₂, SO₄²⁻, Cl⁻, F⁻, and Fe of majority of the samples are exceeds BIS permissible limits due to industrial activities. There is also a possible for more metals to seep into the soil to reach the ground water and due to higher withdrawal of groundwater leading to intrusion of seawater in and around SIPCOT area Tuticorin. Hence, it is indention to prevent ground water contamination at the earliest in this area and save the human health.

Keywords: SIPCOT-Tuticorin, Ground Water, Water quality parameter

1. Introduction

Water is the most essential and the prime commodity in our life. Water covers about 75% of earth's surface, of the total volume of water available, 97% is in vast oceans which is of no use to our daily needs, 2% is in the forms of icebergs and less than 1% is available as fresh water (Ponnusamy et al., 2014 & 2013). Water is subjected to pollution easily due to the excessive use of fertilizers, pesticides, discharge effluents from industries and runoff water from agricultural fields. Ground water is an important source of fresh water supply globally. It is readily available than surface water.

It is a major source of drinking water for urban and rural areas. The rapid growth of urban areas has adversely affected the ground water quality due to over exploitation of resources and improper waste disposal practices (Harilal et al., 2004).

Due to the constant addition of industrial, agricultural and domestic water the ground water resource are degrading and are contaminated greatly in many parts of India. At present, effluents are being discharged into sewer but surrounding land receives them due to over flow of sewer system (Sastry et al., 2003).

Polluted water can act as a key vehicle in the direct transmission of various diseases (Jain et al., 2003). The present study is an attempt to examine the ground water quality in the SIPCOT, Tuticorin that includes a

network of some major industries (Thillai Arasu et al., 2007).

2. Material and Method

The study was carried out in the SIPCOT industrial complex, Tuticorin. The Latitude and Longitude of SIPCOT Tuticorin is 8.8075 ° N and 78.0829 ° E respectively. It is 8 km away from Tuticorin town. This industrial complex mainly hosts the chemical industries and marine food processing industries. Twelve ground water samples are collected from bore wells and open wells near the study area within a distance of 1 to 2 km (Table-1).

The bore wells were among the range of 40 to 60 ft. The water samples collected during February 2008.

Table 1: Sample number and Sample Sites

Sl.No.	Sample No.	Site / Location of the Sampling
1	S1	Kilburn Chemicals
2	S2	Sterlite Industries
3	S3	KTV Oil company
4	S4	Amulya Sea foods
5	S5	Tuticorin Alkali Chemical(TAC)
6	S6	Heavy Water Plant (HWP)
7	S7	SPIC Industries
8	S8	Thermal Power Station
9	S9	Old Bus Stand
10	S10	Rahmathullapuram Mosque
11	S11	Kamaraj College

12 S12 VOC College

The water samples were collected in polyethylene bottles which were well sealed with stoppers. The samples were analyzed for various water quality

parameters as per standard procedures (APHA, 1998) and the values were compared with standard values recommended by Bureau of Indian Standards (BIS) (BIS, 2009) (Table-2) for drinking purpose.

Table 2: Physico-Chemical Parameters of groundwater in and round SIPCOT, Tuticorin

Sample No.	p ^H	TDS	TH	Acidity	Alkalinity	Nitrate	Sulphate	Chloride	Fluoride	Iron
		mg/lit	mg/lit	mg/lit	mg/lit	mg/lit	mg/lit	mg/lit	mg/lit	mg/lit
S1	8.61	2170	660	30	41	9	700	1230	0.6	0.16
S2	8.91	1100	560	40	46	11	488	270	1.4	0.16
S3	7.83	1950	1600	46	20	10	53	1300	0.2	0.08
S4	7.93	1720	1200	30	20	12	60	1020	0	0.08
S5	9.01	698	500	43	55	15	188	150	1.2	0.16
S6	7.78	459	200	40	36	2	145	104	1	0.24
S7	8.05	585	324	34	38	24	275	108	0.8	0
S8	8.8	228	112	10	24	17	500	364	1.4	0.24
S9	7.13	228	68	0	5	4	18	26	0.2	0.24
S10	8.13	517	256	32	36	1	11	28	0.2	0.08
S11	8.09	345	128	28	35	9	60	122	0.2	0
S12	9.93	3720	2600	39	39	1	30	36	2.6	0.56
Mean	8.35	1143.3	684	31	32.92	9.58	210.67	396.5	0.82	0.17

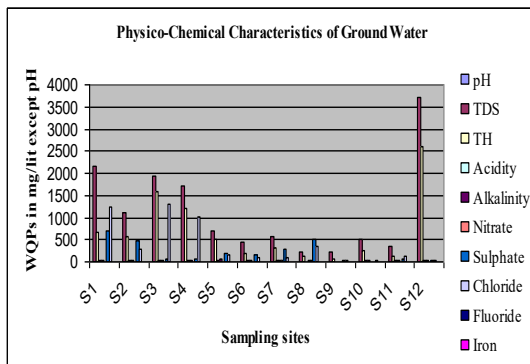


Fig 1: Physico-Chemical Parameters of groundwater in and round SIPCOT, Tuticorin

2.1. Methods and Instrument used for analysis

pH of the water sample were measured with digital pH meter of Elico make model L1-20 using a coupled glass gel-filled electrode and a calomel reference electrode of pH range 0-14.

Total dissolved solids were determined from the residue left after evaporation and drying the water sample. The presence of total hardness and total alkalinity in water sample were determined by volumetrically. The availability of nitrate and sulphate in water sample were estimated by UV-spectrophotometric method of the type UV-Visible - spectrophotometer-SL-159. The presence of Chloride in water sample was determined volumetrically by the method called the "Mohr Method". The fluoride of water samples was measured by adopting colorimetric

technique in a fluoride meter of Elico make mode CL 352. The presence of iron in water sample was determined volumetrically.

3. Result and Discussion

The graphical representation of Physico-Chemical Parameters of groundwater data in and round SIPCOT, Tuticorin shown in the Fig.1. The high level alkalinity indicates the presence of weak and strong bases, such as carbonates, bicarbonates and hydroxides in the water body. The pH reduces the germicidal potential of chlorine and indicates the formation of toxic trihalomethanes (Trived and Goel., 1984). pH ranges from 7.13 to 9.93. The mean value of pH is 8.35. The results show that all the water samples were within the BIS permissible limits except S1, S2, S5, S8 and S12. This value shows that pH of water sample was slightly alkaline. The pH does not have any direct adverse effect on health but it alters the taste of water and shows effect indirectly in the long run (Saravanakumar and Ranjith Kumar., 2011). TDS in the study area varied from 228 to 3720 mg/lit. The mean value is 1143.33 mg/lit. This results show that sample numbers S1 and S12 were not within BIS standards.

The reason for the high concentration of TDS in these areas is due to higher withdrawal of groundwater leading to intrusion of seawater (Nathanson., 2002) and pollution by domestic and industrial wastage.

The total hardness ranges from 68 to 2600 mg/lit. The mean value is 684 mg/lit. The results show that sample number S6, S8, S9, S10 and S11 of water

samples were within BIS permissible limits. The higher disease rates are mainly associated with higher concentration of total hardness present in this area ground water. Alkalinity is due to presence of carbonate and bicarbonate ions. The value ranges from 5 to 55mg/lit. The mean value of alkalinity is 32.92 mg/lit. All the samples are within The BIS permissible limits. So it does not cause any adverse effect on human health.

Nitrate concentration varies from 1 to 24 mg/lit in the ground water samples of the study area, but all of them fall within the permissible limit. The mean value of nitrate is 9.58 mg/lit. Nitrate itself is not toxic but poses a problem only when it is converted to nitrite in the human body by causing diseases like "blue baby syndrome, gastric cancer and some other health disorders (Majumdar and Gupta., 2000). Sulphate concentration of all samples was within the permissible limits except samples S1, S2 & S8. The mean value is 210.67 mg/lit. This higher in values of above samples may be due to the discharge of the industrial effluent and sewage in to the ground water. Excess sulphate content induces cathartic effect on human health (Rao and Mamtha., 2004).

The chloride ranges from 26 to 1300 mg/lit. The mean value of chloride is 396.5 mg/lit. Out of twelve water samples, chloride content of S1, S2, S3, S4 & S8 lie out of the BIS permissible limits. This ensures that the chloride ions are present mainly in the form of highly soluble salts like NaCl and KCl. Chloride in excess (>250 mg/lit) imparts a salty taste to water and people who are not adapted to high chlorides can be subjected to laxative effects (Parkash et al., 1989). All the sample stations are coastal area and the soils are sand soils. The possible reason for the high levels of chloride content in the sampling stations is mainly due to improper disposal of sewage and septic tank.

Fluoride used in the insecticides, disinfectants and preservatives is the potential source of fluoride present in the ground water. They are found in large quantities in super phosphate, brick making and aluminium extraction process. Use of phosphate fertilizers may also contribute to high fluoride content in the ground water. Fluoride is the most exclusive bone-seeking element owing to its affinity for the normal development of bones. The mean value of fluoride is 0.82 mg/lit. In general it should not exceed 1.5mg/lit in BIS standard except S12. When its concentration exceed standard limit it causes various types of fluorosis starting from dental to skeleton. The prolonged use of ground water of source S12 may cause for drinking purpose may create teeth fluorosis. Waste material dumped near the factories which is subjected to reaction with percolating rain water picks of a large number of trace metals and reaches the aquifer system and hence degrades the ground water quality (Raman and Sathiyarayanan., 2011). The mean value of iron is 0.17 mg/lit. The maximum BIS permissible limits of iron content in drinking water

are set as 0.3mg/lit (IS). Beyond this limit the iron content in water sample may cause discolouration of clothes. The iron content of all the water samples with an exception of sample numbers S12 lie within the limits.

4. Conclusion

The ground water show that all the twelve samples collected from the places located in and around the industrial belt of SIPCOT has been grossly polluted. The present study clearly highlight that the physico-chemical parameters like pH, TDS, TH, NO₂, SO₄²⁻, Cl⁻, F⁻ and Fe of majority of the samples are exceeds BIS permissible limits. Pollution occurred due to industrial activities and urbanization; anthropogenic activities increased human interventions in the ground water have been ascertained. The major challenge in this study was to distinguish saline water of different origins. Based on the results the hydro geochemical variance of the water samples appears to characterize first the water-rock interaction processes, responsible for the high loadings in Cl⁻, Na+K, TDS and TH (Ganapathi Subramanian et al, 2011). There is also a possible for more metals to seep into the soil to reach the ground water in and around SIPCOT area, Tuticorin. Hence, it is indention to prevent ground water contamination at the earliest in this area to save the human health.

References

- [1] Ponnusamy Thillaiarasu, Arumugam Murugan and Jeslin Kanaga Inba (2014) Atomic Absorption Spectrophotometric Studies on Heavy Metal Contamination in Groundwater in and around Tiruchendur, Tamilnadu, India. *Chemical Science Transactions*, 3(3), pp 812-818.
- [2] Ponnusamy Thillaiarasu and Arumugam Murugan (2013) Physico Chemical Study On the Sea water Intrusion in Tuticorin Coastal area, *International Journal of ChemTech Tesearch*, 5(4), pp1824-1828.
- [3] Harilal, C.C. and Sasikala, K (2004) Bacterial contamination of well water in and around Thiruvalla municipal area of Pathanamthitta District, *Indian Journal of Environmental Protection*, 24 (1), pp25-28.
- [4] Sastry, K.V., Vineeta Shukla and Sharda Abusaria (2003) Impact assessment of industrial pollution on groundwater, *Indian Journal of Environmental Protection*, 23(3), pp250-255.
- [5] Jain, C.K., Bhatia, K.K.S., Kumar, C.P. and Purandara, B.K (2003) Groundwater Quality in Malaprapha Sub-basin, Karnataka, *Indian Journal of Environmental Production*, 23(3), pp321-329.
- [6] Thillai Arasu, P., Hema S. and Neelakantan, M.A (2007) Physico-chemical analysis of Tamirabarani river water in South India, *Indian Journal of Science and Technology*, 1(2), pp1-6.

- [7] APHA (American Public Health Association) (1998) Standard methods for the examinations of Water and Waste Water, 20th edition, Washington DC.
- [8] BIS (Bureau of Indian Standards), (2003). Indian standard drinking water specifications; IS 10500: 1991, Edition 2.2 (2003 - 09), Bureau of Indian Standards, New Delhi.
- [9] Trivedy, R.K. and Goel, P.K (1984) Chemical and biological methods for water pollution studies, Environ Publications, Karad, Maharashtra, India.
- [10] Saravanakumar, K. and Ranjith Kumar, R (2011) Analysis of water quality parameters of groundwater near Ambattur industrial area, Tamil Nadu, India, *Indian Journal of Science and Technology*, 4(5)., pp660-662.
- [11] Jerry, A. Nathanson (2002) Basic Environmental Technology, Fourth Edition, Prentice- Hall of India Private Limited. New Delhi, pp136-138.
- [12] Majumdar, D. and Gupta, N (2000) Nitrate pollution of groundwater and associated human health disorders, *Indian Journal of Environmental Health*, 42(1)., pp28-39.
- [13] Rao, S.M. and Mamtha, P (2004) Water quality in sustainable water management, *Current Science*, 87., pp942-947.
- [14] Parkash, Ravi, S. and Krishna Rao, G (1989) The chemistry of groundwater in Paravada area with regard to their suitability for domestic and irrigational purposes, *Indian Journal of Geochemistry*, 4., pp39-54.
- [15] Raman, N. and Sathiyarayanan, D (2011) Quality assessment of groundwater in Pallavapuram Municipal solid waste dumpsite area nearer to Pallavaram in Chennai, Tamil Nadu, *Rasayam Journal of Chemistry*, 4(2)., pp481-487.
- [16] Ganapathi Subramanian, R, Subramanian, V and Sukumar. S (2011) Pre-and Post-Monsoon variation in Physico-chemical characteristics in Groundwater quality of parts of Tirunelveli District, Tamil Nadu, India, *International Journal of Geomatics and Geosciences*, 2(1)., pp300-310.

Biosynthesis of Silver Nanoparticles Using *Saccharomyces Cerevisiae* with Different pH and Study of Antimicrobial Activity against Bacterial Pathogens

M. SHEIK MUHIDEEN BADHUSHA^{1*} and M.M. ABDUL KADER MOHIDEEN²,

¹Department of Chemistry, Sadakathullah Appa College, Tirunelveli, Tamil Nadu, India

²Department of Microbiology, Sadakathullah Appa College, Tirunelveli, Tamil Nadu, India
drbadhunano@gmail.com

Received 24 May 2016 / Revised 30 June 2016 / Accepted 15 July 2016

Abstract: Extracellular biosynthesis of silver nanoparticles (Ag-NPs) using the *Saccharomyces cerevisiae* (Yeast) was carried out. The pH of the medium play a vital role in the synthesis of control shaped and sized nanoparticles. Morphological observation and characterization of biosynthesized silver nanoparticles were performed by UV-Visible spectroscopy, Scanning electron microscopy and Fourier transform infrared spectroscopy. The biosynthesized silver nanoparticles showed a maximum absorption in the visible region *Saccharomyces cerevisiae* strains showed a maximum absorption at 420-460 nm respectively and the size was ranged from 60-110 nm and 10-40 nm respectively. The antibacterial activities of silver nanoparticles (Ag-NPs) were studied with *Staphylococcus aureus* (Gram-positive) and *Escherichia coli* (Gram-negative). The silver nanoparticles were synthesized at pH 6 that showed maximum antibacterial activity. This method is a promising eco-friendly alternative to chemical method.

Keywords: *Saccharomyces cerevisiae*, Biosynthesis, Extracellular synthesis, Nanoparticles, Antimicrobial activity

Introduction

One of the most important criteria of nanotechnology is that of the development of clean, nontoxic and environmentally acceptable “green chemistry” procedures, involving organisms ranging from bacteria to fungi and even plants^{1,2}. The interactions between microorganisms and metals have been well documented and the ability of microorganisms to extract and accumulate metals is already employed in biotechnological processes such as bioleaching and bioremediation.

It is known that a large number of organisms, both unicellular or multi cellular, are able to produce inorganic nanomaterials, either intracellularly or extracellularly. It seems that especially the yeast and fungi are very good candidates for the synthesis of silver nanoparticles because these types of biomasses are easily handled³.

Yeast being a member of the class Ascomycetes also called sac fungi in kingdom fungi, it has been taken into regular use as media supplement in different culture procedures and this organism itself has been a very good source of different enzymes and vitamins. Eco-friendly approach for nanomaterials synthesis should not use toxic chemicals in the synthesis protocol. In the present effort, the baker's yeast (*Saccharomyces cerevisiae*) has been taken in order to assess its potential as candidate fungal genera for the transformation of silver nanoparticles³.

In this study, the silver nanoparticles were synthesized by an extracellular synthesis process using *Saccharomyces cerevisiae* cell culture and then the effect of pH on the synthesis of silver nanoparticles was examined by changing the pH of the aqueous cell filtrate with 0.1 N sodium hydroxide and hydrochloric acid. The synthesized nanoparticles were characterized. The antibacterial activity of silver nanoparticles was examined against *E. coli* and *Staphylococcus aureus*

Experimental

Silver nitrate, nutrient agar, nutrient broth, luria bertani medium, sodium chloride, hydrochloric acid were obtained from Himedia Pvt.Ltd., India. Yeast (*Saccharomyces cerevisiae*) was isolated from graph juice. Pathogens *Staphylococcus aureus* and *Escherichia coli* were isolated from clinical samples.

Extracellular synthesis of silver nanoparticles

Saccharomyces cerevisiae was inoculated at 0.5% level in 2 L Erlenmeyer flasks containing 1L growth medium (2% tryptone, 1% yeast extract and 2% glucose, pH 5.6). The flasks were incubated at 30 °C on a rotary shaker set at 100 rpm. Upon attaining the mid-log phase (between 9 and 10 h, O.D.600=2), the cells were separated from the culture medium by centrifugation (5000 rpm) and the cell-free medium was used for the recovery of precipitated silver nanoparticles. 1 mM of silver nitrate was added to the cell-free medium for the synthesis. The silver nanoparticles were incubated further in dark for 24 h. The UV absorption spectrophotometer reading was taken at different time intervals to monitor the synthesis of silver nanoparticles extracellularly.

Effect of pH on the extracellular synthesis of silver nanoparticles

The influences of pH on the extracellular synthesis of silver nanoparticles were carried out by changing the pH of the cell-free medium. The different pH was taken (4 and 6) to examine the effect of pH on the synthesis of silver nanoparticles using *Saccharomyces cerevisiae*. The pH of the cell-free medium was changed using 0.1 N hydrochloric acid and 0.1 N sodium hydroxide. UV spectrophotometer was used to take the absorption at 24 h of incubation.

Characterization of biosynthesized silver nanoparticles

The UV absorbance spectra were taken at various time intervals at different wavelength. Scanning electron microscope used to identify the shape of the synthesized silver nanoparticles. The functional groups of biologically synthesized dried nanoparticles observed using Fourier Transform Infrared Spectrometer.

Antibacterial activity of silver nanoparticles

The antibacterial activity of biosynthesized silver nanoparticles was carried out against *Staphylococcus aureus* and *Escherichia coli*. Various concentrations (10 µL, 20 µL, 30 µL, 40 µL and 50 µL) of silver nanoparticles were synthesized with different pH (4 and 6). The well-diffusion method was used to determine the antibacterial activity of silver nanoparticles.

The well was formed in the medium using cork borer. The silver nanoparticles were pipette out into the wells, and then the plates were incubated at 37 °C for 24 h. After 24 h of incubation, the plates were observed for the zone of inhibition.

Results and Discussion

Extracellular synthesis of silver nanoparticles

The preliminary confirmation for the formation of silver nanoparticles was the visual observation of colour change of the aqueous solution of yeast culture. Before the addition of silver nitrate the culture was in yellow colour. After the addition of silver nitrate, the extracellular culture colour changed to white precipitate and at 24 h of reaction, the colour of the solution changed to brown (Figure 1). Synthesized silver nanocrystals using *Sacharomyces cerevisiae* they obtained the similar colour changes during the formation of silver nanoparticles⁴.

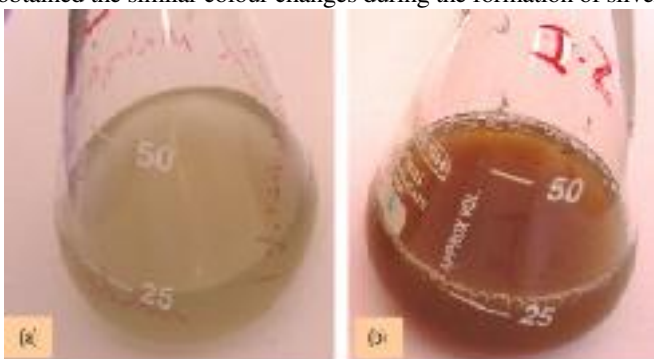


Figure 1. Culture filtrate with silver nitrate solution at the (a) beginning of the reaction and (b) after 24 h of reaction

Characterization of biosynthesized silver nanoparticles

UV Absorption spectrum

The UV absorption spectral studies were carried out to confirm the formation of silver nanoparticles using *Sacharomyces cerevisiae*. Figure 2 shows the peak found at 420 nm. The peak appears very broad with number of sub peaks and shoulders and it is proposed that such a broad peak indicates that there exists a wide range of nanoparticle sizes.

Figure 3 shows the effect pH on the synthesis of silver nanoparticles at pH 6. The maximum production of silver nanoparticles occurred. The absorption peak occurred at 420 nm and 460 nm for pH 6 and pH 4 respectively. The band at 420 nm indicated the spherical shape of nanoparticles, whereas at 480 nm the particles are different shapes⁵.

SEM

Silver nanoparticles were synthesized using pH 4. The synthesized particles were hexagonal in shape and the size of the nanoparticles was in the range of 60-110 nm. Figure 4a and Figure 4b shows the SEM images of the silver nanoparticles synthesized using pH 6. The particles were spherical and the obtained particles are 10-40 nm in size. The size of nanoparticles is high at acidic pH, because the nucleation process for the formation of silver nanocrystal at acidic pH is slow. The low amount of large size particles were formed. While at high pH, more nucleation process occurred because of the accessibility of –OH ions. Thus high amount of small size particles formed⁶.

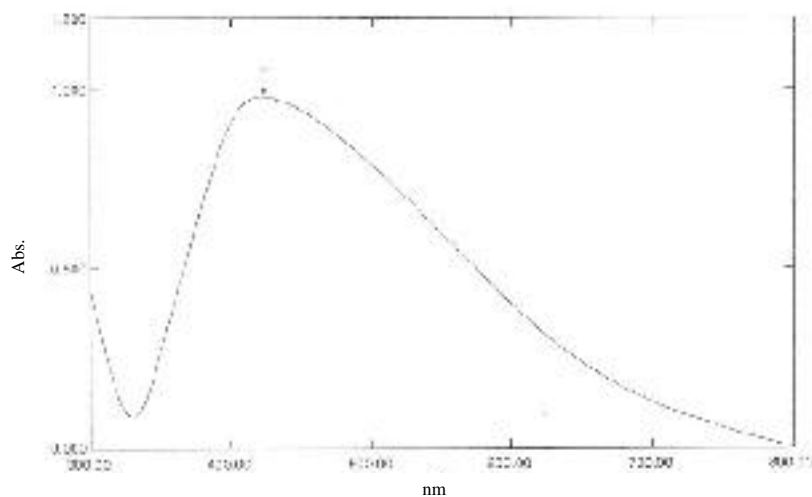


Figure 2. UV- Absorption spectrum, the peak found at 420 nm the peak appears very broad with number of sub peaks and shoulders and it is proposed that such a broad peak indicates that there exists a wide range of nanoparticle sizes

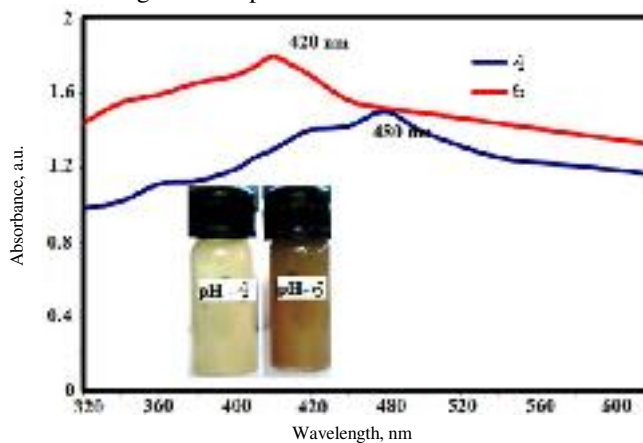


Figure 3. UV-Spectrophotometer absorption of the effect of pH on the synthesis of silver nanoparticles. Inset shows the colour variation at pH-4. The synthesis of silver nanoparticles is low and at pH-6 the production of silver nanoparticles is high

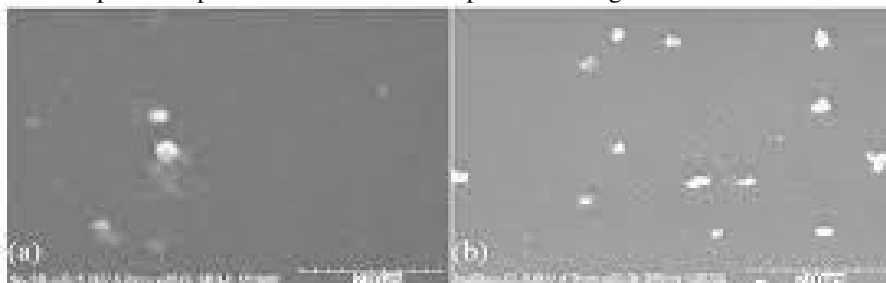


Figure 4. SEM image of the synthesized silver nanoparticles (a) pH 5, (b) pH 9

FTIR

The FTIR spectrums of silver nanoparticles were synthesized using *Sacharomyces cerevisiae* (Figure 5). The band at 3412 cm^{-1} and 2918 cm^{-1} represent the O-H, C-C stretching vibration⁷. The band at 1634 cm^{-1} represents the -NH stretching vibration of the amide group⁸. The bands at 1381 cm^{-1} and 1058 cm^{-1} represent the aromatic and aliphatic amines of C-N stretching vibrations of protein⁹. The FTIR results confirmed that protein might be responsible for the formation of silver nanoparticles^{10,11}.

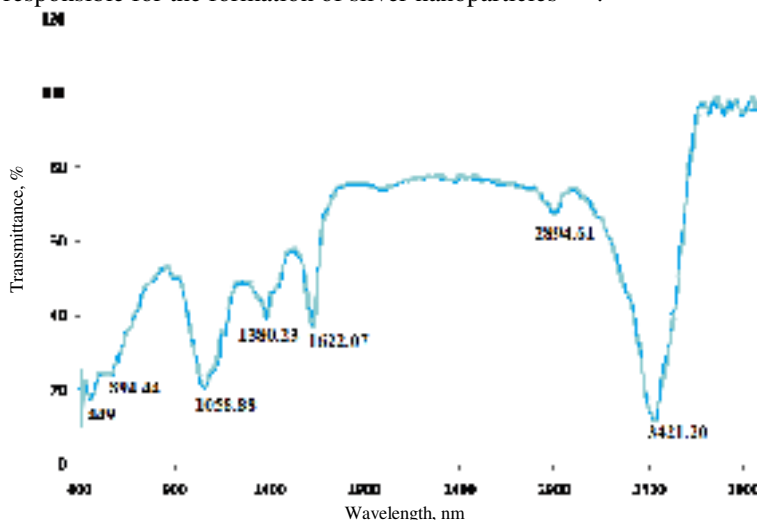


Figure 5. FTIR Spectrum of biosynthesized silver nanoparticles using *Saharomyces Cerevisiae*

Antibacterial activity

The well diffusion method was used to provide evidence for the antibacterial activity of biosynthesized silver nanoparticles against *E.coli* and *Staphylococcus aureus* Figure 6 and Figure 7 shows the antibacterial activity of silver nanoparticles synthesized using pH 4 and pH 6 against *E.coli* and *Staphylococcus aureus*. The antibacterial activity of silver nanoparticles indicated by the formation of the zone and the zone of inhibition measured as mm/diameter. The maximum zone of inhibition occurred at $50\ \mu\text{L}$ concentration of silver nanoparticles. The silver nanoparticles synthesized using pH 6 show higher antibacterial activity against *E.coli* and *Staphylococcus aureus*^{12,13}.



Figure 6. Antibacterial activity of biosynthesized silver nanoparticles synthesized using pH 4 against *E.coli* and *Staphylococcus aureus*

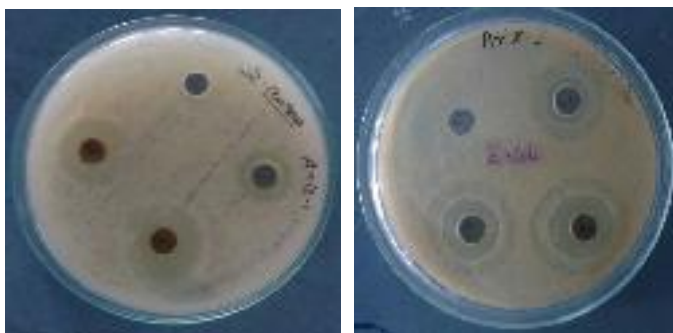


Figure 7. Antibacterial activity of biosynthesized silver nanoparticles synthesized using pH 6 against *E.coli* and *Staphylococcus aureus*

Conclusion

The silver nanoparticles were synthesized using *Saharomyces cerevisiae* by extracellular method. The different sized and shaped nanoparticles formed while changing the pH of the aqueous solution. The proteins which are present in the bacteria may be a possible reason for the synthesis of silver nanoparticles. The pH of the aqueous solution plays an important role in the antibacterial activity of silver nanoparticles. The smallest nanoparticles synthesized using pH 6 showed more antibacterial activity than large particles which are synthesized using original pH and pH 4.

References

1. Duran N, Marcato P L, Alves O L and De Souza G I, *J Nanobiotechnol.*, 2005, **3(1)**, 7.
2. Sastry M, Ahmad A, Khan M I and Kumar R, *Curr Sci.*, 2003, **85(2)**, 162-170.
3. Kowshik M, Ashtaputre S, Kharrazi S, Vogel W, Urban J, Kulkarni S K and Paknikar K M, *Nanotechnology*, 2003, **14(1)**, 95-100; DOI:10.1088/09574484/14/1/321
4. Ahmad A, Mukherjee P, Senapati S, Mandal D, Khan M I, Kumar R and Sastry M, *Colloids Surf B Biointerfaces*, 2003, **28(4)**, 313-318; DOI:10.1016/S0927-7765(02)00174-1
5. Melaiye A, Sun Z, Hindi K, Milsted A, Ely D, Reneker D H, Tessier C A and Youngs W J, *J Am Chem Soc.*, 2005, **127(7)**, 2285-2291; DOI:10.1021/ja040226s
6. Bhattacharya D and Rajinder G, *Crit Rev Biotechnol.*, 2005, **25(4)**, 199-204; DOI:10.1080/07388550500361994
7. Das J, Paul Das M and Velusamy P, *Spectrochim Acta Part A: Mol Biomol Spec.*, 2013, **104**, 265.
8. Kamat P V and Meisel D, *Curr Opin Collaid Interface Sci*, 2002, **7**, 282-287.
9. Islam Bhuyan N, Begum J and Sultana M, *J Bangladesh Pharmacol Soc.*, 2009, **4**, 150-153
10. Bhainsa K C and D'Souza S F, *Colloids Surf B: Biointerfaces*, 2006, **47(2)**, 160-164; DOI:10.1016/j.colsurfb.2005.11.026
11. Mandal D, Bolander M E, Mukhopadhyay, Sarkar G and Mukherjee P, *J Appl Microbiolbiotechnol.*, 2006, **69(5)**, 485-492; DOI:10.1007/s00253-005-0179-3
12. Gericke M and Pinches A, *Hydrometallurgy*, 2006, **83(1-4)**, 132-140; DOI:10.1016/j.hydromet.2006.03.019
13. Whitesides G M, *Nat Biotechnol.*, 2003, **21**, 1161-1165; DOI:10.1038/nbt872



Journal homepage: <http://www.journalijar.com>

INTERNATIONAL JOURNAL
OF ADVANCED RESEARCH

RESEARCH ARTICLE

STUDY OF QUALITY OF GROUND WATER FOUND IN KALLUR VILLAGE, TIRUNELVELI, TAMILNADU, INDIA.

S. L. Sathya Saibaba¹, H. Perumpadaiyan², M. Sheik Muhideen Badhusha³,
S. Kamalesu⁴, A. Anish Babu⁴ and P. Karthiga⁴.

1. Department of Chemistry, Thamirabharani Engineering College, Tirunelveli - 627358, Tamil Nadu, India.
2. Department of Chemistry, Sri K.G.S. Arts College, Srivaikundam, Tuticorin - 628619, Tamil Nadu, India.
3. Department of Chemistry Sadakathullah Appa College, Tirunelveli - 627011, Tamil Nadu, India.
4. Department of Chemistry, Manonmaniam Sundaranar University, Tirunelveli - 627012, Tamil Nadu, India.

Manuscript Info

Manuscript History:

Received: 17 January 2016
Final Accepted: 18 February 2016
Published Online: March 2016

Key words:

Ground water, physico-chemical parameters, Biological parameters, Kallur.

*Corresponding Author

M. Sheik Muhideen
Badhusha.

Copy Right, IJAR, 2016.. All rights reserved.

Abstract

The study was conducted to evaluate the ground water quality of Kallur, Tirunelveli district, India. Groundwater samples were collected from five locations S1, S2 S3, S4, S5 and these samples were analyzed for more than 15 water quality parameters. High coefficient of variance indicates variability of physico-chemical parameters in ground water. From correlation analysis it was observed that very strong correlations exist between total hardness of samples S2, S3, S4, S5 and TDS of S1 exceeds the permissible limit. Potassium concentration (26 mg/l), chloride concentration (610 mg/l), and ammonia concentration (0.8 mg/l) are very higher than standard values. Biological parameters such as COD and BOD also analysed.

Introduction:-

Water is the vital for the survival of any type of life. On a normal, a person expends around two liters of water each day¹. Groundwater resource is under threat from pollution either from human life style manifested by the low level of hygiene practiced in the developing nations². With increasing industrialization, urbanization and growth of population, India's environment has become fragile and has been causing concern³. Pollution of water is due to use of fertilizers in agriculture and man- made activities^{4,5}. Once the ground water contaminated, its quality cannot be restored by stopping the pollutants from the source, therefore it becomes very important to regularly monitor the quality of groundwater.

Many studies have been carried out and reported in literature. Trace metal concentration and physico-chemical analysis of ground water of Tadpatri, India, by S. Ramanjulu et al. The physico-chemical characteristics and concentration of twelve trace metals in the ground water of Tadpatri (India) were reported⁶. Ground water quality assessment in Dharmapuri district has been done by K.P. Elango et.al., Cations and anions concentration of most of the locations are within the permissible limit, indicating that the water is suitable for drinking and irrigation purposes⁷. Study of ground water quality has helped in evolving a management plan for ground water development.

In the present study groundwater samples were analysed the physico-chemical parameters such as pH, turbidity, electrical conductivity, total dissolvedsolids (TDS), total alkalinity, acidity, total hardness, calcium, magnesium, sodium, potassium, iron, manganese, ammonia, nitrite, nitrate, chloride, fluoride, sulphate, phosphate, dissolvedoxygen (DO), biochemical oxygen demand (BOD) and chemical oxygen demand (COD) respectively.

Materials and methods:-

Polythene cans of two liter capacities were used for the collection of water samples. Acids, alkalis, indicator, buffer reagents and mineral salts were analytical grade of high purity purchased from Merck India and it is used without further purification. All the other reagents used were of reagent grade.

Sites of Collection:-

Five ground water samples S1, S2, S3, S4 and S5 were collected from bore wells and hand pumps around Kallur, Tirunelveli district. The table 1. indicates where the water samples was collected.

TABLE:1 Places of the water samples collected

S.No.	Sample	Place	Source
1	S1	Near Railway station	HP
2	S2	Near water tank	PP
3	S3	Middle street	HP
4	S4	Durkaiamman koil Street	HP
5	S5	Near Govt. Hr. Sec. School	PP

Results and Discussion:-

Physico-Chemical Characteristics:-

The physico-chemical characteristics such as pH, turbidity, electrical conductivity, TDS, total alkalinity, acidity and total hardness of all the five samples were showed in Table 2.

Table 2: Physicochemical Parameters of the Ground water from the Kallur Area

Sample	pH	Turbidity (NTU)	EC(μ mhos/cm)	TDS(mg/l)	TA(mg/l)	Acidity(mg/l)	TH(mg/l)
S1	7.29	3	436	279	160	20	160
S2	7.69	1	1250	825	240	28	368
S3	7.39	3	3048	2134	448	35	920
S4	7.51	2	2003	1402	320	31	500
S5	7.79	0	2867	2007	400	32	600

pH:-

The pH of natural water is neutral (i.e. 7.0) due to the buffering capacity of the carbonate - bicarbonate system in a water solution⁶. pH is also an important factor in water analysis, since it enters into the calculation of acidity, alkalinity and processes like coagulation, disinfection and corrosion control. The limit of pH value of drinking water is specified to be 6.5-9.2 (WHO standard). In the present study, pH value varies from 7.29 to 7.79 which are found to be weakly alkaline.

Turbidity:-

WHO permissible limit for Turbidity is between 5-25 NTU. Falling within the permissible limit, the turbidity values of present study ranges from 0 to 3.

Electrical Conductivity:-

The electrical conductivity of water is due to dissolved and dissociated inorganic substances. WHO permissible limit for electrical conductivity is 300 μ mhos/cm. The variation in EC ranges between 436 and 3048 μ mhos/cm in water samples. The high values of electrical conductivity may be due to the high concentrations of ionic constituents present in the water bodies under study and reflect the pollution by domestic wastes⁷.

Total Dissolved Solids:-

TDS indicates the general nature of the water quality or salinity. WHO permissible limit for TDS is 500 mg/l. Water containing more than 500 mg/l of TDS is not desirable for drinking water purposes, In the present study the Concentrations of the total dissolved solids are in the range between 279 and 2134 mg/l. Since the samples S3 and S5 have high values of TDS, they cannot be used for drinking as well as for construction purpose⁸. So people of this area have laxative and sometimes the reverse effect due to the high solid content⁹. However, the possibilities of higher concentration of TDS in this area are due to higher withdrawal of ground water leading to poor sanitation and

Pollution by domestic wastage. The untreated water, which shows higher value of TDS is ingested, would lead to gastrointestinal disorder.

Total Alkalinity:-

The high level alkalinity indicates the presence of bicarbonates in the water body. Bicarbonate represents the major form since they are formed in considerable amount from the action of carbonates upon the basic materials in the soil. The WHO permissible limit is 120 mg/l. In the present study it varies from 120 to 448 mg/l. All the samples exceeded the permissible limit.

Acidity:-

Acidity in all the samples lie within the range of 20 mg/l to 35 mg/l. WHO permissible limit is 30-150 mg/l. All the samples well below the permissible limits.

Total Hardness:-

In the study area, total hardness varies from 160 to 920 mg/l. Calcium and Magnesium along with their carbonates, sulphates and chlorides makes the water hard both temporary and permanent¹⁰. The desirable limit according to IS limit is 300 mg/l. All the water samples of the study area except S1 exceeds the permissible limit.

Trace Metals In Water:-

The basic radicals or cations present in the water samples are Calcium, Magnesium, Sodium, Potassium, Iron and Manganese are given in Table-3.

Table-3 Inorganic constituents of water Samples mg/l

Sample	Ca	Mg	Na	K	Fe	Mn
S1	38	15	22	1	0.18	0
S2	96	31	84	26	2.24	0
S3	320	29	215	15	0	0
S4	160	24	240	25	0.12	0
S5	216	14	350	15	0	0

Calcium:-

Calcium is an essential mineral required for diverse physiological and biochemical functions in the human body¹¹. Hardness of water mainly depends upon the amount calcium salts. Calcium concentration in the present study ranges between 38 and 320 mg/l. The calcium content of samples S2, S3, S4 and S5 exceeds the permissible limit 75 mg/l, and are not suitable for domestic applications.

Magnesium:-

Hardness also depends upon the amount of the Magnesium salts¹⁰. In the study area its concentration varies from 10 to 31mg/l. Thus the Magnesium content in the present study is within the WHO permissible limit 50 mg/l.

Sodium:-

Sodium concentration observed in the study area is between 22 and 350 mg/l. Sodium rich water may cause the ground water alkaline in the presence of bicarbonate ions. Alkalinity mainly depends upon the amount of sodium salts. Alkalinity of water is a measure of its capacity to neutralize acids. Sodium ranks sixth among the elements in order of abundance and is present in most natural waters. Soil permeability may be affected by a high sodium content.

Potassium:-

Alkalinity also depends upon the amount of Potassium salts. Figure 1 shows potassium concentration observed in the study area is between 1 and 26 mg/l. The Potassium concentration of samples S2, S3, S4 and S5 exceeds the permissible limit.

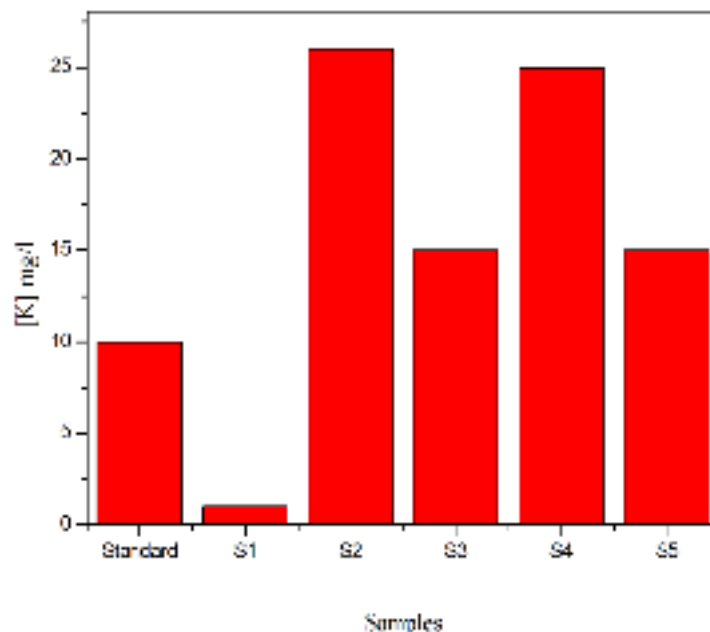


Figure.1 Potassium concentration in S1, S2, S3, S4 and S5 samples.

Iron:-

Iron in the ground water is mostly in the form of inorganic complexes. The concentration of iron in the study area ranges from 0.00 to 2.24 mg/l. The main source of iron in ground water is the weathering of rock and discharge of waste effluents on land.

Manganese:-

Hardness in water causes by the presence of divalent metallic cation Manganese. Concentration of Manganese in natural water is generally 0.2 mg/l or less. More than 0.2 mg/l precipitates upon oxidation and causes undesirable tastes. The Manganese content in the study area is 0.00 mg/l. Thus all the samples in the study area are well within the permissible limit. Water in these areas are safe of domestic purpose.

Major constituents (anionic):-

Phosphate:-

Phosphorous is essential for the growth of organisms and phosphorous present as phosphate in natural water is a growth limiting nutrient. The concentration of phosphate in all the water samples in the study area ranges from 0 to 0.16 mg/l. The values are well within the WHO permissible limit of 0.64 mg/l.

Nitrite And Nitrate:-

Nitrate is widely present in the environment. Natural waters are naturally deficient of nitrates, this restricts the algal growth. Some groundwater naturally has high nitrate concentration. The results indicates that the concentration of nitrate varies from 4 to 7 mg/l. In the present study, the concentration of nitrite ranges from 0.03 to 1.79 mg/l.

Sulphate:-

Higher concentration of sulphate may induce diahorrea, whereas lower concentration causes the laxative effect and respiratory diseases. It was observed that the stagnated water had familiar pungent odour of H_2S even at surface level. Sulphate in the study area lies between 21 and 235 mg/l. The sulphate content of samples in the study area other than S4 are well below the permissible limit 235 mg/l.

Chloride:-

Chloride in the form of Cl^- ions is one of the major inorganic anions in water. The water containing 250 mg/l chloride may have a detectable salty taste if the cation is sodium. WHO permissible limit for chloride is 200 mg/l. Figure-2 shows the concentration of chloride in all the samples in the study area ranges between 20 and 610 mg/l.

The higher chloride content in ground water may be attributed to the presence of soluble chlorides from rocks, saline intrusion, connate and juvenile water.

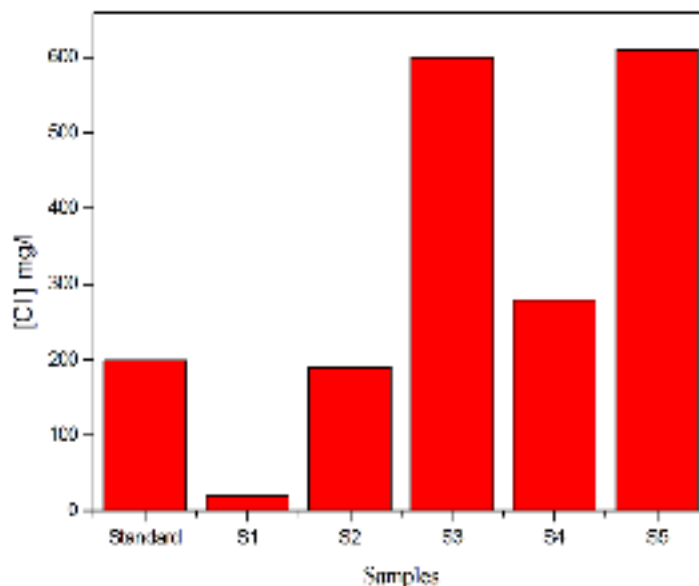


Figure 2. Chloride concentration in S1, S2, S3, S4 and S5 samples

Ammonia:-

Figure-3 shows the ammonia concentration ranges from 0 to 0.8 mg/l. The WHO permissible limit is 0.5 mg/l. Mixing sewage water and septic tank nearer to the water sources causes an increase in the concentration of ammonia. Concentration of Ammonia in all the samples are within the permissible limit.

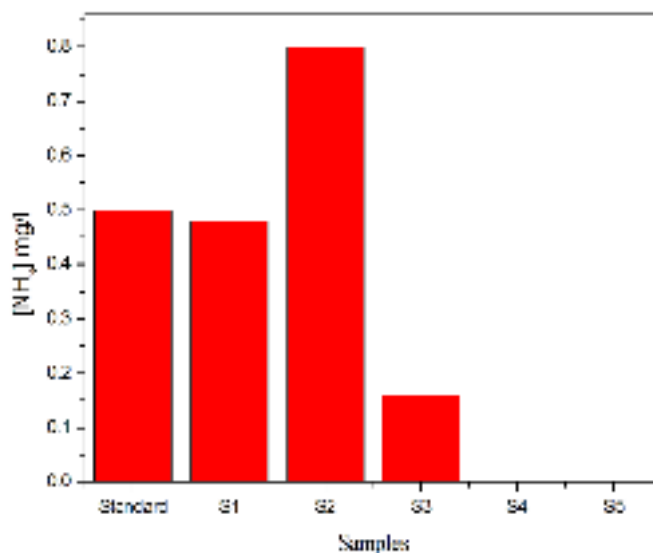


Figure.3 Ammonia concentration in S1, S2, S3, S4 and S5 samples.

Fluoride:-

Excess Fluoride intake paralyzes the fluoride metabolism and are deposited over teeth and skeletal structures which lead to many health problems¹³ called fluorosis. The concentration of fluoride in the present study ranges from 0 to 0.6 mg/l. The results indicate that all the samples contain fluoride well below the permissible limit 1.5 mg/l.

BOD and COD:-

The BOD and COD parameters measure not only the oxidatively decomposable organic components but also the level of pollution. WHO permissible limit for BOD and COD is 6 and 7 mg/l respectively. BOD values ranges from 2 to 3.1 mg/l and COD values ranges from 2 to 4.1 mg/l were noted in the present investigation.

Conclusion:-

pH values for the study area varies from 7.29 to 7.79. Among the five samples, All of them within the permissible limit (WHO 6.5-9.2). pH values has been reported all the samples are said to be weakly alkaline in nature because due to bicarbonate salts. Except S1, all the samples exceeded the permissible limit of TDS. Hence they are not suitable for domestic purposes. The Total Hardness values of S2, S3, S4 and S5 samples are exceeded the permissible limit. Hardness in water is mainly due to its Calcium and Magnesium contents. Hardness make the water unsuitable for several domestic operations such as washing, cooking etc. Remaining samples have well below the permissible limit of 300 mg/l, ICMR. Hardness of water mainly depends upon the amount calcium salts. Calcium concentration in the present study ranges between 38 and 320 mg/l. WHO permissible limit for calcium is 75 mg/l. The calcium content of samples S2, S3, S4 and S5 exceeds the permissible. Potassium concentration for the water samples varies from 1 to 26 mg/l, About 80% of the samples such as S2, S3, S4, S5 exceeded the Standard permissible limit of 10 mg/l, WHO.

References:-

1. Kant, P. P. and Deepti, G. (2005): Environment and Ecology, 2nd ed, Sun India publications, New Delhi, pp. 4.1- 4.5.
2. Ikem, A., Osibanjo, O., Sridhar, M. K. C. and Sobande, A. (2002): Evaluation of groundwater quality characteristics near two waste sites in Ibadan and Lagos, Nigeria: Water, Air and Soil Pollution, Vol. 140(1-4) pp. 307-333.
3. Mohapatra, U. K. and Singh, B. C. (1999): Trace metals in drinking water from different sources in old capital city of Cuttak. Indian Journal of Environmental Health, Vol. 41(2), pp. 115-120.
4. Anwar, K. M. and Aggarwal, V. (2014): Curr. World Environ., 9, pp. 851-857.
5. Rao, Subba, M. V., Rao V. D. and Anand Andrews, B. S. (2012): Assessment of Quality of Drinking Water at Srikuram in Srikakulam District, Andhra Pradesh, India, International Research Journal of Environmental Science, Vol. 1(2), pp.13-20.
6. Ramanjulu, S., Suresh, A., Suresh Kumar, C., Mahendra Varma, B. and Surendranath, B., (1992): Trace metal concentration and physico-chemical analysis of ground water of Tadpatri, India, Env. Eco., 10(1), pp. 213-215.
7. APHA, AWWA, WEF, (1992): STANDARD METHODS FOR THE EXAMINATION OF Washington, water and waste water 18th edition.
8. Shanmugha Sundarraj, A., Karthikeyan, G. and Elango, K.P., (2004): Fluoride dependence on water quality parameters and Mapping of Fluorotic areas of Bargur block of Dharmapuri District - A case study, Ind. J. Env. Protection., 24(3), pp. 202-206.
9. Thillai Arasu, P., Jeyakumar, T. and Indira, S., (2003): Status of ground water quality and public health around Tiruchendur, Ind. J. Env. Protection., 23(3), pp. 256-260.
10. Pallav Sengupta, Potential Health Impacts of Hard Water. (2013) : Int. J. Prev. Med. 4(8), pp. 866-875.
11. A. Anish Babu., S. Kamalesu., P. Karthiga., M. Jaya Brabha and S. S. Sajitha., (2016): Int. J. Engineering Research and Technology, 5(2), pp. 353-355.
12. Kaza, S. R., Prasad, W. D. N., Someswara Rao, B., Mohana Rao, M., Kiska, and M., Rambabu C., (1991):Monitoring the ground waters of Musunur Mandal, Krishna dist, (AP), Polln Res, 10 (3), pp. 165-171.
13. WHO (1977), Environmental Health Criteria-3, WHO, Geneva.

Biosynthesis of ZnO Nanoparticles using *Ficus Carica* leaf extract and their biological evolution of antibacterial activity

Dr. M. Sheik Muhideen Badhusha¹

Abstract: In this study, zinc oxide nanoparticles were biologically synthesized using the leaf extract of *Ficus Carica* (ZnO (AZ)). The synthesized ZnO (AZ) NPs was characterized by UV-Vis spectrophotometer, FT-IR, SEM and XRD analysis. Mainly, the present results depicted that the synthesized nanoproducts are moderately stable, hexagonal phase, roughly cluster like morphology with maximum particles in the size range within 50 - 130 nm in diameter. The antibacterial activity was tested by the well diffusion method in the solid agar medium. The antibacterial activity was tested for gram-positive bacterium like *S. aureus*, *K. Phenemonia* and *Salmonella typhi*. The results reveal that green synthesized ZnO nanoparticles showed the highest antibacterial activity when compared to that of bare ZnO nanoparticles. Further, the present investigation suggests that ZnO NPs has the potential applications for various medical and industrial fields.

Keywords: Green synthesis, Zinc oxide, Antibacterial activity, *Ficus Carica*

1. Introduction

In recent years, the use of inorganic antimicrobial agents has been an attracting interest for the control of microbes. The key advantages of inorganic antimicrobial agents are improved safety and stability when compared with organic antimicrobial agents [1]. At present, most antibacterial inorganic materials are metallic nanoparticles [2] and metal oxide nanoparticles like zinc oxide [3].

Green synthetic strategic-approach is one of the eco-friendly methods for preparing nanoparticles. Synthesis of nanomaterials using biosynthesis over chemical synthesis could avoid many problems because the synthesis method does not use any toxic reagent in the preparation method. Three types of materials are commonly used in the biosynthesis process, including enzymes [4], microorganisms [5] and plant extracts [6]. Among them, synthesis of nanomaterials using plant extracts is the simplest approach

¹ Assistant Professor, Department of Chemistry, Sadakathullah Appa College (Autonomous), Tirunelveli, India.

because of its low cost, abundant resource and simple operation requirement. Zinc oxide (ZnO) is a n-type wide-bandgap semiconductor and large excitonic binding energy (60MeV), and it is much higher than those of other prospective materials like ZnSe(22MeV) and ZnS(40MeV)[7] which is widely used in many technological applications such as solar cells [8], diluted magnetic semiconductors [9], (DMSs), nanopiezotronics [10], UV detectors [11], gas sensors [12], light emitting diodes (LEDs) [13].

Hence, the present task was carried out to synthesis and characterization of ZnO nanoparticles using leaf extract of *Ficus Carica* and finally to evaluate its antibacterial activities.

2. Materials and methods

2.1 Preparation of aqueous *Ficus Carica* leaf extract:

The collected *Ficus Carica* leaves were first washed with tap water and then with distilled water for removing the unwanted impurities. The leaves were allowed to dry in room temperature (32 °C). The dried leaves were powdered in a laboratory mill. *Ficus Carica* leaf extract was prepared by placing 10 g of dried powder in 500 mL glass beaker along with 400 mL of sterile distilled water. The mixture was then boiled for 5 minutes until the colour of aqueous solution changed from watery to yellow. Then the mixture was cooled to room temperature and filtered with Whatman No. 1 filter paper before centrifuging at 1200 rpm for 2 minutes to remove biomaterials. The extract was stored at room temperature in order to be used for further experiments.

2.2 Synthesis of ZnO nanoparticles by chemical precipitation method:

For the synthesis of ZnO NPs, 50mL of extract was taken and boiled at 80 °C by using a stirrer-heater for 20 min. Then, 5 g of Zinc sulphate was added to the solution and was kept under continuous stirring at 80°C for 2 h. Then the mixture was boiled until it becomes a deep yellow colored paste. This paste was then collected in a ceramic crucible and heated in an air heated furnace at 400 °C for 2 h. A light white coloured powder was obtained and this powdered product (ZnO (AZ)NPs) was used for the further studies.

2.3 Characterization of ZnO nanoparticles

The optical properties investigated using a UV-Visible spectrophotometry were recorded at room temperature in the wave length range of 200-800 nm using Shimadzu UV - 2450 spectrophotometer. Surface structure was characterized by a Fourier-transform infra red (FT-IR) spectrophotometer (JASCO FT-IR 460 plus). The crystalline structure of the nanoparticles was studied by an X-ray diffractometer (XRD; XPERT PRO

X-RAY) with Cu K α radiation at 25 °C and the structural assignments were made with reference to the JCPDS powder diffraction files. The surface morphology was examined using scanning electron microscopy (SEM) (JSM 6701F - 6701) in both secondary and backscattered electron modes and the elemental analysis was also detected.

2.4 Measurement of antimicrobial activity

Well diffusion method was used to observe the dose dependent antibacterial activity of ZnO NPs on bacterial species. Bacterial inoculums were prepared by growing a single colony overnight in nutrient broth and adjusting the turbidity to 0.5 McFarland standards. Mueller–Hinton agar (MHA) plates were inoculated with this bacterial suspension and 200 mg/mL of ZnO NPs were added to a center well with a diameter of 8 mm. These plates were incubated at 37 °C for 24 h. The zone of inhibition (ZO) was measured by subtracting the well diameter from the total inhibition zone diameter. The tetracycline was used as a standard drug for bacterial species. All experiments were done in triplicates and the results were concurrent and calculated standard deviations [14].

3. Results and Discussion

3.1 UV-Visible spectroscopy

The room temperature UV-Vis absorption spectrum of ZnO (AZ) NPs is shown in Fig. 1. The spectrum reveals a characteristic absorption peak of ZnO at wavelength of 459 nm, which can be assigned to the intrinsic band-gap absorption of ZnO due to the electron transitions from the valence band to the conduction band. The band gap energy of samples is determined by the formula $\alpha h\nu = E_d(h\nu - E_g)^2$ where α is absorption coefficient, $h\nu$ is the energy of photon, E_g is the direct band gap and E_d is the constant. By plot of $(\alpha h\nu)^{1/2}$ vs $h\nu$ and extra plotting the linear region of the curve to absorption equal to zero as shown in the Fig(2) gives the value of direct band gap (E_g).

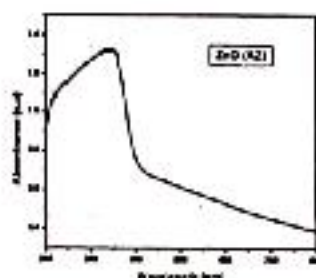


Figure 1 UV-vis-spectrum of ZnO (AZ) NPs



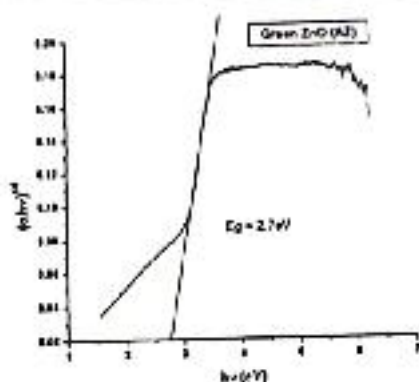


Figure 2 Tauc plot of ZnO (AZ) NPs

3.2 XRD Analysis

The crystalline size and structural properties of the ZnO NPs are revealed by powder X-ray diffraction. The XRD is carried out with Cu K α radiation ($\lambda = 0.1540$ nm) and 2 Theta ranges from 20 to 80. The XRD pattern of bio-synthesized ZnO (AZ) NPs is shown in Fig. 3. The diffractogram of XRD are very well matched with the hexagonal wurtzite structure in comparison with the data from JCPDS card No. 89-1397. The size of ZnO nanoparticles was obtained by Debye-Scherrer's formula given by the equation $D = K\lambda/(\beta\cos\theta)$, where K is the scherrer constant, λ the X-ray wavelength, β the peak width of half maximum, and θ is the Bragg diffraction angle. The Debye-Scherrer approximation allows to estimate the average size of the biosynthesized ZnO nanoparticles which is found to be ~ 21.5 nm.

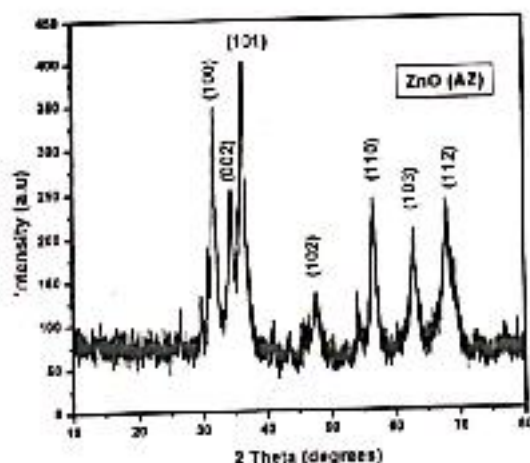


Figure 3 XRD patterns of ZnO (AZ) NPs

3.3 FT-IR Analysis

The peak in the region between 400 and 600 cm^{-1} is allotted to Zn-O [15]. The bands at 3416 cm^{-1} and 1580 cm^{-1} are characteristic for hydroxyl group (O-H). The peaks at 1384 cm^{-1} and 1118 cm^{-1} may be ascribed to -C-O and -C-O-C stretching modes. Peak at 1405 cm^{-1} may be assigned to symmetric stretching of the carbonyl side groups in the amino acid residues of the protein molecules [16].

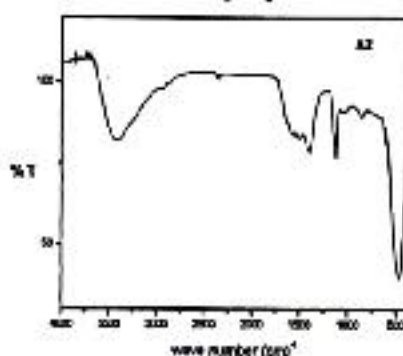


Figure 4 FT-IR spectrum of ZnO (AZ) NPs

3.4 SEM Analysis

Fig. 5 demonstrates SEM images showing the surface morphology of ZnO (AZ) NPs. It shows ZnO (AZ) NPs is in cluster-based frameworks with a diameter in range of 50 - 130 nm.



Figure 5 SEM image of ZnO (AZ) NPs

3.5 Antibacterial activity

The antibacterial properties of the ZnO (AZ) Nps were tested against pathogenic bacterium like *S. aureus*, *K. Phenemania* and *Salmonella typhi* using agar well diffusion method. The ZnO (AZ) Nps showed significant antibacterial activity on all the bacterial strains. The zone of inhibition is shown in Fig. 6. The data is shown in Table. 1.



Figure 6 Antibacterial activity of ZnO(AZ) NPs

Table 1

Antibacterial activity of ZnO (AZ) nanoparticles synthesized by green method

S. No	Sample	Bare ZnO	ZnO (AZ) NPs	Control	Standard
1	<i>Salmonella</i>	8	20	-	21
2	<i>Klebsiella</i>	10	23	-	6
3	<i>Staph. aureus</i>	6	17	-	24

4. Conclusion:

The present biosynthesis method is a green, low cost approach capable of producing ZnO NPs at nearby room temperature. ZnO NPs at obtained were should be targeted for the potentials of antimicrobial applications. UV-vis studies confirmed the indirect band gap 2.7. eV spectrum showed the peak at 459 nm indicated the characteristic absorption peak of ZnO nanoparticles. XRD results confirmed the size of the ranging from 16 to 37 nm. FTIR study confirmed that zinc-oxygen bands at 478 cm^{-1} . Finally it can be concluded that microbial activity of ZnO NPs is

more susceptible *Klebsiella* than the other micro organisms. The present study is so helpful and useful to the scientific community for using the ZnO NPs has potent applications to the antidiabetic and antihyperlipidemic activities. In addition, it is inexpensive, stable and non-toxic, safe and eco-friendly without any side effects for human beings. Therefore, the present research was designed to be eco-friendly, stable and non-toxic for biosynthesis of ZnO nanoparticles using the *Ficus Carica* leaf extract.

References:

- [1] J. Sawai, *J. Microbiol. Methods* 54 (2003) 177.
- [2] F. Furno, K.S. Morley, B. Wong, B.L. Sharp, P.L. Arnold, S.M. Howdle, R. Bayston, P.D. Brown, P.D. Winship, H.J. Reid, *J. Antimicrob. Chemother.* 54 (2004) 1019.
- [3] N. Ciofi, L. Torsi, N. Ditaranto, G. Tantillo, L. Ghibelli, L. Sabatini, T. Bleve-Zache
- [4] Y. Konishi, K. Ohno, N. Saitoh, T. Nomura, S. Nagamine, H. Hishida, Y. Takahashi and T. Uruga, *J. Biotechnol.*, 128 (2007) 649
- [5] S.K. Das, C. Dickinson, F. Lafir, D.F. Brougham and E. Marsili, *Green Chemistry*, 14 (2012) 1322
- [6] H. Abdul Salam, R. Sivaraj and R. Venckatesh, *Materials Letters*, 131 (2014) 16
- [7] G. Sangeetha, S. Rajeshwari and R. Venckatesh, *Mater. Res. Bull.*, 46 (2011) 2560
- [8] P. Rajiv, S. Rajeshwari and R. Venckatesh, *Spectrochimica acta. Part A, Molecular and biomolecular spectroscopy*, 112 (2013) 384
- [9] D. Apurba, S. Chavdhuri, B.N. Dev, *Bull. Mater. sci.* 31 (2008) 281-285.
- [10] P.S. Reddy, G.R. Chetty, S. Uthanna, B.S. Naidu, P.J. Reddy, *Solid State Commun* 77 (12) (1991) 899-901.
- [11] I. Djerdj, G. Garnweitner, D. Arcon, M. Pregelj, Z. Jaglicic, M. Niederberger, *J. Mater. Chem.* 18 (2008) 5208-5217.
- [12] J. Volk, T. Nagata, R. Erdelyi, I. Barsoni, A.L. Toth, I.E. Lukacs, Z. Czigany, H. Tomimoto, Y. Shingaya, T. Chikyow, *Nanoscale Res. Lett.* 4 (2009) 699-704.
- [13] A. Bechen, M. Durr, L.P. Nostro, P. Baglioni, *J. Nanoparticle Res.* 10 (2008) 679-689.
- [14] A.J. Kora, R. Manjusha, J. Arunachalam, *Mater. Sci. Eng. C* 29 (2009) 2104-2109.
- [15] D. Kushal et.al, *Material Letters*. 77 (2012) 93-95.
- [16] S. K Das, A. R. Das, A. K. Guha, *Langmuir*, 25(2009) 8192.



Green synthesis and characterization of Fe doped ZnO nanoparticles and their interaction with bovine serum albumin

M. Sheik Muhideen Badhusha ^a  , C. Joel ^b, R. Imran Khan ^a, N. Vijayakumar ^c

Show more 

 Outline |  Share  Cite

<https://doi.org/10.1016/j.jics.2021.100197>

[Get rights and content](#)

Highlights

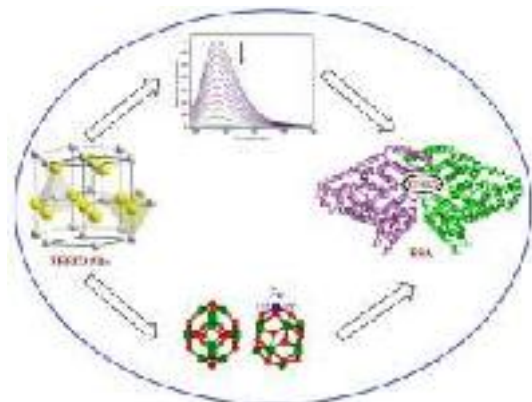
- We have synthesized Fe doped ZnO nanoparticles using *Thespesia polpulanea* flower extract.
- The XRD pattern indicates the formation of ZnO nanoparticles in wurtzite structure.
- The morphology and optical properties of ZnO and Fe doped ZnO nanoparticles have been studied.
- The binding affinities of the nanoparticles were studied with plasma protein BSA.

Abstract

Herein we report an eco-friendly and cost efficient synthesis of Fe doped ZnO (TPFZO) nanoparticles using the extract of *Thespesia polpulanea* flowers as a stabilizing agent. The synthesized NPs have been characterized by XRD, FT-IR, UV-DRS, SEM, EDAX and TEM studies. The synthesized NPs were found to have the crystallite size in the range of 30–60 nm. The

calculated band gap energies for ZO and TPFZO nanoparticles were 3.00 eV and 1.97 eV respectively. The size distribution of the ZO and TPFZO obtained from TEM were observed to be lying in the range 50–120 nm and 4–22 nm respectively. The interaction of TPFZO NPs with bovine serum albumin (BSA) has been studied using fluorescence and absorption titration methods. The results indicated that the nanoparticles quenched the BSA fluorescence at 340 nm via static quenching mode having a bimolecular quenching rate constant value of $6.21 \times 10^{13} \text{ Lmol}^{-1}\text{s}^{-1}$.

Graphical abstract



[Download : Download high-res image \(198KB\)](#)

[Download : Download full-size image](#)

[<](#) Previous

Next [>](#)

Keywords

Green synthesis; ZnO; *Thespesia polpulanea*; BSA; Fluorescence quenching

[Recommended articles](#)

Cited by (1)

Strain Induced by Temperature Evolution of Green Hydrothermally Synthesized Photoresponsive Mesoporous ZnO Nanopowders and its Effect on Structural, Optical and I-V Properties

2022, SSRN

[View full text](#)

© 2021 Indian Chemical Society. Published by Elsevier B.V. All rights reserved.



Copyright © 2022 Elsevier B.V. or its licensors or contributors.
ScienceDirect® is a registered trademark of Elsevier B.V.



Theoretical Study on Indacaterol by DFT Study

J. Winfred Jebaraj¹, P. Muthuselvan¹, D. Jim Livingston¹, I. Antony Danish²

¹Department of Chemistry, St. John's College, Palayamkottai, India – 627002

²Department of Chemistry, Sadakathullah Appa College, Palayamkottai, India – 627011

Abstract: Quantum chemical calculations were carried out to study the molecular structure for indacaterol. To investigate the optimized molecular structure, bond length, bond angle and tetrahedral angles, Mullikan atomic charges, HOMO, LUMO energy levels, energy gap, dipole moment, total energy and some other physical parameters, DFT calculations were carried out using 6-31G basis set with B3LYP.

Keywords: Dipole moment, HOMO-LUMO energy gap, Indacaterol, Mullikan charges.

I. Introduction

Indacaterol is a drug used for the treatment of chronic obstructive pulmonary disease (COPD). Its chemical name is 5-((1R)-2-[(5,6-diethyl-2,3-dihydro-1H-inden-2-yl)amino]-1-hydroxyethyl)-8-hydroxy-2(1H)-quinolinone maleate. It is an ultra long acting beta adrenoceptor agonist. According to WHO, there are more than two hundred million people have moderate to severe COPD worldwide. It is in essential need of the theoretical properties. B3LYP/DFT/631-G basis set is used to calculate some physical properties of the target molecule with the help of Gaussian 09 software.

II. Computational details

The combination of quantum chemical calculation is very effective to understand the structure and behavior of the compound. The various analysis of the present study of the compound under investigation are carried out by DFT with three parameter hybrid [1,2] functional (B3) [3] for the exchange part and Lee Yang–Parr [4] (LYP) correlation functional using 6-31G basis set. The Gaussian 09 package is used for this calculation [5].

III. Result and Discussion

3.1 Optimized molecular structure

The list of atoms for the target molecule is shown in Table 1. The optimized molecular structure is shown in Fig 1. The optimized bond length, bond angle and tetrahedral angles for Indacaterol molecule at both levels of theory are listed in Tables 2,3 and 4 respectively.



Fig 1: The 2D and 3D optimized molecular structure of Indacaterol

Table 1: The atom list of Indacaterol

1	2	3	4	5	6	7	8
C	C	C	C	C	C	C	C
9	10	11	12	13	14	15	16
C	C	C	C	C	N	C	C
17	18	19	20	21	22	23	24
O	C	C	C	C	C	O	N
25	26	27	28	29	30	31	32
C	C	O	C	C	H	H	H

33	34	35	36	37	38	39	40
H	H	H	H	H	H	H	H
41	42	43	44	45	46	47	48
H	H	H	H	H	H	H	H
49	50	51	52	53	54	55	56
H	H	H	H	H	H	H	H
57							
H							

Table 2: Bond length of optimized Indacaterol molecule by 631-G calculation

Sl.no	Code	Bond	Bond distance (Å)	Sl.no	Code	Bond	Bond distance (Å)
1	R1	R(1,2)	1.5464	31	R31	R(12,13)	1.3937
2	R2	R(1,30)	1.0965	32	R32	R(13,46)	1.0879
3	R3	R(1,31)	1.0959	33	R33	R(14,15)	1.4659
4	R4	R(1,32)	1.0959	34	R34	R(14,47)	1.0193
5	R5	R(2,3)	1.5207	35	R35	R(15,16)	1.5351
6	R6	R(2,33)	1.0977	36	R36	R(15,48)	1.0976
7	R7	R(2,34)	1.0964	37	R37	R(15,49)	1.1044
8	R8	R(3,4)	1.421	38	R38	R(16,17)	1.4839
9	R9	R(3,13)	1.4066	39	R39	R(16,18)	1.5186
10	R10	R(4,5)	1.5265	40	R40	R(16,50)	1.0957
11	R11	R(4,7)	1.407	41	R41	R(17,51)	0.9789
12	R12	R(5,6)	1.5361	42	R42	R(18,19)	1.4295
13	R13	R(5,35)	1.1009	43	R43	R(18,29)	1.3943
14	R14	R(5,36)	1.099	44	R44	R(19,20)	1.4487
15	R15	R(6,37)	1.0961	45	R45	R(19,25)	1.4144
16	R16	R(6,38)	1.0955	46	R46	R(20,21)	1.3602
17	R17	R(6,39)	1.0962	47	R47	R(20,52)	1.0838
18	R18	R(7,8)	1.3952	48	R48	R(21,22)	1.459
19	R19	R(7,40)	1.0845	49	R49	R(21,53)	1.0826
20	R20	R(8,9)	1.5159	50	R50	R(22,23)	1.2532
21	R21	R(8,12)	1.4036	51	R51	R(22,24)	1.3985
22	R22	R(9,10)	1.572	52	R52	R(24,25)	1.3831
23	R23	R(9,41)	1.0961	53	R53	R(24,54)	1.0129
24	R24	R(9,42)	1.1021	54	R54	R(25,26)	1.4105
25	R25	R(10,11)	1.5565	55	R55	R(26,27)	1.3935
26	R26	R(10,14)	1.4635	56	R56	R(26,28)	1.3851
27	R27	R(10,43)	1.0991	57	R57	R(27,55)	0.9747
28	R28	R(11,12)	1.5145	58	R58	R(28,29)	1.4079
29	R29	R(11,44)	1.0953	59	R59	R(28,56)	1.0864
30	R30	R(11,45)	1.1022	60	R60	R(29,57)	1.0826

It is predicted that the longest and possibly weakest bonds are R1, R5, R10, R12, R20, R25, R28, R35 and R39 involving C-C bonds. The shortest and possibly strongest bonds are R41 and R57 involving O-H bond.

Table 3: Bond angle of optimized Indacaterol molecule by 6-31G calculation

Sl.no	Code	Bond	Bond angle (°)	Sl.no	Code	Bond	Bond angle (°)
1	A1	A(2,1,30)	110.8945	55	A55	A(8,12,11)	110.6888
2	A2	A(2,1,31)	110.6033	56	A56	A(8,12,13)	119.7246
3	A3	A(2,1,32)	111.401	57	A57	A(11,12,13)	129.585
4	A4	A(30,1,31)	108.1923	58	A58	A(3,13,12)	120.7643
5	A5	A(30,1,32)	108.0415	59	A59	A(3,13,46)	118.931
6	A6	A(31,1,32)	107.5726	60	A60	A(12,13,46)	120.3035
7	A7	A(1,2,3)	113.1311	61	A61	A(10,14,15)	116.6752
8	A8	A(1,2,33)	108.5676	62	A62	A(10,14,47)	112.2483
9	A9	A(1,2,34)	109.1776	63	A63	A(15,14,47)	110.1864
10	A10	A(3,2,33)	108.8281	64	A64	A(14,15,16)	112.0089
11	A11	A(3,2,34)	110.7046	65	A65	A(14,15,48)	108.8955
12	A12	A(33,2,34)	106.1729	66	A66	A(14,15,49)	112.562
13	A13	A(2,3,4)	121.9505	67	A67	A(16,15,48)	109.3157
14	A14	A(2,3,13)	118.4691	68	A68	A(16,15,49)	106.933

15	A15	A(4,3,13)	119.5664	69	A69	A(48,15,49)	106.9627
16	A16	A(3,4,5)	120.006	70	A70	A(15,16,17)	108.299
17	A17	A(3,4,7)	118.9815	71	A71	A(15,16,18)	117.3853
18	A18	A(5,4,7)	121.0051	72	A72	A(15,16,50)	106.6921
19	A19	A(4,5,6)	116.2799	73	A73	A(17,16,18)	111.0973
20	A20	A(4,5,35)	108.8641	74	A74	A(17,16,50)	103.928
21	A21	A(4,5,36)	109.0978	75	A75	A(18,16,50)	108.5141
22	A22	A(6,5,35)	108.4027	76	A76	A(16,17,51)	109.0385
23	A23	A(6,5,36)	108.4157	77	A77	A(16,18,19)	118.851
24	A24	A(35,5,36)	105.2162	78	A78	A(16,18,29)	122.1208
25	A25	A(5,6,37)	111.757	79	A79	A(19,18,29)	119.0269
26	A26	A(5,6,38)	110.0556	80	A80	A(18,19,20)	124.2265
27	A27	A(5,6,39)	111.605	81	A81	A(18,19,25)	119.2921
28	A28	A(37,6,38)	107.5817	82	A82	A(20,19,25)	116.481
29	A29	A(37,6,39)	107.9654	83	A83	A(19,20,21)	121.6817
30	A30	A(38,6,39)	107.7003	84	A84	A(19,20,52)	118.4848
31	A31	A(4,7,8)	120.7492	85	A85	A(21,20,52)	119.7913
32	A32	A(4,7,40)	119.8168	86	A86	A(20,21,22)	122.4013
33	A33	A(8,7,40)	119.4335	87	A87	A(20,21,53)	121.7888
34	A34	A(7,8,9)	129.1896	88	A88	A(22,21,53)	115.8073
35	A35	A(7,8,12)	120.2124	89	A89	A(21,22,23)	125.0916
36	A36	A(9,8,12)	110.5972	90	A90	A(21,22,24)	113.9689
37	A37	A(8,9,10)	102.9867	91	A91	A(23,22,24)	120.938
38	A38	A(8,9,41)	113.4793	92	A92	A(22,24,25)	125.2027
39	A39	A(8,9,42)	111.0859	93	A93	A(22,24,54)	116.8442
40	A40	A(10,9,41)	112.7322	94	A94	A(25,24,54)	117.9529
41	A41	A(10,9,42)	109.5127	95	A95	A(19,25,24)	120.2448
42	A42	A(41,9,42)	107.0519	96	A96	A(19,25,26)	120.2644
43	A43	A(9,10,11)	104.4006	97	A97	A(24,25,26)	119.4906
44	A44	A(9,10,14)	117.2919	98	A98	A(25,26,27)	114.9554
45	A45	A(9,10,43)	107.5829	99	A99	A(25,26,28)	120.0758
46	A46	A(11,10,14)	111.9368	100	A100	A(27,26,28)	124.9675
47	A47	A(11,10,43)	108.1677	101	A101	A(26,27,55)	112.474
48	A48	A(14,10,43)	107.1117	102	A102	A(26,28,29)	120.1199
49	A49	A(10,11,12)	103.4178	103	A103	A(26,28,56)	120.075
50	A50	A(10,11,44)	111.9544	104	A104	A(29,28,56)	119.8051
51	A51	A(10,11,45)	109.5582	105	A105	A(18,29,28)	121.1875
52	A52	A(12,11,44)	114.1293	106	A106	A(18,29,57)	118.9597
53	A53	A(12,11,45)	111.0329	107	A107	A(28,29,57)	119.8227
54	A54	A(44,11,45)	106.7575				

From the Table 3, it is clear that A37, carbon atoms – 8,9,10 present in the five membered ring system shows the shortest angle while A57, carbons atoms 11,12,13 shows the largest angle.

From the tetrahedral values in Table 4, it is clear that the atoms of D1, D8, D19, D22, D23, D30, D31, D32, D33, D35, D43, D44, D45, D46, D53, D54, D55, D56, D87, D88, D89, D90, D131, D132, D135, D136, D137, D139, D140, D141, D142, D143, D144, D145, D146, D147, D148, D149, D150, D151, D152, D153, D154, D155, D156 and D157 lie in same plane.

Table: 4 Tetrahedral angle of optimized Indacaterol molecule by 631-G calculation

Sl.no	Code	Bond	Bond angle (°)	Sl.no	Code	Bond	Bond angle (°)
1	D1	D(30,1,2,3)	179.6524	81	D81	D(10,11,12,8)	17.085
2	D2	D(30,1,2,33)	58.7415	82	D82	D(10,11,12,13)	-163.3913
3	D3	D(30,1,2,34)	-56.5944	83	D83	D(44,11,12,8)	138.9567
4	D4	D(31,1,2,3)	59.6169	84	D84	D(44,11,12,13)	-41.5196
5	D5	D(31,1,2,33)	-61.294	85	D85	D(45,11,12,8)	-100.3317
6	D6	D(31,1,2,34)	-176.6299	86	D86	D(45,11,12,13)	79.192
7	D7	D(32,1,2,3)	-59.9717	87	D87	D(8,12,13,3)	0.0259
8	D8	D(32,1,2,33)	179.1174	88	D88	D(8,12,13,46)	-179.5661
9	D9	D(32,1,2,34)	63.7815	89	D89	D(11,12,13,3)	-179.4609
10	D10	D(1,2,3,4)	87.9956	90	D90	D(11,12,13,46)	0.947
11	D11	D(1,2,3,13)	-90.6379	91	D91	D(10,14,15,16)	177.9432
12	D12	D(33,2,3,4)	-151.2412	92	D92	D(10,14,15,48)	56.9156

13	D13	D(33,2,3,13)	30.1254	93	D93	D(10,14,15,49)	-61.5179
14	D14	D(34,2,3,4)	-34.9152	94	D94	D(47,14,15,16)	-52.5504
15	D15	D(34,2,3,13)	146.4514	95	D95	D(47,14,15,48)	-173.578
16	D16	D(2,3,4,5)	2.6785	96	D96	D(47,14,15,49)	67.9884
17	D17	D(2,3,4,7)	-178.305	97	D97	D(14,15,16,17)	55.4567
18	D18	D(13,3,4,5)	-178.7027	98	D98	D(14,15,16,18)	-71.2904
19	D19	D(13,3,4,7)	0.3138	99	D99	D(14,15,16,50)	166.793
20	D20	D(2,3,13,12)	178.3238	100	D100	D(48,15,16,17)	176.2411
21	D21	D(2,3,13,46)	-2.0786	101	D101	D(48,15,16,18)	49.494
22	D22	D(4,3,13,12)	-0.343	102	D102	D(48,15,16,50)	-72.4226
23	D23	D(4,3,13,46)	179.2545	103	D103	D(49,15,16,17)	-68.2993
24	D24	D(3,4,5,6)	-177.6214	104	D104	D(49,15,16,18)	164.9536
25	D25	D(3,4,5,35)	59.6414	105	D105	D(49,15,16,50)	43.0369
26	D26	D(3,4,5,36)	-54.6776	106	D106	D(15,16,17,51)	-106.512
27	D27	D(7,4,5,6)	3.3824	107	D107	D(18,16,17,51)	23.7938
28	D28	D(7,4,5,35)	-119.3548	108	D108	D(50,16,17,51)	140.303
29	D29	D(7,4,5,36)	126.3262	109	D109	D(15,16,18,19)	-165.2877
30	D30	D(3,4,7,8)	0.0282	110	D110	D(15,16,18,29)	14.286
31	D31	D(3,4,7,40)	-179.7115	111	D111	D(17,16,18,19)	69.3413
32	D32	D(5,4,7,8)	179.0345	112	D112	D(17,16,18,29)	-111.085
33	D33	D(5,4,7,40)	-0.7052	113	D113	D(50,16,18,19)	-44.3166
34	D34	D(4,5,6,37)	-61.4123	114	D114	D(50,16,18,29)	135.2571
35	D35	D(4,5,6,38)	179.1202	115	D115	D(16,18,19,20)	-2.8007
36	D36	D(4,5,6,39)	59.6019	116	D116	D(16,18,19,25)	177.4303
37	D37	D(35,5,6,37)	61.5658	117	D117	D(29,18,19,20)	177.6122
38	D38	D(35,5,6,38)	-57.9017	118	D118	D(29,18,19,25)	-2.1567
39	D39	D(35,5,6,39)	-177.42	119	D119	D(16,18,29,28)	-177.9588
40	D40	D(36,5,6,37)	175.2888	120	D120	D(16,18,29,57)	4.0389
41	D41	D(36,5,6,38)	55.8213	121	D121	D(19,18,29,28)	1.6142
42	D42	D(36,5,6,39)	-63.697	122	D122	D(19,18,29,57)	-176.3882
43	D43	D(4,7,8,9)	179.3098	123	D123	D(18,19,20,21)	178.9093
44	D44	D(4,7,8,12)	-0.3476	124	D124	D(18,19,20,52)	-3.4588
45	D45	D(40,7,8,9)	-0.9495	125	D125	D(25,19,20,21)	-1.3158
46	D46	D(40,7,8,12)	179.3931	126	D126	D(25,19,20,52)	176.3161
47	D47	D(7,8,9,10)	163.1545	127	D127	D(18,19,25,24)	-178.8929
48	D48	D(7,8,9,41)	40.977	128	D128	D(18,19,25,26)	1.2363
49	D49	D(7,8,9,42)	-79.6964	129	D129	D(20,19,25,24)	1.3205
50	D50	D(12,8,9,10)	-17.1618	130	D130	D(20,19,25,26)	-178.5502
51	D51	D(12,8,9,41)	-139.3393	131	D131	D(19,20,21,22)	0.2105
52	D52	D(12,8,9,42)	99.9873	132	D132	D(19,20,21,53)	179.5953
53	D53	D(7,8,12,11)	179.8979	133	D133	D(52,20,21,22)	-177.3911
54	D54	D(7,8,12,13)	0.3206	134	D134	D(52,20,21,53)	1.9938
55	D55	D(9,8,12,11)	0.1815	135	D135	D(20,21,22,23)	-179.5874
56	D56	D(9,8,12,13)	-179.3957	136	D136	D(20,21,22,24)	0.8649
57	D57	D(8,9,10,11)	26.7374	137	D137	D(53,21,22,23)	0.9934
58	D58	D(8,9,10,14)	151.2438	138	D138	D(53,21,22,24)	-178.5543
59	D59	D(8,9,10,43)	-88.0377	139	D139	D(21,22,24,25)	-0.8665
60	D60	D(41,9,10,11)	149.4167	140	D140	D(21,22,24,54)	179.2401
61	D61	D(41,9,10,14)	-86.0769	141	D141	D(23,22,24,25)	179.565
62	D62	D(41,9,10,43)	34.6416	142	D142	D(23,22,24,54)	-0.3284
63	D63	D(42,9,10,11)	-91.52	143	D143	D(22,24,25,19)	-0.2338
64	D64	D(42,9,10,14)	32.9864	144	D144	D(22,24,25,26)	179.6379
65	D65	D(42,9,10,43)	153.7049	145	D145	D(54,24,25,19)	179.6585
66	D66	D(9,10,11,12)	-26.6923	146	D146	D(54,24,25,26)	-0.4697
67	D67	D(9,10,11,44)	-150.0108	147	D147	D(19,25,26,27)	179.8699
68	D68	D(9,10,11,45)	91.7531	148	D148	D(19,25,26,28)	0.2725
69	D69	D(14,10,11,12)	-154.5542	149	D149	D(24,25,26,27)	-0.0018
70	D70	D(14,10,11,44)	82.1273	150	D150	D(24,25,26,28)	-179.5992
71	D71	D(14,10,11,45)	-36.1088	151	D151	D(25,26,27,55)	179.9594
72	D72	D(43,10,11,12)	87.6703	152	D152	D(28,26,27,55)	-0.4657
73	D73	D(43,10,11,44)	-35.6482	153	D153	D(25,26,28,29)	-0.8531
74	D74	D(43,10,11,45)	-153.8843	154	D154	D(25,26,28,56)	179.1297

75	D75	D(9,10,14,15)	65.7398	155	D155	D(27,26,28,29)	179.5923
76	D76	D(9,10,14,47)	-62.7784	156	D156	D(27,26,28,56)	-0.4249
77	D77	D(11,10,14,15)	-173.6299	157	D157	D(26,28,29,18)	-0.107
78	D78	D(11,10,14,47)	57.8519	158	D158	D(26,28,29,57)	177.8783
79	D79	D(43,10,14,15)	-55.2252	159	D159	D(56,28,29,18)	179.9102
80	D80	D(43,10,14,47)	176.2566	160	D160	D(56,28,29,57)	-2.1045

3.2 Mullikan charges

The bonding ability of a molecule depends on the electronic charge on the chelating atoms. The atomic charge values have been obtained by the Mullikan population analysis [6]. To confirm the reliability of the result, the Mullikan population analysis of the target molecule has been calculated using B3LYP/6-31G basis set. The Mullikan charges are given in Table 5. From the results, it is clear 22 C is having very high value, since it attached with nitrogen atom and oxygen atom. Also 26 C shows higher value due to the attachment of oxygen atom. All the hydrogen atoms were found to possess positive charge.

Table 5: Mullikan atomic charges of Indacaterol (Hartree)

Sl. No	Atoms	Atomic charges with B3LYP	Sl. no	Atoms	Atomic charges with B3LYP	Sl. no	Atoms	Atomic charges with B3LYP
1	C	-0.398892	20	C	-0.092165	39	H	0.140695
2	C	-0.316669	21	C	-0.163114	40	H	0.120137
3	C	0.071831	22	C	0.506772	41	H	0.136876
4	C	0.085315	23	O	-0.470661	42	H	0.142955
5	C	-0.326371	24	N	-0.787431	43	H	0.138033
6	C	-0.410013	25	C	0.320134	44	H	0.142010
7	C	-0.195206	26	C	0.245138	45	H	0.139564
8	C	0.068281	27	O	-0.639857	46	H	0.116046
9	C	-0.317758	28	C	-0.129374	47	H	0.275737
10	C	0.023848	29	C	-0.157536	48	H	0.138440
11	C	-0.313620	30	H	0.131596	49	H	0.131058
12	C	0.082292	31	H	0.138839	50	H	0.148660
13	C	-0.199152	32	H	0.139910	51	H	0.363617
14	N	-0.589553	33	H	0.132681	52	H	0.173499
15	C	-0.085881	34	H	0.132069	53	H	0.154086
16	C	0.024189	35	H	0.145855	54	H	0.354835
17	O	-0.608652	36	H	0.145341	55	H	0.385164
18	C	0.002986	37	H	0.139700	56	H	0.127041
19	C	0.030804	38	H	0.131869	57	H	0.174004

3.3 Dipole moment, Quadrupole moment and various energies

The dipole moment is the first derivative of the energy with respect to an applied field. It is a measure of the asymmetry in the molecular charge distribution and is given as a vector in three dimensions. The theoretical dipole moment (in Debye) is shown in Table 6. The total dipole moment is found to be 7.0504 Debye.

Table 6: The Dipole moment (in Debye) of Indacaterol

B3LYP/6-31G			
X	Y	Z	Total
-6.0446	3.2090	-1.6949	7.0504

The predicted quadrupole moment for the target molecule is given in Table 7. It is clear that the molecule is slightly elongated along the XX axis in both levels of theory.

Table 7: The quadrupole moment of Indacaterol

B3LYP/6-31G		
XX	YY	ZZ
-229.5692	-155.9353	-171.2368

Thermo chemical analysis for the molecule is carried out at 298.15K and 1 atmospheric pressure. The energies of thermal, constant volume heat capacity and entropy due to electronic, translational, rotational and vibrational energies are given in Table 8. It is seen that vibrational energy accounts for almost all of the total energy. It is observed that the constant volume heat capacity due to vibrational energy is greater than all other. Similarly, the translational energy causes more entropy.

Table 8: Various energies of Indacaterol

Parameters	B3LYP/6-31G		
	E (Thermal) KCal/Mol	CV Cal/Mol- Kelvin	S Cal/Mol-Kelvin
Total	321.175	104.734	183.275
Electronic	0.000	0.000	0.000
Translational	0.889	2.981	43.792
Rotational	0.889	2.981	37.013
Vibrational	319.397	98.772	102.471

The zero point correction, thermal correction to energy, thermal correction to enthalpy, thermal correction to Gibbs free energy, sum of electronic and zero point energy, sum of electronic and thermal energies, sum of electronic and thermal enthalpies and sum of electronic and thermal free energies are shown in Table 9. It is clear that the data are well correlated for both levels of theories.

Table 9: Thermo-chemistry of Indacaterol

Parameters	B3LYP/6-31G (Hartree/Particle)
Zero-point correction	0.484975
Thermal correction to Energy	0.511825
Thermal correction to Enthalpy	0.512769
Thermal correction to Gibbs Free Energy	0.425689
Sum of electronic and zero-point Energies	-1265.789516
Sum of electronic and thermal Energies	-1265.762667
Sum of electronic and thermal Enthalpies	-1265.761723
Sum of electronic and thermal Free Energies	-1265.848803

3.4 Electrostatic Potential Map (ESP)

ESP gives the electrostatic potential at location on a particular surface most commonly a surface of electron density to over all molecular size. In this target molecule (Fig 3) the colors near red represent large negative values [electron rich] while the colors near blue represent large positive values [electron poor] and the colors green and yellow represent intermediate values of the potential. [7] In this case, red, green, and yellow colors appeared near --OH, aromatic regions, -NH groups respectively.

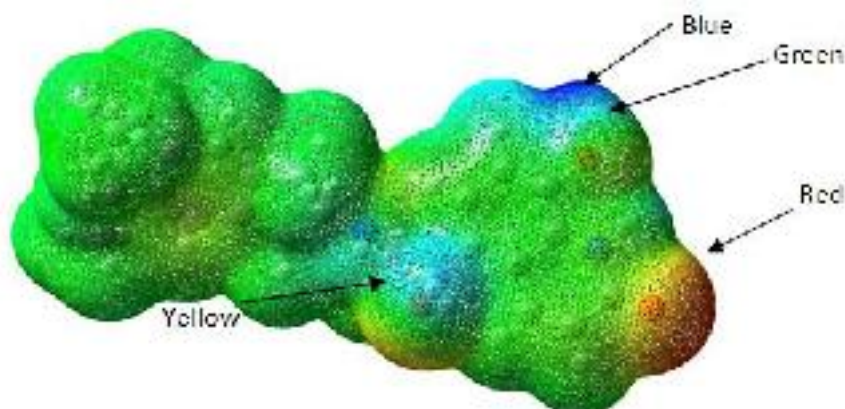


Fig 3: Electrostatic potential map of Indacaterol

3.5 HOMO – LUMO and total energy

From the Table 10, it is clear that the energy gap between HOMO and LUMO are high and hence the molecule is found to be stable. The total energy of the target molecule is found to be -1266.2744917 a.u.



a. (HOMO) b.(LUMO)

Fig 4: HOMO and LUMO of Indacaterol**Table 9:** Physical parameters of Indacaterol

	6-31G
HOMO (a.u)	-0.21177
LUMO (a.u)	-0.05805
Energy gap (a.u)	-0.15372
Total energy (a.u)	-1266.2744917

IV. Conclusion

In this present study, computational methods are used to predict the molecular dynamics of indacaterol. The equilibrium geometry of Indacaterol molecule was analyzed at DFT/B3LYP/6-31G basis set. The HOMO, LUMO, energy gap, dipole moment and total energy etc., were calculated theoretically, The ESP has also been used to understand the activity of the molecule.

References

- [1]. Dong Jun K, and Byung Tae C., *Bulletin of Korean Chem. Soc.*, 24, 2003, 1641-1648.
- [2]. Krishnamoorthy B, Kannan, Tangirala P, *Saudi Pharmaceutical Journal*, 20, 2012, 53–61.
- [3]. Becke AD, *J.ChemPhys*, 98, 1993, 5648.
- [4]. Lee C, Yang W X Par R.G, *Phys Rev*, 37B, 1988, 785.
- [5]. Gaussian 09, Revision D.01, M. J. Frisch, G. W. Trucks, H. B. Schlegel, G. E. Scuseria, M. A. Robb, J. R. Cheeseman, G. Scalmani, V. Barone, B. Mennucci, G. A. Petersson, H. Nakatsuji, M. Caricato, X. Li, H. P. Hratchian, A. F. Izmaylov, J. Bloino, G. Zheng, J. L. Sonnenberg, M. Hada, M. Ehara, K. Toyota, R. Fukuda, J. Hasegawa, M. Ishida, T. Nakajima, Y. Honda, O. Kitao, H. Nakai, T. Vreven, J. A. Montgomery, Jr., J. E. Peralta, F. Ogliaro, M. Bearpark, J. J. Heyd, E. Brothers, K. N. Kudin, V. N. Staroverov, R. Kobayashi, J. Normand, K. Raghavachari, A. Rendell, J. C. Burant, S. S. Iyengar, J. Tomasi, M. Cossi, N. Rega, J. M. Millam, M. Klene, J. E. Knox, J. B. Cross, V. Bakken, C. Adamo, J. Jaramillo, R. Gomperts, R. E. Stratmann, O. Yazyev, A. J. Austin, R. Cammi, C. Pomelli, J. W. Ochterski, R. L. Martin, K. Morokuma, V. G. Zakrzewski, G. A. Voth, P. Salvador, J. J. Dannenberg, S. Dapprich, A. D. Daniels, Ö. Farkas, J. B. Foresman, J. V. Ortiz, J. Cioslowski, and D. J. Fox, Gaussian, Inc., Wallingford CT, 2009.
- [6]. Mullikan, R. S, *J.Chem. Phys.*, 23, 1955, 1833.
- [7]. Warren J Hehre, *A Guide to Molecular Mechanics and Quantum Chemical Calculations* Page 77.



Developmental Studies on Novel Biodegradable Polyester Films from Maravetti Oil

T. Sahaya Maria Jeyaseeli¹, I. Antony Danish², J. Shakina^{1*}

¹Department of Chemistry, Sarah Tucker College, Tirunelveli, TN, India.

²Department of Chemistry, Sadakathullah Appa College, Tirunelveli, TN, India.

*shakinajudson@gmail.com

ABSTRACT

A unique biodegradable polyester film was made from naturally accessible Maravetti crude (*Hydnocarpus wightianus*), formic acid, and 30% hydrogen peroxide utilising a stepwise polymerisation technique. The polymer was created by reacting resin with styrene. UV, FTIR, and NMR spectral studies were utilized to identify the structural characteristics of the polymer product. The biodegradability of the polyester film was investigated using a soil burial test. The thermal deterioration was investigated using TG-DTA analysis at various time intervals. The cross-linking potential of the polymers was determined using DSC analysis. Tensile and impact strength were assessed, as well as other mechanical parameters. The resultant polymers have acceptable mechanical characteristics and cure quickly.

Keywords: Cross-linking; Degradation; Polymer Soil Burial; Styrene.

1. INTRODUCTION

In our world over 6.3 billion plastics are generated, only 9% is recycled, 12% incinerated, 79% accumulated in natural environment. In the production of plastics, monomers used which are derived from fossil hydrocarbons. Most of the plastics are slow to degrade (Roland *et al.* 2017). Because of increasing price of petroleum and environmental awareness, researchers are interested in the synthesising of polymers from renewable resources of plants. Plant oils are considered building blocks of polymers due to their low cost, availability and eco-friendly (Barnes *et al.* 2009). Active functional groups such as double bonds, ester groups and hydroxyl groups, on the triglyceride chain make the polymer to be chemically modified and to synthesis polymers with desirable properties (Wang *et al.* 2008). *Hydnocarpus* is a kind of *Hydnocarpus*. *Wightiana* seed oil, also known as chaulmoogra oil or Maravetti oil, comes from the seeds of the *Wightiana* plant. As a paste suspended in gum or as an emulsion, it has been used in medicine as an antibiotic for the treatment of many skin diseases and leprosy (Nortan, 1994). The oil is unusual in not being made up of straight chain fatty acids but acids with a cyclic group at the end of the chain.

2. EXPERIMENTAL METHODS

2.1 Materials

The thermal deterioration was investigated using TG-DTA analysis at various time intervals. The cross-

linking potential of the polymers was determined using DSC analysis. Tensile and impact strength were assessed, as well as other mechanical parameters. The resultant polymers have acceptable mechanical characteristics and cure quickly. In the curing procedure, benzoyl peroxide was used as a radical initiator and N, N-Dimethyl aniline was used as an accelerator.

2.2 Synthesis of *Hydnocarpus wightianus* Oil Polyol

Three-necked reagent flask with a water condenser was filled with 100 g of *Hydnocarpus wightianus* oil. 100 mL formic acid (97%) and 55 mL hydrogen peroxide (30%) were added to the flask, which was vigorously stirred about 16 hr. Externally, the temperature was maintained below 400 °C. The emulsion was then put into a separating funnel and removed using ether. The polyol resin from *Hydnocarpus wightianus* oil was obtained by drying the ether layer over anhydrous sodium sulphate.

2.3 Synthesis of Polyesters

The polyol resin product was heated in a three necked reagent flask and maleic anhydride was added in 1:2 ratio at 70 °C. Morpholine was used as a catalyst. After 2 hrs. a viscous liquid with golden yellow colour was formed which indicates the formation of oligomerised *Hydnocarpus wightianus* oil fumarate resin.

2.4 Synthesis of Polyester Film from Oligomerised *Hydnocarpus wightianus* Oil Fumarate Resin and Co-Monomer Styrene

Utilizing the homopolymer (*Oligomerised Hydnocarpus wightianus* oil fumarate resin) and styrene at various concentrations, aliphatic polyester was synthesised using a free radical addition polymerisation process with benzoyl peroxide as catalyst and Dimethyl aniline as accelerator. At room temperature, the viscous liquid is poured into a glass mould covered with silicon oil. From homo polymer and styrene, polyester thin films of various concentrations such as 1:0.5, 1:1, and 1:2 were synthesised. Finally, the yellow polyester sheets were taken out of the mould.

2.5 Characterisation of Resins

The UV and FTIR analysis were carried out for *Hydnocarpus wightianus* oil, hydroxylated *Hydnocarpus*

wightianus oil and also the resin. The $^1\text{H-NMR}$ spectra for epoxy resin, polyols and pre-polymers were dissolved in CDCl_3 and recorded using BRUKER AVANCE III, 400 MHz FT NMR SPECTROPHOTOMETER. Cured samples were also checked to see the degree of curing.

3. RESULT AND DISCUSSION

3.1 FTIR Analysis

The FTIR spectra of *Hydnocarpus wightianus* oil, Hydroxylated *Hydnocarpus wightianus* oil and the resins were recorded between 500 cm^{-1} to 4000 cm^{-1} (Rohan *et al.* 2018). In hydroxylated MVO, the FTIR spectra showed a strong absorption band at 3522.74 cm^{-1} , due to the presence of free-OH group in the molecule, which is absent in MVO. A strong absorbance band in 1734.85 cm^{-1} is due to the presence of $\text{C}=\text{O}$ in esters. A strong band in 2927.68 cm^{-1} due to the symmetrical-C-H bond in $-\text{CH}_2-$ group of the side chain.

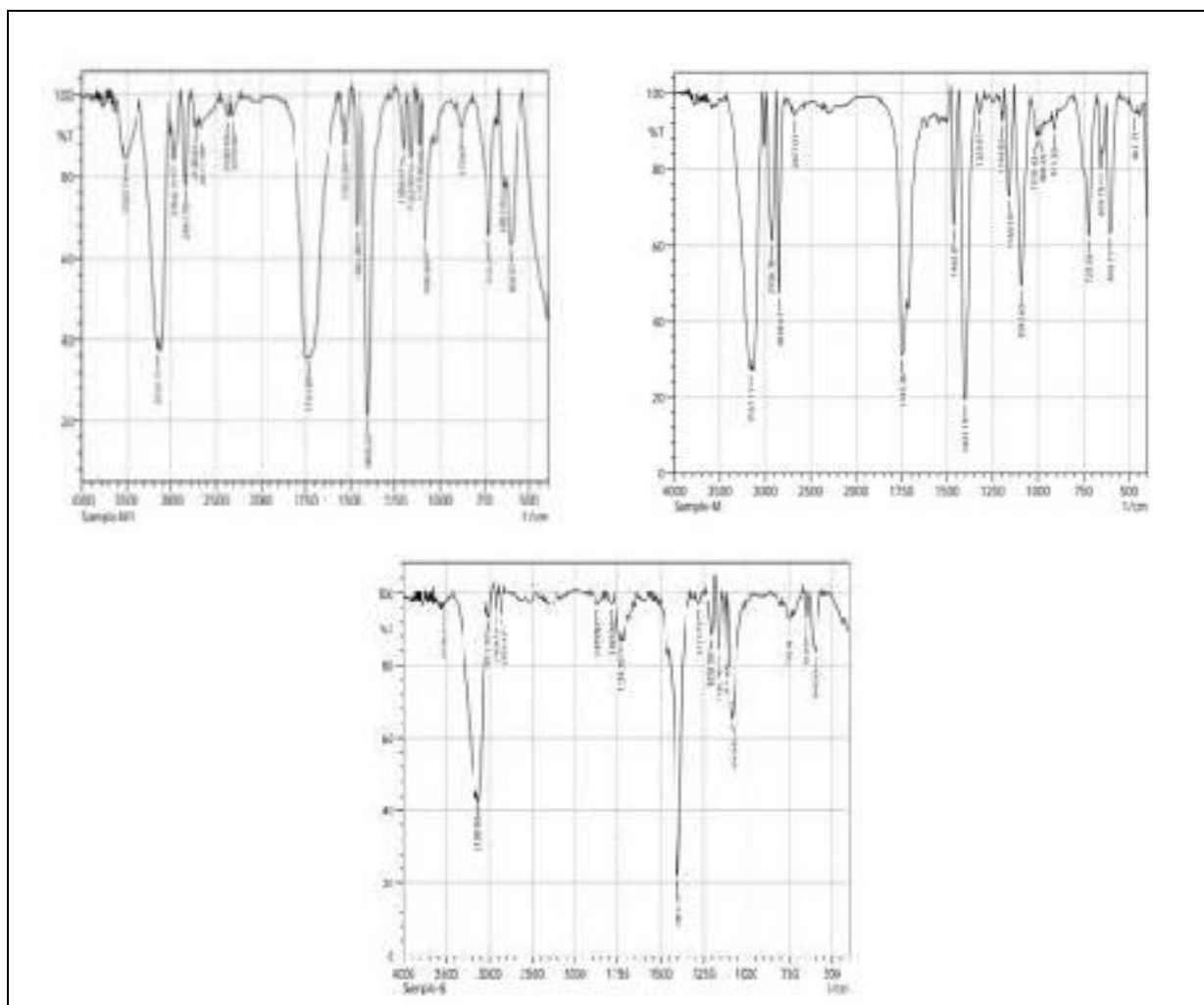


Fig. 1: FTIR spectra of MVO, Hydroxylated MVO and MVO Resin

Table 1. FT-IR probable assignment

Probable assignment	MVO (cm ⁻¹)	Hydroxylated MVO (cm ⁻¹)	MVO Resin (cm ⁻¹)
-CH ₂ Group	2927.68	2966.31	2926.78
-C- O Group in GM	2848.67	2847.7	-
C=O in esters	1745.46	1733.89	1734.85
Terminal CH ₃ Groups	1 194.82	1200.61	1202.53
Carboxyl Group of acids	1160.10	1163	1163.96
-CH-CH- Stretching	1092.60	1084.88	1082.96
CH ₂ -sequences of the aliphatic chains	720.36	722.29	755.08
-OH Group	3161.11	3522.74	3536.24

3.2 UV Analysis

The ultraviolet spectra of the resin, hydroxylated triglyceride oil, and resins have been studied (220 nm - 800 nm). The electronic absorption band in the resin sample was at 239 nm. When compared to the original oil, the hydroxylated resin showed a blue shift, which is due to the hydroxyl group being substituted at the unsaturated moiety. The replacement of the hydroxyl group at the olefinic double bond, as well as geometric distortion, cause a drop in absorbance as compared to parent oil. The substitution of the fumarate group caused a significant red shift in electronic absorption in the resin, as well as a distortion in the molecule's shape owing to the insertion of the fumarate group (Priya *et al.* 2015).

3.3 ¹H-NMR spectral studies

The ¹H-NMR spectra recorded from resin of chosen resin are shown in Fig 3. The peaks in ¹H-NMR for quantitating unsaturated fatty acids are those of the terminal methyl protons (0.85-0.89 ppm), olefinic protons (5.4-5.6 ppm), methylene -CH₂- (1.1-1.6 ppm) protons attached to allylic carbon (2.01-2.05 ppm) and protons attached to the bis-allylic carbons (2.2 - 2.7 ppm). The corresponding olefinic protons peak in the hydrolysis products have almost disappeared, revealed the double bonds in resin is replaced by the hydroxyl group. This peak is shifted to 8.1 ppm in the chosen resin due to the de-shielding effect of hydroxyl and carboxylate ester linkages (Shakina *et al.* 2012).

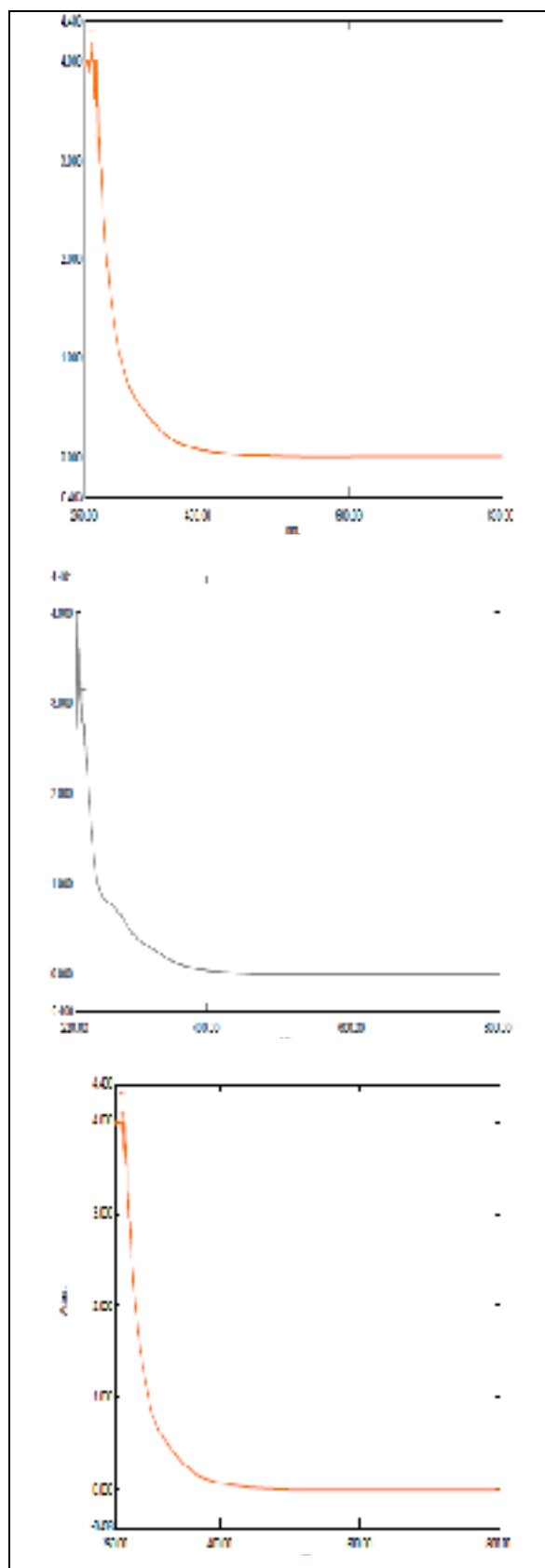


Fig. 2: UV spectra of MVO, Hydroxylated MVO and MVO Resin

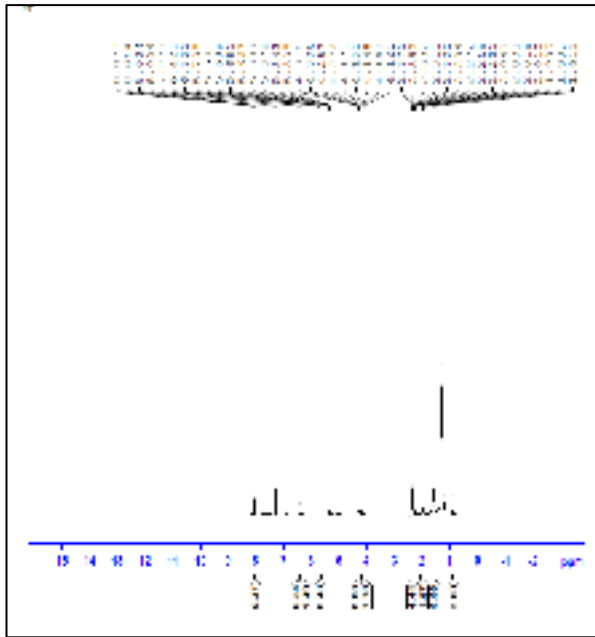


Fig. 3: NMR Spectrum of MVO Resin

3.4 XRD Pattern of Polymer Composite

From XRD analysis, average crystallite size is 7.02 nm. Peak is narrow, hence the polymer composite is crystalline (Birendra Pratap Singh *et al.* 2012).

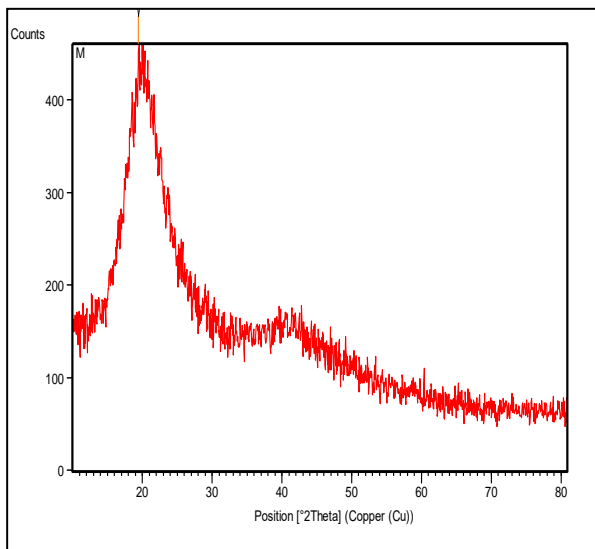


Fig. 4: XRD pattern of MV polymer

3.5 Thermal Analysis

The degree of cross linking influenced the properties of the polymer, which was associated with the monomer's functionality. The thermosetting resin's curing outcomes may be checked using DSC. The peak temperature for the sample with cross linker is 527.19 °C, indicating that this resin will cure the fastest at this temperature. For this

resin, the start of the cure peak is 412.00 °C, and the total heat of the reaction is 3853J/g (Li *et al.* 2017).

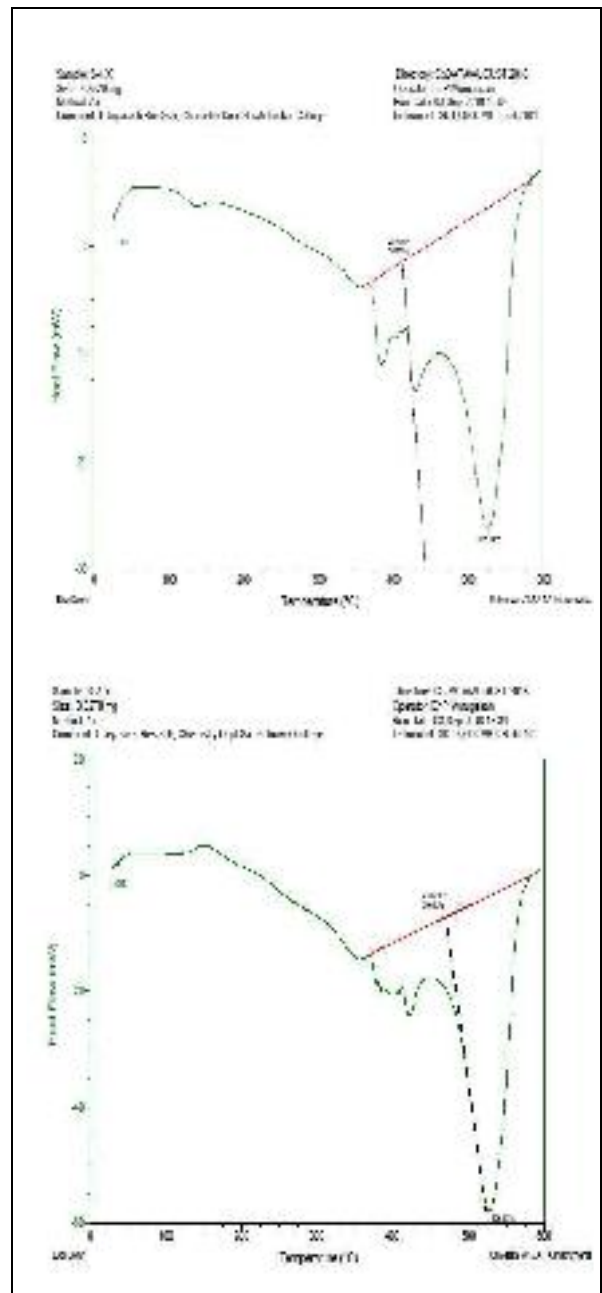


Fig. 5: DSC thermograms of polymer composite and without cross linker

The peak for the chosen material without cross linker is 527.8 °C, indicating the fastest cure for this resin will occur at the temperature. The onset of the cure peak for this resin is 471.64 °C and the total heat of the reaction is 2964J/g. It can be seen that resins with cross linker released out more heat during the curing process, which indicate more double bonds inside the resin. TGA for resins was conducted to identify their degradation characteristics.

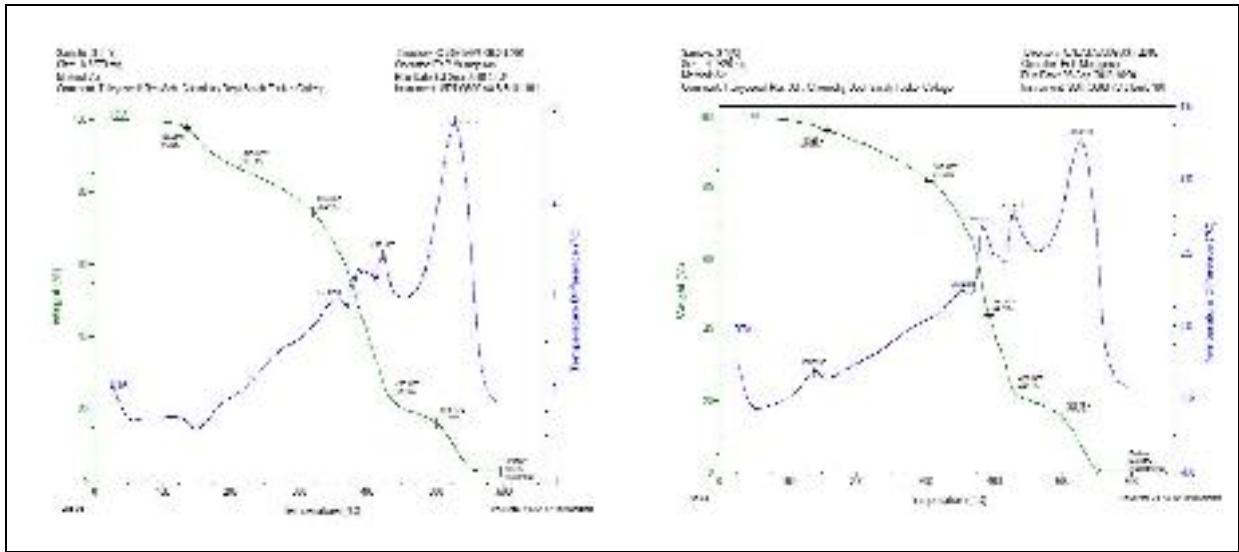


Fig. 6: TGA, DTA thermograms of sample with and without cross linker

The resin with cross linker was stable up to 150 °C with no significant weight loss, the initial weight loss was observed at 157.21 °C, indicating the loss of volatiles and moistures. Significant weight loss began at 306.36 °C due to the degradation of the resin. When the temperature reached 499.46 °C, weight loss was recorded. The maximum rate of decomposition occurred at 525.21 °C; the residual mass is around 0.009847 mg. The resin without cross linker was stable upto 130 °C with no significant weight loss; the initial weight loss was observed at 135.91 °C, indicating the loss of volatiles and moistures. Significant weight loss began at 320.35 °C due to the degradation of the resin. When the temperature reached 511.25 °C, weight reduced was found. The maximum rate of decomposition recorded at 528.22 °C; the residual mass is around 0.256 mg. It is clear that for resins with cross linkages are more resistive to

temperature, this is due to cross linkages increased the cross linking network of the oil. The percentage of residue is some what lower than resins without cross linkage (Sathishkumar *et al.* 2013).

3.6 FTIR-ATR Analysis

The samples were analysed over the range of 400 cm^{-1} – 4000 cm^{-1} with a spectrum resolution of 4 cm^{-1} . All spectra were averaged over 64 scans. The cross linking was confirmed through the ATR spectral studies.

The strong peaks observed at 1737.76 cm^{-1} and 1754.23 cm^{-1} indicate that the surface of the sample with and without cross linker are comprised predominantly with ester linkages (Shakina *et al.* 2014).

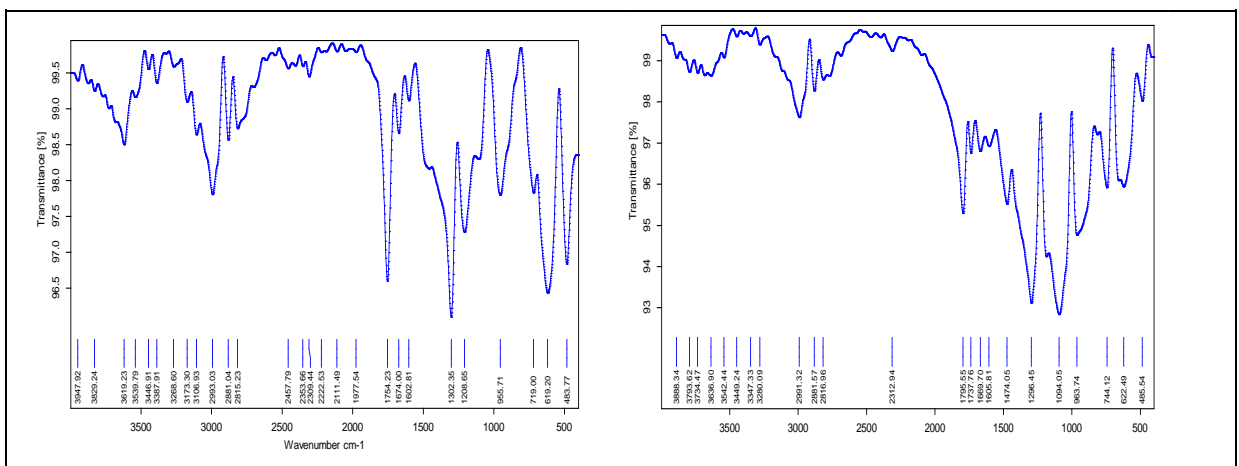


Fig. 7: ATR Spectrum of polymer composite with and without cross linker

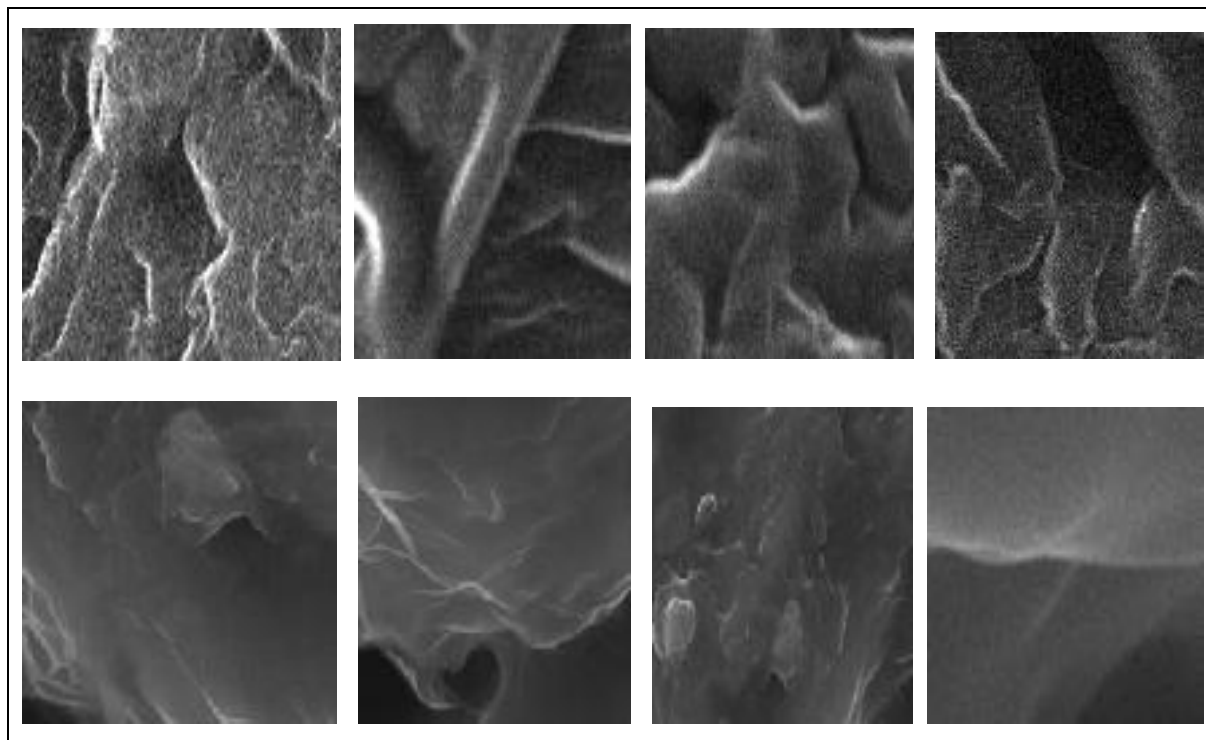


Fig. 8: SEM Photographs of polymer composite with and without cross linker

3.7 SEM Analysis

SEM micrographs reveal that the composite without cross linker has stronger bonding than the composite with cross linker. As indicated by the virtually total absence of holes surrounding the matrix and the lack of bio-flour breaking during tensile fracture, these results obviously offer strong interfacial adhesion and excellent wetting (Prabha *et al.* 2015).

3.8 Microbial Studies

Antibacterial activities were found in the sample by Agar well diffusion method using bacterial strains *Actinomyces Israelii* and *Aeromonas hydrophilla*. As prepared biopolyesters showed potential antibacterial characteristics against micro organisms. Antifungal present in the sample was detected by Agar well diffusion method using fungal strain *Aspergillus Niger*. The newly prepared biopolyesters showed potential antifungal activity against micro organisms (Shakina *et al.* 2012).

4. CONCLUSION

The fatty acid from *Hydnocarpus wightiana* seed oil was used to create Bio-based thermoset resin. It was hydroxylated using hydrogen peroxide and formic acid, and then maleic anhydride was added to the resulting

resin. The resins that were obtained were utilised to make bio-based composites. The mechanical properties of the composite shows better flexural strength and impact strength.

ACKNOWLEDGEMENTS

The authors registered their grateful thanks to the Principal, Sarah Tucker College, Tirunelveli, Tamilnadu for rendering their support to this work. The authors acknowledge The Director CECRI, Karaikudi, Tamilnadu, India, for providing all facilities for the evaluation of polymer samples.

REFERENCES

- David K. A. Barnes, Francois Galgani, Richard C. Thompson and Morton Barlaz, Accumulation and fragmentation of plastic debris in global environments, *Philos. Trans. R. Soc. Lond. B: Biol. Sci.*, 364(1526), 1985–1998 (2009).
<https://dx.doi.org/10.1098/rstb.2008.0205>
- Rohan Dassanayake, S., Sanjit Acharya, Nouredine Abidi, Biopolymer-based materials from polysaccharide properties, processing, characterization and sorption Applications, *Advanced Sorption Process Applications* (2018).
<https://dx.doi.org/10.5772/intechopen.80898>

- Birendra Pratap Singh, Jai Prakash Singh, Shruti Shukla, Shanti Sharma, Synthesis and characterization of inorganic polymer nano-composites, *Der Chemica Sinica*, 3(2), 521-526 (2012).
- Norton, S. A., Useful plants of dermatology, I. Hydnocarpus and chaulmoogra, *J. Am. Acad. Dermatol.*, 31(4), 683-686 (1994).
<https://dx.doi.org/10.1016/s0190-9622>
- Prabha Littis, G. S., Malar, S. and Begila David, Studies on polyester elastomers using palm olein for drug delivery, *Int. J. Sci. Eng. Appl. Sci.*, 1(5), 142-148 (2015).
- Priya Rajini, K. and Begila David, S., Synthesis and comparative study of novel cross linked biopolymers from Linseed Oil, *Int. J. Eng. Res. Appl.*, 5(8), 09-15 (2015).
- Roland Geyer, Jenna Jambeck, R. and Kara Lavender, Law, Production, use and fate of all plastics ever made, *Sci. Adv.*, 3(7), 01-05 (2017).
<https://dx.doi.org/10.1126/sciadv.1700782>.
- Sathishkumar, T. P., Navaneethakrishnan, P. and Shankar, S., Characterization of natural fiber and composites-A review, *J. Reinf. Plast. Compos.*, 32(19), 1457-1476 (2013).
<https://dx.doi.org/10.1177/0731684413495322>
- Shakina, J., Anita, A. and Alamelu, K., Polymers from renewable resources: polyester resin based upon acid anhydride-cured hydroxylated soybean oil, *Indian J. Sci.*, 8(20), 44-54 (2014).
- Shakina, J., Sathiya Lekshmi, K. and Allen Gnana Raj, G., Microbial degradation of synthetic polyesters from renewable resources, *Indian J. Sci.*, 1(1), 21-28 (2012).
- Shakina, J., Sathiya Lekshmi, K. and Allen Gnana Raj, G., Synthesis and characterisation of Novel cross linked biopolyesters from olive oil as eco-friendly biodegradable materials, *E-J Chem.*, 9(1), 181-192(2012).
- Li, Y. T., Yang, L. T., Zhang, H. and Tang, Z. J., Synthesis and properties of a novel bio based polymer from modified soy bean oil, *IOP Conf. Series: Mater. Sci. Eng.*, 17, 012010 (2017).
<https://dx.doi.org/10.1088/1757-899X/170/1/012010>
- Wang, H. J., Rong, M. Z. and Zhang, M. Q., Biodegradable foam plastics based on castor oil, *Biomacromolecules*, 9(2), 615-623 (2008).
<https://dx.doi.org/10.1021/bm7009152>

Multi Scale Plant Based Polymer Matrix: Synthesis, Biodegradation And Thermal Studies

T. Sahaya Maria Jeyaseeli, I. Antony Danish, J. Shakina

Abstract: In this study, cross linked polymers were synthesized from plant oils (Maravetti and Neem oil). Plant oil triglycerides were reacted with maleic anhydride and were treated with a monomer. The resulting polymer products were studied by FT-IR. The cross-linking ability of the polymers were checked by DSC analysis. TGA analysis was conducted to identify the thermal degradation patterns. NMR studies carried out to identify the nature of polymer. SEM analysis confirmed that the polymer was biodegradable. The synthesized polymers were characterized by solubility studies, soil burial test and microbial studies. The synthesized polymers may serve as a replacement in many applications.

Keywords: cross-linking, degradation, microbial, neem oil, polymer, solubility, soil burial

1. INTRODUCTION

Due to the environmental issues, vegetable oils are used as raw materials for their inherent biodegradability, low cost, societal favorably advantages and availability [1]. Bio-based polymers show better properties than petroleum products [2]. Because of lack of food value, Non-edible vegetable oil is used as alternative source of resin synthesis [3]. The widespread use of synthetic polymers in technology and in everyday life is an accepted feature of modern civilization. Plant oils are mainly constituted by triglycerides. The modification of triglycerides can be performed using the reactivity of the functional groups in their structure. Hydnocarpus Wightiana seed oil or chaulmoogra oil also known as Maravetti oil. Chemical constituents of Maravetti oil are Chaulmoogric acid, hydnocarpic acid, apigenin, hydnocarpin, fixed oils, tannins. The Maravetti oil has been shown to be highly active against fungal plant pathogens including *Aspergillus Niger* and *Rhizopus Nigricans* and also having anti bacterial activity against *Actinomycetes Israelii* and *Aeromonas Hydrophilla* [4]. The three most fatty acids of this type are 11 - cyclopent - 2-enyl-undecanoic (hydnocarpic), 13 - cyclopent - 2-enyl - tridecanoic (chaulmoogric) and 13 - cyclopent - 2-enyltridec - 6 - enoic (garlic) acids and lower cyclic homologues, myristic acid, palmitic acid, stearic acid, palmitoleic acid, oleic acid, linoleic acid and linolenic acid [5]. *Azadirachta indica* oil known as neem oil is composed mainly of triglycerides and contains many triterpenoid compounds, which are responsible for the bitter taste. It has the Iodine value 65-95. It is hydrophobic in nature; in order to emulsify it in water for application purposes, it must be formulated with appropriate surfactants. It has been used as an antiseptic, antifungal, antipyretic and antihistamine [6]. It is rich in medicinal properties which are what makes it a great ingredient in cosmetics and other beauty products: soaps, hair oil, hand wash soap etc. It can treat a bunch of skin diseases and is known to be an excellent mosquito repellent. It can be used to protect other plants.

- T. Sahaya Maria Jeyaseeli, Department of Chemistry and Research Centre, Sarah Tucker College (Autonomous), affiliated to Manonmaniam Sundaranar (M.S.) University, Tirunelveli, India, E-mail: jeyaseelit3@gmail.com
- I. Antony Danish, Department of Chemistry, Sadakathullah Appa College (Autonomous), Tirunelveli affiliated to M.S. University, Tirunelveli, India, E-mail: antonydanish@gmail.com.
- J. Shakina, Department of Chemistry and Research Centre, Sarah Tucker College (Autonomous), affiliated to M. S. University, Tirunelveli, India, E-mail: shakinajudson@gmail.com.

TABLE 1
FATTY ACID COMPOSITION OF OILS

Acid	Maravetti oil	Neem oil
Hydnocarpic acid	22.9	-
Chaulmoogri acid	35.0	-
Gloric acid	12.8	-
Lower cyclic homologs	4.6	-
Myristic acid(C14:0)	0.8	-
Palmitic acid(C16:0)	5.6	16-33
Stearic acid(C18:0)	4.7	9-24
Palmitoleic acid(C16:1)	0.5	-
Oleic acid(C18:1)	3.6	25-54
Linoleic acid(C18:2)	1.8	6-16

TABLE 2
PHYSICAL PROPERTIES OF OILS

Property	Maravetti oil	Neem oil
Refractive index, at 40°C	1.472	1.432
Iodine value	98-103	65 to 95
Saponification value	198-204	160 to 205
Acid value	25.0%	24.2%
Melting point	20-25°C	25°C
Specific gravity (at 25°C)	0.950-0.960	0.852- 0.95

2. EXPERIMENTAL

Maravetti oil (MVO) and Neem oil (NMO) were purchased from local market, Formic acid (97%) (Rankem), Hydrogen peroxide (30%) (Rankem) were used in the first step functionalisation. Maleic acid (Rankem) and Morpholine (Rankem). Benzoyl peroxide (Rankem) was used as a radical initiator and N, N-Dimethyl aniline (Rankem) was used as accelerator in the curing process. Styrene (Rankem) was used as a vinyl comonomer.

2.1 Synthesis of Maravetti / Neem oil polyol

100 g of Maravetti / Neem oil was taken in a three necked flask fitted with condenser and thermometer. 100 ml of 97% formic acid and 55ml of 30% hydrogen peroxide was added and the reaction mixture was vigorously stirred over 16h. Ice water bath was used externally to keep the temperature below 40°C. The resulting emulsion was poured into a separating funnel and extracted with ether. The ether layer was dried over anhydrous sodium sulphate and the resulting product was polyol resin from Maravetti / Neem oil.

2.2 Synthesis of polyesters

The polyol resin was heated in a three necked flask and maleic anhydride was added in 1:2 ratio at 70°C. Morpholine was used as a catalyst. After 2 hours a golden yellow viscous

liquid formed indicating the formation of oligomerised maravetti / neem oil fumarate resin.

2.3 Synthesis of polyester film from oligomerised maravetti or neem oil fumarate resin and co-monomer styrene

Synthesis of aliphatic polyester was carried out by free radical addition polymerization reaction using the homopolymer (oligomerised maravetti or neem oil fumarate resin) and styrene at different concentration with benzoyl peroxide as catalyst and Dimethylaniline as accelerator. The viscous liquid is transferred in to glass mould coated with silicon oil at room temperature. The polyester thin film of different concentration such as 1:0.5, 1:1 and 1:2 were synthesized from homopolymer and styrene. Finally the yellow colored polyesters sheets were removed from the mould.



Figure 1. MVO polymer film sheet



Figure 2. NMO polymer film sheet

2.4 Characterization of polymers

UV and FT-IR spectroscopy were used to characterize the synthesized resins in order to testify the chemical modification reactions. The UV and FTIR analysis were carried out for MVO and NMO, hydroxylated MVO and NMO and also the respective resins. Cured samples were also checked to see the degree of curing. The $^1\text{H-NMR}$ spectra for epoxy resin, polyols and pre-polymers were dissolved in CDCl_3 and recorded using BRUKER AVANCE III, 400 MHz FT NMR SPECTROPHOTOMETER. The mechanical studies of the biopolyesters were determined using Dumbbell shaped cut from the specimen. The Thermo Gravimetric Analysis (TGA) was done by using TGA instrument. The Differential Scanning Calorimetry (DSC) analysis was done by a TA instrument. XRD analysis was used to calculate crystal size of the polymers. SEM analysis was carried out to know about the surface property of the polymer. Microbial studies were carried out by agar diffusion method.

3. RESULT AND DISCUSSION

3.1 UV analysis

UV spectra of MVO and Hydroxylated MVO and MVO Resins have been investigated (220 nm - 800 nm). The MVO sample showed an electronic absorption band around 239 nm. Similarly UV spectra of NMO and Hydroxylated NMO and NMO Resins have been investigated (180 nm - 520 nm). The NMO sample showed an electronic absorption band around 262 nm. The hydroxylated resin exhibited a blue shift when

compared with the corresponding parent oil which is attributed to the substitution of hydroxyl group at the unsaturated moiety. There is also decrease in the absorbance in comparison with that of parent oil is due to the substitution of the hydroxyl group at the olefinic double bond and also distortion of geometry. The substantial red shift in electronic absorption exhibited in resins due to the substitution of the fumarate group and also due to the distortion in geometry of the molecule by the introduction of fumarate group [7].

3.2 IR analysis of the synthesized resins

The FTIR spectra of MVO, Hydroxylated MVO and MVO Resins are recorded between 500 cm^{-1} to 4000 cm^{-1} [8]. In hydroxylated MVO, the FTIR spectra showed a strong absorption band at 3522.74 cm^{-1} , due to the presence of free-OH group in the molecule, which is absent in MVO. A strong absorbance band in 1734.85 cm^{-1} is due to the presence of C=O in esters. A strong band in 2926.78 cm^{-1} is due to the symmetrical aliphatic-C-H bonding in $-\text{CH}_2-$ group of the side chain of triglyceride moiety. In hydroxylated NMO, the FTIR spectra showed a strong absorption band at 3565.17 cm^{-1} , due to the presence of free -OH group in the molecule, which is absent in NMO. A strong absorbance band in 1726.17 cm^{-1} is due to the presence of C=O in esters. A strong band in 2927.74 cm^{-1} is due to the symmetrical -C-H bond in $-\text{CH}_2-$ group of the side chain.

TABLE 3
FT-IR PROBABLE ASSIGNMENT

Probable assignment	MVO (cm^{-1})	HMVO (cm^{-1})	MVO Resin (cm^{-1})	NMO (cm^{-1})	HNMO (cm^{-1})	NMO Resin (cm^{-1})
$-\text{CH}_2$ Group	2926	2966.31	2926.7	2927.7	2927.7	2929.6
-C- O Group in GM	2848.67	2847.7	-	2854.4	2855.4	2855.4
C=O in esters	1745.46	1733.89	1734.8	1745.4	1726.1	1729.0
Terminal CH_3 Groups	1194.82	1200.61	1202.5	1209.2	1400.2	1460.0
Carboxyl Group of acids	1160.10	1163	1163.9	1167.8	1178.43	1374.1
-CH-CH- Stretching	1092.60	1084.88	1082.9	1072.3	1076.2	1058.8
CH_2 -sequences of the aliphatic chains	720.36	722.29	755.08	649	725.18	723.26
-OH Group	3161.11	3522.74	3536.2	3658.7	3565.1	3268.1

MVO= Maravetti Oil, NMO = Neem Oil, HMVO =Hydroxylated Maravetti Oil, HNMO = Hydroxylated Neem Oil

3.3 ^1NMR spectral studies

The $^1\text{H-NMR}$ spectra recorded from resin of MVO are shown in figure 3. The peaks in $^1\text{H-NMR}$ for quantitating unsaturated fatty acids are those of the terminal methyl protons (0.86 -0.88 ppm), olefinic protons (5.3-5.6 ppm), methylene $-\text{CH}_2-$ (1.2-1.6 ppm) protons attached to allylic carbon (2.00-2.04 ppm) and protons attached to the bis-allylic carbons (2.2-2.6 ppm). The corresponding olefinic protons peak in the hydroxylated product has almost disappeared, showing the double bonds in oil is replaced by the hydroxyl group. This peak is shifted to 8.0 ppm in the MVO resin due to the deshielding effect of hydroxyl and carboxylate ester linkages [9].

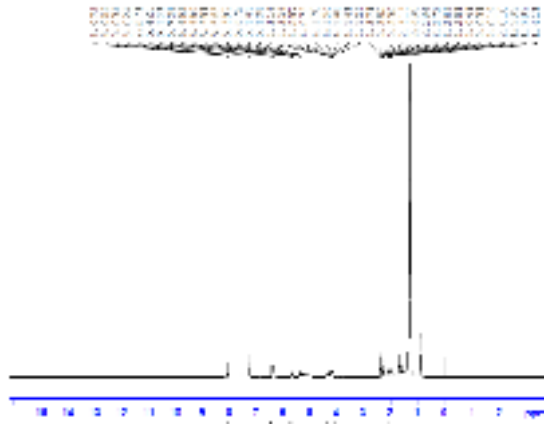


Figure 3. ^1H NMR Spectrum of MVO Resin

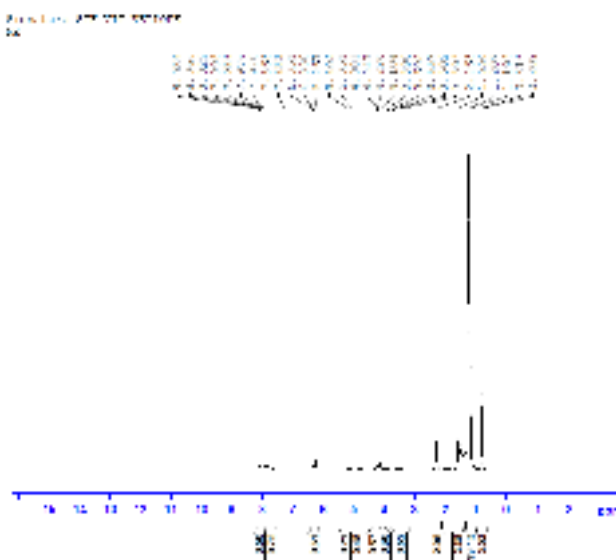


Figure 4. ^1H NMR Spectrum of NMO Resin

The ^1H NMR spectra recorded from resin of NMO are shown in figure 4. The spectra show the double bond hydrogen at 5.37 to 5.26 ppm. The corresponding olefinic protons peak in the hydroxylated product has almost disappeared; showing the double bonds in oil is replaced by the hydroxyl group. This peak is shifted to 8.0 ppm in the NMO resin due to the deshielding effect of hydroxyl and carboxylate ester linkages.

3.4 XRD pattern

XRD is a primary technique to determine the degree of crystallinity in polymers. The XRD patterns of the MVO and NMO polymers shows that they are semi crystalline. The results suggest that the MVO polymers have sharp peak compared to NMO polymer, so the MVO polymers are more crystalline than NMO polymers [10].

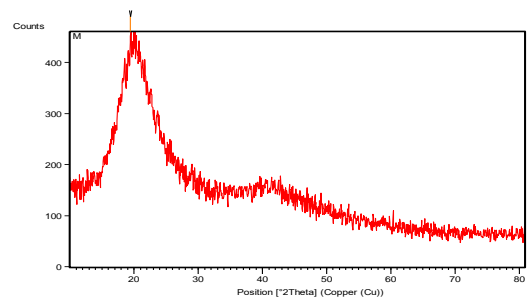


Figure 5. XRD patterns of MVO polymer

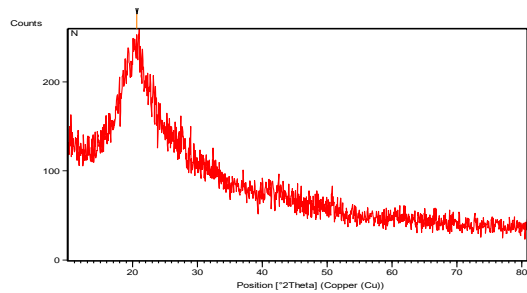


Figure 6. XRD Patterns of NMO polymer

3.5 Thermal analysis:

TGA for polymer was conducted to identify their degradation characteristics. The MVO polymer was stable up to 130 °C with no significant weight loss; the initial weight loss was observed at 135.91°C, indicating the loss of volatiles and moistures. Significant weight loss began at 320.35°C due to the degradation of the resin. The maximum rate of decomposition occurred at 527.42°C, the residual mass is around 0.2557 mg. The residue percentage is 2.896%.

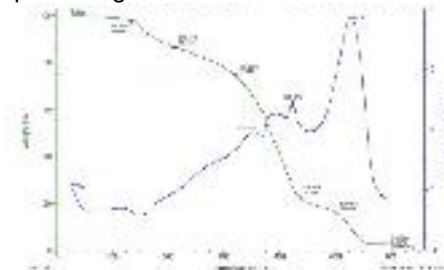


Figure 7. TGA, DTA thermograms of MVO polymer

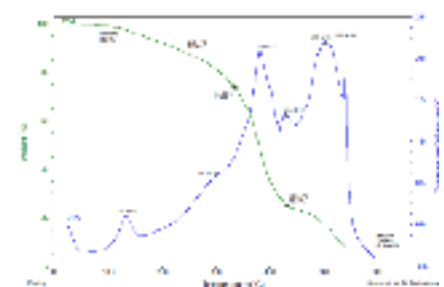


Figure 8. TGA, DTA thermograms of NMO polymer

The NMO polymer was stable up to 120 °C with no significant weight loss; the initial weight loss was observed at 243.11°C, indicating the loss of volatiles and moistures. Significant weight loss began at 334.99°C due to the degradation of the resin. When the temperature reached 431.54°C, weight loss was recorded. The residual mass is around 0.5444 mg. From

this, we see that polymers are more resistive to temperature increasing. The residue percentage is 7.434%. Thermal analysis indicates that both the polymers are semi crystalline in nature [11].

TABLE 4.
THE TGA DATA OF CROSS LINKED POLYESTERS

Polyesters	Initial loss Temp/°C	Significant Temp/°C	90%weight loss Temp/°C	Derivative Temp/°C	Residue (Wt %)
MVO	213.14	320.35	501.45	527.42	2.896
NMO	243.11	334.99	431.54	539.4	7.434

TABLE 5.
THE DTA DATA OF CROSS LINKED POLYESTERS

Polyesters	Exothermic response(°C)		
	Exo1	Exo2	Exo3
MVO	353.18	423.10	527.42
NMO	301.20	503.34	539.41

Properties of polymer affected by the cross linking degree, which correlated with the degree of functionality of the monomer. DSC can be used to check the curing results of the thermosetting resin. Both the MVO and NMO polymers were analyzed by DSC.

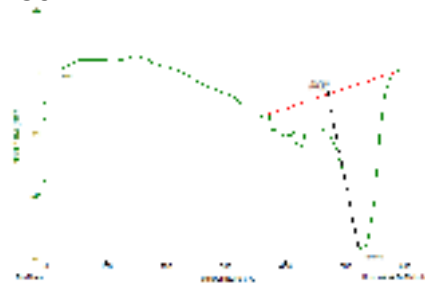


Figure 9. DSC thermogram of MVO polymer

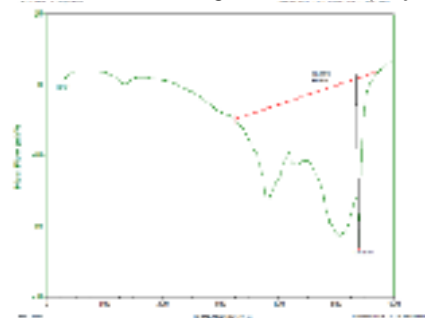


Figure10. DSC thermogram of NMO polymer

TABLE 6.
THE DSC DATA OF CROSS LINKED POLYESTERS

Polyesters	Onset temperature (°C)	Derivative Temperature (°C)	Heat of exotherm (J/g)
MVO	470.73	528.6	2965
NMO	534.98	539.26	4469

The peak for the MVO polymer is 528.6°C indicating the fastest cure for this resin will occur at the temperature. The onset of the cure peak for this resin is 470.73°C and the total heat of the reaction is 2965 J/g. The peak for the NMO polymer is 539.26°C, indicating the fastest cure for this resin will occur at the temperature. The onset of the cure peak for this resin is 534.98°C and the total heat of the reaction is 4469 J/g. It can be seen that Neem resins released out more heat during the curing process, which indicate more double bonds inside the resins [12].

3.6 Mechanical Analysis

Tensile strength helps to determine the effectiveness and behavior of a material when a stretching force acts on it. Mechanical properties of the polymers were evaluated based on tensile studies, the tensile strength of the polyesters MVO and NMO were 14.50 MPa and 2.90 MPa respectively. From this, MVO polymer possesses more tensile strength than NMO polymer [13].

3.7 SEM analysis

Scanning electron microscope is a multifold tool for the characterization of polymers and shows the information about the surface topography and properties of polymer [14]. It is possible to identify all the different elements that the polymers contain. Surface of both the MVO and NMO polymer composites have symmetric chain units in parallel and network patterns, among them Neem oil polymer has a good network pattern.

3.8 Swelling Property

The percentages of swelling in polyesters were studied systematically. The polymeric samples were allowed in alkaline and acidic medium for 72 hours at room temperature. All the polymeric samples show minimum swelling in both acid and alkaline medium.

3.9 Soil Burial Method

After soil burial test the Scanning electron micrographs of MVO and NMO are represented in figures 11 and 12. Hollow cavities and cracks appear in the SEM images of the polyesters. From the SEM pattern the biodegradation pattern was more in NMO polymer than the MVO polymer due to its low tensile and crosslink density. The IR spectrum of MVO polymer (after soil burial) clearly depicts the breaking of ester linkage and the complete degradation of the functional groups [15].

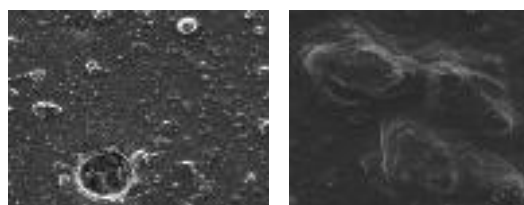


Figure11. SEM images of MVO after soil burial

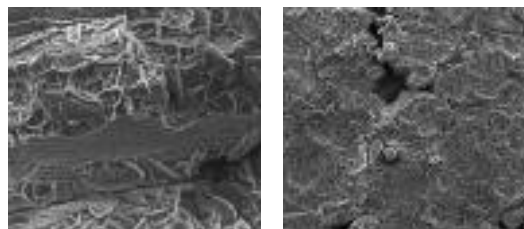


Figure12. SEM images of NMO after soil burial

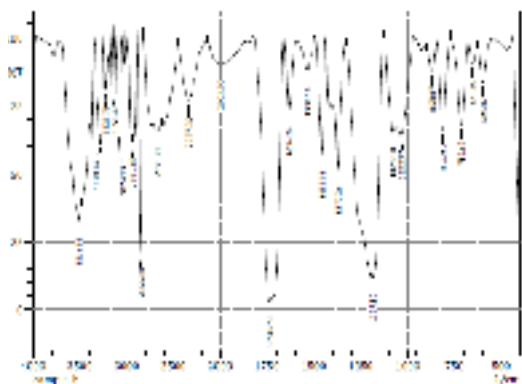


Figure 13. IR Spectra of MVO Polymer before the soil burial

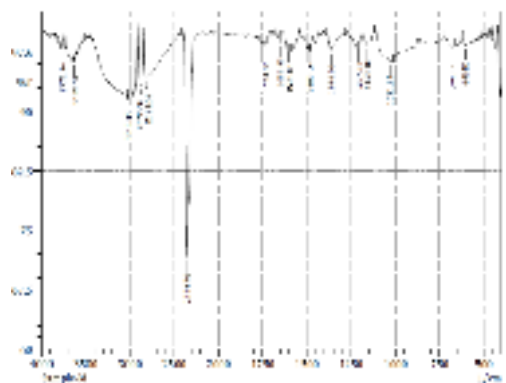


Figure 14. IR Spectra of MVO Polymer after the soil burial

4 CONCLUSIONS

Bio-based polymers were synthesized from MVO and NMO. From UV analysis; we infer that the MVO & NMO oils have ethylenic double bonds. In FTIR analysis, the presence of functional group is confirmed. Thermal analysis indicates that both the polymers are semi crystalline in nature. From the XRD patterns of the polymers, it shows that they are crystalline. SEM analysis shows that they have good network pattern. The antimicrobial activity of these bio polyesters is also realised to some extent. NMO polymer has more antibacterial activity. In this experimental investigation; we infer that they are biodegradable and environmental friendly.

ACKNOWLEDGEMENTS

The authors wish to thank the management and Principal, Sarah Tucker College (Autonomous), Tirunelveli for their support to undertake this research programme. The authors acknowledge the staff of CECRI, Karaikudi for the assistance in the evaluation of polymer samples.

REFERENCES

- [1] S. G. Tan & W.S.Chow, "Biobased Epoxidized Vegetable Oils and Its Greener Epoxy Blends: A Review," *Polymer-Plastics Technology and Engineering*, vol.49, no.15, pp. 1581-1590, Dec 2010.
- [2] Xujuan Huang, Xinxin Yang, He Liub, Shibin Shangb, Zhaosheng Caia, Kang Wuc, "Bio-based thermosetting epoxy foams from epoxidized soybean oil and rosin with enhanced properties," *Industrial Crops and Products*, vol.139, pp.111540, Jul 2019.
- [3] Montu Moni Bora, Riblu Deka, Nuruddin Ahmed, Dilip Kumar Kakati, "Karanja (*Milletia pinnata* (L.) Panigrahi)

- seed oil as a renewable raw material for the synthesis of alkyd resin," *Industrial Crops and Products*, vol.61, pp. 106–114, Nov 2014.
- [4] A.Sengupta, J.K.Gupta, J.Dutta and A.Ghosh, "The component fatty acids of chaulmoogra oil," *Journal of the Science of Food and Agriculture*, vol.24, no.6, pp.669-674, Feb 1973, doi:10.1002/jsfa.2740240606
- [5] N.V.Bringi, "Non-Traditional Oilseeds and Oils in India", Oxford & IBH Publishing Co. PVT. Ltd, ISBN 81-204-0190-5, pp.231-235, 1987.
- [6] Frank R. Stermitz, Peter Lorenz, Jeanne N. Tawara, Lauren A. Zenevicz and Kim Lewis, "Synergy in a medicinal plant: Antimicrobial action of berberine potentiated by 5-methoxyhydnocarpin, multi drug pump inhibitor", *Proceedings of the National Academy of Sciences*, vol.97, no.4, pp1433-1437, Feb 15, 2000, doi:10.1073/pnas.030540597.
- [7] M. S. Dahiya and Astha Pandey, "Extraction of Neem oil from Neem seeds of different geographical regions of India by two processes and study of their properties for standardization of parameters useful for coating of urea fertilizer," *European Journal of Biomedical and Pharmaceutical sciences (EJBPS)*, Vol.5, no.3, pp.565-570, Feb 2018.
- [8] P. Neerada and S. Mutta Reddy, "Neem oil emulsion formulation overview and further scope of improvements/development," *International Journal of Pharmacy and Biological Sciences*, Vol.8, no.2, pp.295-299, Apr-Jun 2018.
- [9] J. Shakina, A. Anita, K. Alamelu, "Polymers from renewable resources: polyester resin based upon acid anhydride-cured hydroxylated soybean oil," *Indian Journal of Science*, vol.8, no. 20, pp.44-54, Feb 2014.
- [10] T.P. Sathishkumar, P. Navaneethakrishnan, S. Shankar, R. Rajasekar and N. Rajini, "Characterization of natural fibre and composites-A review," *Journal of Reinforced Plastics and Composites*, vol.32, no.19, pp.1457-1476, Dec 2013, doi: 10.1177/0731684413495322
- [11] Birendra Pratap Singh, Jai Prakash Singh, Shruti Shukla and Shanti Sharma, "Synthesis and characterization of Inorganic Polymer Nano Composites," *Derchemica indica*, vol.3, no.2, pp.521-526, 2012.
- [12] Rohan S. Dassanayake, Sanjit Acharya and Nouredine Abidi, "Biopolymer-Based Materials from Polysaccharides: Properties, Processing, Characterization and Sorption Applications," *Advanced Sorption Process Applications*, 2019, doi:10.5772/intechopen.80898.
- [13] M.L.Ginju and S. Begila David, "Characteristic Studies on Novel Biodegradable Polyurethane Thin Films from Soyabean oil," *Oriental Journal of Chemistry*, vol.35, no.2, pp.877-884, Mar 2019, doi: http://dx.doi.org/10.13005/ojc/350252
- [14] J.Shakina, K.Sathiya Lekshmi and G.Allen Gnana Raj, "Synthesis and characterisation of novel cross linked biopolyesters from olive oil as eco-friendly biodegradable materials," *E-Journal of Chemistry*, vol.9, no.1, pp.181-192, 2012.
- [15] G.S.Prabha Littis Malar, S.Begila David, "Studies on polyester elastomers using palm olein for drug delivery," *International Journal of Scientific Engineering and Applied Science*, vol.1, no. 5, pp.1442-148, Aug 2015.



SYNTHESIS, CHARACTERIZATION AND THERMAL BEHAVIOR OF THERMOSETTING POLYESTERS FROM BIO-DEGRADABLE PLANT OIL

T. Sahaya Maria Jeyaseeli^a, I. Antony Danish^b, J. Shakina^{c*}

^aDepartment of Chemistry, Sarah Tucker College, (Autonomous) Tirunelveli - 627 007, affiliated to Manonmaniam Sundaranar University, Tirunelveli, Tamilnadu, India.

^bAssistant Professor, Department of Chemistry, Sadakathullah Appa College, (Autonomous) Tirunelveli - 627 011, Affiliated to Manonmaniam Sundaranar University, Tirunelveli, Tamilnadu, India

^cAssociate Professor, Department of Chemistry, Sarah Tucker College, (Autonomous) Tirunelveli - 627 007, affiliated to Manonmaniam Sundaranar University, Tirunelveli, Tamilnadu, India.

*Corresponding author E-mail: shakinajudson@gmail.com

Abstract

Thermal Analysis (TA) is an essential analytical technique in the polymer research. In polymer science Thermal Characterization of Polymers is an extreme analysis and brief assessment of the application of thermal analysis this technique is used for evaluation of comparative thermal stability of different polymers. The following materials were synthesized from Odal, Chennakai, Neem and Thennamarakudi oils. They were synthesized and characterized by UV-Visible and IR Spectra. NMR spectral studies carried out to identify the nature of the polymer formed. SEM analysis confirmed that the polymer was biodegradable in nature. The thermal degradation at different time intervals was analyzed by TG-DTA analysis. TGA analysis was conducted to identify the thermal degradation patterns and to determine product performance. The cross-linking ability of the resins was checked by DSC analysis.

Keywords: Polymer, Cross- linking, Biodegradability, Thermal analysis, Degradation,

Introduction

Researchers are attracted towards polymeric materials due to economic and environmental concerns. The utilization of renewable resources for the production of polymeric materials can reduce the plastic pollution.ⁱ Vegetable oils are considered as good starting materials for polymer production. Due to ready availability, their low cost and versatile applications, vegetable oils are encouraging renewable resources for polymers. The plant oils are composed of triglycerides which can be modified using the reactivity of the functional groups in their structure.ⁱⁱ Synthesis of resins from plant oil involves chemical modifications of unsaturated oils to undergo crosslinking. This cross linking was responsible for good

mechanical and thermal properties of the resins.ⁱⁱⁱ

Synthesis of polymers from renewable resources of plants is attractive because of increasing price of petroleum.^{iv} Biodegradable and inexpensive polymers are obtained from low cost and readily available raw materials.^v Plant oil is a biodegradable triglyceride with unsaturation.^{vi} It has unsaturated double bonds which are easily reactive and induce functional groups including epoxy, hydroxyl and other more active double bonds. The chemical modification of the triglyceride of plant oil is preferred, enabling the synthesis of oligomeric triglyceride resin in the way to target polymeric materials. The chemical transformation of the non-edible oil triglyceride affords a wide variety of monomers for the synthesis cross linked structural polymers. The modification of triglycerides can be performed using the reactivity of the functional groups in their structure.

Experimental

Materials

Odal, Chennakai, Neem and Thennamarakudi oils were purchased from local market, Formic acid (97%) (Rankem), Hydrogen peroxide (30%) (Rankem) were used in the first step fractionalization. Maleic anhydride (Rankem) and Morpholine (Rankem). Benzoyl peroxide (Rankem) was used as a radical initiator and N, N-Dimethyl aniline (Rankem) was used as accelerator in the curing process. Styrene (Rankem) was used as a vinyl co-monomer.

Synthesis of plant oil polyol

100 g of Odal / Chennakai / Neem / Thennamarakudi oil was taken in a three necked flask fitted with condenser and thermometer. 100 ml of 97% formic acid and 55 ml of 30% hydrogen peroxide was added and the reaction mixture was vigorously stirred over 16h. Ice water bath was used externally to keep the temperature below 40°C. The resulting emulsion was poured into a separating funnel and extracted with ether. The ether layer was dried over anhydrous sodium sulphate and the resulting product was polyol resin from Odal / Chennakai / Neem / Thennamarakudi oil.

Synthesis of polyesters

The polyol resin was heated in a three necked flask and maleic anhydride was added in 1:2 ratio at 70°C. Morpholine was used as a catalyst. After 2 hours a golden yellow viscous liquid formed it indicates the formation of oligomerised Odal / Chennakai / Neem / Thennamarakudi oil fumarate resin.

Synthesis of polyester film from oligomerised Odal / Chennakai / Neem / Thennamarakudi oil fumarate resin and co-monomer styrene

Synthesis of aliphatic polyester was carried out by free radical addition polymerization reaction by using the homopolymer (oligomerised Odal / Chennakai / Neem / Thennamarakudi oil fumarate resin) and styrene at different concentration using benzoylperoxide as catalyst and Dimethylaniline as accelerator. The viscous liquid is transferred in to glass mould coated with silicon oil at room temperature. The polyester thin films were synthesized from homopolymer and styrene. Finally the yellow colored polyesters sheets were removed from the mould.

Characterization of polymer

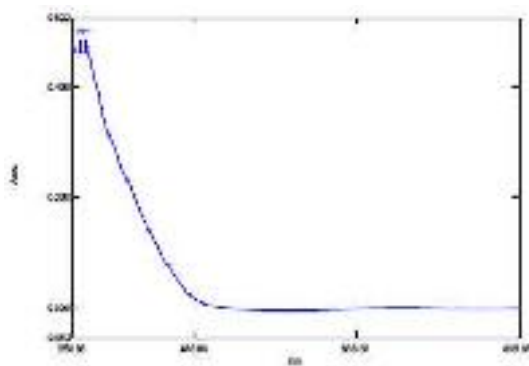
Double-beam UV/visible spectrometer is used to verify the characteristic absorption of the polymer composites. Fourier transform infrared (FTIR) spectra of polymers were obtained using Shimadzu FT-IR spectrophotometer using KBr pellet at wave-lengths between 4000 cm^{-1} and 400 cm^{-1} at 27°C. ATR spectra were obtained using BRUKER Optic GmbH FTIR SPECTROMETER with KBR crystal in the range of 4000 cm^{-1} – 400 cm^{-1} . The ¹H-NMR spectra for epoxy resin, polyols and pre-polymers were dissolved in CDCl₃ and recorded using BRUKER AVANCE III, 400 MHz FT NMR SPECTROPHOTOMETER. The

chemical shift in ppm for ^1H NMR Spectra were obtained relative to TMS as internal reference. TG/DTA thermo grams of the post-polymers were obtained at a scanning speed of $10^\circ\text{C min}^{-1}$ in the range of 40°C - 700°C under the flow of nitrogen gas using PERKIN ELMER, DIAMOND TG/DTA. The SEM analysis of the polymers was obtained using VEGA3TESCAN.

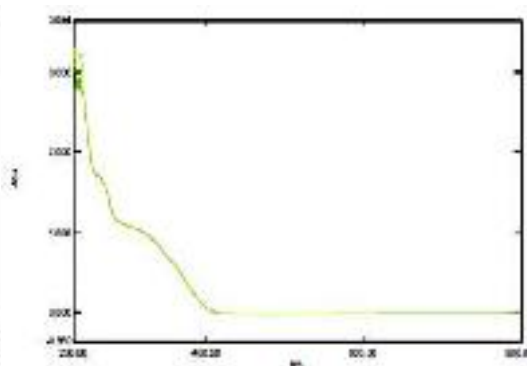
Result and discussion

UV Analysis

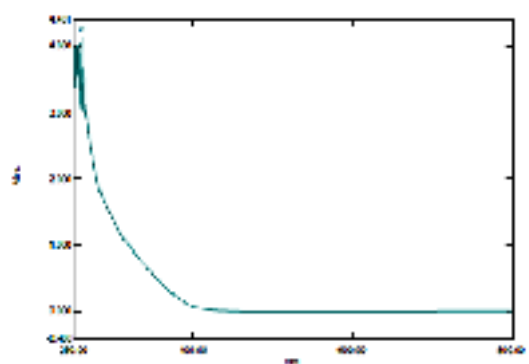
Figure 1 shows the UV spectra of Odal/ Chennakai/ Neem / Thennamarakudi oil, hydroxylated triglyceride oil resins and O-PTF resins. They have been investigated (230 nm - 800 nm). The oil samples (Odal, Chennakai, Neem and Thennamarakudi) showed an electronic absorption band around 238,295.50,262 and 270.50 nm respectively. The hydroxylated resins exhibited a blue shift when compared with the corresponding parent oil which is attributed to the substitution of hydroxyl group at the unsaturated moiety.^{vii}



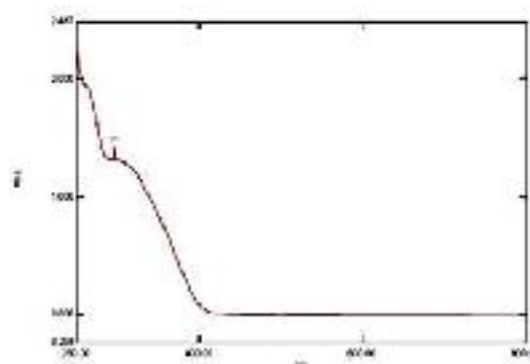
(a)



(b)



(c)



(d)

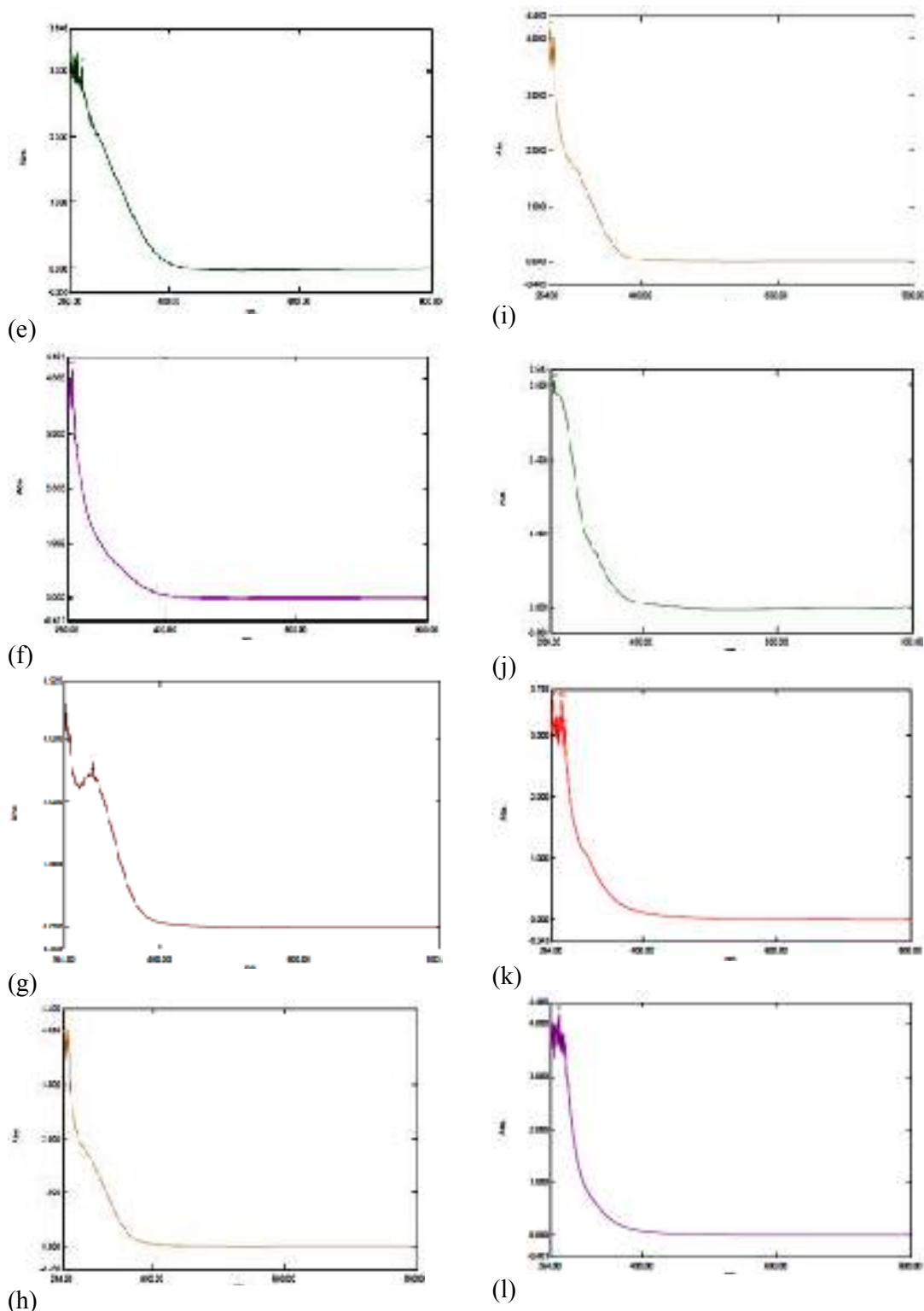
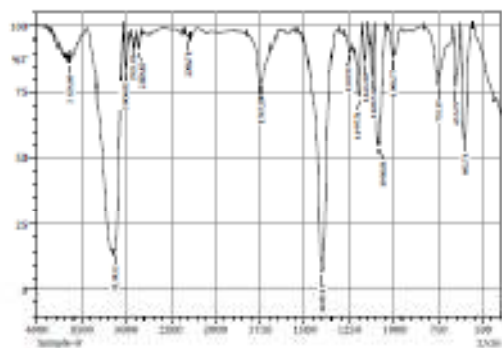


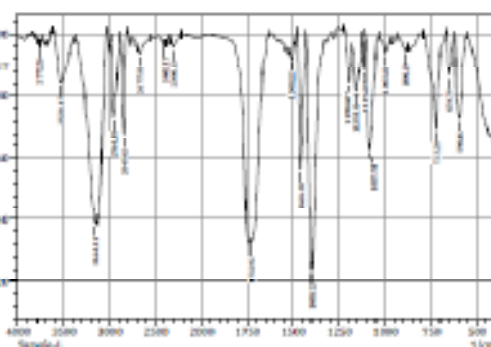
Figure 1. UV Spectrum of (a) Odal oil (b) Hydroxylated Odal oil (c) Odal Resin (d) chennakai oil (e) Hydroxylated Chennakai oil (f) Chennakai Resin (g) Neem oil (h) Hydroxylated Neem oil (i)Neem Resin (j) Thennamarakudi oil (k)HydroxylatedThennamarakudi oil (l) Thennamarakudi Resin

FTIR spectral analysis

Figure 2 shows the IR spectra of Odal/ Chennakai/ Neem / Thennamarakudi oil, hydroxylated triglyceride oil and resins. They have been investigated between 500 cm^{-1} to 4000 cm^{-1} . In hydroxylated triglyceride resins, FT-IR spectra showed a strong absorption band at 3772.5 , 3770.58 , 3565.17 and 3172.68 cm^{-1} respectively, due to the presence of free –OH group in the molecule. The corresponding peaks are completely reduced in the resins indicates the entire OH group get substituted.^{viii}



(a)

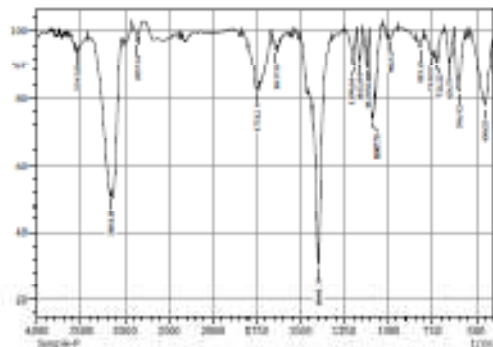


(b)

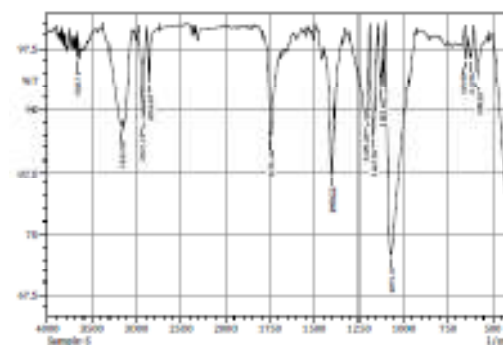
(c)((((((((

(c)

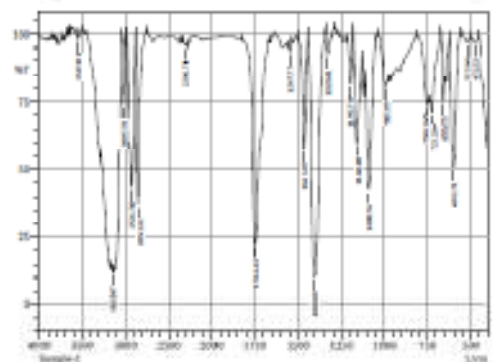
ccccccg



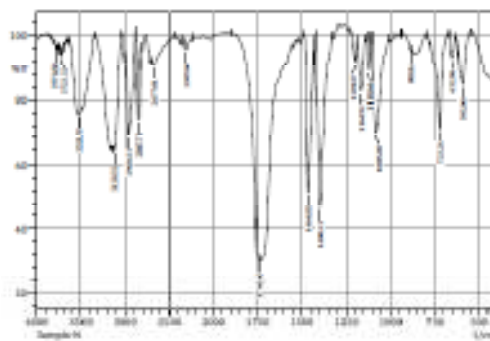
(d)



(g)



(e)



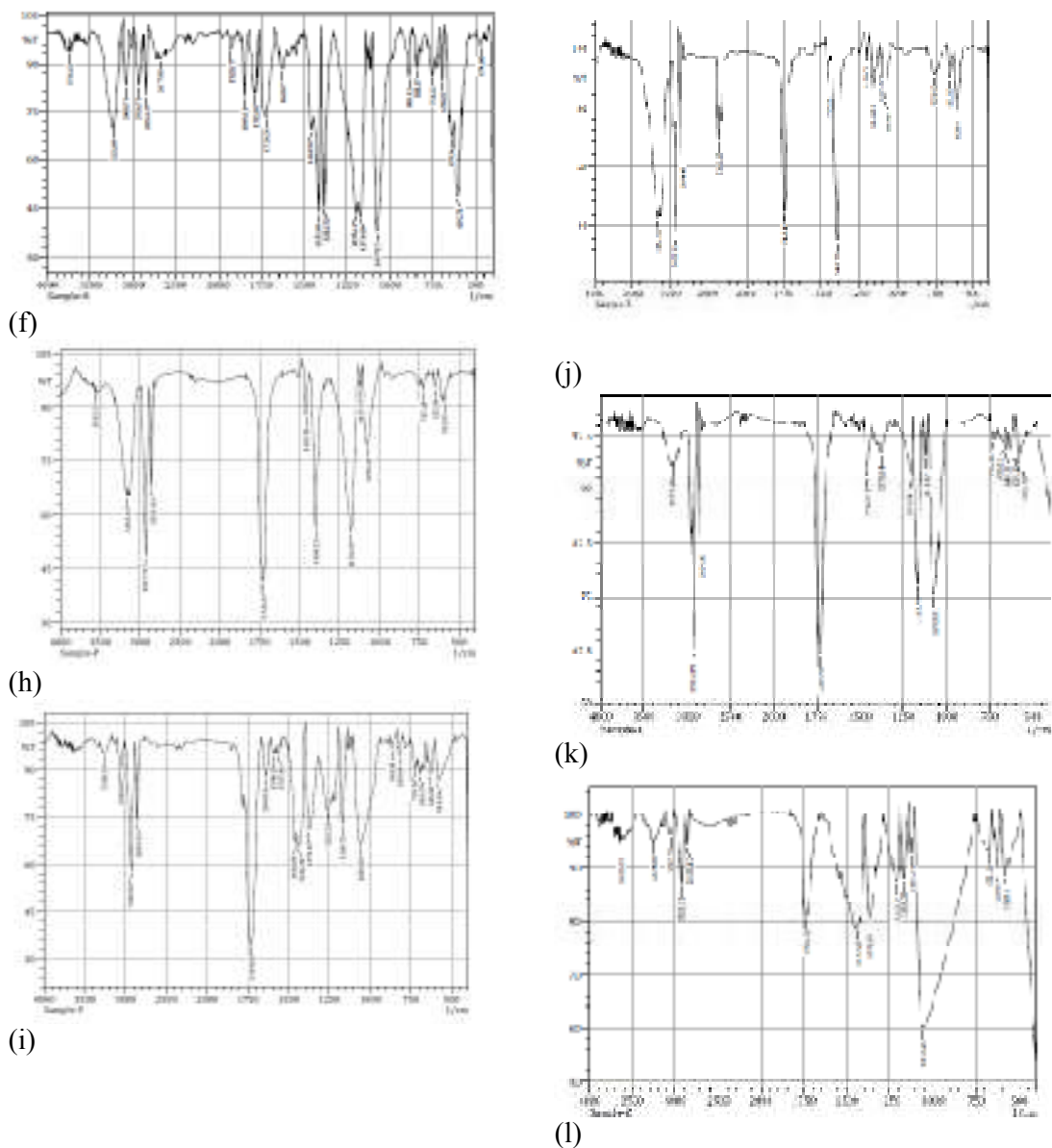


Figure 2. IR Spectrum of (a) Odal oil (b) Hydroxylated Odal oil (c) Odal Resin (d) Chennakai oil (e) Hydroxylated Chennakai oil (f) Chennakai Resin (g) Neem oil (h) Hydroxylated Neem oil (i) Neem Resin (j) Thennamarakudi oil (k) Hydroxylated Thennamarakudi oil (l) Thennamarakudi Resin

Table1: FT-IR probable assignment of Odal and Chennakai oil

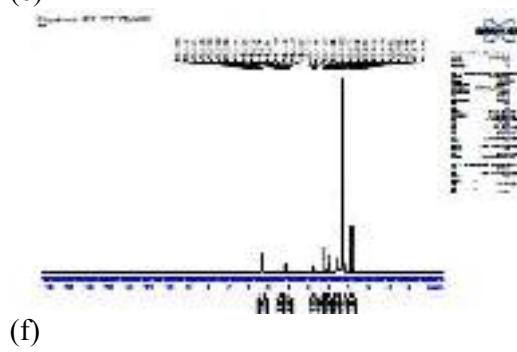
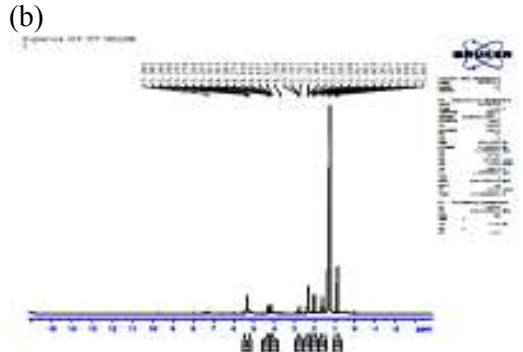
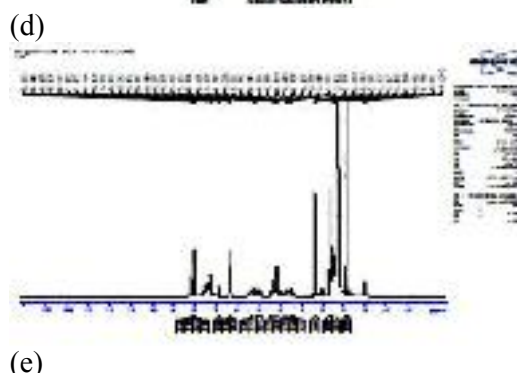
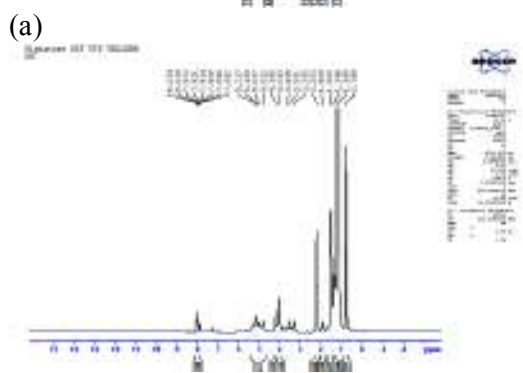
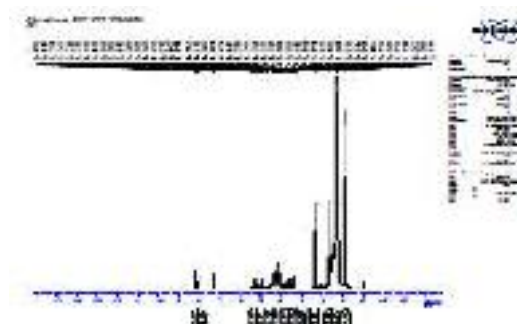
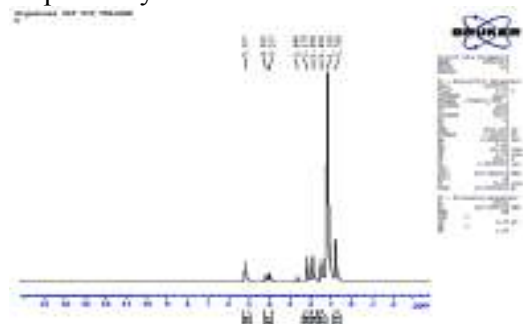
Probable assignment	Odal oil (cm ⁻¹)	Hydroxylated Odal oil (cm ⁻¹)	Odal Resin (cm ⁻¹)	Chennakai oil (cm ⁻¹)	Hydroxylated Chennakai oil (cm ⁻¹)	Chennakai Resin (cm ⁻¹)
-CH ₂ Group	2925.81	2961.49	2961.49	2926.78	2960.53	2926.78
-C- O Group in GM	2306.71	2308.71	2854.34	2852.52	2347.21	2853.49
C=O in esters	1747.39	1732.92	1751.24	1746.42	1746.42	1783.07
Terminal CH ₃ Groups	1197.71	1119.6	1199.64	1195.78	1464.83	1199.64
Carboxyl Group of acids	1163	1159.14	1401.19	1160.1	1164.92	1171.68
-CH-CH- Stretching	1086.81	1087.78	1087.78	1088.74	1085.85	1077.17
CH ₂ -sequences of the aliphatic chains	752.19	723.26	748.33	750.26	723.26	751.22
-OH Group	3634.6	3772.5	3545.88	3547.81	3770.58	3736.82

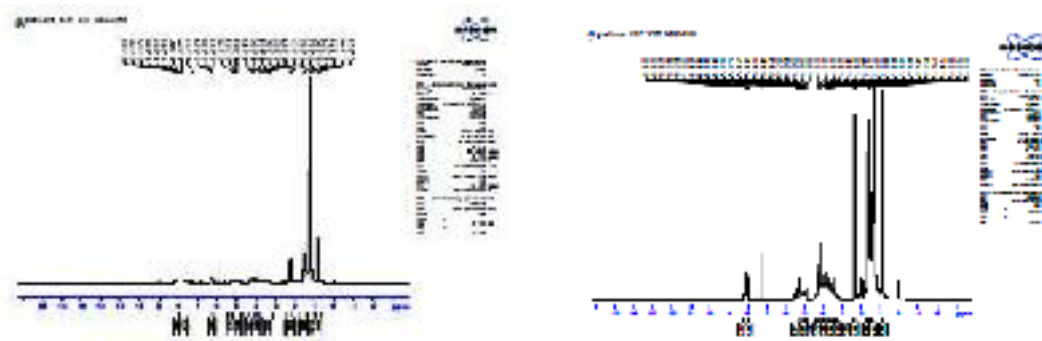
Table2: FT-IR probable assignment of Neem and Thennamarakudi oil

Probable assignment	Neem oil (cm ⁻¹)	Hydroxylated Neem oil (cm ⁻¹)	Neem Resin (cm ⁻¹)	Thennamarakudi oil (cm ⁻¹)	Hydroxylated Thennamarakudi oil (cm ⁻¹)	Thennamarakudi Resin (cm ⁻¹)
-CH ₂ Group	2927.74	2927.74	2929.67	2925.81	2926.78	2928.71
-C- O Group in GM	2854.45	2855.45	2855.42	2854.4	2854.45	2855.42
C=O in esters	1745.46	1726.17	1729.06	1746.42	1730.99	1734.85
Terminal CH ₃ Groups	1209.28	1400.22	1460.01	1196.75	1116.71	1168.78
Carboxyl Group of acids	1167.82	1178.43	1374.19	1162.03	1145.75	1132.14
-CH-CH- Stretching	1072.35	1076.21	1058.85	1086.81	1073.31	1055.95
CH ₂ -sequences of the aliphatic chains	649	725.18	723.26	753.15	723.26	671.18
-OH Group	3658.71	3565.17	3268.15	3161.11	3172.68	3635.57

¹H NMR spectral studies

In this study, the NMR spectrum of plant oils, the peak at 4.0-5.2 ppm shows the presence of methylene protons. The peak at 2.6-2.1 ppm indicate the presence of hydrogen in ethylenic bond. The peak at 5.2 ppm shows the olefin proton present in plant oils.^{ix} The chemical shift associated at 4.1 ppm shows methylene protons of ester associated with triglyceride molecule. In the ¹H-NMR spectrum of polyol of plant oils show the presence of hydroxyl group at 8.0 ppm. Thus the formation of polyol confirmed from these studies. The chemical shift at lower region from 5.2-0.7 ppm supports oleic and saturated fatty acids respectively.

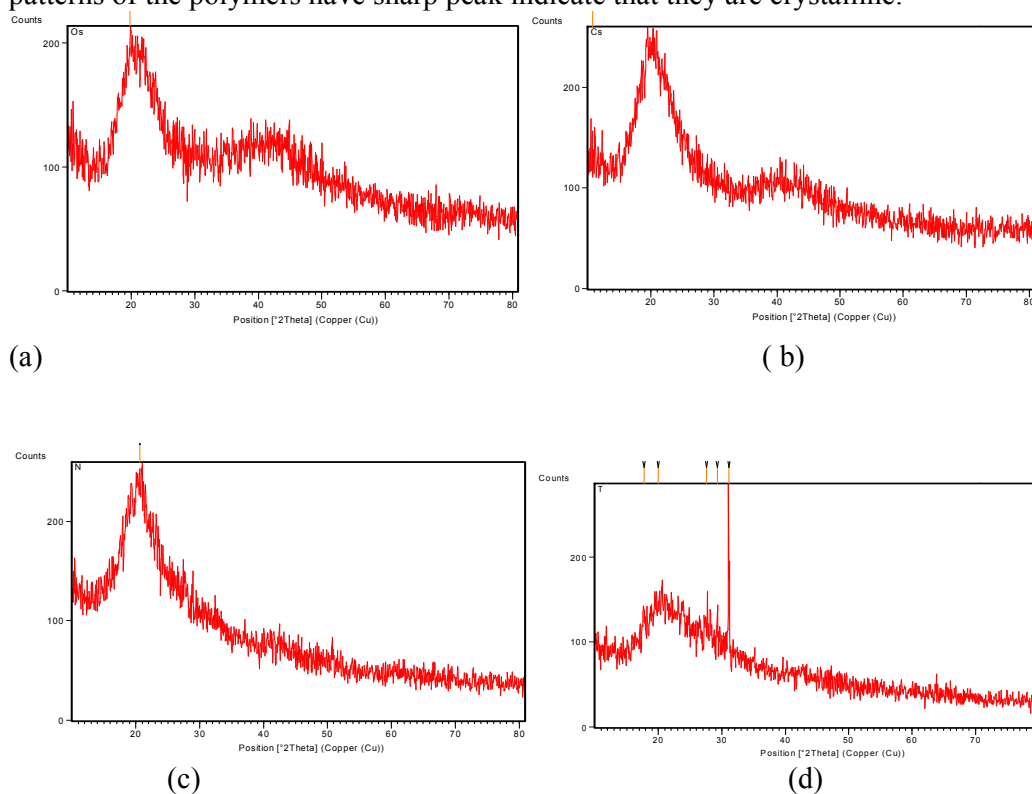




(g) (h)
Figure3. NMR Spectrum of (a) Odal oil (b) HydroxylatedOdal oil (c) Chennakai oil (d) HydroxylatedChennakai oil (e) Chennakai Resin (f) HydroxylatedNeem oil (g) Neem Resin (h) Thennamarakudi oil

XRD pattern

XRD is primary techniques to determine the degree of crystallinity in polymers.^x The size of crystallites can be determined from XRD patterns using Scherer's equation. XRD patterns of the polymers have sharp peak indicate that they are crystalline.



(a) (b) (c) (d)
Figure4. XRD patterns of (a) Odal oil (b) Chennakai oil(c) Neem oil (d) Thennamarakudi oil

Thermal analysis:

The Odal polymer was stable up to 80 °c with no significant weight loss; the initial weight loss was observed at 359.39°c, indicating the loss of volatiles and moistures.^{xi} Significant

weight loss began at 397.15⁰c due to the degradation of the resin. When the temperature reached 432.48⁰c, weight loss was recorded. The residual mass is around 0.07298 mg .From this we see that polymers are more resistive to temperature increasing. The residue percentage is 1.200%.

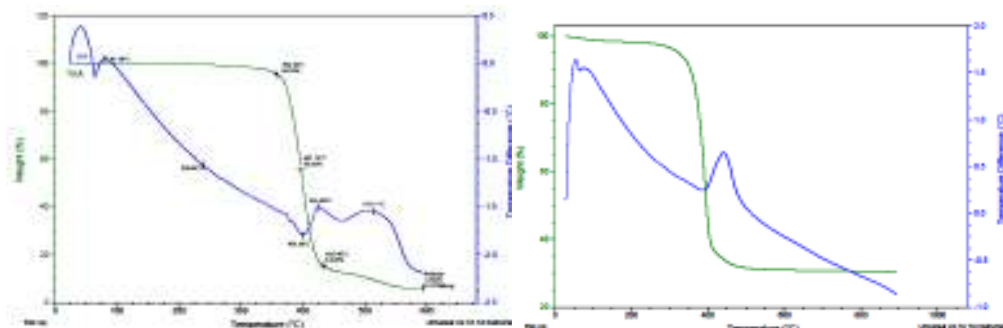


Figure 5. TGA, DTA thermograms of Odal polymer and Chennakai polymer

The Chennakai polymer was stable up to 100 °c with no significant weight loss; the initial weight loss was observed at 355.209⁰c, indicating the loss of volatiles and moistures. Significant weight loss began at 400.03⁰c due to the degradation of the resin. When the temperature reached 452.76⁰c, weight loss was recorded. The residual percentage 1.454%.

The Neem polymer was stable up to 120 °c with no significant weight loss; the initial weight loss was observed at 243.11⁰c, indicating the loss of volatiles and moistures. Significant weight loss began at 334.99⁰c due to the degradation of the resin. When the temperature reached 431.54⁰c, weight loss was recorded. The residual mass is around 0.5444 mg. The residue percentage is 7.434%. Thermal analysis indicates that both the polymers are semi crystalline in nature. The peak for the Neem polymer is 539.26⁰c, indicating the fastest cure for this resin will occur at the temperature. The onset of the cure peak for this resin is 534.98⁰c and the total heat of the reaction is 4469J/g

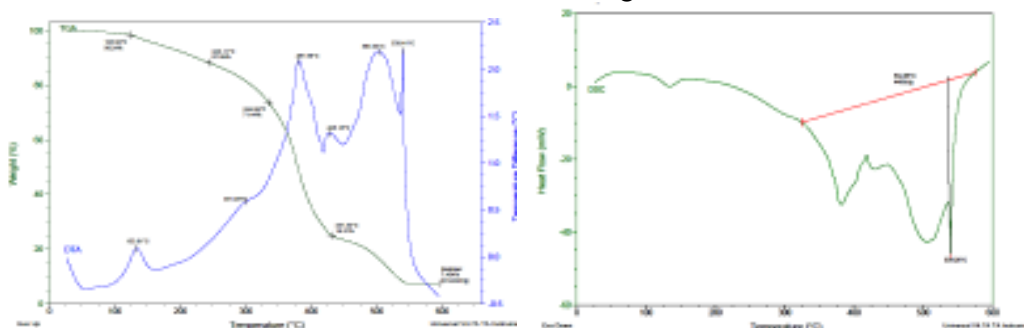


Figure 6. TGA, DTA thermograms of Neem polymer

The Thennamarakudi polymer was stable up to 120 °c with no significant weight loss; the initial weight loss was observed at 243.11⁰c, indicating the loss of volatiles and moistures. Significant weight loss began at 334.99⁰c due to the degradation of the resin. When the temperature reached 431.54⁰c, weight loss was recorded. The residual mass is around 0.5444 mg. The residue percentage is 7.434. The peak for the sample is 501.21⁰c, indicating the fastest cure for this resin will occur at the temperature. The onset of the cure peak for this resin is 473.09⁰c and the total heat of the reaction is 3508J/g

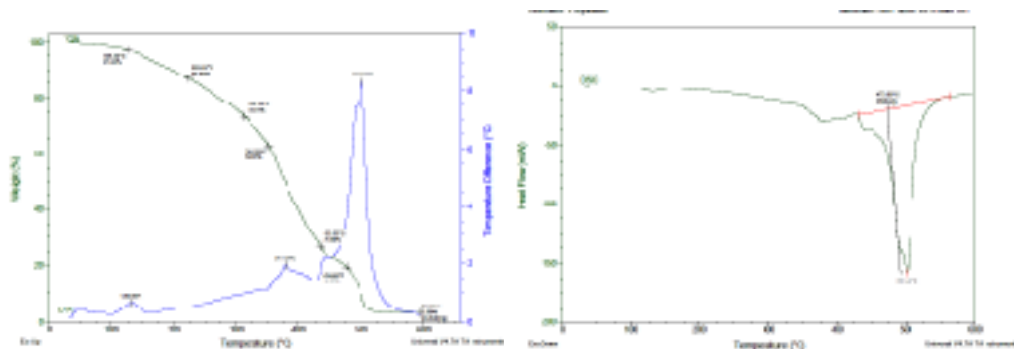


Figure7. TGA, DTA thermograms of Thennamarakudi polymer

Thermal analysis indicates that the polymers are semi crystalline in nature.

SEM analysis

Scanning electron micrographs of Odal, Chennakai, Neem and Thennamarakudi oil polymers are shown in figure8. Surface SEM images of the polyesters have symmetric chain units in parallel, uniformly distributed and has a good network pattern.^{xii}

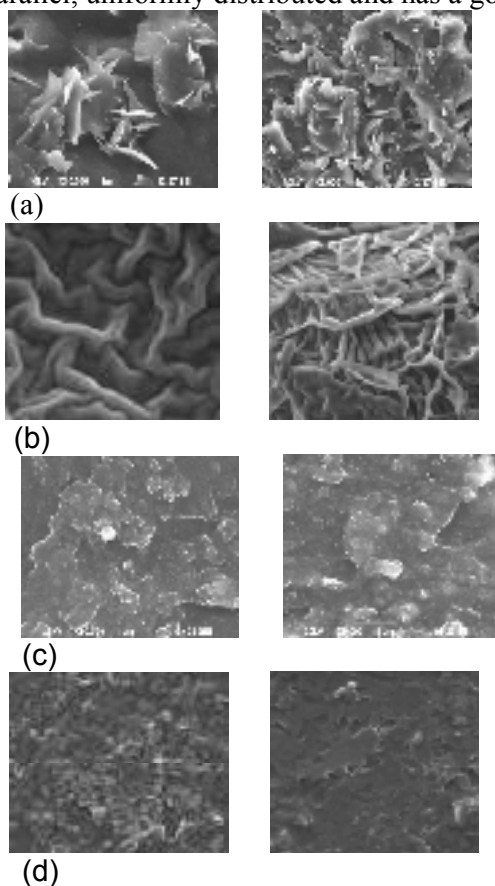


Figure8. SEM photographs of (a) Odal oil polymer (b) Chennakai polymer (c) Neem polymer (d) Thennamarakudi polymer

Conclusion

We have synthesized plant oil polymers from Odal, Chennakai, Neem and Thennamarakudi oils were synthesised. The reaction mechanism was determined by FTIR and H^1 NMR spectroscopy. XRD patterns show that they are crystalline. SEM analysis shows that they have good network pattern. Thermal analysis confirms the thermal stability of the polymers. In this experimental investigation, it is possible to develop low cost polyesters from naturally available non-edible oil for consumer applications.

Acknowledgements

The authors wish to thank the management and Principal, Sarah Tucker College (autonomous), Tirunelveli for their support to undertake this research programme. The authors acknowledge the staff of CECRI, Karaikudi for the assistance in the evaluation of polymer samples.

References

- i. K.PriyaRajini, S.Begila David, Synthesis and comparative study of novel cross linked bio polymers from linseed oil, *Int. Journal of Engineering Research and Applications*,**5**,9(2015)
- ii. Fana Teffera, Michael J. Forrester, and Eric W. Cochran *Plant Oil-Based Polyether. Bio-Based Plant Oil Polymers and Composites*, 87 (2016)
- iii. Sachin Mane, Surendra Ponrathnam and Nayaku Chavan* Effect of Chemical Cross-linking on Properties of Polymer Microbeads: A Review ,**3**,473(2015)
- iv. Kunwei Liu , Chaoqun Zhang , and Samy A. Madbouly Fiber Reinforced Plant Oil-Based Composites *Bio-Based Plant Oil Polymers and Composites*, 167 (2016)
- v. Ginju.M.I and Dr.S .Begila David, Characteristic Studies on Novel Biodegradable Polyurethane Thin Flims from Soyabean Oil, *International Journal of Advanced Scientific Research and Management*, 4(219)
- vi. Y T Li,L T Yang, H Zhang,z j Tang,Synthesis and properties of a novel bio-based polymer from modified soybean oil,*Materials Science and Engineering* ,170(2017)
- vii. J.Shakina, K.SathiyaLekshmi and G.AllenGnana Raj, Synthesis and characterisation of novel cross linked biopolyesters from olive oil as eco-friendly biodegradable materials. *E-Journal of Chemistry* **9**, 181(2012)
- viii. G.S.PrabhaLittis Malar, S.Begila David, Stydies on Polyester elastomers using Palmolein for Drug delivery, *International Journal of Scientific Engineering and Applied Science* ,**1**(2015)
- ix. M.L.Ginju, Dr.S.Begila David, Synthesis and Characterisation of Novel CrosslinkedBiopolyurethane from Soyabean oil as eco-friendly Biodegradable Material,*International Journal of Interdisciplinary Research and Innovations***6**,423(2018)
- x. Obi Reddy, K., Sivamohan Reddy, G., Uma Maheswari, C., VaradaRajulu, A., & MadhusudhanaRao, K. Structural characterization of coconut tree leaf sheath fiber reinforcement. *Journal of Forestry Research*, **21**, 53(2010)
- xi. J.Shakina, A.Anita, K.Alamelu, Polymers from renewable resources: polyester resin based upon acid anhydride-cured hydroxylated soybean oil, *Indian Journal of Science*, **8**, 44(2014).
- xii. G.S.PrabhaLittis Malar, S.Begila David, Synthesis and Characterization of Biodegradable Polyesters Based on Sesame Oil for Biomedical Field, *International Journal of Science and Research* ,**4** (2015).

Received on December 4, 2019.

DEVELOPMENTAL STUDIES OF BIODEGRADABLE PRESSURE SENSITIVE ADHESIVES AND FIBER REINFORCED POLYMER FROM NEEM OIL

T. SAHAYA MARIA JEYASEELI¹, I. ANTONY DANISH² AND J. SHAKINA³

¹Department of Chemistry, Sarah Tucker College, (Autonomous) Tirunelveli - 627 007, affiliated to Manonmaniam Sundaranar University, Tirunelveli, Tamilnadu, India.

²Assistant Professor, Department of Chemistry, Sadakathullah Appa College, (Autonomous) Tirunelveli - 627 011, Affiliated to Manonmaniam Sundaranar University, Tirunelveli, Tamilnadu, India

³Associate Professor, Department of Chemistry, Sarah Tucker College, (Autonomous) Tirunelveli - 627 007, affiliated to Manonmaniam Sundaranar University, Tirunelveli, Tamilnadu, India.

*Corresponding author E-mail: shakinajudson@gmail.com Mobile Number: 9384218533

ABSTRACT

In this experimental study, there are different composite samples were fabricated by using coconut fiber using oligomeric polymer resin. Scanning electron microscopy (SEM) analysis is carried out to study the fiber matrix interfaces and analyse the structure of the fractured and water absorbed surfaces. The lower weight of FRP materials makes handling and installation significantly easier than in case of steel plates. Degradation studies show that the pressure sensitive adhesives (PSA) is biodegradable. These may be suitable for non occlusive PSA tapes there by decrease the level of skin irritation considerably and also minimize the incidence of bacterial infection. It allows the migration and transmission of moisture. It also serves as a bacteriostatic-prevent the growth of bacteria on the plastic surface. The results show that Neem oil - based PSA films and tapes have great potential to replace petro-based PSAs for a broad range of applications including flexible electronics and medical devices because of their thermal stability, transparency, chemical resistance, and potential biodegradability from triglycerides.

Keywords: Green materials, Polymer, Transparency, Degradation, Moisture

1. INTRODUCTION

Plant fibres can also be regarded as fillers to replace the more expensive polymers and improve the green credentials of the final composite parts. The concern for the environmental pollution and the prevention of resources has attracted researchers to develop new eco-friendly green materials based on sustainability principles. Synthesis of polymers from renewable resources of plants is attractive because of increasing price of petroleum. Biodegradable and inexpensive polymers are obtained from low cost and readily available raw materials.

Neem oil is a biodegradable triglyceride with unsaturation. It has unsaturated double bonds which are easily reactive and induce functional groups including epoxy, hydroxyl and other more active double bonds. The chemical modification of the triglyceride of Neem oil is preferred, enabling the synthesis of oligomeric triglyceride resin in the way to target polymeric materials. The chemical transformation of the non- edible oil triglyceride affords a wide variety of monomers for the synthesis of cross linked structural polymers. The modification of triglyceride can be performed using the reactivity of the functional groups in their structure.

2. EXPERIMENTAL

2.1 MATERIALS

Neem oil (NMO) was purchased from local market, Formic acid (97%) (Rankem), Hydrogen peroxide (30%) (Rankem) were used in the first step functionalization. Maleic anhydride (Rankem) and Morpholine (Rankem). Benzoyl peroxide (Rankem) was used as a radical initiator and N, N-Dimethyl aniline (Rankem) was used as accelerator in the curing process. Styrene (Rankem) was used as a vinyl co-monomer.

2.2 SYNTHESIS OF NMO POLYOL

100 g of NMO was taken in a three necked flask fitted with condenser and thermometer. 100 ml of 97% formic acid and 55 ml of 30% hydrogen peroxide was added and the reaction mixture was vigorously stirred over 16h. Ice water bath was used externally to keep the temperature below 40°C. The resulting emulsion was poured into a separating funnel and extracted with ether. The ether layer was dried over anhydrous sodium sulphate and the resulting product was polyol resin from NMO.

2.3 SYNTHESIS OF POLYESTERS

The polyol resin was heated in a three necked flask and maleic anhydride was added in 1:2 ratio at 70°C. Morpholine was used as a catalyst. After 2 hours a golden yellow viscous liquid formed it indicates the formation of oligomerised NMO fumarate resin.

2.4 SYNTHESIS OF POLYESTER FILM FROM OLIGOMERISED NMO FUMARATE RESIN AND CO-MONOMER STYRENE

Synthesis of aliphatic polyester was carried out by free radical addition polymerisation reaction by using the homopolymer (oligomerised NMO fumarate resin) and styrene at different concentration using benzoyl peroxide as catalyst and Dimethyl aniline as accelerator. The viscous liquid is transferred in to glass mould coated with silicon oil at room temperature. The polyester thin film of different concentration such as 1:0.5, 1:1 and 1:2 were synthesised from homo polymer and styrene. Finally the yellow coloured polyesters sheets were removed from the mould.

2.5 CHARACTERISATION OF RESINS

The UV and FTIR analysis were carried out for NMO, hydroxylated NMO and also the resin. The ¹H-NMR spectra for epoxy resin, polyols and pre-polymers were dissolved in CDCl₃ and recorded using BRUKER AVANCE III, 400 MHz FT NMR SPECTROPHOTOMETER. Cured samples were also checked to see the degree of curing. The Thermo Gravimetric Analysis (TGA) was done by using TGA instrument. The Differential Scanning Calorimetry (DSC) analysis was done by a TA instrument.

3. RESULT AND DISCUSSION

3.1 UV ANALYSIS

The UV spectra of NMO, hydroxylated triglyceride oil and the resin have been investigated (220 nm - 800 nm). The NMO sample showed an electronic absorption band around 239 nm. The hydroxylated oil exhibited a blue shift when compared with the corresponding parent oil which is attributed to the substitution of hydroxyl group at the unsaturated moiety. There is also decrease in the absorbance in comparison with that of parent oil is due to the substitution of the hydroxyl group at the olefinic double bond and also distortion of geometry. The substantial red shift in electronic absorption exhibited in the resin due to the substitution of

the fumarate group and also due to the distortion in geometry of the molecule by the introduction of fumarate group.

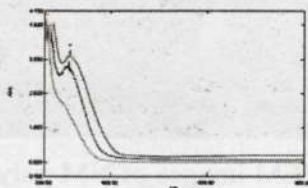


Fig.1. UV Spectra of NMO, Hydroxylated NMO and resin

3.2 IR SPECTRA

An invaluable tool in organic structure determination and verification involves the class of electromagnetic radiation (EM) with frequencies between 4000 and 400 cm^{-1} (wave numbers). The category of EM radiation is termed infrared (IR) radiation, and its application to organic chemistry is known as IR spectroscopy. Radiation in this region can be utilized in organic structure determination by making use of the fact that it is absorbed by inter atomic bonds in organic compounds. The samples were analysed over the range 500 cm^{-1} to 4000 cm^{-1} . The strong peaks absorbed at 1732.92 cm^{-1} indicate that the surface of the polymer is comprised predominantly with ester linkages.

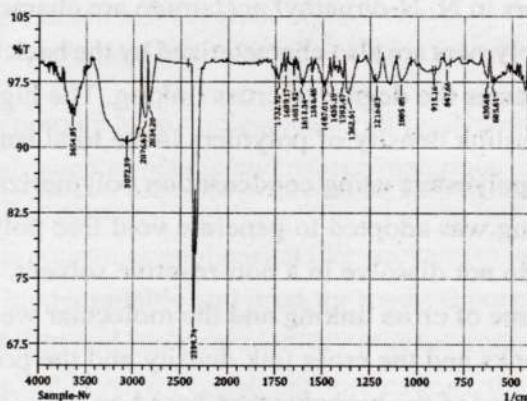


Fig.2. IR Spectra of NM polymer

Probable assignment	Neem Polymer
-C-O- Group in GM	2359.74
C=O esters	1732.92
Terminal -CH ₃ -Groups	1487.01
Carboxy Group of acids	1362.61
-CH-CH- Streching	1085.85
CH ₂ -sequence of the aliphatic chains	630.68

Table1.FT-IR probable assignment

3.3 SEM ANALYSIS

Scanning electron microscope is a technique to find out the surface morphology of the samples. SEM micrographs show the strong bonding in polymer.



Fig.3. SEM images of NM polymer

3.4 SWELLING PROPERTIES

Cross link density and voids play an important role in determining the properties of crosslinked polymers. The effective cross link density is the total sum of chemical and physical cross links. The swelling studies of the newly prepared polyesters have been carried out in solvents having different solubility parameters, methanol (13.5), ethanol (12.3), dimethylacetamide (10.8), tetra hydro furan (9.3) and dimethyl formamide (12.1). All these polyesters undergo slight swelling in solvents methanol, ethanol, tetrahydrofuran, dimethyl formamide and benzene and undergo appreciable swelling in and dimethyl acetamide alone. Low swelling in solvents methanol, ethanol, tetrahydrofuran, N, N-dimethyl formamide and benzene reveal that present polyesters are also cross linked. Due to the higher degree of swelling (swelling coefficient) only in N, N-dimethyl acetamide, it is understood that the solubility parameter of the new polyester is 10.8. The value of the swelling coefficient (degree of swelling) of the polyesters in N, N-dimethyl acetamide are characteristic of a cross linked system. Molecular weights of cross linked polymers are also characterized by the back bone chain length. The molecular weight between cross links M_c indicates the degree of cross linking. The higher value of M_c , the lower is the crosslink density. The effective crosslink density of polymers is the total sum of chemical cross links. Plant oils were used to prepare biostable polyesters using condensation polymerization. In the present studies addition polymerization and cross linking was adopted to generate void free polyesters. The present cross linked biopolyesters CPB only swell and do not dissolve in a non-reactive solvent. The degree of swelling in a non-reactive solvent determines the degree of cross linking and the molecular weight between the cross links. The molecular weights between cross links and the cross link density and the present materials confirm the cross linked character. The cross link density of the biopolyesters based on poly (NMO fumarate) is comparatively higher than the other oil based polyesters. The cross link density of the cross linked biopolyesters based on styrene is comparatively higher than the corresponding vinyl based materials.

3.5 STABILITY IN ORGANIC SOLVENTS

The non – reactive chemical environment influences the stability of polyesters by solvation and discussion of polymers. Diethyl ether which is compatible for dissolution of vegetable oil resins and aliphatic organic solvent, dimethyl acetamide which is compatible for the dissolution of polyesters are selected for the present studies on the effect of organic solvents. In addition to these two organic solvents, the commonly used aromatic solvent viz toluene and benzene are used in the present study. The polyesters show largest degradation rate, this is due to the hydrophobic nature of this polymer network that rises from long aliphatic hydrocarbon chain of fatty acid part of the oil chemical structure.

3.6 BIODEGRADATION

Biodegradation is the decomposition of organic material by micro organisms. The term biodegradation is often used in relation to sewage treatment, environmental remediation and to plastic materials. Biodegradable polymers are polymers which break down after its planned use. The degradation of the polymer results in the

formation of natural byproducts such as oxygen, nitrogen, carbon dioxide, water, biomass and inorganic salts. In general biodegradable polymers break down to form gases, salts, and biomass. Complete biodegradation is said to occur when there are no oligomers or monomers left. The breakdown of these polymers depend on a variety of factors including the polymers.

0.498g weight of NM film was buried in the soil mixed with municipal sewage sludge for six months. The Fig.4 shows the photograph of polyesters after soil burial degradation test for 30 days. The original polymer film exhibits a relatively smooth surface. However after 30 days in the soil, large number of holes, cavities, and pin hole were observed in polymer film and the polymer surface was attacked by the microorganism under soil environment.



Fig.4. Biodegradation test (degradation 30 days, 60days, 70days)

4. CONCLUSION

- The purpose of this work is to prepare high molecular weight polymers and it would be alternative petroleum based polymeric materials such as plastic and rubber materials.
- The outcome of these studies has revealed that the prepared cross linked bio polyesters are potential biodegradable material for various consumer application like package materials and agricultural applications.
- The cured polyester films are biodegradable and used for medical purpose as absorbable sutures and agricultural films. In bio-compatibility and bio-degradability play an important role.
- Development of biodegradable polymers for consumer applications, that can fulfill processing and property requirements for many applications in which biodegradability would be an important materials property is a major challenge.

ACKNOWLEDGEMENTS

The authors wish to thank the management and Principal, Sarah Tucker College (Autonomous), Tirunelveli for their support to undertake this research programme.

REFERENCES

1. Soden P.D., Kaddour A.S. Failure Criteria in Fibre-Reinforced-Polymer Composites: The World-Wide Failure Exercise. Elsevier 2004.
2. Tong L., Mouritz A.P., Bannister M. 3D Fibre Reinforced Polymer Composites. Elsevier 2002.
3. Ravi Jain, Luke lee. Fiber Reinforced Polymer (FRP) Composites for Infrastructure Applications. Focusing on Innovation, Technology Implementation and Sustainability. Springer 2012.
4. King Hwee TAN. Fibre Reinforced Polymer. Reinforcement for Concrete Structures. Proceedings of the Sixth International Symposium on FRP Concrete Structures, volume 1-2 (FRPRCS-6). World Scientific 2003.
5. Erki M.A. and Rizkalla S.H. FRP Reinforcement for Concrete Structures. Concrete International (1993)

6. W. Kraus, "Biologically active ingredients-azadirachtin and other triterpenoids", in: H. Schutterer (Ed.), *The Neem Tree Azadirachta indica. Juss and Other Meliaceous Plants*, Weinheim, New York, 1995, p 35-88
7. Aubourg, P.F., Crall C., Hadley J., Kaverman R.D., and Miller D.M. *Glass Fibers, Ceramics and Glasses. Engineered Materials Handbook, Vol. 4.* ASM International, 1991
8. McLellan, G.W. and Shand E.B. *Glass Engineering Handbook.* McGraw-Hill, 1984.
9. Pfaender, H.G. *Schott Guide to Glass.* Van Nostrand Reinhold Company, 1983.
10. Tooley, F.V. "Fiberglass, Ceramics and Glasses", in *Engineered Materials Handbook, Vol. 4.* ASM International, 1991, pp. 402-08.
11. Hnat, J.G. "Recycling of Insulation Fiberglass Waste". *Glass Production Technology International*, Sterling Publications Ltd., pp. 81-84.
12. Webb, R.O. "Major Forces Impacting the Fiberglass Insulation Industry in the 1990s". *Ceramic Engineering and Science Proceedings*, 1991, pp 426-431.
13. How fiberglass is made - material, used, processing, components, dimensions, composition, product, industry, machine, Raw Materials, The Manufacturing Process of fiberglass, Quality Control <http://www.madehow.com/Volume-2/Fiberglass.html> 1027-31
14. Copyright © 2005 American Chemical Society Lippard, S.; Chapter 1 Metal Ion Chemistry for Sustaining Life, , In *Medicinal Inorganic Chemistry*; Sessler, J., et al.; ACS Symposium Series; American Chemical Society: Washington, DC, 2005
15. M.R. Malik et al., *Inorg. Chim. Acta* (2011), doi:10.1016/j.ica.2011.06.017 Monti, Laura
16. Kim, T. N., Q. L. Feng, J. O. Kim, J. Wu, H. Wang, G. C. Chen, F. Z. Cui. *Journal of Materials Science: Materials in Medicine* 9 (1998) 129-134 Antimicrobial effects of metal ions Ag(I), Cu(II), Zn(II) in hydroxyapatite
17. Kozarich, John W. *Medicinal Inorganic Chemistry: Promises and Challenges*, *Medicinal Inorganic Chemistry*, Chapter 2, pp 4-14 ACS Symposium Series, Vol. 903, and ISBN13: 9780841238992 eISBN: 9780841220218 Publication Date (Print): August 25, 2005.
18. Copyright © 2005 American Chemical Society Lippard, S.; Chapter 1 Metal Ion Chemistry for Sustaining Life, , In *Medicinal Inorganic Chemistry*; Sessler, J., et al.; ACS Symposium Series; American Chemical Society: Washington, DC, 2005
19. M.R. Malik et al., *Inorg. Chim. Acta* (2011), doi:10.1016/j.ica.2011.06.017
20. Morais Leme D, Marin-Morales MA (2009) *Allium cepa* test in environmental monitoring review on its application. *Mutat Res* 682:71-81

CHARACTERISTIC STUDIES ON NOVEL BIODEGRADABLE POLYESTER FILMS FROM MARAVETTI OIL

T. SAHAYA MARIA JEYASEELI¹, I. ANTONY DANISH² AND J. SHAKINA³

¹Department of Chemistry, Sarah Tucker College, (Autonomous) Tirunelveli - 627 007, Affiliated to Manonmaniam Sundaranar University, Tirunelveli, Tamilnadu, India.

²Assistant Professor, Department of Chemistry, Sadakathullah Appa College, (Autonomous), Tirunelveli - 627 011, Affiliated to Manonmaniam Sundaranar University, Tirunelveli, Tamilnadu, India

³Associate Professor, Department of Chemistry, Sarah Tucker College, (Autonomous) Tirunelveli - 627 007, Affiliated to Manonmaniam Sundaranar University, Tirunelveli, Tamilnadu, India.

*Corresponding author E-mail: shakinajudson@gmail.com Mobile Number: 9384218533

ABSTRACT

Novel biodegradable polyester film was synthesised from naturally available Maravetti oil, formic acid and 30% hydrogen peroxide by stepwise polymerisation technique. The polymer was prepared by resin react with styrene. The UV, FTIR and NMR spectral studies carried out to identify the nature of the polymer formed. SEM analysis confirmed that the polymer was biodegradable in nature. The biodegradability of the polyester film was studied by soil burial test. The thermal degradation at different time intervals were analysed by TG-DTA analysis. The cross-linking ability of the polymers was checked by DSC analysis. Mechanical properties like tensile strength and impact strength were characterized. The resulted polymers have satisfied mechanical performance and fast curing speed.

Keywords: Cross-linking, Degradation, Polymer, Soil Burial, Styrene

1. INTRODUCTION

In our world over 6.3 billion plastics are generated, only 9% is recycled, 12% incinerated, 79% accumulated in natural environment. In the production of plastics, monomers used which are derived from fossil hydrocarbons. Most of the plastics are slow to degrade. Because of increasing prize of petroleum and environmental awareness; researchers are interested in the synthesising of polymers from renewable resources of plants. Plant oils are considered building blocks of polymers due to their low cost, availability and eco-friendly. Active functional groups such as double bonds, ester groups and hydroxyl groups, on the triglyceride chain make the polymer to be chemically modified and to prepare polymers with desirable properties.

Hydnocarpus Wightiana seed oil or chaulmoogra oil also known as Maravetti oil. It has been used in medicine as antibiotics for the treatment of several skin diseases and leprosy as a mixture suspended in gum or as an emulsion. The oil is unusual in not being made up of straight chain fatty acids but acids with a cyclic group at the end of the chain.

2. EXPERIMENTAL

2.1 MATERIALS

Maravetti oil (MVO) was purchased from local market, Formic acid (97%) (Rankem), Hydrogen peroxide (30%) (Rankem) were used in the first step functionalization. Maleic anhydride (Rankem) and Morpholine (Rankem). Benzoyl peroxide (Rankem) was used as a radical initiator and N, N-Dimethyl aniline (Rankem) was used as accelerator in the curing process. Styrene (Rankem) was used as a vinyl co-monomer.

2.2 SYNTHESIS OF MARAVETTI OIL POLYOL

100 g of MVO was taken in a three necked flask fitted with condenser and thermometer. 100 ml of 97% formic acid and 55 ml of 30% hydrogen peroxide was added and the reaction mixture was vigorously stirred over 16h. Ice water bath was used externally to keep the temperature below 40°C. The resulting emulsion was poured into a separating funnel and extracted with ether. The ether layer was dried over anhydrous sodium sulphate and the resulting product was polyol resin from MVO.

2.3 SYNTHESIS OF POLYESTERS

The polyol resin was heated in a three necked flask and maleic anhydride was added in 1:2 ratio at 70°C. Morpholine was used as a catalyst. After 2 hours a golden yellow viscous liquid formed it indicates the formation of oligomerised MVO fumarate resin.

2.4 SYNTHESIS OF POLYESTER FILM FROM OLIGOMERISED MVO FUMARATE RESIN AND CO-MONOMER STYRENE

Synthesis of aliphatic polyester was carried out by free radical addition polymerisation reaction by using the homopolymer (oligomerised MVO fumarate resin) and styrene at different concentration using benzoyl peroxide as catalyst and Dimethyl aniline as accelerator. The viscous liquid is transferred in to glass mould coated with silicon oil at room temperature. The polyester thin film of different concentration such as 1:0.5, 1:1 and 1:2 were synthesised from homo polymer and styrene. Finally the yellow coloured polyesters sheets were removed from the mould.

2.5 CHARACTERISATION OF RESINS

The UV and FTIR analysis were carried out for MVO, hydroxylated MVO and also the resin. The ¹H-NMR spectra for epoxy resin, polyols and pre-polymers were dissolved in CDCl₃ and recorded using BRUKER AVANCE III, 400 MHz FT NMR SPECTROPHOTOMETER. Cured samples were also checked to see the degree of curing. The Thermo Gravimetric Analysis (TGA) was done by using TGA instrument. The Differential Scanning Calorimetry (DSC) analysis was done by a TA instrument.

3. RESULT AND DISCUSSION

3.1 UV ANALYSIS

The UV spectra of the MVO, hydroxylated MVO and for the resin have been investigated (220 nm - 800 nm). The MVO sample showed an electronic absorption band around 239 nm. The hydroxylated oil exhibited a blue shift when compared with the corresponding parent oil which is attributed to the substitution of hydroxyl group at the unsaturated moiety. There is also decrease in the absorbance in comparison with that of parent oil is due to the substitution of the hydroxyl group at the olefinic double bond and also distortion of geometry. The substantial red shift in electronic absorption exhibited in the resin due to the substitution of the fumarate group and also due to the distortion in geometry of the molecule by the introduction of fumarate group.

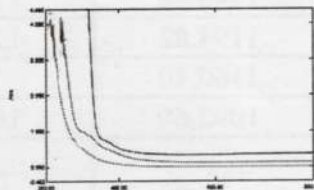


Fig.1. UV spectra of MVO, Hydroxylated MVO and MV Resin

3.2 XRD PATTERN OF POLYMER COMPOSITE

This module provides an introduction to X-ray Diffraction (XRD), which is a versatile, non-destructive technique that reveals detailed information about the chemical composition and crystallographic structure of materials.

From XRD analysis, average crystallite size of the MV polymer is 7.02 nm. Peak is narrow; hence the polymer composite is crystalline.

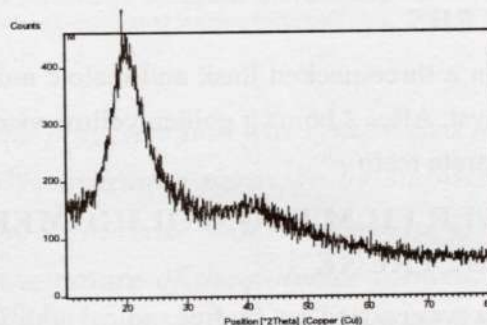


Fig.2.XRD pattern of MV polymer

3.3 FT-IR ANALYSIS

The FT-IR spectra of MVO, hydroxylated MVO and the resin were recorded between 500 cm^{-1} to 4000 cm^{-1} [5]. In hydroxylated MVO, the FTIR spectra showed a strong absorption band at 3522.74 cm^{-1} , due to the presence of free-OH group in the molecule, which is absent in MVO. A strong absorbance band in 1734.85 cm^{-1} is due to the presence of C=O in esters. A strong band in 2926.78 cm^{-1} due to the symmetrical-C-H bond in $-\text{CH}_2-$ group of the side chain.

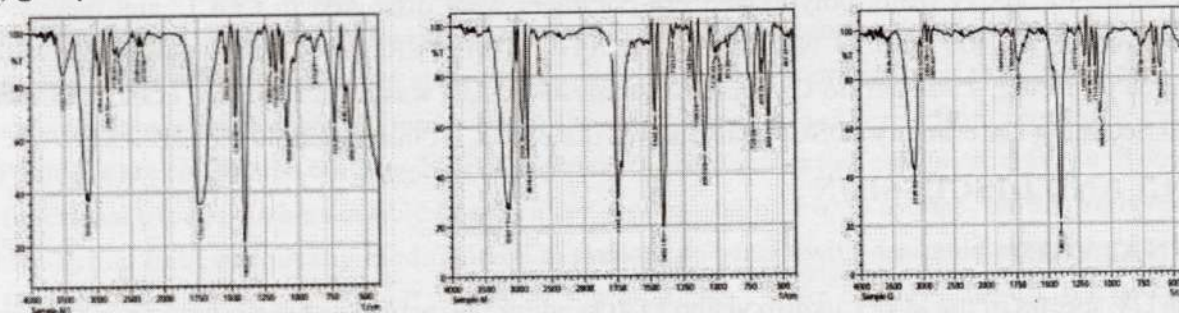


Fig.3.IR spectra of MVO, hydroxylated MVO and MV resin

TABLE 1: FT-IR PROBABLE ASSIGNMENT

Probable assignment	MVO(cm^{-1})	Hydroxylated MVO (cm^{-1})	MV resin (cm^{-1})
-CH ₂ Group	2926.78	2966.31	2926.78
-C- O Group in GM	2848.67	2847.7	-
C=O in esters	1745.46	1733.89	1734.85
TerminalCH ₃ Groups	1194.82	1200.61	1202.53
Carboxyl Group of acids	1160.10	1163	1163.96
-CH-CH-Stretching	1092.60	1084.88	1082.96
CH ₂ -sequences of the aliphatic chains	720.36	722.29	755.08
-OH Group	3161.11	3522.74	3536.24

3.4 THERMAL ANALYSIS

Properties of polymer affected by the cross linking degree, which correlated with the degree of functionality of the monomer. DSC can be used to check the curing results of the thermosetting resin. Both resins with cross linker and without cross linker were analysed by DSC. The peak for the sample with cross linker is 527.19°C, indicating the fastest cure for this resin will occur at the temperature. The onset of the cure peak for this resin is 412.00°C and the total heat of the reaction is 3853J/g.

The peak for the sample without cross linker is 528.6 °C, indicating the fastest cure for this resin will occur at the temperature. The onset of the cure peak for this resin is 470.73°C and the total heat of the reaction is 2965J/g. It can be seen that resins with cross linker released out more heat during the curing process, which indicate more double bonds inside the resins. TGA for resins was conducted to identify their degradation characteristics.

The resin with cross linker was stable up to 150°C with no significant weight loss; the initial weight loss was observed at 157.21°C, indicating the loss of volatiles and moistures. Significant weight loss began at 306.36°C due to the degradation of the resin. When the temperature reached 499.46°C, weight loss was recorded. The maximum rate of decomposition occurred at 525.21°C; the residual mass is around 0.009847 mg. The resin without cross linker was stable upto 130°C with no significant weight loss; the initial weight loss was observed at 135.91°C, indicating the loss of volatiles and moistures. Significant weight loss began at 320.35°C due to the degradation of the resin. When the temperature reached 510.45°C, weight loss was recorded. The maximum rate of decomposition occurred at 527.42°C; the residual mass is around 0.2557 mg. From this, we see that for resins with cross linker are more resistive to temperature increasing, this is due to cross linker increased the cross linking network of the resins. The residue percentage is lower than resins without cross linker.

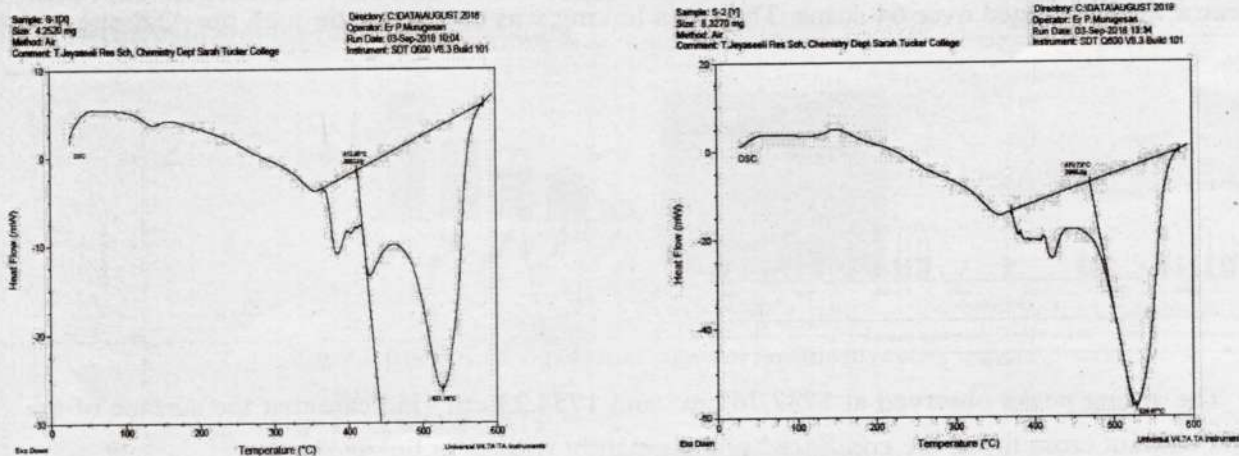


Fig.4.DSC thermograms of polymer composite and without cross linker

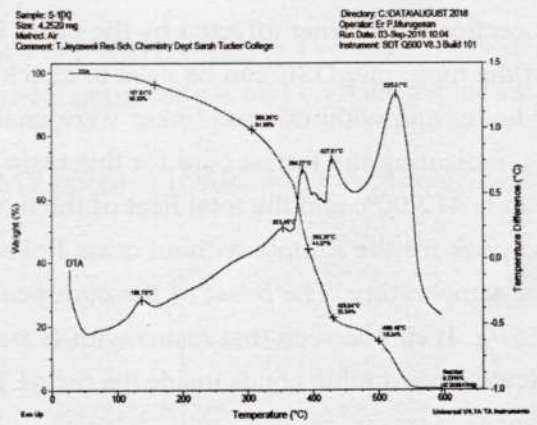
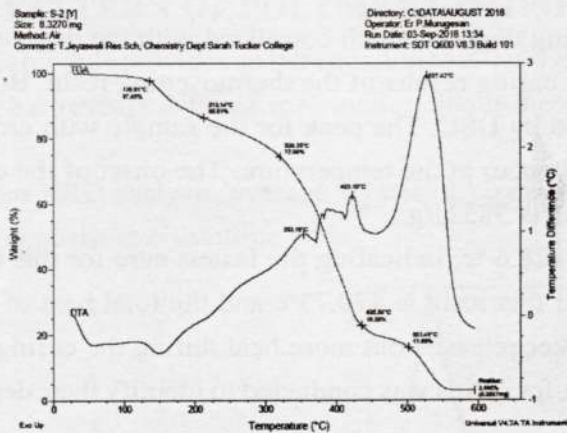
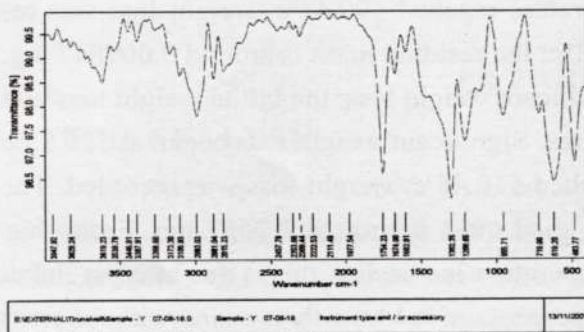


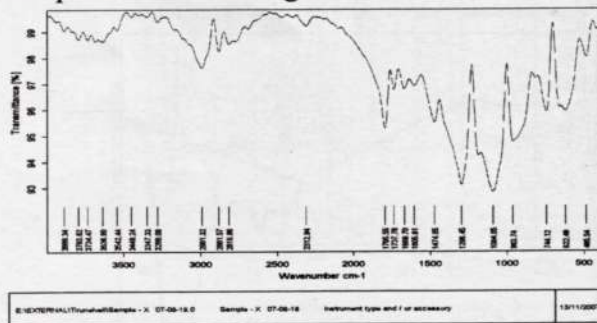
Fig.5.TGA, DTA thermograms of sample with and without cross linker

3.5 FTIR-ATR ANALYSIS



Page 1/1

The samples were analysed over the range of 400cm^{-1} - 4000 cm^{-1} with a spectrum resolution of 4cm^{-1} . All spectra were averaged over 64 scans. The cross linking was confirmed through the ATR spectral studies.



Page 1/1

The strong peaks observed at 1737.76 cm^{-1} and 1754.23 cm^{-1} indicate that the surface of the sample with and without cross linker are comprised predominantly with ester linkages.

Fig .6.ATR Spectrum of polymer composite with and without cross linker

3.6 SEM ANALYSIS

SEM micrographs show the strong bonding in composite without cross linker than in with cross linker. These results clearly provide strong interfacial adhesion and good wetting, as evidenced by the almost complete absence of holes around the matrix.



Fig.7.SEM Photographs of polymer composite with and without cross linker

3.7 DNA BINDING ASSAY

A polymer binds to DNA through intercalation usually results in hypochromism and bathochromism, due to a strong stacking interaction between a polymer and the base pairs of DNA.

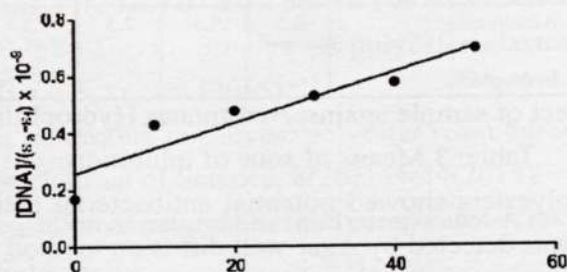


Fig.8. Plots of $[DNA]/(\epsilon a - \epsilon f)$ versus $[DNA]$

Table.2 OD values of polymer treated

Drug Treated	Concentration	OD Value
50 $\mu\text{g/ml}$ of the R	0	0.17
10 μM CT DNA + 50 $\mu\text{g/ml}$ of the R	10	0.43
20 μM CT DNA + 50 $\mu\text{g/ml}$ of the R	20	0.479
30 μM CT DNA + 50 $\mu\text{g/ml}$ of the R	30	0.53
40 μM CT DNA + 50 $\mu\text{g/ml}$ of the R	40	0.576
50 μM CT DNA + 50 $\mu\text{g/ml}$ of the R	50	0.697

The intrinsic binding constant K_b of the polymer with CT-DNA was -3.717×10^{-4}

3.7 MICROBIAL STUDIES

Antibacterials present in the sample were detected by Agar well diffusion method using bacterial strains *Actinomyces israelii* and *Aeromonas hydrophilla*.

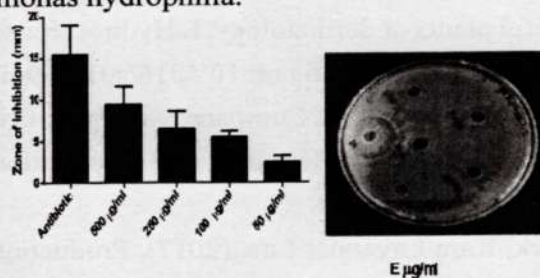
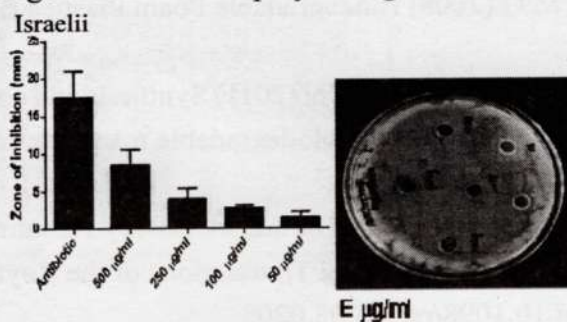


Fig.9. Effect of MV polymer against *Actinomyces israelii*



S. No	poly-mer sample	Name of the test organism	Zone of inhibition (mm)				
			500 µg/ml	250 µg/ml	100 µg/ml	50 µg/ml	AB
1.	MV	Actinomyces israelii	9.5	6.5	5.5	2.5	15.5
2.	MV	Aeromonas hydrophilla	6.5	5.5	2.5	1.5	12.5

Fig.10.Effect of sample against Aeromonas Hydrophilla

Table: 3 Means of zone of inhibition

The newly prepared biopolyesters showed potential antibacterial activity against micro organisms. Antifungal present in the sample was detected by Agar well diffusion method using fungal strain *Aspergillus Niger*. The newly prepared biopolyesters showed potential antifungal activity against micro organisms.

4. CONCLUSION

We have synthesized Bio-based thermoset resin from *Hydnocarpus wightiana* seed oil fatty acid. It was hydroxylated by hydrogen peroxide and formic acid; the resulted resin was modified by maleic anhydride. The obtained resins were used in the preparation of the bio based composites. The composites were characterised by different mechanical analysis and showed relatively good flexural and impact strength which is comparable with the glass fibre reinforced composites.

ACKNOWLEDGEMENTS

The authors wish to thank the management and Principal, Sarah Tucker College (Autonomous), Tirunelveli for their support to undertake this research programme. The authors acknowledge the staff of CE-CRI, Karaikudi for the assistance in the evaluation of polymer samples.

5. REFERENCE

1. Norton, SA (October 1994). Useful plants of dermatology. I. *Hydnocarpus* and *chaulmoogra*. *Journal of the American Academy of Dermatology*. 31(4): 683-6. doi: 10.1016/s0190-9622 (08) 81744-6. PMID8089304.
2. K.Priya Rajini and S.Begila David, Synthesis and Comparative Study of Novel Cross Linked BioPolymers from Linseed Oil, *Int.Journal of Engineering Research and Applications*, Vol.5, Issue 8(Part-5) August 2015, pp 09-15
3. Roland Geyer, Jenna R. Jambeck, Kara Lavender Law (2017). Production, use and fate of all plastics ever made. *Science Advances*, 3(7), e1700782. doi:10.1126/sciadv.1700782.
4. Wang H J, Rong M Z and Zhang M Q (2008) Biodegradable Foam Plastics Based on Castor Oil, *Biomacromolecules*, 9, 615-623.
5. J.Shakina, K.Sathiya Lekshmi and G.Allen Gnana Raj (2011) Synthesis and characterisation of Novel cross linked biopolyesters from olive oil as eco-friendly biodegradable materials. *E-Journal of Chemistry* 2012, 9(1), 181-192
6. Barnes, D. K. A., Galgani, F., Thompson, R. C., & Barlaz, M. (2009). Accumulation and fragmentation of plastic debris in global environments. *Philosophical Transactions of the Royal Society B: Biological Sciences*, 364(1526), 1985–1998. doi:10.1098/rstb.2008.0205
7. Bio polymer-based materials from polysaccharide properties, processing, Characterization and sorption Applications. By Rohan S. Dassanayake, Sanjit Acharya and Nouredine Abidi Submitted: February 28th 2018. Reviewed: August 13th 2018 Published: November 5th 2018, DOI: 10.5772/intechopen.80898

8. Shakina J , Sathiya Lekshmi K , Allen Gnana Raj G , Microbial degradation of synthetic polyesters from renewable resources, Indian Journal of Science, 2012, 1(1), 21-28
9. Synthesis and properties of a novel bio based polymer from modified soy bean oil IOP Conf. Series: Materials Science and Engineering 17(2017) 012010 doi:10.1088/1757-899X/170/1/012010
10. G.S.Prabha Littis Malar,S.Begila David, Studies on polyester elastomers using palm olein for drug delivery,IJSEAS-Volume-1,Issue-5,August (2015).
11. Shakina et al.Polymers from renewable resources: polyester resin based upon acid anhydride-cured hydroxylated soybean oil, Indian Journal of Science, 8(20), 44-54(2014).
12. Sathish Kumar et.al.Characterization of natural fiber and composites-A review.Journal of Reinforced Plastics and Composites.32 (19)1457-1476
13. Birendra Pratap Singh et al. Synthesis and characterization of Inorganic Polymer Nano-Composites, Der Chemica Sinica, 2012, 3(2):521-526.

**RECENT ADVANCES IN MECHANICAL BEHAVIOR OF FIBRE REINFORCED SMART BIODEGRADABLE POLYMERS****T. Sahaya Maria Jeyaseeli¹, I. Antony Danish², J. Shakina*¹, P. Tharmaraj³**¹Department of Chemistry and Research Centre, Sarah Tucker College, (Autonomous) Tirunelveli, Tamilnadu, India²Department of Chemistry and Research Centre, Sadakathullah Appa College (Autonomous) Tirunelveli, Tamilnadu, India³Department of Chemistry and Research Centre, Thiyagarajar College, Affiliated to Madurai Kamaraj University, Madurai, Tamilnadu, India*Corresponding author: shakinajudson@gmail.com**ABSTRACT**

Fibre-reinforced polymer composites have been developed from the reaction of fumarate resin with natural material Perch fibre. The composite material is fabricated by hand layup technique. The fabricated composite material was tested for its mechanical properties such as Tensile Strength, Flexural Strength and Impact Strength. The composite specimens for the above-mentioned test were prepared as per the ASTM standards. The fibre reinforcement influenced the improvement of mechanical properties of polymers and surface morphology of the polymer was analysed by Scanning Electron Microscope. Moisture absorption and vibration damping with polymers and its effect on mechanical properties can also be studied. Tensile strength, flexural strength and impact strength were observed and compared to each other. Tensile test showed maximum ultimate tensile strength for untreated 80 mm length fibre compared to others. Flexural test showed maximum ultimate flexural strength for untreated 80 mm length fibre compared to others. Impact test showed higher impact energy for treated 40 mm length fibre compared to others.

Keywords: Biodegradable, Eco-friendly, Thermoset, Mechanical, Moisture, Vibration.**1. INTRODUCTION**

Natural fibres are recently attracted towards researchers due to their low cost, eco-friendly, low density, good mechanical properties and as a renewable source [1]. Natural fibres offer many technological and environmental benefits to reinforce low density materials with high strength and is favourable as a reinforcement in making lightweight polymers with good mechanical properties [2]. A special benefit of using fibre reinforced polymer is its biodegradability and extremely available from a renewable resource. As fibre contents increases, the mechanical properties such as tensile, impact and flexural strengths of these properties also increases [3]. Different kinds of tests have been performed on the polymer composites and the reports reveal that they have interesting mechanical properties [4]. Due to various chemical treatments on fibres, the hydrophilic behaviour of the fibres was reduced to improve mechanical strength in natural fibre reinforced polymers [5]. Fibre reinforced polymers assist to expand strength and ductility without increase in stiffness [6].

2. EXPERIMENTAL**2.1. Materials**

Azadirachta Indica oil (AIO) and Thennamarakudi oil (TKO) were purchased from local market, Formic acid (97%) (Rankem), Hydrogen peroxide (30%) (Rankem) were used in the first step fractionalization. Maleic anhydride (Rankem) morpholine (Rankem) and benzoyl peroxide (Rankem) was used as a radical initiator and N, N- dimethyl aniline (Rankem) was used as accelerator in the curing process. Styrene (Rankem) was used as a vinyl co-monomer.

2.2. Synthesis of plant oil polyol

A 100 g of AIO/TKO was taken in a three necked flask fitted with condenser and thermometer. 100 mL of 97% formic acid and 55 mL of 30% hydrogen peroxide was added. Ice water bath was used externally to keep the temperature below 4°C. The reaction mixture was vigorously stirred over 16hr. The resulting emulsion was poured into a separating funnel and extracted with ether. The ether layer was dried over anhydrous sodium sulphate and the resulting product was polyol resin obtained from AIO/ TKO.

2.3. Synthesis of polyesters

The polyol resin was heated in a three necked flask and maleic anhydride was added in 1:2 ratio at 70°C. Morpholine was used as a catalyst. After 2 hours a golden yellow viscous liquid formed it indicates the formation of oligomerised AIO/TKO fumarate resin.

2.4. Synthesis of polyester film from oligomerised AIO/TKO fumarate resin and comonomer styrene

Synthesis of aliphatic polyester was carried out by free radical addition polymerization reaction by using the homopolymer (oligomerised AIO/TKO fumarate resin) and styrene at different

concentration using benzoyl peroxide as catalyst and N,N-dimethyl aniline as accelerator. The viscous liquid is fabricated with different weight ratio of Perch fish fibre and is transferred in to glass mould coated with silicone oil at room temperature. The polyester thin films were synthesized from homopolymer and styrene. Finally, the fibre reinforced polyesters sheets were removed from the mould.

2.5. Characterization of Polymers

Double-beam UV/visible spectrometer is used to verify the characteristic absorption of the polymer composites. Fourier transform infrared (FTIR) spectra of polymers were obtained using Shimadzu FT-IR spectrophotometer using KBr pellet at wavelengths between 4000 cm^{-1} and 400 cm^{-1} at 27°C. SEM analysis was carried out to know about the surface property of the polymer. The mechanical studies of the biopolyesters were determined using dumbbell shaped cut from the specimen according to ASTM D3039 standards.

3. RESULT AND DISCUSSION

3.1. UV analysis

Figure 1 shows the UV spectra of AIO and TKO, hydroxylated triglyceride oils and their resins. They have been investigated (230 nm-800 nm). The AIO and TKO samples showed an electronic absorption band around 262 nm and 270.50 nm, respectively. The hydroxylated resins exhibited a blue shift when compared with the corresponding parent oil which is attributed to the substitution of hydroxyl group at the unsaturated moiety.

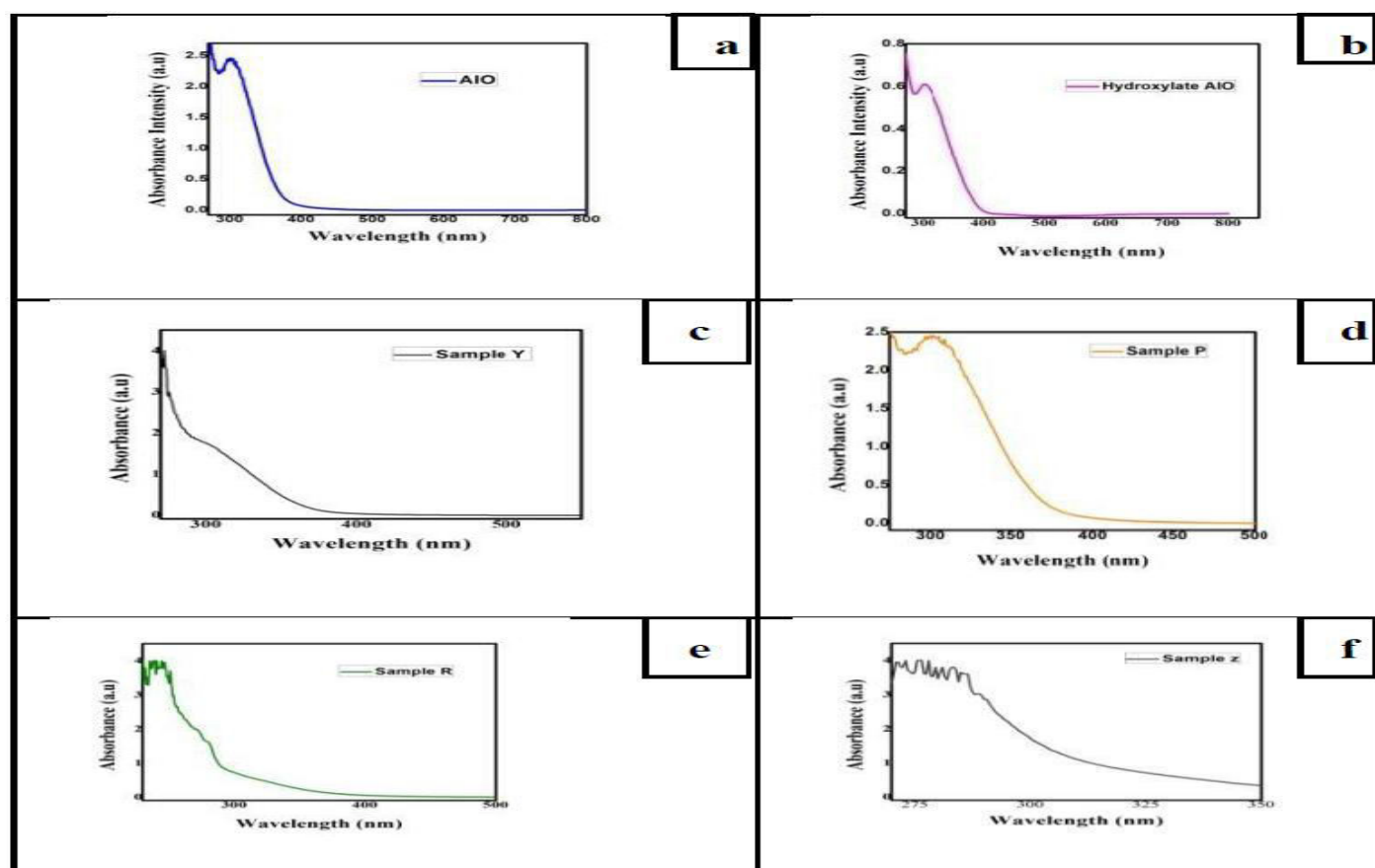


Fig. 1: UV Spectra of a) AIO b) HAIO c) PAIOFRS d) TKO e) HTKO and f) PTKOFRS

3.2. FTIR spectral analysis

Table 1 shows the IR spectra of AIO, TKO, hydroxylated triglyceride oils and their resins. They have been investigated between 500 cm^{-1} to 4000 cm^{-1} . In hydroxylated triglyceride oils, FT-IR spectra showed

a strong absorption band at 3565.17 cm^{-1} and 3172.68 cm^{-1} , respectively due to the presence of free -OH group in the molecule. The corresponding peaks are completely reduced in the resins indicates the entire OH group get substituted.

Table 1: FT-IR probable assignments of AIO and TKO

Probable assignment	AIO (cm^{-1})	HAIO(cm^{-1})	AIOFRS (cm^{-1})	TKO (cm^{-1})	HTKO (cm^{-1})	TKOFRS (cm^{-1})
- CH ₂ Group	2927.74	2927.74	2929.67	2925.81	2926.78	2928.71
-C- O Group in GM	2854.45	2855.45	2855.42	2854.4	2854.45	2855.42
C=O in esters	1745.46	1726.17	1729.06	1746.42	1730.99	1734.85
TerminalCH ₃ Groups	1209.28	1400.22	1460.01	1196.75	1116.71	1168.78
CarboxylGroupof Acids	1167.82	1178.43	1374.19	1162.03	1145.75	1132.14
-CH-CH-Stretching	1072.35	1076.21	1058.85	1086.81	1073.31	1055.95
CH ₂ -sequences of the aliphatic chains	649	725.18	723.26	753.15	723.26	671.18
-OH Group	3658.71	3565.17	3268.15	3161.11	3172.68	3635.57

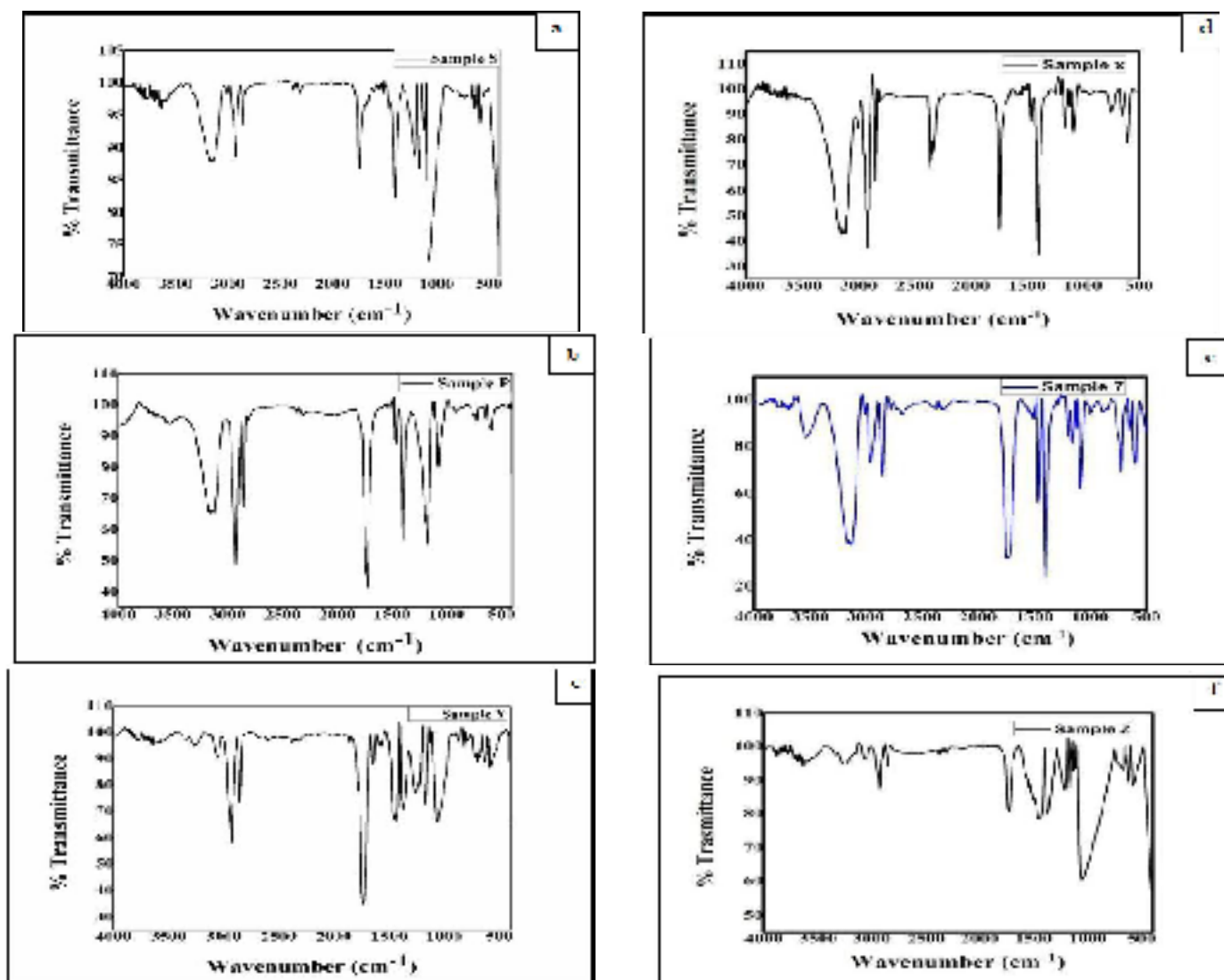


Fig. 2: IR spectrum of a) AIO b)HAIO c)PAIOFRS d)TKO e)HTKO and f)PTKOFRS

3.3. XRD Pattern

XRD patterns explain the crystallographic structure of polymers. AIO and TKO polymers have broad peaks indicate that they are semi crystalline in nature.

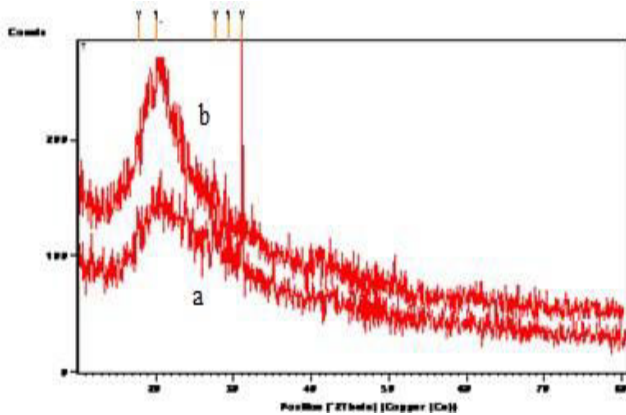


Fig. 3: XRD Patterns of a) AIO polymer b) TKO polymer

3.4. SEM analysis

Scanning electron micrograph provides the information about surface morphology of polymers. Figure 4 and 5 represent the SEM images of untreated and treated AIO and TKO polymers. They have symmetric chain units in parallel and have a good network pattern. The SEM images show the adhesion between the fibres and matrix.

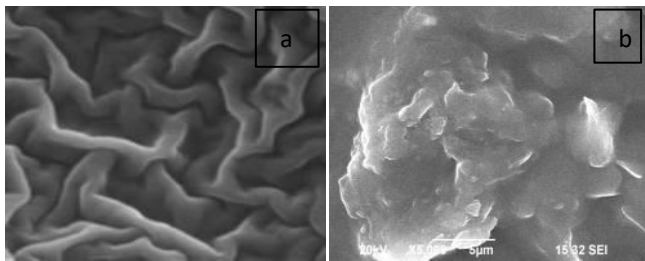


Fig. 4: SEM images of a) untreated AIO b) treated AIO

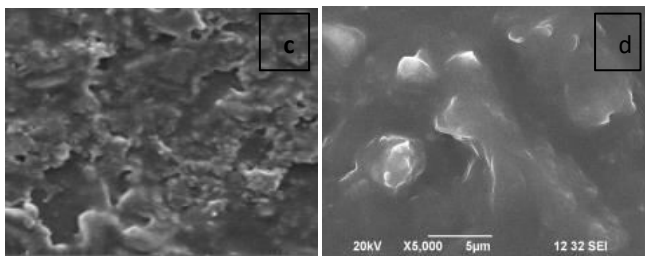


Fig. 5: SEM images of a) untreated TKO b) treated TKO

The above images are of sample with composition of 30 %Perch Fish Fibres and 70% Resin. Figure 4 shows image of surface without any fracture. There are some voids seen in image which are caused because of manually stirred resin mixture and it also may be caused because of random orientation of fibres.

SEM images prove that the polymer composite has strong bonding between resin and fibres and it also shows that the fibres are completely immersed within resin. Scanning electron microscopy (SEM) study revealed excellent interfacial bonding between the fibre and the resin matrix of AIO/fish fibre reinforced fumarated hybrid composite that evince the improvement in the tensile and flexural properties of the material. Moreover, when compared to other composites, AIO/ Perch fish fibre and TKO/ Perch fish fibre composite absorbs more energy during impact loading that makes the material a good competitor in automotive and textile sectors.

3.5. Mechanical property

The mechanical properties of the polymers prepared were shown in Table 2. To evaluate the tensile properties of the TKO and AIO polymers, tensile tests were conducted according to ASTM D3039 to measure the force required to break the polymer composites.

Table 2: Mechanical properties of the polymers

Polymer sample	Tensile strength (Map)	%of Elongation	Flexural strength (Mpa)	flexural Strain (%)
TKO	28.9	16.4	26.43	7
TKO1	30.5	16.08	25.2	7.2
TKO2	31.3	14.18	27.5	6.7
TKO3	32.5	18.94	26.6	7.1
AIO	4.9	20.57	34	7.9
AIO1	6.6	18.4	32.5	8.2
AIO2	6.9	23.9	33.2	8.5
AIO3	10.39	19.4	36.3	7

A standard specimen is subjected to gradually increasing uniaxial tensile load until it fractures. Tensile strength of developed TKO and AIO polymers were found to be 28.9 Mpa and 4.9Mpa. Fig.6 shows the comparison of AIO and TKO polymers of a) Tensile and Flexural strength b) Elongation and Flexural strength c) Impact strength. Among the polymers, tensile strength is high in TKO polymer due to higher cross link density and flexural strength is high in AIO polymer [8]. From the graph, elongation and flexural strain is greater in AIO

polymer and impact strength of TKO polymer is greater than AIO polymer. Figure 7 shows that the tensile and impact strength of various fibre ratio of TKO and AIO polymer. From the graph, tensile and impact strength is greater in TKO polymer and flexural strength is greater in AIO polymer.

3.6. Moisture Absorption of Polymers

Fig. 8 shows the curves of percentage of water absorption as a function of time in sea water, distilled water and drinking water. To measure the strength or quality of the polymer, the water absorption tests were performed according to ASTM D570 on a universal test machine. From the graph, water absorption increases with absorption time [9]. Due to the high cellulose content, the percentage of weight of the fibre in the polymer increased as the moisture absorption was decreased. Moisture absorption of fibre reinforced TKO and AIO polymers causes the swelling of fibre as a result of the formation of micro cracks at fibre-matrix space. Due to the damages of the fibre, interfacial bonding and the strength is decreased, which in turn caused degradation of polymers.

3.7. Vibration damping with Polymers

Dampers based on polymers have many applications due to their low cost, light weight and flexibility. The damping factor was determined by using free vibration method as per ASTM standard (D 790). The damping factors were calculated by taking the values of successive peak from the vibration response graph. From the graph, damping factor increases with frequency [10]. Fibre reinforced TKO and AIO polymers exhibit greater vibration damping because fibres are stiff and the fibre-matrix interface increases the damping properties and energy dissipation.

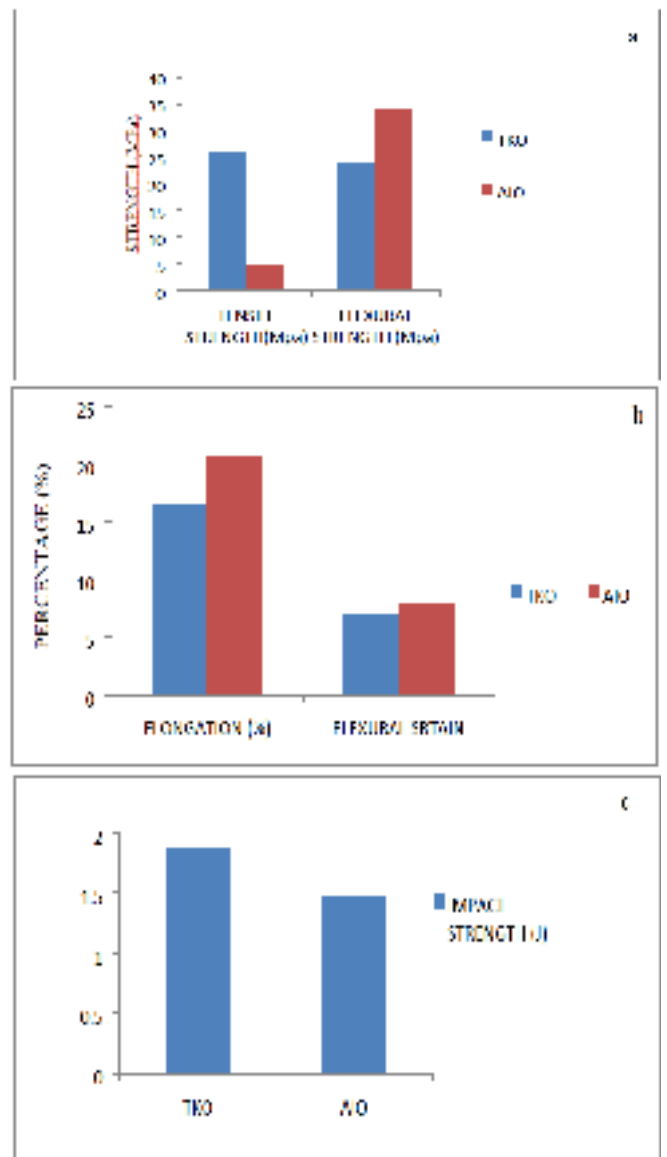
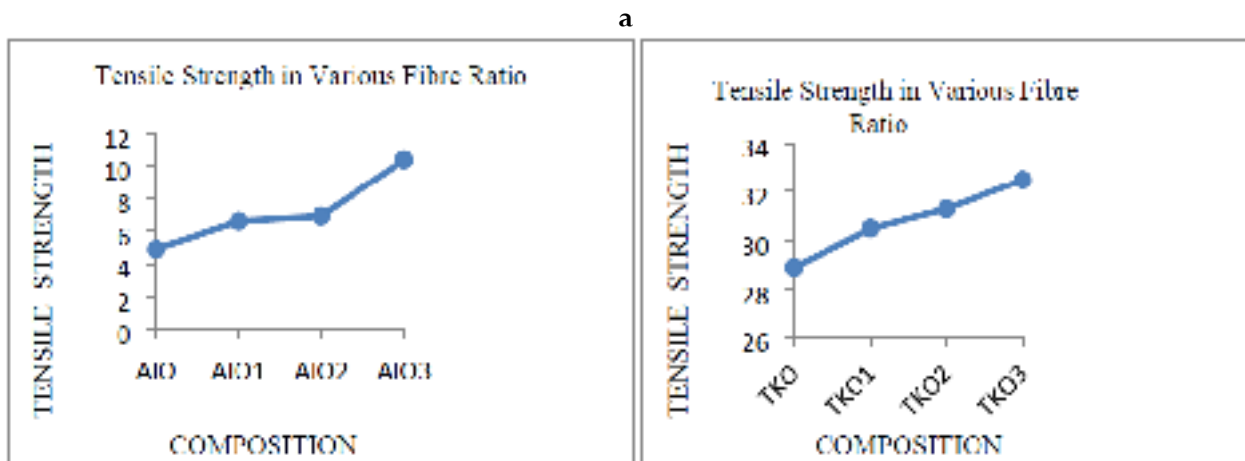


Fig. 6: Comparison of TKO and AIO polymers of a) Tensile and Flexural strength b) Elongation and Flexural strength c) Impact strength



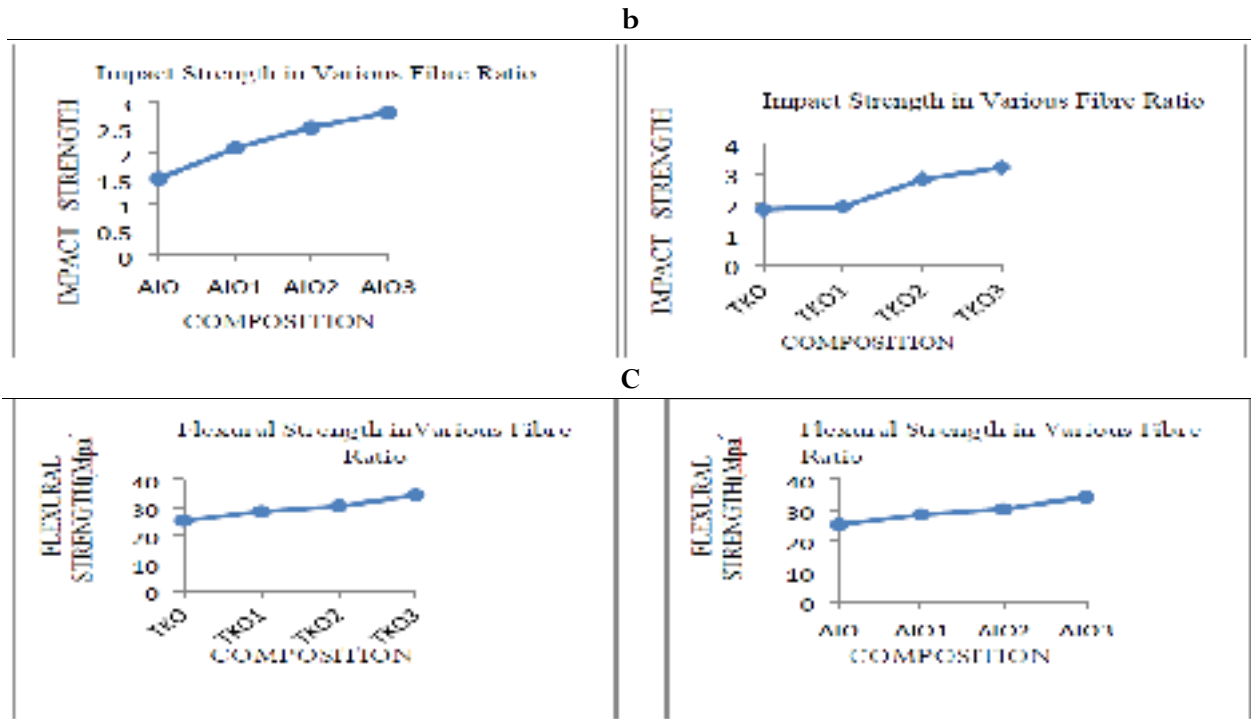


Fig. 7: Various fibre ratio of AIO and TKO polymers of a) Tensile b) Impact c) Flexural strength

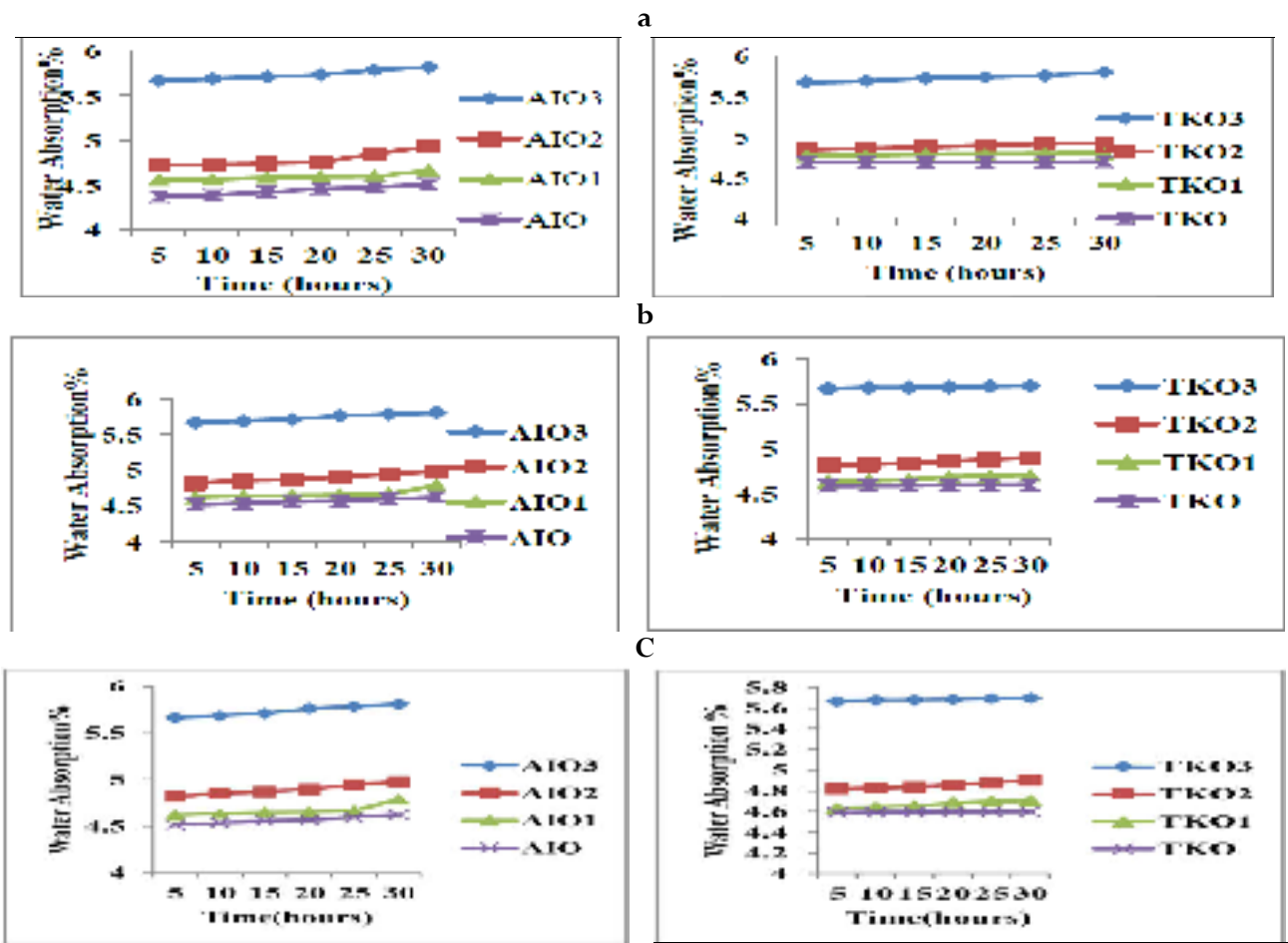


Fig. 8: Water Absorption curves of AIO and TKO polymers in a) sea water b) distilled water c) drinking water

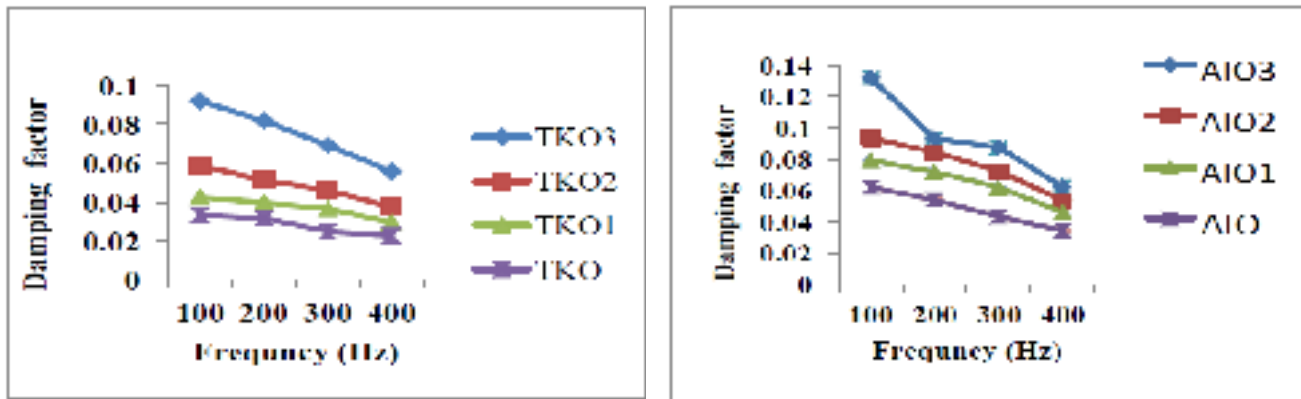


Fig. 9: Damping curves of a) AIO polymer b) TKO polymer

4. CONCLUSION

We have successfully synthesized fibre reinforced polymers. Mechanical characterization of newly synthesised polymers was studied. AIO based polymeric material was more flexible compared to TKO based bio material. TKO based polymer has more stiffness than AIO based polymer. Tensile strength and impact strength is high in fibre reinforced polymers of TKO and flexural strength, elongation and flexural strain is high in fibre reinforced polymers of AIO moisture absorption increases; the degradation of TKO and AIO polymers will also increase. They exhibit greater vibration damping. The newly prepared polymer is biodegradable.

5. ACKNOWLEDGEMENTS

The authors wish to thank the management and Principal, Sarah Tucker College (Autonomous), Tirunelveli for their support to undertake this research programme. The authors acknowledge the Lab facilities provided by Govt. Engineering College (Mechanical Trade), Tirunelveli, for the assistance in the evaluation of polymer samples.

6. REFERENCES

1. Chandramohan D, Bharanichandar J. *American Journal of Environmental Science*, 2013; **9(6)**: 494-504.
2. Ramanaiah K, Ratna Prasad AV, Hema Chandra Reddy K. *International Journal of Polymer Anal. Charact*, 2013; **18(2)**:126-136.
3. Aadekomaya O, Adama K. *Nigerian Journal of Technology*, 2017; **36(3)**:782-787.
4. EshetieKasseгна, Frederik Desplentereb, Temesgen Berhanuc. *Branna Journal of Engineering and Technology*, 2019; **1(1)**:20-36.
5. Layth Mohammed, Ansari MNM, Grace Pua, Mohammad Jawaid, Saiful Islam M. *International Journal of Polymer Science*, 2015; 1-15. DOI:10.1155/2015/243947
6. Sandeep S. Pendhari, Tarun Kant, Yogesh M. Desai. *Composite Structures*, 2008; **84(2)**:114-124.
7. PrabhaLittis Malar GS, Begila David S. *International Journal of Scientific Engineering Science*, 2015; **1(5)**:142-148.
8. Sridhar R, Athijayamani A, Stalin B, Sankar Ganesh R., *IJAER*, 2015; **10(55)**:4076-4080.
9. Mohd Hafizuddin Ab Ghani, Sahrim Ahmad. *Advances in Materials Science and Engineering*, 2011; 1-4.
10. Geethamma VG, Asaletha R, Nandakumar kalarikkal, Sabu Thomas. *Resonance*, 2014; **19(9)**:821-833.



DFT, NBO, HOMO-LUMO, NCI, stability, Fukui function and hole – Electron analyses of tolcapone

Isravel Antony Danish^a, Jeyaraj Jebasingh Kores^b, Thangasamy Sasitha^c,
John Winfred Jebaraj^{c,*}

^a Research Department of Chemistry, Sadakathullah Appa College* (Autonomous), Tirunelveli, Tamil Nadu 628251, India

^b Research Department of Physics, Pope's College* (Autonomous), Sawyerpuram, Tamil Nadu 628257, India

^c Research Department of Chemistry, St. John's College*, Palayamkottai, Tamil Nadu 627002, India

ARTICLE INFO

Keywords:

NBO
HOMO-LUMO analysis
Non Covalent interaction
Tolcapone
Hole - Electron Interaction
DFT

ABSTRACT

Parkinson's disease is a neurodegenerative disorder that damages the nervous system. The treatment of this disease is carried using tolcapone as a drug combination with Levodopa. Tolcapone is investigated by the B3LYP/6-311G method by using DFT calculations. HOMO-LUMO results and fingerprint analysis reveal that it is a hard, stable molecule with hydrogen bond donor and acceptor system. According to NBO analysis, the presence of hydrogen bond, conjugation of double bonds, and CT nature enhances the stability. Fukui function analysis suggests that this molecule is more prone to nucleophilic attack. Multiwfn 3.8 is used to interpret the following results. NCI interaction study reveals that it is having steric effect, Van der Waals force, and hydrogen bond. Hole-electron interaction studies reveal that S1, S5, and S6 undergo a charge transfer excitation. The simulated Scanning Tunneling Microscope (STM) analysis shows that the tunneling current is located at C12 and H26.

1. Introduction

Parkinson's disease is a common neurodegenerative disorder that damages the nervous system like the slowness of movement and balance impairment. A huge volume of research has shown that the treatment of Parkinson's disease (PD) is carried using tolcapone as a drug combination with Levodopa. In the past decade, it is reported that, a common neurodegenerative disorder that causes major damage to the nervous system is due to Parkinson's disease. It results in rest rigidity, tremor, balance impairment, and slowness of movement, and this disability can be cured through the pharmacological correction of brain dopamine deficiency in Parkinson affected patients [1–2].

A huge volume of continuous research has shown that levodopa is considered an important drug for the healing of Parkinson's disease. On oral intake, Levodopa undergoes decarboxylation in the presence of *aromatic acid decarboxylase* in the brain after crossing the blood–brain barrier and to produce dopamine in the periphery [3–4]. The mechanism of action of levodopa showed that the inhibition of COMT would reduce the degradation of levodopa, hence the administration of it with a *dopamine decarboxylase* inhibitor (DDCI), will increase the dopamine simulation. Hence there will be a reduction in the exposure to levodopa.

Tolcapone is a strong, nitrocatechol-type inhibitor of the enzyme *catechol-O-methyltransferase* (COMT) [5]. Tolcapone is used as an add-on to levodopa with carbidopa combination of levodopa with benserazide medications. Levodopa is a prodrug for dopamine [6]. When compared with levodopa and catecholamines, tolcapone is highly selective and binds with the central nervous system (CNS) with a superior affinity [7]. Thus tolcapone hinders the 3-O-methylation of levodopa by generating 3-O-methyl-dopa, which is a key metabolite to compete with levodopa to cross the blood–brain barrier. As a result, the concentration of levodopa will be more when it reaches the CNS. The previously remaining concentration of levodopa is converted into dopamine at the CNS. The degradation of dopamine is inhibited by tolcapone which in turn controls the COMT activity. Hence, tolcapone improves the bioavailability thereby diminishing the clearance of levodopa and subsequently dopamine from the CNS [8]. The clinical trials in PD have established that tolcapone improves the benefits of levodopa [9].

Owing to its pharmacological importance, but with limited reports on the structural characteristics, tolcapone attracted us to conduct a study on the NBO and excitation studies etc., The observations from the NBO analysis will further enlighten to understand the stability of the molecule. Also, the NCI analysis confirms the presence of intra-

* Corresponding author at: Research Department of Chemistry, St. John's College*, Palayamkottai, Tamil Nadu 627002, India.

E-mail address: winfred.chem@stjohnscollege.edu.in (W.J. John).

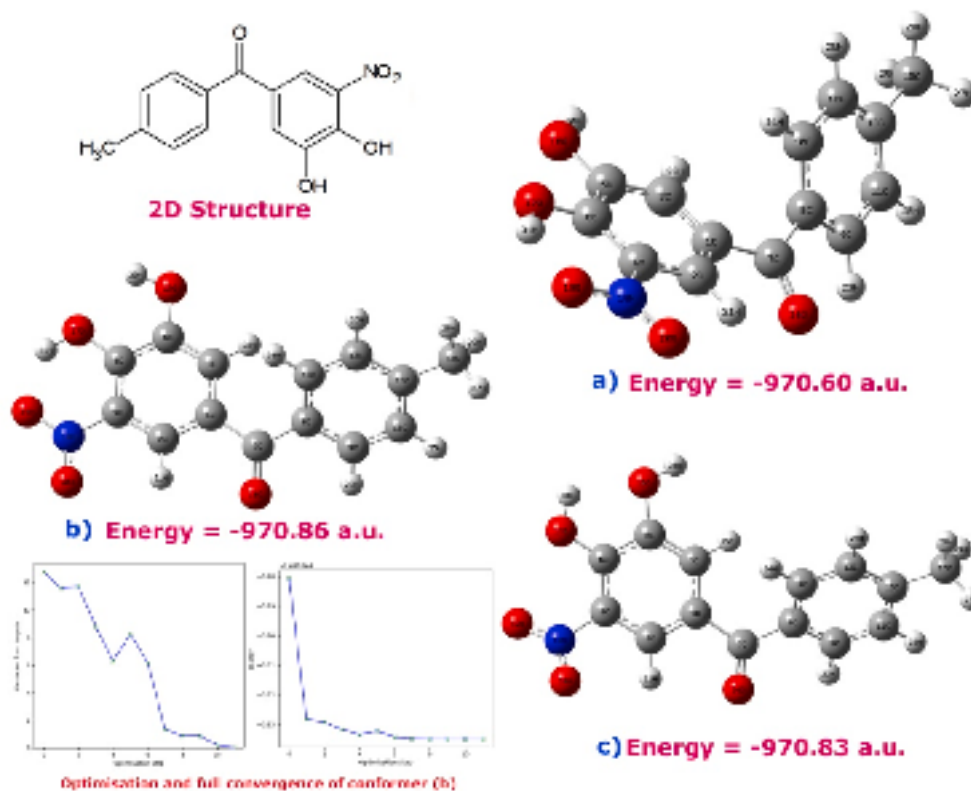


Fig. 1. Geometry and optimization of tolcaponone conformers

molecular hydrogen bond enhances the stability of the molecule.

2. Computational details

The electronic structural calculation is performed for the target molecule by using the Gaussian 16 W package [10]. The molecule is viewed by Gauss View 6. The software is implemented on an Intel® Core™ i-7 8700 CPU @ 3.20 GHz processor with 32 GB RAM. All the calculations are carried out by using the Density Functional Theory (DFT) and Becke's three-parameter functional (B3LYP) method with the 6-311G basis set [11–12]. Usually, B3LYP along with DFT calculation is widely used and shows better results with experimental values [13]. Multiwfn 3.8 tool is used to calculate various parameters like NCI, Shaded surface map with a projection of LOL, hole – electron interaction, and STM analysis. VMD 1.9.3 is used to visualize some results.

The NBO analysis highlights the role of intermolecular orbital interactions or exchange transfer in a molecule. It is always calculated by considering all possible interactions between filled donor and empty acceptor NBOs. Also, it is estimating their energetic importance by second-order perturbation theory. The stabilization energy (E_a) combined with electron delocalization between electron donor NBO (i) and electron acceptor NBO (j) is calculated according to the following equation [14–15].

$$E_2 = (\Delta E_{ij}) = q_i \frac{(F(i,j))^2}{E_j - E_i} = q_i \frac{(F_{ij})^2}{\Delta E} \quad (1)$$

where $q \rightarrow$ is the orbital occupancies E_i and E_j are diagonal elements and F_{ij} is the off diagonal NBO Fock matrix element.

3. Results and discussion

3.1. Optimization and electronic structure analysis

The geometry of tolcaponone has consecutive electron donors (OH

groups) and acceptors (NO_2 group) in one of the phenyl rings. So it is essential to carry out conformational analysis and the conformations along with their energies are produced in Fig. 1. The conformer Fig. 1(b) with the least energy (-970.86 a.u.) is considered for further investigations. The absence of negative frequency values in the imaginary frequency calculations for the selected minimum energy conformer Fig. 1(b) confirms that the molecule is completely converged and attains minimum energy configuration. The complete optimization of the molecule is further confirmed by Gausssum 03 tool and the picture is produced in Fig. 1.

The bond length, bond angle, and dihedral angles are calculated for the optimized tolcaponone molecule in the gaseous phase and are reproduced in supplementary Table S1. The shortest bond length is seen between 16O-30H (0.976 Å) and the longest bond length is located at 13C-15C (1.510 Å). The shortest bond angle is located on 27H-15C-29H as 107.2° and the largest bond angle is seen at 4C-6C-17O as (126.3°) . The calculated bond angle, bond distance, and dihedral angles between C, H, N, O are compared with the literature values and they agree well [16].

3.2. Natural charge analysis

The calculation of Mulliken atomic charge of a molecule or complex has a vital role in the application of chemical calculations, since atomic charges affect the physical properties like molecular polarizability, dipole moment, electronic structure, and other various properties of a molecular system [17–18]. But the natural analysis is an alternative to conventional Mulliken population analysis. It seems to reveal numerical stability and to better explain the electron distribution in a molecule. The charge distribution on the atom reveals the formation of pairs of donor and acceptor, which can involve the charge transfer (CT) in the molecule. The atomic charge has been used to explain the process of electronegativity equalization and CT in chemical reactions [19–20].

The natural charges for the title molecule are calculated by the

Table 1
Natural atomic charges for tolcapone molecule

Natural atomic charge (a.u.)			
Atom	Charge	Atom	Charge
C1	-0.120	O17	-0.682
C2	-0.146	N18	0.448
C3	-0.189	O19	-0.435
C4	0.016	O20	-0.321
C5	0.284	H21	0.264
C6	0.294	H22	0.241
C7	0.511	H23	0.227
C8	-0.141	H24	0.213
C9	-0.140	H25	0.207
C10	-0.171	H26	0.207
C11	-0.205	H27	0.212
C12	-0.209	H28	0.207
C13	0.017	H29	0.216
O14	-0.545	H30	0.487
C15	-0.594	H31	0.509
O16	-0.664		

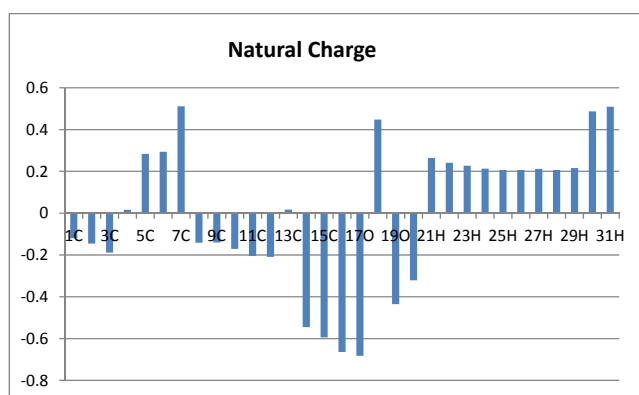


Fig. 2. Plot of Natural atomic charges for tolcapone.

B3LYP/6-311G method is displayed in Table 1 and shown in Fig. 2. It is important to mention that C4, C5, C6, C7, and C13 atoms of the title compound exhibit positive charge since all the substituents like -OH, -NO₂, -CH₃ are attached with these carbons while C1, C2, C3, C8, C9, C10, C11, C12, (carbons in the aromatic ring without any substituents), and C15 atoms exhibit negative charges. Among these C7 (carbonyl carbon) has the highest charge of 0.511 a.u. whereas the lowest charge is located on C15 (methyl carbon).

All the oxygen atoms are carrying negative charges. Among these, O20 is having a very high amount of charge (-0.321 a.u.) while the lowest charge is seen on O17 (-0.682 a.u.). The charge on N18 is determined as 0.448 a.u. All the hydrogen atoms are having a positive charge. The lowest charge among hydrogen atoms is located on H25 (0.207 a.u.) while the highest charge is placed on H31 (0.509 a.u.). The presence of a negative charge on oxygen atoms and a net positive charge on hydrogen atoms may reveal the formation of an intra-molecular interaction in solid forms [21].

3.3. HOMO – LUMO calculations

The HOMO – LUMO values are very important quantum mechanical descriptors. They play a vital role to govern a wide range of chemical interactions [22]. The Frontier Molecular Orbital (FMO) provides an insight to determine properties like molecular electrical transport, conductivity, biological properties, chemical reactivity, kinetic stability, etc., of a chemical structure [23]. Also, the gap between HOMO and LUMO explains molecular stability [24]. The energy gap is greatly responsible for the spectroscopic and chemical properties of a chemical structure [25]. The HOMO LUMO values are calculated by B3LYP/6-

Table 2
HOMO – LUMO energy gap and other physical relationship for tolcapone

Sl. no	Parameter	Formula	Charge (eV)
1	HOMO		-6.949
2	LUMO		-3.657
3	Energy gap		3.292
4	Ionization potential	IP = - E _{HOMO}	6.949
5	Electron affinity	Ea = - E _{LUMO}	3.657
6	Electro negativity	$\chi = \frac{IP + Ea}{2}$	5.303
7	Hardness	$\eta = \frac{IP - Ea}{2}$	1.646
8	Chemical potential	$\mu = -(X)$	-5.303
9	Softness	$S = \frac{1}{\eta}$	0.608

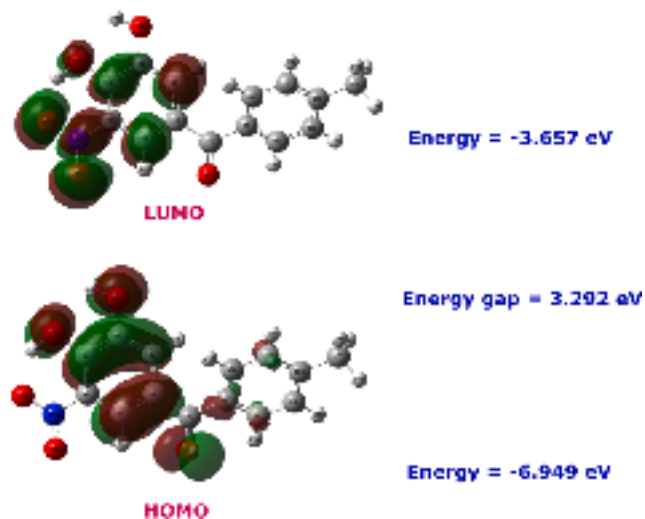


Fig. 3. Frontier energy gap of the target molecule

311G level of theory. The various physical parameters calculated from HOMO – LUMO are displayed in Table 2. The HOMO and LUMO is displayed in Fig. 3.

The HOMO appears all over the phenyl ring except the nitro group and LUMO has developed over the phenyl ring except one of the -OH groups of the target molecule. The energy gap is found to be 3.292 eV. This large gap shows that the molecule is a stable one. The electron affinity (Ea) and ionization potential (IP) can be calculated from HOMO and LUMO energies IP = -E_{HOMO} and Ea = -E_{LUMO}. The formulae to calculate hardness, softness, and chemical potential are given below [26].

$$\text{Hardness } \eta = \frac{1}{2} \left(\frac{\delta^2 E}{\delta N^2} \right) V = \frac{1}{2} \left(\frac{\delta \mu}{\delta N} \right) V = \frac{(IP - Ea)}{2} \quad (2)$$

$$\text{Chemical potential } \mu = \left(\frac{\delta E}{\delta N} \right) V = - \frac{(IP - Ea)}{2} \quad (3)$$

Where V represents external potential and E denotes the electronic energy of N electron system

$$\text{Softness } S = \frac{1}{\eta} \quad (4)$$

The ionization potential and electron affinity of the target molecule are 6.949 and 3.657 eV respectively. The chemical hardness, softness, and electronegativity values are calculated as 1.646, 0.608, and 5.303 eV respectively. From the values shown in Table 2, it is clear that the molecule is hard and stable.

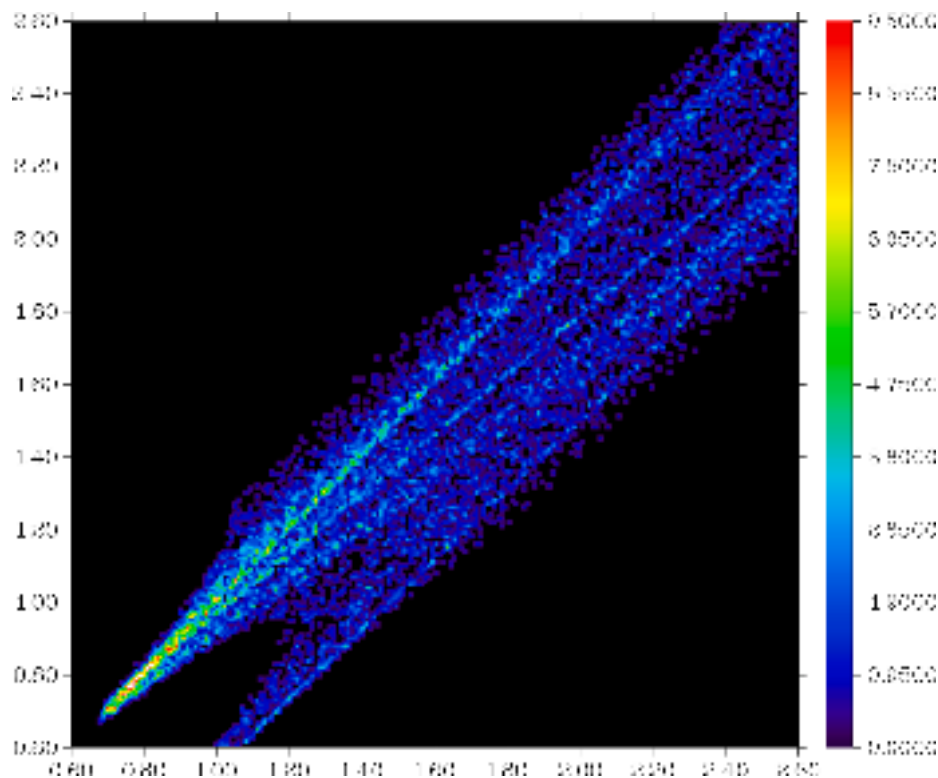


Fig. 4. Finger print plot of tolcapone

3.4. Fingerprint plot of tolcapone

The fingerprint plot defined in the framework of Hirshfeld surface analysis is very helpful to investigate the noncovalent interactions like hydrogen bond donor and acceptor in molecular system. For tolcapone molecule, the fingerprint plot is analyzed with the help of the Multiwfn 3.8 tool and shown in Fig. 4. X and Y axes in this plot correspond to parameters d_i and d_e , respectively. The plot is created by binning (d_i , d_e) pairs in certain intervals and colouring each bin of the resulting 2D histogram as a function of the number of surface points in that bin, ranging from purple (few points) through green to red (many points). Black region means there are not surface points.

From Fig. 4, we could able to see a pair of spikes at the bottom left of the plot. The observation hints that tolcapone behaves as both hydrogen bond acceptor (the lower spike $d_i > d_e$) and hydrogen bond donor (the upper spike $d_i < d_e$). The donor and acceptor numbers for tolcapone are determined from swissADME (<http://www.swissadme.ch/index.php>). The numbers of donor and acceptor of tolcapone are found to be 2 and 5 respectively.

3.5. Second order perturbation theory analysis

Interaction of electron delocalization can be quantitatively reflected using stabilization energy $E(2)$. It is estimated based on the theory of second-order perturbation [27]. The stabilization energy can be calculated by

$$E(2) = \Delta E_{i,j} = q_i \frac{F_{ij}^2}{E_i - E_j} \quad (5)$$

where $E(2)$ is orbital stabilization energy; q_i is the occupancy of donating orbitals; E_i and E_j are the energy of NBO donor and acceptor respectively and F_{ij} is the Fock matrix element between NBO orbitals i and j [13].

The NBO calculation of some selected donors and acceptors are displayed in Table S2 along with the electron density, $E(2)$, $E(j) - E(i)$,

and $f(i,j)$ values. The NBO analysis, stabilization energy $E(2)$ is used to characterize the interaction between occupied and unoccupied NBO type Lewis orbitals, since they contribute to the electron delocalization from bonding (BD) or lone pair (LP) orbitals to anti-bonding (BD*) orbitals [28]. The larger the $E(2)$ value, the more intensive is the interaction between the donors and acceptors [29].

For the title molecule, tolcapone, the LP (3) O19 \rightarrow π (N18-O20) has a very strong interaction of 128.30 kJ/mol favors the stabilization of the molecules greatly. The donor π (C4-C6) to the acceptor π^* (N18-O20) has the stabilization energy of 38.83 kJ/mol also supports the stabilization. A hydrogen bond is seen between O19 of the nitro group with nearby hydrogen of O17-H31 group. The stabilization energy is found to be 16.10 kJ/mol. Due to the presence of an intra-molecular hydrogen bond, the molecule is stabilized further. The stabilization energy of 27.62 kJ/mol for the donor-acceptor system of O16 LP(2) \rightarrow σ^* (C3-C5) helps for the stabilization. The interaction between the donor O17 \rightarrow the acceptor σ^* (C4-C6) plays a vital role in the CT excitation with 33.12 kJ/mol. In this molecule, the presence of conjugation in the aromatic ring, hydrogen bond, and charge transfer between molecules help the molecule's stabilization. Along with these stabilization energies, other donor-acceptor systems enhance the stability of the molecule and hence this title molecule is highly stable.

3.6. Fukui function

DFT is one of the best methods to realize familiar chemical concepts like electronegativity, electron affinity, ionization potential, and chemical potential etc., Kolandaivel *et.al.*, initiated the atomic descriptors to calculate the local reactive sites of the molecule [30]. In this present work, the optimized geometry is used in a single point energy calculation, which has been carried out at the DFT level theory for the anions and cations for the title molecule along with neutral molecule. The individual atomic charge calculated by NPA (Natural Population Analysis) and MPA (Mulliken Population Analysis) have been used to determine Fukui function. Usually Fukui function is calculated [31] by

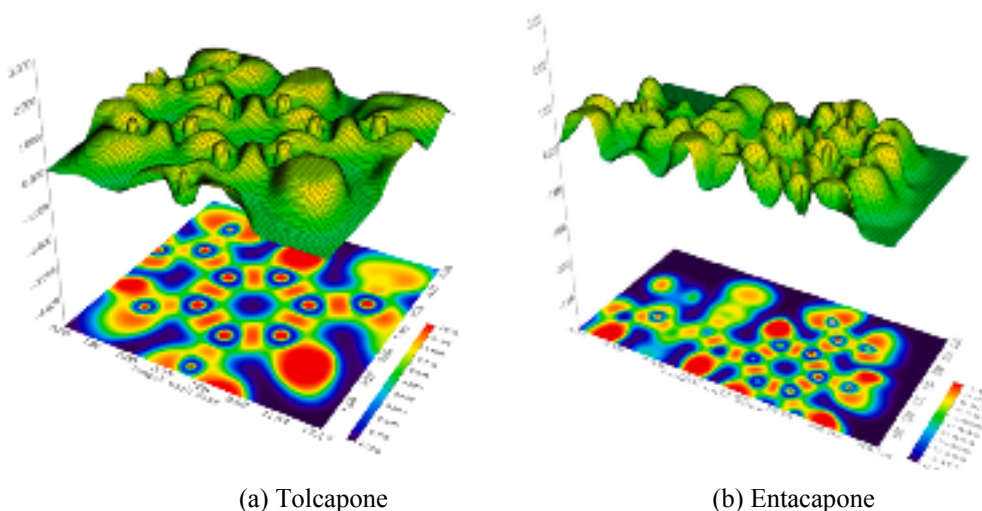


Fig. 5. Shaded surface map with a projection of localized orbital locator (LOL) analysis of tolcapone and entacapone (Here the Z-axis is LOL)

$$f_j^+ = q_j(N+1) - q_j \quad (6)$$

$$f_j^- = q_j(N) - q_j(N-1) \quad (7)$$

$$f_j^0 = \frac{1}{2} [q_j(N+1) - q_j(N-1)] \quad (8)$$

Table S3 shows the f_k^+ , f_k^0 and f_k^- values for the title molecule, tolcapone which is calculated by NPA and MPA gross charges at the DFT level of theory with the basis set B3LYP/6-311G. From Table S3, it is clear that for MPA analysis the 19O, 31H and 17O are having more positive values for cation, neutral and anions respectively. They are more prone to nucleophilic attacks. The NPA analysis suggests that the N18 is having more positive value and hence it is more prone to nucleophilic attack. The order of nucleophilic attack for the cationic, neutral and anionic attack is $18N > 7C > 31H > 30H > 6C$. The values which are almost equal or equal to zero denote the chance for radical attacks. The atoms which are having negative charges are more prone to electrophilic attack. If anyone compares the three kinds of attacks, it is possible to find out that the nucleophilic attack has a larger reactivity compared to the other electrophilic and radical attacks.

3.7. Shaded surface map with a projection of localized orbital locator (LOL) analysis

Multiwfn 3.8 tool is used to interpret the shaded surface map with a projection of LOL to analyze the electron depletion area and electron-rich area [32]. Schmider and Becke explained that Localized Orbital

Locator (LOL) is a function that is used for locating localized high localization regions [33]. It is defined as,

$$\text{LOL}(\mathbf{r}) = \frac{\tau(\mathbf{r})}{1 + \tau(\mathbf{r})} \quad (9)$$

Where $\tau(\mathbf{r})$ (dimensionless variable) is $g_0(\mathbf{r}) / g(\mathbf{r})$. It always depends on positive one electron kinetic energy and defined as,

$$g(\mathbf{r}) = \frac{1}{2} \sum \nabla \Psi_i(\mathbf{r}) \nabla \Psi_i(\mathbf{r}) \quad (10)$$

where $\Psi_i(\mathbf{r})$ is the Hatree – Fock or the Kohn Sham orbital.

In a particular region, the larger LOL is more likely the electron motion is restricted within it. For the target molecule, the shaded surface map with a projection of localized orbital locator is analyzed and shown in Fig. 5 (a). In this, the high electron depletion regions between the valence shell and inner shell are represented by blue color circles around the nucleus. Most of them are appeared in the phenyl rings. The red color area represents the high localized electron regions. In order to stabilize the molecule, the electrons lean to be localized in the outer side of the molecule tolcapone.

The same study is performed for the case of entacapone, a molecule with a similar structure, which is also used as a drug to treat Parkinson's disease and shown in Fig. 5 (b). Like tolcapone, entacapone also shows a high electron depletion area around the nucleus. Electrons are richer in $-\text{NH}_2$ and $-\text{OH}$ groups which are attached with the nucleus. Like tolcapone, electrons are occupying the outer side of the molecule and thus the molecule is stabilized.

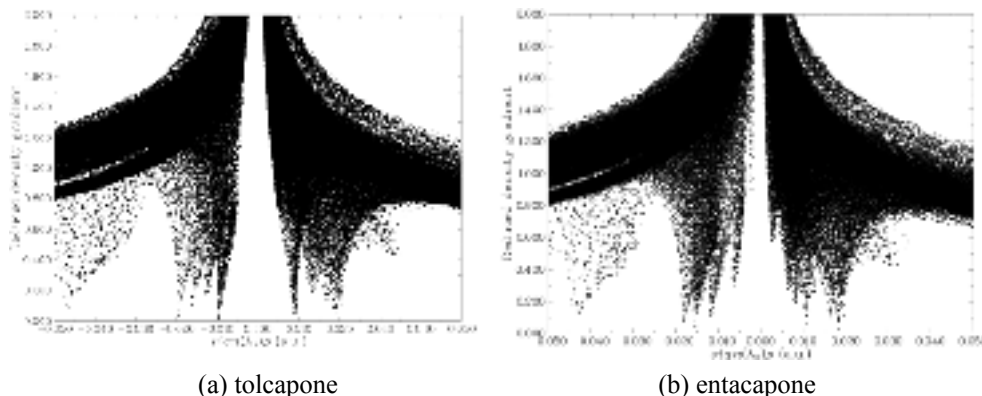


Fig. 6. The non covalent interactions in tolcapone and entacapone by NCI analysis

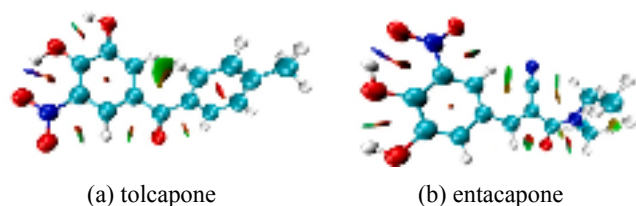


Fig. 7. Reduced Density Gradient (RDG) isosurface function for tolcapone and entacapone derived from VMD 1.9.3 software.

Table 3
Maxima and minima isosurface values of tolcapone.

Maxima		Minima	
Atom number	Energy (kcal/mol)	Atom number	Energy (kcal/mol)
C12	385.87	C6	295.86
C2	379.95	C9	219.76
C3	361.48	H25	220.11
C5	361.45		

3.8. Study of weak interactions

Multiwfn 3.8 software is used to study the weak interaction of the molecule tolcapone. Atoms in a molecule (AIM) theory is useful to explain the weak interaction within a molecule. Reduced Density Gradient (RDG) isosurface function is used to calculate the non-covalent interaction and is defined as,

$$\text{RDG}(r) = \frac{1}{2(3\pi^2)^{1/3}} \frac{|\nabla\rho(r)|}{\rho(r)^{4/3}} \quad (11)$$

NCI plot is generated by plotting Reduced Density Gradient (s) versus sign of λ_2 (Eigen values the electron density of Hessian matrix) multiplied by the density ρ . The plot indicates spikes in the low-density gradient region. It is a classic trace of NCI interaction is stronger and stronger when it moves away from zero [34]. The NCI plots of RDG for tolcapone and entacapone molecules are shown in Fig. 6 (a) and (b) respectively. From Fig. 6, it is evident that the spike around -0.040 a.u. is due to the presence of a hydrogen bond. The spikes near -0.010 to $+0.010$ a.u. are due to the presence of weak Van der Waals attraction. The spikes near $+0.020$ a.u. represent the presence of the steric effect. Since the structures are almost similar, they produce an almost similar pattern.

The isosurface of the molecules, tolcapone and entacapone are compared with each other and reproduced in Fig. 7. The blue color isosurface is developed for both the molecules near $-\text{NO}_2$ and $-\text{OH}$ indicates the presence of hydrogen bond which is responsible for the spikes near -0.040 a.u. in the NCI plot. The red isosurface have seen in the middle of the benzene ring of both the molecules indicate the presence of a steric effect. They are responsible for the spikes above 0.020 a.u. in NCI plots. Low electron densities (greenish-red isosurface) have appeared around the benzene rings of the molecules in which $-\text{OH}$ and $-\text{NO}_2$ groups are present.

The isosurface of the molecules, tolcapone and entacapone are compared with each other and reproduced in Fig. 7. The blue color isosurface is developed for both the molecules near $-\text{NO}_2$ and $-\text{OH}$ indicates the presence of hydrogen bond which is responsible for the spikes near -0.040 a.u. in the NCI plot. The red isosurface have seen in the middle of the benzene ring of both the molecules indicate the presence of a steric effect. They are responsible for the spikes above 0.020 a.u. in NCI plots. Low electron densities (greenish-red isosurface) have appeared around the benzene rings of the molecules in which $-\text{OH}$ and $-\text{NO}_2$ groups are present.

3.9. Study of orbital overlap distance function $D(r)$

The quantitative analysis orbital overlap length function $D(r)$ on molecular electron density isosurface of tolcapone is studied with the Multiwfn 3.8 software. The selected minima and maxima values are listed in Table 3.

The isosurface of maxima and minima for tolcapone is shown in Fig. 8. In Fig. 8, the red spheres represent the maxima and the blue spheres represent minima. From

Fig. 8 and Table 3, it is clear that the maxima is developed on C12 (385.87 kcal/mol) whereas the minima is located on C9 (219.76 kcal/mol) [35].

3.10. Hole – Electron interaction analysis

Multiwfn 3.8 is a very big and strong tool to perform electron excitation analysis. It also provides very deep insight into all types of electron transfer characters. It is a very practical way to reveal the nature of the electron excitations [36]. Tolcapone has two $-\text{OH}$ groups (electron donors) with a π linker (benzene) and a strong electron-withdrawing group ($-\text{NO}_2$) on one part of its structure. In the other part, it has a $-\text{CH}_3$ group (electron donor), a π linker (benzene), and an electron-withdrawing group

(-COR). Hence it is decided to investigate the electron excitation properties for this molecule of interest.

First, the molecule is optimized by B3LYP/6-311G method. Then

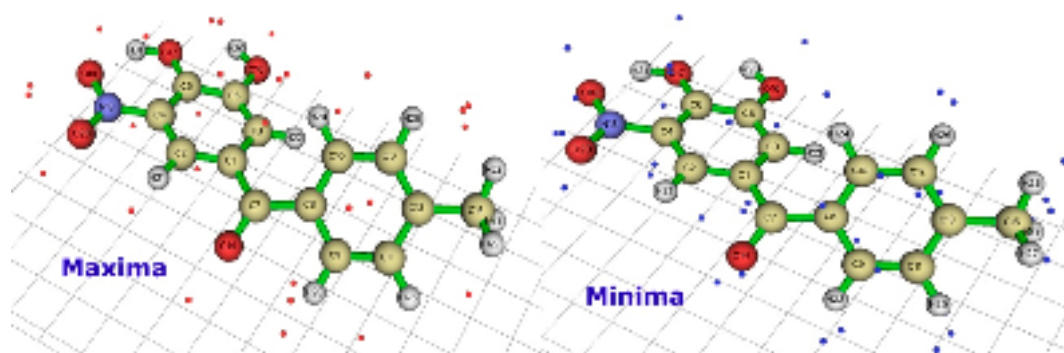


Fig. 8. Maxima and minima isosurface values of tolcapone.

Table 4
Hole – electron interaction properties for tolcapone.

Excitation	Sm(a.u.)	Sr(a.u.)	D index(Å)	H index(Å)	τ index(Å)	Excitation energy(eV)	Coloumb attractive energy (eV)	$\Delta r(\text{Å})$	Λ
S1	0.2535	0.5161	2.336	2.181	0.925	3.368	5.2727	2.5766	0.4384
S2	0.2608	0.5030	0.691	1.609	-0.400	3.538	8.7643	1.0375	0.4807
S3	0.2496	0.5162	0.860	1.888	-0.221	3.661	7.2624	1.3989	0.5447
S4	0.2596	0.5150	0.651	1.790	-0.592	4.051	8.0711	0.9975	0.5011
S5	0.3385	0.6469	1.882	2.282	0.330	4.457	5.6033	2.8114	0.4880
S6	0.0722	0.2581	5.125	2.469	3.227	4.607	3.2292	5.8393	0.1656

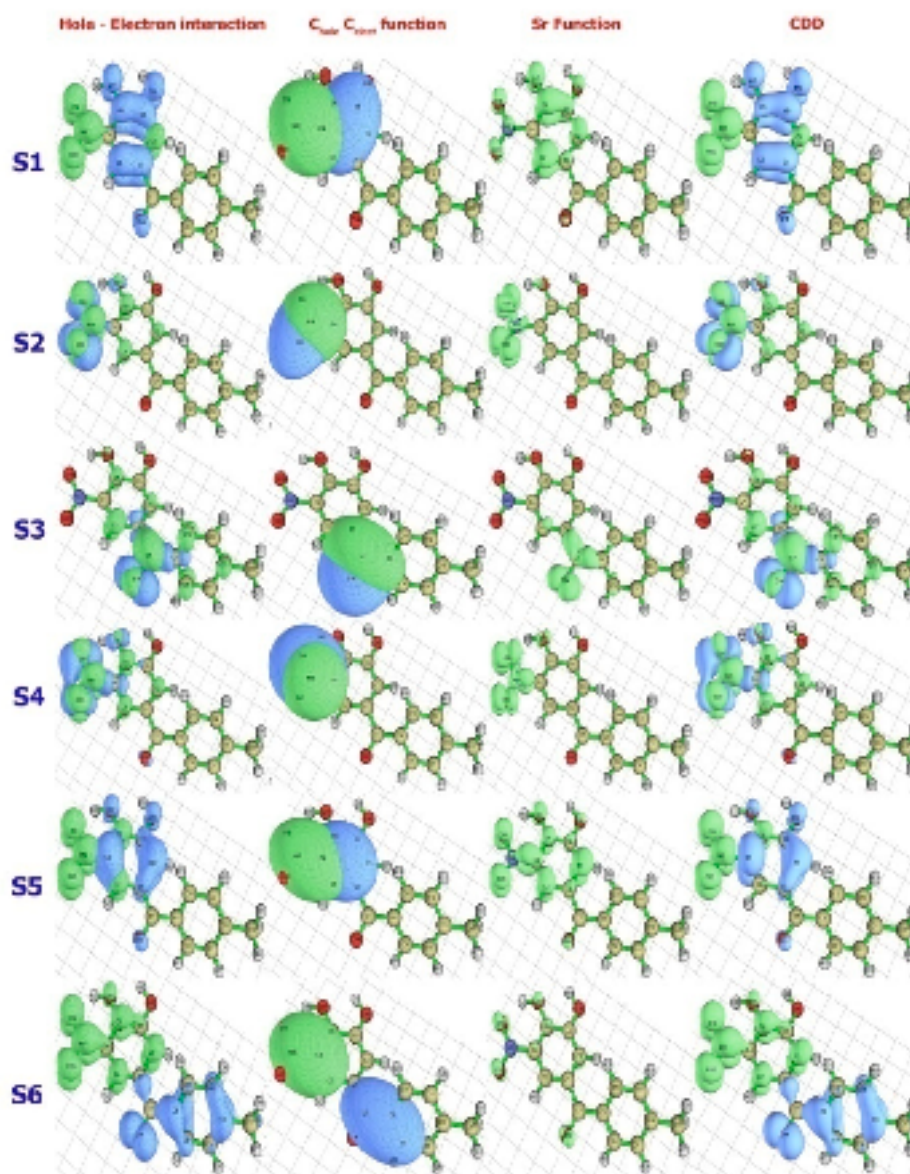


Fig. 9. The hole-electron distribution, $c_{\text{hole}} - c_{\text{elec}}$ function, Sr function and charge density difference (CDD) of tolcapone for lowest six excitation states.

TDDFT calculation is carried out with the CAM-B3LYP basis set with the IOp(9/40 = 4) keyword. The six lowest singlet excited states are analyzed. The Sm, Sr, D index, H index, and τ index, excitation energy, Coloumb attractive energy, Δr , and Λ (Lambda) values are analyzed at the same level of theory and erected in Table 4. The hole-electron distribution, $c_{\text{hole}} - c_{\text{elec}}$ function, Sr function and Charge Density Difference (CDD) are collected and shown in Fig. 9.

The large D index value is observed at $S_0 \rightarrow S_6$ excitation (5.125 Å) and can be obviously considered as charge transfer (CT) excitation. Also from Fig. 9, for $S_0 \rightarrow S_6$ it can be seen that the distance between the centre of the blue (hole) and green (electron) isosurfaces (centeroids of $c_{\text{hole}} - c_{\text{elec}}$) is large. The D index for $S_0 \rightarrow S_1$ (2.336 Å) and $S_0 \rightarrow S_5$ (1.882 Å) are also high and they may follow CT excitation.

The Sr index values of all the excited states are relatively larger (except $S_0 \rightarrow S_6$) and may follow $n \rightarrow \pi^*$ transition on the benzene ring (or) nitro group (or) keto group. For $\pi \rightarrow \pi^*$ transition, the values should be around 0.8 a.u. The absence of these values predicts that there is no $\pi \rightarrow \pi^*$ transition in lower six excitation states.

The breadth of the average distribution of hole and electron is denoted by the H index. It can be observed that the hole and electron

map that both the hole and electron of $S_0 \rightarrow S_2$, S_3 , and S_4 are distributed in the local region. So that their H index values are not large. Since the distribution of hole and electron corresponding to the excitation from $S_0 \rightarrow S_1$, S_5 and S_6 are evidently wider, their H index values are larger.

The τ indices of $S_0 \rightarrow S_1$, S_5 , and S_6 are positive, indicating that the separation of hole and electron is palpable. So we can understand that these three excitations are of charge transfer (CT) type. The τ indices for other excitations from $S_0 \rightarrow S_2$, S_3 , and S_4 are perceptible negative values, proposing that the degree of separation of hole and electron is very low. Thus they follow the local type (LE) of excitation.

The hole – electron Coulomb attractive energy indicated in Table 4 is associated with the electron excitation characteristics and the most influential factor should be the D index. The larger the D index is, the farther the distance between the main distribution of hole and electron, and the Coulomb energy weakens. From the data, it is evident that the Coulomb attraction energy for $S_0 \rightarrow S_6$ is the smallest one (3.2292 eV) of that of all the other excitations. For the excitation of $S_0 \rightarrow S_1$, S_2 , S_3 , S_4 , and S_5 , since their D index values, are small, and according to the H index, the spatial extent of this hole and electron is very narrow. So the

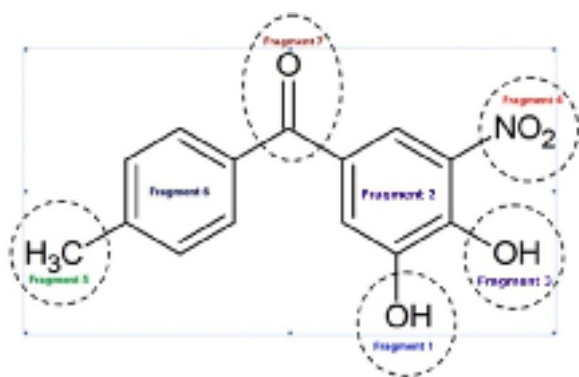


Fig. 10. Fragmentation pattern for IFCT calculation for the title molecule.

corresponding Coulomb attraction energy is very strong.

The Δr values imply that the excitation from $S_0 \rightarrow S_1$, S_5 , and S_6 may have strong CT character since they have large Δr values, 2.5766,

2.8114, and 5.8393 eV respectively. For other excitations, they are very small. (In the original paper, the Δr value suggests using 2.0 Å as a criterion for distinguishing LE and CT excitations). Since S_1 , S_5 , and S_6 are having positive τ values, as well as high Δr values, they only follow CT excitation and the other excitations follow the local type of excitation (LE).

It is evident that the Lambda (Λ) is nearly inversely proportional to the Δr values. The larger the hole – electron overlapping extent, generally the shorter is the hole – electron separation distance. Here the Λ value, 0.1656, which is obtained for $S_0 \rightarrow S_6$ excited state is shorter when compared to other values.

By the analysis of the above isosurface maps (Fig. 9) and Table 4, the following conclusions are made.

$S_0 \rightarrow S_1$ CT type of excitation of $n-\pi^*$ on the nitro group and benzene ring

$S_0 \rightarrow S_2$ LE type of excitation of $n-\pi^*$ on the nitro group

$S_0 \rightarrow S_3$ LE type of excitation of $n-\pi^*$ on the C=O group

$S_0 \rightarrow S_4$ LE type of excitation of $n-\pi^*$ on the nitro group

$S_0 \rightarrow S_5$ CT type of excitation of $n-\pi^*$ on the nitro group and benzene

Table 5

Transferred electrons between the fragments and net transferred electrons for the title molecule at S_1 transition.

excitation	Donor	OH 1 (Fragment 1)	Benzene 1 (Fragment 2)	OH 2 (Fragment 3)	Nitro (Fragment 4)	CH ₃ (Fragment 5)	Benzene 2 (Fragment 6)	CO (Fragment 7)	
S1	Transferred electrons between fragments (diagonal terms corresponds to amount of intrafragment electron redistribution)								
	OH 1	0.0000	0.0007	0.0001	0.0014	0.0000	0.0000	0.0000	
	Benzene 1	0.0003	0.0232	0.0018	0.0467	0.0000	0.0007	0.0006	
	OH 2	0.0003	0.0026	0.0002	0.0052	0.0000	0.0001	0.0001	
	Nitro	0.0000	0.0035	0.0002	0.0070	0.0000	0.0001	0.0001	
	CH ₃	0.0000	0.0068	0.0005	0.0137	0.0000	0.0002	0.0001	
	Benzene 2	0.0000	0.1516	0.0116	0.3049	0.0000	0.0048	0.0041	
	CO	0.0018	0.1282	0.0098	0.2577	0.0000	0.0040	0.0034	
	Net transferred electrons between fragments								
	Donor		OH 1 (Fragment 1)	Benzene 1 (Fragment 2)	OH 2 (Fragment 3)	Nitro (Fragment 4)	CH ₃ (Fragment 5)	Benzene 2 (Fragment 6)	CO (Fragment 7)
	OH 1	—	—	0.0004	0.0000	0.0013	-0.0000	-0.0018	-0.0015
	Benzene 1	—	—	—	-0.0008	0.0432	-0.0068	-0.1508	-0.1275
	OH 2	—	—	—	—	0.0049	-0.0005	-0.0116	-0.0098
Nitro	—	—	—	—	—	-0.0136	-0.3048	-0.2576	
CH ₃	—	—	—	—	—	—	0.0001	0.0001	
Benzene 2	—	—	—	—	—	—	—	-0.0000	
CO	—	—	—	—	—	—	—	—	

Table 6

Transferred electrons between the fragments and net transferred electrons for the title molecule at S_5 transition.

excitation	Donor	OH 1 (Fragment 1)	Benzene 1 (Fragment 2)	OH 2 (Fragment 3)	Nitro (Fragment 4)	CH ₃ (Fragment 5)	Benzene 2 (Fragment 6)	CO (Fragment 7)	
S5	Transferred electrons between fragments (diagonal terms corresponds to amount of intra-fragment electron redistribution)								
	OH 1	0.0001	0.0171	0.0014	0.0442	0.0000	0.0005	0.0012	
	Benzene 1	0.0020	0.2013	0.0158	0.5198	0.0002	0.0060	0.0135	
	OH 2	0.0001	0.0137	0.0011	0.0354	0.0000	0.0004	0.0009	
	Nitro	0.0002	0.0207	0.0016	0.0533	0.0000	0.0006	0.0013	
	CH ₃	0.0000	0.0000	0.0000	0.0000	0.0000	0.0000	0.0000	
	Benzene 2	0.0000	0.0039	0.0003	0.0101	0.0000	0.0001	0.0003	
	CO	0.0001	0.0086	0.0007	0.0221	0.0000	0.0003	0.0006	
	Net transferred electrons between fragments								
	OH 1	—	—	0.0151	0.0012	0.0440	0.0000	0.0005	0.0011
	Benzene 1	—	—	—	0.0023	0.4991	0.0002	0.0050	0.0050
	OH 2	—	—	—	—	0.0338	0.0000	0.0001	0.0002
	Nitro	—	—	—	—	—	0.0000	-0.0095	-0.0207
CH ₃	—	—	—	—	—	—	-0.0000	-0.0000	
Benzene 2	—	—	—	—	—	—	—	0.0000	
CO	—	—	—	—	—	—	—	—	

Table 7

Transferred electrons between the fragments and net transferred electrons for the title molecule at S6 transition.

excitation	Donor	OH 1 (Fragment 1)	Benzene 1 (Fragment 2)	OH 2 (Fragment 3)	Nitro (Fragment 4)	CH ₃ (Fragment 5)	Benzene 2 (Fragment 6)	CO (Fragment 7)	
S6	Transferred electrons between fragments (diagonal terms corresponds to amount of intra-fragment electron redistribution)								
		OH 1	0.0001	0.0007	0.0000	0.0014	0.0000	0.0000	0.0000
		Benzene 1	0.0003	0.0232	0.0018	0.0467	0.0000	0.0007	0.0006
		OH 2	0.0000	0.0026	0.0002	0.0052	0.0000	0.0001	0.0000
		Nitro	0.0000	0.0035	0.0003	0.0070	0.0000	0.0001	0.0000
		CH ₃	0.0000	0.0068	0.0005	0.0137	0.0000	0.0002	0.0001
		Benzene 2	0.0018	0.1516	0.0005	0.3049	0.0000	0.0048	0.0040
		CO	0.0015	0.1282	0.116	0.2577	0.0000	0.0041	0.0034
		Net transferred electrons between fragments							
		OH 1	—	0.0004	0.0000	0.0013	−0.0000	−0.0018	0.0015
		Benzene 1	—	—	−0.0008	0.0432	−0.0068	−0.1509	−0.1275
		OH 2	—	—	—	0.0049	−0.0005	−0.0116	0.0098
		Nitro	—	—	—	—	−0.0136	−0.3048	−0.2576
		CH ₃	—	—	—	—	—	0.0001	0.0001
		Benzene 2	—	—	—	—	—	—	−0.0000
		CO	—	—	—	—	—	—	—

ring

S0 → S5 CT type of excitation of n-π* on the nitro group

3.11. The inter-fragment charge transfer (IFCT) analysis

The inter-fragment charge transfer (IFCT) is a technique that is derived based on the hole – electron analysis for quantitatively investigating the amount of charge transfer between different fragments for S0 → S1, S0 → S5, and S0 → S6. For this type of calculation, the optimized molecule with B3LYP/6-311G basis set is subjected to the analysis with usual TDDFT/CAMB3LYP basis set, IOp(9/40 = 9) keyword and n = 6 states condition.

For this molecule, there are two benzene rings attached to the keto group. The fragmentation patterns are mentioned in Fig. 10.

The inter fragment charge transfer (IFCT) for S0 → S1, S0 → S5, and S0 → S6 transition details are shown in Tables 5 – 7 respectively. In each table, the upper portion represents the transferred amount of electrons between the fragments and the bottom portion explains the net transferred electrons respectively. The diagonal terms in the upper portion of S1, S5, and S6 represent the amount of intra-fragment electron distributions.

For the S0 → S1 excitation, from Table 5, it is clear that 0.0007 electrons are donated from fragment 1 (–OH 1) to fragment 2 (benzene

1) and at the same time 0.0003 electrons are back donated to fragment 1 by fragment 2. So the net electrons transfer from fragment 1 to fragment 2 is 0.0004 electrons. Likewise, all the electron distribution is mentioned in Table 5. From the data, it is clear that the electron-donating group, i. e., fragment 1 (–OH) transfers 0.0004 electrons to the π linker (benzene) and also transfers 0.0013 electrons to the electron-withdrawing group (–NO₂). This transfer of electrons from an electron-donating to the electron-withdrawing group through a π linker causes charge transfer (CT) excitation in S0 → S1. Also, it is noted that fragment 3 (–OH 2) group donates 0.0049 electrons to the nitro group, while fragment 2 (benzene) governs 0.0432 electrons. In this excitation state, the nitro group (electron-withdrawing group) withdraw electrons from both electron donors (–OH groups) through the π linker, benzene ring.

Likewise for the S0 → S5 excitation, from Table 6, it is clear that 0.0171 electrons are donated from fragment 1 (–OH 1) to fragment 2 (benzene 1) and at the same time, 0.0020 electrons are back donated to fragment 1 by fragment 2. So the net electrons transfer from fragment 1 to fragment 2 is 0.0151 electrons. Likewise, all the electron distribution is mentioned in Table 6. From the data, it is clear that the electron-donating group, i. e., fragment 1 (–OH) transfers 0.0151 electrons to the π linker (benzene) and also transfers 0.0440 electrons to the electron-withdrawing group (–NO₂). This transfer of electrons from an electron-donating to electron-withdrawing group through a π linker

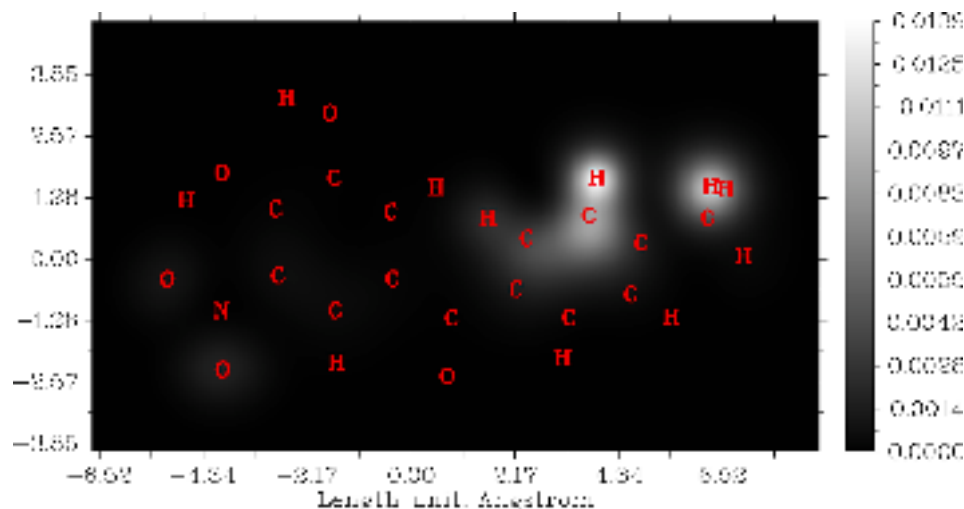


Fig. 11. STM image for tolcapone.

causes the charge transfer (CT) excitation in $S_0 \rightarrow S_5$. Also, it is noted that the fragment 3 (-OH 2) group donates 0.0338 electrons to the nitro group, while fragment 2 (benzene) governs 0.4991 electrons. In this excitation state also, the nitro group (electron-withdrawing group) is withdrawing electrons from both electron donors (-OH groups) through the π linker, benzene ring.

It is surprising that the transfer of electrons from electron donor (-OH 1) to a neighboring benzene ring through keto group ($>C=O$). Fragment 1 (-OH 1) transfers 0.0011 electrons to the keto group (fragment 7) and thus transfers 0.0005 electrons to fragment 6 (benzene 2). The fragment 3 (-OH 2) also involves in the transfer of electrons feebly to the neighbouring benzene ring, fragment 6 (0.0001 electrons) through keto group (0.0002 electrons) which has the double bond in its structure.

Similarly for the $S_0 \rightarrow S_6$ excitation, from Table 7, it is clear that 0.0007 electrons are donated from fragment 1 (-OH 1) to fragment 2 (benzene 1) and at the same time 0.0003 electrons are back donated to fragment 1 by fragment 2. So the net electrons transfer from fragment 1 to fragment 2 is 0.0004 electrons. Likewise, all the electron distribution is mentioned in Table 7 for this transition.

From the data, it is clear that the electron-donating group, i.e., fragment 1 (-OH) transfers 0.0004 electrons to the π linker (benzene) and also transfers 0.0013 electrons to the electron-withdrawing group (-NO₂). This transfer of electrons from an electron-donating to an electron-withdrawing group through a π linker causes charge transfer (CT) excitation in $S_0 \rightarrow S_6$. Also, it is noted that the fragment 3 (-OH 2) group donates 0.0049 electrons to the nitro group, while fragment 2 (benzene) governs 0.0432 electrons. In this excitation state also, the nitro group (electron-withdrawing group) withdraw electrons from both electron donors (-OH groups) through the π linker, benzene ring. In this excitation, both the electron donors (fragments 1 and 3) transfers 0.0015 and 0.0098 electrons to the keto group respectively. But in this transition, no electrons flow beyond the keto group.

3.12. Simulating constant height of STM image for tolcapone

Multiwfn 3.8 is used to calculate the simulated STM (Scanning Tunneling Microscope) image and is plotted in Fig. 11. The maximum local density of states (LDOS) value is calculated as 0.0061 a.u. In this map, the brighter the white, the larger the LDOS and thus the stronger is the tunneling current (I). According to Tersoff – Hamann model, the tunneling current is positively proportional to LDOS. In this case, 'I' is more predominant at the benzene ring (at C12 and H26) in which -CH₃ group is attached.

4. Conclusion

For the title molecule, tolcapone, Mulliken charge analysis, HOMO-LUMO related physical properties, NBO analysis, stabilization energies, and delocalization properties are studied along with Fukui functions etc. Based on the results, the following conclusions are made.

- i) The molecule is prone to nucleophilic attack rather than electrophilic and radical attacks
- ii) Electron depletion areas are seen in aromatic rings
- iii) The molecule has weak Van der Waals interaction, intramolecular hydrogen bond, and steric effects
- iv) The maximum isosurface energy is found in C12 and the minima is present on C9
- v) Three CT excitations (S1, S5, and S6) are found within the lowest six excitations
- vi) The tunneling current is found to be maximum at C12 and H26 for tolcapone
- vii) The molecular structure of tolcapone is compared with entacapone, a drug for Parkinson's disease, produces almost similar NCI plots and shaded surface map with LOL surfaces.

Declaration of Competing Interest

The authors declare that they have no known competing financial interests or personal relationships that could have appeared to influence the work reported in this paper.

Acknowledgement

The authors are thankful to the Principal, the Secretary and the Management of St. John's College, Palayamkottai for providing the computer and software facilities.

Funding

This research did not receive any specific grant from funding agencies in the public, commercial, or not-for-profit sectors.

Appendix A. Supplementary data

Supplementary data to this article can be found online at <https://doi.org/10.1016/j.comptc.2021.113296>.

References

- [1] M.J. Savitt, L.V. Dawson, M.T. Dawson, Diagnosis and treatment of Parkinson disease: Molecules to Medicine, *J. Clin. Invest* 116 (2006) 1744–1754, <https://doi.org/10.1172/JCI29178>.
- [2] J.G. Greenfield, F.D. Bosanquet, The brain-stem lesions in Parkinsonism, *J. Neurol. Neurosurg. Psychiatry* 16 (1953) 213–226, <https://doi.org/10.1136/jnnp.16.4.213>.
- [3] D.D. Truong, Tolcapone: Review of its pharmacology and use as adjunctive therapy in patients with Parkinson's disease, *Clinical Interventions in Aging* 4 (2009) 109–113, <https://doi.org/10.2147/CLIA.S3787>.
- [4] S. Kaakkola, Effects of Drugs and Catechol-O-methyltransferase Inhibitors on Hydration Status, *Drugs* 29 (2000) 1233–1250, <https://doi.org/10.2165/00003495-200059060-00004>.
- [5] K.M. Jorga, B. Fotteler, P. Heizmann, G. Zürcher, Pharmacokinetics and pharmacodynamics after oral and intravenous administration of tolcapone, a novel adjunct to Parkinson's disease therapy, *Europ. J. of Clin. Pharm.* 54 (5) (1998) 443–447, <https://doi.org/10.1007/s002280050490>.
- [6] F. Haddad, M. Sawalha, Y. Khawaja, A. Najjar, R. Karaman, Dopamine and Levodopa prodrugs for the treatment of Parkinson's Disease, *Molecules* 23 (1) (2018) 40, <https://doi.org/10.3390/molecules23010040>.
- [7] D. Deleu, M.G. Northway, Y. Hanssens, Clinical Pharmacokinetic and Pharmacodynamic properties of drugs used in the treatment of parkinson's disease, *Clinical Pharmacokinetics* 41 (4) (2002) 261–309, <https://doi.org/10.2165/00003088-200241040-00003>.
- [8] K. Jorga, B. Fotteler, P. Heizmann, R. Gasser, Metabolism and excretion of tolcapone, a novel inhibitor of catechol-O-methyltransferase, *British Journal of Clinical Pharmacology* 48 (4) (2001) 513–520, <https://doi.org/10.1046/j.1365-2125.1999.00036.x>.
- [9] A. Napolitano, P.D. Dotto, L. Petrozzi, Pharmacokinetics and pharmacodynamics of L-Dopa after acute and 6-week tolcapone administration in patients with Parkinson's disease, *Clin. Neuropharmacol* 22 (1999) 24–29, <https://doi.org/10.1097/00002826-199901000-00005>.
- [10] Gaussian 16, Revision B.01, M.J. Frisch, G.W. Trucks, H.B. Schlegel, G. E. Scuseria, M.A. Robb, J.R. Cheeseman, G. Scalmani, V. Barone, G.A. Petersson, H. Nakatsuji, X. Li, M. Caricato, A.V. Marenich, J. Bloino, B.G. Janesko, R. Comperts, B. Mennucci, H.P. Hratchian, J.V. Ortiz, A.F. Izmaylov, J.L. Sonnenberg, D. Williams-Young, F. Ding, F. Lipparini, F. Egidi, J. Goings, B. Peng, A. Petrone, T. Henderson, D. Ranasinghe, V.G. Zakrzewski, J. Gao, N. Rega, G. Zheng, W. Liang, M. Hada, M. Ehara, K. Toyota, R. Fukuda, J. Hasegawa, M. Ishida, T. Nakajima, Y. Honda, O. Kitao, H. Nakai, T. Vereven, K. Throssell, J.A. Montgomery, Jr., J.E. Peralta, F. Ogliaro, M.J. Bearpark, J.J. Heyd, E.N. Borherters, K.N. Kudin, V.N. Staroverov, T.A. Keith, R. Kobayashi, J. Normand, K. Raghavachari, A.P. Rendell, J.C. Burant, S.S. Iyengar, J. Tomasi, M. Cossi, J.M. Millam, M. Klene, C. Adamo, R. Cammi, J.W. Ochterski, R. L. Martin, K. Morokuma, O. Farkas, J.B. Foresman, and D.J. Fox Gaussian, Inc., Wallingford CT, 2016.
- [11] A.D. Becke, Density-functional thermochemistry. III. The role of exact exchange, *J. Chem. Phys* 98 (1993) 5648–5652, <https://doi.org/10.1063/1.464913>.
- [12] C. Lee, W.X. Yang, R.G. Par, Development of the Colle-Salvetti correlation-energy formula into a functional of the electron density, *Phys. Rev* 37B (1988) 785–789, <https://doi.org/10.1103/physrevb.37.785>.
- [13] N. Singla, P. Chowdhury, Density functional investigation of photo induced Intramolecular proton transfer (IPT) in Indole-7-carboxaldehyde and its experimental verification, *J. Mol. Struct* 1045 (2013) 72–80, <https://doi.org/10.1016/j.molstruc.2013.04.015>.
- [14] F. Weinhold, C.R. Lanois, Natural bond orbitals and extensions of localized bonding concepts, *Chemistry Education Research and Practices* 2 (2001) 91–104, <https://doi.org/10.1039/b1rp90011k>.

- [15] N.K. Nobel, K. Bamba, Q.W. Partridge, N. Ziao, NBO population analysis and electronic calculation of four azopyridine ruthenium complexes by DFT method, *Comput. Chem* 5 (2017) 51–64, <https://doi.org/10.4236/cc.2017.51005>.
- [16] FTIR, FT-Raman spectra and ab initio DFT vibrational analysis of 2,4-dichloro-6-nitrophenol, *Spectrochimica Acta Part A* 65 (2006) 1053–1062, <https://doi.org/10.1016/j.saa.2006.01.041>.
- [17] P. Rubarani, Gangadharan, S. Sampath Krishnan, Natural bond orbital (NBO) population analysis of 1-Azanaphthalene-8-ol, *Acta Physica Polonica A*, 125, (2014), 18–22. <https://doi.org/10.12693/APhysPolA.125.18>.
- [18] J. Sidir, Y.G. Sidir, M. E, Tasal, *Ab initio* Hartree-Fock and density functional theory investigations on the conformational stability, molecular structure and vibrational spectra of 7-acetoxy-6-(2,3-dibromopropyl)-4,8-dimethylcoumarin molecule, *J. Mol. Struct* 134 (2010) 964, <https://doi.org/10.1016/j.molstruc.2009.11.023>.
- [19] K. Jug, Z. B. Maksic, Z. B. Maksic Part 3, Springer, Berlin, 1991.
- [20] S. Flisazar, Springer, New York, 1983.
- [21] L.X. Hong, L.X. Ru, Z.X. Zhou, Calculation of vibrational spectroscopic and NMR parameters of 2-Dicyanovinyl-5-(4-N, N-dimethylaminophenyl) thiophene by ab initio HF and density functional methods, *Comput. Theor. Chem* 969 (2011) 27–34, <https://doi.org/10.1016/j.comptc.2011.05.010>.
- [22] Z. Zhou, R.G. Parr, Thermodynamic hardness and the maximum hardness principle, *J. Am. Chem. Soc* 112 (1990) 5720–5724, <https://doi.org/10.1021/ja00171a007>.
- [23] H. Singh, A DFT approach for theoretical and experimental study of structure, electronic, Hirshfeld surface and spectroscopic properties of 12-(4-bromophenyl)-2-(prop-2-ynyloxy)-6,10-dihydro-8H-benzo[α]xanthen-11(12H)-on single crystal, *Chemical Physics* 524 (2019) 1–13, <https://doi.org/10.1016/j.chemphys.2019.05.003>.
- [24] R.G. Pearson, Absolute electronegativity and hardness: applications to organic chemistry, *J. Org. Chem* 54 (1989) 1423–1430, <https://doi.org/10.1021/jo00267a034>.
- [25] K. Fukui, T. Yonezawa, H. Shingu, A molecular orbital theory of reactivity in aromatic hydrocarbons, *J. Chem. Phys* 20 (1952) 722–725, <https://doi.org/10.1063/1.1700523>.
- [26] B. Sylaja, S. Gunasekaran, S. Srinivasan, Vibrational, NLO, NBO, NMR, frontier molecular orbital and molecular docking studies of diazepam, *Mat. Resea. Inno.* 22 (6) (2018) 361–373, <https://doi.org/10.1080/14328917.2017.1324356>.
- [27] S. Rahmawati, C.L. Radiman, M.A.K. Martoprawiro, Density Functional Theory (DFT) and Natural Bond Orbital (NBO) Analysis of Intermolecular Hydrogen Bond Interaction in “Phosphorylated Nata De Coco - Water”, *J. Chem* 18 (1) (2018) 173–178. <https://doi.org/10.22146/jc.25170>.
- [28] H.Y. Chen, H.B. Ji, Alkaline hydrolysis of cinnamaldehyde to benzaldehyde in the presence of β cyclodextrin, *AlChE.J* 56 (2) (2010) 466–476, <https://doi.org/10.1002/aic.12017>.
- [29] O. Erdogan, M. Unsalan, M. Amalanathan, I. Hubert Joe, Infrared and Raman spectra, vibrational assignment, NBO analysis and DFT calculations of 6-aminoflavone, *J. Mol. Struct* 980 (2010) 24–30, <https://doi.org/10.1016/j.molstruc.2010.06.032>.
- [30] P. Kolandaivel, G. Praveena, P. Selvarengan, Study of atomic and condensed atomic indices for reactive sites of molecules, *J. Chem. Sci* 117 (2005) 591–598, <https://doi.org/10.1007/bf02708366>.
- [31] Z. Demircioğlu, C.G.A. Kaştaş, O. Büyükgüngör, Theoretical analysis (NBO, NPA, Mulliken Population Method) and molecular orbital studies (hardness, chemical potential, electrophilicity and Fukui function analysis) of (E)-2-((4-hydroxy-2-methylphenylimino)methyl)-3-methoxyphenol, *J. of Mol. Stru.* 1091 (2015) 183–195, <https://doi.org/10.1016/j.molstruc.2015.02.076>.
- [32] T. Lu, F. Chen, Multiwfn: A multi wave function analyzer, *J. Comput. Chem* 33 (2012) 580–592, <https://doi.org/10.1002/jcc.22885>.
- [33] H. L. Schmider, A. D. Becke, Chemical content of the kinetic energy density, *J. of Mol. Struct: TheoChem*, 527 (2000), 51 – 61. [https://doi.org/10.1016/S0166-1280\(00\)00477-2](https://doi.org/10.1016/S0166-1280(00)00477-2).
- [34] A.P. Bandyopadhyay, A. Karmakar, J. Deb, U. Sarkar, Md.M. Seikh, Non-covalent interactions between epinephrine and nitroaromatic compounds: A DFT study, *Spectrochimica Acta Part A* 228 (2019), 117827, <https://doi.org/10.1016/j.saa.2019.117827>.
- [35] T. Lu, Multiwfn: Software Manual, version 3.8, 2020.
- [36] Z. Liu, T. Lu, Q. Chen, An sp hybridized all-carboatomic ring, cyclo[18]carbon: electronic structure, electronic spectrum, and optical nonlinearity, *Carbon* 165 (2020) 461–467, <https://doi.org/10.1016/j.carbon.2020.05.023>.



Research article

Spectral, NBO, NLO, NCI, aromaticity and charge transfer analyses of anthracene-9,10-dicarboxaldehyde by DFT

J. Jebasingh Kores^{a,1}, I. Antony Danish^{b,1}, T. Sasitha^{c,1}, J. Gershom Stuart^{c,1}, E. Jimla Pushpam^{c,1}, J. Winfred Jebaraj^{c,*,1}^a Department of Physics, Pope's College (Autonomous), Sawyerpuram, 628251, Tamilnadu, India^b Department of Chemistry, Sadakathullah Appa College (Autonomous), Tirunelveli, 627011, Tamilnadu, India^c Department of Chemistry, St. John's College, Tirunelveli, 627002, Tamilnadu, India

ARTICLE INFO

Keywords:

Anthracene-9,10-dicarboxaldehyde

DFT

Docking

NBO

Non-covalent interaction

HOMA

ABSTRACT

Anthracene-9,10-dicarboxaldehyde (ADCA) is a polynuclear aromatic compound that has a planar structure with double bonds which are in conjugation. The molecule is subjected to theoretical investigation with DFT/B3LYP/6-311++G(d,p) basis set to find out the electronic structural properties and stability. Theoretical and experimental vibrational analyses are carried out. NBO studies predict that the molecule has high stability. NCI interaction studies reveal that Van der Waals force and steric effect are seen in the molecule. A shaded surface map with a projection of LOL analysis pointed out that electron depletion area is seen in this molecule. The tunnelling current is more in the boundary rings than the central ring. It is docked with the protein 4COF and the binding energy is found to be -6.6 kcal/mol. Electrons excitation analysis is performed and found that local excitation takes place for the lowest five excitations. The aromaticity of the molecule is also thoroughly investigated.

1. Introduction

Poly-nuclear aromatic compounds like anthracene are having a π conjugated electron system which has a great impact in many research areas like material science [1, 2]. The organic π electron systems have attracted great interest from both the scientific communities and industrialists on the basis of the potential applications as active elements in LED (Light-emitting electrode). The distribution of electron clouds on the aromatic moiety determines the optical and electro-physical properties. Ionization potential and electron affinity are always related to this kind of charge carriers. The mobility of the charge from one place to another is a key factor for the development of new organic optoelectronic material or devices. Normally anthracene and its derivatives have applications in organic electroluminescence investigations [3, 4, 5] and molecule conductivity studies [6]. The rich π conjugated system has a rigid planar structure.

The arrival of computational practices assists to predict the properties of molecules and to explore the chemical dependences. Usually DFT approach can give more accurate results than semi empirical methods [7]. This molecule has three rings, i.e., two terminals and one centre ring

with electron withdrawing substitution at the two corners of it. So it is decided to check how the aromaticity is varied? Properties like electronic structure, NBO (Natural Bond Orbital), NLO (Non Linear Optical), ESP (Electrostatic Potential), Frontier energy gap, Mulliken charge prediction, and theoretical spectral analysis, etc., are useful to interpret about a molecule completely. But unfortunately there is no such work has been done on this molecule. Hence it is decided to explore the properties by DFT and wave function analysis for the structurally important molecule. DFT investigation of anthracene-9,10-dicarboxaldehyde is carried out to investigate all the above said properties clearly. Since the molecule is a planar poly-nuclear ring system, the stability is expected to be very much. So we tried to identify which parameters are helpful to enhance the stability of this molecule. A thorough NBO study is carried out to know about the stability of the molecule. Wave function analyses which furnish more clarity about the structural properties like, NCI (Non Covalent Interaction), Shaded surface map determination, Hole-electron excitation, aromaticity determination, etc., are carried out.

The molecule under investigation is checked with PASS online tool to have an idea about the choice of proteins to bind. Interestingly the results suggested that this molecule can be docked well with around 200

* Corresponding author.

E-mail address: winfred.chem@stjohnscollege.edu.in (J. Winfred Jebaraj).¹ Affiliated to Manonmaniam Sundaranar University, Abishekapatti, Tirunelveli- 627012, Tamilnadu, India.

proteins of various domains. From the results, it is found that this molecule under investigation can be used for phobia disorders. The human protein 4COF is related to this disease so it is decided to extend for molecular docking. The docking pattern of the target molecule with 4COF protein is investigated by PyRx tool and viewed by PyMOL programme.

2. Computational details

The gas-phase molecular geometry is optimized in the neutral state with the help of DFT using the B3LYP functionals. Becke's three-parameter hybrid exchange functional [8] combined with the Lee-Yang-Parr correlation functional basis set [9] with the diffuse function namely 6-311++G basis is implemented in Gaussian 16 package [10]. A valence double zeta set augmented with *d* polarisation function with *s* and *p* diffusion functions for each atom except for hydrogen is also included.

Basis sets with diffuse functions are important for systems where electrons are relatively far away from the nucleus and systems with low ionization potentials and so on. Unrestricted B3LYP formalism is used to carry out all the calculations. Recently DFT has appeared as a steadfast standard method for the theoretical research of geometrical and electronic properties like ionization potential, electronic excitation spectrum, etc., They have high accuracy for the wide range of the systems.

Multiwfn 3.8 tool is used to calculate NCI, shaded surface map, hole electron transfer, aromaticity, and simulated STM (Scanning Tunneling Microscope) deeply. PyRx and PyMOL tools are used to investigate the docking studies.

3. Experimental details

The FT-IR spectrum for the molecule is recorded in the 4000–400 cm^{-1} region with a Nicolet 1S5R FT-IR spectrometer using KBr pellets (AR) with diamond crystal plate. The UV-Visible spectrum is recorded by double beam UH-5300 spectrophotometer by dissolving 0.5 mg of the sample in 10 ml of absolute ethanol.

4. Results and discussion

4.1. Electronic structure determination

The molecule, anthracene-9,10-dicarboxaldehyde (ADCA) is optimized to obtain the fully converged structure. The convergence and full optimization are confirmed by GaussSum 3.0 tool. The absence of imaginary frequencies determined by Gaussian 16W tool also reveals that the molecule is fully optimized. The investigated molecule has 28 atoms and 122 electrons. It is found to be neutral and singlet in nature. The 2D and optimized 3D structures of the target molecule are shown in Figure 1 (a) and (b) respectively.

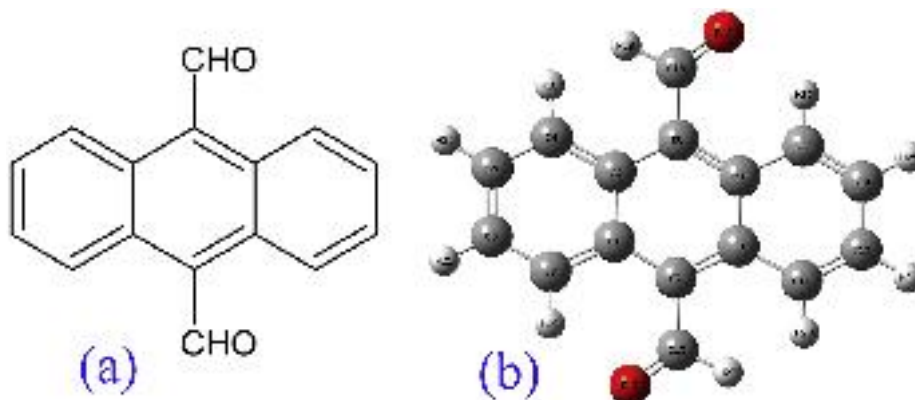


Figure 1. (a) The 2D and (b) optimized 3D structures of ADCA.

The atom numbering list generated by the Gaussian 16W software is listed in Table 1. The bond angle, bond distance, and dihedral angles for the optimized structure are determined by the DFT/B3LYP/6-311++G(d,p) basis set in the gaseous phase and listed in Table S1 (Supplementary Table 1). Trotter investigated the crystal structure of 9-anthraldehyde. The bond length and bond angle results are compared with the above results and found good [11]. Byru *et al.*, has published a DFT work on the derivative of anthracene-9-carboxaldehyde, in which they specified the electronic structural properties along with XRD data. The measured values of the target molecule are in good agreement with the previous literature reports [12, 13, 14]. The average C–H bond length in anthracene molecule is estimated as 1.08 Å theoretically. The shortest C–H bond length of 1.076 Å is observed at 3C–19H and 13C–25H respectively. The longest bond of 1.492 Å is observed at 7C–15C and 9C–16C respectively. Two aldehyde carbons are attached to the aromatic ring. The calculated average bond angles between CCC are found to be 120.3° which are in good agreement with the reported experimental value of 120.9°. Likewise, the average bond angle between CCH is found to be 118.8°. The bond angle between CCH of aldehyde groups [(7C–15C–27H) and (9C–16C–28H)] are found to be 114.9° respectively. The angle between the CCO of aldehyde groups (9C–16C–18O) and (7C–15C–17O) are found to be 127.7° respectively.

4.2. Mulliken charge analysis

Mulliken charge for the target molecule is calculated at the same level of the basis set and is given in Table 2 and the plot generated is shown in Figure 2. From Table 2 and Figure 2, it is clear that the two oxygen atoms 17O and 18O are having almost the same charge (−0.215 a.u.). 1C, 2C, 7C, 8C, 9C, 10C are having positive charges and remaining carbon atoms are possessing negative charges.

1C is having greater charge of 0.8063 a.u. while the 4C is having the least charge of -0.7181 a.u. All the hydrogen atoms are having a positive charge. Among these 27H and 28H hydrogen atoms are having 0.1575 a.u. each since they are attached with carbonyl carbons. 21H and 26H atoms are having the charge of 0.1779 a.u. each respectively.

Table 1. The atom numbering list of ADCA.

1	2	3	4	5	6	7
C	C	C	C	C	C	C
8	9	10	11	12	13	14
C	C	C	C	C	C	C
15	16	17	18	19	20	21
C	C	O	O	H	H	H
22	23	24	25	26	27	28
H	H	H	H	H	H	H

Table 2. Mulliken charge of ADCA by B3LYP/6-311++G(d,p) method.

Atom	Charge (a.u.)	Atom	Charge (a.u.)
1C	0.8063	15C	-0.4298
2C	0.6310	16C	-0.4300
3C	-0.6784	17O	-0.2158
4C	-0.7181	18O	-0.2159
5C	-0.4100	19H	0.1885
6C	-0.3066	20H	0.0435
7C	0.5712	21H	0.1779
8C	0.6310	22H	0.1827
9C	0.5714	23H	0.0436
10C	0.8063	24H	0.1828
11C	-0.7180	25H	0.1885
12C	-0.3067	26H	0.1779
13C	-0.6782	27H	0.1575
14C	-0.4100	28H	0.1575

4.3. Chemical reactivity

Density functional theory is a very useful framework for the study of chemical reactivity. Four decades ago DFT theory of chemical reactivity has been born. It provides the electronic structure of the chemical species [15]. Using HOMO and LUMO values the chemical reactivity parameters are calculated for ADCA using DFT with B3LYP/6-311++G(d,p) level of theory, and the values are listed in Table 3. The HOMO and LUMO are seen on overall molecule and exposed in Figure 3.

Electron affinity and ionization potential: Electron affinity (A) and ionization potential (I) measure the ability of chemical species to accept and donate one electron (Eqs. (1) and (2)). They are defined as,

$$A = -E_{LUMO} \quad (1)$$

$$I = -E_{HOMO} \quad (2)$$

E_{HOMO} and E_{LUMO} are the energies of highest occupied and lowest unoccupied molecular orbitals respectively.

Electro negativity and chemical potential: Electronegativity (χ) is one of the most used chemical concepts, a tendency of an atom or group that attracts an electron towards itself (eqn.3). It is the minus of chemical potential (μ). According to Mulliken [16, 17] it is defined as,

Table 3. Chemical reactivity parameters of ADCA at B3LYP/6-311++G(d,p) level.

S. No	Physical parameter	Charge (eV)
1	HOMO	-6.3003
2	LUMO	-3.4989
3	Energy gap (ΔE)	2.8014
4	Ionization potential (I)	6.3003
5	Electron affinity (A)	3.4989
6	Electronegativity (χ)	4.8996
7	Chemical hardness (η)	1.4007
8	Global softness (S)	0.7139
9	Chemical potential (μ)	-4.8996
10	Electrophilicity index (ω)	8.5693
11	Net electrophilicity ($\Delta\omega^\pm$)	-4.8997
12	Electron donating capability (ω^-)	11.1942
13	Electron accepting capability (ω^+)	6.2945
14	Additional electronic charge (ΔN_{max})	3.4979

$$\chi = \frac{I + A}{2} \quad (3)$$

Using Koopman's theorem [16, 17, 18], the electron affinity and ionization potential can be replaced by the lowest unoccupied molecular orbital (LUMO) energy and highest occupied molecular orbital (HOMO) energy respectively (eqn.4).

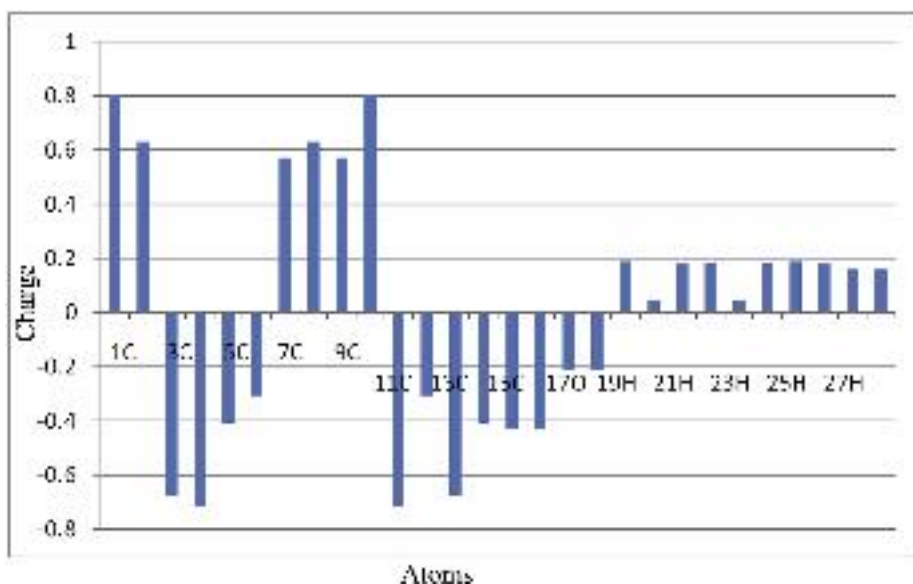
$$\chi = -\mu = -\frac{E_{HOMO} + E_{LUMO}}{2} \quad (4)$$

Global hardness and softness: Global hardness (η) is equal to the energy difference between the occupied and unoccupied molecular orbitals (eqn.5). It is related to another molecular property global softness (S) (eqn.6). It is a reciprocal of hardness [17].

$$\eta = \frac{E_{LUMO} - E_{HOMO}}{2} \quad (5)$$

$$s = \frac{1}{\eta} \quad (6)$$

Electrophilicity and net electrophilicity: The ability of an electrophile to accept electrons from the nucleophile is called electrophilicity (eqn.7).

**Figure 2.** Mulliken charge plot of ADCA by B3LYP/6-311++G(d,p) method.

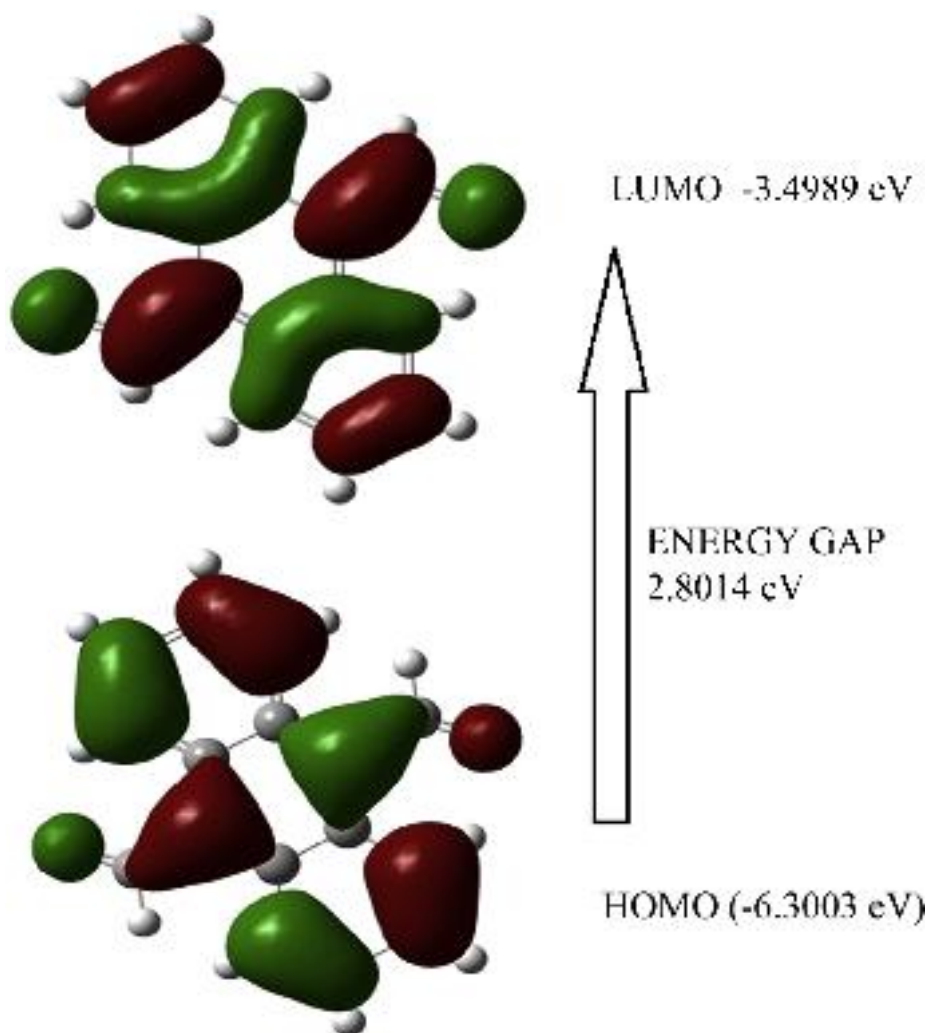


Figure 3. HOMO – LUMO of ADCA

In DFT, electrophilicity has been calculated by both chemical potential and hardness [19, 20].

$$\omega = \frac{\mu^2}{2\eta} \quad (7)$$

Using electron-accepting (ω^+) and electron-donating (ω^-) powers, net electrophilicity ($\Delta\omega^\pm$) (eqn.8) have been proposed [21].

$$\Delta\omega^\pm = \omega^+ - (\omega^-) \quad (8)$$

where

$$\omega^- = \frac{(3I + A)^2}{16(I - A)} \quad (9)$$

$$\omega^+ = \frac{(I + 3A)^2}{16(I - A)} \quad (10)$$

The additional electronic charge is defined as (eqn.11)

$$\Delta N_{\max} = \frac{-\mu}{\eta} \quad (11)$$

The energy difference between HOMO and LUMO of ADCA is 2.8014 eV. So this molecule can be a stable molecule. The global hardness, softness, chemical potential, electronegativity, and electrophilicity index

of ADCA are found to be 1.4007, 0.7139, -4.8996, 4.8996, and 8.5692 eV respectively.

4.4. Molecular electrostatic potential (ESP) analysis

Molecular electrostatic potential of a molecule gives information about the properties like molecular size, dipole moment, shape, electronic density, hydrogen bonding interactions, and chemical reactivity etc., [22]. In molecular electrostatic potential, the surfaces are represented in red, blue, light blue, yellow, and green colors. The red colour represents the electron-rich (partially negative charge) area whereas the blue colour represents the electron poor (partially positive charge) locations. Light blue colour represents slightly electron-deficient region while the yellow colour represents a slightly electron-rich domain. The green colour represents a neutral charge location [23]. The electrostatic potential map for the title molecule is investigated by B3LYP/6-311++G(d,p) method and the electrostatic potential map with different colour representation is shown in Figure 4 (a). The region of red colour (electron-rich) is located around the oxygen atoms of the two aldehyde groups in which electrophilic attack is possible. Blue colour region (electron-poor) region is spread all over the molecule around hydrogen atoms which is prone to nucleophilic attack. The contour map of the investigated molecule is also analysed and shown in Figure 4 (b). From the map it is clear that the contour map spreads through all the atoms.

4.5. Non linear optical effect

The dipole moment, mean polarizability and first-order hyperpolarizability of the title compound is calculated by DFT/B3LYP/6-311++G(d,p) level of theory based on finite field approach. The first order hyperpolarizability is a third rank tensor that can be described by the $3 \times 3 \times 3$ matrix. Due to Kleinman symmetry [24] the 27 component of the 3D matrix can be reduced to 10 components.

The β components are defined as the coefficient in the Taylor series expansion (eqn.12) of the energy in the external electric field, which is weak and homogenous. This expansion is as follows

$$E = E^0 - \mu_\alpha F_\alpha - \frac{1}{2} \alpha_{\alpha\beta} F_\alpha F_\beta - \frac{1}{6} \beta_{\alpha\beta\gamma} F_\alpha F_\beta F_\gamma + \dots \quad (12)$$

where E^0 is the energy of the unperturbed molecules, μ_α , $\alpha_{\alpha\beta}$ and $\beta_{\alpha\beta\gamma}$ are the component of the dipole moment, polarizability and first-order hyperpolarizability respectively. Using x, y, z components the dipole moment, polarizability and hyperpolarizability are defined as follows (Eqs. (13), (14), (15), and (16)) [25, 26],

$$\mu = \sqrt{\mu_x^2 + \mu_y^2 + \mu_z^2} \quad (13)$$

$$\alpha = \frac{\alpha_{xx} + \alpha_{yy} + \alpha_{zz}}{3} \quad (14)$$

$$\Delta\alpha = \frac{1}{\sqrt{2}} \sqrt{(\alpha_{xx} - \alpha_{yy})^2 + (\alpha_{yy} - \alpha_{zz})^2 + (\alpha_{zz} - \alpha_{xx})^2 + 6\alpha_{xx}^2} \quad (15)$$

$$\beta_{tot} = \sqrt{(\beta_x)^2 + (\beta_y)^2 + (\beta_z)^2} \quad (16)$$

where,

$$\beta_x = \beta_{xxx} + \beta_{xyy} + \beta_{xzz}$$

$$\beta_y = \beta_{yyy} + \beta_{yzz} + \beta_{yxx}$$

$$\beta_z = \beta_{zzz} + \beta_{zxx} + \beta_{zyy}$$

The polarizability and first-order hyper polarizability values of the Gaussian 16W output in atomic units, and the calculated values are converted into electrostatic units (For α , 1 a.u. = 0.1482×10^{-24} e.s.u.; for β , 1 a.u. = 8.6391×10^{-30} e.s.u.) [27]. They are shown in Table 4. As seen in Table 4, the calculated dipole moment, polarizability, anisotropy of polarizability and first-order hyperpolarizability of the title molecule are found to be 0.3621 Debye, 31.7134×10^{-24} and 0.8989×10^{-30} e.s.u. respectively.

Table 4. Dipole moment, polarizability and hyper polarizability of the target molecule determined by DFT method using the basis set B3LYP/6-311++G(d,p).

Parameters	B3LYP/6-311++G(d,p)	Parameters	B3LYP/6-311++G(d,p)
α_{xx}	231.128	β_{xzz}	-5.1214
α_{yy}	163.052	β_{yyy}	-3.5436
α_{zz}	247.793	β_{xxy}	2.2736
α_{Tot}	31.7134×10^{-24} e.s.u	β_{yyz}	2.8320
$\Delta\alpha$	60.4370×10^{-24} e.s.u	β_{zzz}	90.2024
β_{Tot}	0.3621 Debye	β_{xxx}	3.2548
μ_{xxx}	2.1240	β_{yzz}	3.6820
β_{xyy}	-35.7641	β_{Tot}	0.8989×10^{-30} e.s.u.

4.6. Natural bond orbital analysis

The natural bond orbital analysis is a useful method to provide information about the interactions of both filled and virtual orbital spaces. It can enhance the prediction of inter and intra-molecular interactions. The natural bond orbital analysis has been performed by Gaussian 16W program package at the DFT/B3LYP/6-311++G(d,p) method. The electron donor-acceptor overlap orbitals on its stabilization energy $E(2)$ arises from second-order perturbation theory and it can be calculated from the following equation (eqn. 17) [28],

$$E(2) = \frac{q_i F(i,j)^2}{\epsilon_j - \epsilon_i} \quad (17)$$

where, q_i is the population of donor orbitals; ϵ_i , ϵ_j are the diagonal elements of NBO orbitals; $F(i,j)$ is the off-diagonal NBO Fock matrix element between i and j NBO orbitals. Some important interactions between the donor-acceptor NBOs are shown in Table S2 (Supplementary Table 2).

The largest stabilization energy shows that bonding σ (7C–15C) to anti-bonding σ^* (4C–20H) orbital having the highest $E(2)$ value of 96.27 kcal/mol. The interaction between σ (1C–7C) \rightarrow σ^* (9C–10C); σ (2C–4C) \rightarrow σ^* (4C–20H); σ (7C–8C) \rightarrow σ^* (9C–10C) stabilizes the molecule with the energy of 49.76, 54.83 and 91.15 kcal/mol respectively. The σ (16C–18O) \rightarrow σ^* (9C–10C) helps the molecule to stabilize with the energy of 62.90 kcal/mol. The interaction between lone pair to anti bonding orbital shows LP (1) 17O \rightarrow σ^* (9C–10C) and σ^* (4C–20H) interaction gives stabilization energy of 73.58 and 26.08 kcal/mol respectively. The interaction of LP(1) 18O \rightarrow σ^* (4C–20H) system also enhances the stability by 90.94 kcal/mol. NBO analysis revealed that the π (3C–5C) \rightarrow π^* (4C–6C), π (4C–6C) \rightarrow π^* (13C–14C), π (11C–12C) \rightarrow π^* (2C–9C) and π (13C–14C) \rightarrow π^* (11C–12C) interactions give a strong stabilization energy of the title compound by 35.33, 34.37, 36.65 and 17.43 kcal/mol respectively. The presence of other conjugated double bonds and their interactions also enhance the stability further.

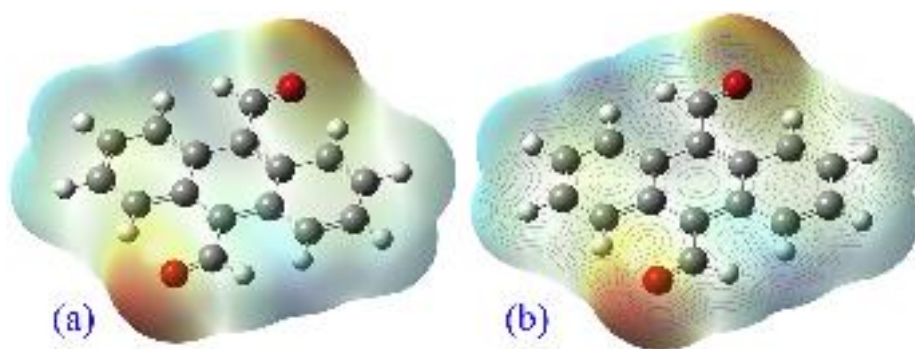


Figure 4. (a) ESP and (b) contour diagram of ADCA.

4.7. Hole electron interaction analysis

The hole-electron analysis module of Multiwfn 3.8 is reasonably very authoritative to analyze all kinds of electron excitations that take place within a molecule. It is useful to analyze the electronic excitation character of a molecule. The molecule under investigation is first optimized by the B3LYP/6-311++G(d,p) basis set. Then time-dependent density functional theory (TDDFT) calculation is carried out for the five lowest singlet excited states. The CAM-B3LYP method is employed with IOp(9/40 = 4) keyword. The fch file is generated and analyzed. The various results obtained are tabulated in Table 5. The hole-electron distribution, Chole-Celectron function, S_r , and Charge density difference (CDD) functions are shown in Figure 5.

The S_r index values are greater than 0.5 a.u. for all excitations (the theoretical upper limit is 1), which is a larger value, inferring that about half part of hole and electron has perfectly matched. This prediction confirms the presence of a typical local type of excitation (LE). The S_r indices value for the entire excited state is relatively larger. Particularly the excitation from $S_0 \rightarrow S_4$ is rather large up to 0.8547 a.u. The main reason for this higher value is highly localized $\pi-\pi^*$ type of excitation is present on the aromatic ring. In the other excitations, only $n-\pi^*$ type of excitation is involved.

The H index reflects the breadth of the average distribution of hole and electron. Table 5 gives information about the H index and it is found to be large. Since the distribution of hole and electron corresponding to all the excitations from S_0 to S_5 are evidently wider, their H indices are evidently larger (Figure 5).

All the τ index values are negative (much less than zero) which means there is no significant separation of hole and electron distributions. This also confirms the absence of charge transfer (CT) type of excitation and insists on the presence of LE type of excitation only.

The hole-electron Coulomb attractive energy is closely related to electron excitation properties. Always D index influences on it. The larger the D index is, the farther the distance between the main distribution regions of hole and electron, and thus the weaker the Coulomb attractive energy. Among all the excitations, $S_0 \rightarrow S_4$ is slightly larger (5.2152 eV). From the above results, we can conclude that,

- $S_0 \rightarrow S_1$: LE type of excitation with $n \rightarrow \pi^*$ transition
- $S_0 \rightarrow S_2$: LE type of excitation with $n \rightarrow \pi^*$ transition
- $S_0 \rightarrow S_3$: LE type of excitation with $n \rightarrow \pi^*$ transition
- $S_0 \rightarrow S_4$: LE type of excitation with $\pi \rightarrow \pi^*$ transition
- $S_0 \rightarrow S_5$: LE type of excitation with $n \rightarrow \pi^*$ transition

According to Kasha's rule, the first excited state ($S_0 \rightarrow S_1$) of a singlet system is usually the critical state to emit fluorescence and hence plays an important role in molecular photo-physics [29].

The percentage of the hole-electron for all the excitation states are investigated and reproduced in Table 6 and shown in Figure 6. From Table 6 and Figure 6, we can easily understand that $S_0 \rightarrow S_1$ has more percentage of holes and electrons (97 and 98 respectively).

4.8. Aromaticity determination

The wave function of the title molecule is generated at the B3LYP/6-311G++(d,p) level of theory. Since the title molecule has three fused

aromatic ring structure, it is decided to find out the electron conjugation character. The Multicenter bond order and Normalized multicenter bond order are calculated by using Multiwfn 3.8 tool and listed in Table 7, which indicates that the central aromatic ring has weaker electron conjugation character than the boundary rings for the title molecule. Becke's fuzzy atomic space is used to study the aromaticity of different rings of the title molecule.

Aromaticity cannot be observed directly. So several definitions are of aromaticity have been proposed [30]. The aromatic nature of a molecule can be evaluated from its structural, magnetic, and energetic properties [31, 32, 33, 34, 35, 36]. The PDI (Para Delocalization Index), FLU (Fluctuation Index), PLR (Para Linear Response index) and HOMA (Harmonic Oscillator Measure of Aromaticity) values are calculated from Multiwfn 3.8 package and listed in Table 7 for the molecule ADCA. PDI value is just the average of the DIs (Delocalisation Index) between 8C-14C, 10C-12C, 13C-11C for left; 1C-10C, 2C-8C, 9C-7C for center and 1C-6C, 2C-5C, 4C-3C for right rings. From the PDI values, it is concluded that the electron delocalization is stronger in boundary rings than the central ring. So it is also evidence that the boundary rings are having stronger aromaticity.

From the FLU values, it is observed that the central ring has higher values than the boundary rings. Hence it is evident that the boundary rings are more typical aromatic system (benzene) and hence possess larger aromaticity than the central ring. The PLR value also validates this conclusion that boundary rings have larger aromaticity than the central ring. Since the HOMA values of boundary rings are larger than the center ring and it also confirms the aromaticity is larger in boundary rings than the middle ring of the target molecule.

4.9. Simulated scanning tunnelling microscope (STM) analysis

Scanning tunnelling microscope is a powerful tool to record the spatial variations of the tunnelling current in the junction between a sharp metallic tip and a conducting probe surface [37]. Simulating scanning tunnelling microscope images for the title molecule and the anthracene molecule are generated and analysed by using Multiwfn 3.8 tool and is shown in Figure 7 (a) and (b) respectively. The local density of states (LDOS) value for the investigated molecule and anthracene are found to be 0.0009 and 0.0003 a.u. respectively at $V = -2V$ and $Z = 2.2 \text{ \AA}$. In these maps, the brighter the white, the larger is the LDOS and thus the stronger the tunnelling current (I). The Tersoff-Hamann model shows that I is positively proportional to LDOS. It can be seen that I signal is more prominent over the two boundary six-membered rings than the central ring for ADCA and anthracene molecules.

4.10. Non-covalent interaction analysis

Non-covalent interaction, otherwise called as RDG, which is a powerful tool to understand the non-covalent interaction within a molecule. RDG (eqn.18) is defined as,

$$RDG(r) = \frac{1}{2(3\pi^2)^{1/3}} \frac{|\nabla\rho(r)|}{\rho(r)^{4/3}} \quad (18)$$

When $\text{sign}(\lambda_2)\rho$ (a.u.) is plotted against RDG, some spikes are

Table 5. Various excitation parameters of ADCA.

Excitations	S_m (a.u.)	S_r (a.u.)	D index (\AA)	H index (\AA)	τ index (\AA)	Excitation energy (eV)	Coulomb attractive energy (eV)
S1	0.4845	0.7751	0.000	3.037	-1.974	2.626	5.0374
S2	0.2756	0.5489	0.007	3.246	-2.576	2.935	5.0510
S3	0.2971	0.5748	0.007	3.273	-2.574	3.138	5.0095
S4	0.5698	0.8547	0.001	2.960	-2.222	3.487	5.2152
S5	0.3521	0.6414	0.000	3.036	-1.967	3.692	5.0240

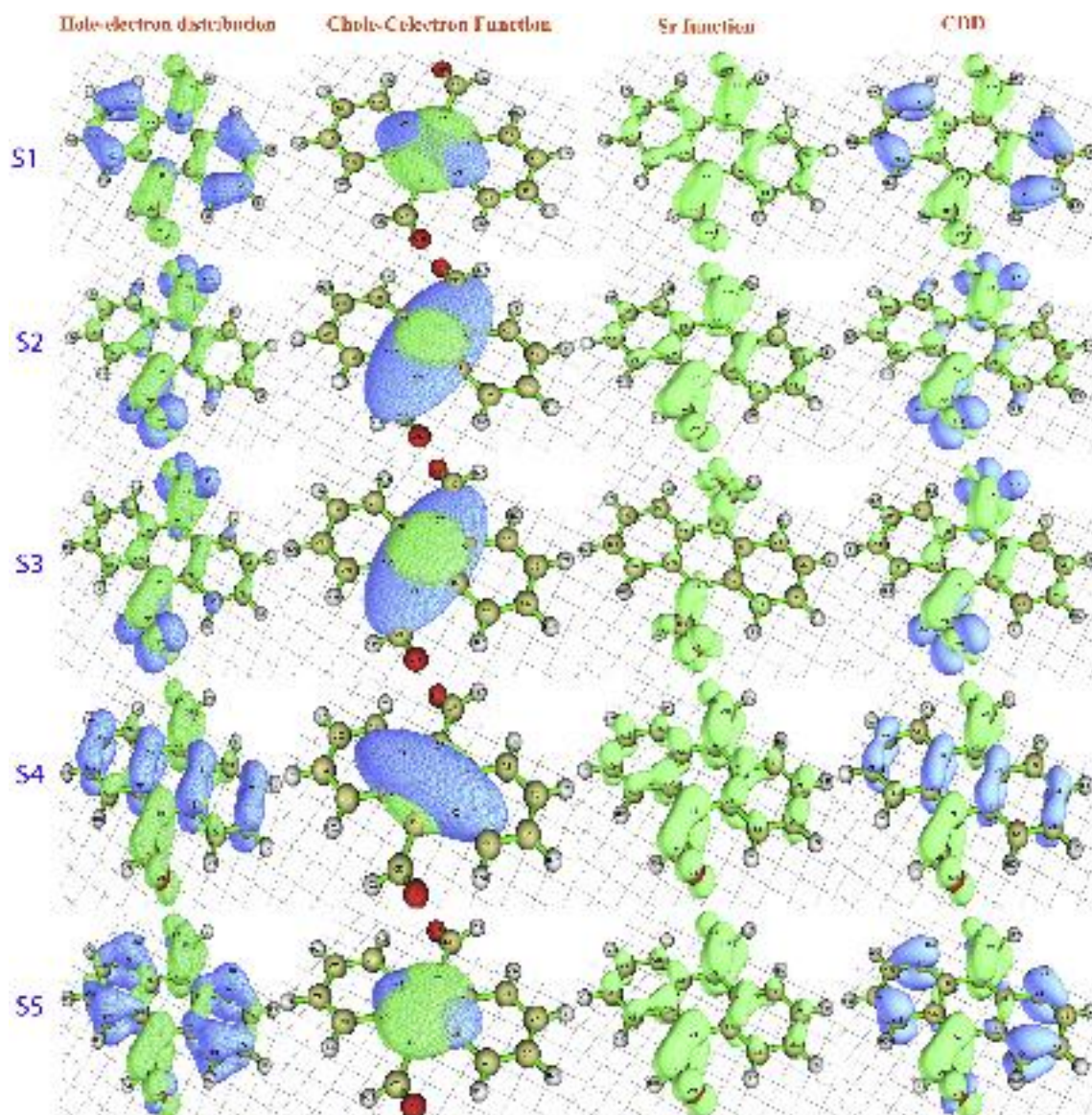


Figure 5. The Hole-Electron distribution, Chole-Celextron function, S_r , and CND representations for all the excitations.

Table 6. Hole-electron percentage involved in various electronic excitations of ADCA.

Excitations	MO	Occupancy	Hole (%)	Electron (%)
S1	61	2.0000	97.265	0.000
	62	0.0000	0.0000	98.490
S2	60	2.0000	82.395	0.000
	62	0.0000	0.0000	94.491
S3	58	2.0000	85.676	0.000
	62	0.0000	0.0000	92.236
S4	59	2.0000	69.376	0.000
	62	0.0000	0.0000	80.311
S5	57	2.0000	86.561	0.000
	62	0.0000	0.0000	96.590

developed. According to the $\text{sign}(\lambda_2)$ and the ρ values, the following regions are defined well.

Strong attraction: halogen bond and hydrogen bond ($\rho > 0$ and $\lambda < 0$).

Van der Waals interaction: ($\rho \approx 0$ and $\lambda \approx 0$).

Strong repulsion: Steric effect in the ring and gage ($\rho > 0$ and $\lambda > 0$).

The NCI (Non-Covalent Interaction) for the title molecule and anthracene are investigated with the help of Multiwfn 3.8 program and the pictures obtained are reported in Figure 8. From Figure 8, it is evident that the target molecule has a steric effect and Van der Waals interactions. The spikes around -0.020 and $+0.010$ a.u. represents the Van der Waals force of attraction. The spike developed around 0.020 a.u. epitomizes the steric effect present in the ring. In order to prove these facts, two cube files (.cub) are generated by Multiwfn 3.8 and viewed in VMD 1.9.3 tool and the isosurface formed is shown in Figure 8 itself. The brownish green colour spheres represent the presence of Van der Waals force in the molecule and the red spheres in the middle of aromatic rings represent the presence of steric interaction. The same study is carried out for anthracene molecule. In the case of anthracene, the spikes in the negative sign area are missed due to the absence of Van der Waals forces. The spike near $+0.020$ a.u. is responsible for the steric effect, which is shown as a red sphere in the isosurface of all the aromatic rings.

4.11. Shaded surface map with a projection of LOL investigation

LOL (eqn.19) is a function for locating high localisation regions and it is defined by Schmider and Becke [38, 39].

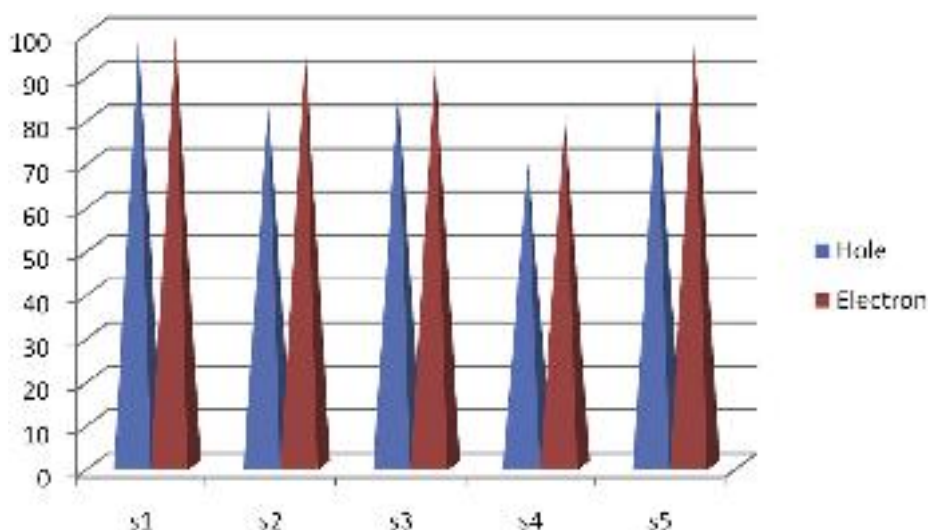


Figure 6. Plot of hole-electron percentage involved in various electronic excitations of ADCA.

Table 7. Various aromaticity parameters of ADCA.

Aromatic ring	Multicenter bond order	Normalized bond order	PDI	FLU	PLR	HOMA
Left	0.0465	0.5996	0.0688	0.0168	0.3821	0.6233
Centre	0.0386	0.5813	0.0549	0.0213	0.3652	0.5673
Right	0.0464	0.5995	0.0688	0.0168	0.3821	0.6233

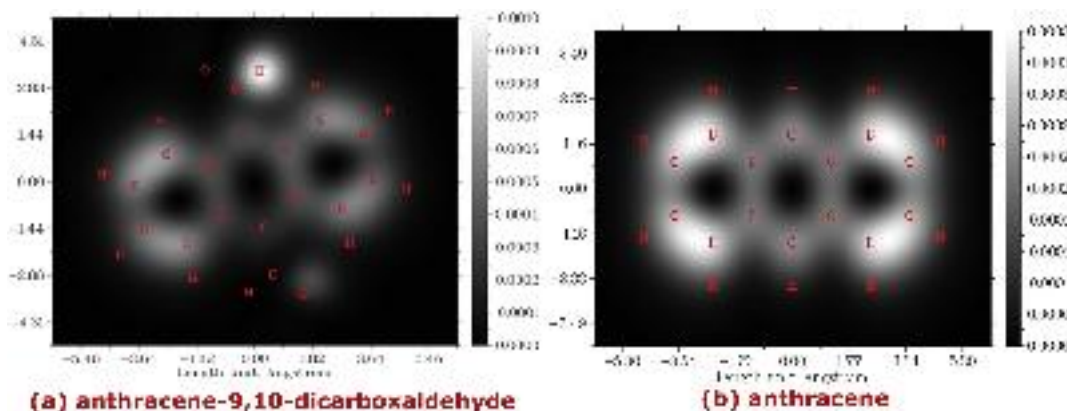


Figure 7. Simulated Scanning Tunneling Microscope (STM) image of (a) ADCA and (b) anthracene.

$$LOL(r) = \frac{\tau(r)}{1 + \tau(r)} \tag{19}$$

where the dimensionless variable $\tau(r)$ is $g_0(r)/g(r)$ and always depends on positive one electron kinetic energy density where, $\phi_i(r)$ are the Hartree – Fock of the Kohn-Sham orbitals. The larger the LOL is in a particular region, the more likely the electron motion is cramped within it. The shaded surface map with a projection of localised orbital locator (LOL) for the title molecule, (ADCA) and anthracene are analysed and the result is evinced in Figure 9 (a) and (b) respectively. In Figure 9, the blue colour in all the carbon atoms represents the depleted electron regions and red colour is related to high localized electron regions. Also, it is evident that all the carbons are having electron depleted area and aromatic hydrogen atoms are having high localized electron regions. It is also evident that the electrons tend to be localised in the outer side of the

rings to stabilise them. Since the backbones of both the rings are same, anthracene also produces similar type of shaded surface map.

4.12. Vibrational studies

4.12.1. Vibrational assignments

Vibrational spectroscopy is the measurement of the interaction between IR radiation and the matter. It is used to study and identify the chemical structure and functional groups in solid, liquid and gaseous forms. The target molecule has 28 atoms in various planes and it undergoes 78 group vibrational modes and finger print vibrations are possible. They are distributed as 28 out of plane vibrations and 50 in-plane vibrations. By adopting DFT/B3LYP/6-311++G(d,p) basis set, the theoretical vibrations are calculated for the title molecule and have been presented in Table 8. The experimental and theoretical IR spectra

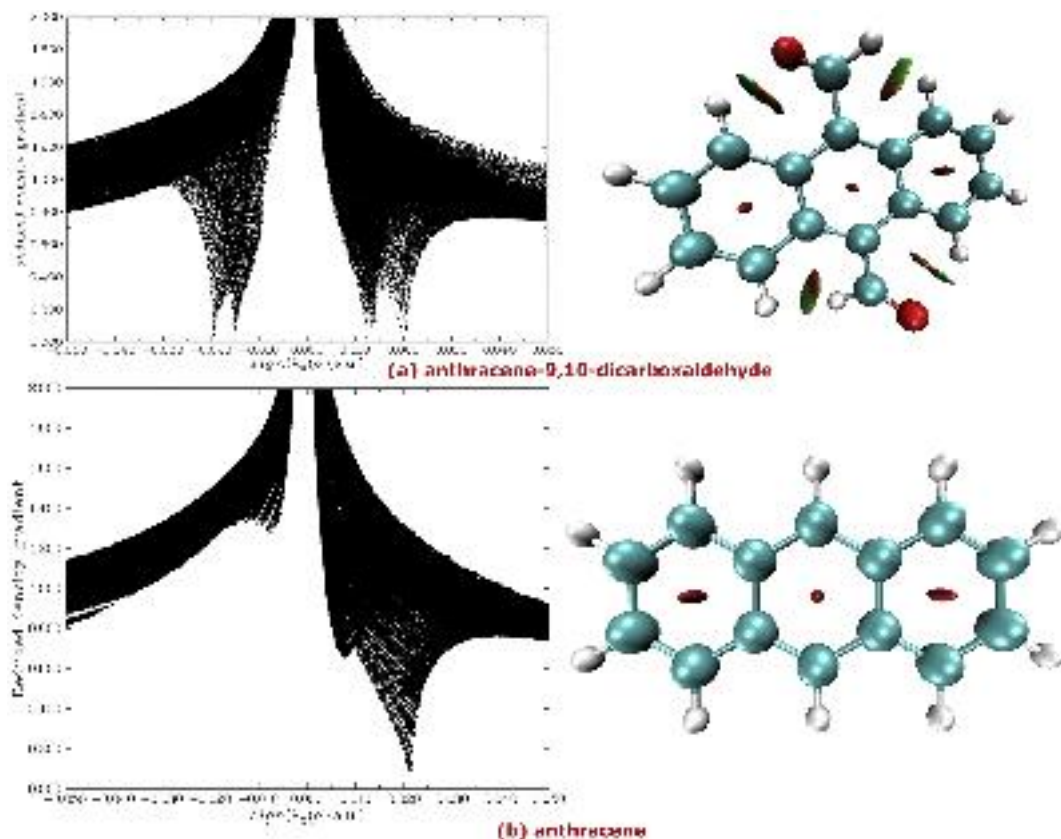


Figure 8. The non covalent interaction of (a) ADCA and (b) anthracene.

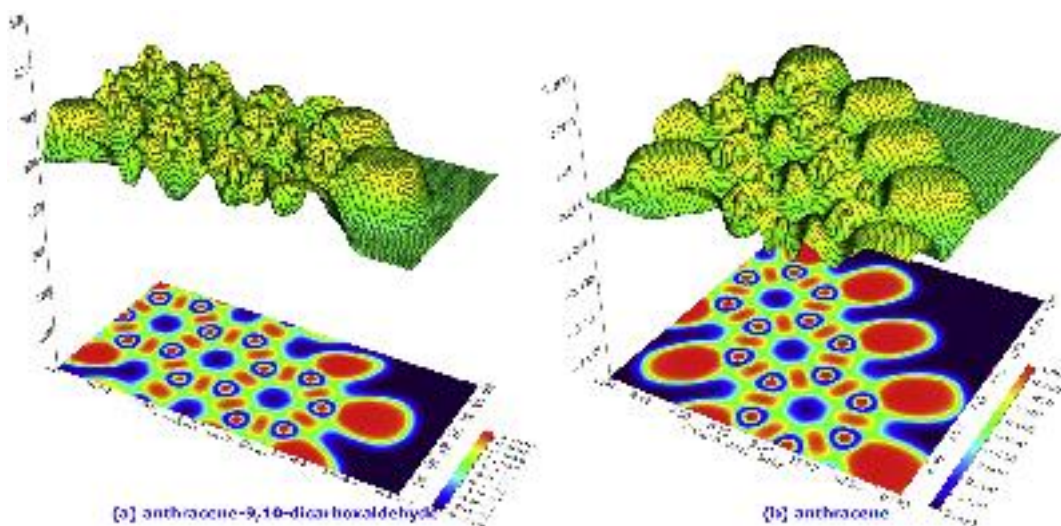


Figure 9. Shaded surface map with projection effect of electron localization function (ELF) in the central QM structures of (a) ADCA and (b) anthracene. In this figure, the Z-axis is Localised Orbital Locator (LOL).

are jointly shown in Figure 10 as (A) and (B) respectively. The scaling factor used to calculate the scaled value is 0.967. When compared with the theoretical values, experimental values are found to be lesser. For this study, the results are compared with the work done by Jeyachitra *et al.*, on 10-methyl anthracene-9-carboxaldehyde and found that the results are in good agreement with them [40].

4.12.2. C–H vibrations

Eight C–H bonds are present in the poly-aromatic anthracene moiety and two hydrogen atoms are attached with the two aldehyde groups. The

C–H stretching vibrations for anthracene can be observed around 3095–2850 cm^{-1} [41]. For the present molecule, the signals at 3154, and 3132 cm^{-1} are allotted to aromatic C–H stretching. The signals at 3081 and 3080 cm^{-1} are fixed to aromatic symmetric C–H stretching while the signal at 3066 cm^{-1} is allotted to aromatic asymmetric C–H stretching. Based on the literature, it is found that the aromatic C–H in-plane bending and out-plane bending modes of vibrations are located in the region 1300–940 cm^{-1} and 1000–720 cm^{-1} respectively [42, 43]. In this investigated molecule, the in-plane bending and out-plane bending modes of vibrations are located at 1514, 1484, 1453, 1427, 1420, 1415,

Table 8. Theoretical and experimental vibrational analysis for the investigated molecule.

SL. NO	Experimental (cm ⁻¹)	Theoretical (cm ⁻¹)		Intensity	Assignment of vibrations
		Unscaled	Scaled		
1	3444	3261	3154(w)	19.6876	ν(CH) _{aro}
2	—	3261	3154(w)	11.7990	ν(CH) _{aro}
3	—	3239	3132(vw)	0.1174	ν(CH) _{aro}
4	—	3239	3132(w)	16.7834	ν(CH) _{aro}
5	—	3186	3081(w)	11.1489	ν _s (CH) _{aro}
6	2923	3185	3080(w)	21.5008	ν _s (CH) _{aro}
7	—	3170	3066(w)	3.4093	ν _{as} (CH) _{aro}
8	2853	3170	3066(w)	10.3916	ν _{as} (CH) _{aro}
9	2361	3016	2917(vw)	0.2173	ν(CH) _{ald}
10	1827	3016	2916(S)	125.4329	ν(CH) _{ald}
11	—	1740	1682(vw)	0.0009	ν(CO)
12	1673	1730	1673(VS)	696.2012	ν(CO)
13	—	1665	1610(w)	11.0639	ν(CCC) _{aro}
14	—	1651	1597(vw)	0.0030	ν(CCC) _{aro}
15	—	1589	1537(vw)	0.0018	ν(CCC) _{aro}
16	1527	1573	1521(w)	15.9255	ν(CCC) _{aro}
17	—	1566	1514(vw)	0.0002	ν(CCC) _{aro} , δ(CH) _{ald}
18	—	1535	1484(vw)	0.0000	δ(CH) _{aro} , δ(CH) _{ald}
19	—	1503	1453(w)	18.6415	δ(CH) _{aro} , δ(CH) _{ald}
20	—	1476	1427(w)	24.5438	δ(CH) _{aro}
21	1443	1468	1420(w)	47.7916	δ(CH) _{aro}
22	—	1464	1415(vw)	0.0097	δ(CH) _{ald} , δ(CH) _{aro}
23	—	1419	1372(vw)	0.0002	ν(CCC) _{aro}
24	—	1413	1366(vw)	0.0002	δ(CH) _{aro}
25	1350	1365	1320(m)	91.3256	δ(CH) _{aro}
26	—	1348	1304(m)	56.6941	δ(CH) _{aro}
27	—	1308	1265(vw)	1.0133	δ(CH) _{aro} , δ(CH) _{aro}
28	1279	1291	1249(w)	32.3180	δ(CH) _{aro} , δ(CCC) _{aro}
29	—	1263	1222(vw)	0.0002	α(CCC) _{aro} , δ(CH) _{aro}
30	—	1257	1216(vw)	0.0002	δ(CH) _{aro}
31	—	1212	1172(vw)	0.0004	δ(CH) _{aro}
32	1180	1209	1169(w)	36.3148	δ(CH) _{aro}
33	1167	1193	1154(w)	36.1447	δ(CH) _{aro}
34	1114	1131	1094(vw)	0.0001	δ(CH) _{aro} , δ(CCC) _{aro}
35	1022	1072	1036(w)	23.6337	δ(CH) _{aro}
36	—	1070	1035(vw)	0.0011	ν(CC) _{ald-aro}
37	—	1064	1029(vw)	0.0077	α(CCC) _{aro}
38	—	1023	989(S)	110.3002	δ(CCC) _{aro}
39	—	1021	988(vw)	0.0063	δ(CH) _{aro}
40	—	1020	987(w)	1.3988	γ(CH) _{aro}
41	—	995	962(vw)	0.0000	γ(CH) _{aro} , γ(CH) _{ald}
42	—	991	959(vw)	0.0383	γ(CH) _{aro} , γ(CH) _{ald}
43	—	982	949(vw)	0.6203	γ(CH) _{aro} , γ(CH) _{ald}
44	—	979	947(vw)	0.0000	γ(CH) _{aro} , γ(CH) _{ald}
45	890	953	922(vw)	0.0000	δ(CCC) _{aro}
46	—	913	883(w)	30.2829	δ(CCC) _{aro}
47	—	868	839(vw)	0.0150	γ(CH) _{aro}
48	799	867	839(w)	4.0290	γ(CH) _{aro}
49	—	780	754(vw)	0.0000	γ(CH) _{aro}
50	—	765	739(vw)	0.0003	γ(CH) _{aro}
51	—	764	739(S)	116.8936	γ(CCC) _{aro}
52	745	759	734(S)	101.2938	β(CCC) _{aro}
53	—	751	726(w)	13.6584	β(CCC) _{aro}
54	—	748	723(vw)	0.0001	γ(CCC) _{aro}
55	655	672	650(vw)	0.0000	γ(CCC) _{aro}
56	—	657	635(w)	14.2354	γ(CCC) _{aro}
57	593	599	579(w)	28.1706	γ(CCC) _{aro}

Table 8 (continued)

SL. NO	Experimental (cm ⁻¹)	Theoretical (cm ⁻¹)		Intensity	Assignment of vibrations
		Unscaled	Scaled		
58	—	593	574(vw)	0.0000	γ(CCC) _{aro}
59	562	575	556(w)	20.5710	γ(CCC) _{aro}
60	—	517	500(vw)	0.0000	γ(CCC) _{aro}
61	—	497	481(vw)	0.1079	γ(CCC) _{aro}
62	454	475	459(vw)	0.0000	γ(CCC) _{aro}
63	—	455	440(w)	3.4996	γ(CCCC)
64	—	425	411(vw)	0.0000	γ(CCCC)
65	—	411	397(vw)	0.0000	γ(CCCC)
66	—	389	376(w)	5.8765	γ(CCC) _{aro}
67	—	344	333(vw)	0.0000	γ(CCC) _{aro}
68	—	329	318(vw)	0.0000	γ(CCCC)
69	—	287	277(vw)	0.0002	γ(CCCC)
70	—	277	268(w)	7.0224	γ(CCCC)
71	—	271	262(w)	9.7337	δ(CH) _{ald}
72	—	233	225(vw)	0.0000	γ(CCCC)
73	—	160	155(vw)	0.0238	γ(CH) _{ald}
74	—	158	152(w)	13.9439	γ(CH) _{ald}
75	—	126	122(vw)	0.5092	γ(CCCC)
76	—	67	65(vw)	0.5156	γ(CCCC)
77	—	56	54(vw)	0.0004	γ(CCCC)
78	—	18	17(w)	6.5780	γ(CCCC)

VS – Very Strong; S – Strong; m – medium, w – weak, vw – very weak; s – symmetric; as – Asymmetric; ν - stretching; δ - in plane bending; γ - out plane bending; α - breathing mode; β - Butterfly type; aro – aromatic; ald - aldehyde.

1366, 1265, 1249, 1222, 1216, 1172, 1169, 1154, 1094, 1036 cm⁻¹ and 988, 987, 962, 959, 949, 947, 839, 754, 739 cm⁻¹ respectively. Some of the in-plane bending vibrations are found well above the expected values may be due to the influence of the two aldehyde groups present in the molecule. The other vibrational signals are located below the expected region. Aromatic C–H butterfly style of vibrations are found at 734 and 726 cm⁻¹. C–H stretching of aldehyde group can be observed at 2917 and 2916 cm⁻¹ respectively for both the aldehyde groups. The C–H of aldehyde groups produces signals at 1514 and 1484, 1453 and 1415 cm⁻¹ for in-plane bending while their out-plane bending vibrations are located at 962, 959, 949, 947 cm⁻¹ as very weak signals.

4.12.3. C=O vibrations

The carbonyl group vibration is always prominence its location between 1750 and 1600 cm⁻¹ as a strong intense peak [44]. Two aldehyde groups are attached with the middle aromatic ring of anthracene directly and it is possible to obtain two C=O vibrational peaks. They appear at 1682 and 1673 cm⁻¹ in the simulation spectrum. Interestingly the experimental value is also found to be placed exactly on 1673 cm⁻¹ as a single strong peak.

4.12.4. C–C vibrations

The poly-nuclear system, anthracene has carbon atoms in its skeleton. They are having some C–C and C=C bonds. The entire C=C and C–C stretching vibrations will be observed in the region 1650–1400 cm⁻¹ [40]. In this molecule of interest, the C=C stretching vibrations are located at 1610, 1597, 1537, 1521, 1514, and 1372 cm⁻¹. The C–C stretching vibrations are located at 1320, 1304, 1265, 1249, and 1094 cm⁻¹. The peaks appear in the expected region are in good agreement with the literature which insists the core bond steadiness. The CCC in-plane bending vibrations are observed at 989, 922, 883 cm⁻¹ with strong intensities. The CCC out-plane bending vibrations have been seen at 739, 723, 650, 635, 579, 574, 556, 500, 481, 449, 376, 333 cm⁻¹. The middle ring of anthracene molecule breaths at 1222 cm⁻¹ and the terminal rings breathe at 1029 cm⁻¹.

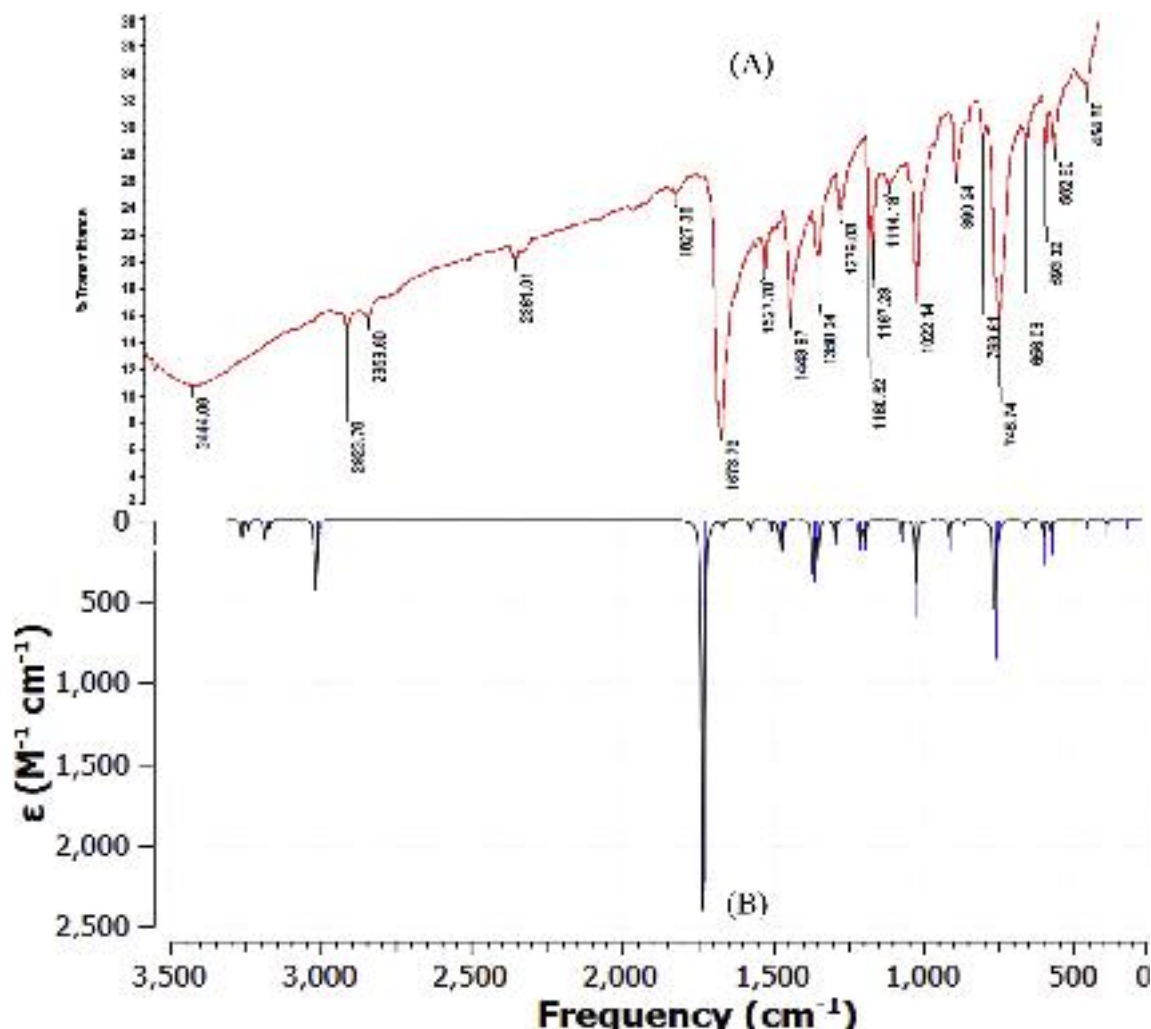


Figure 10. Experimental (A) and simulated (B) IR spectra of ADCA.

4.12.5. CHO vibrations

The aldehyde carbon attached with the nucleus undergoes stretching and is observed at 1035 cm^{-1} . The aldehyde in-plane bending and out-plane bending vibrations are observed at 262, 155, and 152 cm^{-1} respectively.

4.12.6. CCCC and CCCO vibrations

The CCCC and CCCO out plane vibrations for the title molecule are seen at 440, 411, 397, 318, 277, 268, 225, 122, 65, 54, and 17 cm^{-1} .

4.13. UV-visible spectral analysis

The UV Visible spectrum of the target molecule is analysed theoretically from fully optimized ground state structure using ZINDO calculation at the B3LYP/6-311++G(d,p) basis set in ethanol solvent. Experimental UV also has been recorded in ethanol solvent and the two spectra are put together shown in Figure 11. GaussSum 3.0 is used to investigate the other properties like energy, oscillator strength, major contributions and minor contributions etc., and listed in Table 9. Two peaks have appeared for the experimental spectrum (418 and 276 nm) and three spectral values (480, 405, and 398 nm) are obtained for the simulated UV spectrum.

The absorption band appeared at 480 nm in ethanol with molar absorption coefficient (ϵ) of 20801.85 cm^{-1} arises due to the major electronic transitions from HOMO to LUMO which makes 97%. The absorption band appeared at 405 nm with molar absorption coefficient

(ϵ) of 24662.01 cm^{-1} arises due to the major electronic transitions from HOMO-4 to LUMO+2 (32%), HOMO-3 to LUMO (40%), while minor transitions include HOMO-3 to LUMO+3 (16%), HOMO-3 to LUMO+6 (2%). Similarly, the peak appeared at 398 nm with molar absorption coefficient (ϵ) of 25090.29 cm^{-1} arises due to the major electronic transitions from HOMO-4 to LUMO (34%), HOMO-4 to LUMO+3 (18%), HOMO-3 to LUMO+2 (35%), while minor transitions include HOMO-9 to LUMO+2 (3%), HOMO-4 to LUMO+6 (3%) and HOMO-2 to LUMO (2%). The oscillator strengths for the three absorptions are evaluated as 0.4777, 0.0019 and 0.0 respectively.

4.14. Docking studies

4.14.1. In silico prediction of activity spectra for substance (PASS)

The prediction for the activity of anthracene-9,10-dicarboxaldehyde is done with the help of computer programme PASS online server. It predicts the activity spectrum of the compounds as probable activity (Pa) and probable inactivity (Pi). The ratio varies between 0.000 and 1.000. If $\text{Pa} > 0.7$ means, the probability of pharmacological action is high, and if $0.5 < \text{Pa} < 0.7$, the probability of pharmacological action is less. If Pa is less than 0.5, the compound is unlikely to show pharmacological action [45]. The prediction of activity spectra for substance (PASS) for the target molecule is analysed to find a better choice. From the results obtained, it is decided to carry out docking studies on phobic disorder treatment [$\text{Pa} < 0.7$ (0.849) and $\text{Pa} > 0.017$]. Phobia is a type of anxiety disorder which results in a rapid onset of fear. In Asia, 2-4 % and in Western world 6-8 %

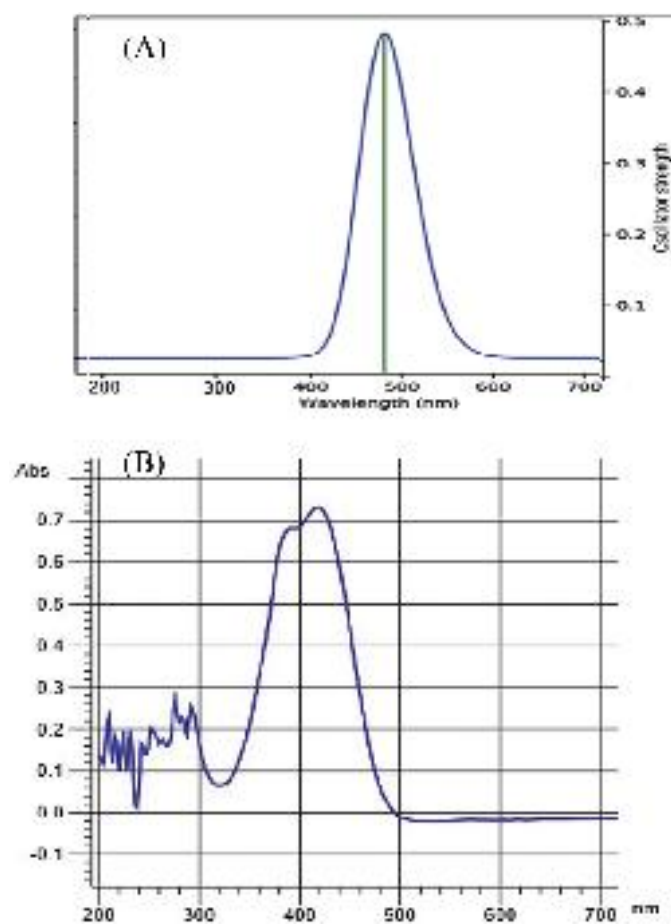


Figure 11. Theoretical (A) and experimental (B) UV – Visible absorption spectra of ADCA.

of people are affected by Phobia. Women are affected by phobias about twice of often as men [46]. Many phobia cases end with suicide. Considering these views, it is decided to carryout research on phobia. So 4COF protein is selected for docking.

4.14.2. Preparation of protein

The X – ray crystal structure of human gamma-aminobutyric acid receptor, GABA(A)R-beta3 homopentamer (PDB ID: 4COF) is retrieved from protein data bank (<https://www.rcsb.org/structure/4COF>). Before docking, the structure of the protein is prepared by using Discovery Studio 4.1 Visualizer (<https://discover.3ds.com/discovery-studio-visualizer-download>). Water molecules and the small ligands like hetero-atoms are removed from the protein to make the complex receptor-free of any ligand before docking. Polar hydrogen atoms are added to the protein which is a very essential and crucial step for the computation of partial atomic charges. The force field applied is CHARMM and the partial charge applied is Momany–Rone. Finally, the

Table 9. Experimental and theoretical electronic absorption spectra of ADCA.

No.	Wavelength (nm)		Energy (cm ⁻¹)	Oscillator strength	Major contributions	Minor contributions
	Experimental	Theoretical				
1	—	480.7266	20801.85	0.4777	HOMO→LUMO (97%)	—
2	418.0	405.4819	24662.01	0.0019	H-4→L+2 (32%), H-3→LUMO (40%)	H-3→L+3 (16%) H-3→L+6 (2%)
3	276.0	398.5605	25090.29	0.0	H-4→LUMO (34%), H-4→L+3 (18%), H-3→L+2 (35%)	H-9→L+2 (3%), H-4→L+6 (3%), H-2→LUMO (2%)

Table 10. Various properties of the ligand ADCA.

1	Molecular formula	C ₁₈ H ₁₄ O ₂
2	Molecular weight	262.10
3	Number of HBA	2
4	Number of HBD	0
5	MolLogP	4.59
6	MolLogS	-4.56 (in Log(moles/L)) 7.28 (in mg/L)
7	MolPSA	27.35 Å ²
8	MolVol	272.35 Å ³
9	pKa of most Basic/Acidic group	<0./16.79
10	Number of stereo centers	0
11	nviolations	0
12	nrotb	2
13	Volume	243.12
14	Druglikeness	Yes
15	Lipinski	Yes
16	Ghose	Yes
17	Veber	Yes
18	EGAN	Yes
19	Muegge	Yes
20	Bioavailability score	0.55

Table 11. Docking results and hydrogen bond interaction of ADCA with 4COF.

PDB ID	Ligand	Binding affinity (kcal/mol)	No. of hydrogen bonds developed	H bond distance (Å)	Atom of Ligand	Residue of protein
4COF	ADCA	-6.6	2	2.5	Oxygen	SER-427
				3.2	Oxygen	LEU-294

protein is subjected to energy minimisation. Ramachandran plot is analyzed for the prepared protein and found that more than 90% of residues fall under the most favoured region.

4.14.3. Preparation of ligand

The 2D structure of the title molecule is drawn with the help of Chemsketch software (<https://www.acdlabs.com/resources/freeware/chemsketch/index.php>) and saved as .mol file which is then converted to energy minimized 3D structure with the help of Avogadro tool (<https://avogadro.cc/>) and saved as .pdb. Optimisation of ligand leads to a stable conformation of coordinates with minimum energy. The force field applied is MMFF94 with steepest descend algorithm. The various properties of the ligand are checked for Lipinski's Rule of five from which is presented in Table 10. From that, we could see that the present molecule obeys the rule. SwissADME (<http://www.swissadme.ch/>) online tool is used to calculate the other properties like bioavailability, drug-likeness etc., and exposed in Table 10. This molecule obeys all the theories and has good drug-likeness property. Also, the bioavailability score is found to be 0.55.

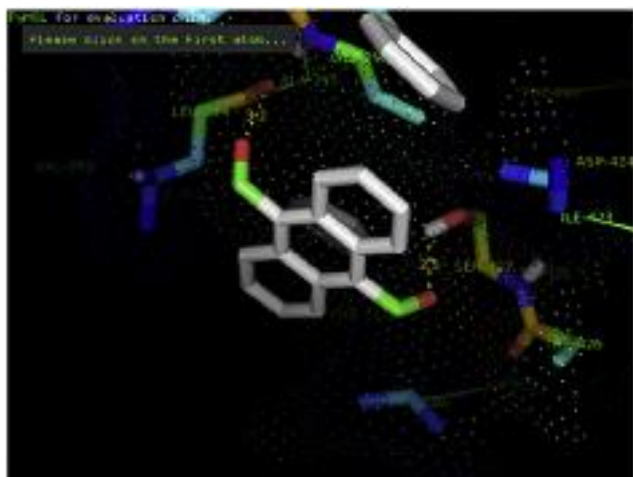


Figure 12. The docking pattern of ADCA with the protein 4COF.

4.14.4. Docking

PyRx is a powerful tool that can be used for docking of ligands with proteins. The target molecule is docked with 4COF and the results are analyzed with the help of PyMOL software. Two hydrogen bonds are developed strongly between the ligand and the protein. The docking results are shown in Table 11.

The two oxygen atoms present in the two aldehyde groups of the aromatic rings are bonded with the residues SER-427 and LEU-294 with the hydrogen bond distance of 2.5 and 3.2 Å respectively. The docking score is found to be -6.6 kcal/mol. It clearly suggests that the ligand fits well with the protein, 4COF. The docking pattern viewed by PyMOL is shown in Figure 12.

5. Conclusion

Anthracene-9,10-dicarboxaldehyde is a wonderful molecule with a multinuclear planar system with conjugated double bonds. It has many significant applications in medicinal and industrial fields. The electronic structure and its properties are analyzed theoretically by DFT/B3LYP/6-311++G(d,p) basis set by using Gaussian 16W software. All the bond angle, bond distance and dihedral angles are perfectly matched with the earlier reports well. From the HOMO – LUMO values, it is clear that the molecule is a hard molecule and it is stable. The ESP studies reveal that the molecule is more prone to electrophilic attack near the oxygen atoms of aldehyde groups. NBO study interprets that this is a stable molecule due to high conjugation of double bonds. By using Multiwfn 3.8 tool, the aromaticity of the molecule is determined. It is found that the aromaticity of the central ring is lower than the terminal rings. The STM studies inform that the terminal rings are having more tunneling current than the central ring. The NCI study reveals that the molecule is having steric effect and Van der Waals force of attraction within the molecule. The hole-electron transfer analysis proposes that all the lowest five excitations are of LE type only. Electron depletion area and LOL are determined and interpreted thoroughly for the title molecule through a shaded surface map. IR spectrum is recorded theoretically and experimentally to analyze the various types of vibrations. By using PyRx and PyMOL tools, the docking pattern of the small molecule with 4COF protein is performed and reported.

Declarations

Author contribution statement

J. Jebasingh Kores: Performed the experiments; Analyzed and interpreted the data; Contributed reagents, materials, analysis tools or data; Wrote the paper.

I. Antony Danish: Performed the experiments; Analyzed and interpreted the data; Contributed reagents, materials, analysis tools or data; Wrote the paper.

T. Sasitha: Conceived and designed the experiments; Performed the experiments; Contributed reagents, materials, analysis tools or data; Wrote the paper.

J. Gershom Stuart: Performed the experiments; Contributed reagents, materials, analysis tools or data.

E. Jimla Pushpam: Analyzed and interpreted the data; Contributed reagents, materials, analysis tools or data; Wrote the paper.

J. Winfred Jebaraj: Conceived and designed the experiments; Analyzed and interpreted the data; Contributed reagents, materials, analysis tools or data; Wrote the paper.

Funding statement

This research did not receive any specific grant from funding agencies in the public, commercial, or not-for-profit sectors.

Data availability statement

Data included in article/supplementary material/referenced in article.

Declaration of interests statement

The authors declare no conflict of interest.

Additional information

Supplementary content related to this article has been published online at <https://doi.org/10.1016/j.heliyon.2021.e08377>.

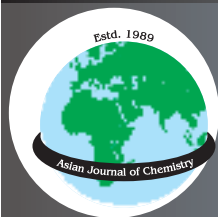
Acknowledgements

The authors are thankful to the Principal, the Secretary and the management of St. John's College, Palayamkottai for providing the computer and software facilities.

References

- [1] R. Ruiterkamp, N.L.J. Cox, M. Spaans, L. Kaper, B.H. Foing, F. Salama, P. Ehrenfreund, PAH charge state distribution and DIB carriers: implications from the line of sight toward HD 147889, *Astron. Strophys.* 432 (2005) 515–529.
- [2] A.V. Kukhta, I.N. Kukhta, N.A. Kukhta, O.L. Neyra, E. Meza, DFT study of the electronic structure of anthracene derivatives in their neutral, anion and cation forms, *J. Phys. B Atom. Mol. Opt. Phys.* 41 (2008) 205701 (7pp).
- [3] H. Okii, H. Hara, Y. Ohba, Electroluminescence in perylene-and-tetracene-doped anthracene films, *Jap. J. Appl. Phys.* 31 (Part 2 No. 4A) (1992) L416–L418.
- [4] D.J. Fatemi, H. Murata, C.D. Merritt, Z.H. Kafafi, Highly fluorescent molecular organic composites for light emitting diodes, *Synth. Met.* 85 (1997) 1225–1228.
- [5] M.X. Yu, J.P. Duan, C.H. Lin, C.H. Cheng, Y.T. Tao, Diaminoanthracene derivatives as high-performance green host electroluminescent materials, *Chem. Mater.* 14 (2002) 3958–3963.
- [6] J.R. Quinn, F.W. Foss Jr., L. Venkataraman, M.S. Hybertsen, R. Breslow, Single-molecule junction conductance through diaminoacenes, *J. Am. Chem. Soc.* 129 (2007) 6714–6715.
- [7] S.E. Adeniji, Density functional theory (DFT) approach for kinetic and thermodynamic study of reaction mechanism of copper(II) complex from 2-hydrazinyl-4,5-dihydro-1h-imidazole and anthracene-9-carbaldehyde, *J. Turk. Chem. Soc. Chem. A* 7 (1) (2020) 77–86.
- [8] A.D. Becke, Density-functional thermochemistry. III. The role of exact exchange, *J. Chem. Phys.* 98 (1993) 5648–5652.
- [9] C. Lee, W. Yang, R. Parr, Development of the Colle-Salvetti correlation-energy formula into a functional of the electron density, *Phys. Rev. B* 37 (1988) 785–789.
- [10] Gaussian 16, Revision C.01, M.J. Frisch, G.W. Trucks, H.B. Schlegel, G.E. Scuseria, M.A. Robb, J.R. Cheeseman, G. Scalmani, V. Barone, G.A. Petersson, H. Nakatsuji, X. Li, M. Caricato, A.V. Marenich, J. Bloino, B.G. Janesko, R. Gomperts, B. Mennucci, H.P. Hratchian, J.V. Ortiz, A.F. Izmaylov, J.L. Sonnenberg, D. Williams-Young, F. Ding, F. Lipparini, F. Egidi, J. Goings, B. Peng, A. Petrone, T. Henderson, D. Ranasinghe, V.G. Zakrzewski, J. Gao, N. Rega, G. Zheng, W. Liang, M. Hada, M. Ehara, K. Toyota, R. Fukuda, J. Hasegawa, M. Ishida, T. Nakajima, Y. Honda, O. Kitao, H. Nakai, T. Vreven, K. Throssell, J.A. Montgomery Jr.,

- J.E. Peralta, F. Ogliaro, M.J. Bearpark, J.J. Heyd, E.N. Brothers, K.N. Kudin, V.N. Staroverov, T.A. Keith, R. Kobayashi, J. Normand, K. Raghavachari, A.P. Rendell, J.C. Burant, S.S. Iyengar, J. Tomasi, M. Cossi, J.M. Millam, M. Klene, C. Adamo, R. Cammi, J.W. Ochterski, R.L. Martin, K. Morokuma, O. Farkas, J.B. Foresman, D.J. Fox, Gaussian, Inc., Wallingford CT, 2016.
- [11] J. Trotter, The crystal structure of some anthracene derivatives VI. 9-anthraldehyde, *Acta Crystallogr.* 12 (1959) 922–928.
- [12] P. Pavitha, J. Prashanth, G. Ramu, G. Ramesh, K. Mamatha, B. Venkatram Reddy, Synthesis, structural, spectroscopic, anti-cancer and molecular docking studies on novel 2-[Anthracene-9-ylmethylene]amino]-2-methylpropane-1,3-diol using XRD, FTIR, NMR, UV-Vis spectra and DFT, *J. Mol. Struct.* 1147 (2017) 406–426.
- [13] I.A. Fedorov, Y.N. Zhuravlev, V.P. Berveno, Electronic structure and chemical bond in naphthalene and anthracene, *Phys. Chem. Chem. Phys.* 13 (13) (2011) 5679–5686.
- [14] K.E. Srikanth, K. Ramaiah, D.J. Rao, K.P. Rao, J.L. Naik, A. Veeraiyah, J. Prashanth, Experimental and theoretical analyses on structural (monomer and dimeric form), spectroscopic and electronic properties of an organic semiconductor 2,6-dimethoxyanthracene, *Indian J. Phys.* 94 (8) (2019) 1153–1167.
- [15] J.L. Gazquez, Perspectives on the density functional theory of chemical reactivity, *J. Mexi. Chem. Soc.* 52 (1) (2008) 3–10.
- [16] L.I.U. Shu-Bin, Conceptual density functional theory and some recent developments, *Acta Phys. Chim. Sin.* 25 (3) (2009) 590–600.
- [17] P. Geerlings, F. De Proft, W. Langenaeker, Conceptual density functional theory, *Chem. Rev.* 103 (5) (2003) 1793–1874.
- [18] H. Chermette, Chemical reactivity indexes in density functional theory, *J. Comput. Chem.* 20 (1) (1999) 129–154.
- [19] L.H. Mendoza-Huizar, Chemical reactivity of isoproturon, diuron, linuron, and chlorotoluron herbicides in aqueous phase: a theoretical quantum study employing global and local reactivity descriptors, *J. Chem.* 2015 (2015) 1–9.
- [20] P.K. Chattaraj, U. Sarkar, D.R. Roy, Electrophilicity index, *Chem. Rev.* 106 (6) (2006) 2065–2091.
- [21] J.I. Martínez-Araya, G. Salgado-Morán, D. Glossman-Mitnik, Computational nano chemistry report on the oxicams conceptual DFT indices and chemical reactivity, *J. Phys. Chem. B* 117 (21) (2013) 6339–6351.
- [22] C.Y. Panicker, H.T. Varghese, K.R. Ambujakshan, S. Mathew, S. Ganguli, A.K. Nanda, C.V. Alsenoy, *J. Raman Spectrosc.* 40 (2009) 527–536.
- [23] R. Arulraj, S. Sivakumar, S. Suresh, K. Anitha, Synthesis, vibrational spectra, DFT calculations, Hirshfeld surface analysis and molecular docking study of 3-chloro-3-methyl-2,6-diphenylpiperidin-4-one, *Spectrochim. Acta Part A Mol. Biomol. Spectrosc.* 232 (2020) 118166.
- [24] D.A. Kleinmen, Nonlinear dielectric polarization in optical media, *Phys. Rev.* 126 (1962) 1977–1979.
- [25] T. Rajamani, S. Muthu, Electronic absorption, vibrational spectra, non-linear optical properties, NBO analysis and thermodynamic properties of 9-[(2-hydroxyethoxy) methyl] guanine molecule by density functional method, *Solid State Sci.* 16 (2013) 90–101.
- [26] A.E. Reed, L.A. Curtius, F. Weinhold, Intermolecular interactions from a natural bond orbital, donor-acceptor viewpoint, *Chem. Soc.* 102 (1988) 899–926.
- [27] B. Rajasekhar, P.K.M. Hijaz, T. Swu, Computational study on non-linear optical property of wittig based Schiff-base ligands (both Z & E isomers) & copper(II) complex, *J. Mol. Struct.* 1168 (2018) 212–222.
- [28] Z. Demircioglu, A. Kastas, O. Buyukgungor, Theoretical analysis (NBO, NPA, Mulliken Population Method) and molecular orbital studies (hardness, chemical potential, electrophilicity and Fukui function analysis) of (E)-2-((4-hydroxy-2-methylphenylimino)methyl)-3-methoxyphenol, *J. Mol. Struct.* 1091 (2015) 183–195.
- [29] Z. Liu, T. Lu, Q. Chen, An sp-hybridized all-carboatomic ring, cyclo[18]carbon: electronic structure, electronic spectrum, and optical nonlinearity, *Carbon* 165 (2020) 461–467.
- [30] E. Matito, M. Duran, M. Sola, The aromatic fluctuation index (FLU): a new aromaticity index based on electron delocalization, *J. Chem. Phys.* 122 (2005), 014109.
- [31] T.M. Krygowski, M.K. Cyrański, Structural aspects of aromaticity, *Chem. Rev.* 101 (2001) 1385–1420.
- [32] F. De Proft, P. Geerlings, Conceptual and computational DFT in the study of aromaticity, *Chem. Rev.* 101 (2001) 1451–1464.
- [33] A.R. Katritzky, K. Jug, D.C. Oniciu, Quantitative measures of aromaticity for mono-, Bi-, and tricyclic penta- and hexatomic heteroaromatic ring systems and their interrelationships, *Chem. Rev.* 101 (2001) 1421–1450.
- [34] J. Gomes, R.B. Mallion, Aromaticity and ring currents, *Chem. Rev.* 101 (2001), 1349–1349.
- [35] M.N. Glukhovtsev, Aromaticity today: energetic and structural criteria, *J. Chem. Educ.* 74 (1) (1997) 132.
- [36] T.M. Krygowski, M.K. Cyrański, Z. Czarnocki, G. Häfelinger, A.R. Katritzky, Aromaticity: a theoretical concept of immense practical importance, *Tetrahedron* 56 (2000) 1783–1796.
- [37] B. Donner, M. Kleber, C. Bracher, H.J. Kreuzer, A simple method for simulating scanning tunneling images, *Am. J. Phys.* 73 (2005) 690–700.
- [38] H.L. Schmider, A.D. Becke, Chemical content of the kinetic energy density, *J. Mol. Struct. (Theochem)* 527 (2000) 51–61.
- [39] M.R. Bozorgmehr, J. Chamani, G. Moslehi, Spectroscopic and DFT investigation of interactions between cyclophosphamide and aspirin with lysozyme as binary and ternary systems, *J. Biomol. Struct. Dyn.* 33 (8) (2015) 1669–1681.
- [40] S.M. Beck, D.E. Powers, J.B. Hopkins, R.E. Smalley, Jet-cooled naphthalene. I. Absorption spectra and line profiles, *J. Chem. Phys.* 73 (1980) 2019–2028.
- [41] K. Jayachitra, P.C. JobePrabakar, S. Ramalingam, Vibrational, NMR and UV Visible spectroscopic investigation on 10-methylanthracene-9-carbaldehyde using computational Calculations, *J. Mol. Struct.* 1217 (2020) 128435.
- [42] A.G. Ozkabak, L. Goodman, K. Wiberg, The benzene ground state potential surface. V. Criteria for theoretical modeling of the B2u harmonic force field, *J. Chem. Phys.* 92 (1990) 4115–4124.
- [43] Y. Haas, S. Zilberg, The .nu.14(b2u) mode of benzene in S0 and S1 and the distortive nature of the .pi. Electron system: theory and experiment, *J. Am. Chem. Soc.* 117 (1995) 5387–5388.
- [44] W.R. Ware, B.B. Baldwin, Effect of temperature on fluorescence quantum yields in Solution, *J. Chem. Phys.* 43 (1965) 1194–1197.
- [45] D. Butina, M.D. Segall, K. Frankcombe, Predicting ADME properties in silico: methods and models, *Drugs Disc. Today* 7 (11) (2002) S83–S88.
- [46] Diagnostic and Statistical Manual of Mental Disorders, fifth ed., American Psychiatric Publishing, Arlington, 2013, p. 204, 218–219.



A Size Controlled Synthesis of Magnetite Nanoparticles in Pure Inorganic Medium

M. THAMEEM ANSARI

Department of Chemistry, Sadakathullah Appa College (Autonomous), Tirunelveli-627 011, India

Corresponding author: Fax: +91 462 2540033; Tel: +91 462 2540763; E-mail: thameemnano@gmail.com

Received: 9 August 2016;

Accepted: 15 October 2016;

Published online: 30 November 2016;

AJC-18176

An extensive research has been carried out on the synthesis of magnetite nanoparticles by co-precipitation technique. Most of the co-precipitation technique shows the improper size and size distribution of the magnetite nanoparticles. In few reports organic stabilizers were employed to control the synthesis of magnetite nanoparticle. In this work, the pure inorganic precursors were employed for the synthesis of magnetite nanoparticles. The reports showed that pure form of magnetite nanoparticles with good size distribution. Hence this is the facile approach for the synthesis of magnetite nanoparticles; which can be employed for the various biomedicine applications.

Keywords: Magnetite nanoparticles, VUSPIO, Superparamagnetic, Nanomaterials.

INTRODUCTION

A number of synthetic methods have already been reported in literatures for the preparation of magnetite nanoparticles. Among them the co-precipitation technique is possibly the simplest and most competent chemical pathway to obtain magnetite nanoparticles. The main advantage of the co-precipitation process is that it can be easily scaled up for bulk preparation. However, the control of particle size distribution is limited, because only the kinetic factors control the growth of the crystal. Size controlled magnetite nanoparticles of range 10-40 nm were prepared through co-precipitation method [1-3]. The magnetite nanorods with anisotropic property have been synthesized by reverse co-precipitation technique with the support of magnetic field. The magnetic fluid has been synthesized from magnetite nanoparticles and hydrophilic surfactant Tween 80 through co-precipitation for the applications in MRI and magnetic fluid hyperthermia. In the co-precipitation process, two stages are involved (i) a short burst of nucleation occurs when the concentration of the species reaches critical super saturation and (ii) slow growth of the nuclei by diffusion of the solute to the surface of the crystal. To produce monodisperse iron oxide nanoparticles, these two stages should be separate, *i.e.*, nucleation should be avoided during the period of growth [4-7].

The magnetite nano crystals of size 2-4 nm can be synthesized by a chemical co-precipitation method in which the particle size was controlled by the reaction temperature [7-13]. The mechanism of the first stage of formation of magnetite nanoparticle synthesized by chemical precipitation

technique and the rate of nanoparticle formation is high in its initial period of time and then found decreasing due to the decrease in the number of combining molecules in the solution. Thus the rate of nanoparticle growth depends on its size because the mean size of nanoparticles depends on the physical properties of the medium (viscosity, temperature, *etc.*) [14-17]. Magnetite particles with an average size of 39 nm and good monodispersity have been synthesized by co-precipitation at 70 °C from ferrous Fe²⁺ and ferric Fe³⁺ ions by a tetra methyl ammonium hydroxide solution, followed by hydrothermal treatment at 250 °C. Further this report explains the conversion of magnetite to other iron oxide phases at elevated temperature [18,19]. Hence the above reports show that the synthesis of magnetite nanoparticles by co-precipitation technique can be achieved only by adding organic stabilizer or tedious reaction setup. In this work the pure magnetite nanoparticles were prepared by using inorganic precursors with facile chemicals.

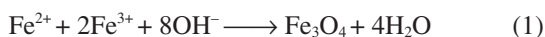
EXPERIMENTAL

The magnetite nanoparticle is prepared by using analytical grade of iron(II) perchlorate [Fe(ClO₄)₂, Alfa Aesar] and iron(III) perchlorate [Fe(ClO₄)₃, Sigma Aldrich] as iron precursor solution in the 1:2 M ratio, respectively. Sodium hydroxide (1 M, Fisher India) is used to maintain the pH of the solution to be 9. Water utilized in the experiments was Milli-Q (Millipore) deionized water. Septum sealed twin neck 100 mL round bottom flask is employed as a reaction container and it was maintained in an inert atmosphere by an argon balloon to prevent the oxidation of magnetite to maghemite

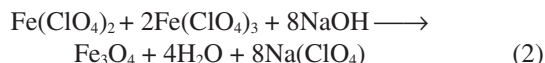
conversion during the process. Both the iron precursor solutions were added in equal amount of 10 mL each and stirred with magnetic pellet. The colour of the solution was monitored till turns into yellow colour. The pH of the reaction is increased by adding 10 mL of 1 M NaOH dropwise using a syringe. With continuous stirring for 10 min, the solution turns into black colour colloidal which indicates the formation of magnetite nanoparticle. The black colour colloidal solution was washed with water for several times to remove the unreacted excess of alkali, carefully dried and used for further characterization. To optimize the formation of magnetite nanoparticle the process has been carried out with different temperatures such as 30, 40 and 50 °C.

RESULTS AND DISCUSSION

The co-precipitation technique is the simplest possible method and most competent chemical pathway to obtain magnetite nanoparticles. Magnetite nanoparticles are usually prepared by ageing a mixture of ferrous and ferric perchlorate salts in aqueous medium. In this co-precipitation process, the chemical reaction has been deduced by the following stoichiometric equation (eqn. 1) which represents the formation of magnetite nanoparticles from 1:2 mixture of Fe²⁺ and Fe³⁺. The pH of solution is attuned to 9 by adding 1 M NaOH solution.



The present work is based on the combination of iron(II) perchlorate and iron(III) perchlorate as a (precursor) formulating materials for the preparation of magnetite nanoparticles. This co-precipitation reaction is represented in eqn. 2.



To optimize the size and shape of the nanoparticle the co-precipitation reaction has been regulated with two different parameters like temperature and concentration of iron precursor solution.

X-ray diffraction studies: The coprecipitation reactions are carried out at different temperatures *viz.*, 30, 40 and 50 °C and the corresponding X-ray diffraction data are depicted in Fig. 1(a-c), respectively. The X-ray diffraction pattern of magnetite nanoparticle (Fig. 1b) prepared at 40 °C showed a slight variation as compared to magnetite nanoparticle prepared at 30 °C. The intensity of the peak for plane 311 is reduced for magnetite nanoparticle synthesized at 40 °C which is the typical diffraction for magnetite. The particle size of magnetite nanoparticle corresponding to the most intense peak of 311 plane ($2\theta = 35.43$) is found to be 98 nm. The particle sizes were calculated by using Debye Scherrer equation (eqn. 3) and the result is consistent with the scanning electron microscopic results.

$$D = 0.98\lambda/\beta \cos \theta \quad (3)$$

where, $\beta = X_{\text{diff}} \times \pi/180$.

X-ray diffraction for magnetite nanoparticle prepared at 50 °C [Fig. 1(c)] showed the peak found at $2\theta = 75^\circ$ representing the maghemite diffraction associated with the magnetite peaks.

The result reveals that during the co-precipitation reaction, the oxidation of magnetite into the most thermodynamically stable iron oxide forms of maghemite has occurred at 50 °C.

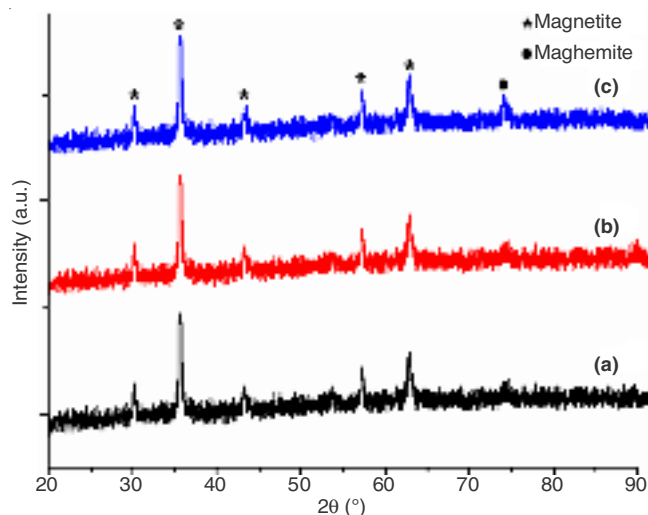


Fig. 1. XRD patterns of magnetite nanoparticle synthesized at various temperatures in 1:2 M of iron(II) perchlorate and iron(III) perchlorate (a) 30 °C, (b) 40 °C and (c) 50 °C

FT-IR spectral analysis: The FT-IR spectra of magnetite nanoparticles synthesized by co-precipitation method at different temperatures 30, 40 and 50 °C were depicted in Fig. 2a-c. The spectrum obtained for 30 °C shows the typical peak for magnetite nanoparticles (Fig. 2a). The FT-IR spectrum acquired for 40 and 50 °C show the high transmittance in the region of 1800-1200 cm⁻¹ compared to the spectrum obtained for 30 °C (Fig. 2b-c). Further the peak at 50 °C appeared at 900 cm⁻¹ corresponds to the other iron oxide phases like maghemite and hematite. Hence from the result it can be concluded that at higher temperature (50 °C) the magnetite could oxidize to its other iron oxide phases namely maghemite.

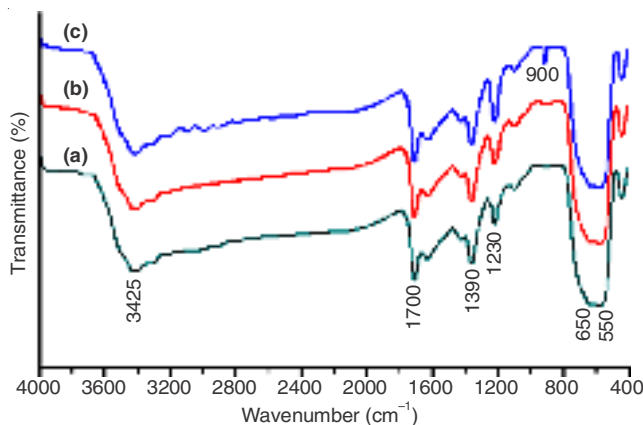


Fig. 2. FT-IR spectra of magnetite nanoparticles synthesized at various temperatures in 1:2 M of iron(II) perchlorate and iron(III) perchlorate (a) 30 °C, (b) 40 °C and (c) 50 °C by co-precipitation method

Raman analysis: The influence of temperature on the formation of magnetite nanoparticle has been evaluated by means of Raman spectroscopy and the spectra are given in Fig. 3a-c. The Raman spectrum of magnetite nanoparticle synthesized at 40 °C shows the typical Raman active bands as received magnetite. Further the increase of temperature to 50 °C leads to the formation of maghemite which is evident from the characteristic peak of maghemite at 700, 500 and 350 cm⁻¹ along with the magnetite peaks. Thus elevation of

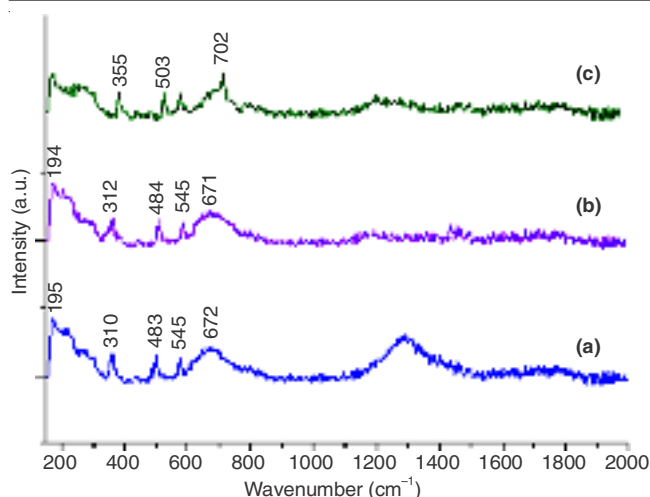


Fig. 3. Raman spectra of magnetite nanoparticles synthesized by co-precipitation method at (a) 30 °C, (b) 40 °C and (c) 50 °C

reaction temperature results in the formation of maghemite. Hence it is concluded that in the co-precipitation technique, the optimum temperature for the formation of magnetite is 40 °C.

Vibrating sample magnetometer studies: Further the M-H analysis has been carried out for the magnetite nanoparticles synthesized by co-precipitation at different temperature 30-50 °C and the hysteresis curves have been shown in Fig. 4. M_s value for the magnetite nanoparticle synthesized at 50 °C is 29.5 emu g^{-1} and magnetite nanoparticle prepared at 40 °C is 29 emu g^{-1} . Hence increasing the temperature of the co-precipitation reaction slightly varies the saturation magnetization value compared to the reaction carried out at 30 °C. Further the existence of small coercivity confirms the ferromagnetic properties of magnetite nanoparticle.

Scanning electron microscopic analysis: The scanning electron micrographs of the magnetite nanoparticle prepared at an elevated temperature (40-50 °C) from 1 M concentration of precursor solution have been shown in Fig. 5a-b. The temperature of the reaction has remarkable influence on the particle distribution which can be evidenced by SEM micrographs. The magnetite nanoparticle synthesized at 50 °C shows the better particle distribution rather than at 40 and 30 °C.

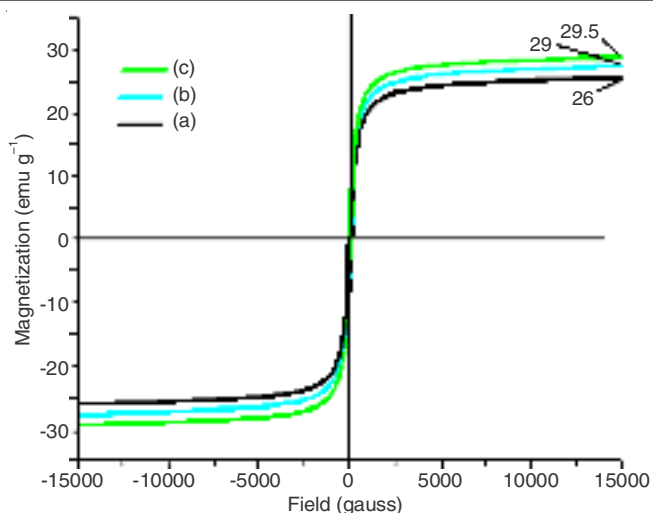


Fig. 4. VSM hysteresis curves of magnetite nanoparticles synthesized by co-precipitation method at (a) 30 °C (b) 40 °C and (c) 50 °C

In co-precipitation technique, the effect of concentration of iron precursors is optimized and it has been observed that 1:2 M ratio of iron(II) perchlorate and iron(III) perchlorate at 40 °C is the best among the other various conditions. Further the effect of temperature shows the better particle distribution but structural study shows the phase transformation of magnetite to magnetite maghemite at elevated temperature 50 °C. The overall SEM results show that the average size of the particles exists as randomized and in the range of 70 to 336 nm. Hence this technique is not efficient method for the synthesis of mono-disperse nanoparticles.

Conclusion

The composition of iron(II) perchlorate and iron(III) perchlorate media is best precursor for the preparation of magnetite nanoparticles. The size distribution of the nanoparticles is controlled by optimizing the temperature of the reaction medium. The optimum temperature for the synthesis of magnetite nanoparticles is 40 °C. At high temperature the magnetite nanoparticles were transformed to the maghemite. It is evidenced by the Raman and FT-IR spectral studies. Further it is confirmed by the X-ray diffraction studies. Scanning electron

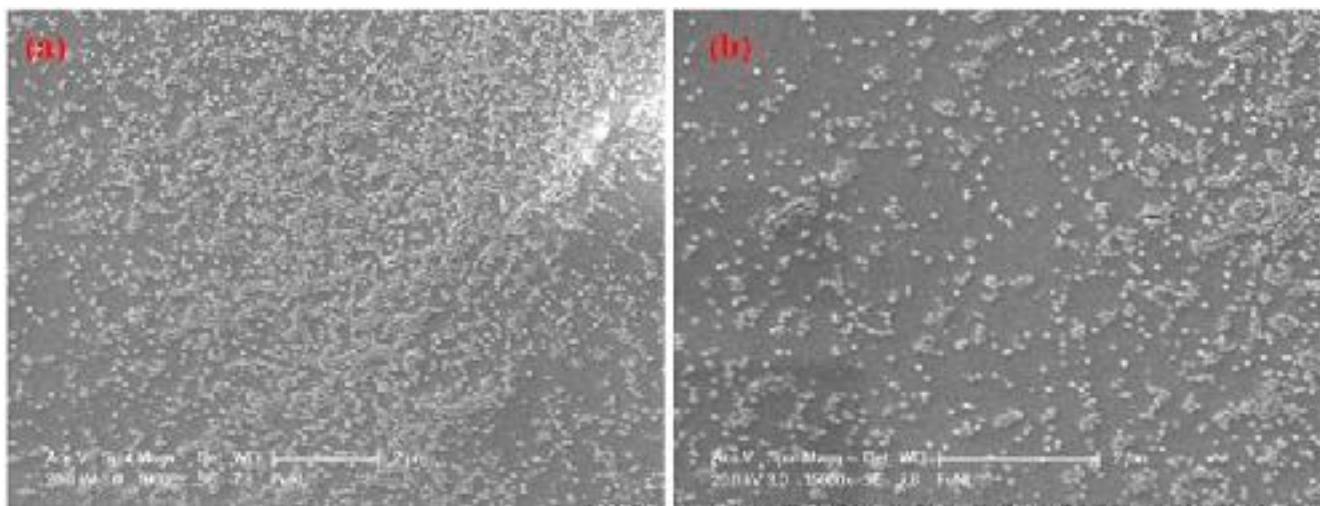


Fig. 5. Scanning electron micrograph of magnetite nanoparticle prepared in 1:2 M of iron precursors at (a) 40 °C and (b) 50 °C

microscopic analysis provides an insight on the morphological features of as-synthesized powders. The particle size has been observed in the range of 80-150 nm and they are in uniform size distribution.

REFERENCES

1. J.A. Blackman and C. Binns, in ed.: P. Misra, Handbook of Metal Physics Metallic Nanoparticles, Elsevier, Oxford: UK, edn 1 (2009).
2. D. Thompson, *Gold Bull.*, **40**, 267 (2007).
3. P. Moriarty, *Rep. Prog. Phys.*, **64**, 297 (2001).
4. Z.L. Wang and J.H. Song, *Science*, **312**, 242 (2006).
5. M. Law, L.E. Greene, J.C. Johnson, R. Saykally and P. Yang, *Nat. Mater.*, **4**, 455 (2005).
6. K. Petcharoen and A. Sirivat, *Mater. Sci. Eng. B*, **177**, 421 (2012).
7. Y.M. Wang, X. Cao, G.H. Liu, R.Y. Hong, Y.M. Chen, X.F. Chen, H.Z. Li, B. Xu and D.G. Wei, *J. Magn. Magn. Mater.*, **323**, 2953 (2011).
8. L. Li, Y. Yang, J. Ding and J. Xue, *Chem. Mater.*, **22**, 3183 (2010).
9. H.T. Hai, H. Kura, M. Takahashi and T. Ogawa, *J. Colloid Interface Sci.*, **341**, 194 (2010).
10. X. Yang, W. Jiang, L. Liu, B. Chen, S. Wu, D. Sun and F. Li, *J. Magn. Magn. Mater.*, **324**, 2249 (2012).
11. J.H. Wu, S.P. Ko, H.L. Liu, M. Jung, J.H. Lee, J. Ju and Y.K. Kim, *Colloids Surf. A*, **313-314**, 268 (2008).
12. D. Gopi, M.T. Ansari, E. Shinyjoy and L. Kavitha, *Spectrochim. Acta A Mol. Biomol. Spectrosc.*, **87**, 245 (2012).
13. D. Gopi, M.T. Ansari and L. Kavitha, *Arab. J. Chem.*, **9**, S829 (2016).
14. Y. Wu, W. Jiang, X. Wen, B. He, X. Zeng, G. Wang and Z. Gu, *Biomed. Mater.*, **5**, 015001 (2010).
15. N. Tran and T.J. Webster, *Acta Biomater.*, **7**, 1298 (2011).
16. F.P. Filho, R.E.F.Q. Nogueira, M.P.F. Graça, M.A. Valente, A.S.B. Sombra and C.C. Silva, *Physica B*, **403**, 3826 (2008).
17. S. Zhang, X. Liu, L. Zhou and W. Peng, *Mater. Lett.*, **68**, 243 (2012).
18. T. Ikoma, T. Tonegawa, H. Watanaba, G. Chen, J. Tanaka and Y. Mizushima, *J. Nanosci. Nanotechnol.*, **7**, 822 (2007).
19. A. Mir, D. Mallik, S. Bhattacharyya, D. Mahata, A. Sinha and S. Nayar, *J. Mater. Sci. Mater. Med.*, **21**, 2365 (2010).



Research Journal of Pharmaceutical, Biological and Chemical Sciences

Formulation Of Innovative Water Quality Index For Assessing Sugar Mill Effluent.

M A Sabitha*.

Department of Chemistry, Sadakathullah Appa College (Autonomous), Tirunelveli - 627 011, Tamil Nadu, India.

ABSTRACT

The objective of water quality index calculation is to change complex water quality data into information that is understandable and useable by the public. In other word, water quality index is a tool used to summarize large amounts of complex, highly technical water quality data into a simple, easy-to-understand message. There are various water quality index calculation method developed in the world. The new index was applied to the sugar mill effluent and the results gave a quantitative picture for the water quality situation. Heber water quality index method has been successfully applied to measure water quality of effluent from sugar mill. The parameters analyzed were Temperature, pH, Total Solids, Turbidity, Dissolved Oxygen, Biochemical Oxygen Demand and Total Phosphate. The total HWQI values are in the range of 0.45-11.97. These values suggest that almost all the water samples collected during different months are bad in quality and must be treated before discharge.

Keywords: Heber water quality index-1, total solids, turbidity, dissolved oxygen, biochemical oxygen demand, total phosphate.

**Corresponding author*



INTRODUCTION

Environmental pollution has become appreciable recently as it adversely affects human and the biosphere (Sabitha et al, 2009). Industrial wastes make the ground water polluted and unfit for human consumption (Nyroos, 1994). Chemical industries discharge tons of untreated effluents with heavy metals and toxic organic and inorganic pollutants into the ground water, making it poisonous for plants and living organisms (Gupta et al., 1997). In India, there are 369 sugar factories (Manohar Rao, 1987). Indian economy mainly depends on these industries which provide employment to large sectors. Tons of waste materials both organic and inorganic loads are released from sugar industries (Rajukkannu and Manickam, 1997).

The effluents generated from Nizam Deccan Sugar factory at Bodhan, Nizamabad, District of Andhra Pradesh, India showed electrical conductivity between 1557-13050 $\mu\text{mhos/cm}$ and higher BOD values (Dasarath et al., 2005). The studies proved that the water cannot be used for irrigation or human consumption. Studies of Nomulwar et al (2005) on the sugar factory effluents revealed that most of the parameters such as colour, odour, total dissolved solids, chemical oxygen demand, total alkalinity, pH, temperature, phosphate and sulphate have exceeded ISI limits. The effluent contain high amount of total hardness, total dissolved solids, biological oxygen demand (BOD) and chemical oxygen demand (COD).

The water quality standards and maximum pollution load for water body are framed by Total Maximum Daily Load (TMDL) regulations (Copeland 2002). Water quality index (WQI) is developed by regulatory agencies to indicate the quality of water in terms of water quality variables, such as dissolved oxygen (DO), conductivity, turbidity, total phosphorus, and fecal coliform, each of which has specific impacts to beneficial uses.

The general WQI was developed by Brown et al., (1970) and improved by Deininger for the Scottish Development Department (1975). Overall index has been framed by Horton (1965). Water quality index provides sufficient information about the quality of water and proved to be effective tool. WQI is defined as a rating reflecting the composite influence of different water quality parameters (Atulegwu and Njoku, 2004).

The following are the major objectives of this investigation:

- (a) To visit the sugar mill to collect important information regarding the nature of the effluent discharged.
- (b) To check whether the effluent discharged by the mill is properly treated or not.
- (c) To assess the quality of the collected water samples during different months using Heber Water Quality index (HWQI).

The quality of water can be assessed using more than 35 parameters. As it is difficult to analyze all the parameters, important seven parameters related to climatic conditions are taken into consideration for framing new, effective and successful water quality index. Heber Water Quality index (HWQI) is a novel method to determine the quality of water (Rajendran et al., 1999). The parameters considered for calculating Heber Water Quality index (HWQI) are temperature, pH, total solids, turbidity, Dissolved Oxygen, Biochemical Oxygen Demand and total phosphate.

MATERIALS AND METHODS

Ground water forms the source for drinking and domestic usage in India. It becomes important to formulate a method which is reliable and cost effective to analyze water and predict the usability (Rajendran et al., 1999). The important parameters which determine the water quality as prescribed by National Sanitation Foundation (NSF) of USA, are temperature, pH, total solids, turbidity, Dissolved Oxygen, Biochemical Oxygen Demand and total phosphate. Analysis of these parameters provide weighing curve values (Q-values) and weightage factor from which the water quality index is determined.

Ground water quality can be assessed using new water quality index. Temperature is an important parameter from which other data such as density, viscosity can be calculated. It also affects the chemical and biological reactions of organisms in water. Temperature variation causes depletion of oxygen dissolved in water, changes in taste and odour and also affects the rate of photosynthesis.



Temperature change and phosphate are not usually considered as pollutants as they change according to the climatic conditions (Rajendran et al., 1999). Since India is a tropical country, the variation in temperature of aquatic system is high. The contribution of thermal power plants to temperature change is also minimal. Hence the parameter gains less importance in calculating the index (Rajendran et al., 2000). Heber Water Quality Index (HWQI) makes use of the seven parameters namely temperature, pH, total solids, turbidity, Dissolved Oxygen, Biochemical Oxygen Demand and total phosphate (Kumar et al., 1993). The Heber Water Quality Index (HWQI) is formulated by arranging the seven parameters in decreasing order of importance with scores of 0-9 from low (0) to high value (9) and weighing curve value is assigned to each parameter.

Sampling station

Water samples were collected from sugar mill. Seven Water quality parameters for calculating HWQI were analyzed.

From the effluent discharge stream of sugar mill, the effluent samples were collected in 2 litre polythene can (Rainwater et al., 1960). The bottles for sample preservation were thoroughly cleaned by rinsing with 8M Nitric acid solution, distilled water, double distilled water and effluent samples. It was stored in a refrigerator at temperature approximately 4°C, after adding the necessary preservatives, (APHA, 1985). Preservatives are added to retard biological action. These samples were used for analysis of water quality parameters such as turbidity (AOAC, 1998), pH, temperature, total solids, (APHA, 1985; Jeffery et al., 1996), BOD and DO (USEPA, 1986; Young et al., 1981) and total phosphate (APHA, 1998).

The percent saturation chart was used to determine the dissolved oxygen present in water at a given temperature. A straight line joining the water temperature of the sample site and the dissolved oxygen in mg/l is drawn. The percent saturation at the intercept on the sloping scale was recorded.

Procedure for determining Q-value

The test value line intersects the weighing curve and a horizontal line was drawn to the “Y” axis which is the point of intersection Q-value. It was recorded in the table. The weighing curve value (i.e., Q-value) for each test was multiplied by the weighing factor listed in the table for a particular test. Similarly, the weighing factors for different parameters such as pH, turbidity, BOD and total phosphate (according to HWQI) were determined. The overall water quality index (WQI) for the sampling station during different months was determined by adding the total of the seven test results.

The weighing factor for the parameters was given in table 2. The overall HWQI values were calculated to be 39.37 (Table 3) during October, 38.69 (Table 4) during November, 24.79 (Table 5) during December, 23.48 (Table 6) during January, 23.73 (Table 7) during February and 23.83 (Table 8) during March respectively which indicates that the effluent are bad during October and November whereas it is very bad during December, January, February and March as given by the quality rating table 1.

Table 1: Quality Rating

Range	Quality
90-100	Excellent
70-90	Good
50-70	Medium
25-50	Bad
0-25	Very Bad

**Table 2: Weighing Factor for parameters**

S.NO.	Parameter	Weighing Factor
1	pH	0.117
2	Turbidity	0.09
3	BOD	0.126
4	DO	0.133
5	Temperature	-
6	Total solids	0.09
7	Total Phosphate	0.1

Table 3: Heber Water Quality Index (HWQI) during October

S.NO.	Parameter	Test Result	Q-Value	HWQI Weighing Factor	Total
1	pH	7.3	93	0.117	10.88
2	Turbidity (NTU)	2.8	91	0.09	8.19
3	BOD (mg/l)	59	5	0.126	0.63
4	DO (mg/l)	84%	90	0.133	11.97
5	Temperature °C	25	16	-	-
6	Total solids (mg/l)	1908	20	0.09	1.80
7	Total Phosphate (mg/l)	0.522	59	0.1	5.9
HWQI = 39.37					

Table 4: Heber Water Quality Index (HWQI) during November

S.NO.	Parameter	Test Result	Q-Value	HWQI Weighing Factor	Total
1	pH	7.2	92	0.117	10.76
2	Turbidity (NTU)	2.6	91	0.09	8.19
3	BOD (mg/l)	51	5	0.126	0.63
4	DO (mg/l)	71%	76	0.133	10.11
5	Temperature °C	24.8	16	-	-
6	Total solids (mg/l)	1687	20	0.09	1.80
7	Total Phosphate (mg/l)	0.391	72	0.1	7.2
HWQI = 38.69					

Table 5: Heber Water Quality Index (HWQI) during December

S.NO.	Parameter	Test Result	Q-Value	HWQI Weighing Factor	Total
1	pH	7.6	92	0.117	10.76
2	Turbidity (NTU)	100	17	0.09	1.53
3	BOD (mg/l)	153	5	0.126	0.63
4	DO (mg/l)	Nil	2	0.133	0.27
5	Temperature °C	24.5	16	-	-
6	Total solids (mg/l)	839	20	0.09	1.80
7	Total Phosphate (mg/l)	0.055	98	0.1	9.8
HWQI = 24.79					

**Table 6: Heber Water Quality Index (HWQI) during January**

S.NO.	Parameter	Test Result	Q-Value	HWQI Weighing Factor	Total
1	pH	7.8	90	0.117	10.53
2	Turbidity (NTU)	118	5	0.09	0.45
3	BOD (mg/l)	159	5	0.126	0.63
4	DO (mg/l)	Nil	2	0.133	0.27
5	Temperature °C	26.7	14	-	-
6	Total solids (mg/l)	873	20	0.09	1.80
7	Total Phosphate (mg/l)	0.062	98	0.1	9.8
HWQI = 23.48					

Table 7: Heber Water Quality Index (HWQI) during February

S.NO.	Parameter	Test Result	Q-Value	HWQI Weighing Factor	Total
1	pH	7.4	93	0.117	10.88
2	Turbidity (NTU)	126	5	0.09	0.45
3	BOD (mg/l)	167	5	0.126	0.63
4	DO (mg/l)	Nil	2	0.133	0.27
5	Temperature °C	26.5	14	-	-
6	Total solids (mg/l)	966	20	0.09	1.80
7	Total Phosphate (mg/l)	0.065	97	0.1	9.7
HWQI = 23.73					

Table 8: Heber Water Quality Index (HWQI) during March

S.NO.	Parameter	Test Result	Q-Value	HWQI Weighing Factor	Total
1	pH	7.5	93	0.117	10.88
2	Turbidity (NTU)	115	5	0.09	0.45
3	BOD (mg/l)	147	5	0.126	0.63
4	DO (mg/l)	Nil	2	0.133	0.27
5	Temperature °C	26.9	13	-	-
6	Total solids (mg/l)	897	20	0.09	1.80
7	Total Phosphate (mg/l)	0.052	98	0.1	9.8
HWQI = 23.83					

RESULTS AND DISCUSSION

Dissolved oxygen is one of the most important parameters in water quality assessment and reflects the physical and biological processes taking place in it. The dissolved oxygen means oxygen is in dissolved state obtained by absorption from the atmosphere. It keeps water fresh and its depletion is a signal severe pollution. Most aquatic plants and animals need a certain level of oxygen dissolved in the water for survival. Dissolved Oxygen was mostly affected by chemical effluents as seen in the present study. The percent saturation level of DO was 84% and 71% during October and November whereas it became 0% during December to March (working season).

The much of dissolved oxygen is consumed in waters of high BOD as Biochemical Oxygen Demand and Dissolved Oxygen are inversely related. Low BOD values (59 and 51 mg/l) were recorded during October and November where the DO was 84% and 71%. When the BOD reached high values of 153 mg/l, 159 mg/l, 167 mg/l and 147 mg/l during December to March, the corresponding DO values were zero.



pH is the measure of the intensity of acidity or alkalinity and measures the concentration of hydrogen ions in water. Depending upon the nature of the dissolved salts and minerals in water, it may be alkaline or acidic. For potable water, pH value should be between 6.5 and 8.5 and for public water supplies, the pH value cause tuberculation and corrosion. The higher values cause incrustation, sediment deposition, difficulty in chlorination and other ill-effects on the human using the water. The pH value is very important in industries since many chemical and Biochemical reactions take place at low pH value or high range of pH value. The control of pH value is particularly much important in the chemical flocculation or trade wastes, treatment by digestion of sewage sludges and of trade wastes. As for as the pH parameter is concerned the effluent is slightly alkaline which will not harm the aquatic system.

The high total solids and turbidity might be due to the fact that the effluent was rich of some sulphates and chlorides. The total phosphorus of the effluent was very high during all the seasons which exceeded the standard limit of 0.0326 mg/l. It will stimulate the growth of algae and other aquatic plant forms, leading to a condition called "Eutrophication". "Eutrophication" is a condition where a water body becomes loaded with nutrients and dissolved solids with a decrease in the transparency of the water column which in turn reduces the DO in water and light penetration.

CONCLUSION

The overall water HWQI values for samples collected during different months were 28.98. This indicates that the quality ranking of the effluent was very bad. It poses serious threat to the environment. This method was found to be more suitable, reliable, less time consuming and less consumption of chemicals. From the data obtained by the analysis of the effluent taken from the sugar mill during different seasons, it was found that total HWQI value was 28.98 which suggest that the quality of the effluent was very bad. Based on the above findings and reasons, it was concluded that effective measures are to be taken before discharging the effluent into ground water system. In a developing country like India people especially living in semi urban area depend mostly on ground water for their drinking and other domestic uses.

REFERENCES

- [1] Sabitha MA, Sarala Thambavani D and Selvasundari R. The Asian Journal of Experimental Chemistry 2009; 4(1&2): 126-132.
- [2] Nyroos H. Publication of the water and environment research institute 1994; 14: 1-85.
- [3] Gupta AK and Sexena GC. Indian J. Environ. Protection 1997; 17(6): 434-441.
- [4] Manohar Rao AJ. Development of Indian sugar industry, Historical Bharathya Sugar Directory, (2nd edn), ISMA, New Delhi, 1987.
- [5] Rajukkannu K and Manickam TS. In: Proc.Sixth National Symposium on Environment, Tamil Nadu Agricultural University, Coimbatore, India 1997; pp 286-290.
- [6] Dasarath D Reddy E and Narasimha. Chemistry 2005; 21(2): 283-286.
- [7] Nomulwar, Poonam and Patil PM. Journal of Aquatic Biology 2005; 20(1): 45-48.
- [8] Copeland C. Water quality: Implementing the Clean Water Act 2002; available at: http://www.policymanc.org/environment/archive/crs_water_quality.shtml.
- [9] Brown RM, McClelland NI, Deininger RA and Tozer RG. Water & Sewage Works 1970; 117: 339-343.
- [10] Scottish Development Department. Report of a River Pollution Survey of Scotland 1975.
- [11] Horton RK. Journal-Water Pollution Control Federation 1965; 37: 300-305.
- [12] Atulegwu PU and Njoku JD. Int. Res. J. Eng. Sci. Technol. 2004; 1: 47-52.
- [13] Rajendran A, Sharon AA, Jeyakar Chellaraj DA and Princy Merlin J. Indian J Environ. Protection 1999; 19(1): 842-845.
- [14] Rajendran A, Gugan S, Ramesh Kumar C, Princy Merlin J and Jeyakar Chellaraj DA. Poll Res. 2000; 19 (3): 485-489.
- [15] Kumar S and Singh KP. Indian J. Environ. Protection 1993; 13(5): 349-345.
- [16] Rainwater FH and Thatcher LL. U.S. Government print office, Washington. D.C., U.S.A. 1960.
- [17] American Public Health Association (APHA). Standard methods of the examination of water/wastewater, 16th Edition. APHA, AWWA, and WPCF, New York 1985.
- [18] AOAC. Official methods of analysis of the Association of Official Analytical Chemists. Alexandria, VA: Association of Official Analytical Chemists 1998; 432-444.



- [19] Jeffery GH. Vogel's textbook of quantitative chemical analysis (5th edn), Addison Wesley Longman Limited, Harlow, England 1996.
- [20] USEPA. Environmental Monitoring and Support Lab., Cincinnati, Ohio 1986.
- [21] Young JC, McDermott GN and Jenkins D. Journal of Water Pollution Control Federation 1981; 53: 1253-1253.
- [22] American Public Health Association (APHA). Standard Methods for the Examination of Water and Wastewater, 20th edn. Washington, D.C 1998.

A Comparative Analysis of Ascorbic Acid Content in Selected Citrus Fruits and Manufactured Tablets Collected from Periyakulam District, Tamil Nadu

Dr. Sabitha, M.A.¹

Abstract

*Human body creates antioxidants to neutralize the free radicals which were produced in the body to destroy bacteria and viruses. Due to the increase in environmental toxins, the body is incapable of producing ample antioxidants. Citrus fruits loaded with high antioxidants supply the necessary antioxidants to get rid of these free radicals. The present study was undertaken to analyze the ascorbic acid content of the following fruits: cherry (*Muntingia calabura*), goose berry (*Phyllanthus emblica*), grapes (*Vitis vinifera*) and orange (*Citrus sinensis*). Vitamin c tablets were also analyzed for antioxidant content. Numbers of moles of antioxidant present in various fruits were analyzed using redox titration with Iodine and Indophenol method. The number of moles of antioxidant per 100 gm using redox titration was 0.0167, 0.056, 0.1725, 0.0645 and 70.5 for cherry, grapes, gooseberry, orange and vitamin C tablet, respectively and using Indophenol method were 0.3182, 0.0775, 0.0850, 0.0875 and 30.0000, respectively. The results of the analysis carried out on the fruits indicate that all the fruits contain ascorbic acid and in turn antioxidising activities at varied levels. As Vitamin C is rich in antioxidants, it is recommended to take cherry, grapes, gooseberry or orange in small quantity per day to fulfill the antioxidant requirement. Since overdose of ascorbic acid leads to nausea and diarrhea, it is recommended to adhere to natural fruits. Hence, it is preferable to take 3-70 gm of cherry or 15-20 gm of grapes or 7-14 gm of gooseberry or 13-20 gm of orange per day. This will enable the human free from diseases and to lead a healthy life.*

Keywords: Free radicals, Cherry (*Muntingia calabura*), Goose berry (*Phyllanthus emblica*), Grapes (*Vitis vinifera*), Orange (*Citrus sinensis*).

¹ Assistant Professor, Department of Chemistry, Sadakathullah Appa College (Autonomous), Rahmath Nagar, Tirunelveli, Tamil Nadu, India.

**PHYTOREMEDIATION OF LABORATORY WASTE WATER USING
OCIMUM SANCTUM, *CYMBOPOGON CITRATUS*, *ALOE BARBADENSIS*
AND REUSING FOR DOMESTIC PURPOSES.**

Dr. M. A. Sabitha¹, Dr. A. Syed Mohamed²

¹Assistant Professor & PG Head, Department of Chemistry, Sadakathullah Appa College (Autonomous), Tirunelveli, Tamil Nadu, India, drsabithama@sadakath.ac.in

²Associate Professor & Research Head, Department of Chemistry, Sadakathullah Appa College (Autonomous), Tirunelveli, Tamil Nadu, India, asm2032@sadakath.ac.in

ABSTRACT

Water samples were collected from the chemistry laboratory. Daily lab discharge water was collected for one week. Water sample was treated by biosorption technique using *Ocimum sanctum*, *Cymbopogon citratus* (Lemon Grass) and *Aloe barbadensis miller*. The water analysis was carried out before and after treatment. 35 physico-chemical parameters were analyzed. pH, electrical conductivity, total dissolved solid and total hardness were reduced to permissible limits. Percentage of reduction was high in sodium, calcium, magnesium, bicarbonate and chloride. The decrease in carbonates, bicarbonates, nitrates, chloride, sulphate and phosphate were high. Even though the concentration of trace metals was low, the biosorption had reduced the concentration further. It was evident from this work that *Ocimum sanctum*, *Cymbopogon citratus* (Lemon Grass) and *Aloe barbadensis miller* could be efficiently used for treating laboratory waste water.

Keywords: *Aloe barbadensis miller*, biosorption, *Cymbopogon citrates*, *Ocimum sanctum*, total dissolved solid.

I. INTRODUCTION

Every natural response happen in water and it is the coordinated arrangement of organic metabolic responses in a fluid arrangement that is fundamental for the support of life. Human beings rely on water in one manner or other. It might be noticed that man's initial home and human advancement jumped up along the banks of waterways. In spite of the fact that the outside of our planet is about 71% water, just 3% of it is new. Of these 3% about 75% is tied up

in icy masses and polar ice sheets, 24% in groundwater and 1% is accessible as new water in streams, lakes and lakes appropriate for human utilization [1].

India faces a serious threat due to water pollution. Nearly 70% of surface water resources and groundwater reserves are contaminated by tones of various pollutants. These resources become unsafe for human consumption as well as for other activities. Because of the degradation of water quality, it will lead to water scarcity. In India, the Central Pollution Control Board (CPCB) in the year 1995 predicted that 18 major rivers are severely polluted. All these rivers run through urban area [2].

Wastes created in households, sewage, effluents from industries and agriculture run off pollutes the water resources. These wastes are loaded with chemicals and toxic substances which affect animals, plants and human beings. Solid wastes dumped in rivers and lakes affect the aquatic life. Due to the spilling of oil in sea pollutes the water becomes toxic for aquatic lives.

Iron coagulants are ferric sulphate ($\text{Fe}_2(\text{SO}_4)_3$), ferrous sulphate (FeSO_4) and ferric chloride (FeCl_2). Iron compounds are generally cheaper, produce a heavier flocculent and perform over a wider pH range than aluminium coagulants. However, iron coagulants are not used as much as aluminium due to staining equipment, corrosiveness, and they require more alkalinity than alum.

Although water treatment chemicals are effective and used worldwide, scientific evidence shows that exposure to chemicals during coagulation with metal salts could be associated with adverse health effects [3]. Aluminium, which is the major component of aluminium sulphate (alum), polyaluminium chloride (PAC) and polyaluminium silica sulphate (PASS), could induce Alzheimer's disease and other similar related problems that are associated with residual aluminium in treated water [4].

It becomes important to pursue research for effective, more cheap and economic way of treating water using natural adsorbents. Hence the present work is carried out using *Ocimum sanctum*, *Cymbopogon citrates* and *Aloe barbadensis* to treat waste water from laboratory and paving way for reuse of lab water for domestic purposes.

II. MATERIALS AND METHODS

Water samples are collected from the Chemistry laboratory of Sadakathullah Appa College. Daily lab discharge water is collected for one week. Sample was preserved by addition of sulphuric acid to $\text{pH} < 2$ (USEPA 600/4-82/029) and stored in refrigerator. Water sample was treated by biosorption technique using *Ocimum sanctum*, *Cymbopogon citratus* (Lemon Grass) and *Aloe barbadensis miller*. The leaves of *Ocimum sanctum* and *Cymbopogon citratus* (Lemon Grass) were collected and dried along with the gel of *Aloe barbadensis miller*. Then dried content were powdered. The weighed 5g powder was kept in muslin cloth and packed. This packet was put in the one litre water sample and then tightly closed. This set up was kept undisturbed for one week. After one week this sample is filtered and again the physico-chemical parameters were analyzed.

The following physico-chemical parameters such as pH, electrical conductivity, total dissolved solids, salinity, total hardness, sodium, calcium, potassium, magnesium, bicarbonate, carbonate, chloride, sulphate, nitrate, phosphate and fluoride [5,6] were determined before and after treatment of water.

III. RESULTS AND DISCUSSION

The waste water collected from the laboratory was soaked with *Ocimum sanctum*, *Cymbopogon citratus* (Lemon Grass) and *Aloe barbadensis miller*. The water analysis was carried out before and after treatment and was tabulated in table 1 and represented in figure 1.

The waste water was also analyzed for trace metals such as lead, arsenic, beryllium, cadmium, vanadium, chromium, nickel, molybdenum, silver, strontium, barium, rubidium, copper, iron, zinc, manganese, aluminium, cobalt, selenium and antimony before and after treatment of water. The results were tabulated in table 2 and represented in figure 2.

pH level of laboratory water was above 8.5 which indicate that a high level of alkanity and minerals were present. High pH causes many problems such as

- ❖ Scale build up on fixtures and shower doors.
- ❖ Reduced water flow.
- ❖ Scale accumulation at the bottom of tank water heater.

❖ Bitter taste.

On treatment with *Ocimum sanctum*, *Cymbopogon citratus* (Lemon Grass) and *Aloe barbadensis miller* pH level was decreased and lies within the permissible level of 7.34 which is very much near to neutral pH. TDS permissible limit for domestic water was less than 300 mg/L. The laboratory water showed 20 times more than the allowed limit. The treatment made an effective purification of waste water and the TDS level fell to 50 mg/l. The value was reduced by 99% from the before treatment value. A high level of TDS creates health problems in human. The presence of potassium, sodium and chloride increase the TDS level in water.

The present study showed electrical conductivity of 11,280 and 74 $\mu\text{S}/\text{cm}$ for waste water and treated water respectively. The permissible limit for EC must be less than 400 $\mu\text{S}/\text{cm}$. The treated water indicated that the value was decreased by greater extent. High electrical conductivity was due to dissolved substances and the presence of heavy metals. These substances affect the aquatic life system when discharged untreated.

The total hardness of the waste water was found to be three times more than the prescribed limit of 0- 60 mg/l. The value was declined to 19 mg/l after treatment with bioadsorbent. The hardness was well below the limiting value. The classification of water based on hardness was given in the table 3.

Based on the classification, the untreated very hard water had been changed to soft water after treatment. Hard water can cause the following effects:

- ❖ Reduce the life of equipment,
- ❖ Raise the costs of heating the water,
- ❖ Lower the efficiency of electric water heaters, and clog pipes.

The permissible limit for sodium in domestic water was 30- 60 mg/l. The untreated water exhibited 652 mg/l and the treated water had 62 mg/l. Although the treated water exceeds the limit, there was 90% reduction in the value. The level of calcium was reduced to 23 mg/l when treated with bioadsorbents which was below the permissible limit of 40- 80 mg/l. The potassium and magnesium levels were highly reduced from 56 mg/l to 6 mg/l and 562 mg/l to 31 mg/l respectively. 94 % decline in magnesium values was observed. The classification of water based

on magnesium was tabulated in table S4. Based on magnesium level, the waste water was graded as very hard which had been modified to slightly hard.

The carbonate and bicarbonate levels reached 101 mg/l and 0 mg/ l from 3 mg/l and 333 mg/l respectively. The levels of carbonate and bicarbonate represent the alkalinity of the samples. When these salt increases, the usage of such water creates health issues.

Chloride and sulphate amounts were reduced by 77% and 85% respectively. The amount of nitrate, phosphate and fluoride also showed slight decrease. Phosphorus is an essential element for plant life, but when there is too much of it in water, it can speed up eutrophication (a reduction in dissolved oxygen in water bodies caused by an increase of mineral and organic nutrients) of rivers and lakes. This method using can be used to prevent those conditions.

Even though the concentrations of lead, arsenic, vanadium, nickel, strontium, barium, cobalt, selenium and antimony were very low, the bio-adsorbents were able to further reduce these amounts. Manganese, iron, copper, and zinc are essential micronutrients. When the concentrations of these elements increase, it creates serious threats to the environment. The bioadsorbents can effectively used to reduce the concentrations of micro nutrients and also trace elements. Concentration of beryllium and nickel were decreased to permissible limit. Similarly the concentrations of silver and molybdenum were declined below the limiting value of 0.2-0.3 μ g/l and < 10 μ g/l respectively. Also aluminium concentration was reduced from 0.23 mg/l to 0.15mg/l.

The flavinoids and tannins present in *Cymbopogon citratus* provide antibacterial effect against gram positive bacteria. Quercitin and tannic acid contained in *Cymbopogon citratus* has efficacious effect against *P. Aeruginosa* [7]. In addition to antibacterial activity, *Cymbopogon citratus* possess antiamoebic, antifilarial and antifungal properties [8]. Studies reveal that aromatic grasses such as lemon grass, vetiver and palmarosa are used for phytoremediation of heavy metal contaminated sites. Also, Ocimum, Methe and Lavender help to remove metals [9]. *Cymbopogon citratus* is used to reclaim the toxic copper tailings [10]. Lead can be conveniently removed from waste water using lemon grass [11].

The effective bioadsorbition capacity of lemon grass for metals such as lead, cadmium and zinc is proved by Hassan et al., [12]. *Cymbopogon citratus* is an efficient accumulator of

aluminium, zinc, cadmium, lead, chromium, arsenic and nickel [13,14]. The efficient biosorption of iron and lead using *Ocimum sanctum* is studied which revealed that alcohol, carboxylamino and sulphonic groups play significant role in biosorption [15]. The high phenolic contents in these medicinal plants pave way for removal of metals due to high metal chelation potential [16]. *Ocimum sanctum* is considered as queen of herbs as it shows antiviral, antioxidative and antimicrobial properties [17].

Aloe barbadensis miller is a hyper accumulator of chromium, copper, nickel, cadmium and lead [18]. Rai et al., [19] confirmed that aloe vera can be effectively used for the biosorption of potassium, sodium, calcium, magnesium, phosphorus, iron, copper, zinc, cadmium and lead. The surface studies of *Aloe barbadensis miller* is being carried out by Malik et al., in 2015 [20]. They showed that carboxyl group, hydroxyl group and carbonyl group are present on the surface. The mechanism for the removal of metals is that the electrostatic attraction between charged groups in cell wall and metals in the pH range of 1.0 to 4.0 [21]. At this pH range, ionic exchange will be the reason for the removal of metals and at high pH, the removal is possible by means of precipitation. High potential of antiviral, antibacterial and antifungal properties are shown by *Aloe barbadensis miller* [22,23].

The main reaction involved in metal removal in these plant leaves are chemical reaction between functional groups on the surface of adsorbent and metals which forms metal- organic complexes. When the pH varies, other possible mechanisms of diffusion, bulk transport in liquid phase and mass transport processes occur. The biosorption of *Cymbopogon citratus* for the metals are in the order Zn (II) > Cd (II) > Pb (II) [24]. The metal removal efficiency of *Ocimum sanctum* for iron is 73.62% and that of lead is 95.63%. When *Aloe barbadensis miller* along with coconut husk is used for metal removal, the efficiency is found to be 99.99% for lead, 86.41% for zinc, 91.97% for nickel and 93.21% for copper [25]. Different bioadsorbents show different removal efficiency for various metals. Hence the combination of these bioadsorbents will produce effective results. So, the three plant species are chosen to effect maximum removal of metals and to incorporate antimicrobial activities.

Conclusion

The increasing population and the demand for underground water have created awareness for rain water harvesting and search of new techniques to reuse waste water. This methodology of using *Ocimum sanctum*, *Cymbopogon citratus* (Lemon Grass) and *Aloe barbadensis miller* for purification of most polluted laboratory waste water was cost effective and efficient. It can be applied to purify any water and the water can be used for domestic purpose. The proposed work can be extended to large scale waste water purification by constructing water tank made with three layers of sand and pebbles, sand and ceramic membrane coated with *Ocimum sanctum*, *Cymbopogon citratus* (Lemon Grass) and *Aloe barbadensis miller* leaf powders.

Acknowledgments

The authors acknowledge the financial support received from Sadakathullah Appa College, Tirunelveli, for their support and encouragement in carrying out this work.

V. REFERENCES

1. Dugan, P.R. (1972). Bio Medical Ecology of Water Pollution. Plenum press London, 159.
2. Central Pollution Control Board (CPCB), (1995). Annual Report 1993/94, Central Pollution Control Board, Ministry of Environment & Forests, Government of India, New Delhi, 154 pp.
3. Hahn, H.H. and Kunte, R. (1990). Chemical Water and Wastewater Treatment. Proceedings of the 4th Gottenburg Symposium ed. Klute, R. Madrid, Spain. Oct.1990. pp 37-409.
4. American Water Works Association (AWWA), (1990). Water Quality and Treatment: A Hand book of Public Water Supplies, 4th edition, New York, McGraw Hill.
5. APHA (American Public Health Association), (2012). Standard Methods for the Examination of Water and Wastewater (22nd ed.), American Public Health Association, Washington, DC.
6. USEPA (1992). Guidelines for Exposure Assessment. EPA/600/Z-92/001. US Environmental Protection Agency, Risk Assessment Forum, Washington, DC.
7. Geetha Subramaniam, Xin YingYew and Lalita Ambigai Sivasamugham, (2020). Antibacterial activity of *Cymbopogon citratus* against clinically important bacteria, South African Journal of Chemical Engineering, 34: 26- 30.

8. Shah, A.P., Nongthomba, U., Kelly Tanaka, K.K., Denton, M.L., Meadows, S.M., Bancroft, N., Molina, M.R., Cripps, R.M. (2011). Cardiac remodeling in *Drosophila* arises from changes in actin gene expression and from a contribution of lymph gland-like cells to the heart musculature. *Mech. Dev.* 128(3-4): 222--233.
9. Janhvi Pandey, Rajesh Kumar Verma and Saudan Singh, (2019). Suitability of aromatic plants for phytoremediation of heavy metal contaminated areas: a review, *International Journal of Phytoremediation*, <https://doi.org/10.1080/15226514.2018.1540546>.
10. Das M, Maiti SK. 2009. Growth of *Cymbopogon citratus* and *Vetiveria zizanioides* on Cu mine tailings amended with chicken manure and manure-soil mixtures: a pot scale study. *Int J Phytoremediation*. 11(8):651–663.
11. Lal K, Yadav RK, Kaur R, Bundela DS, Khan MI, Chaudhary M, Meena RL, Dar SR, Singh G. 2013. Productivity, essential oil yield, and heavy metal accumulation in lemon grass (*Cymbopogon flexuosus*) under varied wastewater–groundwater irrigation regimes. *Ind Crops Prod.* 45:270–278.
12. Hassan E. 2016. Comparative study on the biosorption of Pb (II), Cd (II) and Zn (II) using Lemon grass (*Cymbopogon citratus*): kinetics, isotherms and thermodynamics. *Chem Int.* 2(2):89–102.
13. Gautam M, Pandey D, Agrawal M. 2017. Phytoremediation of metals using lemongrass (*Cymbopogon citratus* (DC) Stapf.) grown under different levels of red mud in soil amended with biowastes. *Int J Phytoremediation*. 19(6):555–562.
14. Lee LY, Lee XJ, Chia PC, Tan KW, Gan S. 2014. Utilisation of *Cymbopogon citratus* (lemon grass) as biosorbent for the sequestration of nickel ions from aqueous solution: equilibrium, kinetic, thermodynamics and mechanism studies. *J Taiwan Institut Chem Eng.* 45(4):1764–1772. doi:10.1016/j.jtice.2014.02.002.
15. Sreelakshmi C D, (2017). Heavy Metal Removal from Wastewater using *Ocimum Sanctum*, *International Journal of Latest Technology in Engineering, Management & Applied Science*, 6(4): 85- 90.
16. Rice-Evans CA, Miller NJ, Paganga G. Structure-antioxidant activity relationships of flavonoids and phenolic acids. *Free Radical Biol Med.* 1996;20:933–956. doi: 10.1016/0891-5849(95)02227-9.

17. Pramod K Raghav and Mitu Saini, (2018). Antimicrobial properties of Tulsi (*Ocimum sanctum*), *International Journal of Green and Herbal Chemistry*, 7(1): 20-32.
18. Fatemeh Shokri, Parisa Ziarati and Zahra Mousavi, (2016). Removal of Selected Heavy Metals from Pharmaceutical Effluent by Aloe Vera L., *Biomed Pharmacol. J.*, 9(2), <https://dx.doi.org/10.13005/bpj/993>
19. Rai TS, Puri A, McBryan T, Hoffman J, Tang Y, Pchelintsev NA, van Tuyn J, Marmorstein R, Schultz DC, Adams PD. 2011. Human CABIN1 is a functional member of the human HIRA/UBN1/ASF1a histone H3.3 chaperone complex. *Mol Cell Biol* 31: 4107–4118.
20. Malik, R. 1 Saini, N. 1 Ahlawat, S. 2 Singhal, S. 3 and Lata, S., (2019). Convenient and Efficient Elimination of Heavy Metals from Wastewater Using Smart Pouch with Biomaterial, *Pollution*, 5(1): 13- 31.
21. Sag Y, Ozer D and Kutsal T, (1995). A comparative study of the biosorption of lead (II) ions to *Z. ramigera* and *R. arrhizus*. *Process Biochemistry* 30 169–174.
22. Ramasubramanian TS, Sivakumar VT, Thirumalai AV., (2010). Antimicrobial activity of *Aloe vera* (L.) Burm. f. against pathogenic microorganisms. *J Bio Sci Res.*, 4:251–8.
23. Arunkumar S, Muthuselvam M., (2009). Analysis of phytochemical constituents and antimicrobial activities of *Aloe vera* L. against clinical pathogens. *World J Agric Sci.*, 5(5):572–6.
24. Babarinde A, Ogundipe K, Sangosanya KT, Akintola BD, Hassan AOE (2016) Comparative study on the biosorption of Pb(II), Cd(II) and Zn(II) using lemon grass (*Cymbopogon citratus*): kinetics, isotherms and thermodynamics. *Chem Int* 2:89–102.
25. Malik, R. 1 Saini, N. 1 Ahlawat, S. 2 Singhal, S. 3 and Lata, S., (2019). Convenient and Efficient Elimination of Heavy Metals from Wastewater Using Smart Pouch with Biomaterial, *Pollution*, 5(1): 13- 31.

TABLE 1: Physico-chemical parameters of waste water collected from laboratory before and after treatment

S. No.	Physico-chemical parameters	Value before treatment	Value after treatment	Standard value
1	pH	8.55	7.34	7.0-8.0
2	TDS mg/L	7400	50	Less than 300
3	EC μ S/cm	11280	74	< 400
4	Total hardness mg/L	270	19	0-60
5	Sodium mg/L	652	62	30-60
6	Calcium mg/L	159	23	40-80
7	Potassium mg/L	56	9	-
8	Magnesium mg/L	562	31	17.1-60
9	Bi carbonate mg/L	333	101	-
10	Carbonate mg/L	3	0	Below 60
11	Chloride	888	201	>250
12	Sulphate	651	89	1-770
13	Nitrate	10	7	10
14	Phosphate	6	2	0.5 -1.5
15	Fluoride	0.8	0.6	-

TABLE 2: Trace metals in waste water collected from laboratory before and after treatment.

S. No.	Trace metals	Values before treatment mg/L	Values after treatment mg/L	Standard value
1	Lead	0.006	0.001	400ppm
2	Arsenic	0.23	0.16	0.05mg/L
3	Beryllium	0.13	0.009	0.01µg/L
4	Cadmium	0.33	0.02	0.005mg/L
5	Vanadium	0.001	0	5.1µg/L
6	Chromium	0.42	0.12	0.1mg/L
7	Nickel	0.12	0.003	100-400µg/L
8	Molybdenum	0.002	0	<10µg/L
9	Silver	0.23	0.11	0.2-0.3µg/L
10	Strontium	0.0001	0.0001	7.0mg/L
11	Barium	0.001	0.001	2.0mg/L
12	Rubidium	0.002	0.002	-
13	Copper	0.13	0.05	<30mg/L
14	Iron	0.23	0.12	1-3mg/L
15	Zinc	0.45	0.14	0.01-0.05mg/L
16	Manganese	0.56	0.12	<300µg/L
17	Aluminum	0.23	0.15	-
18	Cobalt	0.002	0	0.02-53.2µg/L
19	Selenium	0.003	0.003	0.06µg/L
20	Antimony	0.002	0.001	0.1-0.2µg/L

TABLE 3: Classification of water based on hardness

S. No.	Classification	Hardness in mg-CaCO ₃ /L
1	Soft	0-60
2	Moderately hard	61-120
3	Hard	121-181
4	Very hard	≥ 181

TABLE 4: Classification of water based on magnesium level.

Classification	Magnesium level (mg/L)
Slightly hard	17.1-60
Moderately hard	60-120
Hard	120-180
Very hard	180 & over

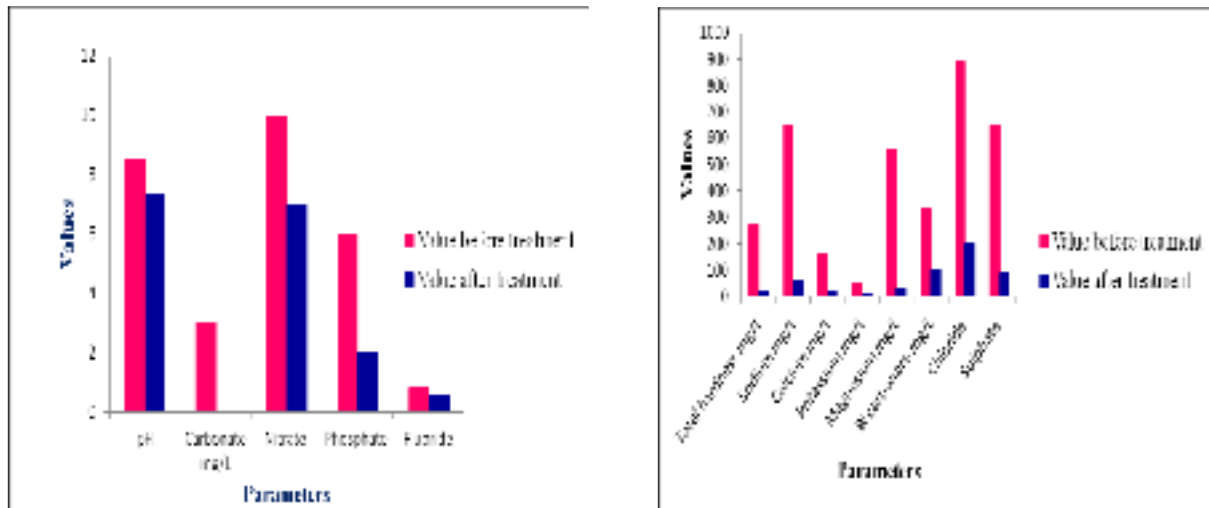


Fig. 1: Variation of physico-chemical parameters of laboratory waste water before and after treatment

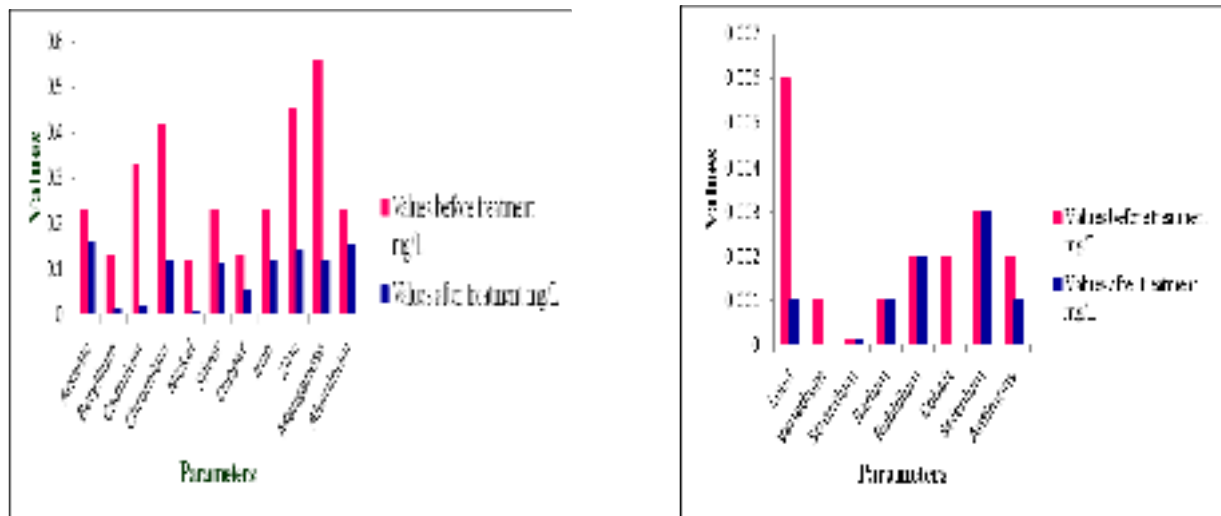


Fig. 2: Trace metals in waste water collected from laboratory before and after treatment.

See discussions, stats, and author profiles for this publication at: <https://www.researchgate.net/publication/355058190>

Green synthesis and characterization of reduced graphene oxide using polysaccharides extracted from *Solanum tuberosum* peels

Article in *Wutan Huatan Jisuan Jishu* · October 2021

CITATIONS

0

READS

96

2 authors, including:



Sabitha M. A.

Sadakathullah Appa College

15 PUBLICATIONS 70 CITATIONS

SEE PROFILE

Some of the authors of this publication are also working on these related projects:



Phytoremediation of laboratory waste water using *Ocimum sanctum*, *Cymbopogon citrates* *Aloe barbadensis* and reusing for domestic purposes. [View project](#)



Preparing biodegradable mask using natural antiviral agents [View project](#)

Green synthesis and characterization of reduced graphene oxide using polysaccharides extracted from *Solanum tuberosum* peels

Dr. M. A. Sabitha¹, Dr. A. Syed Mohamed²

¹Assistant Professor & PG Head, Department of Chemistry, Sadakathullah Appa College (Autonomous), Tirunelveli, Tamil Nadu, India, drsabithama@sadakath.ac.in

²Associate Professor & Research Head, Department of Chemistry, Sadakathullah Appa College (Autonomous), Tirunelveli, Tamil Nadu, India, asm2032@sadakath.ac.in

ABSTRACT

Green technique for the reduction of graphene oxide is utterly important on account of its industrial application. The available methods involve the use of hydrazine which is a very harmful chemical. Hence an eco-friendly method is to be suggested for producing reduced graphene oxide. The current study paves way for efficient, cost effective and greener synthesis of reduced graphene oxide using waste materials. The peels of *Solanum tuberosum* which is rich in polysaccharides are utilized for the reduction and stabilization of reduced graphene oxide. The extracted polysaccharides are tested and used for the reduction. The reduced graphene oxide is characterized using UV-Visible spectroscopy. The red shift of the spectrum to 274 nm and peak at 300 nm confirms the formation of reduced graphene oxide.

Key words: graphene oxide, polysaccharides, *Solanum tuberosum*, red shift, reduced graphene oxide.

I. INTRODUCTION

Graphene, graphene oxide and their derivatives is currently the subject of a great deal of research, both in terms of their fundamental physical, chemical, and materials science properties, as well as the exciting promise of their practical applications in diverse fields [1]. The tuning of defects in graphene based materials is of interest for application in several areas. The remarkable

potential of graphene-based technologies has prompted researchers to explore several areas of application centered on the controlled reduction of graphene oxide to varying degrees and consequently also a partial restoration of its network system [2].

Graphene has wide applications in the industries. It is very difficult to prepare graphene in pure form and in large quantity. The reduction of graphene oxide which is hydrophilic to reduced graphene oxide which is hydrophobic and similar in structure to graphene is easy [3]. Reduced graphene retains the hexagonal structure of graphene with sp^2 hybridized carbon-carbon bonds with all the functional groups removed.

Reduced graphene oxide with similar structure to graphene has wide range of applications. Reduced GO is preferable over graphene, because of the ease of production and low cost [4]. Bulk quantities can be produced at cheaper cost. The methods involved in the reduction of graphene oxide to reduced graphene are chemical reduction, thermal reduction, solvothermal, photolytic, hydrothermal and microwave irradiation. There are advantages and disadvantages involved in each process [5].

The sheets of graphene oxide sheets are insulating with sheet resistance (R_s) of 1012 Ω /sq. This is due to the presence of sp^3 hybridized carbon cluster and other defects. Reduction of graphene oxide can make it electrically conductive. Heat treatment of graphene oxide decomposes the oxygen functionalities and restores the sp^2 carbon clusters which lead to higher electrical conductivity [6].

Hence a greener, cost effective and easy method is to be designed for the bulk production of reduced graphene oxide. The present study involves an eco-friendly method utilizing the waste material for the production. Several nutritionally beneficial compounds were present in

Solanum tuberosum peels which can be utilized in many ways. The peel extract exhibits antioxidant property. Phenolic compounds are found predominantly (about 90%) in potato peels. Many researchers reported the presence of caffeic acid in *Solanum tuberosum* [7].

The peels also contain non-starch polysaccharides of about 30%. These polysaccharides show antioxidant properties. It exhibits radical scavenging activity and reducing capacity. Hence, it can be utilized in the reduction and stabilization of graphene oxide.

II. MATERIALS AND METHODS

Solanum tuberosum was obtained from a local market in Tirunelveli, Tamilnadu. The adhered surface dust particles on the peels were removed by washing in tap water and then in distilled water. After washing, the peels were removed. The peels were dried at 50°C in an oven for 48 h and ground in a mixer grinder (Moulinex). It was then stored at room temperature (25 ± 5°C) until use. The methodology for the extraction of polysaccharides was done as suggested by Ding *et al.*, (2012) with some modifications [8].

The peels (20 g) were mixed with 500 ml of distilled water in a 1 L flask, and boiled under reflux with a heating mantle. The solution was filtered and recovered after 4 hours. The extraction was repeated to ensure complete removal of polysaccharides. The filtrates obtained were combined and concentrated by means of a rotary evaporator maintained at 50°C under vacuum. Recovery of the polysaccharides was performed by ethanol precipitation for one night at -20°C, followed by centrifugation for 15 min at 5300xg. The polysaccharide was re-solubilized in distilled water. A dialysis step against double-distilled water was carried out for 3 days to remove inorganic salts, prior to freeze-drying for three days to obtain water-soluble polysaccharides [9, 10].

Test for polysaccharides

Iodine test

1 ml of a given sample is taken in a clean, dry test tube. Control of 1ml of distilled water is taken in another tube. About 2-3 drops of Lugol's solution is added to both the tubes and mixed in a vortex. The appearance of color in the test tube is observed. It is heated in the water bath until the color disappears. The test tubes are cooled. The appearance of color seen in the test tubes is noted. Appearance of blue black color indicates the presence of polysaccharides (starch) [11].

Reduction of graphene oxide

1 g of graphene oxide powder was mixed with 5 g of polysaccharides and dissolved in 250 ml water and stirred continuously for 72 hours. This process was done by using deionized water and centrifugation at 5000 rpm for 15 minutes. The step was repeated twice along with ultrasonification of 10 minutes before every centrifugation to disperse sample in deionized water. The product was dried in an oven at 80°C for 24 hours.

Characterization

The dried powder was characterized using UV-Visible spectrophotometer.

III. RESULTS AND DISCUSSION

A green method to reduce graphene oxide (RGO) was developed using polysaccharide obtained from *Solanum tuberosum* peels which acts as as both reducing agent and stabilizing agent. The reaction conditions are analyzed for optimum production of reduced graphene oxide and the product is characterized using UV-Visible spectrophotometer. Reduction of graphene oxide using polysaccharides obtained from waste proves to be an efficient and cost effective green methodology. The degree of reduction can be determined by λ_{\max} of UV-Visible spectrum. As conjugation increases, less energy is needed for π - π^* transitions and the λ_{\max} value increases [12].

The spectrum of graphene oxide has an absorption peak at 230 nm which is shifted to 274 nm in reduced graphene oxide. This is red shift due to electronic configuration in reduced graphene oxide. The absorption peak at 230 nm is attributed to π - π^* transition of aromatic C-C ring. The UV spectra of reduced graphene oxide on the other hand show the red shift at 274 nm. This absorption peak is due to n- π^* transition of C-O bonds. The UV spectrum for graphene oxide and reduced graphene oxide are given in the figures 5.1 and 5.2 respectively.

The optical absorption for graphene oxide appears at 230 nm corresponding to the π - π^* plasmon peak [13]. The nano meter scale sp^2 clusters and chromophore units such as C=C, C=O and C-O are responsible for π - π^* plasmon peak [11]. The conjugative effect of chromophore produces the π - π^* plasmon peak for graphene oxide. n- π^* transition of the carbonyl groups (C=O) appears as shoulder at 300 nm [14,15, 16].

The red shift to 274 nm suggests the presence of conjugation followed from graphene oxide after reduction. The peak at 300 nm in reduced graphene oxide results from the removal of oxygen. The change in color of the solution from brown to black also indicates the formation of reduced graphene oxide. Conventional methods involve the use of hydrazine which is very

harmful. This greener methodology provides cost effective route for the reduction of graphene oxide [17].

Although methodologies are available for reduction of graphene oxide using polysaccharides such as glucose, this method involves the use of polysaccharides extracted from waste peels. The incorporation of waste materials for the production of commercially important product paves way for cost effective, novel and eco-friendly process.

IV. CONCLUSION

The reduced graphene oxide has high commercial application. Hence an eco-friendly and cheap method to reduce graphene oxide will pave way for huge application in various fields. The present method involves the reduction of graphene oxide using easily available, cost effective and reuse of waste form vegetable (peels of *Solanum tuberosum*). The result indicated the formation of reduced graphene oxide which is characterized by UV-Visible spectrum with λ_{\max} at 230 and 274 nm for graphene oxide and reduced graphene oxide respectively. Further studies can be carried out to inspect the structural morphology and applications of reduced graphene oxide.

V. REFERENCES

1. B. L. Dasari, J. M. Nouri, D. Brabazon, and S. Naher, (2017). Graphene and derivatives – synthesis techniques, properties and their energy applications, *Energy*, vol. 140(1): 766–778.
2. B. C. Brodie, (1860). Researches on the atomic weight of graphite, *Quarterly Journal of the Chemical Society of London*, 12(1): 261–268.
3. O. Leenaerts, B. Partoens, and F. M. Peeters, (2009). Water on graphene: Hydrophobicity and dipole moment using density functional theory, *Phys. Rev. B*, 79(23): 235440-5.

4. D. A. Dikin, S. Stankovich, E. J. Zimney, R. D. Piner, G. H. B. Dommett, G. Evmenenko, S. T. Nguyen, and R. S. Ruoff, (2007). Preparation and characterization of graphene oxide paper, *Nature*, 448(7152): 457–460.
5. N. Syed, N. Sharma, and L. Kumar, (2017). Synthesis of graphene oxide (go) by modified hummers method and its thermal reduction to obtain reduced graphene oxide (rgo), *Graphene*, 6(1): 1-18.
6. S. Pei and H.-M. Cheng, (2012). The reduction of graphene oxide, *Carbon*, 50(9): 3210–3228.
7. Al-Weshahy A., Venket Rao A., (2009). Isolation and characterization of functional components from peel samples of six potatoes varieties growing in Ontario. *Food Res. Int.*, 42: 1062–1066.
8. Khawla Ben Jeddou, Fatma Chaari, SamehMaktouf, Oumèma Nouri-Ellouz, Claire Boisset Helbert and Raoudha Ellouz Ghorbel, (2016). Structural, functional, and antioxidant properties of water-soluble polysaccharides from potatoes peels, *Food Chemistry*, 205: 97-105.
9. Yi Ding, Huhu Cheng, Ce Zhou, Yueqiong Fan, Jia Zhu, Huibo Shao and Liangti Qu, (2012). Functional microspheres of graphene quantum dots, *Nanotechnology*, 23(25): 6494-6498.
10. Juan Yu, Hai-Yu Ji, Yu-Fang Wang and An-Jun Liu, (2018). Polysaccharides from Pomelo Peels: Extraction, Optimization and their Antioxidant Activity In Vitro, *Current Topics in Nutraceutical Research*, 17(1): 56-63.
11. Blance, D.E., GaillardNorman, S., Thompson Alfred J., Morak, (1969). The interaction of polysaccharides with iodine: Part I. Investigation of the general nature of the reaction, *Carbohydrate Research*, 11(4): 509-519.
12. D.C. Marcano, D.V. Kosynkin, J.M. Berlin, A. Sinitskii, Z. Sun, A. Slesarev, J.M. Tour, (2010). Improved synthesis of graphene oxide, *ACS Nano*, 4 (8): 4806-4814.

13. Goki Eda, Yun-Yue Lin, Cecilia Mattevi, Hisato Yamaguchi, Hsin-An Chen, I-Sheng Chen, Chun-Wei Chen, Manish Chhowalla, (2010). Blue Photoluminescence from Chemically Derived Graphene Oxide, *Advanced Materials*, 22(4): 505-509.
14. W. Cai, R.D. Piner, F.J. Stadermann, S. Park, M.A. Shaibat, Y. Ishii, R.S. Ruoff, (2008). Synthesis and solid-state NMR structural characterization of ^{13}C -labeled graphite oxide, *Science*, 321(5897): 1815-1817.
15. Lawrence Verbit, (1965). The Benzene Ring as an Optically Active Chromophore, *Journal of the American Chemical Society*, 87(7): 1617-1619.
16. Haruo Hosoya, Jiro Tanaka, and Saburo Nagakura, (1962). Ultraviolet absorption spectra of monomer and dimer of benzoic acid, *Journal of Molecular Spectroscopy*, 8(1-6): 257-275.
17. Adere Tarekegne Habte and Delele Worku Ayele, (2019). Synthesis and Characterization of Reduced Graphene Oxide (rGO) Started from Graphene Oxide (GO) Using the Tour Method with Different Parameters, *Advances in Materials Science and Engineering*, vol-2019, <https://doi.org/10.1155/2019/5058163>.

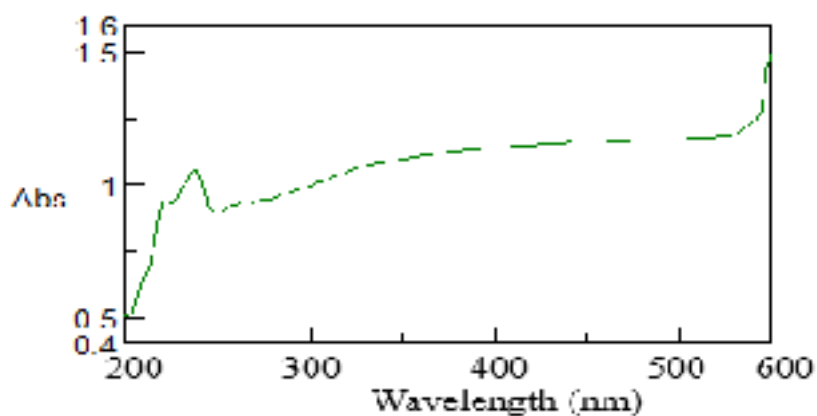


Figure 1 UV- Visible spectrum of Graphene oxide

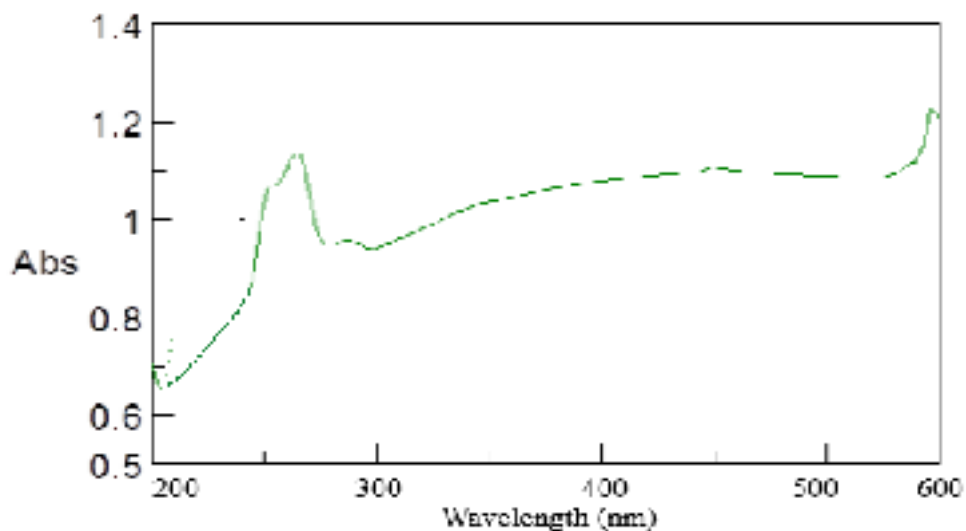
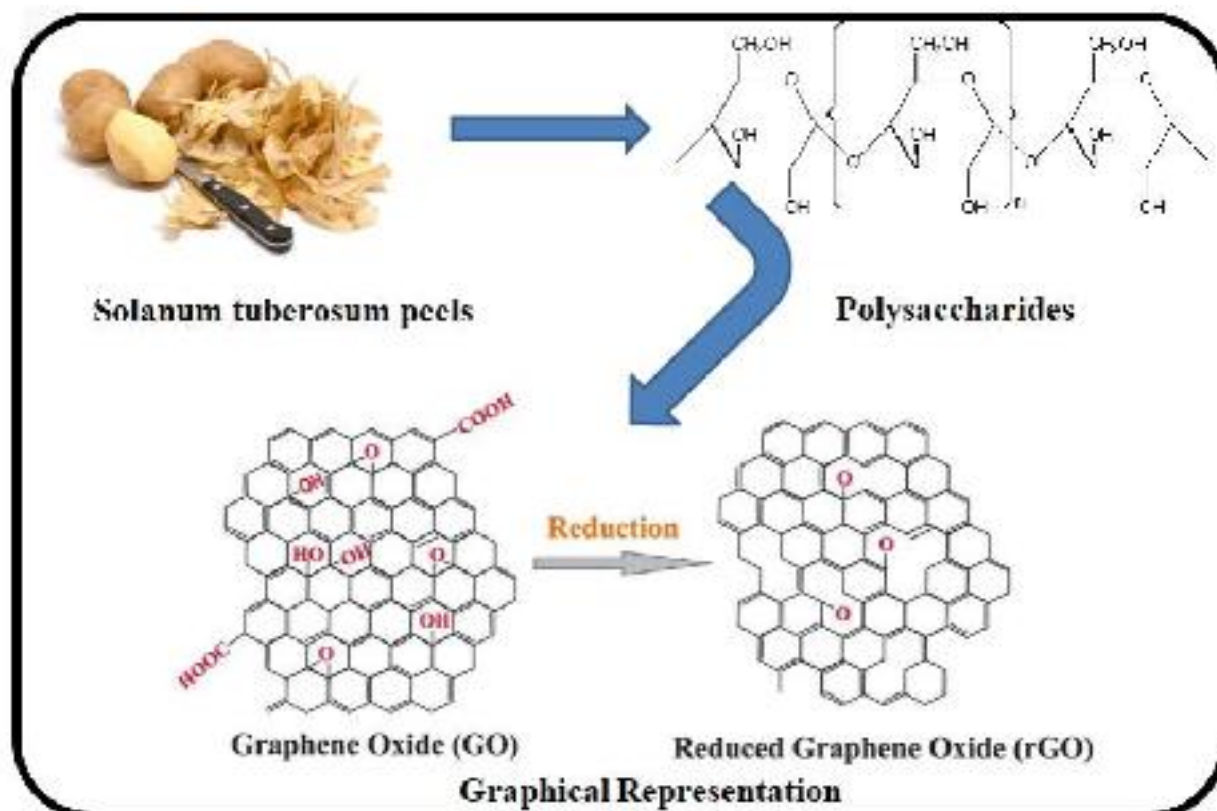


Figure 2 UV-Visible spectra of Reduced Graphene oxide



Antimicrobial activity of combined extracts of *Carica papaya* peels and *Glycyrrhiza glabra* roots

Dr. M. A. Sabitha¹*, Dr. A. Syed Mohamed²

¹Assistant Professor & PG Head, Department of Chemistry, Sadakathullah Appa College (Autonomous), Tirunelveli, Tamil Nadu, India.

²Associate Professor & Research Head, Department of Chemistry, Sadakathullah Appa College (Autonomous), Tirunelveli, Tamil Nadu, India.

Abstract: *The use of plants for medication in India is common among tribal and ethnic groups. The phytochemical constituents present in the plants ensure antibacterial, antifungal and anti-cancer properties. The present study is initiated to study the antimicrobial property of Carica papaya peels and Glycyrrhiza glabra roots. The extracts of these components are prepared in different ratios and analyzed for antimicrobial and phytochemical constituents. The results showed that the presence of phenol, saponins, flavonoids, steroids, terpenes and reducing sugar in the extract. The extract in the ratio of 2:1 exhibited effective antibacterial activity against Klebsiella pneumoniae whereas the ratio of 1:1 had effectiveness against Pseudomonas aeruginosa and Staphylococcus aureus. The antifungal studies provided the data that 1:1 extract is effective against Rhizopus microspores while 2:1 ratio proved to be effective against Aspergillus flavus and Candida albicans.*

Keywords: *Carica papaya, Glycyrrhiza glabra roots, phenol, Klebsiella pneumonia, Staphylococcus aureus, Rhizopus microspores.*

1. Introduction

Treatment with medicinal plants is the prime medication in many countries. Most of the world's population depends on crude plants for medicinal use. The tree barks, leaves, stem, flowers and roots are utilized for medication (Barrett and Kieffer 2001). The active phytochemical constituents are made use as starting materials for the preparation of drugs. The side effects produced in consuming the synthetic drugs provided importance to the ancient medicinal plant constituents. Numerous plants which are used in folk medication are approved as medicines by extracting the bioactive component of the mixture. An example is morphine extracted from opium.

Research on medicinal plants involves numerous fields of study and analysis. The different field of study involved is botanist to collect plants, ethnopharmacologist to diagnose the medicinal value, chemist to analyze the component responsible for therapeutic action and pharmacologist to isolate and make it suitable for medication (Baker et al., 1995). The phytochemical constituents are important source of new drugs and lead compounds (Newman et al., 2000; Newman et al., 2003).

India occupies an important place in the plant resources. About lakhs of traditional medicinal practitioners are available in India. Millions of people receive the welfare of Siddha, Unani and Ayurvedic medicine. Recent years the medical field is attracted much towards the use of plants. The reason lies in non-toxic and lack of side effects of using natural cure (Mukherjee 2001). The traditional medicine requires extensive research with technological advances and logical justifications to be utilized.

The use of plants as medicine has started from vedic period. Charak Samhita described about 341 medicinal plants in 1900 BC. Baghahtta of Sind, Madhab Nidana and Bhava Mishra wrote books on medicinal plants. About 1250 plants have been utilized in Ayurveda. Many Ayurvedic plants have now been used in preparing modern medicines. Nearly 70% of organic constituents in British Pharmacopoeia of 1932 are derived from plants. The lacking in the use of traditional medicine lies in the backlog of research in the plant derived products and scientific reasoning of the components (Miller and Gerean 1992).

Antibacterials derived from plants have served better than synthetic due to lesser side effects. The active components of plant origin are a best alternative to control pathogens (Kumaraswamy et al., 2008). The bioactive components are essential for the determination of therapeutic action and medicinal value of the plants. The chemical constituents mostly found in plants are flavonoids, alkaloids, phenolic compounds and tannins. Ethnopharmacological information in phytochemistry will pave way for discovery of new therapeutic agent with fewer side effects (Chhetri et al., 2008). The phenolic compounds and flavonoids present in plants have therapeutic values such as anti-inflammatory, analgesic, antimicrobial and antitumour properties (Wink, 1999). Flavonoids can also act as antioxidants (Gurib-Fakim, 2006).

Recent advancement in technology and isolation processes pave way for the extraction and purification of phytochemical constituents. Numerous plant species still remain unexplored. Some examples of plant components with high efficiency are mevastatin obtained from penicillin, quinine, rapamycin and etoposide (Kingston et al., 1992). According to the World Health Organization report, around 20, 000 medicinal plants are used worldwide as medicine.

The demand for herbal drugs is increasing day by day. The efficacy, lack of side effects and therapeutic long term action make these drugs essential for analysis of bioactive components. People rely on Ayurveda for medicinal purposes during ancient times and the period changed when their hope shifted to allopathic medicine. Now due to lack of long term therapeutic effects and safety, the attention is much diverted to herbal medicines. Hence it becomes important to analyze the bioactive ingredients of these plants for effective medicinal use.

International Pharmacopoeia has included several herbal drugs and traditional medicines. The guidelines and methodology must be regularized for the usage of these bioactive components. The plants must be chosen based on easy availability, phytochemical components and therapeutic value.

Glycyrrhiza glabra is one of the oldest traditional medicinal plants of India. The components of the plant are saponins, flavonoids, glycyrrhizin and in addition the root exhibits sugar and proteinous substances. Glycyrrhizin, a triterpenoid compound, represents the sweet taste of root. The yellow shade of *G.glabra* is due to the flavonoid substance such as liquiritin, isoliquiritin (a chalcone) and other compounds. The concentrates are frequently utilized as an enhancing agent in present day medication. The plant has been used as pigments, food additives, insecticides and in perfume industries. It has been used in folk medicine to reduce fever and curing tooth aches (Kumar and Dora, 2012). Alkaloids present in the roots are active constituent with therapeutic value.

Licorice hinders the growth and cytopathology of numerous random DNA and RNA viruses. Glycyrrhizic corrosive represses cyclooxygenase movement and prostaglandin development, as well as by implication restraining platelet aggregation (Acharya et al., 1993). Specifically, glycyrrhizin has antiviral action against and is prepared to do irreversibly inactivating the virus. Although it is an extensively studied plant, the effect of the root components against some particular bacteria and fungus remains unexplored (Ajagannavar et al., 2014).

Not only plant parts but also the wastes obtained from the fruits can also be used for medicine. One such plant is *Carica papaya* where the peels of fruits contain bioactive ingredients. The peels are rich in phenol, vitamin c, fibres, copper, sulphur, calcium, iron, magnesium and potassium. The presence of phenol provides antioxidant property. Also, vitamin c content helps to cure inflammation and can be utilized for antimicrobial activities (Didier et al., 2017).

The present study is carried out to analyze the combined effects of extracts of *Glycyrrhiza glabra* root and *Carica papaya* peels in different ratios against certain bacteria and fungi.

2. Materials and Methods

Carica papaya peels were cut in to small pieces and weighed. Samples were exposed to air dry for three days, lyophilized for 8 hours using a freeze dryer and exposed to temperatures of 50 °C and 80 °C using a laboratory oven for 3 hours. About 2 g of coarse powder was packed in Soxhlet apparatus using ethyl acetate, ethanol and hexane. The extract was collected and stored after evaporating the solvents. Fresh roots of *Glycyrrhiza glabra* Linn commonly known as athimathuram were collected. They were washed and shade dried for 5 to 6 days. The dried samples were finely ground into powder. The fine powdered roots of *Glycyrrhiza glabra* were weighed to determine the dry weight. The extraction was carried out using Soxhlet apparatus with chloroform as solvent. About 10g of dried *G. glabra* was dissolved in 100 ml of chloroform and stirred using stirrer. The sample and solvent was maintained at 1:10 ratio. After extraction, the contents were filtered using Whatmann filter paper No.1. The filtrate was kept on a hot water bath at 75 °C to concentrate the product by evaporating the residual solvents in the filtrate. The samples are mixed with one another in

two different ratios. Sample A and B. Sample A has the ratio of 1:1 (*Carica papaya* peel extract 1ml and extract of *Glycyrrhiza glabra* root 1ml) and sample B has the ratio of 2:1 (papaya peel extract 2ml and extract of *Glycyrrhiza glabra* 1ml), then the samples were analyzed for antimicrobial activity and phytochemical constituents. The presence of bioactive components such as phenols, saponins, flavonoids, steroids, terpenes and reducing sugars were tested. The samples were examined for antibacterial activity against *Klebsiella pneumoniae*, *Pseudomonas aeruginosa* and *Staphylococcus aureus*. Antifungal study was carried out against *Aspergillus flavus*, *Rhizopus microspores* and *Candida albicans* (Yogeshi et al., 2004; Perez et al., 1990).

3. Results and Discussion

Phytochemical analysis indicated the presence of phenol, saponins, flavonoids, steroids, terpenes and reducing sugar in the extract. The phytochemical constituents are tabulated in table 1

Table 1 Antibacterial activity of extracts of *Carica papaya* peels and roots of *Glycyrrhiza glabra*

Phytochemical test	Result
Phenol	+
Saponins	+
Flavonoids	+
Steroids	+
Terpenes	+
Reducing sugars	+

Antibacterial activity

In the present study the samples were subjected to evaluate its antimicrobial activity. Sample A represents *Carica papaya* peel extract of 1ml and *Glycyrrhiza glabra* extract of 1ml whereas Sample B represents the papaya peel extract of 2ml and *Glycyrrhiza glabra* of 1ml. Sample B was highly active against *Klebsiella pneumoniae* than Sample A. The zone of inhibition of sample A was 18 whereas sample B showed 16 against the bacteria *Pseudomonas aeruginosa*. The result for *Staphylococcus aureus* was similar to that of *Pseudomonas aeruginosa*, since sample A showed high zone of inhibition than sample B. Samples A and B displayed nearly equal activity against *Pseudomonas aeruginosa*. The antibacterial results are tabulated in table 2.

Table 2 Antibacterial activity of extracts of *Carica papaya* peels and roots of *Glycyrrhiza glabra*

Microorganisms	Zone of inhibition	
	A*	B*
<i>Klebsiella pneumoniae</i>	15	20
<i>Pseudomonas aeruginosa</i>	18	16
<i>Staphylococcus aureus</i>	20	14

*Sample A - *Carica papaya* peel extract 1ml and extract of *Glycyrrhiza glabra* 1ml

*Sample B- *Carica papaya* peel extract 2ml and extract of *Glycyrrhiza glabra* 1ml



Figure 1 Antibacterial activity of Sample A and Sample B against *Klebsiella pneumoniae*, *Pseudomonas aeruginosa* and *Staphylococcus aureus*

Antifungal activity

Sample B was effective against *Aspergillus flavus* and *Candida albicans* than sample A. The zone of inhibition of sample B was 12 against *Aspergillus flavus*. Both samples A and B showed higher zone of inhibition for *Rhizopus microspores*. The antifungal activity was tabulated in table 3.

Fukai et al. (2002 a) reported certain flavonoids of licorice such as glabridin, glabrene, licochalcone A, licoisoflavone B which showed antibacterial activity against drug resistant *H. pylori*. Fukai et al. (2002 b) further reported antibacterial activity of flavonoid against methicillin resistant strain of *S. aureus*. The presence of these flavonoids resulted in the antibacterial activity of *Glycyrrhiza glabra*. The antimicrobial activity was reported due to the presence of glycyram and licuroside. Glabridin in *Glycyrrhiza glabra* was the main reason for antifungal activity (Fatima et al., 2009).

Table 3 Antifungal activity of extracts of *Carica papaya* peels and roots of *Glycyrrhiza glabra*

Microorganisms	Zone of inhibition	
	A*	B*
<i>Aspergillus flavus</i>	10	12
<i>Rhizopus microsporus</i>	18	16
<i>Candida albicans</i>	15	16

*Sample A - papaya peel extract 1ml and extract of *Glycyrrhiza glabra* 1ml, *Sample B- papaya peel extract 2ml and extract of *Glycyrrhiza glabra* 1ml



Figure 2 Antifungal activity of Sample A and Sample B against *Aspergillus flavus*, *Rhizopus microspores* and *Candida albicans*

The antibacterial activity of papaya peel was due to the presence of alkaloids and tannins (Khalili et al., 2012). The result was further supported by Maria et al., (2019). Their study showed that the presence of phytochemicals such as terpenes, alkaloids and saponins contents in peels of papaya which result in antimicrobial activity.

The mixture of extract was active against *Klebsiella pneumoniae* bacteria which cause severe infections in lungs, bladder, brain, liver, eyes, blood, and wounds. Also the extract was very much effective against *Rhizopus microspores* which can cause mucormycosis in immune-compromised humans.

4. Conclusion

The extracts of *Carica papaya* peels and roots of *Glycyrrhiza glabra* were effective against bacteria such as *Klebsiella pneumonia*, *Pseudomonas aeruginosa* and *Staphylococcus aureus*. The extract showed efficient antifungal activity against *Aspergillus flavus*, *Rhizopus microspores* and *Candida albicans*. The different ratio of mixtures depicted varying activity. The efficiency of the extract can be further increased by analyzing different ratio mixtures and separating the active components.

References

- Bruce Barrett and David Kieffer, Medicinal Plants, Science, and Health Care, *Journal of Herbs Spices & Medicinal Plants* 8(2-3), (2001), 1-36.
- Baker, J.T., Borris, R.P., Carté, B., Cordell, G.A., Soejarto, D.D., Cragg, G.M., Gupta, M.P., Iwu, M.M., Madulid, D.R. and Tyler, V.E. Natural products drug discovery and development: new perspective on international collaboration. *J. Nat. Prod.*, 1995, 58 (9), (1995, 1325-1357.
- Newman, D. J., Cragg, G.M. and Snader, K.M., The influence of natural products upon drug discovery, *Nat. Prod. Rep.* 17 (3), (2000), 215-234.
- Newman, D.J., Cragg, G.M. and Snader, K.M., Natural products as sources of new drugs over the period 1981-2002. *J. Nat. Prod.* 66 (7), (2003), 1022-1037.
- Mukherjee P.K., Quality control of Herbal Drugs, Business Horizons, Pharmaceutical Publisher, 1st ed, 1-29, (2001).

Miller J.S., Gerean R.E., Biologically Active natural products: Pharmaceuticals, ed. Cutler S.J., Cutler H.G., CRC Press, Boca Raton, Florida, 1st Ed. 25-38, (1992).

Kumaraswamy MV, Kavitha HU, Satish S. Antibacterial evaluation and phytochemical analysis of *Betula utilis*. *World Journal of Agricultural Sciences.*, (2008), 4: 661-4.

Himal Paudel Chhetri, Nisha Shrestha, Jyoti Sherchan Panna Thapa, Phytochemical and Antimicrobial Evaluations of some Medicinal Plants of Nepal, *Kathmandu University Journal of Science Engineering and Technology*, 1(5), (2008), 49-54.

Wink, M., Biochemistry of plant secondary metabolism. Annual plant reviews, volume 2. Ch. 1. p. 1-16. Sheffield Academic Press, (1999).

Gurib-Fakim, A., Medicinal plants: Tradition of yesterday and drugs of tomorrow. Review article. *Mol. Aspects Med.* 27 (1), (2006), 1-93.

Kingston D.G.I., Biologically active natural products Pharmaceuticals, ed Cutter S.J., Cutler H.G., CRC Press, Boca Raton, Florida 1st ed, 39-52, (1992).

Acharya SK, Dasarathy S, Tandon A, A preliminary open trial on interferon stimulator (SNMC) derived from *Glycyrrhiza glabra* in the treatment of subacute hepatic failure. *Indian J Med Res Sect A—Infect Dis.*;98, (1993), 69–74.

Ajagannavar SL, Battur H, Shamarao S, Effect of aqueous and alcoholic licorice (*Glycyrrhiza glabra*) root extract against *Streptococcus mutans* and *Lactobacillus acidophilus* in comparison to chlorhexidine: an in vitro study. *J Int Oral Health.*, 6, (2014), 29–34.

Adingra Kouassi Martial-Didier, Konan Kouassi Hubert, Kouadio Eugène Jean Parfait, Tano Kablan, Phytochemical Properties and Proximate Composition of Papaya (*Carica papaya* L. var solo 8) Peels, *Turkish Journal of Agriculture- Food Science and Technology*, 5(6), (2017), 676- 680.

Kumar A and Dora J, Review on *Glycyrrhiza glabra*: licorice. *Journal of Pharmaceutical & Scientific Innovations* 1, (2012), 1-4.

Yogeshi, K. V., Rathish, N., Mayur, S., Shipra, B., Sumitra, C., Synthesis, structural determination and antibacterial activity of compounds derived from vanillin and 4-aminoantipyrine. *J Serb Chem Soc.*, 69, (2004), 991-998.

Fukai T, Marumo A, Kaitou K, Anti-*Helicobacter pylori* flavonoids from licorice extract. *Life Sci.*, 7, (2002), 1449–1463.

Fatima, Z., Saleemi, M., Zia, M., Sultan, T., Aslam, M., Riaz-ur-Rehman, Chaudhary, M.F., Antifungal activity of plant growth-promoting rhizobacteria isolates against *Rhizoctonia solani* in wheat. *Afr. J. Biotechnol.* 8, (2009), 219-225.

Khalili JS, Hanson RW, Szallasi Z 2012. In silico prediction of tumor antigens derived from functional missense mutations of the cancer gene census. *OncolImmunology* 1, (2012), 1281–1289.

Ana Maria Zbancioc and Gabriela Tataringa, Coumarin derivatives with antimicrobial and antioxidant activities, *Intec Open Book Series*, (2019).

Accepted Manuscript

Title: Design and one-pot synthesis of a novel pyrene based fluorescent sensor for selective “turn on”, naked eye detection of Ni²⁺ ions, and live cell imaging

Authors: Raihana Imran Khan, Andy Ramu, Kasi Pitchumani



PII: S0925-4005(18)30635-X
DOI: <https://doi.org/10.1016/j.snb.2018.03.137>
Reference: SNB 24422

To appear in: *Sensors and Actuators B*

Received date: 9-1-2018
Revised date: 21-3-2018
Accepted date: 22-3-2018

Please cite this article as: Raihana Imran Khan, Andy Ramu, Kasi Pitchumani, Design and one-pot synthesis of a novel pyrene based fluorescent sensor for selective “turn on”, naked eye detection of Ni²⁺ ions, and live cell imaging, *Sensors and Actuators B: Chemical* <https://doi.org/10.1016/j.snb.2018.03.137>

This is a PDF file of an unedited manuscript that has been accepted for publication. As a service to our customers we are providing this early version of the manuscript. The manuscript will undergo copyediting, typesetting, and review of the resulting proof before it is published in its final form. Please note that during the production process errors may be discovered which could affect the content, and all legal disclaimers that apply to the journal pertain.

Design and one-pot synthesis of a novel pyrene based
fluorescent sensor for selective “turn on”, naked eye detection of
Ni²⁺ ions, and live cell imaging

Raihana Imran Khan^[a], Andy Ramu^{*[b]} and Kasi Pitchumani^{*[a,c]}

^aSchool of Chemistry, Madurai Kamaraj University, Madurai 625 021, India

^bDepartment of Inorganic Chemistry, School of Chemistry, Madurai Kamaraj University

^cCenter for Green Chemistry Processes, School of Chemistry, Madurai Kamaraj
University

Madurai, India.

*Corresponding author. Tel.: +91 452 2456614; fax: +91 452 2459181.

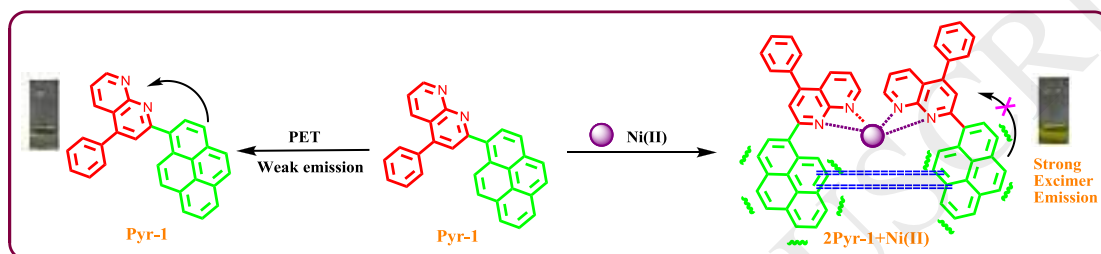
E-mail address: pit12399@yahoo.com (K. Pitchumani)

Highlights:

- ❖ A novel pyrene based fluorescent probe, 4-phenyl-2-(pyren-1-yl)-1,8-naphthyridine (Pyr-1), was designed and synthesized using Qun- β -CD catalyst.
- ❖ Dependence of photoluminescence of Pyr-1 on solvent polarity strongly validates photoinduced electron transfer, which also finds support from DFT studies.
- ❖ The red shifted “*turn-on*” fluorescence enhanced by the addition of Ni^{2+} ion is explained *via* a Photoinduced Electron Transfer (PET).
- ❖ Detection limit as low as 2.56×10^{-7} M.
- ❖ The confocal laser scanning micrographs of HeLa cells confirmed the cell permeability of Pyr-1 and its ability to selectively detect Ni^{2+} ions in living cells.

Abstract: A novel pyrene based fluorescent probe, 4-phenyl-2-(pyren-1-yl)-1,8-naphthyridine (Pyr-1), was designed and synthesized through tandem cyclization of pyrenealdehyde, amine and alkyne in the presence of quinolinium modified β -CD (Qun- β -CD) in water. Pyr-1 was characterized by ^1H NMR, ^{13}C NMR and ESI-MS spectra and was used as a selective “turn-on” and naked eye sensor for Ni^{2+} ion over other cations. The localized frontier molecular orbitals (DFT studies) and the solvent polarity dependent photoluminescence characteristics strongly validate the presence of photo induced electron transfer from pyrene to 1,8-naphthyridine unit in Pyr-1. Upon Ni^{2+} addition, the fluorescence was shifted to 450 nm due to the formation of a square planar 2:1 complex of pyr-1 with Ni^{2+} at room temperature even in the presence of other

interfering ions such as Cd^{2+} and Hg^{2+} . The resultant excimer emission and conquest of photoinduced electron transfer (PET) from pyrene moiety to the 1,8-naphthyridine part is supported by DFT studies. The sensor also exhibited very low cytotoxicity and strong fluorescence emission in living cells, indicating its potential applicability as a novel chemosensor for selective detection of Ni^{2+} ions in biological environment also.



Keywords: Novel pyrene based fluorescent sensor, Qun- β -CD, Ni^{2+} “turn-on” Sensing, Excimer emission, Fluorescence Imaging Studies in HeLa Cells.

Introduction

Fluorescent chemosensors have been widely applied in diverse fields such as biology, chemistry and medicine. Most of the recent research in this area is focused on design and synthesis of organic luminescence materials and their utility in diverse applications [1]. Due to their significantly higher quantum yield and excellent photostability the development of organic luminescence probes achieved importance in of materials chemistry also. Among the various types of fluorophores known, pyrene shows unique photophysical properties and is widely useful as an environmentally benign sensor system [2-3]. Pyrene derivatives are used for constructing

various types of tunable chemosensors, tunable in numerous microenvironments due to their advantages properties such as polarity sensitive vibronic emission, longer fluorescence lifetime, high charge carrier mobility, π - π staking behavior and chemical stability [4-6].

To detect many biologically important metal ions in solution the design and synthesis of supramolecular systems are very useful in the field of supramolecular chemistry. In this context, study of systems involving aggregation of various probes held together by non-covalent interactions such as electrostatic [7], hydrogen bonding [8], dispersion interactions [9], solvophobic effects [10] and π - π stacking [11] are significant. Among them, the π - π stacking interaction is widely known in synthesis of aggregation types of supramolecular probes which are more common in both chemical and biological systems [12-16] and are widely used as fluorescence probes for many biological systems such as, DNA, lectin, pH sensing, *etc* [17-19].

Metal ion recognition with selectivity and sensitivity is of immense interest due to their cost effective, simple, quantitative and qualitative detection of environmentally toxic metal ions and also to understand the role of biological systems. Among the various transition metal ions, nickel is an essential metal for supporting life [20-23], which is also an essential nutrient for living organisms. It is involved in biological processes such as, metabolism, respiration and biosynthesis [24] and is extensively used in a wide variety of metallurgical processes such as, electroplating, pigments of paints, ceramics, surgical, rods for arc welding and dental prostheses [25] and magnetic tapes of computers and nickel-cadmium batteries [26]. Nickel is also well known for its chemical toxicity, which includes effects on the gastrointestinal systems, blood and kidneys [27]. In biological system loss of nickel, is harmful to prokaryotic and eukaryotic organisms and with limited epidemiological evidence, soluble nickel reacts as an enhancer of

cancer risk followed by certain forms of insoluble nickel. Several methods are used to detection of nickel such as, atomic absorbance spectrometry (AAS) [28], inductively coupled plasma-optical emission spectrometry (ICP-OES) [29], electrothermal atomic absorption spectrometry (ETAAS) [30], flame atomic absorption spectrometry (FAAS) [31], spectrophotometry and inductively coupled plasma-mass spectrometry (ICP-MS) [32]. Recently, nickel sensors based on potentiometric methods are also employed [33-36]. Despite this, most of the reported chemosensors for nickel have drawbacks such as, poor water solubility, low sensitivity and selectivity [37]. Therefore, development of new fluorescent probes to selectively sense for nickel, by overcoming the above mentioned issues and also a “turn-on” chemosensor would be desirable [38-40]. This prompted us to develop selective chemosensor for nickel in the acetonitrile as a solvent. To the best of our knowledge, no reports are available for the detection of nickel ion using pyrene derivatives.

Cyclodextrins (CDs) as simple naturally occurring macrocyclic oligosaccharides, possess a hydrophobic cavity that selectively binds substrates and catalyzes chemical reactions through formation of host–guest complexes *via* noncovalent interactions [41-44]. Modification of cyclodextrins offers enormous opportunities and challenges for chemists, ranging from achieving solubility in a desired solvent to selective and specific catalysis. In addition, modified cyclodextrins act as ligands for various metal ions. As part of our continuing interest in developing greener methods for the synthesis of bioactive compounds, we have recently successfully utilized per-6-amino- β -cyclodextrin, and pyridinium modified β -cyclodextrin as useful hosts as well as catalysts for a large number of organic transformations [45-48]. Encouraged by these efforts and aiming further to demonstrate the efficiency and generality of these modified cyclodextrins as unique supramolecular hosts/catalysts, a novel quinolinium

modified β -cyclodextrin (Qun- β -CD) is synthesized. It is soluble in water and exhibits excellent catalytic activity in tandem cyclization reactions starting from simple and easily available starting materials under much milder reaction conditions, in the absence of metals.

In this study, using a quinolinium modified β -cyclodextrin (Qun- β -CD) as catalyst, a one-pot synthesis of a novel, 4-phenyl-2-(pyren-1-yl)-1,8-naphthyridine (Pyr-1) probe, and its characterization using NMR and ESI-MS spectroscopic techniques and study of its photophysical applications [49] are reported. The sensor probe (Pyr-1) is also found to display bio-analytical applications in living systems.

Experimental Section

General Methods

Reactions were carried out under aerobic conditions. All chemicals were used without further purification as commercially available without otherwise noted. Electrospray ionization mass spectrometry (ESI-MS) analyses were recorded in LCQ Fleet, Thermo Fisher Instruments Limited, US. ESI-MS was performed in positive ion mode. NMR spectra were recorded at 300 MHz on a Bruker spectrometer. All ^1H NMR and ^{13}C NMR spectra were measured in DMSO- d_6 and CDCl_3 with TMS as the internal standard. FT-IR spectral analyses were performed using a JASCO FT/IR-410 instrument by the KBr pellet technique in the range of 4000–500 cm^{-1} .

Sensor titrations

Compound Pyr-1 was dissolved in CH_3CN and Pb^{2+} , Al^{3+} , Ag^+ , Cu^{2+} , Fe^{3+} , Ni^{2+} , Hg^{2+} , Zn^{2+} , Na^+ , Co^{2+} , Cr^{2+} , In^{2+} , Cd^{2+} , and Mn^{2+} metal cations were dissolved in water medium at 1×10^{-3} M concentration from their respective chloro and acetate salts.

General procedure for the synthesis of quinolinium modified β -cyclodextrin (Qun- β -CD)

N-pentylquinolin-8-amine (0.66 mmol) was added to a solution of dried mono-tosyl- β -CD (0.22 mmol) in 1 mL DMF. The reaction medium was heated at 90 °C for 48 h. the reaction mixture was then cooled to room temperature and the product was precipitated with acetone (4 mL). The solid was collected by filtration and washed with acetone (2 x 2 mL). Pure product is obtained via acetone diffusion in DMF. The solid was then dissolved in deionised water (12 mL) and anion exchange from tosylate to chloride was performed using an Amberlite IRA-410 Cl⁻ resin to yield Qun-CD as a brown solid (0.15 mmol, 72 %), which was analyzed by NMR spectroscopy (300 MHz, CDCl₃, T=300 K, TMS=0 ppm), and ESI-MS. Melting point 220 °C. Elemental analysis for this Qun-CD (3) was also carried out and the values are as follows: calculated, Carbon, 49.36; Hydrogen, 6.12; Chlorine, 2.33; Nitrogen, 2.16; Oxygen, 39.35 (Figures S1-S3, See supporting information).

General procedure for the synthesis of compound Pyr-1

A reaction tube equipped with a magnetic stirring bar was charged with quinolinium modified β -cyclodextrin (Qun-CD) (0.1 mmol, 1 mol%) dispersed in water (2 mL) for 15 min. Aniline (109 μ L, 1.2 mmol), benzaldehyde (122 μ L, 1.2 mmol) and phenylacetylene (110 μ L, 1mmol) were added with the above reaction mixture at room temperature. After 5 h of stirring the solvent was evaporated under reduced pressure. After completion of the reaction, the product was extracted with ethyl acetate, filtered, dried with sodium sulphate, and concentrated under reduced pressure. The resulting crude product was purified by passing it through a column of silica gel 60–120 mesh using petroleum ether/ethyl acetate (9:1 ratio) as the eluent, afford Pyr-1 (113 mg, 92%) as a yellow solid, m.p. = 138–140 °C. ¹H NMR (300 MHz, CDCl₃) 9.33-9.28 (t, 1H), 9.05-9.02 (d, 1H), 8.82-8.79 (d, 1H), 8.61-8.53 (m, 1H), 8.32-8.29 (m, 2H, J = 8.7 Hz.), 8.19-8.17 (m, 2H, J = 8.7 Hz.), 8.04-8.00 (m, 4H, J = 7.8 Hz.), 7.50-7.48 (m, 1H), 7.42-7.36 (m,

4H), 7.27-7.20 (m, 1H). ^{13}C NMR (75 MHz, CDCl_3) δ 153.63, 150.78, 138.72, 138.06, 136.46, 133.10, 131.88, 131.72, 131.54, 130.57, 130.10, 129.14, 128.93, 128.60, 128.30, 127.69, 127.34, 127.12, 126.96, 126.67, 126.45, 125.43, 124.92, 123.91, 121.87, 119.52. Elemental analysis: cal. (%) for $\text{C}_{30}\text{H}_{18}\text{N}_2$: C, 88.64; H, 4.46; N, 6.89 found: C, 88.12; H, 4.28; N, 6.92 ESI-MS (m/z) calcd for $\text{C}_{30}\text{H}_{18}\text{N}_2$:406.15, found: 427.09 ($\text{M}+\text{Na}$) $^+$ (Figures S4-S6, See supporting information).

MTT Assay

HeLa cells were seeded at 8000 cells in 96-well plates and incubated for 24 hours with 5% of CO_2 at 37 °C. Different concentrations of Pyr-1 were added to each well and the plates were incubated in a humidified CO_2 incubator for a further 12 h at 37 °C. 100 μL of MTT (3-(4,5-dimethylthiazol-2-yl)-2,5-tetrazolium bromide) reagent (1 mg/ mL) was added to each well. After 4 h of incubation, the medium was replaced with 100 μL of dimethyl sulfoxide (DMSO) and the wells were incubated at 37 °C for 1h with shaking. The cytotoxicity of Pyr-1 was exhibited as the percentage of absorbance in a SpectraMax M5 microplate reader at a wavelength of 490 nm.

Cell Imaging

HeLa cells were developed in modified Eagle's medium supplemented with 10% FBS (fetal bovine serum) at 37 °C and were incubated with Pyr-1 (5.0 μM) in PBS buffer, pH = 7.54, containing 1% DMSO as co-solvent. After incubation, the cells were washed thrice with buffer to eliminate excess of probe present in the extracellular media and growth medium. The cells were now imaged through the fluorescence microscope. The probe-treated cells were further

incubated with NiCl₂ (5.0 μM in H₂O) for 1h at 37 °C and imaged again with a fluorescence microscope.

Results and Discussion

Synthesis and AIE properties of Pyr-1

The pyrene based chemosensor 4-phenyl-2-(pyren-1-yl)-1,8-naphthyridine (Pyr-1) was synthesized as depicted in Scheme 1. As a part of our group's interest to develop modified cyclodextrins for sensor and catalytic applications,[50-52] we have synthesized a novel quinoline modified cyclodextrin (Qun-β-CD) which is used as a catalyst to synthesis Pyr-1 through tandem cyclization of pyrenealdehyde, amine and alkyne in water as solvent in 88%. Pyr-1 is characterized by its ¹H, ¹³C-NMR and ESI-MS analyses (Fig S4 – S6).

(Scheme 1)

The UV-Vis absorption and emission spectra of Pyr-1 are recorded in different solvents (Fig S8a). In UV-Vis spectra, peaks are observed at λ_{max} values of 355, 362 and 394 nms characteristic of absorbance by pyrene unit. It is well known that pyrene derived molecules exhibit aggregation induced emission characteristics. Hence the presence of pyrene unit in Pyr-1 stimulated a study on the aggregation induced emission (AIE) of Pyr-1 in THF:water solvent mixtures (Fig. 1a). At 0%, water Pyr-1 exhibits a weak emission peak at 410 nm due to a photoinduced electron transfer from pyrene to 1,8-naphthyridine unit of Pyr-1, and there is no excimer emission. However, upon incremental addition of water, improved excimer emission is observed with red shifted peaks at 460 nm. Maximum excimer emission is noticed in 60% and 90% water. This shift in λ_{max} and increase in intensity in emission spectra are attributed to

aggregation and subsequent excimer emission from the pyrene unit. The addition of water increases the polarity of the solvent medium with a subsequent hydrophobic aggregation between pyrene entities. Due to the presence of monomers also along with excimers, the combination of both the peaks is present (Figure. 1a).

Theoretical Studies

To understand the emission spectra of Pyr-1 during solvent polarity variations DFT computational studies are performed using Gaussian 09 program (Figure S8b). The possible electronic transition involved in Pyr-1 was calculated using TD-DFT method and the results, involve charge transfer from pyrene to 1,8-naphthyridine unit. The basic set B3LYP was used for the pyr-1 and 631G(d) was applied to the basic set for all the atoms which provide reasonably good quality results in reasonable time scales. Visualization of the optimized structures and the MOs were performed using Gauss view 5.0. The frontier molecular orbital of Pyr-1 is shown in figure 1(b). The HOMO is mainly localized on the pyrene unit and LUMO is mainly localized on the 1,8-naphthyridine unit. On the other hand, HOMO-1 is localized on the quinoline unit and LUMO+1 is pyrene unit.

(Figure 1)

The localized frontier molecular orbitals of Pyr-1 clearly indicate that the molecule may redistribute the charge upon excitation. This result is in agreement with the experimentally observed solvent polarity dependent emission characteristics of Pyr-1. The calculated energy gap between HOMO and LUMO of Pyr-1 is 3.40 eV.

Sensor Studies

The potential sensing ability of Pyr-1 probe was studied in CH₃CN and all metal ions were taken as 1×10^{-3} M concentrations. In the sensor titration of Pyr-1, 20 μ M of Pyr-1 was added to an ACN solution followed by addition of 20 μ M (1 equiv.) of metal ions (Pb²⁺, Al³⁺, Ag⁺, Cu²⁺, Fe³⁺, Ni²⁺, Hg²⁺, Zn²⁺, Na⁺, Co²⁺, Cr²⁺, In²⁺, Cd²⁺, and Mn²⁺) in H₂O. Surprisingly, Pyr-1 displays selectivity towards metal ions showing enhancement in absorbance in the UV-Vis peaks at 362 and 394 nms (figure 2a) respectively. The fluorescence measurements were also carried out to study the interaction of Pyr-1 with other metal ions. Figure 2b shows the fluorescence spectra of Pyr-1 in the presence of other metal ions such as, Pb²⁺, Al³⁺, Ag⁺, Cu²⁺, Fe³⁺, Ni²⁺, Hg²⁺, Zn²⁺, Na⁺, Co²⁺, Cr²⁺, In²⁺, Cd²⁺, and Mn²⁺. Pyr-1 displayed a marked increase in excimer emission with a red shift to 450 nm from 420 nm (figure 2b) selectively, upon addition of Ni²⁺ ions. The emission intensity at 420 nm was not affected even in the presence of other metal cations.

To confirm the specific selectivity, the sensory responses of Pyr-1 is also evaluated with other metal cations such as, Pb²⁺, Al³⁺, Ag⁺, Cu²⁺, Fe³⁺, Ni²⁺, Hg²⁺, Zn²⁺, Na⁺, Co²⁺, Cr²⁺, In²⁺, Cd²⁺, and Mn²⁺. However, the probe of Pyr-1 is selective only to Ni²⁺ ions. The photograph of Pyr-1 with different metal ions under day light indicates its selectivity towards Ni²⁺ ion *via* pale green emission, as depicted in figure 2c.

(Figure 2)

To obtain a better insight into the response mechanism of Pyr-1 toward Ni²⁺ ions, spectroscopic titrations were also carried out under the same working conditions. As shown in Fig.3a, when excited at 350 nm, the fluorescence band at 420 nm is increased in intensity and also a red shift is ensued due to an increase in the formation of excimer emission when

increasing the concentration of Ni^{2+} ions from 0 to 40 μM . A satisfactory Boltzmann correlation exists between the fluorescence intensity and the concentration of Ni^{2+} ions within the range from 0 to 40.0 μM .

(Figure 3)

A similar behavior is also observed in UV-Vis spectra also as shown in Fig. 3b, after addition of higher amounts of Ni^{2+} ions, the bands at 362 and 394 nm gradually increased in intensity, which can be ascribed to the charge transfer from pyrene to 1,8-naphthyridine unit. With the concentration of Ni^{2+} ions is varied upto 0-40 μM , the maximum absorbance changes were observed in Fig. 3b.

As selectivity is significant for evaluating the performance of sensing systems, in the present study the selectivity of probe 1 is also extended to various other metal ions, such as Pb^{2+} , Al^{3+} , Ag^+ , Cu^{2+} , Fe^{3+} , Ni^{2+} , Hg^{2+} , Zn^{2+} , Na^+ , Co^{2+} , Cr^{2+} , In^{2+} , Cd^{2+} , and Mn^{2+} . From the results shown in Fig. 4a, it can be perceived that only Ni^{2+} ions prompted fluorescence enhancement, whereas other metal ions lead to a minor or no fluorescence variations. This indicates clearly that the present Pyr-1 based chemosensor has good selectivity towards Ni^{2+} ion over the other competing cations. The effect of other concomitant cations on nickel ion detection is also determined. The fluorescence response of the present sensing system towards Ni^{2+} ions in the presence of alkali, alkaline earth and other transition metal ions are shown in Fig. 4b. The results indicate that the presence of the other selected metal ions does not exhibit any interference with Ni^{2+} binding to the probe, representing that these co-existing ions have insignificant interference effects on Ni^{2+} sensing by the present Pyr-1 system. Fluorescence response is linearly proportional to the concentration of Ni^{2+} in the range of 0-40 μM . From figure 4c, the value of

linearly dependent co-efficient (R^2) is found to be 0.9937. The detection limit (LOD) is measured to be 2.5×10^{-7} M. From the fluorescence data, the stoichiometry of $2\text{Pyr-1} + \text{Ni}^{2+}$ was calculated through Job's plots as shown in Fig. 4d, by plotting mole fraction *Vs* intensity of Pyr-1 at 450 nm in the presence and the absence of respective metal ion concentrations. Upon addition of 0-40 μM of Ni^{2+} ions the fluorescence maximum of Pyr-1 was enhanced with a red shift to 450 nm. But, after the addition of 0.5 equiv. (20 μM) of metal ions, the peak at 450 nm was slightly quenched.

The Job's plot, plotted between mole fraction *Vs* intensity indicates the formation of 2:1 stoichiometry complex. Furthermore, the formation of 2:1 complexes was also confirmed from ESI-MS data (supporting information fig S7).

(Figure 4)

The proposed binding mechanism is depicted in Scheme 2. In the absence of Ni^{2+} ions, Pyr-1 exhibits weak emission attributed to photoinduced electron transfer from pyrene unit to the 1,8-naphthyridine unit. Upon addition, Ni^{2+} ion binds to two molecules of Pyr-1 *via* their 1,8-naphthyridine units to form a square-planer complex, the driving force being π - π staking interaction between the two pyrene units.

(Scheme 2)

This is supported by ESI-MS data (supporting information, fig. S7) which gives the most direct evidence by comparing the mass spectra of compound Pyr-1 and $2\text{Pyr-1} + \text{Ni}^{2+}$. The peak at $m/z = 427.09$ corresponds to $[\text{pyr-1} + \text{Na}]^+$, (See supporting information fig S3) when Ni^{2+} ions are added to Pyr-1, the peak at $m/z = 427.09$ disappear and another peak at $m/z = 871.23$ [2Pyr-

$1+\text{Ni}^{2+}+\text{H}]^+$ is clearly observed, which indicates the formation of the complex $2\text{Pyr}-1+\text{Ni}^{2+}$. To study the reversible and the reproducible nature of the probe Pyr-1 upon Ni^{2+} addition, EDTA titrations were performed (Scheme 2). As shown in figure S9 (in supporting information), the fluorescence of $2\text{Pyr}-1+\text{Ni}^{2+}$ is quenched by the addition of EDTA, suggesting that Ni^{2+} has been removed from the probe indicating complete reversibility due to the interaction of EDTA with Ni^{2+} . These results thus clearly indicate the capability of the present $2\text{Pyr}-1+\text{Ni}^{2+}$ system for quantitative detection of Ni^{2+} and its reversibility upon EDTA addition.

To gain additional support and to know the theoretical basis of photophysical properties of Pyr-1 and their Ni^{2+} complex, density functional theory (DFT) calculations were carried out using Gaussian 09 program.

Figure 5, the geometries of Pyr-1 and $2\text{Pyr}-1+\text{Ni}^{2+}$ adduct were optimized with B3LYP, 6-311G (d,p) and LANL2DZ basis sets. The absorption properties and their corresponding oscillator strengths of the Pyr-1 and $2\text{Pyr}-1+\text{Ni}^{2+}$ were calculated by time dependent DFT calculations with the optimized geometries using same basis sets already mention in above (Figure S10). As shown in figure 5, for Pyr-1 the HOMO is localized on pyrenyl unit, 1,8-naphthyridine unit acting as a LUMO, representing that the Photoinduced electron transfer (PET) takes place from pyrenyl unit to the 1,8-naphthyridine unit resulting in weaker emission, when Ni^{2+} binds with nitrogen atoms of $2\text{Pyr}-1+\text{Ni}^{2+}$ unit, the PET process is inhibited through CHEF effect⁴⁰ and excimer formation and subsequent emission excimer significant resulting in remarkable fluorescence enhancement with a 20 nm red shift.

(Figure 5)

Live cell imaging

The potential for biosensing selectively a guest species in living cells is of very importance for biological applications.¹² Utility of Pyr-1 for imaging of Ni²⁺ ions in living cells was examined using confocal fluorescence microscope studies. The potential efficacy of Pyr-1 is now evaluated for fluorescence imaging of Ni²⁺ in living cell. The cytotoxicity of this probe to HeLa cells was evaluated by standard MTT (3-(4,5-dimethylthiazol-2-yl)-2,5-diphenyltetrazolium bromide) assay (figure S11). The results indicate that the probe is non-toxic to the HeLa cells under the experimental conditions. To observe the applicability of our probe in biological systems, it is applied to human cervical cancer cells (HeLa). HeLa cells pretreated with Pyr-1 for 6h had no noticeable effect on the number and morphology of HeLa cells (Figure S12). Here, both the receptors and Ni²⁺ ion were endurable to uptake by the cells and the images of the cells by fluorescence microscopy with 325 nm excitation are displayed in figure 6. HeLa cells incubated with Pyr-1 (5.0 μM, 1% DMSO) exhibited almost no fluorescence in the intracellular region. After adding NiCl₂ (5.0 μM) to the cells, strong intracellular fluorescence are now observed. These results clearly demonstrate the practical applicability of the present probe for Ni²⁺ ions detection in living cells by fluorescence imaging. These results also demonstrate clearly that the present sensing platform has the potential for monitoring intracellular Ni²⁺ ions.

(Figure 6)

Despite their relevance and biological significance, not many sensors are reported for sensing of Ni²⁺ ions. The sensing ability of the present Pyr-1 systems towards Ni²⁺ ions is also associated with other reported literature methods (Table 1).

(Table 1)

Comparison of the results indicates that the present pyrene system (entry 21) exhibits better ability for Ni²⁺ detection compared than to other systems as the previous reported systems require organic solvents (entries 1, 4, 7, 10, 15 and 19), mixture of solvents (entries 2, 3, 5, 6, 8, 9, 11-13, 16-18, 20). Also many of the reported sensors involve poorer selectivity. On the other hand the present sensing system is cost-effective, selective, exhibits a simple naked-eye sensing and can be utilized in live cell imaging and sensing of Ni²⁺ ions in water.

Conclusions

A novel pyrene based fluorescent probe, 4-phenyl-2-(pyren-1-yl)-1,8-naphthyridine (Pyr-1), was designed and synthesized through tandem cyclization of pyrenealdehyde, amine and alkyne in the presence of quinolinium modified β -CD (Qun- β -CD). Pyr-1 was characterized by ¹H NMR, ¹³C NMR and ESI-MS spectra and was used as a selective “turn-on” and naked eye sensor for Ni²⁺ ion over other cations. The localized frontier molecular orbitals (DFT studies) and the solvent polarity dependent photoluminescence characteristics strongly validate the presence of photoelectron transfer from pyrene to 1,8-naphthyridine unit in Pyr-1. Upon Ni²⁺ addition, the fluorescence was shifted to 450 nm due to the formation of a square planar 2:1 complex of pyr-1 with Ni²⁺ at room temperature even in the presence of other interfering ions such as Cd²⁺ and Hg²⁺. The resultant excimer emission and suppression of photoinduced electron transfer (PET) from pyrene moiety to the 1,8-naphthyridine part is supported by DFT studies. The developed sensor also exhibited very low cytotoxicity and strong fluorescence emission in living cells, indicating its applicability as a novel chemosensor for selective detection of Ni²⁺ ions in biological environments too.

Acknowledgements

KP thanks CSIR, India for financial support and RI thanks to UGC and MKU for UGC Non-NET fellowship.

Reference

- [1] B. Wang, E. V. Anslyn, Eds, *Chemosensor: Principle, Strategies, and Application*; John Wiley and Sons: Hoboken, NJ, 2011.
- [2] T. Liu, A. D. Chien, L. Jiwei, G. Zhang, C. L. Fraser, Arene effects on difluoroboron β -diketonate mechanochromic luminescence, *J. Mater. Chem.* 21 (2011) 8401.
- [3] E. M. Nolan, S. J. Lippard, Tools and Tactics for the Optical Detection of Mercuric Ion, *Chem. Rev.* 108 (2008) 3443.
- [4] G. M. Fischer, C. Jungst, M. Isomaki-Kron Dahl, D. Gauss, H. M. Moller, E. Daltrozzo, A. Zumbusch, Asymmetric PPCys: Strongly fluorescing NIR labels, *Chem. Commun.* 46 (2010) 5289
- [5] X. Chen, X. Zhang, G. Zhang, Wide-range thermochromic luminescence of organoboronium complexes, *Chem. Commun.* 51 (2015) 161.
- [6] N. Kaur, S. Kumar, Colorimetric metal ion sensors, *Tetrahedron.* 67 (2011) 9233.
- [7] Q. He, E. W. Mille, A. P. Wong, C. J. Chang, A Selective Fluorescent Sensor for Detecting Lead in Living Cells, *J. Am. Chem. Soc.* 128 (2006) 9316.
- [8] A. P. D. Silva, H. Q. N. Gunaratne, T. Gunnlaugsson, A. J. M. Huxley, C. P. McCoy, J. T. Rademacher, T. E. Rice, Signaling Recognition Events with Fluorescent Sensors and Switches, *Chem. Rev.* 97 (1997) 1515.

- [9] D. Udhayakumari, S. Velmathi, Azo Linked Polycyclic Aromatic Hydrocarbons-Based Dual Chemosensor for Cu^{2+} and Hg^{2+} Ions, *Ind. Eng. Chem. Res.* 54 (2015) 3541.
- [10] J. M. Lehn, From supramolecular chemistry towards constitutional dynamic chemistry and adaptive chemistry, *Chem. Soc. Rev.* 36 (2007) 151.
- [11] F. Wurthner, T. E. Kaiser, C. R. Saha-Moller, J-Aggregates: From Serendipitous Discovery to Supramolecular Engineering of Functional Dye Materials, *Angew. Chem. Int. Ed.* 50 (2011) 3376.
- [12] D. M. Bassani, I. Jonušauskaite, A. Lavie-Combot, N. D. McClenaghan, J. L. Pozzo, D. Ray, G. Vives, Photoswitchable devices and photochemistry, *Coord. Chem. Rev.* 254 (2010) 2429.
- [13] Y. Bao, H. DeKeersmaecker, S. Corneillie, F. Yu, H. Mizuno, G. Zhang, J. Hofkens, B. Mendrek, A. Kowakzuk, M. Smet, Tunable Ratiometric Fluorescence Sensing of Intracellular pH by Aggregation-Induced Emission-Active Hyperbranched Polymer Nanoparticles, *Chem. Mater.* 27 (2015) 3450.
- [14] X. Wang, J. Hu, G. Zhang, S. Liu, Highly Selective Fluorogenic Multianalyte Biosensors Constructed via Enzyme-Catalyzed Coupling and Aggregation-Induced Emission, *J. Am. Chem. Soc.* 136 (2014) 9890.
- [15] J. H. Wang, H. T. Feng, Y. S. Zheng, Synthesis of tetraphenylethylene pillar[6]arenes and the selective fast quenching of their AIE fluorescence by TNT, *Chem. Commun.* 50 (2014) 11407.
- [16] A. Kathiraven, K. Sundaravel, M. Jaccob, G. Dhinakaran, A. Ramesh Kumar, D. Arul Ananth, T. SivaSudha, Pyrene Schiff Base: Photophysics, Aggregation Induced Emission, and Antimicrobial Properties, *J. Phys. Chem. B.* 118 (2014) 13573.

- [17] M. Shellaiah, T. Simon, K. Fu-Hsiang, L. Ming-Chang, L. Hong-Cheu, Novel pyrene containing monomeric and dimeric supramolecular AIE active nano-probes utilized in selective “off-on” trivalent metal and highly acidic pH sensing with live cell applications, *J. Mater. Chem. C*. 4 (2016) 2056.
- [18] A. Sigel, H. Sigel, and R. K. O. Sigel, *Nickel and its Surprising Impact in Nature*, John Wiley & Sons Ltd, U.K., 2007.
- [19] J. E. R. Goodman, L. Prueitt, D. G. Dodge, S. Thakali, Carcinogenicity assessment of water-soluble nickel compounds, *Crit. Rev. Toxicol.* 39 (2009) 365.
- [20] C. Kokkinos, A. Economou, I. Raptis, T. Speliotis, Disposable mercury-free cell-on-a-chip devices with integrated microfabricated electrodes for the determination of trace nickel(II) by adsorptive stripping voltammetry, *Anal. Chim. Acta.* 622 (2008) 111.
- [21] A. A. Nemeč, G. D. Leikauf, B. R. Pitt, K. Wasserloos, J. A. Barchowsky, A. M. J. Respir. Nickel Mobilizes Intracellular Zinc to Induce Metallothionein in Human Airway Epithelial Cells Antonia A, *Cell Mol. Biol.* 41 (2009) 69.
- [22] M. Costa, T. L. Davidson, H. Chen, Q. Ke, P. Zhang, Y. Yan, C. Huang, T. Kluz, Nickel carcinogenesis: Epigenetics and hypoxia signaling, *Mutat. Res.* 592 (2005) 79.
- [23] D. Zendelovska, G. Pavlovska, K. Cundeve, T. Stafilov, Electrothermal atomic absorption spectrometric determination of cobalt, copper, lead and nickel traces in aragonite following flotation and extraction separation, *Talanta.* 54 (2001) 139.
- [24] M. A. Bezerra, W. N. L. dos Santos, V. A. Lemos, M. Korn, S. L. C. Ferreira, A study of Zn–Mn based sorbent for the high-temperature removal of H₂S from coal-derived gas, *J. Hazard. Mater.* 148 (2007) 334.

- [25] A. U. Karatepe, M. Soylak, L. Elci, Separation/Preconcentration of Copper, Lead, and Iron in Natural Water Samples on Chromosorb-105 Resin Prior to Flame Atomic Absorption Spectrometric Determinations, *Anal. Lett.* 36 (2003) 797.
- [26] E. A. Takara, S. D. Pasini-Cabello, S. Cerutti, J. A. Gasquez, L. D. J. Martinez, On-line preconcentration/determination of copper in parenteral solutions using activated carbon by inductively coupled plasma optical emission spectrometry, *J. Pharm. Biomed. Anal.* 39 (2005) 735.
- [27] T. Stafilov, Determination of trace elements in minerals by electrothermal atomic absorption spectrometry, *Spectrochim. Acta, Part B.* 55 (2000) 893.
- [28] J. Shiowatana, K. Benyatianb, A. Siripinyanond, Pre-concentration and determination of heavy metals on modified activated carbon in real samples, *Spectrochim. Acta, Part B.* 21 (2000) 179.
- [29] K. Jankowski, J. Yao, K. Kasiura, A. Jackowska, A. Sieradzka, Multielement determination of heavy metals in water samples by continuous powder introduction microwave-induced plasma atomic emission spectrometry after preconcentration on activated carbon, *Spectrochim. Acta, Part B.* 60 (2005) 369.
- [30] P. S. Tonello, A. H. Rosa, C. H. Abreu, A. A. Menegario, Use of diffusive gradients in thin films and tangential flow ultrafiltration for fractionation of Al(III) and Cu(II) in organic-rich river waters, *Anal. Chim. Acta.* 598 (2007) 162.
- [31] E. Denkhaus, K. Salnikow, Nickel essentiality, toxicity, and carcinogenicity, *Crit. Rev. Oncol. Hematol.* 42 (2002) 35.

- [32] T. Kiriya, R. Kuroda, Fresenius, Simultaneous determination of silicon and phosphorus in biological standard materials with on-line column flow-injection spectrophotometry, *J. Anal. Chem.* 332 (1988) 338.
- [33] L. Elci, M. Soylak, B. Ozcan, Coprecipitation of Cu(II), Ni(II), Fe(III), Cd(II), Pb(II), and Co(II) in Wastewater, Sediment, and Metallic Zinc Samples with HMDTC–HMA for Flame Atomic Absorption Spectrometric Determination, *Anal. Lett.* 36 (2003) 987.
- [34] L. Prodi, F. Bolletta, M. Montalti, N. Zaccheroni, Luminescent chemosensors for transition metal ions, *Coord. Chem. Rev.* 205 (2000) 59.
- [35] Q. M. Li, X. H. Zhao, K. Jiang, G. G. Liu, Study of spectrophotometric method for determination of trace copper after the separation and enrichment with solid phase extractant-microcrystalline phenolphthalein, *Chin. Sci. Bull.* 52 (2007) 65.
- [36] X.Q. Liu, X. Zhou, X. Shu, J. Zhu, A Polymer-Based Ultrasensitive Metal Ion Sensor, *Macromolecules.* 42 (2009) 7634.
- [37] S. Adewuyi, D. A. Ondigo, R. Zuggle, Z. Tshentu, T. Nyokong, N. Torto, A highly selective and sensitive pyridylazo-2-naphthol-poly(acrylic acid) functionalized electrospun nanofiber fluorescence “turn-off” chemosensory system for Ni²⁺, *Anal. Methods.* 4 (2012) 1729.
- [38] B. Annaraj, L. Mitu, M.A. Neelakantan, Spectroscopic (FT-IR and UV-Vis) and theoretical (HF and DFT) investigation of 2-Ethyl-N-[(5-nitrothiophene-2-yl)methylidene]aniline, *Journal of Molecular Structure.* 1104 (2016) 1.
- [39] D. Ray, P.K. Bharadwaj, A Coumarin-Derived Fluorescence Probe Selective for Magnesium, *Inorg. Chem.* 47 (2008) 2252.

- [40] H. Li, S.J. Zhang, C.L. Gong, Y.F. Li, Y. Liang, Z.G. Qi, S. Chen, Highly sensitive and selective fluorescent chemosensor for Ni²⁺ based on a new poly(arylene ether) with terpyridine substituent groups, *Analyst*. 138 (2013) 7090.
- [41] X. Zhao, X. Liu, M. Lu, Appl. β -cyclodextrin-capped palladium nanoparticle-catalyzed ligand-free Suzuki and Heck couplings in low melting β -cyclodextrin/NMU mixtures, *Organometal Chem.*, 28 (2014) 635.
- [42] F. X. Legrand, M. Menand, M. Sollogoub, S. Tilloya, E. Monflier, An N-heterocyclic carbene ligand based on a β -cyclodextrin-imidazolium salt: synthesis, characterization of organometallic complexes and Suzuki coupling, *New. J. Chem.*, 35 (2011) 2061.
- [43] L. Strimbu, J. Liu, A. E. Kaifer, Cyclodextrin-capped palladium nanoparticles as catalysts for the Suzuki reaction, *Green Chem.*, 19 (2003) 483.
- [44] J. Cao, X. Ma, M. Miu, T. Cao, S. Wu, H. Tian, INHIBIT logic operations based on light-driven β -cyclodextrin pseudo[1]rotaxane with room temperature phosphorescence addresses, *Chem. Commun.*, 50 (2014) 3224.
- [45] I. A. Azath, P. Suresh, K. Pitchumani, Per-6-amino- β -cyclodextrin/CuI catalyzed cyanation of aryl halides with K₄[Fe(CN)₆], *New. J. Chem.*, 36 (2012) 2334.
- [46] P. Suresh, K. Pitchumani, Per-6-amino- β -cyclodextrin as an efficient supramolecular ligand and host for Cu(I)-catalyzed N-arylation of imidazole with aryl bromides, *J. Org. Chem.*, 73 (2008) 9121.
- [47] K. Kanagaraj, P. Suresh, K. Pitchumani, Per-6-amino- β -cyclodextrin as a reusable promoter and chiral host for enantioselective Henry reaction, *Org. Lett.*, 12 (2010) 4070.

- [48] P. Suresh, K. Pitchumani, Per-6-amino- β -cyclodextrin catalyzed asymmetric Michael addition of nitromethane and thiols to chalcones in water, *Tetrahedron: Asymmetry* 19 (2006) 2037.
- [49] V. Tharmaraj, K. Pitchumani, D-Glucose Sensing by (E)-4-((pyren-1-ylmethylene)amino)phenyl)boronic acid *via* Photoinduced Electron Transfer(PET) Mechanism, *RSC Adv.* 3 (2013) 11566.
- [50] S. D. Shahida Parveen, B. Suresh Kumar, S. Raj Kumar, R. Imran Khan, K. Pitchumani, Isolation of biochanin A, an isoflavone, and its selective sensing of copper(II) ion, *Sensors and Actuators B.* 221 (2015) 75.
- [51] R. Imran Khan, K. Pitchumani, β -Cyclodextrin Included Coumarin Derivatives as Selective Fluorescent Sensors for Cu^{2+} Ions in HeLa Cells, *RSC Adv.* 6 (2016) 20269.
- [52] Y. Q. Weng, F. Yue, Y. R. Zhong, B. H. Ye, A Copper(II) Ion-Selective On-Off-Type Fluoroionophore Based on Zinc Porphyrin-Dipyridylamino, *Inorg. Chem.* 46 (2007) 7749.
- [53] A. Kumar, P. S. Chae, Pyreneamide-based dipodal probes for ultra-sensitive and selective detection of 3,5-dinitrosalicylic acid in an aqueous solution, *Dyes and Pigments.* 147 (2017) 400.
- [54] K. L. Reddy, A. Manoj Kumar, A. Dhir, V. Krishnan, Selective and Sensitive Fluorescent Detection of Picric Acid by New Pyrene and Anthracene Based Copper Complexes, *J Fluoresc.* 26 (2016) 2041.
- [55] S. D. Padghan, A. L. Puyad, R. S. Bhosale, S. V. Bhosale, S. V. Bhosale, A pyrene based fluorescent turn-on chemosensor: aggregation-induced emission enhancement and application towards Fe^{3+} and Fe^{2+} recognition, *Photochemical & Photobiological Sciences.* 16 (2017) 1591.

- [56] P. Venkatesan, S. P. Wu, A turn-on fluorescent pyrene-based chemosensor for Cu(II) with live cell application, *RSC Adv.*, 5 (2015) 42591.
- [57] T. Raj, P. Salija, N. Singh, A new class of pyrene based multifunctional chemosensors for differential sensing of metals in different media: Selective recognition of Zn^{2+} in organic and Fe^{3+} in aqueous medium, *Sensors and Actuators B*. 206 (2015) 98.
- [58] T. Simon, M. Shellaiah, V. Srinivasadesikan, C. C. Liu, F. H. Ko, K. W. Sun, M. C. Lin, A simple pyrene based AIE active schiff base probe for selective naked eye and fluorescence off-on detection of trivalent cations with live cell application, *Sensors and Actuators B*. 231 (2016) 18.
- [59] M. Zhao, X. Zhou, J. Tang, Z. Deng, X. Xuan, Z. Cheu, X. Li, L. Yang, L. J. Ma, Pyrene excimer-based fluorescent sensor for detection and removal of Fe^{3+} and Pb^{2+} from aqueous solutions, *Spectrochimica Acta Part A: Molecular and Biomolecular Spectroscopy*. 173 (2017) 235.
- [60] D. Phapale, A. Gaikwad, D. Das, Selective recognition of Cu (II) and Fe (III) using a pyrene based chemosensor, *Spectrochimica Acta Part A: Molecular and Biomolecular Spectroscopy*. 178 (2017) 160.
- [61] F. A. Abebe, C. S. Eribal, G. Ramakrishna, E. Sinn, A 'turn-on' fluorescent sensor for the selective detection of cobalt and nickel ions in aqueous media, *Tetrahedron Letters*. 52 (2011) 5554.
- [62] B. Annaraj, L. Mitu, M. A. Neelakantan, Synthesis and crystal structure of imidazole containing amide as a turn on fluorescent probe for nickel ion in aqueous media. An experimental and theoretical investigation, *Journal of Molecular Structure*. 1104 (2016) 1.

- [63] A. Banerjee, A. Sahana, S. Guha, S. Lohar, I. Hauli, S. K. Mukhopadhyay, J. S. Matalobos, D. Das, Nickel(II)-Induced Excimer Formation of a Naphthalene-Based Fluorescent Probe for Living Cell Imaging, *Inorg. Chem.* 51 (2012) 5699.
- [64] D. Rambabu, C. P. Pradeep, A. Dhir, Nickel–sodium pyrene tetrasulfonic acid based coordination polymer as fluorescent template for recognition of azo dyes, *Sensors and Actuators B.* 225 (2016) 586.
- [65] J. Prabhu, K. Velmurugan, A. Raman, N. Duraipandy, M. S. Kiran, S. Easwaramoorthi, R. Nandhakum, A simple chalcone based ratiometric chemosensor for sensitive and selective detection of Nickel ion and its imaging in live cells, *Sensors and Actuators B.* 238 (2017) 306.
- [66] G. Subashini, R. Shankar, T. Arasakumar, P. S. Mohan, Quinoline appended pyrazoline based Ni sensor and its application towards live cell imaging and environmental monitoring, *Sensors and Actuators B.* 243 (2017) 549.
- [67] M. Saleem, A. Ali, C. S. Choi, B. J. Park, E. H. Choi, K. H. Lee, The smart 2-(2-fluorobenzoyl)-N-(2-methoxyphenyl)hydrazinecarbothioamide functionalized as Ni(II) sensor in micromolar concentration level and its application in live cell imaging, *J Fluoresc.* 24 (2014) 995.
- [68] A. Senthil Murugan, N. Vidhyalakshmi, U. Ramesh, J. Annaraj, A Schiff's base receptor for red fluorescence live cell imaging of Zn^{2+} ions in zebrafish embryos and naked eye detection of Ni^{2+} ions for bio-analytical applications, *J. Mater. Chem. B.* 5 (2017) 3195.
- [69] J. Jiang, C. Gou, J. Luo, C. Yi, X. Liu, A novel highly selective colorimetric sensor for Ni (II) ion using coumarin derivatives, *Inorganic Chemistry Communications.* 15 (2012) 12.

[70] M. R. Ganjali, M. Hosseini, M. Motalebi, M. Sedaghat, F. Mizani, F. Faridbod, P. Norouzi, Selective recognition of Ni²⁺ ion based on fluorescence enhancement chemosensor, *Spectrochimica Acta Part A: Molecular and Biomolecular Spectroscopy*. 140 (2015) 283.

[71] N. Huang, M. M. Siegel, Automation of Fourier transformation ion cyclotron resonance mass spectrometer for acquisition, analysis and E-mailing of high resolution exact-mass electrospray ionization mass spectral data, *J. Am. Soc. Mass Spectrom.*, 10 (1999) 1166.

Biographies

Raihana Imran Khan (1989) received his B.Sc. (Chemistry) degree from Jamal Mohamed College, Trichy in 2010, M.Sc. (Chemistry) from Manonmaniam Sundaranar University, Tirunelveli in 2012, and doing Ph.D. in Madurai Kamaraj University, Madurai, India. He has published few articles in reputed scientific journals. His research interests are organic transformations and designing sensor systems using modified cyclodextrins.

Prof. A. Ramu received his M.Sc degree in Chemistry at Madurai Kamaraj University, Madurai, India (1983). He joined as an Assistant Professor in the Department of Chemistry, ANJA College, Sivakasi, India (1984). He earned his Ph.D at University of Madras, Chennai, India (1993). He joined as a Professor, School of Chemistry, Madurai Kamaraj University, Madurai, India (1999). He has published 50 articles in reputed scientific journals and contributed few chapters in books. His main research area include the Co-ordination chemistry, application of DNA binding by using UV, CD Spectroscopy for stereo-chemical investigations, binding

nature of the complexes, Cytotoxic studies, Geo hydrology-Water quality assessment and water pollution, Phase transfer catalyst and Phytochemistry.

Kasi Pitchumani (1954) received his M.Sc. (Chemistry) from Madurai Kamaraj University, Madurai, India. After receiving Ph.D. degree from the same university in 1981, he became an Assistant Professor in the same year and was appointed as Professor of Organic Chemistry in 1996. Currently he is working as a CSIR Emeritus Scientist in the same university. He did his postdoctoral research with Prof. V. Ramamurthy, University of Miami, USA and Prof. Akihiko Ueno, Tokyo Institute of Technology, Japan. He has 35 year of teaching experience in Organic Chemistry and published 195 research articles in peer reviewed journals. His research interests are supramolecular photochemistry, green chemistry and chemistry in confined media like clays, zeolites, hydrotalcites and cyclodextrins. He is also involved in synthesis of modified cyclodextrins, isolation of natural products and newer nanomaterials for developing sensor applications.

Figure Captions

Scheme 1 Synthetic route to 4-phenyl-2-(pyren-1-yl)-1,8-naphthyridine (Pyr-1)

Figure 1 a) Emission spectra of Pyr-1 in THF:water solvent mixture, b) selected frontier molecular orbitals for Pyr-1.

Figure 2 (a and b) UV-Vis and Fluorescence spectra of Pyr-1 (40 μ M in CH₃CN) λ_{ex} = 350 nm; (c) photograph of sensor selectivity of Pyr-1 visualized is daylight.

Figure 3 (a) Fluorescence ($\lambda_{\text{ex}} = 350 \text{ nm}$) intensity changes as a function of Ni^{2+} ions concentration from 0-40 μM and (b) UV-Vis sensor titrations of Pyr-1 (40 μM in CH_3CN) with 0–40 μM of Ni^{2+} ions in H_2O

Figure 4 a) Histogram representing selectivity of Pyr-1 (20 μM in CH_3CN) towards 20 μM (1 equiv.) of metal ions; (b) Bar chart illustrating fluorescence response in the selectivity of Pyr-1 for Ni^{2+} ion in the presence of other metal ions ($2.5 \times 10^{-6} \text{ M}$). The blue bars represent the fluorescence intensity of Pyr-1 in the presence of other metal ions. The brown bars represent the change in fluorescence intensity that occurs upon subsequent addition of Ni^{2+} to the solution containing Pyr-1 and other metal ions; (c) linear fitting plot and error plot for the detection limit calculation of Ni^{2+} ions (d) Job's plot (based on emission intensity changes) between mole fraction of Pyr-1 and intensity), representing the 2 : 1 (2Pyr-1 Ni^{2+}) complex.

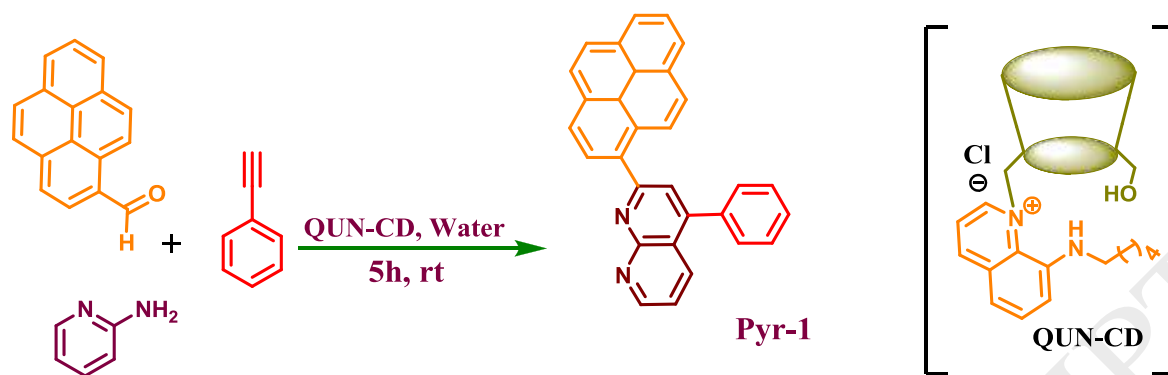
Scheme 2 Plausible mechanism of Pyr-1 complexation with Ni^{2+} ion and removal of Ni^{2+} by EDTA.

Figure 5 Frontier molecular orbitals of Pyr-1 and $2\text{Pyr-1} + \text{Ni}^{2+}$ obtained from the DFT calculations using Gaussian 09 program

Figure 6 Bright field image and fluorescence image of HeLa cells (a) Bright field image HeLa cells incubated with Pyr-1 (5.0 μM) for 1h. (b) Fluorescence image of HeLa cells incubated with Pyr-1. (c) Overlay images of HeLa cells incubated with Pyr-1. (d) Bright field image of Pyr-1 treated HeLa cells again incubated with Ni^{2+} (5.0 μM).

(e) Fluorescence image of Pyr-1 treated HeLa cells with Ni²⁺. (f) Overlay images of Pyr-1 treated HeLa cells with Ni²⁺.

ACCEPTED MANUSCRIPT



Scheme 1

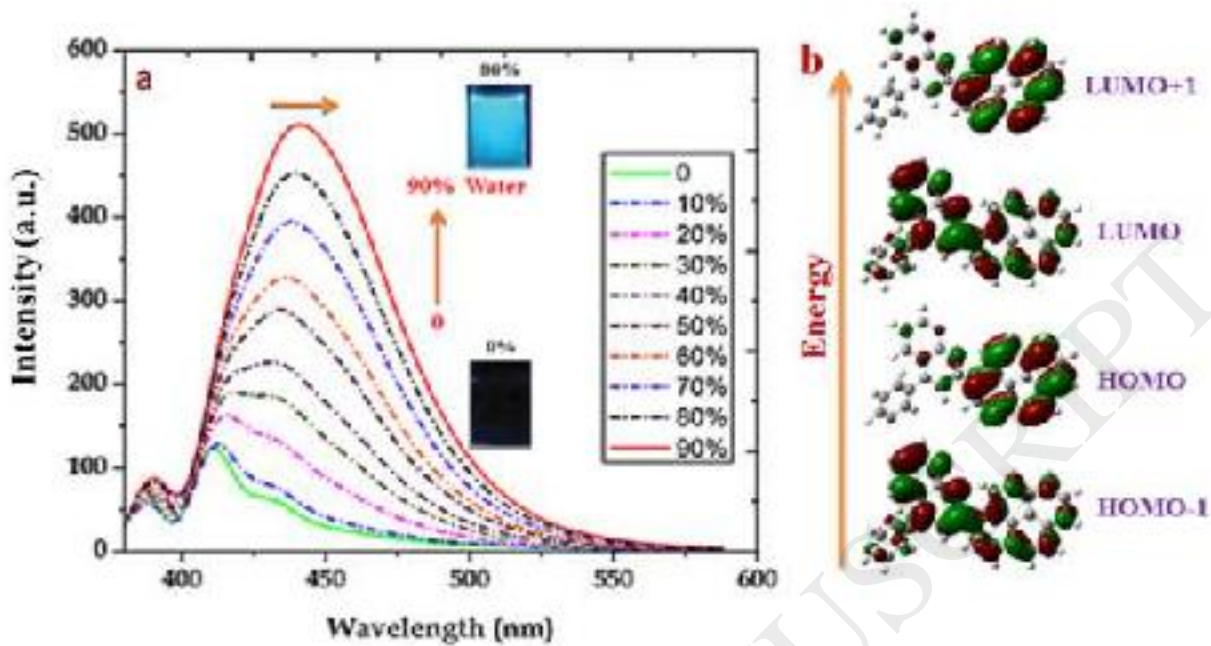


Figure 1

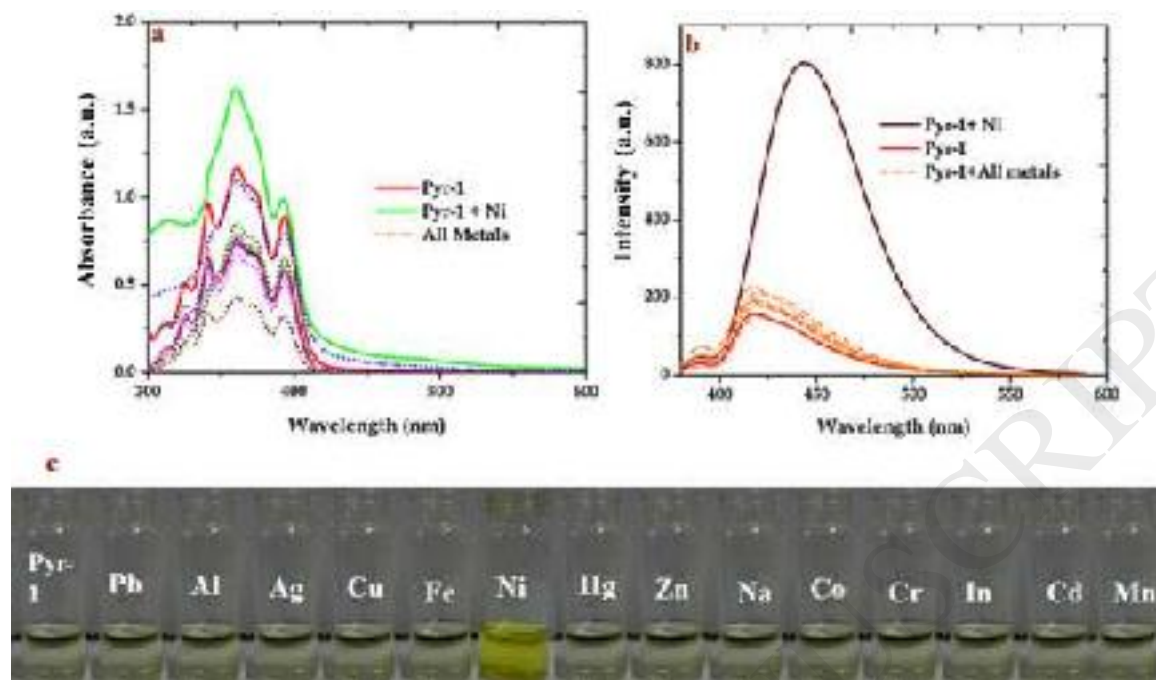


Figure 2

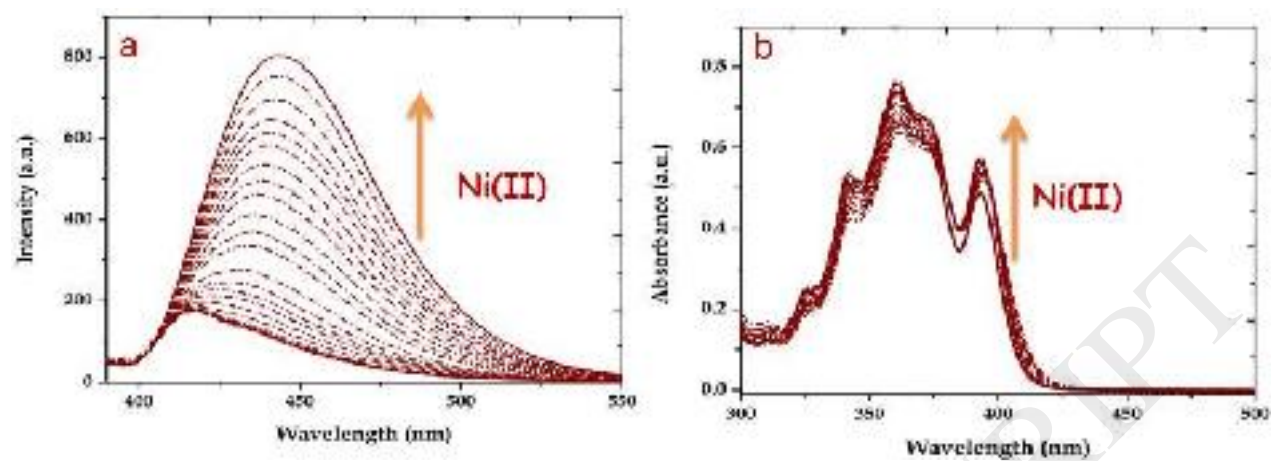


Figure 3

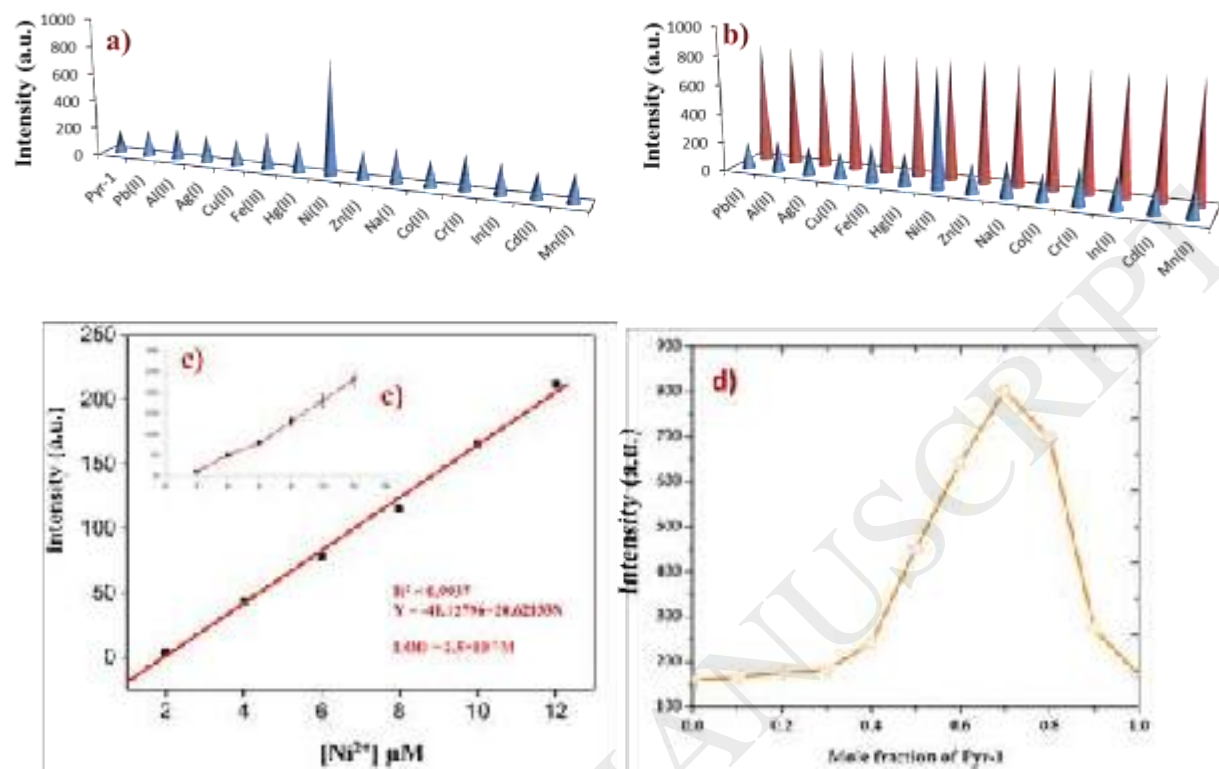
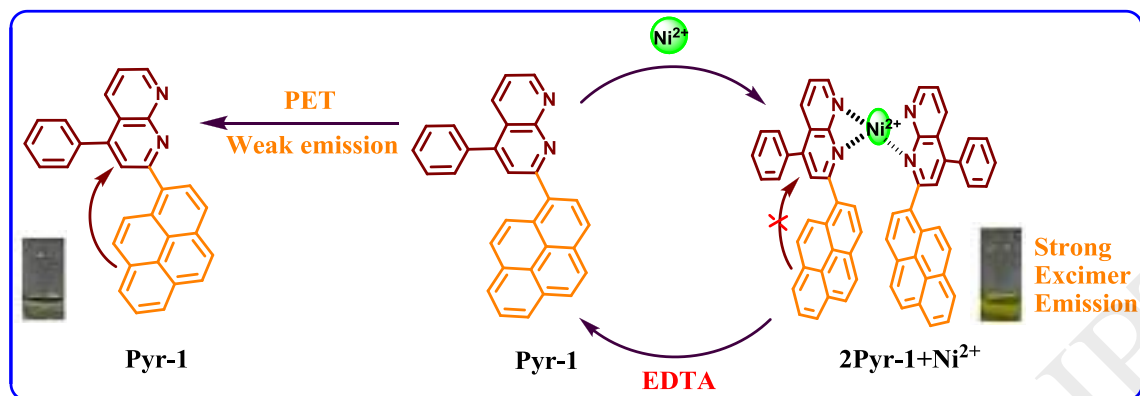


Figure 4



Scheme 2

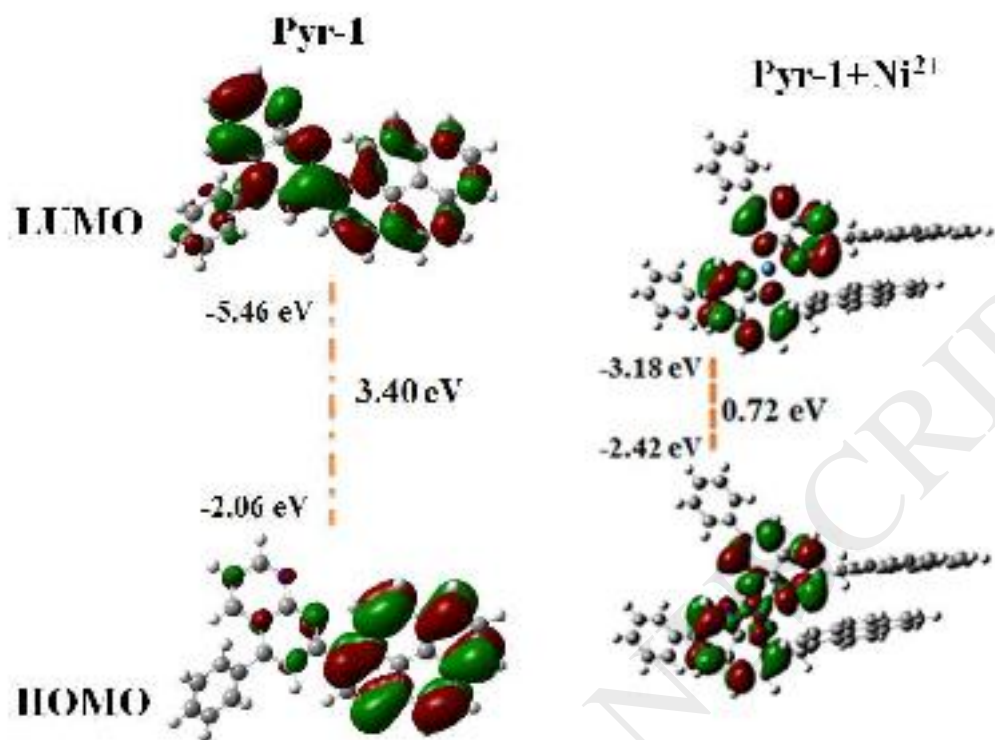


Figure 5

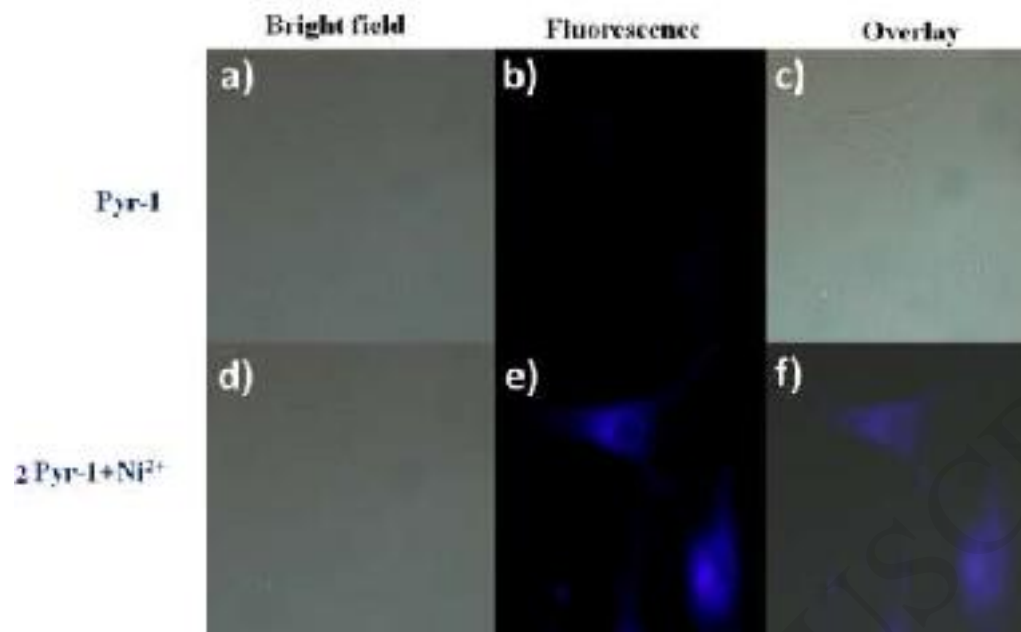


Figure 6

Table 1 Comparison table for pyrene and Ni²⁺ based chemosensor systems.

S. No	Sensing Probe	Sensor for	Medium	Detection Limit	Biological Studies	Ref.
	Pyrene Based Chemosensors					
1	Triazole based pyrene	Picric acid	THF	0.46	-	36
2	Furan-pyrene	Al ³⁺	EtOH:H ₂ O	1.04	-	38
3	Pyrenamide based dipodal probe	3,5-dinitro salicylic acid	DMSO:H ₂ O	1	-	53
4	Cu-pyrene complex	Picric acid	THF:HEBS	1.20	-	54
5	Pyrene based fluorescent	Fe ³⁺ and Fe ²⁺	ACN:H ₂ O	2.61	-	55
6	PHP	Cu ²⁺	ACN:H ₂ O	0.04	RAW264.7	56
7	Pyrene-biginielli reaction	Zn ²⁺ and Fe ³⁺	ACN	7.94	-	57
8	2-((pyren-1-ylmethylene)amino)ethanol	Al ³⁺ , Cr ³⁺ and Fe ³⁺	H ₂ O	2	RAW264.7	58
9	N,N-bi[4(1-pyrene)-butyroyl]ornithine	Fe ³⁺ and Pb ²⁺	H ₂ O:ACN	0.1	-	59
10	1-(pyren-1-yl)-N,N-bis-(pyridine-2-ylmethyl)methanamine	Cu ²⁺ and Fe ³⁺	Methanol	3	-	60
	Chemosensor for Ni²⁺					
11	Rhodamine dyes	Ni ²⁺ and Co ²⁺	DMSO:H ₂ O	-	-	61
12	Imidazole derivative	Ni ²⁺	DMSO:H ₂ O	2.8	-	62
13	Napthalene based fluorescent	Ni ²⁺	DMSO:H ₂ O		A. puberula	63
14	pyrene tetrasulfonic acid	Ni ²⁺ and Na ⁺	H ₂ O	0.64	-	64
15	chalcone	Ni ²⁺	MeOH	5.14	HeLa	65
16	Quinoline-appended pyrazoline	Ni ²⁺	H ₂ O:DMSO	0.5	MG 63	66
17	2-(2-Fluorobenzoyl)-N-(2-Methoxyphenyl)	Ni ²⁺	H ₂ O:ACN	-	L-929	67
18	Quinoline based chemosensor	Ni ²⁺ and Zn ²⁺	DMSO:H ₂ O	6	A-549	68
19	Coumarin derivatives	Ni ²⁺	EtOH	0.5	-	69
20	2-(1- <i>H</i> -benzo[<i>d</i>]imidazol-2yl)-N-phenyl-hydrazine-carbothioamide	Ni ²⁺	ACN:H ₂ O	16	-	70
21	Novel Pyrene derivative (Pyr-1)	Ni²⁺	H₂O	0.3	HeLa	This Work

ADVERTISEMENT

RETURN TO ISSUE

< PREV **RESEARCH ARTICLE** NEXT >[Get e-Alerts](#)

Water-Soluble Palladium Complex of N-(pyridin-2-yl)propane-1,3-diamine modified β -Cyclodextrin: An efficient Catalyst for Transfer Hydrogenation of Carbonyl Compounds

Raihana Imran Khan and Kasi Pitchumani*

Cite this: *ACS Sustainable Chem. Eng.* 2018, 6, 12, 16130–16138Publication Date: November 1, 2018 <https://doi.org/10.1021/acssuschemeng.8b02787>

Copyright © 2018 American Chemical Society

[RIGHTS & PERMISSIONS](#)

Article Views

621

Altmetric

-

Citations

9

[LEARN ABOUT THESE METRICS](#)

Share Add to Export

[Read Online](#)

This website uses cookies to improve your user experience. By continuing to use the site, you are accepting our use of cookies. [Read the ACS privacy policy.](#)

CONTINUE



Synthesis of a water-soluble Pd(II) complex of *N'*-(pyridin-2-yl)propane-1,3-diamine modified β -cyclodextrin (Pd(II)@PyPDA: β -CD) is reported. The synthesized Pd(II)@PyPDA: β -CD, characterized by FT-IR, NMR, mass, UV-vis spectroscopies and molecular modeling studies, is used as a homogeneous, ecofriendly and reusable catalyst under mild reaction conditions for transfer hydrogenation of aromatic ketones to secondary alcohols using isopropyl alcohol as a green reducing agent. This homogeneous catalyst is reused five times with only a small decrease in its catalytic activity. The presence of a chiral cavity in cyclodextrin, is found to facilitate significant chiral induction, evident from preliminary chiral HPLC studies. A plausible mechanism for hydrogenation is proposed. Other significant advantages of the present catalyst, namely, simple preparation, stability, substrate selectivity, easy recovery, and reusability highlight its potential utility in other reactions and also in industrial applications.

KEYWORDS: Pd(II)@PyPDA: β -cyclodextrin catalyst, Transfer hydrogenation, Carbonyl compounds ∇

Supporting Information

The Supporting Information is available free of charge on the [ACS Publications website](https://pubs.acs.org/doi/10.1021/acssuschemeng.8b02787) at DOI: [10.1021/acssuschemeng.8b02787](https://pubs.acs.org/doi/10.1021/acssuschemeng.8b02787).

- The contents of the SI section include ^1H , ^{13}C , ESI-MS and FT-IR of PyPDA: β -CD,

This website uses cookies to improve your user experience. By continuing to use the site, you are accepting our use of cookies. [Read the ACS privacy policy.](#)

CONTINUE

Supporting In

Water Soluble Palladium Complex of N'-(pyridin-2-yl)propane-1,3-diamine modified β -Cyclodextrin : An efficient Catalyst for Transf

Raihana Imran Khan[†] and

[†]Department of Natural Products Chemistry, School of Chemistry, National Institute of Technology, Patna, Bihar, India

[‡]Centre for Green Chemistry Processes, School of Chemistry, National Institute of Technology, Patna, Bihar, India



Terms & Conditions

Most electronic Supporting Information files are available without a subscription to ACS Web Editions. Such files may be downloaded by article for research use (if there is a public use license linked to the relevant article, that license may permit other uses). Permission may be obtained from ACS for other uses through requests via the RightsLink permission system:

<http://pubs.acs.org/page/copyright/permissions.html>.

This website uses cookies to improve your user experience. By continuing to use the site, you are accepting our use of cookies. [Read the ACS privacy policy.](#)

CONTINUE

g... ACS Publications
<https://doi.org/10.1038/s41598-022-08868-9>

2. Sakthinarayanan Jayaraman, Selvarasu Uthayanila, Chandrakasan Vanmathi, Parasuraman Karthikeyan. Metal-free convenient homogeneous bifunctional ionic liquid catalysed selective cross-hydrogenation ketone to alcohol. *Materials Today Sustainability* **2022**, *17*, 100102. <https://doi.org/10.1016/j.mtsust.2021.100102>
3. Sean McCarthy, D. Christopher Braddock, James D.E.T. Wilton-Ely. Strategies for sustainable palladium catalysis. *Coordination Chemistry Reviews* **2021**, *442*, 213925. <https://doi.org/10.1016/j.ccr.2021.213925>
4. Ziya Dağalan, Sepideh Behboudikhiavi, Muhammet Turgut, Melike Sevim, Ahmet Emre Kasapoğlu, Bilal Nişancı, Önder Metin. Nickel–palladium alloy nanoparticles supported on reduced graphene oxide decorated with metallic aluminum nanoparticles (Al-rGO/NiPd): a multifunctional catalyst for the transfer hydrogenation of nitroarenes and olefins using water as a hydrogen source. *Inorganic Chemistry Frontiers* **2021**, *8* (9), 2200-2212. <https://doi.org/10.1039/D0QI01363C>
5. Árpád Molnár. Synthetic Application of Cyclodextrins in Combination with Metal Ions, Complexes, and Metal Particles. *ChemCatChem* **2021**, *13* (6), 1424-1474. <https://doi.org/10.1002/cctc.202001610>
6. Preeti Oswal, Aayushi Arora, Siddhant Singh, Divyanshu Nautiyal, Sushil Kumar, Gyandshwar Kumar Rao, Arun Kumar. Organochalcogen ligands in catalysis of oxidation of alcohols and transfer hydrogenation. *Dalton Transactions* **2020**, *49* (36), 12503-12529. <https://doi.org/10.1039/D0DT01201G>
7. Lu Liu, Bowei Wang, Ruixiao Gao, Dan Zhang, Wensheng Xu, Ligong Chen, Xilong Yan, Yang Li. Biomass-derived Fe-NC hybrid for hydrogenation with formic acid: control of Fe-based nanoparticle distribution. *RSC Advances* **2020**, *10* (18), 10689-10694. <https://doi.org/10.1039/D0RA01356K>
8. Bilal Nişancı, Ziya Dağalan. A facile and highly efficient transfer hydrogenation of ketones and aldehydes catalyzed by palladium nanoparticles supported on mesoporous graphitic carbon nitride. *Journal of Chemical Research* **2020**, *44* (1-2), 14-19. <https://doi.org/10.1177/1747519819883792>
9. Aurélien Cocq, Hervé Bricout, Florence Djedaïni-Pilard, Sébastien Tilloy, Eric Monflier. Rhodium-Catalyzed Aqueous Biphasic Olefin Hydroformylation Promoted by Amphiphilic Cyclodextrins. *Catalysts* **2020**, *10* (1), 56. <https://doi.org/10.3390/catal10010056>

Partners

This website uses cookies to improve your user experience. By continuing to use the site, you are accepting our use of cookies. [Read the ACS privacy policy.](#)

CONTINUE



1155 Sixteenth Street N.W.
Washington, DC 20036
Copyright © 2022
American Chemical Society

About

[About ACS Publications](#)
[ACS & Open Access](#)
[ACS Membership](#)

Resources and Information

[Journals A-Z](#)
[Books and Reference](#)
[Advertising Media Kit](#)
[Institutional Sales](#)
[ACS Publishing Center](#)
[Privacy Policy](#)
[Terms of Use](#)

Support & Contact

[Help](#)
[Live Chat](#)
[FAQ](#)

Connect with ACS Publications



This website uses cookies to improve your user experience. By continuing to use the site, you are accepting our use of cookies. [Read the ACS privacy policy.](#)

CONTINUE